An Investigation of Smart, Inclusion-based Mechanical Metamaterials

Ph.D. Thesis

by

Russell Galea Mifsud

Supervised by: Prof. Ruben Gatt

Co-supervised by: Prof. Vasilis Valdramidis, Prof. Renald Blundell

University of Malta

September 2023

Statement of Authenticity

The undersigned declare that the content of this Ph.D. thesis is based on the work carried out by Russell Galea Mifsud under the supervision of Professor Ruben Gatt.

_____ _____

Russell Galea Mifsud — Professor Ruben Gatt

Candidate — *Supervisor*

Abstract

Mechanical metamaterials have captured the attention of researchers worldwide owing to their exceptional mechanical properties. They are poised to emerge as a pivotal category of materials that will shape the next generation of innovative materials. Research on auxetic materials, a class of mechanical metamaterials, has been ongoing for more than four decades, with recent years witnessing a surge in interest in the design of 3D auxetic metamaterials. Another class of metamaterials that has shown great potential is active metamaterials, which are materials that can have their geometry and/or mechanical properties tuned post-fabrication in response to external stimuli. This thesis delved into the realm of mechanical metamaterials, focusing on these two distinct categories. It introduced a novel design approach for creating 3D auxetic structures and conducted an in-depth exploration of magneto-mechanical active metamaterials. The 3D auxetic systems were intentionally designed to lay the foundation for potential future research, envisioning their transformation into active magneto-mechanical metamaterials. The mechanical properties of the 3D auxetic structures produced in this thesis were investigated through numerical simulations validated by experimental tests. It was demonstrated that a system, created through equally sized voids with a constant cross-sectional area into a solid material at specific locations in various planes, could exhibit a negative Poisson's ratio of approximately -0.5 in multiple directions. This behaviour was observed over a significant range of aperture angles for the cross-sectional areas, especially when the voids were positioned close to each other. A scalable inclusion-based active magneto-mechanical metamaterial consisting of magnetic inclusions embedded within a non-magnetic matrix was also produced. The proposed structure, based on an accordion-like structure, was shown to respond to the magnitude and direction of an external magnetic field by tuning its geometry. The basic unit was then used to create a number of active systems including the auxetic re-entrant honeycomb and egg-rack structures. Finally, iron nanoparticles inclusions were used instead of permanent magnets and successfully produced a magneto elastomer. Through numerical simulations validated by experimental prototypes, the response to an external magnetic field was investigated. The numerical model showed good agreement with the experimental tests and following this the effect of nanoparticle concentration and other geometric parameters were investigated.

Acknowledgements

First and foremost, I would like to express my deepest gratitude to my supervisor, Professor Ruben Gatt, who not only acted as a role model as a researcher and supervisor, but supported and guided me throughout my studies and inspired me in our discussions. I would also like to extend my gratitude to Professor Vasilis Valdramidis, as together they have provided me with invaluable opportunities of collaborating with research groups abroad. I would also like to thank Prof. Pierre Sandre Farrugia and Prof. Krzystof Dudek for their help and the time they dedicated to my work. I would also like to thank Prof. Joseph N. Grima, who without him, my career choices would have been much different and who has been a mentor in all my studies.

I would also like to thank the members of the Metamaterials units, Auxrow and Food science units with whom I have had the pleasure of working with for providing a nurturing and fun environment. Without this, my PhD would have been monotonous and boring. Additionally, funding is key to any research, and therefore I would also like to thank the TESS which funded parts of my research.

I am very thankful for my family, Roger, Roseann, Ricky, and Rebecca who have encouraged me and supported me throughout the years. I could not have arrived where I am today without all of them and for this, I will be eternally grateful. My thanks go to my friends who have been there for me in many ways. Most of all, I am grateful for my wife, Martina Galea Mifsud, words cannot express my gratitude for everything you have done for me and for the patience and support you have given me. This achievement is equally yours as it is mine.

Finally, I am truly indebted and grateful to God, for sustaining me and equipping me with all I needed during my studies.

Table of Contents

List of Figures

List of Tables

Chapter 1 Introduction

Material Science is undergoing a remarkable evolution where new advanced materials are transitioning from static and inert systems to sophisticated ones which can respond to external stimuli, and others which are capable of dynamically morphing and adapting to different environmental conditions. Although these materials are not found on the market at present, ongoing research is paving the way for their emergence. The field of metamaterials holds tremendous potential in unlocking the possibilities of these future materials. Whilst initially the term "Metamaterials" (which refers to materials which exhibit counterintuitive properties) was used within the context of optics and electromagnetism (Cai *et al.*, 2007; Edel *et al.*, 2023; Maurya *et al.*, 2023; Shalaev, 2007; Smith *et al.*, 2004; Sylvere *et al.*, 2021), this notion has branched into other disciplines. In fact, mechanical metamaterials (Gatt *et al.*, 2012; J. N. Grima & Caruana-Gauci, 2012) are a subset of metamaterials which exhibit unusual mechanical properties, typically a negative mechanical index, such as negative Poisson's ratios(Caddock & Evans, 1989; J. N. Grima & Evans, 2000a; R. Lakes, 1987; Wojciechowski, 1995; Wojciechowski K.W., Branka, 1994), negative compressibility (Baughman *et al.*, 1998; Gatt *et al.*, 2009; Nicolaou & Motter, 2012), and negative stiffness (Hewage, Alderson, Alderson, Scarpa, *et al.*, 2016). Their properties are mainly dependent on their geometry and deformation mechanism (W. Yang *et al.*, 2004). An important subset of mechanical metamaterials are auxetic materials, a term coined by Evans (Evans, 1991a). Auxetic materials are materials characterised by a negative Poisson's ratio (NPR), i.e., materials that contract or expand transversely when subjected to a uniaxial compressive or tensile force, respectively, as described by Equation 1.1. This behaviour is unlike that of conventional materials which

expand transversely in response to a uniaxial compressive force (J. N. Grima, Farrugia, Caruana, *et al.*, 2008) as depicted in Figure 1.1.

$$\nu_{ij} = -\frac{\varepsilon_j}{\varepsilon_i} \tag{1.1}$$

where ν_{ij} is the Poisson's ratio in the Ox_i - Ox_j plane, ε_j is the strain observed in the Ox_j direction and ε_i is the strain applied in the Ox_i direction. ε_j may be defined as $\frac{dl_j}{l_j^\circ}$ and ε_i may be defined as $\frac{dl_i}{l_i^\circ}$, where dl_j and dl_i are the changes in length in the Ox_j and Ox_i directions respectively while l_j° and l_i° are the original lengths in the Ox_j and Ox_i directions respectively.

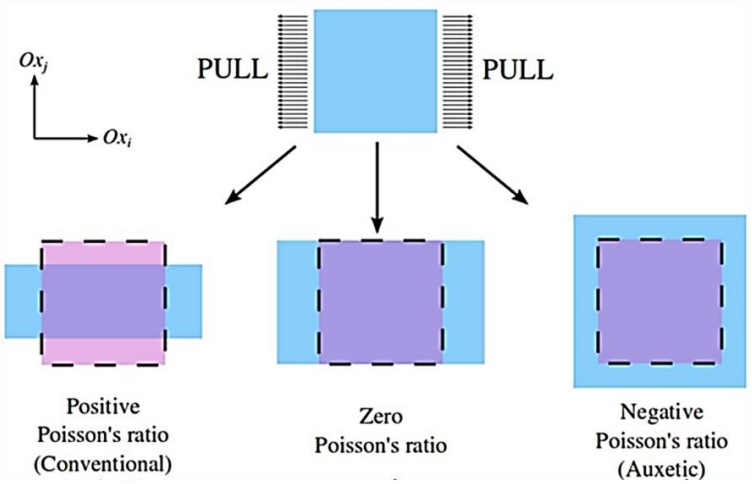

Figure 1.1. A diagram depicting the difference in the response of a positive, zero and negative Poisson's ratio to a uniaxial tensile force. Image adapted from (K. K. Dudek, 2018)

The presence of an NPR is associated with several desirable material properties including superior shear (Fan *et al.*, 2022), indentation (Argatov *et al.*, 2012; Coenen & Alderson, 2011; Z. Li *et al.*, 2021), impact (K. K. Dudek *et al.*, 2019a; T. Li *et al.*, 2020b), fracture resistance (Morin-Martinez *et al.*, 2023), as well as better energy absorption performance (S. Hou *et al.*, 2015; Imbalzano *et al.*, 2016; L. Jiang & Hu, 2017; Steffens *et al.*, 2021), as compared to materials with positive Poisson's ratio. Furthermore, NPR systems can have variable permeability (C. Li *et al.*, 2020a) and exhibit synclastic curvature (S. Hou *et al.*, 2015; Imbalzano *et al.*, 2016; L. Jiang & Hu, 2017). For this

reason, it is expected that auxetic materials and structures can be used to design innovative products having an improved performance across a number of industries including, but not limited to, the biomedical (Y. Kim *et al.*, 2021), textiles (Liaqat *et al.*, 2017; Zeng *et al.*, 2017) (in particular for sports applications (Allen *et al.*, 2017; Sanami *et al.*, 2014)) as well as the automotive (K. K. Dudek *et al.*, 2020; K. K. Dudek, Gatt, *et al.*, 2018; Y. Ma *et al.*, 2013) and aerospace industries (Z. Wang *et al.*, 2016). Examples of such products comprise vibration dampers (K. K. Dudek *et al.*, 2020; K. K. Dudek, Gatt, *et al.*, 2018; Y. Ma *et al.*, 2013), smart sensors (Q. Li *et al.*, 2017; S. L. Zhang *et al.*, 2017), adaptable body armour (K. K. Dudek *et al.*, 2019a), seat cushions (Y. C. Wang & Lakes, 2002), smart filters (A. Alderson *et al.*, 2000; Warmuth *et al.*, 2017), acoustic isolators (Bertoldi *et al.*, 2010), magnetic auxetic systems (K. K. Dudek, Wolak, *et al.*, 2017) such as thin memory films in computer technology (M. R. Dudek & Wojciechowski, 2008) and applications where impact (K. K. Dudek *et al.*, 2019a), indentation and fatigue resistance (K. L. Alderson *et al.*, 2005; Bezazi & Scarpa, 2009) are required.

More recent developments include investigations of active auxetic metamaterials which possess the unique ability to adjust their properties in response to external stimuli (Y. Kim *et al.*, 2018). In this class of materials, magnetically actuated metamaterials have garnered significant attention. These reconfigurable metamaterials offer tunable properties and geometries after fabrication. Their adaptable and programmable geometry has been used in wave manipulation, filtering, and cloaking for aerospace and defence applications (S. Wu *et al.*, 2022). A wide range of magneto-mechanical metamaterials have been proposed (W. Han *et al.*, 2021; X. Liang *et al.*, 2022; Schroeders, 2021), however, the unique properties of metamaterials combined with the magnetically actuated tunable geometry has been particularly advantageous in the design of multifunctional soft robots and biomedical devices (S. Wu *et al.*, 2019).

Another important aspect, which sometimes is not given enough importance, is the ability to manufacture such advanced materials. The extensive studies of 2D auxetic systems has been led to a large selection of manufacturing methods ranging from traditional manufacturing methods namely moulding (Bertoldi *et al.*, 2010; Shen *et al.*, 2014), milling and perforations (Mizzi *et al.*, 2019) to 3D-printing additive manufacturing techniques such as fused deposition modelling (FDM) (Vyavahare & Kumar, 2021), stereolithography (SLA) (Varas *et al.*, 2023), selective laser sintering (SLS) (Geng *et al.*, 2019), selective laser melting (SLM) (Ulbin *et al.*, 2020), electron beam melting (EBM) (Gunaydin *et al.*, 2019) amongst others. However, when considering the complex geometry of 3D auxetic systems, such systems have been predominantly produced through 3D printing (Y. Gao *et al.*, 2021; Khadem-Reza *et al.*, 2022; L. Wang *et al.*, 2022; Zheng *et al.*, 2021). In fact, since 3D printing is difficult to scale up and mass produce, the reliance on this manufacturing method has limited the adoption of 3D auxetic systems for industrial applications.

Notwithstanding all of the above, there are still several lacunae in the scientific knowledge of these systems. For instance, no attempt has been made to propose a design method that can be used to produce 3D auxetic metamaterials having continuous voids of constant cross-sectional area. Furthermore, the field of magnetically actuated mechanical metamaterials is still relatively novel and a wide range of auxetic structures have yet to be explored. Research on magnetically actuated metamaterials exhibiting NPR in multiple planes is still limited and the possibility of implementing this on a milli-, micro- or perhaps nano- scale have yet to be investigated.

In view of the above, this thesis aims: (1) to propose 3D systems having continuous voids of constant cross-sectional area and investigate them *vis-à-vis* their potential to exhibit a negative Poisson's ratio and (2) to develop a scalable inclusion-

based magneto-mechanical metamaterial. In order to achieve these aims, the research performed in this thesis will be divided into two main parts, with the first part focusing on 3D auxetic designed to have continuous voids of constant cross-sectional area and the second part, focusing on active mechanical metamaterial having magnetic inclusions. Furthermore, the use of iron nanoparticles as magnetic inclusions in an active mechanical metamaterial will also be explored and the structures response to an external magnetic field will be studied.

In order to achieve these aims, Chapter 2 will present a literature review where existing literature on auxetic metamaterials will be discussed. Emphasis will be made on the present gaps in the research field and the challenges that this thesis aims to tackle. In Chapter 3 a novel auxetic material will be proposed and investigated which is capable of exhibiting an NPR in multiple directions. This 3D auxetic metamaterial will be composed of continuous diamond-shaped voids of constant cross-sectional area and the study will investigate its NPR. A plethora of structures that arise from this configuration will be discussed and will be later expanded on in Chapter 4 by investigating structures having elliptical and stadium-shaped voids.

In Chapter 5, the focus will shift onto creating an active mechanical metamaterial having magnetic inclusions. Initially an accordion-like base unit will be investigated and its response to an external magnetic field will be explored. This structure will later serve to design multi-layered systems capable of exhibiting an NPR and in Chapter 6 this will be extended to an egg-rack-like system capable of exhibiting NPR. Finally, the accordion-like model will be used as a template to create an active magneto-mechanical metamaterial having iron nanoparticles inclusions. Furthermore, the possibility of a nanoparticle inclusion-based auxetic mechanical metamaterial and its benefits will be discussed.

Chapter 2 Literature Review

The main aim of this chapter is to introduce the subject matter of this thesis i.e., auxetic materials and magnetomechanical metamaterials. Furthermore, since the research in this thesis will be mainly conducted through FEA simulations, this methodology as applied to mechanical metamaterials (particularly auxetic systems) will also be reviewed. In view of this, this chapter will be divided into three main parts. In the first part, a general discussion on the main geometries/deformation mechanisms which has been used to describe auxetic behaviour will be presented. This section of the review will mainly focus on analytical models as further analysis of systems based on these models using FEA will be discussed in the second part of the discussion. Also, since most of these models has been known for some time, this part of the review will be based on literature of the past twenty years. This will be followed by an overview on literature pertaining to the application of Finite Element Analysis as applied to research in auxetic materials. The third and final part of this chapter will focus on perforated auxetic metamaterials and moves on to discuss active auxetic metamaterials with an emphasis on the research of magneto-mechanical metamaterials. Having discussed various research on the subject matter, lacunae identified in this study will be discussed and the main aims and scope of this study will be discussed at the end of this chapter.

2.1 Auxetic Metamaterials

2.1.1 Introduction

The field of auxetic metamaterials is a rapidly growing area in materials science research encompassing a wide range of structures and auxetic systems. The study of materials exhibiting a negative Poisson's ratio sparked from the discovery of naturally occurring auxetic crystalline systems (Aouni & Wheeler, 2008; Berlincourt & Jaffe, 1958; Boppart *et al.*, 1980; Kittinger *et al.*, 1981) and naturally occurring auxetic biomaterials (Gatt, Vella Wood, *et al.*, 2015; Veronda & Westmann, 1970). However, the major leap in research occurred in 1987 when Roderic S. Lakes and his group successfully produced an auxetic foam (R. Lakes, 1987). In this study and subsequent investigations, it was shown that auxetic foams possessed enhanced properties when compared to their conventional counterparts including increased indentation resistance, shear stiffness and damping amongst others (Allen *et al.*, 2015; Bezazi *et al.*, 2008; Bhullar *et al.*, 2014; J. B. Choi & Lakes, 1995; Friis *et al.*, 1988; R. Lakes, 1987; Mohsenizadeh *et al.*, 2019; Scarpa *et al.*, 2002, 2005). It was during this time that other researchers designed and produced structures to exhibit negative Poisson's ratios with pioneers such as Kenneth E. Evans (Caddock & Evans, 1989; Evans, 1991a, 1991b) and Kryzystof W. Wojciechowski (Wojciechowski, 1987, 1989; Wojciechowski & Brańka, 1989) contributing significantly to the research of auxetics investigating other classes of auxetic materials.

In fact in the early days, the theoretical studies by Wojciechowski investigated the a new class of auxetic materials where hard discs were organised and attached in particular arrangement to exhibit auxetic behaviour (Wojciechowski, 1987; Wojciechowski & Brańka, 1989). The hard discs were meant to represent atoms, and in fact the hard cyclic hexamers proposed initially were representative of a 2D model of benzene molecules adsorbed on a surface. Other researchers expanded on the hard discs

concept and with advances in technology, 3D structures were considered resulting in the hard spheres which have been applied in different branches of the nanotechnology industry (Narojczyk *et al.*, 2016, 2019, 2022; Pigłowski *et al.*, 2016; Tretiakov & Wojciechowski, 2014, 2005, 2007; Tretiakov *et al.*, 2016). One of the most investigated arrangements is the FCC (Face-Centered Cubic) crystal structure of Yukawa particles (Narojczyk, Tretiakov, *et al.*, 2022; Tretiakov & Wojciechowski, 2005a) which were shown to be partially auxetic, reaching a negative Poisson's ratio of −0.4 in the direction $[110][1\bar{1}0]$ (Tretiakov & Wojciechowski, 2014). In a recent study by Narojczyk et al, the effect of inclusions on the auxetic properties of FCC hard sphere crystal were investigated. It was found to alter the symmetry of the crystal which decreased the Poisson's ratio, recording values as low as −0.873 (Narojczyk *et al.*, 2019). Other structures were investigated namely hard cyclic tetramers (Tretiakov, 2009; Tretiakov & Wojciechowski, 2020, 2022) and hard dimers (Narojczyk *et al.*, 2016; Tretiakov & Wojciechowski, 2006). This work is especially interesting when taking into account the advances in nanotechnology opening the potential of producing auxetic nanocomposites which would be auxetic at the atomic level.

Another direction in auxetic research led to microstructured polymers exhibiting a negative Poisson's ratio. The first studies investigated polytetrafluoroethylene which was shown to be able of exhibiting a negative Poisson's ratio of −12 in one direction(Caddock & Evans, 1989). Subsequent work on this class of auxetic materials investigated the use of other polymers and the mechanical properties the structures exhibited (K. L. Alderson *et al.*, 2002; Chirima *et al.*, 2009; Pickles *et al.*, 1995; Ravirala *et al.*, 2005, 2006). Over the last few decades, other classes of materials exhibiting a auxetic behaviour have been discovered or produced ranging from the nano-scale to the macro-scale and research has shown that the auxetic behaviour between the different

materials can be distinguished using models based on features in (1) the geometry of the system and (2) the deformation mechanism (A. Alderson, 1999). Ample geometries and deformation mechanisms that exhibit a negative Poisson's ratio has been identified. In view of this, this review, will only highlight research on the most impactful and extensively studied geometries in this field, namely re-entrant structures, chiral structures and rotating rigid unit structures.

2.1.2 Re-entrant Systems

One of the first and most studied re-entrant systems is the hexagonal re-entrant honeycombs depicted in Figure 2.1(b). These systems were developed by Abd el-Sayed *et al.* who derived analytical models investigated the in-plane mechanical properties of hexagonal honeycombs deforming through the flexure of ribs and concluded that the configuration exhibited (Abd El-Sayed *et al.*, 1979). Later theoretical models describing re-entrant honeycombs confirmed that such systems indeed exhibit a negative Poisson's ratio (L. J. J. Gibson *et al.*, 1982) and in the following years, researchers proposed models that would serve as more reliable representations of these systems by considering the deformation of the structure through hinging and stretching in combination with flexure (Evans *et al.*, 1995; L. J. Gibson & Ashby, 1997; Masters & Evans, 1996). These models showed that the Poisson's ratio was dependant on both the geometry and the deformation mechanism of the system, where the conventional honeycomb was shown to exhibit a negative Poisson's ratio when deforming through stretching and a positive Poisson's ratio when deforming through hinging (see Figure 2.1). On the other hand the re-entrant honeycomb was shown to exhibit a positive Poisson's ratio when deforming through stretching and a negative Poisson's ratio when deforming through hinging (see Figure 2.1), emphasising the point that the Poisson's ratio of a system depends on both the

geometry and the deformation mechanism. Subsequent studies on re-entrant honeycombs were carried out over the years investigating their off-axis properties (Grediac, 1993; Ju & Summers, 2011; Scarpa *et al.*, 2000), out-of-plane behaviour (D. H. Chen & Ozaki, 2009; Evans, 1991b; Lorato *et al.*, 2010) and the effect of changes to geometric parameters (Overaker *et al.*, 1998; Whitty *et al.*, 2002; D. U. Yang *et al.*, 2003). In other studies, the acoustic and vibration properties of re-entrant honeycomb structures were shown to be superior to their to their conventional counterparts through their ability to reduce transmissions of vibrations and sound (Sparavigna, 2007a, 2007b).

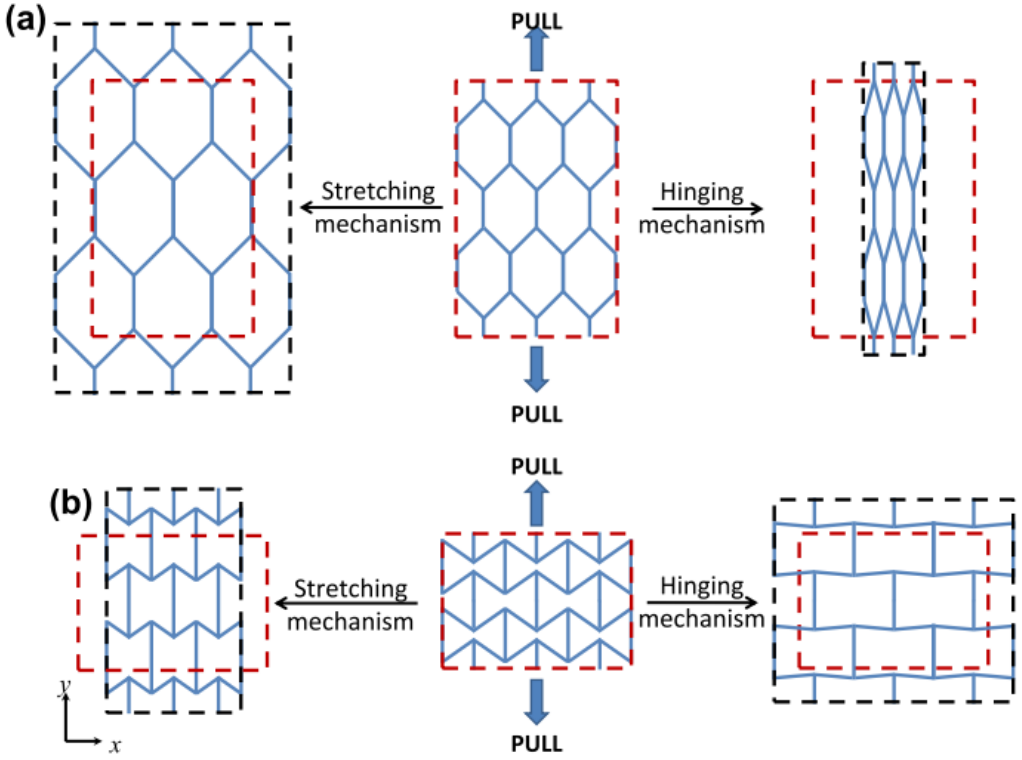

Figure 2.1. Depiction of the effect of geometry and deformation mechanism on the Poisson's ratio of (a) honeycomb and (b) re-entrant honeycomb systems. Image taken from Grima *et al.* (J. N. Grima *et al.*, 2013)

Apart from re-entrant honeycombs, there are also other types of re-entrant systems that may exhibit auxetic behaviour. One such example is structures composed of star-

shaped units, often referred to as STAR-n systems, depicted in Figure 2.2. These structures were investigated in several studies where they were primarily used to design systems with the potential to exhibit negative Poisson's ratio and negative compressibility (A. Alderson, Alderson, Attard, *et al.*, 2010; J. N. Grima, Gatt, *et al.*, 2008). In a study by Rad *et al.* this system was extended to a 3D auxetic system based on the STAR-4 system (Rad *et al.*, 2015). Other noteworthy auxetic systems based on the re-entrant geometry include Almgrem's re-entrant honeycombs having additional rods which was used to produce 2D and 3D auxetic systems (Almgren, 1985) and the arrow-head system proposed by Larsen *et al.* (Larsen *et al.*, 1997), shown in Figure 2.3. Properties of the latter have been investigated numerically and experimentally in several studies indicating that this design is also suitable for the design of more complex mechanical metamaterials (Crumm & Halloran, 2007; Larsen *et al.*, 1997; J. X. Qiao & Chen, 2015; Rafsanjani & Pasini, 2016; Spagnoli *et al.*, 2015).

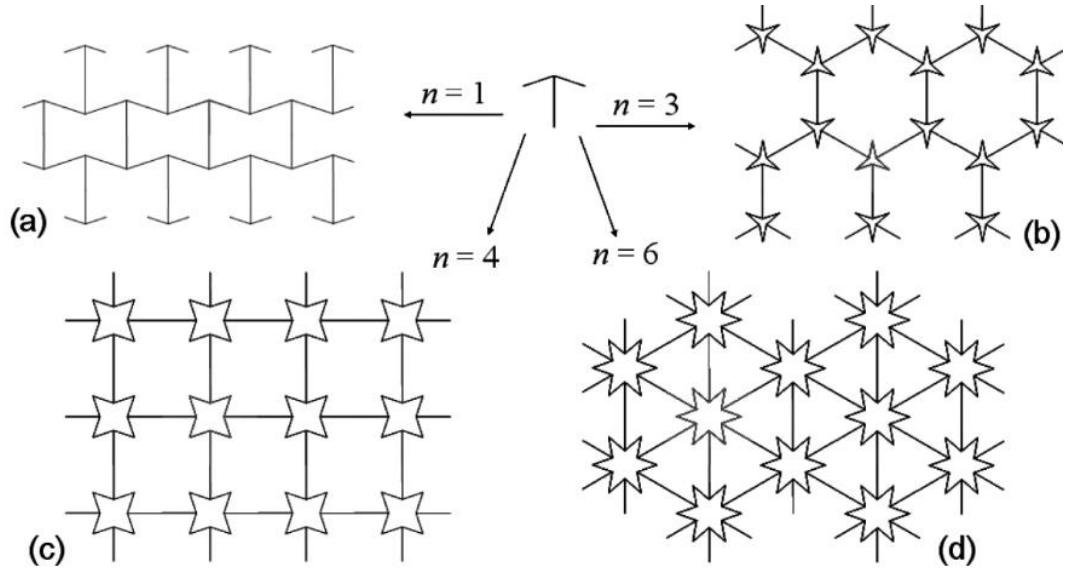

Figure 2.2. A depiction of the various tessellations that can be constructed using the STAR-*n* model where *n* is the rotational symmetry. The structures depicted above were acquire when (a) n = 1, (b) n = 3, (c) n = 4 and (d) n = 6. Image taken from Grima *et al.*(J. N. Grima, Gatt, *et al.*, 2005b).

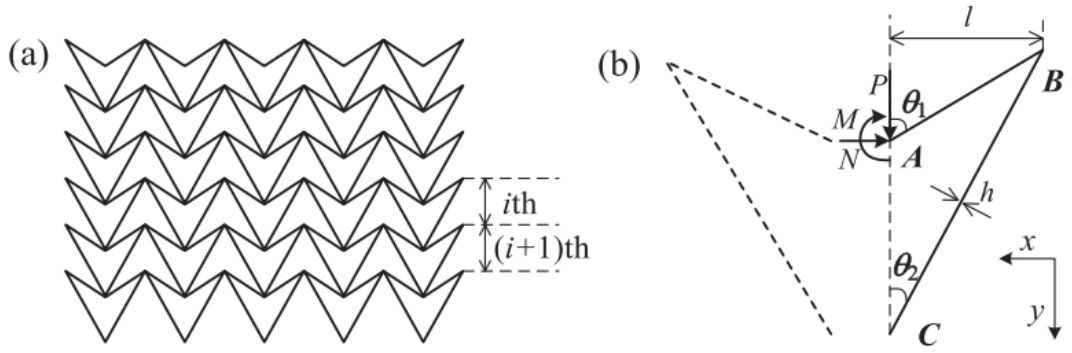

Figure 2.3. (a) Double arrow auxetic honeycomb and (b) the unit cell's parameters suggested by Larsen *et al.* Image taken from Qiao and Chen (J. Qiao & Chen, 2015).

Recently, a shift toward 3D auxetics has led to the design of 3D re-entrant honeycomb structures due to research and advances in manufacturing processes. 3D auxetics offer a number of advantages over their 2D counterparts especially in applications where forces could be applied in multiple directions such as car bumpers and protective equipment. This allows the structure to exhibit indentation and impact resistance in multiple directions. To this end a number of studies proposed re-entrant mechanisms designed to deform auxetically in three-dimensions, with some examples being the tetrakaidecahedron system (see Figure 2.4(a)) (J. B. Choi & Lakes, 1995) and modified version of hexagonal honeycombs (see Figure 2.4(b)) (Almgren, 1985; Evans *et al.*, 1994; J. N. Grima, Caruana-Gauci, *et al.*, 2012a; Krödel *et al.*, 2014; Schwerdtfeger *et al.*, 2012; Shokri Rad *et al.*, 2014; K. Wang *et al.*, 2015). These 3D lattices were experimentally shown to have excellent energy absorption capabilities and compression stiffness and in fact some structures were proposed for the automobile industry as dampers (Lvov *et al.*, 2020; S. Wang *et al.*, 2022) and other protective structures (Teng *et al.*, 2022).

Another type of 3D re-entrant system that can exhibit auxetic behaviour is the so-called “fibril and node” system, whose concept was initially proposed by Alderson *et al.* in 1993 (K. L. Alderson & Evans, 1993). Similarly to their two-dimensional counterparts, these systems can exhibit negative Poisson’s ratio in three dimensions (see Figure 2.4(c-d)) (K. L. Alderson *et al.*, 1997; Gaspar *et al.*, 2011; Z. Zhang *et al.*, 2013; Z. K. Zhang *et al.*, 2013). Other studies produced re-entrant structure which were organised into tubular structure resulting in a structure which was able to deform in three dimensions. An example of this was done in the study by Ruan *et al.* on the intravascular stent (Ruan *et al.*, 2019).

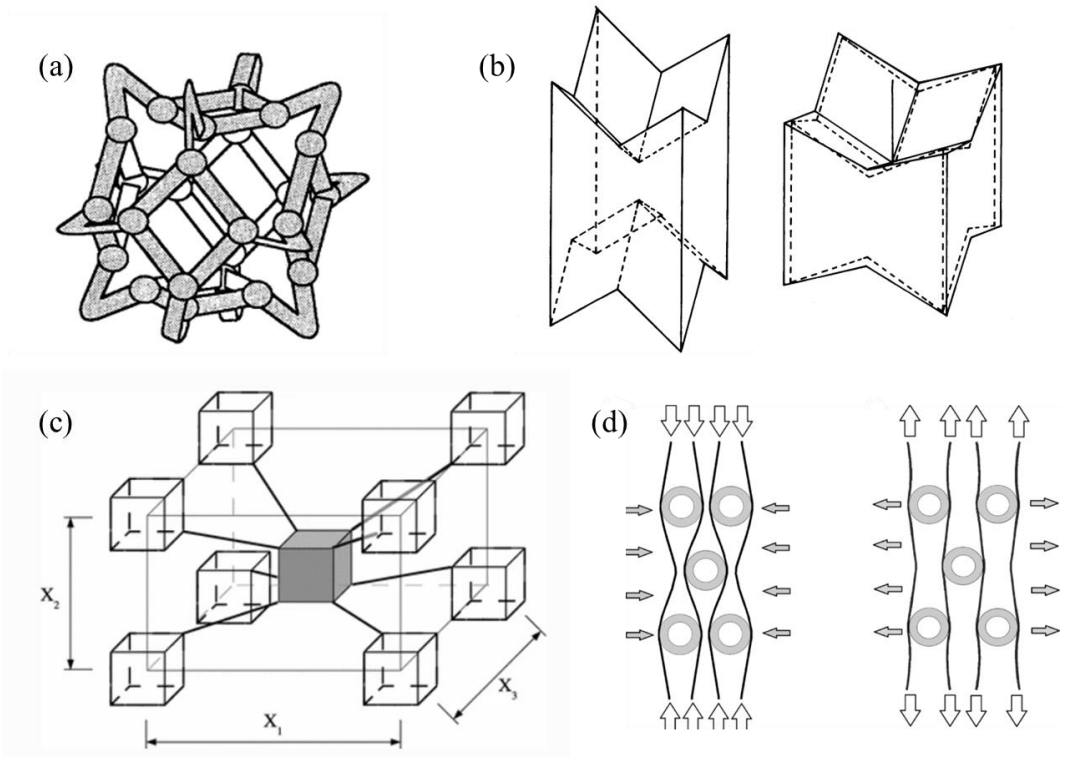

Figure 2.4. Three-dimensional auxetic structures based on the re-entrant mechanism namely; (a) the tetrakaidecahedron system, image taken from Choi *et al.*(J. B. Choi & Lakes, 1995), (b) Three-dimensional re-entrant honeycombs proposed by Evans *et al.*, image taken from Evans *et al.* (Evans *et al.*, 1994), (c-d) fibril and node system, image taken from Gaspar *et al.* and Zhang *et al.* respectively (Gaspar *et al.*, 2011; Z. Zhang *et al.*, 2013).

2.1.3 Chiral

Auxetic chiral systems are another class of auxetic structures in which structure and/or sub-units cannot be superimposed on their mirror image. Chiral systems with a negative Poisson's ratio were first described by Wojciechowski in 1989 (Wojciechowski, 1989) and later implemented as a structure by Lakes (Prall & Lakes, 1997). In his work, Lakes described a structure composed of circular nodes connected to each other by means of ligaments, with each node having six tangentially attached ligaments of equal length. Furthermore, in this structure, two nodes to a single ligament reside on different sides of the ligament. The resulting structure was termed by Lakes and co-workers as hexachiral, see Figure 2.5(a). When loaded, the hexachiral structure was shown to deform through flexure of the ligaments and to exhibit a Poisson's ratio of -1, independently of the size of the nodes and length of the ligaments (R. S. Lakes, 1991; Prall & Lakes, 1997).

Another system made from rigid nodes connected together through ligaments that flex upon deformation was proposed by Sigmund *et al.* (Sigmund *et al.*, 1998; Sigmund & Torquato, 1999). The configuration proposed by Sigmund had four tangentially attached ligaments to each node, with two nodes attached to a single ligament situated on the same side of the ligament (see Figure 2.5). This results in a system that has chiral sub-units (one quarter of a unit cell), but the system as a whole is not chiral. Furthermore, due to the different alignment of the nodes with the ligaments these structures deform in a different manner when compared to the hexachiral system. In fact, in the hexachiral system, the nodes rotate in the same direction when deformed, whilst in the system proposed by Sigmund, neighbouring nodes rotate in opposite directions. A general nomenclature system was then proposed by Grima and co-workers where systems having the nodes on different sides of the connecting ligament were termed as 'Chiral' while those having the nodes on the same side of the connecting ligament were termed as 'anti-

chiral' (J. N. Grima, 2000). Another additional configuration was investigated where both chiral and anti-chiral systems were combined to create meta-chiral systems which are only possible for n = 3 or 4 (J. N. Grima, Gatt, *et al.*, 2008). It is also worth noting that in the case of systems that have ligaments which are tangentially attached to the nodes (having n-fold symmetry), have equal ligament lengths and have equal node sizes, it was shown that space-filling chiral systems may only assume n-fold symmetries which correspond to n = 3, 4, 6 (A. Alderson, Alderson, Attard, *et al.*, 2010), whereas the anti-chiral systems may only form a space-filling configuration for n = 3, 4 (J. N. Grima, Gatt, *et al.*, 2008). These structures were later characterised and the 4- and 6- connected honeycombs were shown to be auxetic, having a Poisson's ratio close to -1 provided that the structure was not allowed to shear. However, trichiral systems were shown to exhibit a positive Poisson's ratio whilst anti-trichiral systems exhibited a negative Poisson's ratios only in the short ligament limit(A. Alderson, Alderson, Attard, *et al.*, 2010).

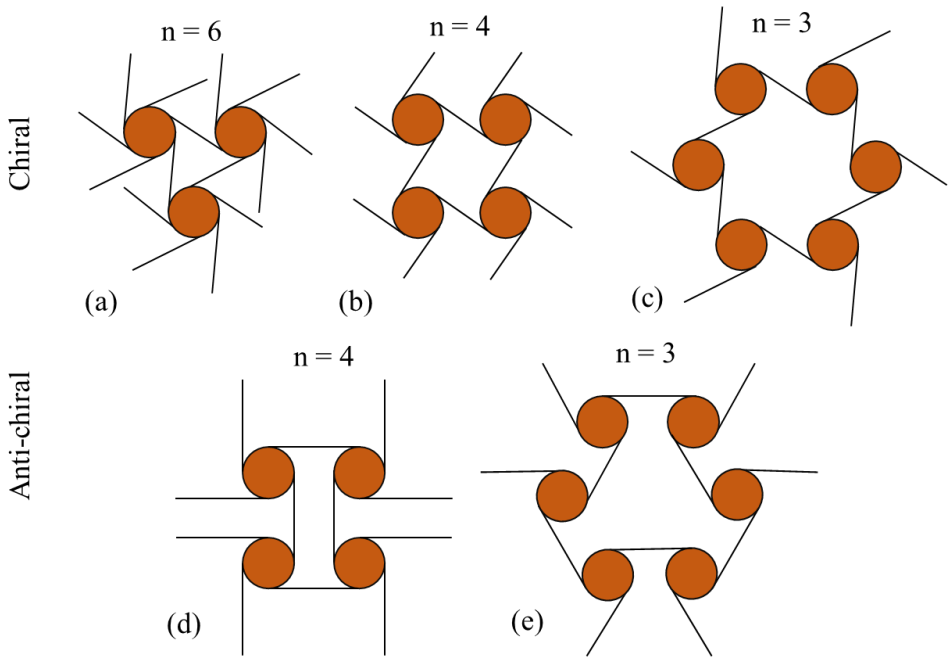

Figure 2.5. The various configurations of space-filling chiral and anti-chiral structures namely (a) hexachiral, (b) tetrachiral, (c) trichiral, (d) anti-tetrachiral and (e) anti-trichiral

Chiral auxetics have gained increasing attention over the years due to the advances in additive manufacturing and in fact numerous chiral and anti-chiral systems are proposed and investigated every year (Afdhal *et al.*, 2023; Bodaghi *et al.*, 2023; Lorato *et al.*, 2010; Miller *et al.*, 2010; Scarpa *et al.*, 2007; Spadoni *et al.*, 2005; Yusuf İnan *et al.*, 2023; Y. Zhou *et al.*, 2023). Studies have established that chiral systems exhibit enhanced flat-wise compressive strength and enhanced transverse shear resistance. In a recent study on the effect of geometric dimensions of a trichiral system on its strength was investigated experimentally. It was shown that whilst thickness, diameter, and length of ligament are inversely related to compressive strength, thickness and ligament length have a parabolic relationship with tensile strength and in fact through changes in geometric dimensions the researchers obtained a 4.5 times increase in tensile strength (Yusuf İnan *et al.*, 2023).

More recently, research in auxetics has shifted to 3D auxetic systems with a number of studies having successfully produced 3D chiral systems namely, cross chiral auxetic structure (Q. Wang *et al.*, 2020), axisymmetric chiral cellular structures (Novak, Mauko, *et al.*, 2022; Novak, Nowak, *et al.*, 2022) and cubic chiral auxetic structure (H.-H. Huang *et al.*, 2016). In the latter study by Huang *et al.* a set of design rules and procedures were developed for creating 3D chiral cubic auxetic structures due to the complexity of these structures (H.-H. Huang *et al.*, 2016). Whilst the complexity of these structure is a significant hurdle, research has sought to bypass this by using computers. In fact, in a recent study by Zhou *et al.*, a ready-to-manufacture optimization design of 3D chiral auxetics for additive manufacturing was developed. In this study, the estimated numerical Poisson's ratio and experimentally tested Poisson's ratio showed good agreement providing a reliable design method (Y. Zhou *et al.*, 2023).

2.1.4 Rotating rigid units systems

In the rotating rigid units mechanism, auxetic behaviour occurs as a result of rigid units connected at their vertices rotating relative to each other upon the application of a stress. The first tesselatable structure based on the rotation of rigid units was proposed by Grima and Evans (J. N. Grima & Evans, 2000a) and Ishibashi and Iwata (Ishibashi & Iwata, 2000), inspired by the design of Sigmund (Sigmund, 1995). The Poisson's ratio may depend on a number of factors, such as the shape of the rigid unit, relative lengths and the angle between the rigid units. For example, it was shown through analytical modelling that systems composed of connected squares (see Figure 2.6(a)) or connected triangles (see Figure 2.6(B)), that deform through relative rotation of connected polygons, yield a Poisson's ratio of -1, with the assumption of having fully rigid units (J. N. Grima & Evans, 2000a, 2000b, 2006).

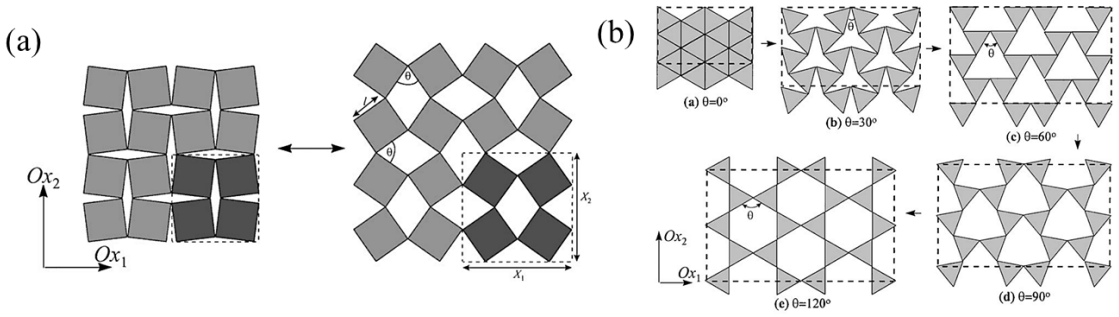

Figure 2.6. A depiction of the auxetic deformation of the proposed (a) rotating rigid squares mechanism (image taken from Grima and Evans (J. N. Grima & Evans, 2000a)) and (b) rotating rigid equilateral triangles (image taken from Ali *et al.*(M. N. Ali *et al.*, 2014a)).

Research was also extended to other geometrical systems made up of rigid rotating units. For example research has shown that changing the geometry from an equilateral triangle to an isosceles or scalene triangle results in a multitude of different Poisson's ratios (both positive and negative) whose magnitude and sign was dependant on the

triangle's shape and angle between the triangles(J. N. Grima, Chetcuti, *et al.*, 2012). Similarly, the rotating rigid squares model was extended to other polygons, namely rectangles, rhombi and parallelograms (see Figure 2.7(a)) (Attard *et al.*, 2016; J. Grima *et al.*, 2004; J. N. Grima, Gatt, *et al.*, 2005; J. N. Grima *et al.*, 2011). When using such polygons, the possibility of having different connectivities arise. When employing rigid rectangles, two types of connectivities are possible (see Figure 2.7(b)). In the first configuration, the long side of a rectangle is joined to the long side of the adjacent rectangles and short side of a rectangle is joined to the short side of the adjacent rectangle, in which case Type I rotating rectangles are obtained. The second possible connection is when the long side of a rectangle is connected to the short side of the adjacent rectangle, in which case Type II rotating rectangles are obtained. The Poisson's ratio obtained is dependent on the type of connectivity. In the case of Type I rotating rigid rectangles, both positive or negative Poisson's ratio may be obtained, depending on the aspect ratio of the rectangle, and the angle between the rectangles, whilst in the case of the Type II rotating rectangles a Poisson's ratio of −1 is always obtained.

In the case of rhombi, it was also determined that two types of connectivities are possible; Type α where the obtuse angle of the rhombus is attached to the acute angle of the adjacent rhombus and Type β, where the obtuse angle of a rhombus is attached to the obtuse angle of the adjacent rhombus (J. N. Grima, Farrugia, Gatt, *et al.*, 2008). Type α rhombi were found to be highly anisotropic and could exhibit both negative and positive Poisson's ratios depending on the shape of the rhombi and the angle between them whereas Type β systems were shown to be isotropic with a constant in-plane Poisson's ratio of –1(Attard & Grima, 2008). When using parallelograms as the rigid units, four different connectivities are possible, Type I and Type II as in the case of the rectangles and Type α and Type β as in the case of the rhombi (Attard, Manicaro, & Grima, 2009a;

J. N. Grima, Farrugia, Gatt, *et al.*, 2008). In the same work, mathematical models were derived describing their behaviour when deforming through hinging from which the Poisson's ratio could be acquired.

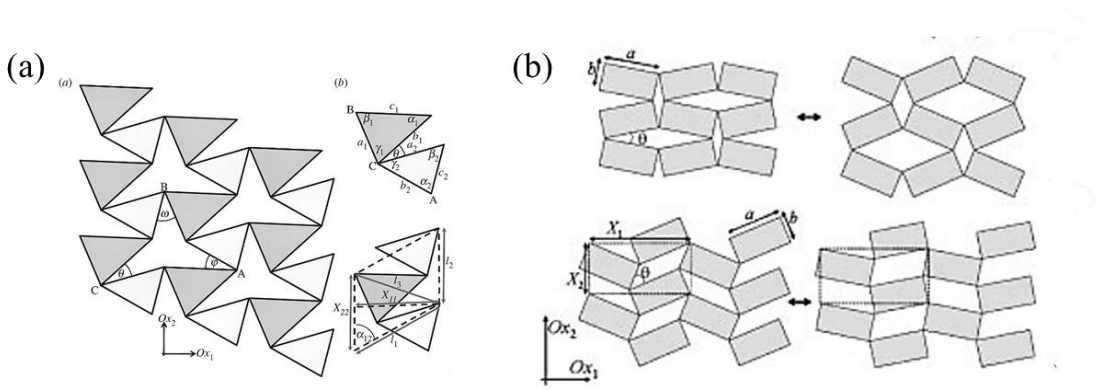

Figure 2.7. Rotating rigid units based on irregular polygons namely (a) scalene triangles (image taken from Grima *et al.*(J. N. Grima, Chetcuti, *et al.*, 2012)) and (b) Type I (above) and Type II (below) rectangles (image taken from Grima *et al.* (J. N. Grima, Gatt, *et al.*, 2005a))

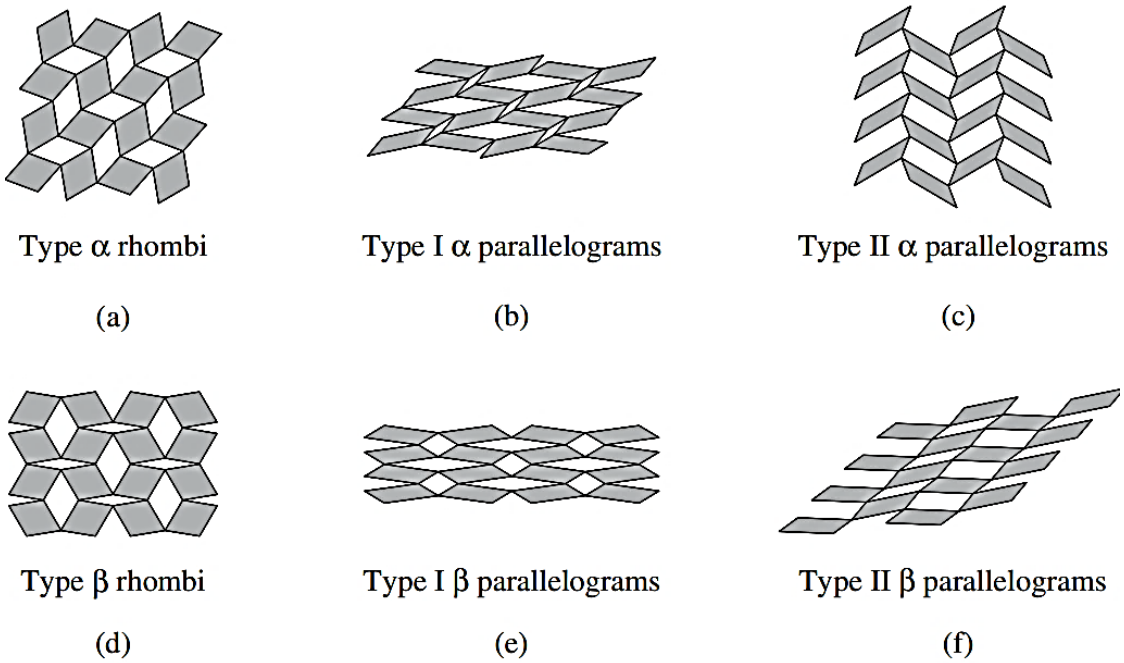

Figure 2.8. A figure depicting six different models; (a) Type α rhombi, (b) Type I α parallelograms, (c) Type II α parallelograms, (d) Type β rhombi (e) Type I β parallelograms, (f) Type II β parallelograms for the rotating rigid units mechanism using rhombi and parallelograms with different connectivity. (Image taken from Grima *et al.* (J. N. Grima, Farrugia, *et al.*, 2008))

Further studies also investigated the auxetic behaviour by connecting different-sized squares and rectangles (see Figure 2.9). In this case it was shown that the resulting Poisson ratios were shown to be dependent on the shape and relative size of the rectangles, the angle between the rectangles and also the direction of loading (J. N. Grima *et al.*, 2011). Other studies also investigated semi-rigid systems where it was found that the deformation of the rigid units compete with the auxetic mechanism and thus the interplay of the deformation mechanisms determine whether the structure would exhibit a positive or negative Poisson's ratio and its magnitude (Attard, Manicaro, Gatt, *et al.*, 2009; Dmitriev, 2007; Dmitriev *et al.*, 2005; J. N. Grima *et al.*, 2007).

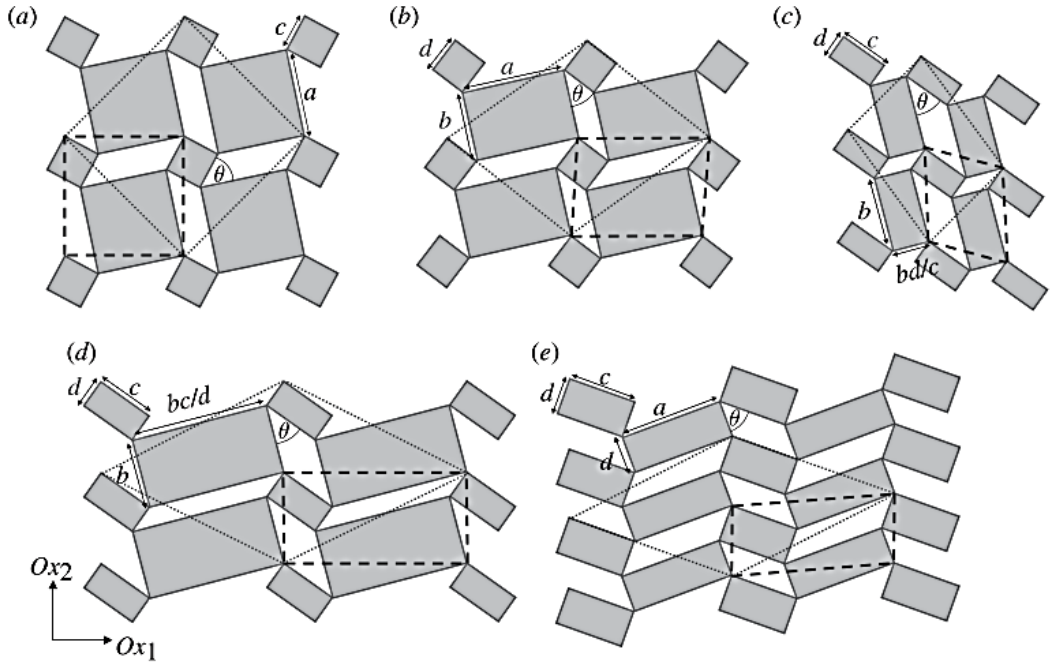

Figure 2.9. Auxetic structures created by connecting (a) different-sized squares, (b) squares and rectangles, (c-e) different-sized rectangles using different connecting points. (Image taken from Grima *et al.* (J. N. Grima *et al.*, 2011).

Another breakthrough in the research on rotating rigid units was proposed by Gatt *et al.* with the introduction of hierarchical auxetic structures based on the rotating rigid units mechanism. The multi-levelled, square-based structure was proposed whose extent of auxeticity, aperture and the several pores' sizes could be controlled through the design

(Gatt, Mizzi, *et al.*, 2015). A number of studies proposed other designs of hierarchical auxetic structures and investigated the enhanced mechanical properties and variable auxeticity that is innately attributed to them due to the nature of hierarchical structures (K. K. Dudek *et al.*, 2022; X. Li *et al.*, 2021; Mizzi & Spaggiari, 2020; Y. Tang & Yin, 2017).

A major leap in auxetic research came with the proposal of 3D auxetic mechanisms which broadened the applicability of the materials in question. As discussed previously, 3D auxetic mechanisms are capable of exhibiting a negative Poisson's ratio in multiple directions and are therefore superior to 2D auxetic mechanisms in areas where forces may be applied from multiple directions. In 2012, Attard and Grima proposed a 3D rotating rigid cuboids mechanism where cuboids were attached solely through the edges, shown in Figure 2.10(a), forming a hexagonal pattern (Attard & Grima, 2012). This structure was shown to exhibit NPR in some planes depending on the angle between the cuboids. In the study, a system in which rotating cubes were joined by their vertices was also suggested to exhibit an NPR. Meanwhile in the work by Andrade *et al.*, they proposed a structure where the cubes were connected through the vertices and edges, shown in Figure 2.10(b), which yielded anisotropic NPR nearing -1 magnitude (Andrade *et al.*, 2018). In the study by Kim *et al.* the Poisson's ratio of three-dimensional structures made of triangular prisms, hexagonal prisms and square prisms connected at their vertices which deformed via a 3D auxetic mechanism was also investigated (J. Kim *et al.*, 2017). In this study an analytical model was derived verified through numerical simulations and the Poisson's ratio formula for three 3D auxetic structures were derived. As manufacturing methods improve, complex architected structures consisting of connected polyhedral units were also produced such as the systems by Sorrentino *et al*. and Tanaka

et al. which were shown to exhibit negative Poisson's ratio (see Figure 2.10(d)) (Sorrentino & Castagnetti, 2023a; Tanaka *et al.*, 2021).

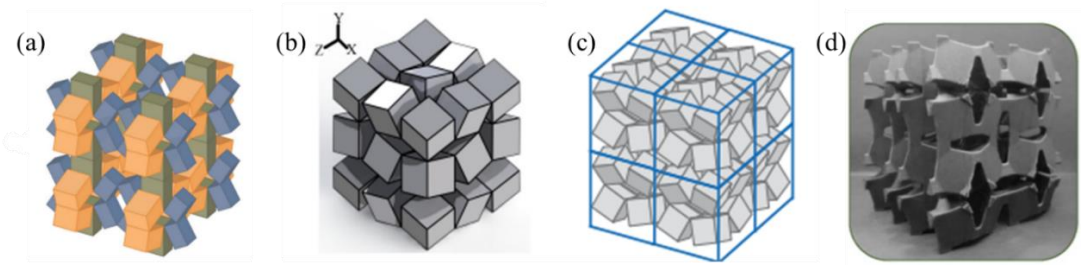

Figure 2.10. Three dimensional structures proposed by (a) Attard and Grima (Attard & Grima, 2012), (b) Andrade *et al.* (Andrade *et al.*, 2018), (c) Kim *et al.* (J. Kim *et al.*, 2017) and (d) Sorrentino *et al.* (Sorrentino & Castagnetti, 2023b), which deform via an auxetic 3D rotating rigid units mechanism. (Images taken from the respective studies)

2.2 Finite Element Analysis in Auxetics Research

2.2.1 Introduction

The last three decades have seen an extensive growth of our knowledge about auxetics. Recognizing the benefits associated with having a negative Poisson's ratio, scientist have availed themselves of various research tools to characterize, optimize end even design *de novo* metamaterials which exhibit a negative Poisson's ratio. In order to advance in the budding field of auxetics with such a wide variety of potential structures, pure experimental research approaches were not always deemed feasible, especially before the advent of 3D printing. This may be attributed in part to complex geometries that auxetic structures, particularly 3D systems have. As a consequence of this, researchers have mostly used numerical analysis to study potential auxetic metamaterials, using experimental results and analytical studies to verify the numerical results obtained (Abbaslou *et al.*, 2023; M. N. Ali *et al.*, 2014b; Alomarah *et al.*, 2019, 2020; S. Z. Khan *et al.*, 2021; C. Li *et al.*, 2021; Shah, Khan, Koloor, *et al.*, 2022; W. Wu *et al.*, 2018b; W. Yang *et al.*, 2022; J. Zhang, Lu, Ruan, *et al.*, 2018; J. Zhang, Lu, Wang, *et al.*, 2018a).

One of the numerical approaches which researchers have used to make significant inroads in the field of auxetics is the Finite Element Analysis (FEA), a method that is able to calculate how a system behaves under specific physical conditions. This method dates back to the 1940s where researchers such as Hrennikoff and Courant sought to overcome the mathematical difficulties when applying the theory of elasticity (Courant, 1943; Hrennikoff, 1941). In 1956, the FEA method was adopted by the aerospace industry, since the method of finite elements allowed the modelling of complex geometries and provided an instant analysis on their mechanical properties (Trivedi, 2014). The method has been shown to determine the location, magnitude, and direction of forces and assign stresses which are then theoretically measured. Furthermore, especially during the design stages, a reliable finite element analysis reduces the need for prototypes as it provides a quick and non-invasive and repeatable analysis (J. Gao *et al.*, 2006; Moens & Vandepitte, 2006; Viceconti *et al.*, 2007).

Within a few decades the method was adopted by a number of research fields from dentistry (Aparna *et al.*, 2021; Srirekha & Bashetty, 2010; Tatarciuc *et al.*, 2021; Thresher & Saito, 1973; Valera-Jiménez *et al.*, 2020) to biomechanics (Galbusera *et al.*, 2020; Huiskes & Chao, 1983; Mengoni, 2020; Phellan *et al.*, 2021) amongst others (Cremonesi *et al.*, 2020; Fadiji *et al.*, 2018; X. Liang *et al.*, 2020; Müzel *et al.*, 2020), since the finite method provided a solution to many of the problems of material analysis by calculating the physical measurements of stress within a structure (Wood *et al.*, 2008). The use of FEA was observed in some of the earliest seminal papers on negative Poisson's ratio by Evans and his group, and was used to model auxetic foams (Evans *et al.*, 1994), continuous fibre composites (Nkansah *et al.*, 1993) and auxetic microporous polymers (A. Alderson & Evans, 1995) even at a time when computational power was much more limited than today. Nowadays, commercially available software such as ANSYS and

ABAQUS combined with high computational power are essential tools when conducting research in the mechanical properties of materials and has thus been utilized by several research groups in the study of auxetic metamaterials (Afshar & Rezvanpour, 2022; K. Chen *et al.*, 2021; Gunaydin & Turkmen, 2019; Kavakli & Ali, 2023; Logakannan *et al.*, 2022; Rad *et al.*, 2019; Y. L. Wei *et al.*, 2021; W. Xu *et al.*, 2020; W. Yang *et al.*, 2022; X. Y. Zhang *et al.*, 2021).

2.2.2 The study of auxetic structures through FEA

2.2.2.1 Two dimensional systems

Since the Poisson's ratio measures a 2D property, many studies were devoted to investigate the mechanical properties of two-dimensional geometries that are capable of exhibiting a negative Poisson's ratio. As discussed above, re-entrant systems are an important subset of auxetic systems and have been research thoroughly. In fact, a number of modified re-entrant structures were tested through FEA in order to optimise the geometry (Gohar *et al.*, 2021; Harkati *et al.*, 2017; Z. Y. Li *et al.*, 2022) and to analyse the resulting mechanical properties such as energy absorption capacity (Gohar *et al.*, 2021), synclastic behaviour (J. Lee *et al.*, 1996; Zied *et al.*, 2015) and impact resistance (Usta *et al.*, 2021, 2022; H. Wang *et al.*, 2019). It is worth discussing the significant studies over the past decade where novel structures were produced and investigated for their properties and the role of FEA in the studies. One major benefit of FEA is the ability to test modified and novel structures in a time-efficient manner. An example of which is the study by Gohar *et al.* where a set of novel re-entrant structures, termed as mixed star structures (shown in Figure 2.11(b)) were designed and investigated. These re-entrant structures were shown to have a number of superior properties, including a high energy absorption capacity (Gohar *et al.*, 2021). Similarly, Huang *et al.* investigated a new type

of honeycomb design consisting of two distinct parts, a re-entrant hexagonal component, and a thin plate section, shown in Figure 2.11(c). The authors created theoretical models to describe the in-plane uniaxial tensile modulus, shear modulus, and Poisson's ratios, which were verified through FEA (J. Huang *et al.*, 2017). Another study was carried out by Zhang *et al.* which investigated two new hybrid metamaterial concepts that combine a core unit cell of re-entrant or cross-chiral shape with lateral missing ribs. FEA simulations were used to optimize specific effective properties, and non-linear simulations were used to understand the Poisson's ratio and stiffness of these metamaterials under large deformations (W. Zhang *et al.*, 2021). Lu *et al.* similarly utilized FEA simulations to calculate the in-plane Poisson's ratio and Young's modulus of modified honeycomb-like configurations under uniaxial loading (Z. Lu *et al.*, 2016).

FEA has also been used to confirm analytical and experimental methods as shown in the work by Khan *et al.* and Mustahsan *et al.* where FEA and experimental testing were used to validate the analytical model accounting for the bending, shear, and axial deformation of modified re-entrant honeycomb structures showing a close agreement between the three methods (S. Z. Khan *et al.*, 2019; Mustahsan *et al.*, 2022)(shown in Figure 2.11(d-e)). Similarly, Li *et al.* proposed a composite auxetic structure, which was studied using FEA in conjunction with experiments and theoretical analysis to investigate the variables affecting the Poisson's ratio and mechanical properties of the structure, as well as shape optimization (Z. Y. Li *et al.*, 2022).

Another major benefit of FEA is that it reveals insight into the internal stresses within the material which is important when understanding the deformation mechanisms when loaded. For example, Harkati *et al.* investigated the shear and axial deformation mechanisms of re-entrant honeycombs using FEA. This analysis successfully provided better insight into the responsible deformation mechanism for auxetic behaviour and the

geometric parameters governing them specifically the cell wall thickness (Harkati *et al.*, 2017) (shown in Figure 2.11a).

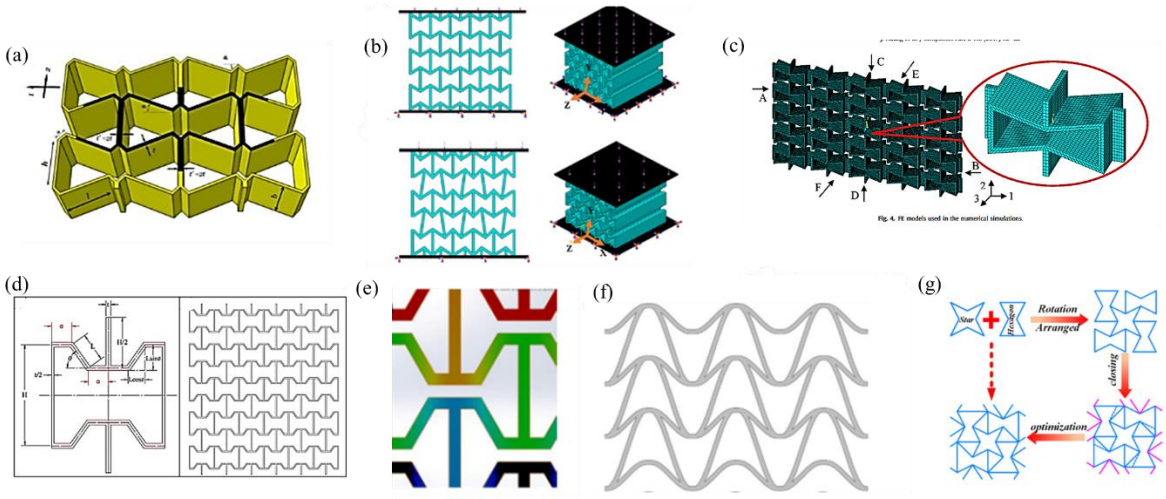

Figure 2.11. Modified re-entrant structures proposed by (a) Harkati *et al.* (Harkati *et al.*, 2017) (b) Gohar *et al.* (Gohar *et al.*, 2021), (c) Huang *et al.* (J. Huang *et al.*, 2017), (d) Khan *et al.* (S. Z. Khan *et al.*, 2019), (e) Mustahsan *et al.* (Mustahsan *et al.*, 2022), (f) Guo *et al.* (M. F. Guo *et al.*, 2020), (g)Wang *et al.* (W. Wang *et al.*, 2023).

Numerous other studies have utilised FEA to investigate a number of 2D-re-entrant honeycomb systems and obtain their mechanical properties in-plane Poisson's ratio and Young's modulus under uniaxial loading (Bezazi *et al.*, 2005; Y. Chen *et al.*, 2022; Etemadi *et al.*, 2023; N. Xu *et al.*, 2021; Zhu *et al.*, 2022). Some noteworthy examples are the investigations on the Double U honeycomb structure in which the arrow-shaped system by Larsen *et al.* was optimised to have better load resistance and a higher energy absorbing capacity (M. F. Guo *et al.*, 2020) (shown in Figure 2.11f) and the WSH honeycombs composed of stars and hexagons and shown to exhibit excellent energy absorption capacity and enhance anti-impact behaviour (W. Wang *et al.*, 2023) (shown in Figure 2.11g). Through FEA simulations, a number of studies were carried out on the shape optimisation of the re-entrant honeycombs by analysing the effect of a number of variables on the physical properties. Most significant of which was the work by Bezazi *et*

al. and Lu *et al.* who employed FEA to study the in-plane Poisson's ratio and Young's moduli under uniaxial loading of modified structures shown in Figure 2.12 and Figure 2.13 respectively. Bezazi *et al.* reported that for certain internal angles, the proposed structure exhibits a decrease in the Poisson's ratio. Also, the presence of edge corners in the proposed configuration gives rise to a cellular structure with enhanced flexibility compared to the classical centrosymmetric one (Bezazi *et al.*, 2005). Moreover, Lu *et al.*, reported that the addition of a narrow rib in the unit cell of re-entrant honeycomb configuration gives rise to a cellular structure with significantly enhanced Young's modulus (Z. Lu *et al.*, 2016).

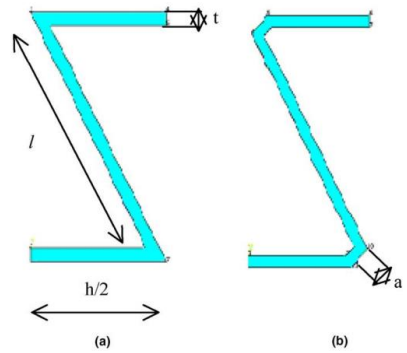

Figure 2.12. Various layouts of centrosymmetric auxetic honeycomb cell. (a) Type 1: classical re-entrant cell. (b) Type 2: new design proposed, re-entrant cell configuration. (Bezazi *et al.*, 2005)

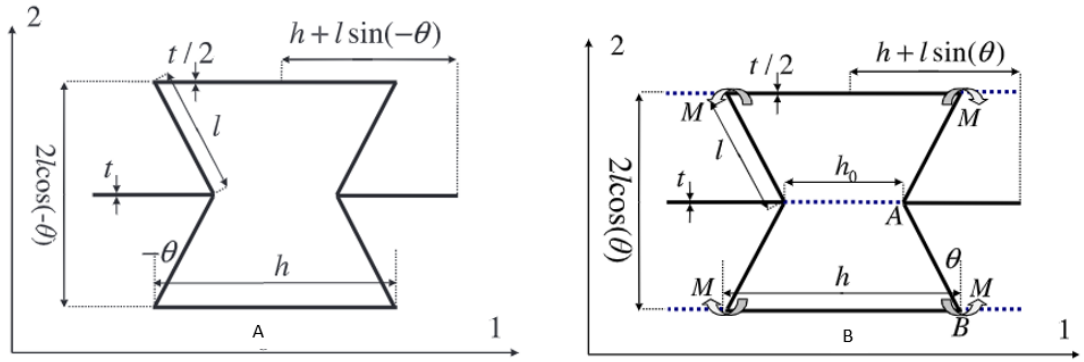

Figure 2.13. New design unit cell geometry and coordinate system for (A) re-entrant cells; (B) unit cell proposed by Lu *et al.* (Z. Lu *et al.*, 2016)

The FEA method has also been used for other auxetic mechanisms including rotating rigid units mechanism and chiral systems. The use of FEA provided insight into the auxetic behaviours of rotating rigid units by highlighting the stresses and strains within the material when loaded, something that could not be shown easily through experimental studies (Chang *et al.*, 2023). This was particularly useful in a study by Afshar *et al.* where non-porous perforated rotating rigid units, having soft inclusion in the perforations, were investigated (see Figure 2.14(a)). It was shown that soft inclusions reduced the auxetic behaviour, however, still exhibited a negative Poisson's ratio which would be useful in applications of non-porous auxetic materials (Afshar & Rezvanpour, 2022). Other studies have been carried out investigating the mechanical properties and deformation mechanisms of rotating rigid units systems, such as the peanut-shaped perforated structures, depicted in Figure 2.14(b) (Atilla Yolcu & Okutan Baba, 2022) and the rectangular perforations by Acuna *et al.* (Acuna *et al.*, 2022), amongst others (Chetcuti *et al.*, 2014; Grima-Cornish *et al.*, 2020; Hur *et al.*, 2021; J. Zhang, Lu, Ruan, *et al.*, 2018). Similarly numerous chiral systems were also investigated where FEA was a key tool when carrying out parametric studies to optimising the geometries of the proposed chiral systems as well as when investigating mechanical properties such as auxeticity, energy absorption capacity, shear resistance and much more (Alomarah *et al.*, 2018; Attard *et al.*, 2020; Gang *et al.*, 2022; D. Gao *et al.*, 2021b; Z. Y. Li *et al.*, 2022; Nečemer *et al.*, 2020; D. Qi *et al.*, 2019; Shim *et al.*, 2013; K. Zhang *et al.*, 2020) (see Figure 2.14(c-d) for examples).

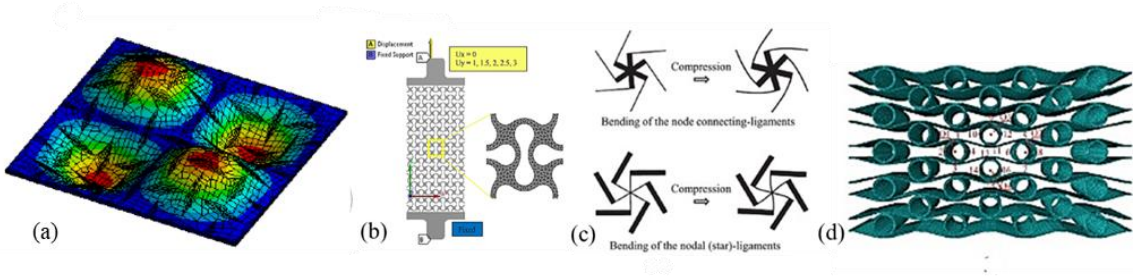

Figure 2.14. Auxetic structures proposed by (a) Afshar *et al.* (Afshar & Rezvanpour, 2022), (b) Atilla *et al.* (Atilla Yolcu & Okutan Baba, 2022), (c) Attard *et al.* (Attard *et al.*, 2020) and (d) Li et al(Z. Y. Li *et al.*, 2022).

In conclusion, FEA has proven to be an essential tool in developing and understanding the mechanical properties of 2D cellular solids, such as honeycomb structures, as well as optimising their geometry to elicit superior properties. These studies highlight the usefulness of FEA in the shape optimization of novel structures, the investigation of their properties under different loading conditions, and the validation of analytical models.

2.2.2.2 Three-Dimensional Systems

More recently, research is shifting to the study of 3D auxetic materials due to the fact that they are capable of exhibiting a negative Poisson's ratio in multiple planes and are therefore useful in applications where forces may be applied in multiple directions. In Section 2.2.2.1, the benefits of FEA when studying 2D materials was discussed. Considering the complexity of 3D auxetics when compared to their 2D counterparts it is evident that FEA is an indispensable tool when studying the auxetic behaviour of 3D materials. In fact FEA has been used when investigating a wide range of 3D auxetic materials including composites (J. N. Grima *et al.*, 2013; Z.-Y. Li *et al.*, 2023; Lyngdoh *et al.*, 2022; Poźniak *et al.*, 2016; Roche *et al.*, 2011), cellular materials (A. Alderson,

Alderson, Chirima, *et al.*, 2010; Atilla Yolcu & Okutan Baba, 2022; Z. Y. Li *et al.*, 2022) and surface auxetic structure (SAS)(Changfang *et al.*, 2022a).

FEA was particularly useful when considering composites, as the structure would be composed of a number of materials and FEA has been shown to be useful in capturing their interaction. In fact, in a study by Grima and his co-workers simulations were employed to investigate an auxetic 3D composite using metal honeycombs embedded in a soft rubbery matrix. FEA allowed the study of the effects of changes in framework geometry in relation to changes in the Poisson's ratio both in-plane and out-of-plane, hence it served as a method to optimise the parameters of the composite for maximum auxetic behaviour (J. N. Grima *et al.*, 2013). These simulations also led to an analytical study to deduce the requirements for an auxetic behaviour. Similarly, Li et. al. (2023) used FEA to investigate the mechanical and auxetic characteristics of a composite fibre-reinforced stacked origami structure (see Figure 2.15(b)). It was deduced that composite stacked origami structures have lower density and better energy absorption characteristics compared to those made from metal using additive manufacturing process (Z.-Y. Li *et al.*, 2023).

This can be extended to other auxetic structures as shown in the study by Wang et. al. on 3D re-entrant honeycomb (depicted in Figure 2.15(a)) (X.-T. Wang *et al.*, 2017) and in the study of cellular structures proposed by Nasim & Etemadi (depicted in Figure 2.15(c)) (Nasim & Etemadi, 2018) where in both cases FEA was used to assess the effect of geometric parameters on the mechanical properties and deformation mechanisms.

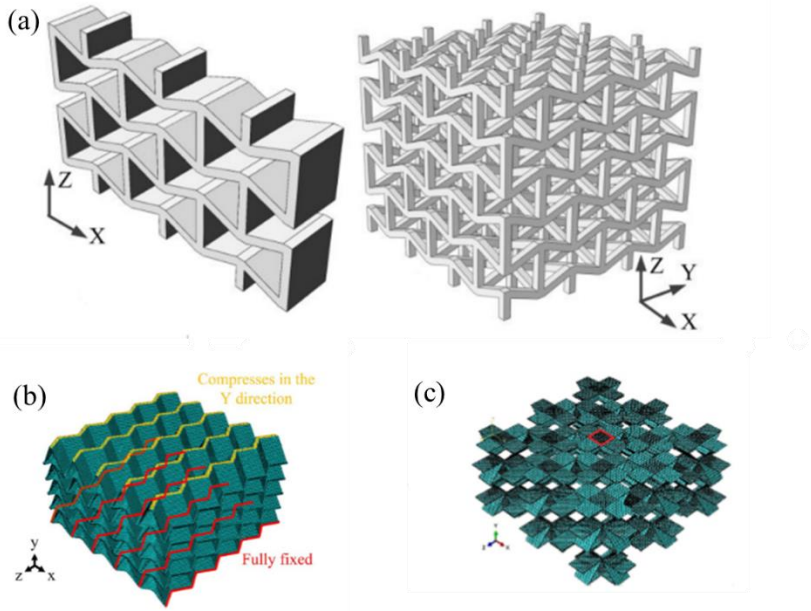

Figure 2.15. Three-dimensional auxetic structures proposed by (a) Wang *et al.* (X.-T. Wang *et al.*, 2017), (b) Li *et al.* (Z.-Y. Li *et al.*, 2023),(c) Nasim & Etemadi (Nasim & Etemadi, 2018)

2.2.2.3 Emulation of properties

As discussed before, since the properties of auxetic materials are interlinked with their geometry, in order to achieve the desired properties, researchers have investigated the effect of the geometric parameters on the mechanical properties. In this area, the use of FEA has been key as it is both more time efficient and cost effective since it eliminates or reduces the production and testing of experimental prototypes with expensive equipment (Q. Gao *et al.*, 2018; Z.-Y. Li *et al.*, 2023) (Nasim & Etemadi, 2018). The FEA method is advantageous as it can accurately acquire the desire mechanical properties and analyse the behaviour of different sections of the material. This is crucial in obtaining the response of the material to loads and other desirable properties as required by the intended application.

In fact, this can be seen in a study by Chow *et al.* where they proposed the use of 3D printed thermoplastic polyurethane (TPU) with an auxetic architecture insert for

pressure therapy to treat hypertrophic scars (HSs). The auxetic structure had to easily accommodate the contours of the human body during joint movement. Prior to any prototyping, the concept was initially tested in FEA where the synclastic effect of out-of-plane bending was investigated. Following this the formability, structural deformation, and auxetic response of re-entrant (RE) and double arrowhead (DAH) auxetic structures are evaluated numerically followed by an experimental prototype. The study successfully showed how the design was able to facilitate a stable level of pressure during body motion, promoting the recovery of HS. (L. Chow *et al.*, 2022).

This section will focus on papers that use FEA to study the mechanical properties and energy absorption capacity of auxetic materials under dynamic and quasi-static loading, analyse the mechanical properties and deformation modes of specific auxetic structures, and investigate the energy absorption capacity of specific auxetic structures.

2.2.2.3.1 Mechanical properties of auxetic materials under dynamic and quasi-static loading

In recent years, there has been growing interest in the mechanical properties and energy absorption capacity of auxetic materials under dynamic and quasi-static loading. One of the key challenges in this area is to develop a deeper understanding of the factors that influence the mechanical properties of auxetic materials under different loading conditions. FEA has been widely used to investigate the mechanical properties and deformation modes of specific auxetic structures.

Han *et al.* used FEA to investigate the mechanical properties and deformation modes of gradient auxetic tube and uniform auxetic tube under axial and inclined loads, shown in Figure 2.16(a). They found that the gradient auxetic tube had better energy

absorption capacity and higher strength compared to the uniform auxetic tube (D. Han, Zhang, *et al.*, 2022). Novak *et al.* explore the mechanical behaviour of chiral auxetic cellular structures under different loading conditions, including quasi-static, low-velocity dynamic compression, and high strain rate loading, as shown in Figure 2.16(c). They use experimental measurements, infrared thermography, high-speed camera images, and computational simulations to study the deformation mechanism of chiral auxetic structures. The computational simulations enable a more detailed analysis of mechanical behaviour at different strain rates and allow for the estimation of plateau stress at arbitrary loading velocities. Overall, the paper provides insights into the use of chiral auxetic structures in crashworthiness, ballistics, and blast protection applications (Novak *et al.*, 2020).

Similarly, W. Wang *et al.* conducted numerical simulations to study the static and dynamic plateau stresses of windmill-like (WSH) honeycombs and their energy absorption capacity, shown in Figure 2.16(b). They found that the windmill-like (WSH) honeycombs had excellent energy absorption performance under both static and dynamic loading conditions(W. Wang *et al.*, 2023). Han, Ren, *et al.* used FEA to investigate a design for ribbed metamaterials with high-quality energy-absorption capabilities speeds (D. Han, Ren, *et al.*, 2022). In the study by Chen *et al.*, the authors propose a set of auxetic lattices with enhanced stiffness by adding a strengthening rib into conventional auxetic unit cells in a direction perpendicular to the re-entrant direction. The effective mechanical properties of these variants are calculated using the fast Fourier transform-based homogenization method, which shows that their Young's modulus in 2D can be improved by approximately 200% along the strengthening direction without significant sacrifice of auxetic property. However, such an enhancement is weakened in 3D. The paper provides

insight into the design of new structures of unit cells with enhanced stiffness and negative Poisson's ratio (Z. Chen *et al.*, 2020)

Other noteworthy studies that have made use of dynamic and quasi-static compression as well as different impact velocities include a number of modified re-entrant diamond structures which exhibited a superior specific energy absorption (J. Liu & Liu, 2022; Logakannan *et al.*, 2020), modified re-entrant honeycombs which were tested for crashworthiness applications (H. Jiang *et al.*, 2020; H. L. Tan *et al.*, 2019) and the investigation of the energy absorption capacity of star-circle honeycomb structures (H. Lu *et al.*, 2021).

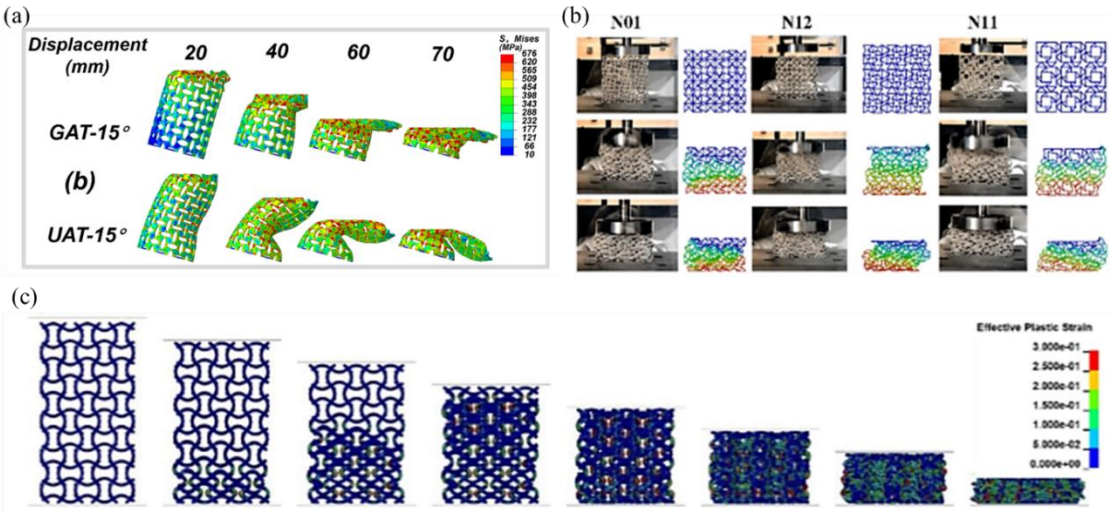

Figure 2.16. The use of FEA to analyse the mechanical properties of auxetic materials when loaded. Images taken from (a) Han *et al.* (D. Han, Zhang, *et al.*, 2022), (b) Wang *et al.* (W. Wang *et al.*, 2023), and (c) Novak *et al.* (Novak *et al.*, 2020)

FEA has also been implemented to expose the materials to dynamic and static crushing conditions. Li *et al.* study the in-plane uniaxial and biaxial crushing characteristics of three honeycombs through explicit dynamic finite element analysis in order to compare the deformation mode, plateau stress, energy absorption, and impact response. (Z. Li *et al.*, 2019). Qi *et al.* analysed in-plane crushing response of tetra-chiral

honeycombs under both quasi-static and dynamic loading conditions which revealed the different modes of deformation in response to the different loading conditions shown in Figure 2.17(a) (C. Qi *et al.*, 2019). A more recent student by the same author made use of the FE predicted deformation to reveal the underlying mechanisms by analysing patterns in the internal stresses. The article identifies three distinctive regions in the REC unit cell configuration map, each corresponding to a meso-scale interaction pattern and a macro-scale deformation mode as shown in Figure 2.17(b) (C. Qi *et al.*, 2021).

Other noteworthy studies analysing the crushing performance through FEA include a paper by Wei *et al.* investigating a new type of auxetic honeycomb structure and its deformation (see Figure 2.17(c)) (L. Wei *et al.*, 2020) and a study by Singh *et al.*, where FEA was used to investigate the deformation mechanisms observed during the static inclined compression of re-entrant honeycomb (RH) auxetic structure. This study introduced a new method to extract micro deformation mechanisms under inclined loading, which were related to the macro deformation regime and the overall mechanical response of the RH structure. By detecting elements experiencing plastic strain of more than 10%, they successfully identified micro modes shown in Figure 2.17(d)(R. Singh *et al.*, 2021). Furthermore a 3D re-entrant structure was also analysed under dynamic crushing condition in order to observe its behaviour under extreme deformation (T. Wang *et al.*, 2019)**.**

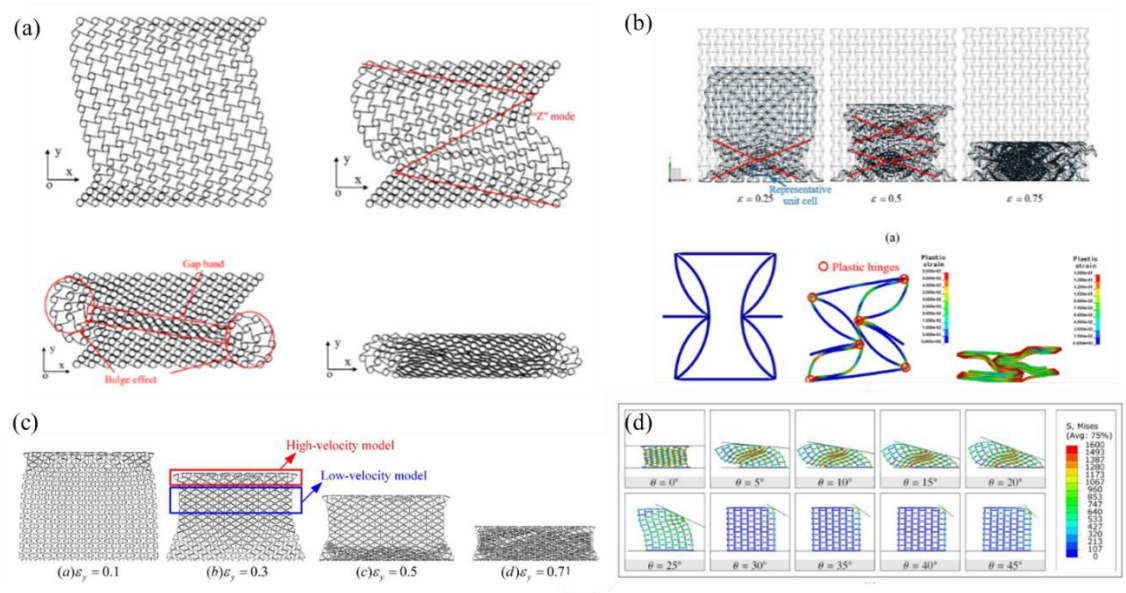

Figure 2.17. Analysis using FEM of the deformation mechanisms during the crushing of auxetic materials taken from (a) Qi *et al.* (C. Qi *et al.*, 2019),(b)Qi *et al.* (C. Qi *et al.*, 2021),(c) Wei *et al.* (L. Wei *et al.*, 2020)and (d) Singh *et al.* (R. Singh *et al.*, 2021)

2.2.2.3.2 FEA analysis of auxetic material behaviour in impact and indent loading

Auxetic materials are also associated with impact resistance and have been proposed in applications of protective gear and automotive bumpers. In recent years, FEA has been used extensively to investigate the behaviour of auxetic materials in impact scenarios which was crucial in material testing for the automotive, aerospace, and other industries. This is due to the fact that FEA is a repeatable and rapid test, *in lieu* or in conjunction with the more time-consuming experimental tests, to investigate the behaviour of auxetic material to impact by analysing the dispersal and redirection of the force as well as the energy absorption properties. This has proved particularly useful in analysing the crushing patterns and the deformations as was shown by Liu *et al.* when loading the re-entrant auxetic honeycomb under different loading speeds, shown in Figure 2.18(a) (W. Liu *et al.*, 2016).

Guo *et al.* investigated the effect of impact velocity and indenter size on a Double U honeycomb structure. They found that the Double U honeycomb structure had better

energy absorption capacity and stress distribution compared to the conventional counterpart (M. F. Guo *et al.*, 2020). Similar to the work above, FEA was used to investigate the effect of impact velocity and crashworthiness of auxetic structures including a number of honeycombs (Ou *et al.*, 2021) and modified honeycombs; the WSH honeycombs(W. Wang *et al.*, 2023), hierarchical honeycombs (H. L. Tan *et al.*, 2019), and chiral auxetic structure, shown in Figure 2.18(b) (D. Gao *et al.*, 2021a).

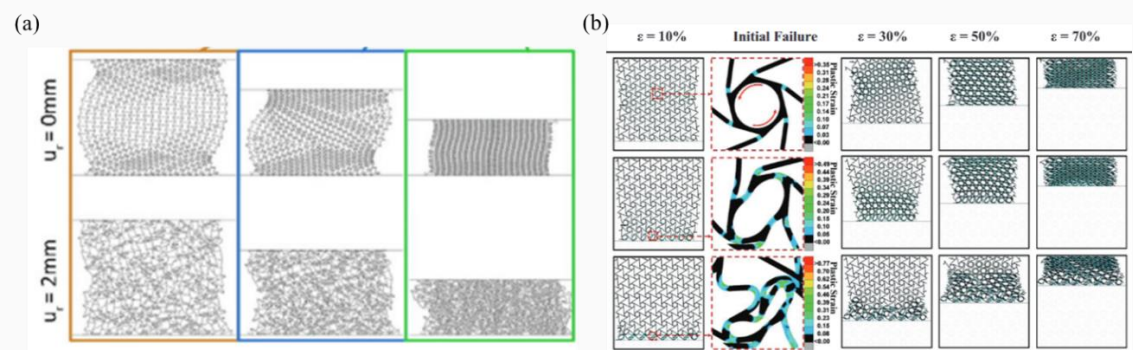

Figure 2.18. Studies carried out by (a) Liu *et al.* (W. Liu *et al.*, 2016) and (b) Gao *et al.* (D. Gao *et al.*, 2021a), investigating the effect of impacts on auxetic materials through FEA.

A number of studies have used FEA in order to investigate the effect of indentation of the deformation mechanism (Z. Li *et al.*, 2021). In two studies, FEA was used to verify the obtained results on indentation resistance of the hexagonal honeycombs (L. L. Hu *et al.*, 2019) and the indentation behaviour of the 3D printed auxetics reinforced composites (T. Li *et al.*, 2020a).

In conclusion, FEA has been an essential tool in the investigation of auxetic materials, and the studies reviewed here demonstrate the usefulness of FEA in analysing the mechanical properties and energy absorption capacity of these materials. The research has shown that auxetic materials have great potential for use in applications requiring high energy absorption capacity, such as in the automotive and aerospace industries.

2.2.2.3.3 Others

FEA has also been used in acoustic and vibration frequency analysis. In two studies by Li *et al.,* they developed and applied a finite element method to evaluate the propagation of acoustic and elastic waves through 3D phononic crystals. The method accurately computed band structures and identified band gaps and eigenmodes. The results showed that the finite element method was precise and efficient for computing band structures of complex phononic crystal structures with irregular unit shapes and could provide accurate results with commercial finite element code (Jianbao *et al.*, 2008; J. Li *et al.*, 2009). The research has been subsequently used by numerous studies (Koutsianitis *et al.*, 2019, 2021) for numerical and experimental investigations of phononic crystal structures and design of new acoustic devices.

In a study by Li *et al.,* the fundamental frequencies for a structure consisting of sandwich plates with functionally graded (FG) auxetic 3D lattice core were modelling, and a non-linear FEA revealed that the effects of FG configurations and strut incline angles are significant, and the FG-X specimen possesses the highest fundamental frequency. The study also investigates the large amplitude vibration characteristics of sandwich plates with FG-NPR 3D lattice core in different thermal environments. The effects of FG configurations on the natural frequencies, non-linear-to-linear frequency ratios of sandwich plates, and Electron Paramagnetic Resonance (EPR)-amplitude curves are studied using full-scale non-linear FE simulations. Results indicate that the FG configurations have a distinct effect on the linear and non-linear vibration behaviour of sandwich plates and that the EPR-amplitude curves become stable when the vibration amplitude is sufficiently large. Overall, the study sheds light on the vibration behaviour

of functionally graded auxetic 3D lattice metamaterials and sandwich plates with such core and provides insights for further investigations (C. Li *et al.*, 2020b).

2.2.2.4 Added understanding

Over the years of research, advances in computational power and improvements in FEA has led to its application to more complex structures. This has allowed the use of FEA to simulate more real and complex scenarios which is required for the end-product design. Recently, Wan et. al. made use of FEA to deduce the ideal 4D printed programmable metamaterial (out of three structures) for biomedical scaffolds, which is shown in Figure 2.19 (c). The analysis illustrated that, the proposed cylindrical shells with desired mechanical properties and configurations demonstrate potential applications in biomedical scaffolds (M. Wan *et al.*, 2022). Similarly, Wu *et al.* studied the mechanical properties of artery stent which are of key importance to both the mechanical integrity and biomechanical performance reliability of stent-plaque-artery system. Wu *et al.* proposed two types of innovative chiral stents with auxetic properties- anti-tetrachiral stent with circular and elliptical nodes and hierarchical anti-tetrachiral stents with circular and elliptical nodes, shown in Figure 2.19 (a). FEA was employed to study the effects of stent geometrical parameters on the tensile mechanical behaviours of the proposed stents. It was deduced that the mechanical behaviours of anti- tetrachiral stent can be tailored through adjusting the levels of hierarchical structures and unit cell design parameters. FEA allowed for the study of the deformation mechanism of the stents during stenting. The proposed structures exhibit remarkable radial expanding abilities while maintaining axial stability, hence allow practical clinical applications (W. Wu *et al.*, 2018a).

Recently, FEA has been employed for the study of surface auxetic structures (SAS). Changfang et. al. studied two types of SAS- RAS (reversed auxetic structure) and CAS (crimped auxetic structure). FEM was employed to conduct compressive simulations of the plane and surface auxetic structures, and hence obtain the mechanical behaviours and energy absorption characteristics. Through this study, it was deduced that RAS realized the auxetic effect of compression shrinkage as well as the supermechanical effect of compression twist. Such behaviour only appeared in the local positions of the beams giving the structure great potential in engineering applications (Changfang *et al.*, 2022b).

Similar studies such as the one carried by Photiou *et al.* and Su et. al. use FEA in order to study the mechanical performance of the proposed SAS. Photiou *et al.* proposed 3D prototypes SAS, whose compression tests demonstrated a Poisson's ratio of -0.6, thus providing support for preliminary finite element studies on unit cells. 3D finite element models were used to replicate the mechanical performance of the auxetic structures. The obtained results illustrated a coherent deformation behaviour with experimental measurements and image analysis (Photiou *et al.*, 2021). Similarly, Su et. al. investigated 3D printable auxetic metamaterial realized by a unique sliding mechanism, shown in Figure 2.19 (d). Both experimental and FEA simulations were carried out to study the mechanical behaviour of the proposed structure. The FEA results illustrated coherence with the experimental results and the proposed structure exhibited superior performance to the 3D re-entrant honeycomb, due to higher compression resistance and more stable auxetic behaviour (Su *et al.*, 2021).

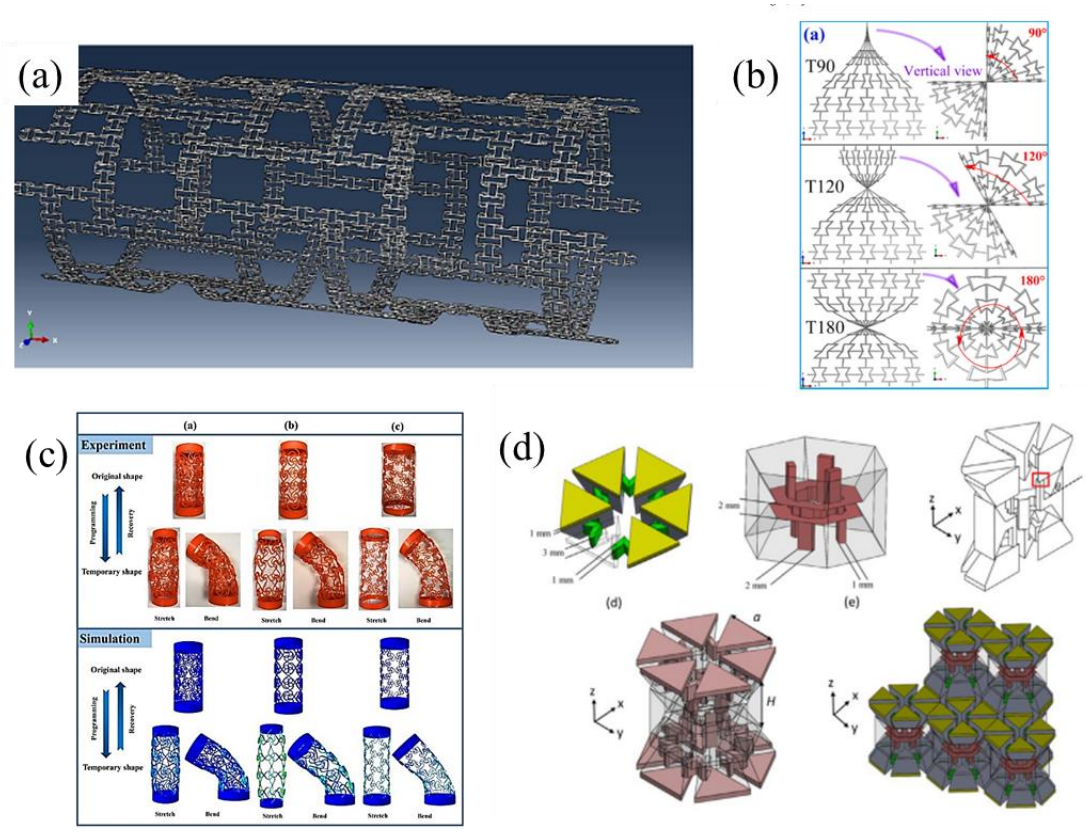

Figure 2.19. Three-dimensional auxetic structures analysed using FEA proposed by; (a) Wu *et al.* (W. Wu *et al.*, 2018a) (b) Changfang *et al.* (Changfang *et al.*, 2022b) (c) Wan *et al.* (M. Wan *et al.*, 2022) and (d) Su *et al.* (Su *et al.*, 2021).

Finite Element Analysis (FEA) is not limited to the conventional test parameters and can more accurately simulate a real-life scenario. Thus, FEA has been used to investigate re-entrant hexagonal honeycombs' post-yield behaviour under tension, shown in Figure 2.20(a), which revealed plastic collapse mechanism and identified three stages of force-displacement curves (J. Zhang, Lu, Wang, *et al.*, 2018b).

FEA has been particularly useful in investigating complex structures such as the proposed hierarchical re-entrant honeycombs (H-ReHs) that exhibit enhanced mechanical properties under compression. The analysis of the deformation to compressions showed that the addition of a 2nd order triangular hierarchy converts the deformation mechanism from bending-dominated to stretching-dominated, shown in Figure 2.20(c), revealing a

unique combination of deformation mechanisms contributing to significant improvement of the mechanical properties of H-ReHs (Zhan *et al.*, 2022). Furthermore, through FEA, a study examined the size effect of mechanical properties for a double-arrowed auxetic honeycomb (DAAH) using a bending energy-based method and a strain-based expansion homogenization method (T. Wang *et al.*, 2022).

Additionally FEA has been applied to a wide range of materials, including composite structures like carbon fibre reinforced polymer(Z. Y. Li *et al.*, 2022), composite origami cellular materials(Z.-Y. Li *et al.*, 2023) and cementitious composites (Lyngdoh *et al.*, 2022). The latter implemented a FEA-based machine learning to generate accurate predictions of auxetic behaviour in cementitious composites (Lyngdoh *et al.*, 2022). Crespo, Duncan, Alderson, & Montáns developed a continuum-equivalent data-driven computational approach for modelling orthotropic auxetic foams in a finite element context. The approach involves resolving a system of functional equations using experimental tests as functional data and energy derivatives as unknowns, depicted in Figure 2.20(b). The algorithms are verified using analytical energies as a reference, and experimental validation from a real specimen is performed. The method is computationally efficient and capable of capturing auxetic behaviour in orthotropic foams (Crespo *et al.*, 2020).

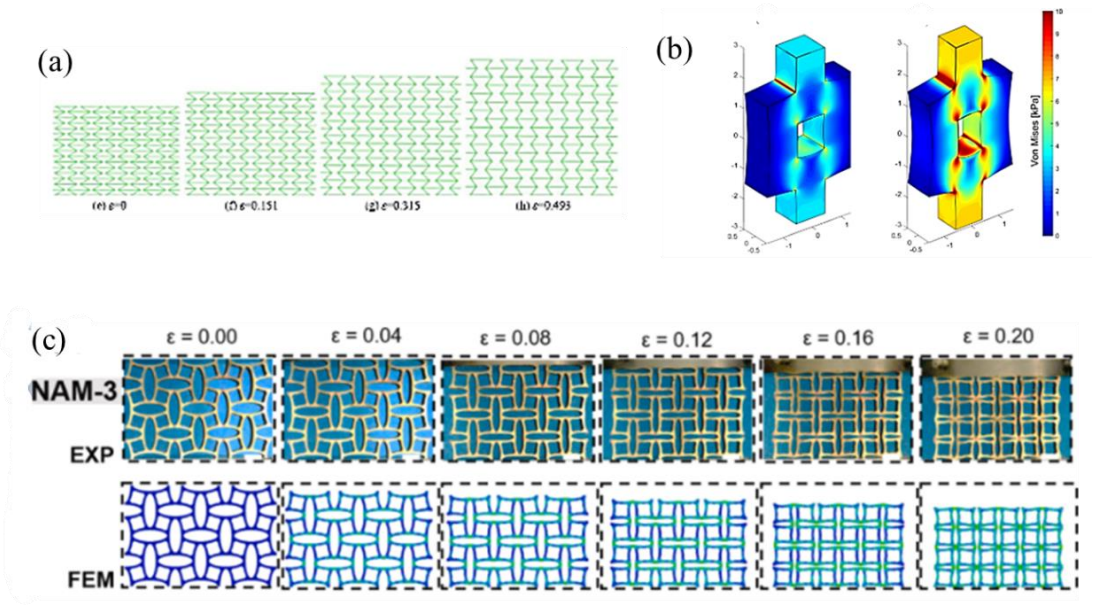

Figure 2.20. (a) The investigation of re-entrant honeycombs under tension by Zhang *et al.* (J. Zhang, Lu, Wang, *et al.*, 2018b) (b) Analysis of energy density by Crespo *et al.* (Crespo *et al.*, 2020) (c) Analysis of deformation mechanisms by Zhan *et al.* (Zhan *et al.*, 2022).

2.2.3 Design of Products

Finite Element Analysis excels at replicating testing scenarios and analysing the behaviour of the material in that particular scenario. Thus, FEA is not limited to the conventional lab testing but can be used to replicate the conditions in which the product is meant to perform and observe the response. In the construction industry, Menon *et al.* used FEA to observe the deflection behaviour of existing auxetic re-entrant beams compared with traditional beam designs, shown in Figure 2.21(a), and proposed two new improved auxetic beam designs with minimal deflection, improved load bearing capacity and 64% reduction in material (Menon *et al.*, 2022). Another study also used FEA to investigate auxetic hexagonal honeycomb sandwich panels for structural application due to the weight reduction provided, shown in Figure 2.21(b) (Sadegh *et al.*, 2018). In a number of studies, FEA was also implemented to replicate loading conditions of a passenger vehicle to investigate auxetic non-pneumatic tyres having different structures

such as the example shown in Figure 2.21(c) (Andriya *et al.*, 2022; T. Wu *et al.*, 2021; Zang *et al.*, 2021). FEA has also been used in the design of anti-tetrachiral stent and hierarchical anti-tetrachiral stent with circular and elliptical nodes. Through FEA the effects of stent geometrical parameters on the tensile mechanical behaviour of these stents were studied (Wu *et al.*, 2018).

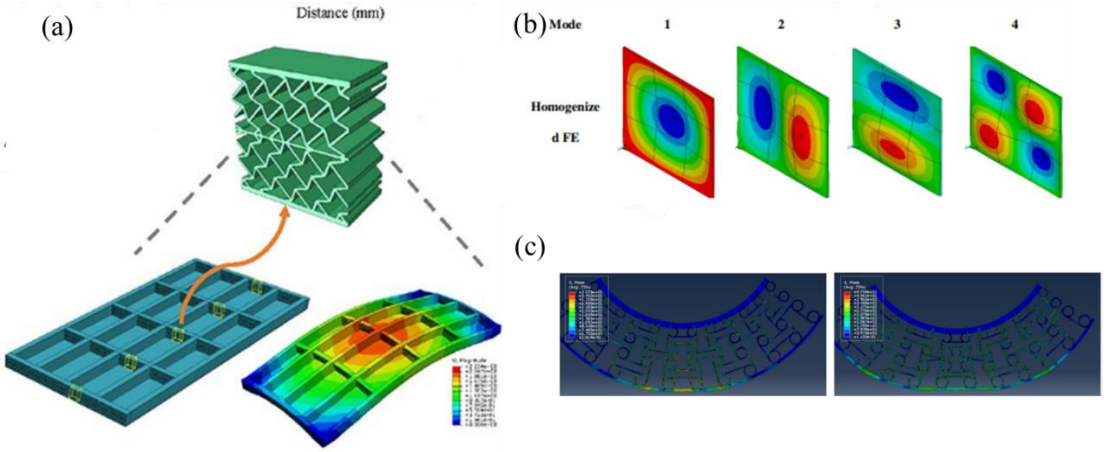

Figure 2.21. Products designed by (a) Menon *et al.* (Menon *et al.*, 2022), (b) Sadegh *et al.* (Sadegh *et al.*, 2018) and (c) (K. Wu *et al.*, 2022) with the aid of FEA.

Given the mimicking of high impacts, with adjustable impact velocities, indents and more, finite element modelling has also been used to facilitate and explore the use of auxetics in military and sports equipment. FEA has already been used to predict material and product behaviour under certain conditions and analyse design parameters in snowboard wrist protectors (Newton-Mann *et al.*, 2018), helmets (Foster *et al.*, 2018; Hernández *et al.*, 2003; Mosleh *et al.*, 2018), and other sports equipment (Allen *et al.*, 2009; Kays & Smith, 2017; Valentini *et al.*, 2016), an example of which is shown in Figure 2.22(a). Within this context, FEA has been used to investigate the effects of unit-cell geometry and Poisson's ratio on mechanical properties in auxetic structures and plates, and to analyse the potential of auxetic constituents in composite materials, similar

to the analysis shown in Figure 2.22(b) comparing the FEA and experimental analysis (Nallavan, 2020; Shepherd *et al.*, 2020).

A number of studies also investigated the ballistic impact behaviour of auxetic material. In the study by Novak, chiral auxetic cellular structures are tested and the effect of ballistic velocity and deformation behaviour of composite sandwich panels, shown in Figure 2.22(c), are evaluated. The experimental results are used for validation of the computational model of cover plates, which is further used for the development of computational models of auxetic composite sandwich panels. The study shows that by using the auxetic sandwich panel, the ballistic performance is enhanced in comparison to the monolithic cover plates (Novak *et al.*, 2019). A recent study analysed the ballistic impact behaviour of auxetic sandwich composite human body armour using finite element analysis. Numerical simulations showed improved indentation resistance and higher energy absorption in the auxetic armour compared to conventional monolithic armour (Shah, Khan, Koloor, *et al.*, 2022). Similar auxetic sandwich panel were also considered for blast protection in military vehicles. The results show that the auxetic sandwich panel performs better in terms of both lightweight and protection than a solid plate and has an advantage in lightweight aspect compared with a square honeycomb core sandwich panel (Y. Wang *et al.*, 2018). Similarly, other studies also investigated the use of auxetics in body protection pads (C. Yang *et al.*, 2020)

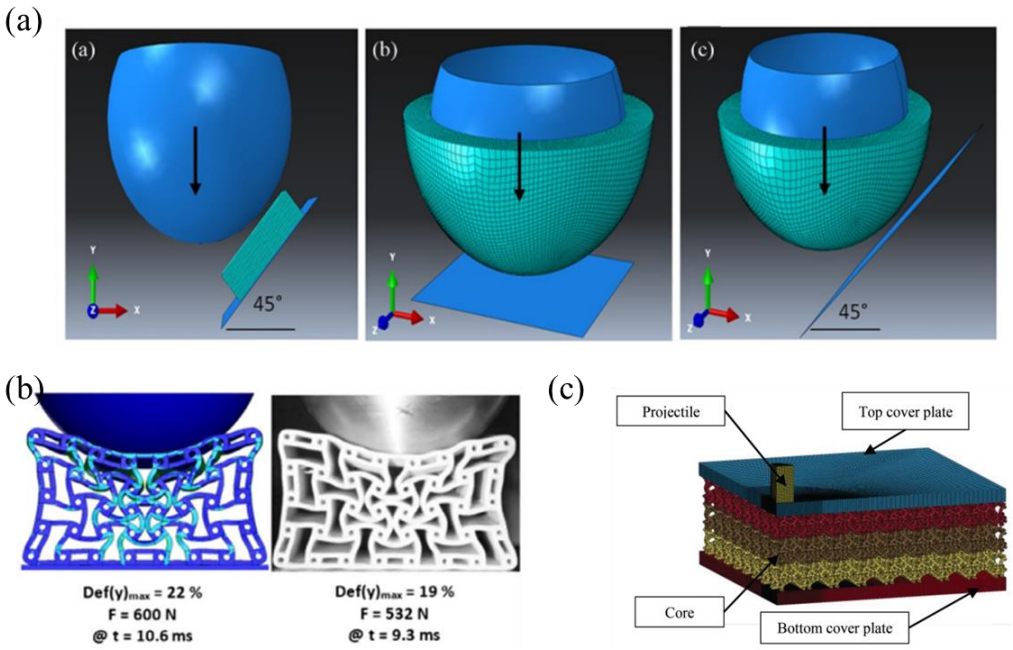

Figure 2.22. The use of FEA in prototyping (a) helmets (Mosleh *et al.*, 2018), (b) sport equipment (Shepherd *et al.*, 2020) and (c) ballistic armour (Novak *et al.*, 2019)

2.2.4 Conclusion

In conclusion, over the years FEA has played a significant role in the study of auxetic materials. Through the use of FEA, researchers are able to model and simulate a wide variety of structures to determine their mechanical properties prior to experimental testing. FEA provides a quick and reliable analysis during the design stages, reducing the need for physical prototypes and accelerating advances in the field. Over the years, FEA has been adopted by a number of research fields and has become an essential tool in the study of mechanical properties of materials. With the availability of commercially available software and high computational power, FEA continues to play a vital role in the study of auxetic materials and other research areas.

2.3 Perforated auxetics

The perforated sheet model, proposed by Grima and Gatt (J. N. Grima & Gatt, 2010), is a model which allows a conventional material to exhibit 2D auxetic behaviour through perforations at strategic loci. In their work, diamond (J. N. Grima & Gatt, 2010), triangle (J. N. Grima, Gatt, *et al.*, 2010) and star-shaped (J. N. Grima & Gatt, 2010; J. N. Grima, Gatt, *et al.*, 2010) perforations were performed strategically to mimic the rotating rigid squares, rectangles and triangles models. Using FEA, the structures were shown to achieve an NPR comparable to the conventional rotating rigid units when the parameter *s*, shown in Figure 2.23, was relatively small.

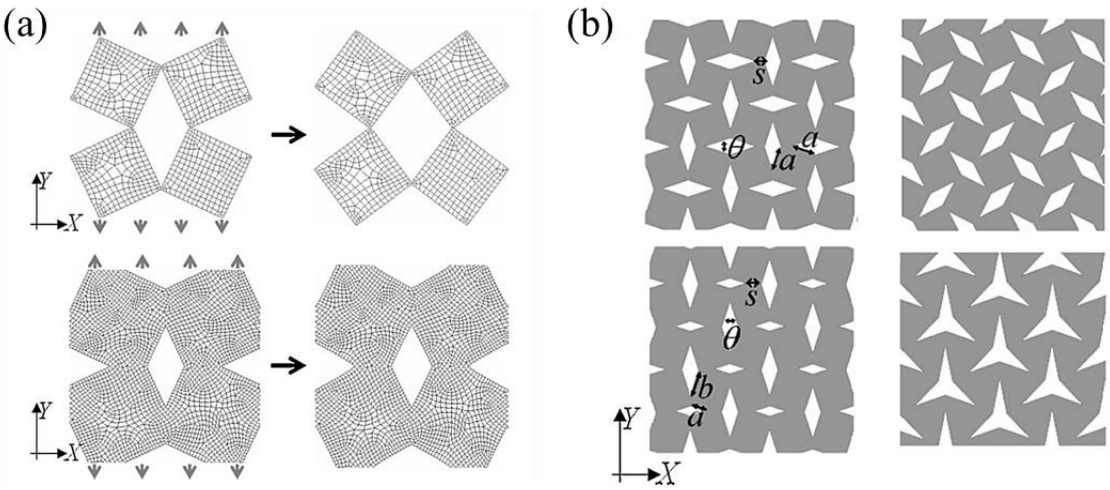

Figure 2.23.(a) A comparison between the rotating rigid squares mechanism and the perforated model mimicking it. (b) Perforated sheets employing diamond and star-shaped perforations to mimic the rotating rigid squares, triangle, and rectangles systems. All images were taken from Grima and Gatt (J. N. Grima & Gatt, 2010).

The simplicity with which the perforated auxetic structures can be produced has revolutionised the production of 2D auxetic metamaterials from conventional materials. In fact, to date; at least forty-four publications have been published describing a wide range of perforated 2D auxetic systems. Studies have investigated the use of a range of perforation shapes, comprising star (J. N. Grima & Gatt, 2010; J. N. Grima, Gatt, *et al.*,

2010; Mizzi, Mahdi, *et al.*, 2018), triangular (J. N. Grima & Gatt, 2010; J. N. Grima, Gatt, *et al.*, 2010), diamond (rhombus)(Attard *et al.*, 2016; Bonfanti & Bhaskar, 2019; Y. Chen & He, 2020; Mizzi *et al.*, 2021; Mohanraj *et al.*, 2016; Y. Zhang *et al.*, 2022), circular and elliptical(Francesconi *et al.*, 2020; Galati *et al.*, 2022; D. Han, Ren, *et al.*, 2022; Hao *et al.*, 2022; Harinarayana, 2022; Harinarayana & Shin, 2022; F. Hou *et al.*, 2021; Linforth *et al.*, 2021; Mizzi *et al.*, 2021; Mullin *et al.*, 2007, 2013; Nedoushan & Yu, 2020; Orhan & Erden, 2022; X. Ren, Shen, *et al.*, 2018; Shim *et al.*, 2013; M. Taylor *et al.*, 2014; Tikariha *et al.*, 2022; H. Wang, Xiao, & Wang, 2021; H. Wang, Xiao, & Zhang, 2021; Yeon *et al.*, 2021; Y. Zhang *et al.*, 2021, 2022), rectangular (Gordanshekan *et al.*, 2022; X. Ren, Shen, *et al.*, 2018; Ripplinger *et al.*, 2018; Slann *et al.*, 2015; Tian *et al.*, 2020; Uddin *et al.*, 2022; Yao *et al.*, 2021; Yeon *et al.*, 2021) and others (Cheng *et al.*, 2022; Sorrentino *et al.*, 2021), leading to systems mimicking the rotating rigid triangles, rotating rigid quadrilaterals and even chiral systems. It is worth noting that studies on circular and elliptical perforation pre-date the development of the perforated sheet model, in investigations of cellular solids and their porous microstructures (Mullin *et al.*, 2007, 2013). The elliptical perforations structure also shares some insight into the essentials of the mechanism as it is not the rigid squares themselves that form the bases of the model but the vertices of the square (Stavric & Wiltsche, 2019). Thus, elliptical, and rectangular perforations allowed for the removal of "non-essential" volume resulting in a lighter and more porous material.

This research has led to applications which were previously simply not feasible and allowed auxetic materials to be seamlessly introduced in existing systems. Through the use of diamond perforations in nylon and short carbon fibre reinforced nylon structures, the previously conventional material having a positive Poisson's ratio yielded an NPR of -1 (Y. Chen & He, 2020) under compression. In fact, despite being a novel

research field introduced in 2010, perforated systems have been implemented in existing systems such as the use of diamond perforations in stretched sheets and membranes implemented in order to suppress the wrinkling (Bonfanti & Bhaskar, 2019) (shown in Figure 2.24(d))and as well as end-product applications have comprised designs for nails (X. Ren, Shen, *et al.*, 2018) (shown in Figure 2.24(c)), electronic skin (Yeon *et al.*, 2021) and body support structures (Mohanraj *et al.*, 2016) making use of elliptical and diamond indents.

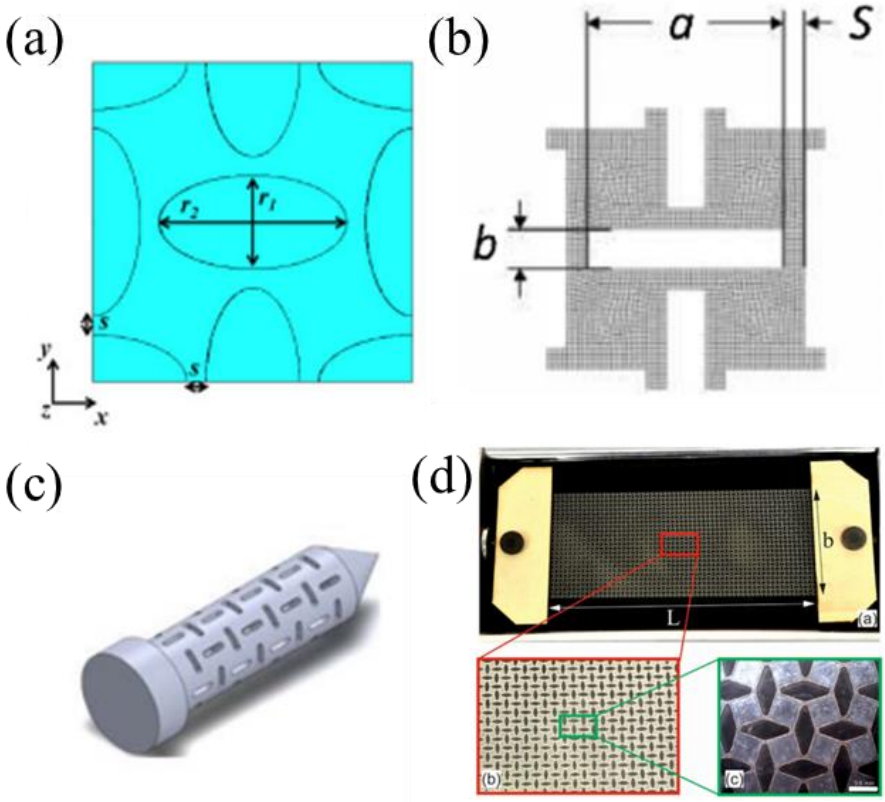

Figure 2.24(a) A proposed perforated system having elliptical indents, image taken from Mizzi *et al.* (Mizzi, Gatt, *et al.*, 2015) (b) A proposed perforated system having rectangular perforations. Image taken from Slann *et al.* (Slann *et al.*, 2015) (c) Application of elliptical indents to design auxetic nails. Image taken from Ren *et al.* (X. Ren, Shen, *et al.*, 2018) (d) Application of rectangular perforations for auxetic membranes. Image taken from Bonfanti and Bhaskar (Bonfanti & Bhaskar, 2019)

The work of Mizzi *et al.* was a major innovation in this field, as it put forward a novel approach using patterned slits (Carta *et al.*, 2016.; Francesconi *et al.*, 2020; Mizzi *et al.*, 2020b, 2020a; Mizzi, Azzopardi, *et al.*, 2015; Shan *et al.*, 2015; Sharma *et al.*, 2019; H. Tang *et al.*, 2020) or I-shaped (Mizzi *et al.*, 2020b, 2020a; Mizzi, Attard, *et al.*, 2018; Mizzi, Azzopardi, *et al.*, 2015; Rafsanjani & Pasini, 2016) perforations to produce systems resembling the 2D re-entrant, chiral, and rotating rigid units mechanisms. Through this method conventional materials have been transformed into auxetic materials through strategic cuts as was the case in the study by Mizzi *et al.* where they introduced patterned nano-slits to create rubber and Kapton metamaterials exhibiting an NPR of − 0.78 through the use of focused ion beam milling (Mizzi *et al.*, 2020a).

Another breakthrough was the proposal of randomly oriented slits in the study by Grima *et al.* shown in Figure 2.25(c). Their use of quasi-random cuts to produce auxetic behaviour (J. Grima *et al.*, 2016) increased the design freedom when generating auxetic materials. In other studies, rectangular (Billon *et al.*, 2016, 2017) and slit perforations (Y. Cho *et al.*, 2014; K. K. Dudek, Gatt, *et al.*, 2017; Y. Tang & Yin, 2017) were used to create 2D hierarchical auxetic systems in order to achieving better compressive and expansive systems while obtaining the enhanced mechanical properties and stability associated with them.

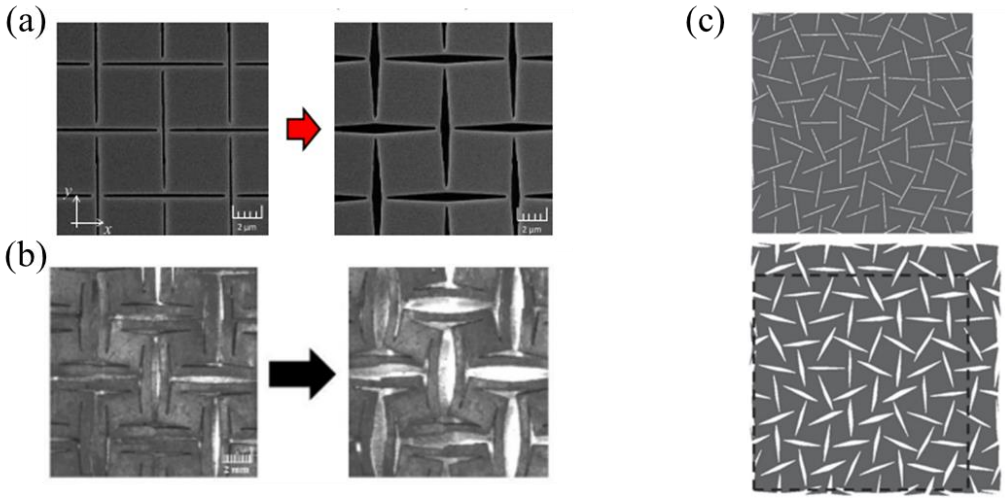

Figure 2.25. Examples of auxetic structures having (a) ordered slits(Mizzi *et al.*, 2020a), (b) I-shaped slits(Mizzi *et al.*, 2020b) and (c) randomly oriented slits (J. Grima *et al.*, 2016)

2.3.1 Active auxetic metamaterials

One of the major limitations of auxetic material is that once manufactured, the mechanical properties of the auxetic metamaterials show a lack of tunability (Montgomery *et al.*, 2020). This limits the use of these materials, where more responsive and adaptable materials with mechanical functionalities beyond those offered by the traditional machines are needed (Lum *et al.*, 2016). To this end, a number of researchers started to investigate shape-programmable metamaterials, i.e. a type of active materials whose geometry can be controlled through specific stimuli such as heat (see Figure 2.26 (b)) (Mohr *et al.*, 2006; Zou *et al.*, 2022), light (see Figure 2.26 (a)) (Lendlein *et al.*, 2005) and magnetic fields (see Figure 2.26 (c)) (K. K. Dudek *et al.*, 2019a, 2020; K. K. Dudek, Gatt, *et al.*, 2018; M. R. Dudek & Wojciechowski, 2008; Fang *et al.*, 2019; J. N. Grima *et al.*, 2013; Jackson *et al.*, 2018; Y. Kim *et al.*, 2018; Lum *et al.*, 2016; Montgomery *et al.*, 2020; Raghunath & Flatau, 2015; Z. Ren *et al.*, 2019; Schaeffer & Ruzzene, 2015b, 2015a; K. Singh *et al.*, 2013; Slesarenko, 2020a; X. Tan *et al.*, 2019; Zou *et al.*, 2022). These materials are capable of providing a more precise and finer control needed in

certain applications (Q. Li *et al.*, 2017; Lum *et al.*, 2016; Montgomery *et al.*, 2020; Scarpa, 2008; S. L. Zhang *et al.*, 2017).

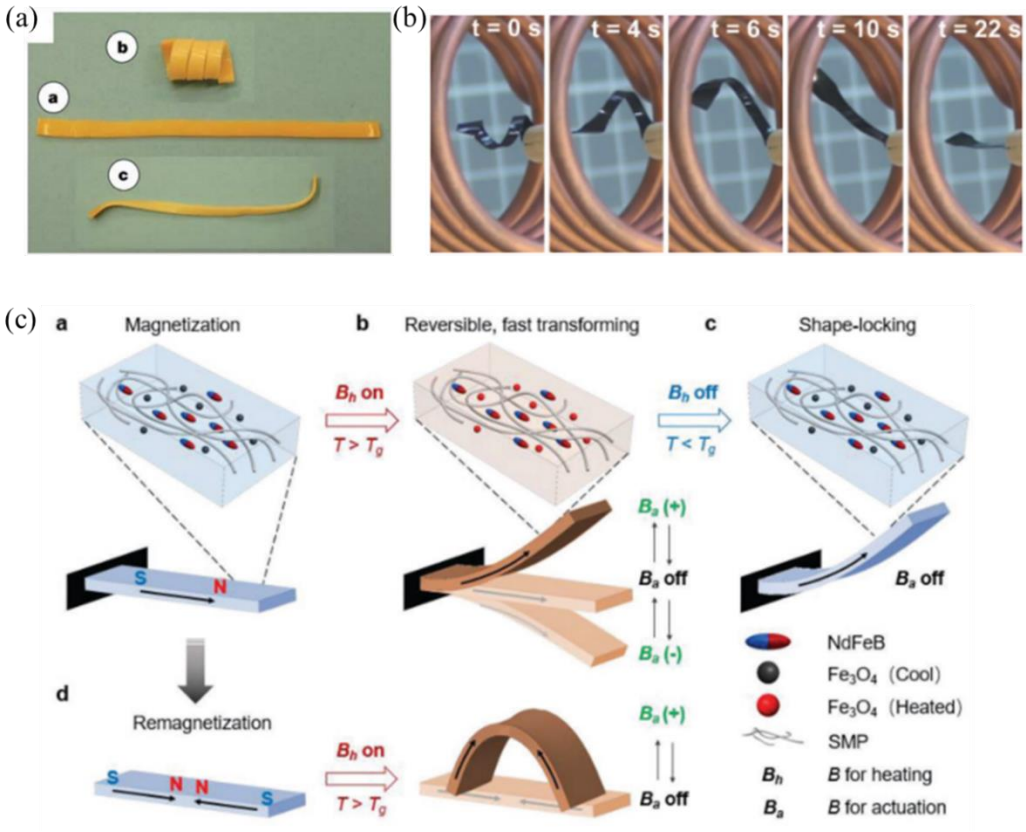

Figure 2.26. Shape-programmable materials which geometry can be manipulated via (a) light (Lendlein *et al.*, 2005),(b) heat (Mohr *et al.*, 2006) and (c) magnetic fields.

2.3.2 Magneto-mechanical metamaterials

One promising class of shape-programmable materials is that of magnetically actuated materials, as their shape can be manipulated not only through the magnitude of the external stimulus, but also through its direction and spatial gradient as well as by the internal interactions between magnetic inclusions (K. K. Dudek *et al.*, 2019a; M. R. Dudek & Wojciechowski, 2008; J. N. Grima *et al.*, 2013; Jackson *et al.*, 2018; Lum *et al.*, 2016; Schaeffer & Ruzzene, 2015a; Slesarenko, 2020a). Combining the unusual properties of auxetic materials and the control that magnetic systems provide results in a magnetic auxetic material which can be manipulated using magnetism. This has resulted

in the control of stiffness even allowing for “negative” stiffness (K. K. Dudek *et al.*, 2020; K. K. Dudek, Gatt, *et al.*, 2018), controlled changes in shape (M. R. Dudek *et al.*, 2007), as well as enhanced impact resistance(K. K. Dudek *et al.*, 2019a) amongst other properties (Scarpa *et al.*, 2004; Schaeffer & Ruzzene, 2015b, 2015c). Applications of these properties range from adaptable body armour (K. K. Dudek *et al.*, 2019a) and vibration dampers (K. K. Dudek *et al.*, 2020; K. K. Dudek, Gatt, *et al.*, 2018) to and magnetic auxetic systems (K. K. Dudek, Wolak, *et al.*, 2017) such as thin magnetic films used as memory elements in computer technology (see Figure 2.27(b)) (M. R. Dudek & Wojciechowski, 2008).

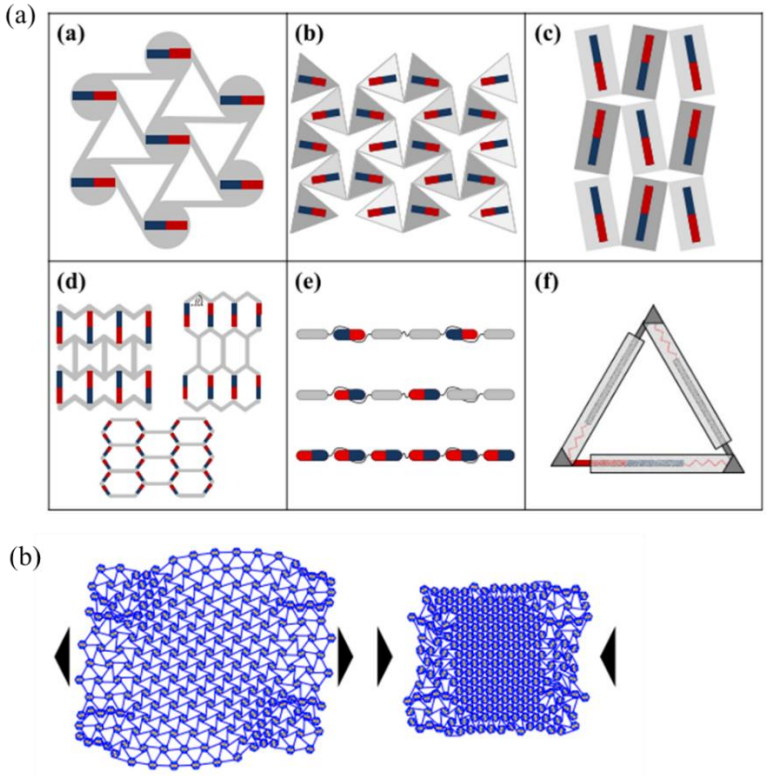

Figure 2.27.(a) Magneto-mechanical materials designs mimicking auxetic systems. (image taken from Grima *et al.*(J. N. Grima *et al.*, 2013). (b) Application of magneto-mechanical materials as memory elements in computer technology (M. R. Dudek & Wojciechowski, 2008).

As the demand for shape-programmable materials has grown, researchers have developed a range of mechanical metamaterials, including magneto-elastic lattices and magneto-mechanical foams (Fang *et al.*, 2019; Raghunath & Flatau, 2015; X. Tan *et al.*, 2019). For instance, Scarpa *et al.* (Scarpa *et al.*, 2004; Scarpa & Smith, 2004), showed that a magneto-mechanical auxetic polyurethane (PU) foam coated in magnetorheological (MR) fluid can have its acoustic absorption coefficient when subjected to magnetic field of constant magnitude, see Figure 2.28(a). Other studies have focused on magneto-mechanical metamaterials able to undergo a reconfiguration under an external magnetic field (Jackson *et al.*, 2018; Lum *et al.*, 2016; Montgomery *et al.*, 2020; Z. Ren *et al.*, 2019; K. Singh *et al.*, 2013), with one of the more notable examples being the work by Kim *et al.* (Y. Kim *et al.*, 2018) where 3D-printed soft structures were built using composite ink with ferromagnetic particles (see Figure 2.28(b-c)). In the work by Kim and co-workers, magnetisable inclusions were embedded in a rubber matrix to create printed auxetic structures which were shown to shrink in response to an external magnetic field. A different approach was taken in the work by Tipton *et al.* (Tipton *et al.*, 2012), where rare-earth magnets were embedded into elastomers. The composite structures proposed in their work were designed to exhibit a coupled twist-buckle behaviour when subjected to large magnetic fields. Other studies investigated structures composed or rigid constituents. For example, Grima *et al.* showed that auxetic behaviour of the rotating squares system can be controlled via an external magnetic field when magnets are placed in the rigid squares themselves (J. N. Grima *et al.*, 2013). The control over the deformation of different other rigid and semi-rigid mechanical lattices with magnetic inclusions was also demonstrated in other studies (K. K. Dudek *et al.*, 2020; K. K. Dudek, Gatt, *et al.*, 2018; J. N. Grima *et al.*, 2013; Schaeffer & Ruzzene, 2015b).

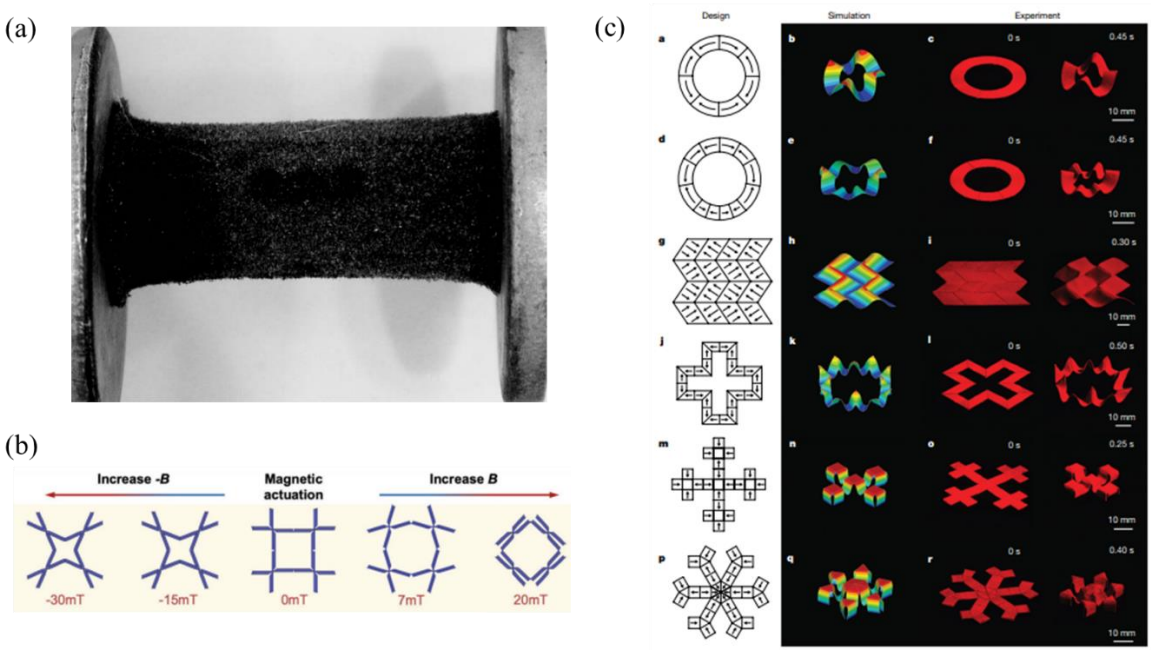

Figure 2.28.(a) PU foam coated in MR fluid proposed by Scarpa *et al.* (Scarpa *et al.*, 2004; Scarpa & Smith, 2004), (b) A depiction of the response of a magneto-mechanical metamaterial to magnetic field of different order and direction. (image taken from Montgomery *et al.* (Montgomery *et al.*, 2020)) (c) Magneto-mechanical metamaterials printed with ferromagnetic composite ink to create magnetically actuated auxetic materials (Image taken from Kim *et al.* (Y. Kim *et al.*, 2018))

Magneto-mechanical metamaterials can also produce unusual mechanical and other types of behaviour that would usually not be possible for similar structures without magnetic inclusions. A very interesting example of this concept is described in the work by Hewage *et al.* (Hewage, Alderson, Alderson, & Scarpa, 2016), where it was shown that a specific quasi two-dimensional mechanical metamaterial composed of hexagonal subunits with magnetic inclusions, as shown in Figure 2.29(c), can exhibit auxetic behaviour and negative stiffness at the same time. This concept was also observed for other quasi two-dimensional magneto-mechanical metamaterials (K. K. Dudek, Gatt, *et al.*, 2018; K. K. Dudek, Wojciechowski, *et al.*, 2018; Slesarenko, 2020a) and extended to three-dimensional structures (K. K. Dudek *et al.*, 2020) , as shown in Figure 2.29(a), something that is particularly important from the point of view of potential applications.

It was also reported that auxetic magneto-mechanical metamaterials can exhibit enhanced wave attenuation (Schaeffer & Ruzzene, 2015a, 2015b) as well as impact resistance (K. K. Dudek *et al.*, 2019b) in the case of a collision with an external body, where these results may lead to the design of superior damping and protective devices. It is also worth noting that magneto-mechanical metamaterials also have a lot of potential at the nanoscale where they can be used to control the magnetic domain evolution(M. R. Dudek *et al.*, 2019; Raghunath & Flatau, 2015) which in turn can result in a strong magneto-caloric effect which may prove to useful in the case of refrigeration technologies.

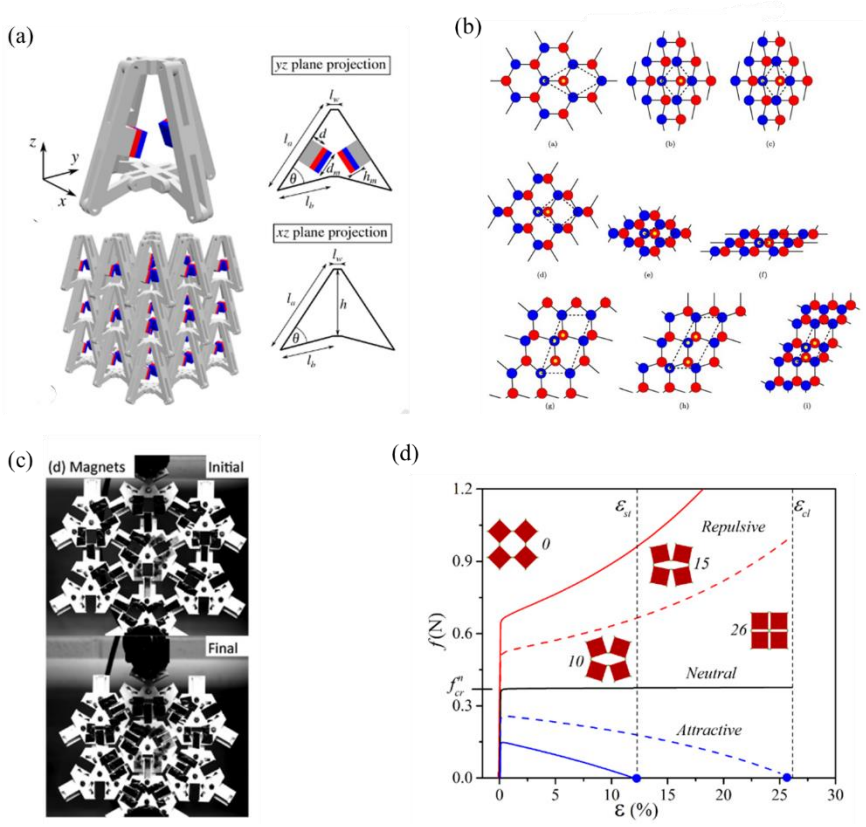

Figure 2.29.(a) A three-dimensional auxetic material with magnetic inclusions, proposed by Dudek *et al.* ((K. K. Dudek *et al.*, 2020) (b) magneto-mechanical lattices proposed by Schaeffer and Ruzzune (Schaeffer & Ruzzene, 2015b) ,(c) A magneto-mechanical metamaterial proposed by Hewage *et al.* which could exhibit negative stiffness and had a negative Poisson's ratio (Hewage, Alderson, Alderson, Scarpa, *et al.*, 2016). (d) A force-strain curves for the magneto-mechanical metamaterial proposed by Slesarenko (Slesarenko, 2020)

Shape-programmable materials have been shown to excel in miniature devices, a few centimetres in size, as it was demonstrated that the locomotion and manipulation capability exceeded their machined counterparts (Bartlett *et al.*, 2015; Frenzel *et al.*, 2017; Novelino *et al.*, 2020). The concept of functionalised miniature devices has a lot of potential amongst others in bioengineering, microfactories and healthcare.

2.4 Conclusion

In the literature review, the most significant research in the field of auxetics and active auxetic metamaterials are highlighted with a particular emphasis on perforated auxetics, 3D auxetic structures and magnetically actuated metamaterials. 3D auxetic structure have shown potential in a number of applications due to their enhanced properties such as high energy absorption, impact and indentation resistance and synclastic properties. Similarly, magnetically actuated metamaterials have also gained increased attention due to their ability to respond to a magnetic stimulus by tuning their geometry and/or mechanical properties which is advantageous in a wide range of applications benefitting from responsive smart materials. Both these fields are still at their infancy and research has to investigate their properties and manufacturing techniques (Novak *et al.*, 2016).

Scope

As detailed in the literature review, there has been a significant advance in the research of novel materials over the past few decades particularly in the field of mechanical metamaterials. Various studies have explored their distinctive mechanical properties, leading to the potential introduction of new advanced materials into the market.

The advent of additive manufacturing via 3D printing has given rise to the design and production of more complex 3D auxetic materials which exhibit an NPR in multiple directions. As discussed in Chapter 2, researchers have successfully produced and characterised a number of 3D auxetic structures. The enhanced properties of auxetic metamaterials have also led to the evolution of the concept of active metamaterials whereby researchers have sought to develop auxetic materials with tunable properties post fabrication. These novel materials are revolutionising the materials science research field by combining the desirable properties in auxetic materials and the responsive and adaptable nature of active materials. Of particular importance is the research on magnetically actuated metamaterials due to their ability to respond to the magnitude and direction of the magnetic field. These materials have been posed to replace traditional machines especially in the fields of soft robotics and biomedical devices especially in miniature devices where the lightweight, untethered, and fine motion of magnetically actuated metamaterials would be advantageous (see Section 2.3.2).

However, despite the advances in auxetic metamaterials research, the research on 3D auxetic metamaterials is still in its infancy. New 3D auxetic structures are constantly being proposed and studied. Similarly significant research is required is in the field of active metamaterials specifically magnetically actuated metamaterials, which is a very new concept and further research is required to fully explored the possible structures that may arise from combining the research fields of active materials and auxetic metamaterials.

In view of the above, this thesis aims: (1) **to propose 3D systems having continuous voids of constant cross-sectional area and investigate them *vis-à-vis* their potential to exhibit a negative Poisson's ratio** and (2) **to design, produce and investigate active magneto-mechanical metamaterials which are able to respond to an external magnetic field**. In order to achieve these aims, the following objectives will be addressed.

- Design 3D systems through the use of diamond-shaped continuous voids, that are capable of exhibiting a 3D auxetic mechanism.
- Investigate through numerical and experimental studies how changes in the relative sizes of the diamond voids and their separation effects the mechanical properties of these 3D auxetic systems.
- Study numerically and experimentally how changes in the shape of the cross-sectional area of these voids effects the mechanical properties of these 3D auxetic systems.
- Design an accordion-like system having magnetic inclusions to produce a magnetically actuated material and investigate dependant parameters.
- Extending the basic unit of the accordion-like system to create multi-layered auxetic systems with tunable geometries.

- Extend the concept of the accordion-like system to an ‘egg-rack’-like geometry to investigate the possibility of having an active 3D auxetic geometry.
- Investigate the effect of using elastic composites having iron nanoparticle inclusion *in lieu* of permanent magnets.

Chapter 3 : 3D Perforated Systems using diamond-shaped perforations[1]

Highlights

- In this chapter, a novel design method is proposed where 3D auxetic metamaterials can be produced by introducing continuous voids of constant cross-sectional area.
- Such voids would be inserted at strategic positions in different perpendicular planes of a solid block to obtain a continuous three-dimensional mechanical metamaterial that can exhibit the desired mechanical characteristics.
- The use of continuous voids to design the 3D metamaterial makes it possible to use a number of manufacturing methods including 3D printing additive manufacturing, subtractive manufacturing as well as casting to produce these systems.
- The resulting group of structures can be described as connected polygons and were found to have the potential to exhibit a negative or zero Poisson's ratio.
- The analysed systems were found to have a strain independent Poisson's ratio up to at least 7% strain.

3.1 Introduction

A significant advancement in auxetic research was attained with the development of 3D systems that are capable of exhibiting an NPR behaviour in at least two planes that are orthogonal to each other i.e., 3D auxetic systems. As discussed in Chapter 2, one such

[1] This chapter has been published in Galea, R., Farrugia, P. S., Dudek, K. K., Attard, D., Grima, J. N., & Gatt, R. (2023). A novel design method to produce 3D auxetic metamaterials with continuous pores exemplified through 3D rotating auxetic systems. Materials & Design, 111596. **(Impact Factor 9.417)**

system is the three-dimensional rotating rigid cuboids structure proposed by Attard and Grima (Attard & Grima, 2012) and later expanded by Kim *et al.* (J. Kim *et al.*, 2017). Manufacturing of such 3D systems is quite challenging, however, with the recent evolution of additive manufacturing the fabrication of 3D auxetic metamaterials has been made more accessible. In fact, additive manufacturing is possibly one of the best fabrication methods for such structures, notwithstanding the number of challenges this technique presents, which include production time, void formation, anisotropic microstructure, and mechanical properties (Ngo *et al.*, 2018).

However, additive manufacturing is not the only method that has been useful to produce auxetic structures. In fact, subtractive manufacturing has been successfully employed for the fabrication of 2D auxetic metamaterials, as discussed in detail in Chapter 2. It has been the focus of extensive research in recent times (Attard *et al.*, 2016; J. Grima *et al.*, 2016; J. N. Grima, Gatt, *et al.*, 2010; Linforth *et al.*, 2021; Mizzi *et al.*, 2021; Nedoushan & Yu, 2020; Scarpa *et al.*, 2004; Slann *et al.*, 2015; H. Wang, Xiao, & Zhang, 2021; Yao *et al.*, 2021) due to the ease and simplicity with which 2D auxetic structures can be produced. Various perforation shapes have been adopted to re-create known 2D auxetic structures(A. Alderson, Alderson, Attard, *et al.*, 2010; Attard, Manicaro, & Grima, 2009b; Chetcuti *et al.*, 2014; K. K. Dudek, Gatt, *et al.*, 2017; Evans *et al.*, 1995; J. N. Grima & Evans, 2000c, 2006; J. N. Grima, Gatt, *et al.*, 2005; Masters & Evans, 1996; Mizzi, Attard, *et al.*, 2018; Prall & Lakes, 1997), including star, diamond (rhombus), elliptical, rectangular, and hexagonal ones, leading to systems mimicking the rotating rigid triangles (J. N. Grima, Gatt, *et al.*, 2010; G. Wu *et al.*, 2015), rotating rigid quadrilaterals (Attard *et al.*, 2016; Bertoldi *et al.*, 2010; J. Grima *et al.*, 2016; J. N. Grima & Gatt, 2010; Mizzi, Azzopardi, *et al.*, 2015; Slann *et al.*, 2015; M. Taylor *et al.*, 2014), and chiral systems (Mizzi, Attard, *et al.*, 2018; Mizzi, Mahdi, *et al.*, 2018; Scarpa *et al.*,

2004; Shim *et al.*, 2013; Slann *et al.*, 2015). Notwithstanding the amount of research in 3D auxetics and 2D perforated auxetic systems, to date, no attempt has been made to propose a design method that can be used to produce 3D auxetic metamaterials having continuous voids of constant cross-sectional area. The structures obtained from such a design method can be produced through various methods, including subtractive manufacturing, additive manufacturing, and casting. Such systems would combine the advantages specific to 3D auxetic structures with multiple streamlined production processes, depending on the case. In view of these considerations, a novel design method will be proposed in this study which utilises the application of continuous voids of constant cross-sectional area on different planes of a solid block of material. This process will be exemplified by using continuous voids having a diamond shaped cross-sectional area. It will be shown for the first time that several 3D auxetic metamaterials, having negative or zero Poisson's ratios can be obtained using such diamond shaped voids.

3.2 Concept

3.2.1 Description of the proposed design method used to produce 3D auxetic metamaterials with continuous voids

In this section a description of how auxetic metamaterials may be produced through the proposed novel design method will be given. To achieve this, continuous voids having a diamond shape perforation will be used as an example (see Figure 3.1). For ease of reference, the continuous voids having a constant cross-sectional area will henceforth be referred to as 'perforations'. Referring to Figure 3.1 (a), without loss of generality, starting from a cube made of conventional material, a first set of perforations can be carried out on the *xy* plane using equally sized diamond shaped perforations (i.e., all diamond shaped perforations have equal side lengths). The perforations traverse the

whole length of the material which is orthogonal to the *xy*-plane, i.e., that is aligned along the *z* axis. Once applied, the pattern of perforations is such that the nearest neighbouring rhombi are rotated by 90° with respect to each other, meaning that their longest diagonals are aligned along perpendicular directions. At the same time, the nearest corners of the diamond shaped perforations are separated by an equal distance *s*. This is required to provide spacing material so as to connect the different rigid units. The resultant structure mimics the 2D rotating squares system. Thus, provided that *s* is small enough, the system is expected to show a negative Poisson's ratio in the *xy* plane, but the constituting material Poisson's ratio in the *yz* and *xz* planes.

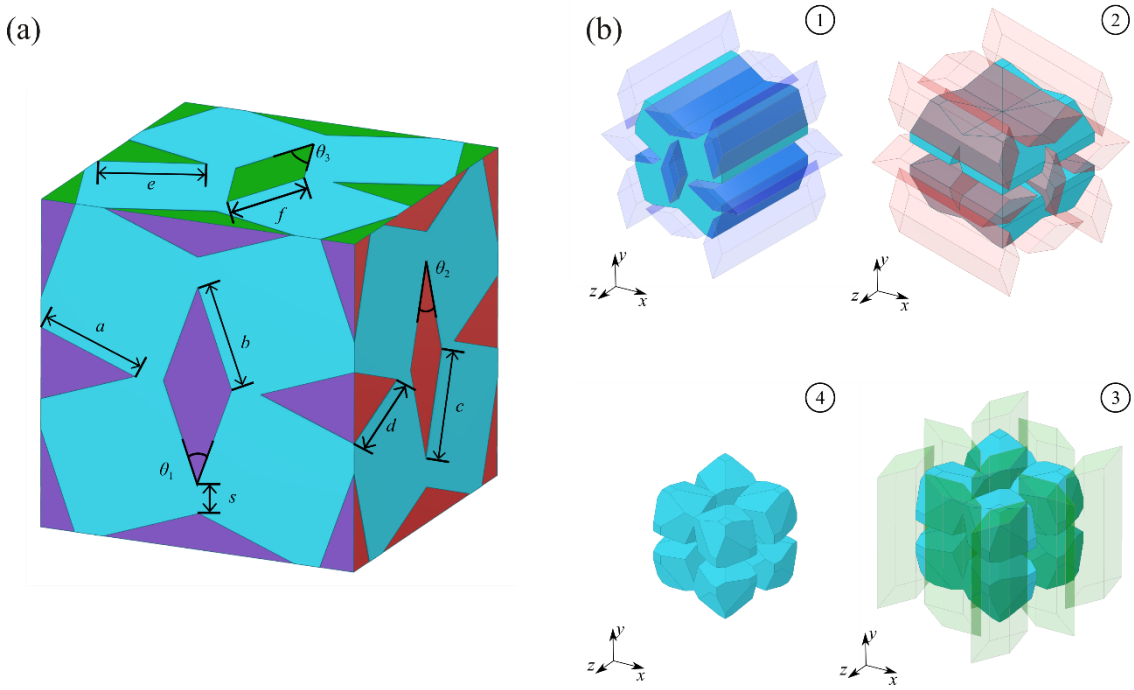

Figure 3.1: (a) The process by which consecutive perforations on different planes are performed (b) A unit cell of the system showing the cross-sectional areas of the continuous columns being removed on each plane.

A second set of analogous perforations can then be performed in the *yz* plane. This will result in a system which has a projected 'rotating squares' geometry in both the *xy* and *yz* planes. It would thus be expected that such a system will exhibit a negative

Poisson's ratio in both planes. To complete the structure, a third set of analogous perforations is performed in the *xz* plane, yielding the 3D polygons system shown in Figure 3.1(b, panel 4). Based on the previous considerations, the resulting system is expected to exhibit a negative Poisson's ratio when loaded in all three planes.

The concept outlined above can easily be extended to one where the diamond shaped perforations are not the same resulting in a cuboidal unit cell shown in Figure 3.2. To do this, diamond perforations having different side length and internal angles need to be used as illustrated in Figure 3.1(a). In this case, it is expected that the Poisson's ratio will depend on the dimensions of the diamond perforations used in each orthogonal plane, meaning that it can vary between planes.

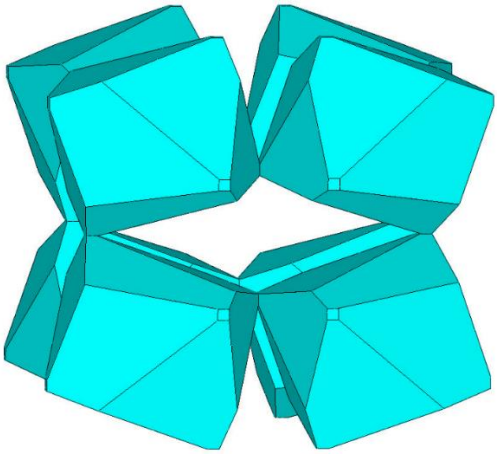

Figure 3.2. 3D perforated system using differently sized diamond perforation.

3.3 Methodology

3.3.1 Geometric considerations of the proposed design method used to produce 3D auxetic metamaterials with continuous voids

In the case of the proposed design method, one must ensure that the perforations performed on one plane do not cut through the material between the different units of another plane as this would result in disjointed parts. The geometric requirements for the

diamond shaped perforations used in this study as an example of the proposed design method are given in this section. The diamond shaped perforations which can be applied to each major plane of a block of material is characterised by the side lengths and internal angles of the diamond/rhombi shaped perforation as well as the separation between the nearest corners of the perforations, *s*. Given the existing relations between the internal angles of a rhombi, only one angle needs to be specified for each plane. This will be referred to as the aperture angle. Considering the simplest case proposed here, whereby all the side length of the rhombi are equal to *a*, and the aperture angle in each plane is also equal, and referenced by θ, the side lengths of the unit cell along the *x*, *y*, and *z* directions are given respectively by:

$$x = y = z = 2\left\{a\left[\cos\left(\frac{\theta}{2}\right) + \sin\left(\frac{\theta}{2}\right)\right] + s\right\} \tag{3.1}$$

The resultant perforated system will henceforth be referred to as the regular 3D perforated system.

In the case that rhombi of different dimensions and internal angles are used, as indicated in Figure 3.1 (a), the side lengths of the unit cell along the *x*, *y*, and *z* directions are given respectively by:

$$x = 2\left[a\cos\left(\frac{\theta_1}{2}\right) + b\sin\left(\frac{\theta_1}{2}\right) + s\right] \tag{3.2}$$

$$y = 2\left[a\sin\left(\frac{\theta_1}{2}\right) + b\cos\left(\frac{\theta_1}{2}\right) + s\right] \tag{3.3}$$

$$z = 2\left[d\cos\left(\frac{\theta_2}{2}\right) + c\sin\left(\frac{\theta_2}{2}\right) + s\right] \tag{3.4}$$

Here, *a* and *b* are the side lengths of the rhombi in the *xy* plane while *c* and *d* are those in the *yz* plane (Figure 3.1 (b)). In addition, θ_1 and θ_2 are respectively the aperture angles in the *xy* and *yz* planes. Geometric analysis shows that the *c*, *d*, and θ_2 are related to each other as well as to the corresponding parameters in the *xy*-plane through the equations,

$$\theta_2 = 2\cos^{-1}\left[\frac{b\cos\left(\frac{\theta_1}{2}\right)}{c}\right] \tag{3.5}$$

$$d = \frac{a\sin\left(\frac{\theta_1}{2}\right)}{\sin\left(\frac{\theta_2}{2}\right)} \tag{3.6}$$

It can be noted from Equation (3.5) that when $c = b\cos\left(\frac{\theta_1}{2}\right)$, the angle θ_2 is equal to zero, implying that no perforations can be made. In practice this sets a minimum value for *c*, as this side length must be larger than $b\cos\left(\frac{\theta_1}{2}\right)$.

In a similar way, the side lengths of the rhombi in the *xz* plane, namely *e* and *f*, and the aperture angle θ_3 are related to the previously defined parameters through the equations,

$$e = \frac{b\sin\left(\frac{\theta_1}{2}\right)}{\sin\left(\frac{\theta_3}{2}\right)} \tag{3.7}$$

$$f = \frac{a\cos\left(\frac{\theta_1}{2}\right)}{\cos\left(\frac{\theta_3}{2}\right)} \tag{3.8}$$

$$\theta_3 = 2\tan^{-1}\left\{\frac{\min\left[c\sin\left(\frac{\theta_2}{2}\right), d\cos\left(\frac{\theta_2}{2}\right)\right]}{a\cos\left(\frac{\theta_1}{2}\right)}\right\} \tag{3.9}$$

where the function "min" returns the minimum of the input values. It should be mentioned that the definition of θ_3 has been chosen so as to prevent the perforations from cutting through the spacing material as this would remove the connection between the different units. This is not the only constraint that is needed to ensure that the geometry is not split up in disjointed parts. Testing has shown that the following relation also needs to hold:

$$f\cos\left(\frac{\theta_3}{2}\right) \leq b\sin\left(\frac{\theta_1}{2}\right) + \frac{b\cos\left(\frac{\theta_1}{2}\right)}{\tan\left(\frac{\theta_1}{2}\right)} \tag{3.10}$$

The constraints mentioned need not be exhaustive of all possible ones. Identifying them would require a thorough investigation of all possible parameter space, something that was considered beyond the scope of the analysis.

The more general system being described here is thus characterised by six lengths (*a, b, c, d, e,* and *f*) and three angles (θ_1, θ_2, and θ_3) leading to a total of nine geometric parameters. In turn, these are related through five equations based on the geometric relations presented above. Hence, only four of the parameters are independent. Without loss of generality, these can be taken to be *a*, *b*, *c* and θ_1. The projections of each plane of the resulting 3D system may be described by Type I rotating rectangles system.

3.3.2 Finite element simulations

3.3.2.1 Pre-processing FEA parameters

To study the mechanical properties of 3D structures produced through the design method proposed in this study, finite element simulations were performed on the 3D structures resulting when using diamond shaped perforations. As explained above, diamond shaped perforations were used as an example of the properties that can be obtained when using this design method. The mechanical properties of the novel 3D perforated systems were investigated using the Finite Element method, using the commercially available software ANSYS® Mechanical APDL Release 13. For the simulations, the symmetry that exists along lines parallel to the principal axes, passing through the middle of the connecting material between the polygons, were availed of. These lines of symmetry exist not only at the edges of the unit cell, but also midway through each side length of the original cuboid. Thus, only one eighth of the unit cell needed to be simulated. A benefit to using a reduced representative volume was a decreased simulation time.

The element type for the simulation was set to SOLID187, this being a higher order 3D element with quadratic displacement behaviour that is able to model both elastic and plastic behaviour, as well as allowing for irregular meshes. For the initial investigation, the Young's modulus was set to 1.1 GPa, while the Poisson's ratio was set to 0.45 (these values were derived from the mechanical properties of plastics in literature).

Symmetry boundary conditions were used for the simulation. In the case of loading in the *x* direction this was attained by applying equal compressive strains on the nodes located on the outer faces aligned perpendicularly to the loading direction as shown in Figure 3.3 as black arrows. The nodes on the face perpendicular to the *y* direction having the minimum value of the *y* coordinate were set to have a zero displacement (depicted by rollers) in the *y* direction whilst those on the opposite side were coupled to move together in the *y* direction with the red boxes indicating coupled nodes. Similar settings were then applied to the nodes on the faces perpendicular to the *z* direction. This allowed the structure to be modelled as an infinite system, with the results providing the bulk properties of the material when loaded in the *x* direction. Inferentially, loading of the *y*, or *z* directions, were thus obtained by interchanging the boundary conditions.

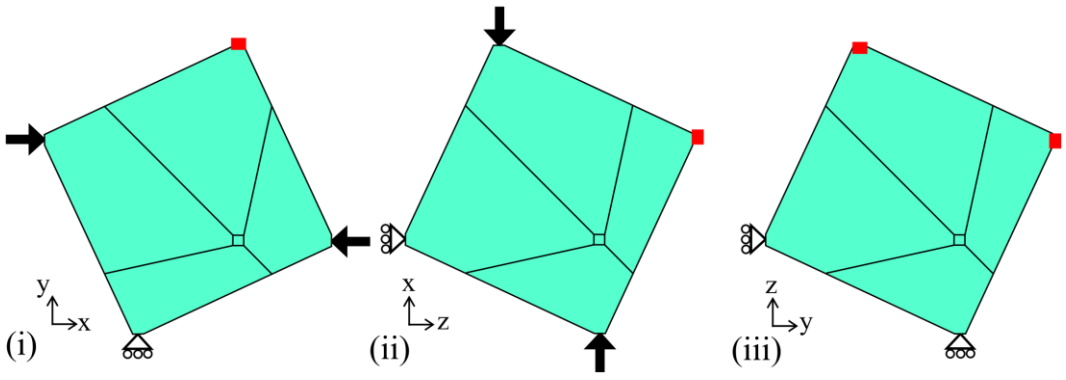

Figure 3.3. A representative drawing of the projections of the 3D perforated system on the (i) *xy*, (ii) *xz*, and (iii) *zy* planes together with the boundary conditions used for loading in the *x* direction.

Prior to performing the simulations, the optimal mesh size had to be determined. This was done to find the right balance between the accuracy of the results and the computational time needed for the solution to be obtained. To this end, eight structures pertaining to the regular 3D perforated system (where a = 10 mm, s = 0.5 mm and θ = 10°, 20°, …, 80°) were analysed using six degrees of increasing mesh refinement. All structures were first meshed using the smart element sizing with the finest mesh configuration. This was followed by a mesh refinement procedure for nodes found at the boundary of the perforations. The mesh refinements which were used are detailed in Table 1 below:

Table 1: Different Levels and Depth use in different sets of mech refinement. The number of elements for the structure with θ = 40°, a = 10 mm and s = 0.5 mm.

Set	*Level*[2]	*Depth*[3]	*Number of elements*
1	0	0	9399
2	1	5	43167
3	2	5	109204
4	3	5	282487
5	4	3	498578
6	5	3	613387

Each set was then compared to the finest mesh (set 6) and their deviations were analysed. The maximum percentage deviation from all computed Poisson's ratio (ν_{xy}, ν_{yx}, ν_{xz}, ν_{zx}, ν_{yz}, and ν_{zy}) and Young's moduli (E_x, E_y and E_z) was used to assess the difference between the generated results.

[2] Amount of refinement to be done
[3] Number of elements to include outward of the selected nodes

3.3.2.2 Parametric analysis using linear simulations.

Initially, a parametric analysis was carried out using linear simulations. The first set of these simulations sought to investigate the relation between the 'degree of openness' of the diamond shaped perforations and the mechanical properties (namely the Poisson's ratios and Young's moduli) of the regular 3D perforated system. For the analysis, the following parameters were used; $a = b = c = 10.0$ mm, $s = 0.5$ mm, while θ was varied between 1° and 90° in increments of 1°.

In the second set of simulations, the effect of s on the mechanical properties of the regular 3D perforated system was investigated. To do so, the following set of parameters was chosen: $a = b = c = 10.0$ mm, s was varied from 0.1 mm to 2.0 mm in increments of 0.1 mm, and angle θ was varied between the values of 10° to 80° in increments of 10°. The third set of simulations considered the more general system. For this case, parameter a was set to 10.0 mm, parameters b and c were varied between 2.0 mm and 20.0 mm in increments of 2.0 mm, s was set at 0.5 mm while angle θ was assigned values from 10° to 80° in increments of 10°. The chosen parameter space allowed the investigation to have the aspect ratios of b/a and c/a span from relatively small to the relatively large values thus encompassing a wide variety of structures. Not all parameter combinations resulted in a tesselatable system due to the constraints mentioned.

From the numerical results obtained, the engineering Poisson's ratio and Young's moduli in all loading directions were derived. Furthermore, the distribution of forces within the material was studied using the strain concentration factor (K_ε) which was defined as:

$$K_{\varepsilon} = \frac{\varepsilon_{\max}}{\varepsilon_{\text{ave}}} \tag{3.11}$$

where $\varepsilon_{\max}$ is the von Mises strain at a specific region and ε_{ave} is the strain applied to the structure.

3.3.2.3 Non-linear Simulations

Based on the analysis of the initial parametric investigation, two structures were identified for further investigation. The first one represented the regular 3D perforated system having dimensions $a = b = c = 4.0$ mm and $\theta = 40°$, while the second one the more general cuboid system having dimensions $a = 4.0$ mm, $b = 4.8$ mm, $c = 4.8$ mm, and $\theta_1 = 40°$. These will be referred to as System I and System II respectively, see Figure 3.4. Non-linear simulations were carried out for these structures with the intention of comparing the results with those of the mechanical testing of physical prototypes. For the purpose, the mechanical properties of the material that was meant to be used for the manufacturing of the prototypes were determined from the mechanical testing of a number of dog bones (see section 3.3.3.1 below).

The Poisson's ratio of the constituting material in the linear region was found to be 0.42 while the Young's modulus was estimated to be 1.52 MPa. Simulations that take into consideration large deflections were then carried out. To do so, the stress-strain results obtained from the dog bones were used as inputs to the hyperelasticity model with the selection of the experimental response function model available in ANSYS APDL. The results could then be compared with those obtained through the mechanical testing of the prototypes.

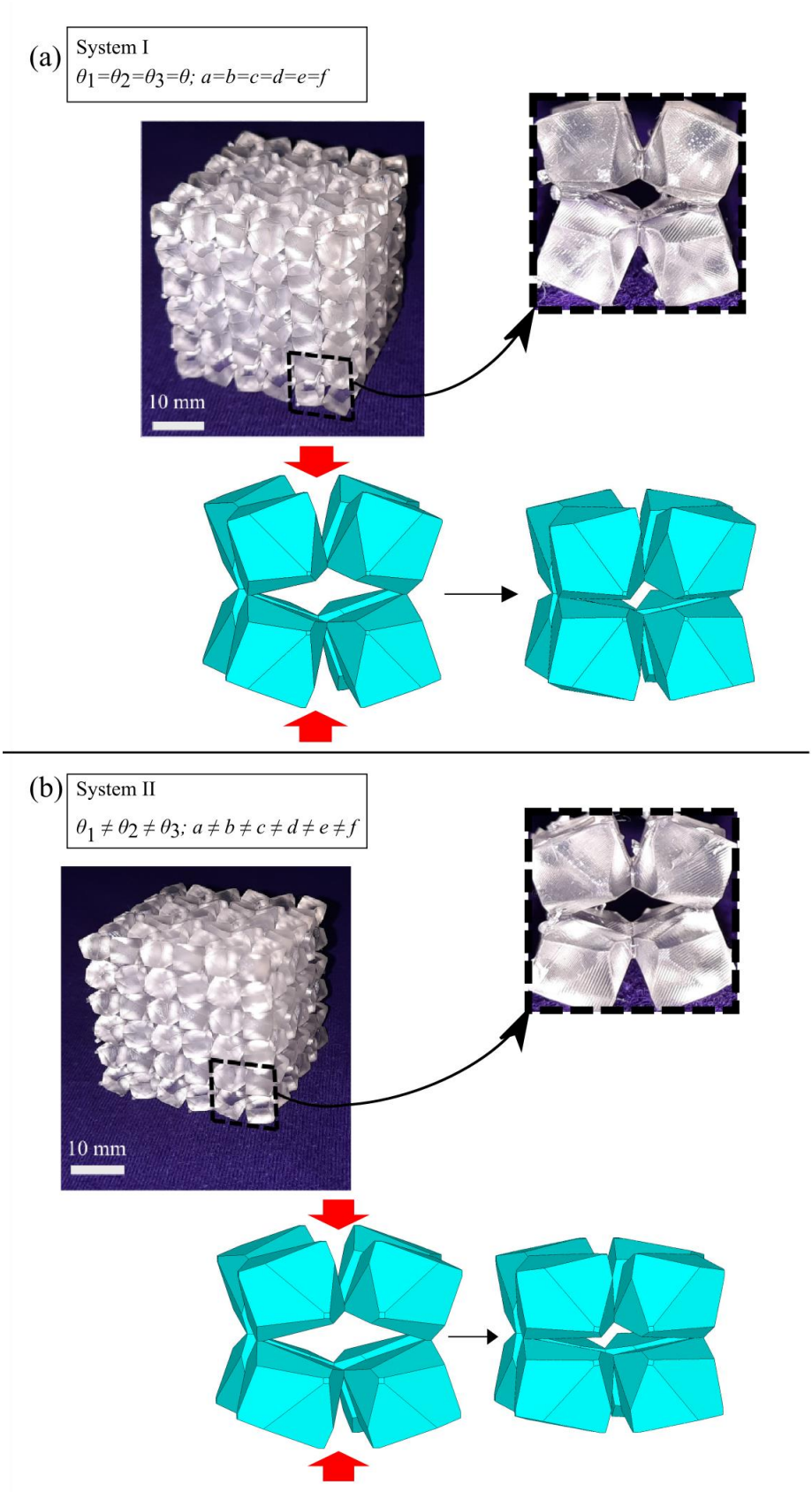

Figure 3.4. A depiction and experimental prototype of (a) System I and (b) System II used in this study.

3.3.3 Experimental method

3.3.3.1 Measuring the mechanical properties of the 3D printing material

As discussed in Section 3.3.2.3, the mechanical properties of the material used to produce the experimental prototypes, three dog bones were 3D printed using the same printer and resin as that adopted for the prototypes. These had a width w = 5.0 mm, a thickness t = 3.0 mm, and a length l = 20.0 mm as shown in Figure 3.5. 3D printing was done by using a Formlabs Form 3 SLA 3D printer using the Elastic 50A resin. The resolution in the *xy* plane was set to 100 µm and a layer thickness of 100 µm was adopted. Once printed the prototypes were washed with isopropyl alcohol (IPA) in the Formlabs Form Wash tank for 10 minutes. The parts were then removed from the build plate and washed once more for 10 minutes. Formlabs Form Cure was then used to cure the prototypes for 20 minutes at 60 °C. The dog bones were loaded under tension using a Testometric universal loading machine (M350-20CT) with a 100 kg load cell (Serial Number: 31931). A 10.0 mm min^{-1} loading rate was used for this analysis. Using a black marker, two sets of two black spots were applied in the axial direction and one set of two black spots was applied in the transverse direction, as illustrated in Figure 3.5. The deformation was recorded with a duly calibrated Messphysik-Videoextensiometer camera. The change in lengths were monitored using the pattern recognition feature found within the videoextensiometer software. This yielded two readings for the axial direction and one reading for the transverse direction from which the Poisson's ratio was then determined. The Young's modulus was calculated using the force displacement data obtained from the universal loading machine.

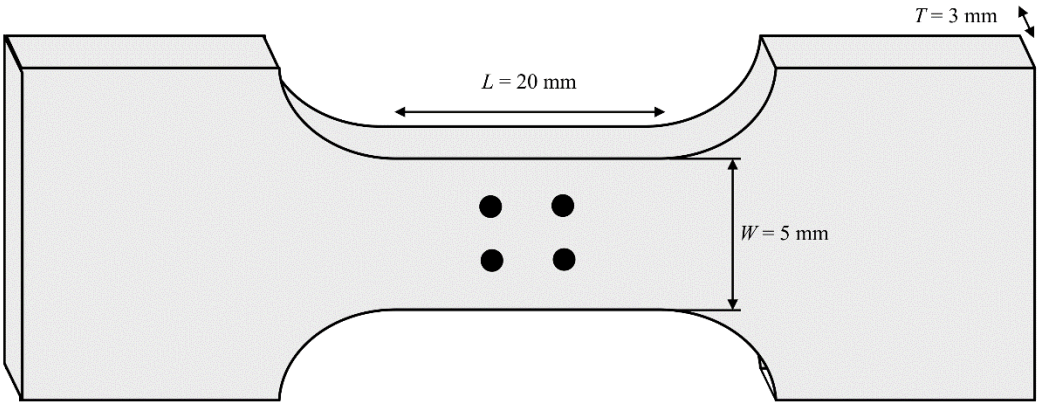

Figure 3.5. Diagram of the dog bone and its dimensions together with the strain-strain and stress-strain plot obtained.

3.3.3.2 Investigation of experimental prototypes

Experimental prototypes of 3D structures obtained by the design method proposed in this study when using diamond shaped perforations were also produced, see Figure 3.4. This was achieved by applying the diamond shaped perforations in-silico and 3D printing the resultant 3D structure, using the same procedure as described in Section 3.3.3.1 above. Once the process was completed, the structure dimensions (parameters *a* and *b*) and the separation between different perforations (parameter *s*) were measured. This was done using a Trinocular Stereo Microscope (HK 1Kins Technology Co Ltd) mounted with a duly calibrated Industrial UHD 4K SONY IMX334 HDMI Measuring Video Camera. One hundred measurements were taken for each parameter considered, from which the average, standard deviation, and distribution were determined.

The prototypes were then loaded under compression using a Testometric universal loading machine (M350-20CT) with a 100 kg load cell (Serial Number: 31931), as shown in Figure 3.6. One set of two black spots were drawn in the axial direction and two sets

of two black spots were drawn in the transverse direction using a black marker. The markings represented the edges of a unit-cell of the system and were used to record the deformations. A compressive strain of circa 7% was then applied at a rate of 10.0 mm min^{-1} on the prototype with the deformation being recorded with a duly calibrated Messphysik-Video extensiometer camera. This yielded one measurement of the change in length in the axial direction and another two for the transverse direction from which the Poisson's ratio was then determined.

Figure 3.6. The experimental setup used to measure the Poisson's ratio and Young's moduli of the experimental prototype.

3.4 Results and Discussion

3.4.1 Mechanical properties for the 3D-printing material used

The data for the dog bones produced using the elastic resin as described in Section 3.3.3.1, is shown in Figure 3.7. The transverse strain against axial strain plot of the material was found to be linear within 50% extension and the value of the Poisson's ratio was found to be 0.42. Meanwhile, the stress against strain plot was found to have a linear region within 7% strain with a resulting Young's modulus of 1.52 MPa.

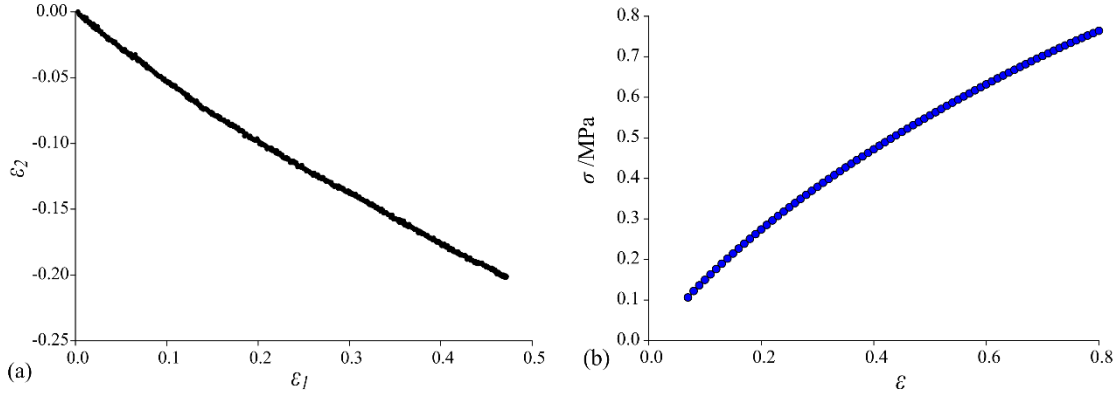

Figure 3.7. (a) The transverse strain against axial strain plot and the (b) the stress against strain plot for Elastic 50A resin as printed using the method described in Section 3.3.3.1.

3.4.2 Mesh-independent analysis

The results of the mesh independence study carried out, indicated that using automatic (smart) element sizing with the finest mesh configuration, followed by a level 4 refinement around boundary nodes up to a depth of three elements inward from these nodes, produced results that were within 1% of those obtained with a finer mesh. It should be noted here that the adopted mesh density required extensive computational resources. In fact, simulating the whole of the unit cell with such a mesh density would not have

been viable. Thus, the use of symmetry considerations to reduce the volume simulated to one eight of the unit cell was, in this case, logistically necessary to obtain the needed results. This is particularly true when considering that in this study 663 simulations were performed.

From the results obtained (see Figure 3.8) it is evident that the first four sets deviate significantly when compared to the finest mesh used. This is especially true for the Young's Modulus. On the other hand, a comparison of set 5 and set 6 shows that the% change between these two sets was of 0.09% and 0.48% for the Poisson's ratio and Young's Modulus respectively. Thus set 5 was deemed to be suitable as it was accurate enough.

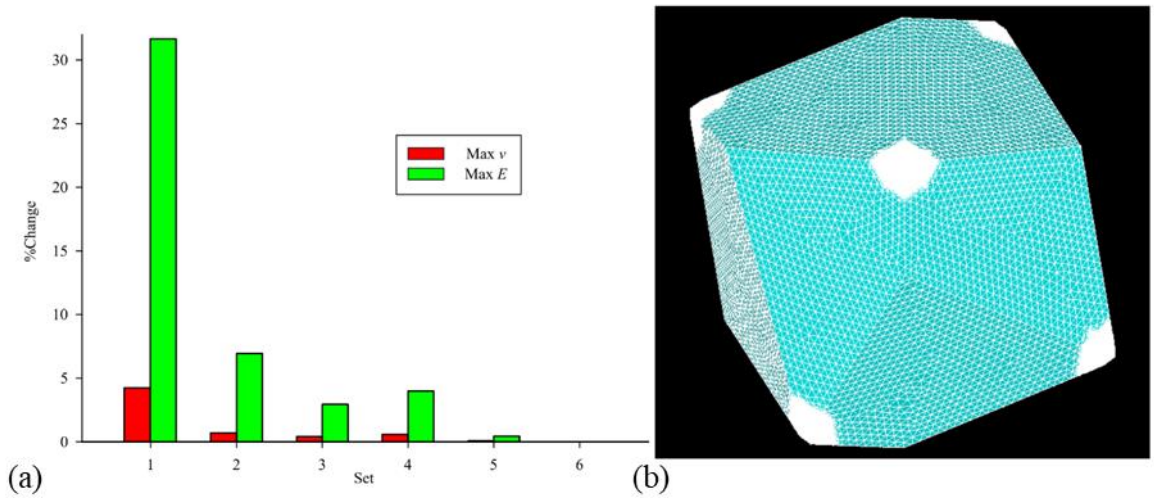

Figure 3.8(a) A bar graph depicting the % change between sets of increasing degrees of mesh refinement. (b) A typical mesh on a regular 3D perforated structure

3.4.3 Regular 3D perforated systems

3.4.3.1 Geometric analysis and volume fraction

For a constant side length of the rhombi, the pore size of this structure can be controlled by changing the angle θ, whereby the larger the value of θ the larger the pore size. This change in pore size will be accompanied by a change in the structure's volume fraction. As it may be anticipated, an increase in θ will result in a decrease of the volume fraction of the regular 3D perforated system. This is clearly shown in Figure 3.9(a) were the change in volume fraction with respect to θ for systems produced from perforations having side lengths, a, of 10.0 mm separated from each other by a distance, s, of 0.5 mm are shown. It is interesting to note that the relation between the volume fraction and the angle θ is not linear. In fact, for small values of θ, an increase in this angle is followed by a relatively large decrease in the material's volume fraction whilst for large values of θ, an increase in this angle is followed by a relatively small change in the material's volume fraction. This is related to the change in volume of the diamond shaped perforations, although it cannot be directly calculated by subtracting the volume of the diamond perforations from the volume of the material. The reason being that there are regions of overlap between the different perforations performed on the different planes.

Further analysis shows that the shape of the polygons resulting from the perforations vary as a function of θ. A system produced by diamond perforations having a very small angle θ may be described as cubes connected through their vertices. As the aperture angle increases, systems composed of irregular dodecahedra connected at their vertices are obtained, while when θ is 90°, the system may be described as being made of rhombic dodecahedron connected through their vertices. The vertices are highlighted through arrows in Figure 3.9(b). It is interesting to note that the resulting polygons are always connected from six vertices. Furthermore, the connectivity area between any two

adjacent polygons is s^2, i.e., it is independent of angle θ. In the case that θ is approaching zero, i.e., the polygon is approaching the shape of a cube, two vertices from each cube will not be connected. On the other hand, in the region where the shape of the polygon may be described as an irregular dodecahedron (i.e., for large θ), eight vertices will not be connected.

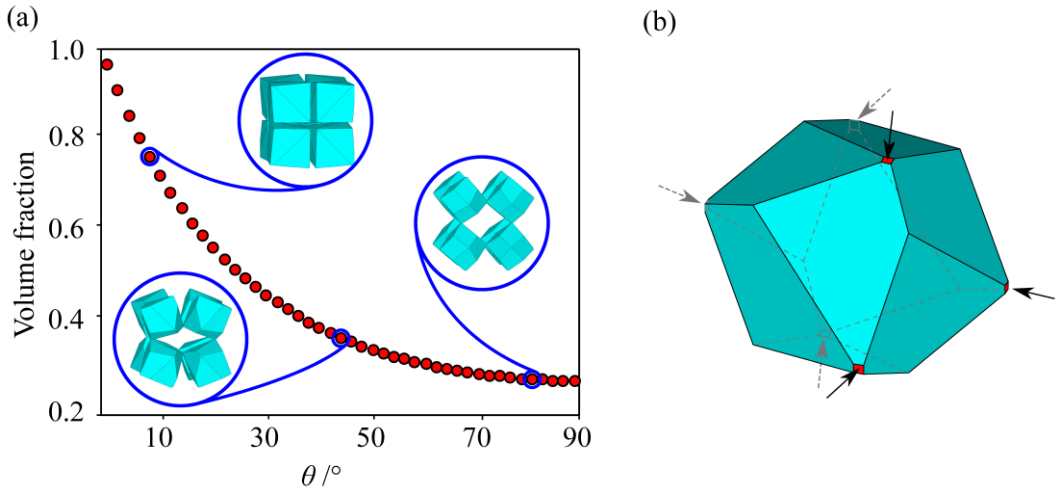

Figure 3.9. (a) Volume fraction against perforation angle with the insets showing structures having a perforation angle, θ, of 10°, 45°, and 80°. (b) An irregular dodecahedron obtained by taking one eighth of a unit cell (θ = 50°).

3.4.3.2 Poisson's ratio and Young's Moduli

The variation of the Poisson's ratios and Young's moduli with θ and s for the regular 3D perforated systems are shown in Figure 3.10. Given the symmetry of the structure, its mechanical properties are the same in the *xy*, *yz*, and *zx* planes. Thus, only those for the *xy* plane will be discussed in detail. With this in mind, it is evident from Figure 3.10 (a) that for the regular system having s = 0.5 mm, a negative Poisson's ratio of circa −0.5 is attained when the values of θ vary between 0° and 70°. Within this range of θ, the material between the perforations is primarily acting as a hinge, allowing the polygons to rotate in three dimensions when a uniaxial load is applied.

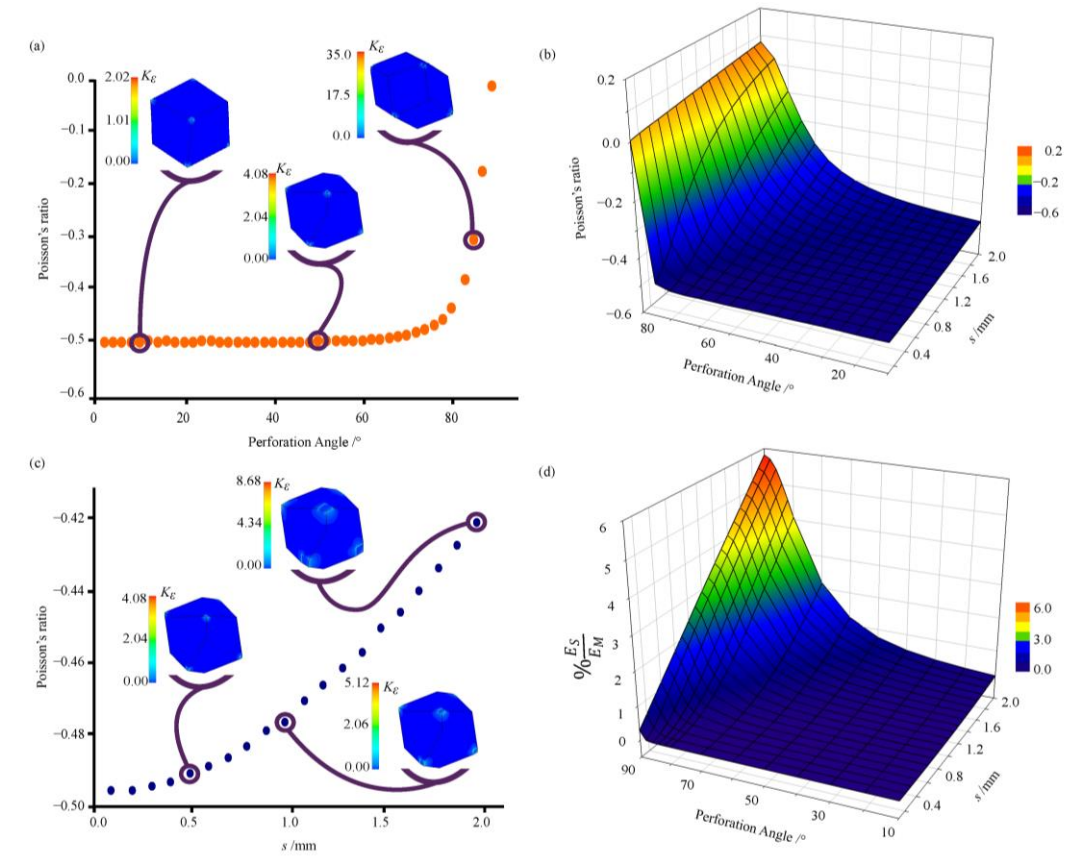

Figure 3.10. Results for the regular 3D perforated system (a) The Poisson's ratio against θ. (b) A 3D plot of the Poisson's ratio for the various combinations of s and θ values (c) The Poisson's ratio against parameter, s, when $\theta = 50°$. (d) A 3D plot depicting the percentage change in the ratio between the Young's modulus of the structure and that of the material for the various combinations of s and θ.

The internal stresses and strains of the regular 3D perforated systems when subjected to compression were analysed in more detail to better understand their distribution (Chapter 4 for a detailed analysis). Figure 3.12, illustrates the effect that the perforation angle (θ) has on the distribution of the von Mises stresses and the strain concentration factor when the distance between the perforations (s) is set to 0.5 mm. From this figure, it can be noted that for all angles considered, the stresses (and hence the strains) are always concentrated in the regions between the polygons, with the other parts experiencing a negligible amount of stress. It then follows that under these conditions these systems may be considered as rigid polygons connected through flexible hinges, this being an integral feature of the rotating rigid units mechanisms, both in 2D and 3D.

Considering further the internal stresses in the *x*, *y*, and *z* directions when $\theta = 10°$ (Figure 3.13), it can be noted that each hinge is characterised by a compressive stress along one edge of the connecting region and a tensorial stress along the opposite edge. This indicates that these hinges are undergoing bending. Additionally, the internal stress profiles at the connection points in the *x*, *y*, and *z* directions are similar, suggesting that this bending behaviour occurs in all three directions. The indications are thus that when the regular perforated system is being compressed in the *x* direction, the rigid polygons rotate relative to each other in the *xy*, *yz*, and *zx* planes.

As the value of θ starts to approach 90°, the rotation of the polygons becomes more difficult. In fact, when θ is equal to 90° the polygons are unable to rotate because the geometry is such that the hinges are aligned along the line of action of the applied uniaxial force. Figure 3.12 also suggests that as the perforation angle becomes larger, the internal stresses experienced by the system become slightly more diffused and larger in magnitude. The increase in von Mises stress in the region between the perforations is mirrored by an increase in the strain concentration factor at the same locations. This indicates that as θ increases, the effect of a second deformation mechanism, whereby the region between the polygons (in the direction of the applied stress) starts to elongate or shorten (depending on if the system is under tension or compression), becomes important. Thus, under these conditions, the Poisson's ratio of the system would depend on the interplay of two mechanisms, namely the polygon rotation and elongation mechanisms.

Interestingly, when $\theta = 90°$ (Figure 3.14), one can observe that the stresses are solely present at the connecting points oriented along the loading direction (the *x* direction in this case). At this point, there could be the expectation that the Poisson's ratio of the structure would be equal to that of the constituting material in view of the fact that the rotation mechanism cannot operate. However, the numerical results obtained indicate

otherwise, with the Poisson's ratio of the structure approaching zero as θ approaches 90°. All stresses within this region are compressive (as the structure is being subjected to a compressive stress) indicating that as expected, no rotations are taking place. The system can be viewed as being constituted of rigid polygons connected together by springs oriented along the *x*, *y*, and *z* directions (see Figure 3.11). The net effect is that the configuration would exhibit a Poisson's ratio of zero. Considering that the induced deformation is localised, this mechanism will henceforth be referred to as the connection point elongation mechanism. It should be noted that in this confirmation, the connection points between the polygons will experience high internal stresses and strains. This can be verified from Figure 3.10 and Figure 3.14 where it can be observed that the strain concentration factor at the connection points increases dramatically as θ increases. For instance, when $s = 0.5$ mm the maximum strain concentration factor increases from 2.0 mm when θ is 10°, 4.1 when θ is 50° to 35.0 when θ is 85° (see Figure 3.10). This is also indicative that as θ increases, the probability of the structure failing at the connection points increases due to the fact that the strain (and stress) experienced by the material in these regions would be relatively large.

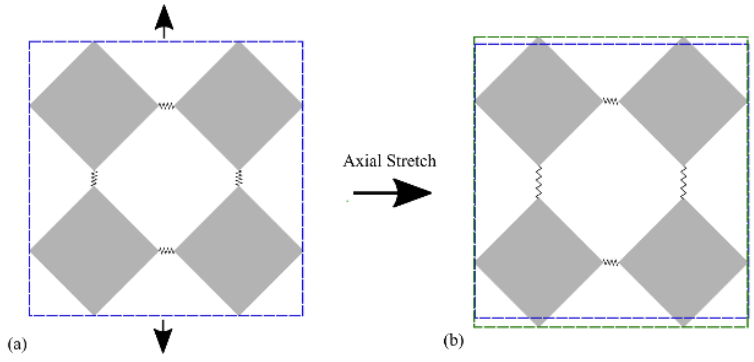

Figure 3.11. An illustration of the deformation of the system when $\theta = 90°$ through which the hinges stretch resulting in a Poisson's ratio of zero.

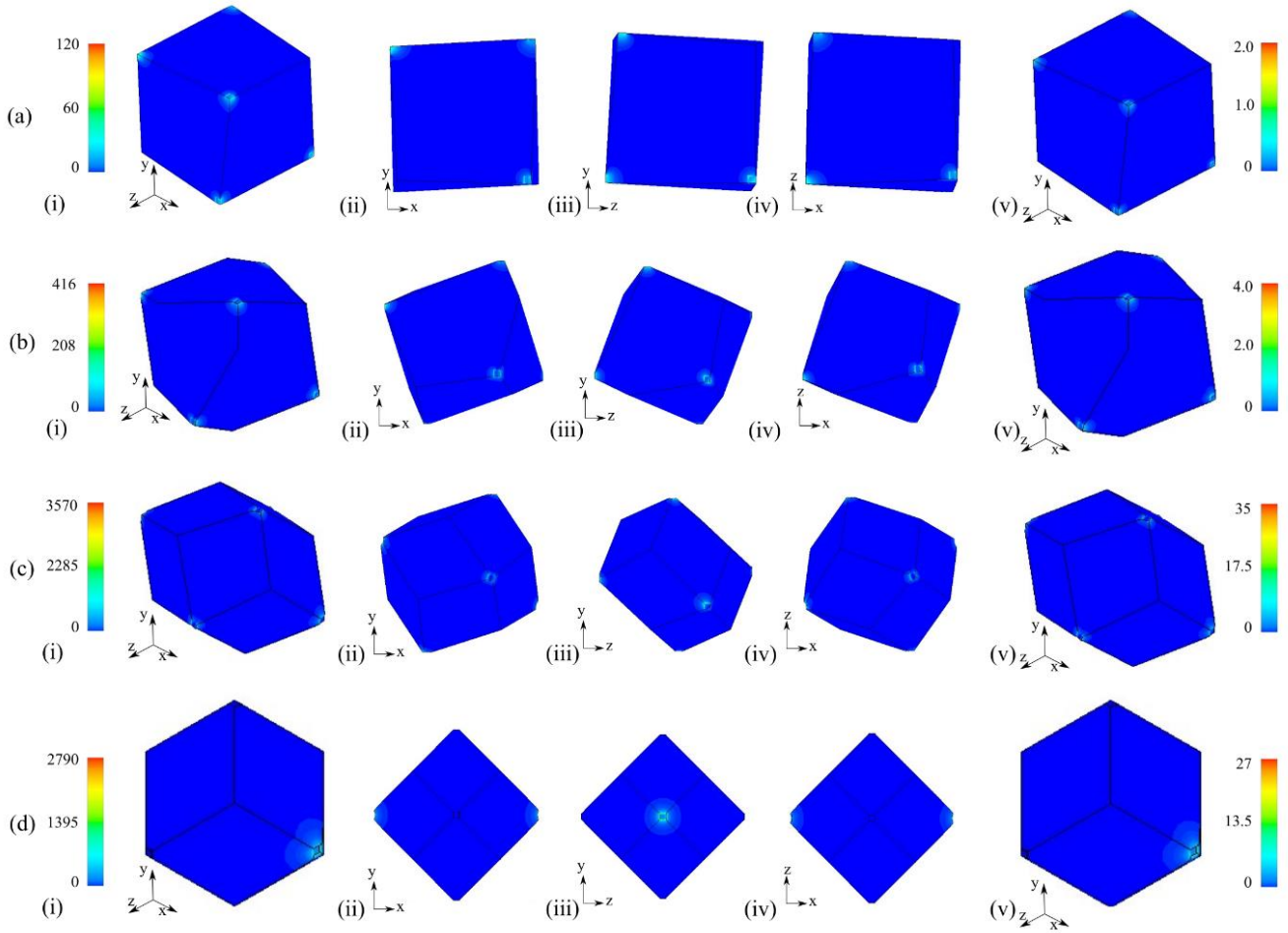

Figure 3.12. The results for the compressed regular 3D perforated system having (a) θ = 10°, (b) θ = 50°, (c) θ = 85°, and (d) θ = 90°. For each panel (i-iv) show the von Mises stresses along planes while (v) the strain concentration factor. In all cases $a = b = c$ = 10.0 mm and s = 0.5 mm.

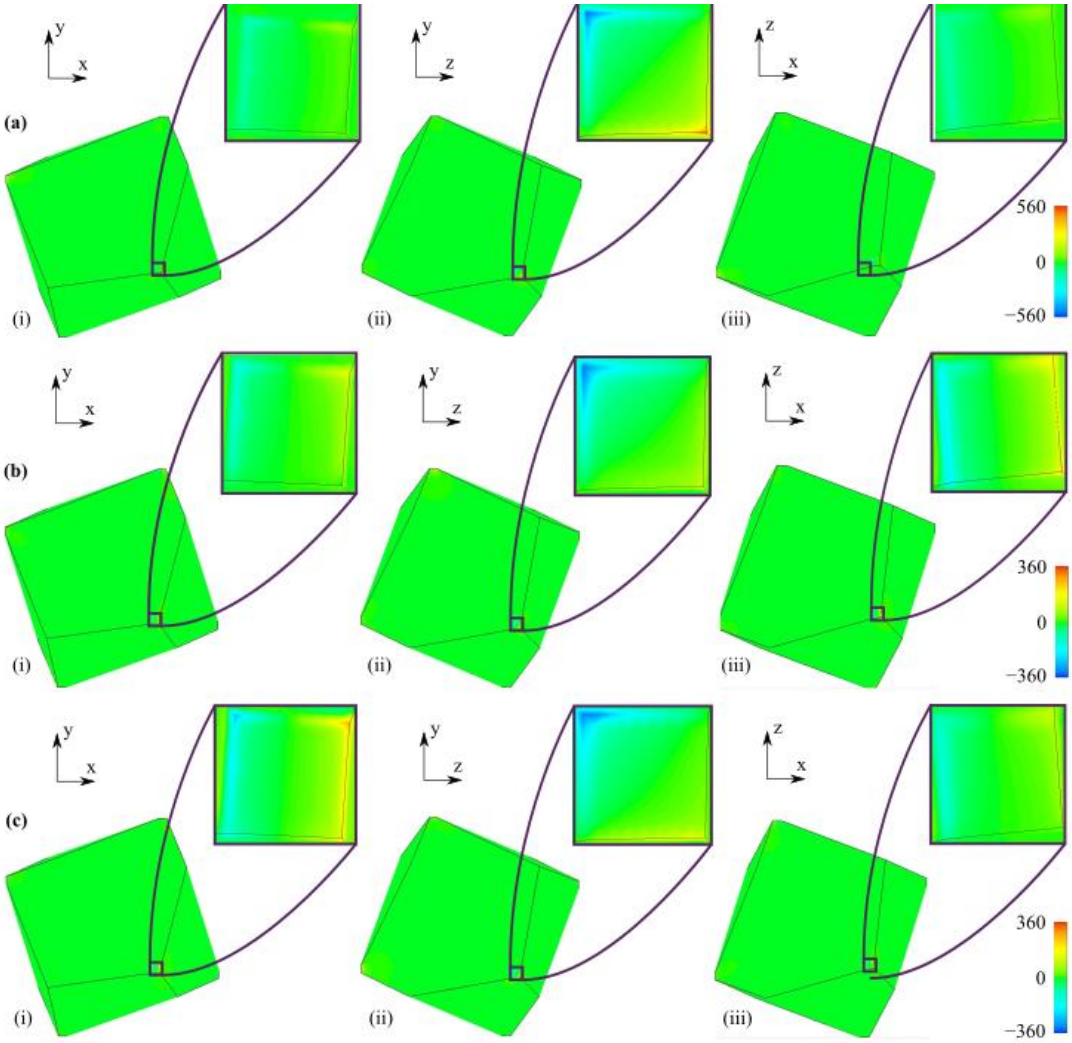

Figure 3.13. Analysis of the regular 3D perforated system, with $\theta = 10°$, $a = b = c = 10.0$ mm, and $s = 0.5$ mm, being subjected to a compression in the x direction. The panels show the resultant internal stresses in the (a) x, (b) y, and (c) z direction. For each panel (i) illustrates the results in the xy plane, (ii) the yz plane, and (iii) xz plane.

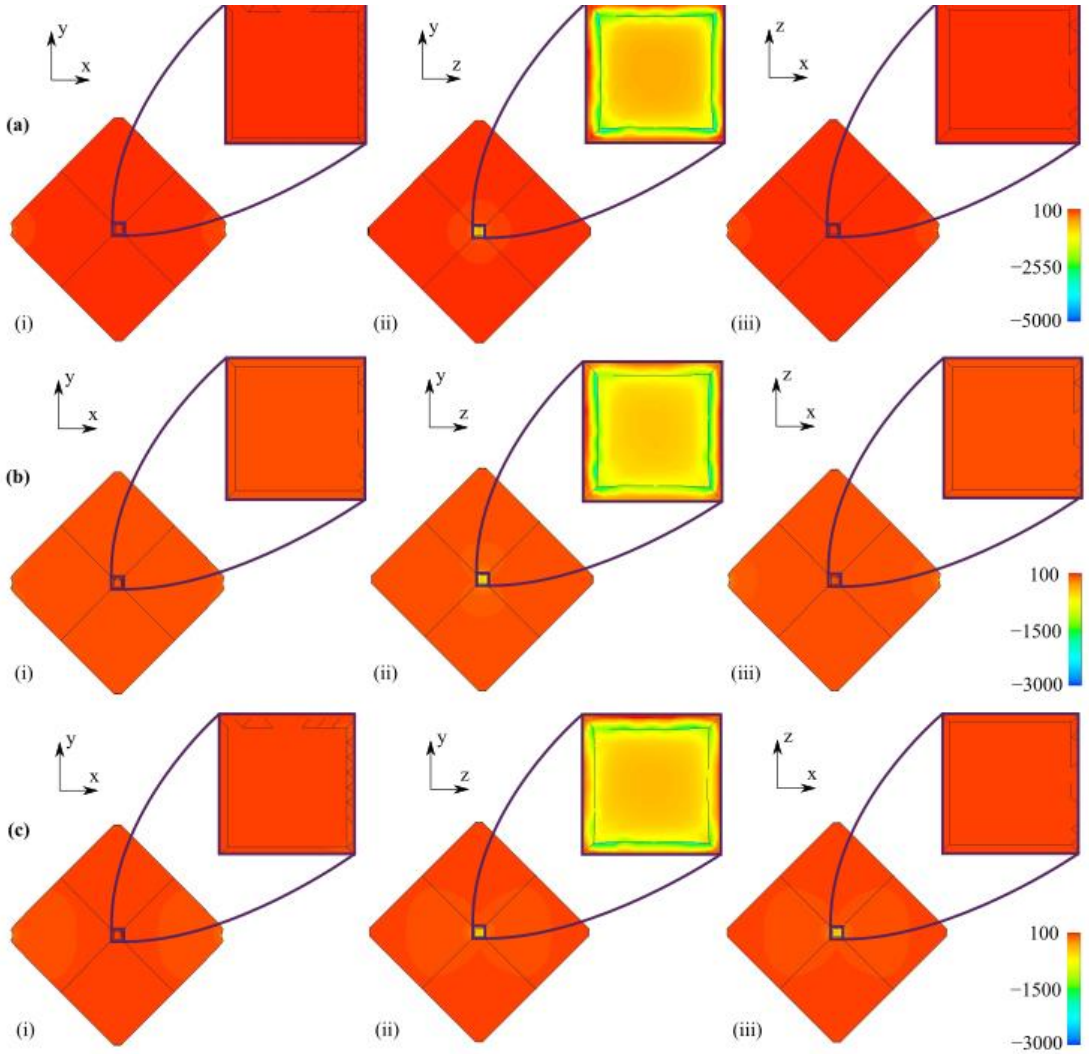

Figure 3.14. Analysis of the regular 3D perforated system, having $\theta = 90°$, $a = b = c = 10.0$ mm, and $s = 0.5$ mm, being subjected to a compression in the x direction. The panels show the resultant internal stresses in the (a) x, (b) y, and (c) z direction. For each panel (i) illustrates the xy plane, (ii) the yz plane, and (iii) xz plane.

The stiffness of the connection between rigid units certainly plays a role in the deformation mechanism. In order to investigate this, a set of simulations were undertaken, whereby the diamond shaped perforations are situated at a larger distance from each other i.e., the parameter s was increased for a number of fixed angles θ. The results indicate that up to moderately small θ (circa 50°) the Poisson's ratio is not affected to a large degree when s is increased from 0.1 to 2.0 mm. For example, when $\theta = 50°$ it changes from −0.495 to −0.419 (see Figure 3.10(c)). On the other hand, for relatively large perforation angles, the changes in Poisson's ratio can be significant. For example, in the case that $\theta = 86°$ the Poisson's ratio changes from −0.479 to −0.039 when s increases from 0.1 to 2.0 mm. Yet, close to the fully open system ($\theta = 90°$), the variation can be small again. For example, when $\theta = 90°$, the Poisson's ratio changes from 0.004 when $s = 0.1$ mm to 0.076 when $s = 2.0$ mm. The way that the Poisson's ratio varies with s and the perforation angle may be understood by taking into consideration the strain concentration factor plots presented in Figure 3.10(c) and the von Mises stress distribution shown in Figure 3.15 and Figure 3.16. These plots indicate that an increase in s is accompanied by a progressive propagation of the deformation of the polyhedrons beyond the connection point. As expected, the stresses in the immediate vicinity of the connection points turn out to be different from those experienced in the rest of the polyhedron. The larger the value of s, the larger the region of the polyhedron which is acting as the 'immediate vicinity' of the point of application of load onto the polyhedron. As s increases, the local deformation at the connection points extends to the bulk of the polyhedrons, something that can be considered as a 'third deformation mechanism'. The deformation of the polygons can be predicted to lead to a positive Poisson's ratio (assuming that the constituting material has a positive Poisson's ratio). In fact, it is expected to approach that of the constituent material as the size of the pores decrease in

relation to the unit cell, something that progressively occurs as s increases. In consequence, the observed Poisson's ratio will be determined through the interplay of these mechanisms acting together.

The degree to which these three types of deformation mechanisms operate will also have an effect on the Young's moduli of the perforated systems proposed here. When s is small, i.e. when the perforated system is mainly deforming through the rotation and connection point deformation mechanisms, the change in the ratio$\%\frac{E_S}{E_M} = \frac{E_S}{E_M} \times 100\%$, where E_S and E_M are respectively the Young's moduli of the structure and the constituting material, Figure 3.10(d)), is always less than 1% across the range of perforation angle. In fact, for s = 0.1 mm the$\%\frac{E_S}{E_M}$ changes from $2.97\times10^{-5}\%$ when $\theta = 10°$ to $2.96\times10^{-1}\%$ when $\theta = 90°$. On the other hand, the Young's modulus of the system changes to higher percentages when s is larger. For example, when s = 2.0 mm the$\%\frac{E_S}{E_M}$ changes from $2.11\times10^{-1}\%$ when $\theta = 10°$ to 5.81% when $\theta = 90°$.

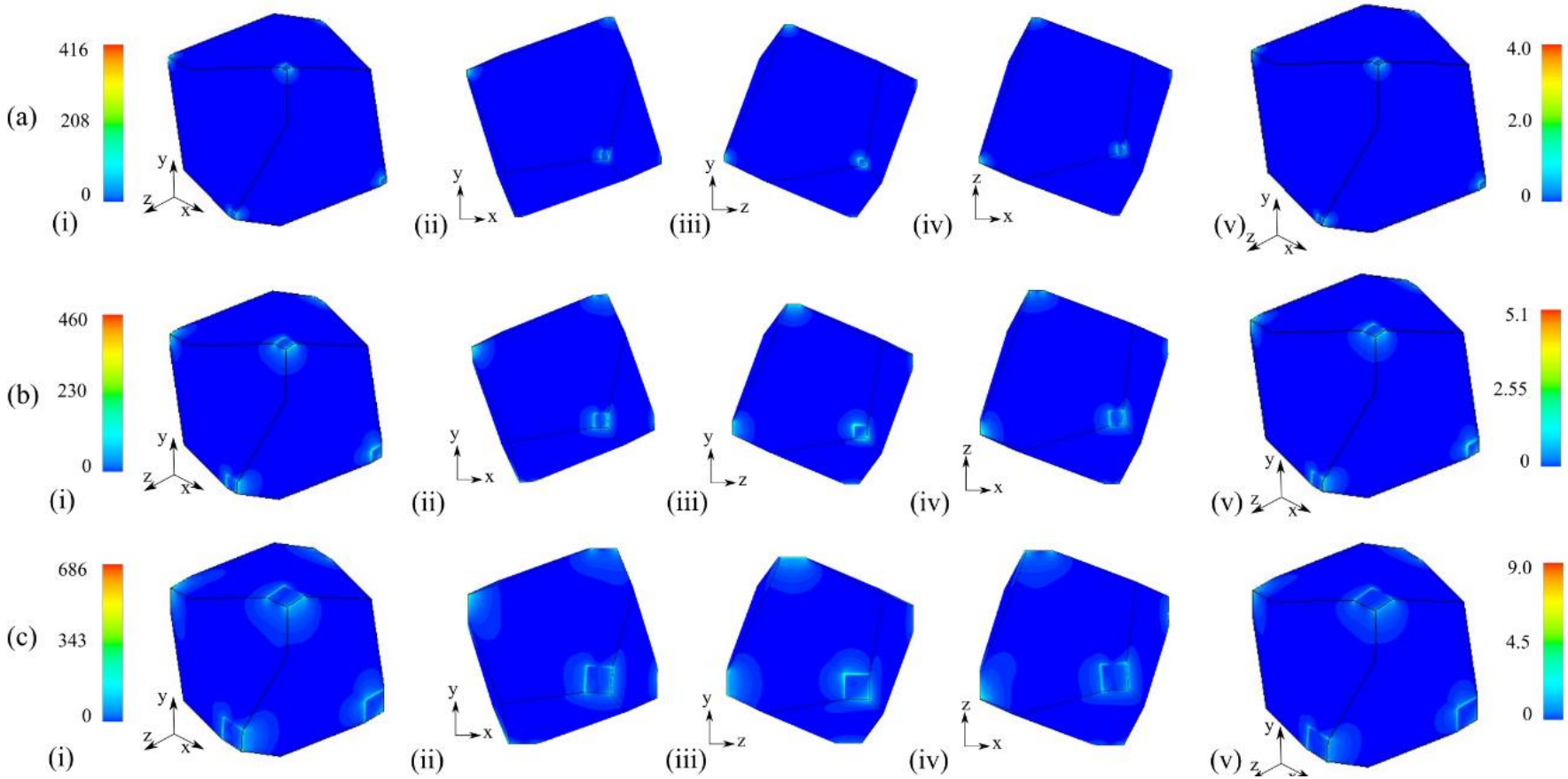

Figure 3.15. The results for the compressed regular 3D perforated system having (a) s = 0.5 mm, (b) s = 1.0 mm, and (c) s = 2.0 mm. For each panel (i-iv) show the von Mises stresses along different planes while (v) the strain concentration factor. In all cases $a = b = c$ = 10.0 mm and $\theta = 50°$

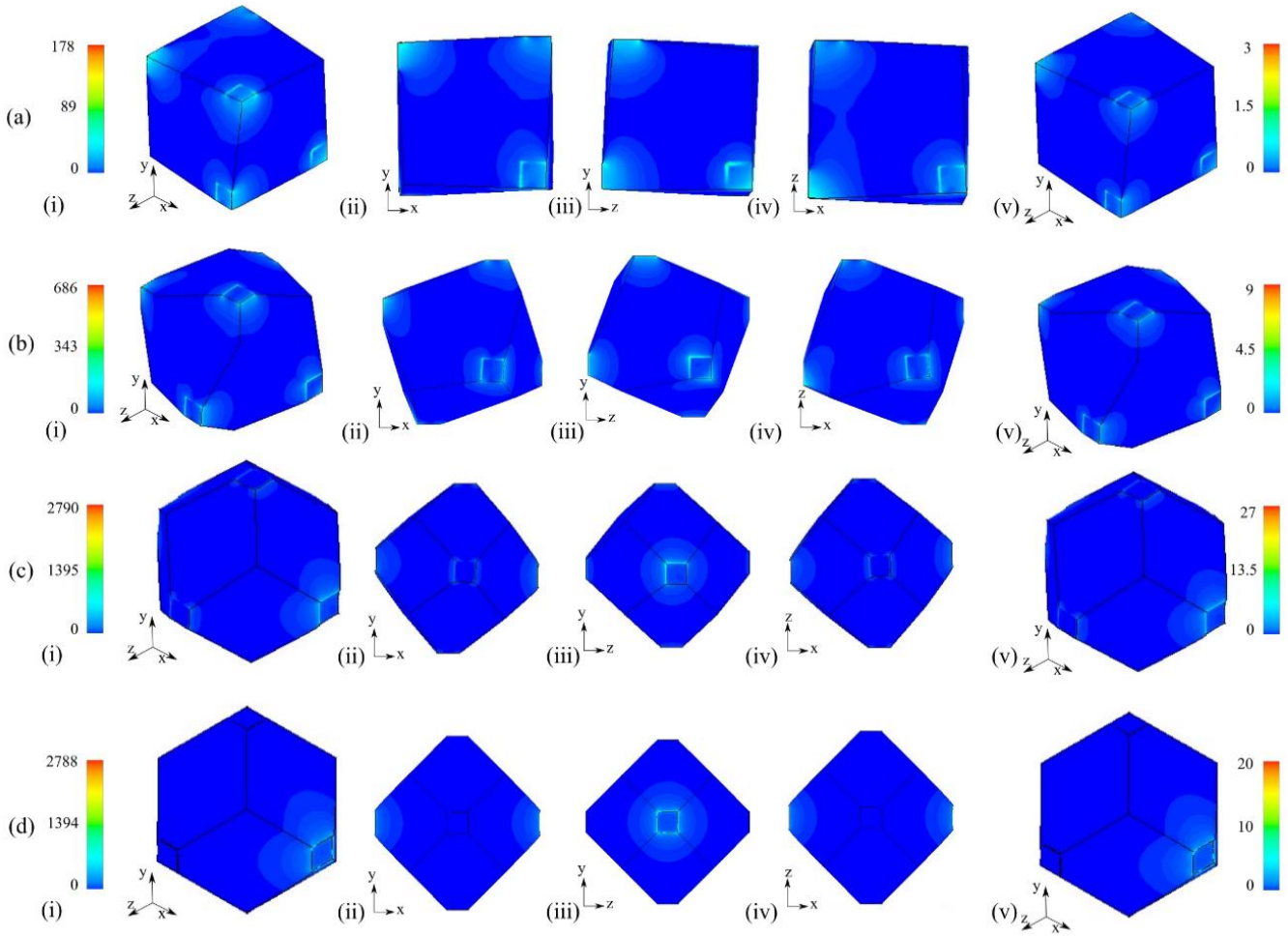

Figure 3.16. The results for the compressed regular 3D perforated system having (a) θ = 10°, (b) θ = 50°, (c) θ = 85°, and (d) θ = 90°. For each panel (i-iv) show the von Mises stresses along different planes while (v) the strain concentration factor. In all cases $a = b = c$ = 10.0 mm and s = 2.0 mm.

3.4.4 General 3D perforated systems with different sized perforations

3.4.4.1 Poisson's ratio

In addition to the range of configurations that can be attained by altering *s* and θ, the perforation of a cuboid using different sized diamonds (see Figure 3.17 and Figure 3.18) can result in a plethora of structures having a diverse range of mechanical properties. In the cases when $a \neq b \neq c$, the projections of the structures in the *xy*, *xz*, and *yz* planes may be described as rectangles connected through their corners, albeit the dimensions of the projected rectangles may be different in different planes. In general, it was observed that such structures exhibited an NPR in at least one direction, the magnitude of which can be relatively large in some cases. From the sets of parameters tested in this study, the most auxetic 3D perforated system (having a = 10 mm, b = 12 mm, c = 10 mm and θ = 70°) had a Poisson's ratio of −13.14 in the *zy* plane, for loading in the *z* direction.

Comprehensive analysis of the result indicated that the deformation of these cuboidal perforated systems is similar to that of the regular 3D perforated system. When the structures are not fully open and *s* is relatively small, they deform mainly through the relative rotation of the polygons (see Figure 3.18). Furthermore, the Young's moduli in the *x*, *y*, and *z* directions were observed to increase to a small extent when the aperture angle θ_1 and/or the ratio b/a increased. This indicates that the connection point elongation mechanism starts to operate when these parameters have large values.

Partial symmetry in the general systems can be attained when any two of the dimensions *a*, *b*, and *c* are equal. In this case, the initial block has the shape of a square cuboid. The resultant perforated system has a projection in one plane that may be described as squares connected through their corners, whilst in the other two planes, the projections may be described as rectangles connected through their corners. These

systems showed a negative Poisson's ratio in all planes investigated (see Figure 3.17). The internal stresses and strains for systems with different sized perforations are shown in Figure 3.19. The von Mises stress distribution displayed a similar trend to that shown in the case of the regular 3D perforated system, with the maximum stress increasing and becoming more diffused as the perforation angle increases.

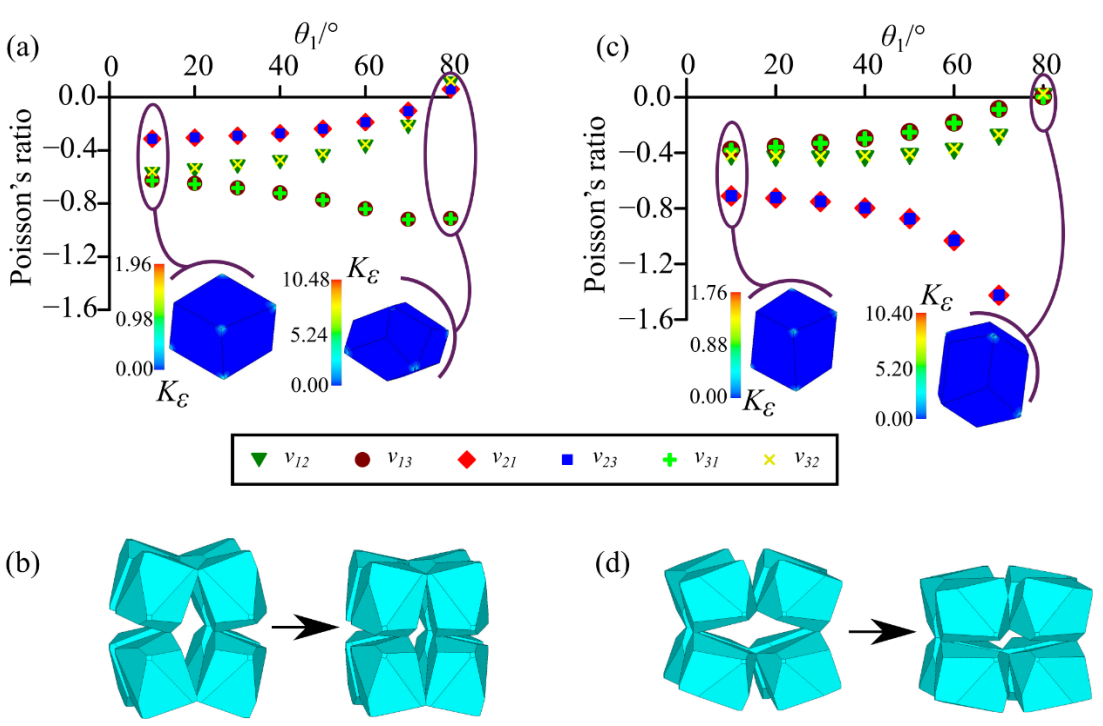

Figure 3.17 (a) Poisson's ratio against θ_1 for the general 3D perforated systems having $b = c = 8.0$ mm and (b) the undeformed and deformed structures for this system when $\theta_1 = 40°$. (c) Poisson's ratio against θ_1 when $b = c = 12.0$ mm and (d) the undeformed and deformed structures for this system when $\theta_1 = 40°$. In all cases, $a = 10.0$ mm, and $s = 0.5$ mm.

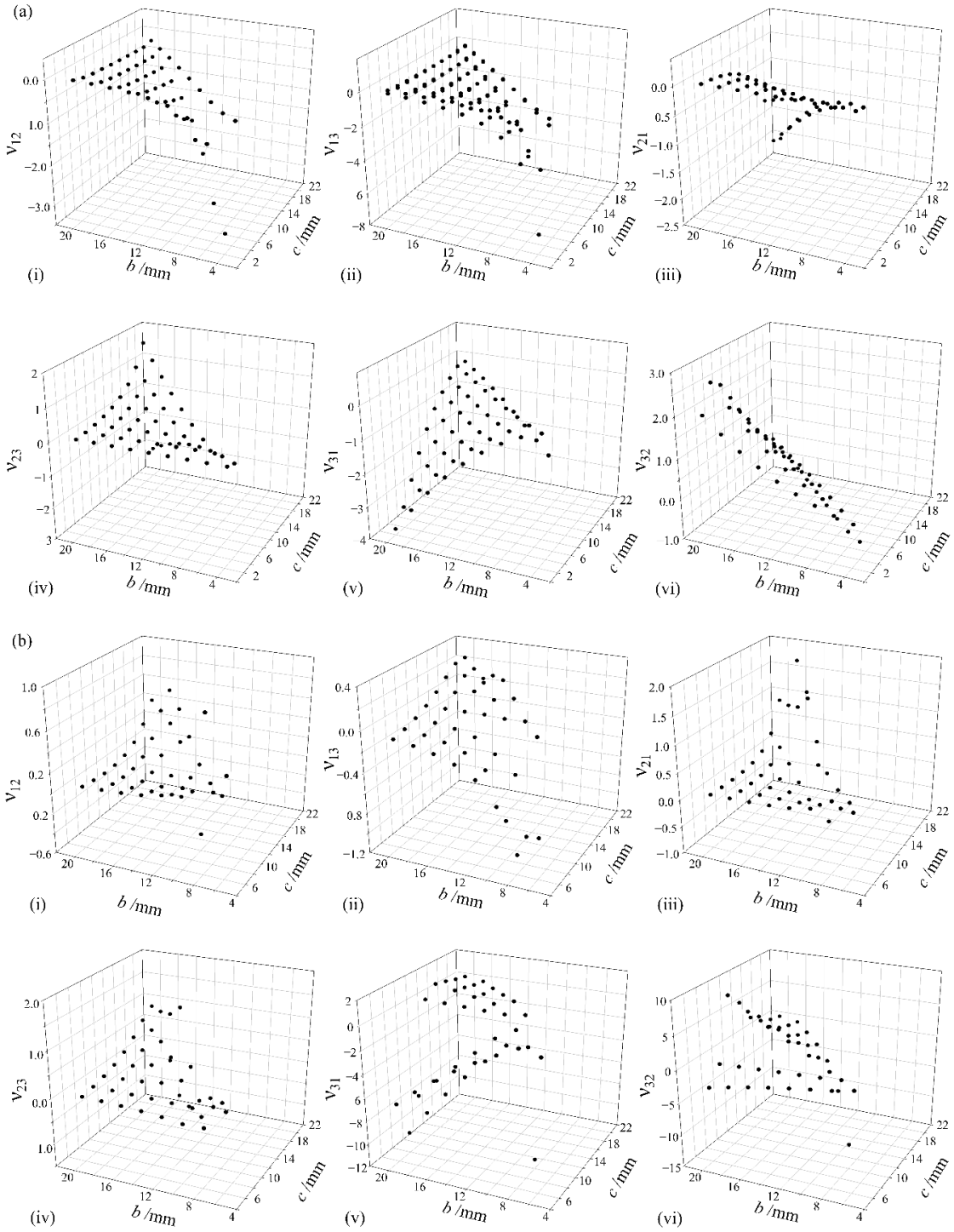

Figure 3.18. The variation of the Poisson's ratio with the lengths *b* and *c* for structures having (a) θ = 10° and (b) θ = 80°. For each panel (i) showing v_{12}, (ii) v_{13}, (iii) v_{21}, (iv) v_{23}, (v) v_{31}, and (vi) v_{32}. In both cases a = 10.0 mm and s = 0.5 mm.

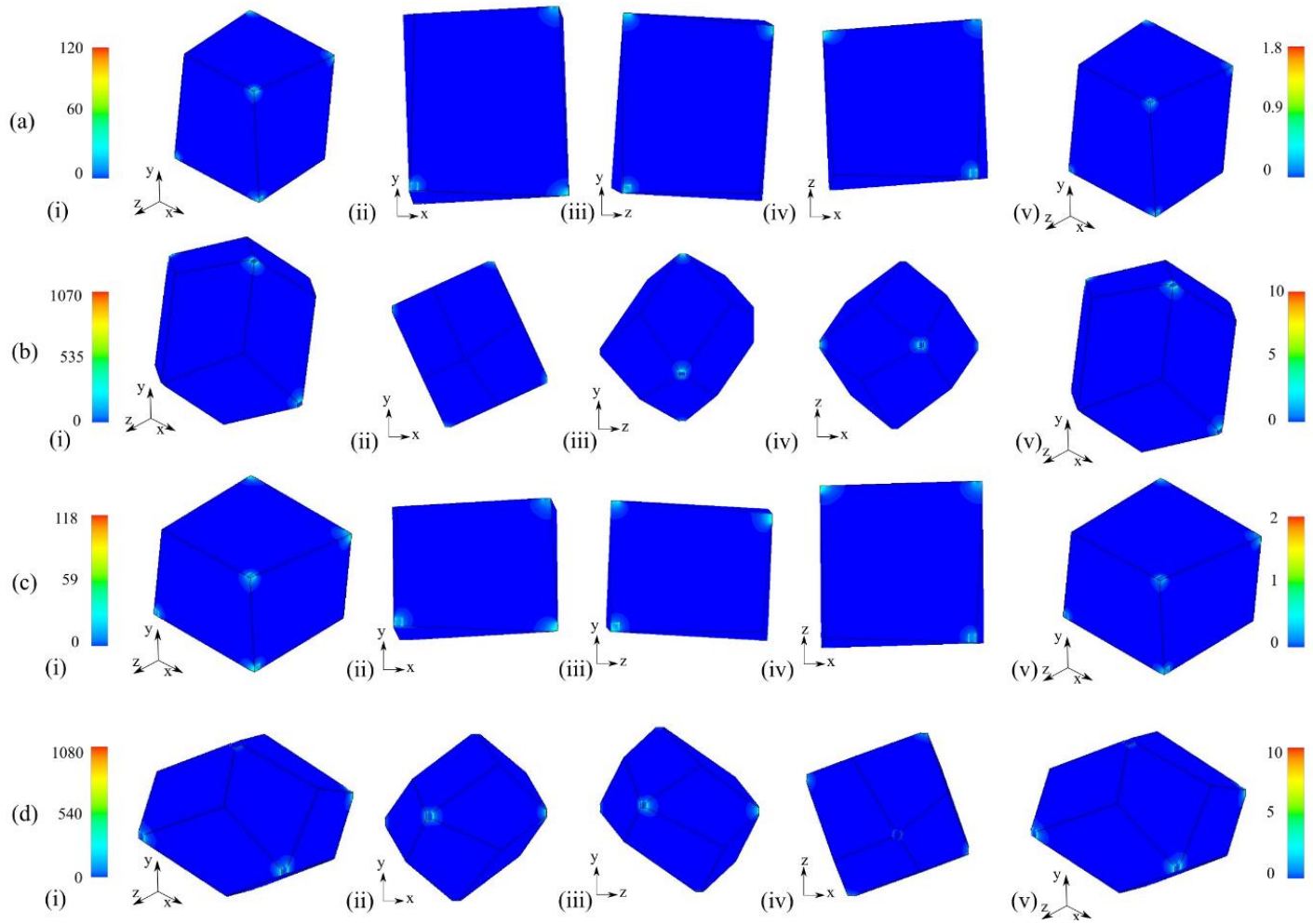

Figure 3.19. The results for the compressed irregular 3D perforated system having (a) b = c = 12.0 mm and θ = 10°, (b) b = c = 12.0 mm and θ = 80°, (c) b = c = 8.0 mm and θ = 10°, and (d) b = c = 8.0 mm and θ = 80°. For each panel (i-iv) show the von Mises stresses along different planes while (v) the strain concentration factor. In all cases a = 10.0 mm and s = 0.5 mm

3.4.5 Experimental and non-linear numerical analysis of Systems I and II

The linear numerical results presented above were also compared to the corresponding non-linear simulations. In the case of the regular 3D perforated system (System I), the structure showed an initial negative Poisson's ratio of −0.44 in all planes studied, as predicted by the linear simulations performed earlier. Furthermore, the non-linear simulations indicate that the Poisson's ratio of this system is strain independent up to the maximum compression used in this study (7% of the original length; see Figure 3.20).

Analysis of the more general cuboid system (System II) gives a similar result whereby the initial Poisson's ratios ν_{ij} are in line with those determined from the linear simulations (see Figure 3.21). More specifically, the values for ν_{xy}, ν_{yx}, ν_{xz}, ν_{zx}, ν_{yz} and ν_{zy} were found to be −0.260, −0.718, −0.305, −0.427, −0.678 and −0.415 respectively. Once again, the Poisson's ratios obtained for the various planes were strain independent up to the maximum strain used in this study. This is a very important result as invariance in Poisson's ratio with strain is rather uncommon amongst auxetic systems mainly due to the fact that during the deformation there is a change in geometry, usually resulting in a change of the ν_{ij}. Thus, these systems can be used for applications where a constant value of the Poisson's ratio is required over a relatively large strain range. Examples of such a situation include any impact absorption setups such as car bumpers and personal protective equipment (Allen *et al.*, 2017; Duncan *et al.*, 2018; Foster *et al.*, 2018; Moroney *et al.*, 2018).

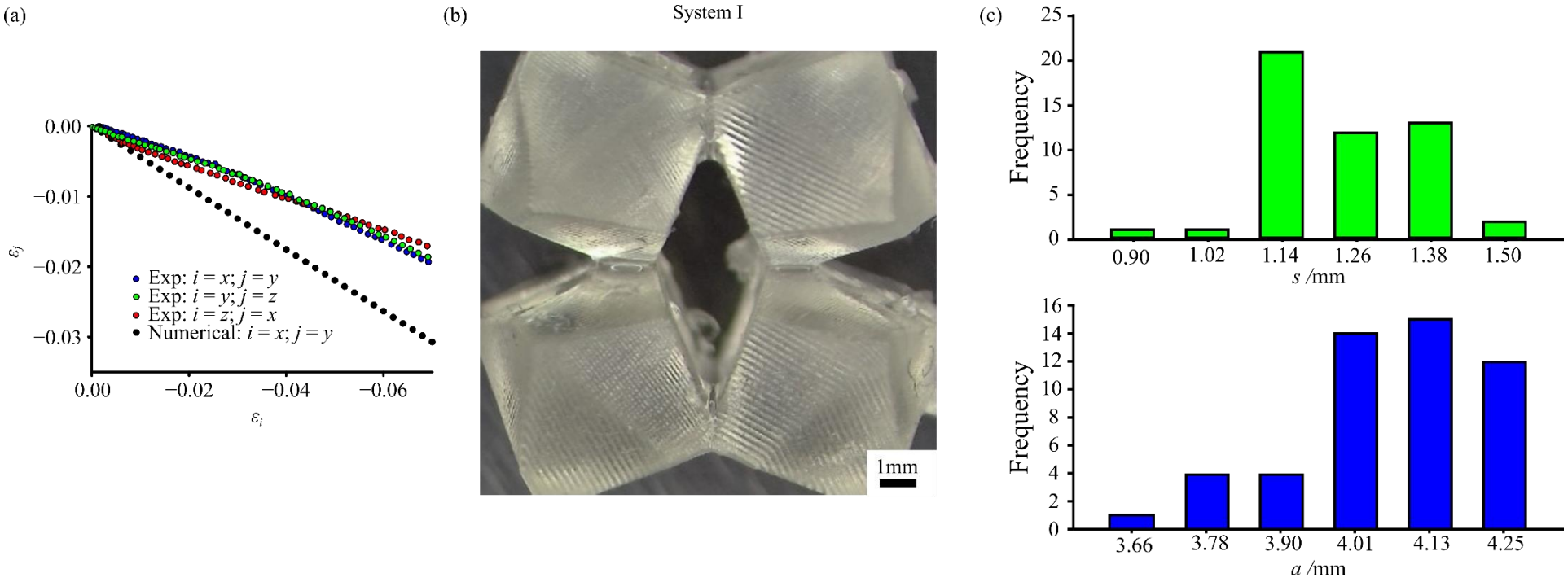

Figure 3.20 (a) Comparison of the Poisson's ratio between the experimental and non-linear numerical results for System I. (b) Part of the experimental prototype of System I. (c) Frequency distribution graphs for different parameters of System I.

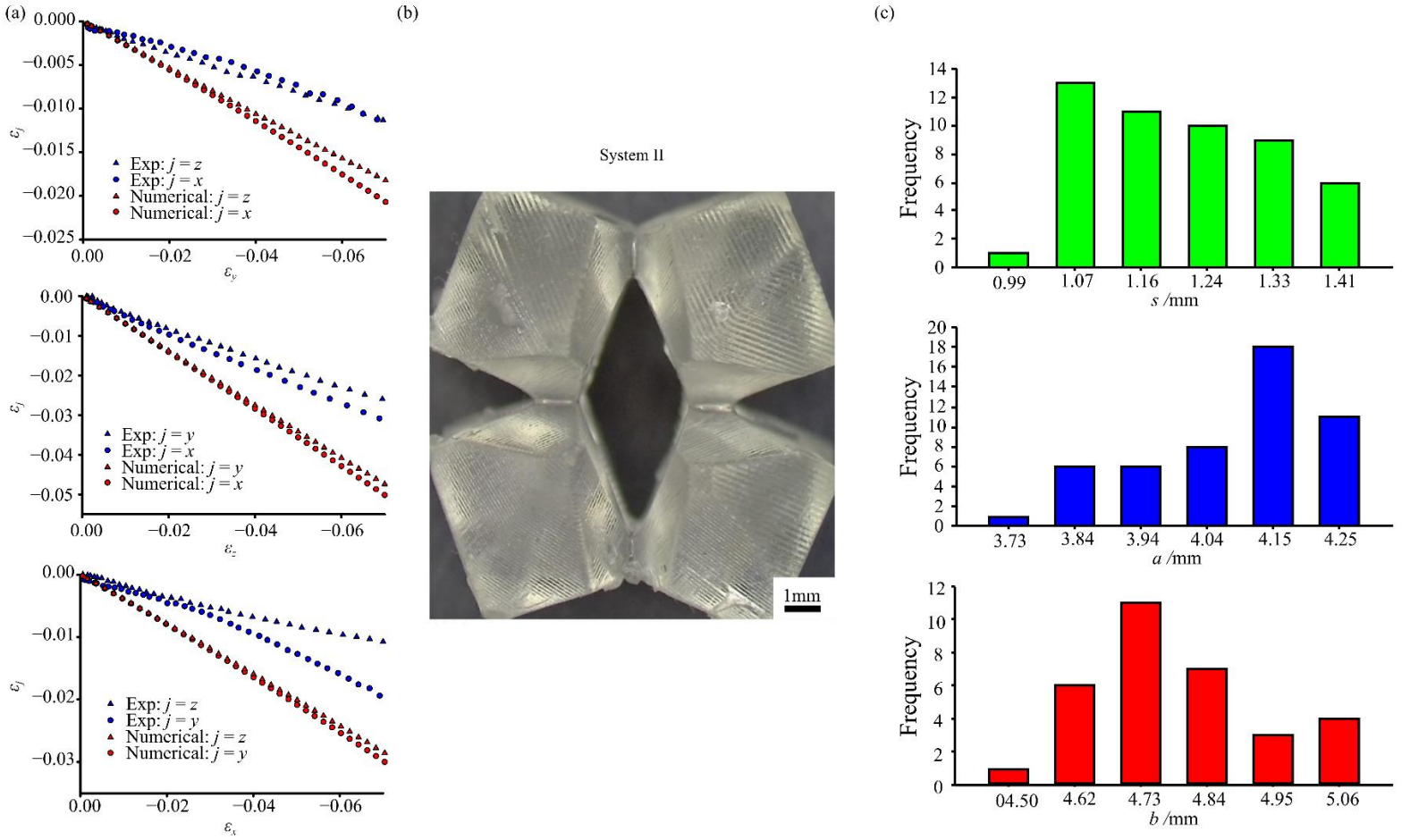

Figure 3.21. (a) Comparison of the Poisson's ratio between the experimental and non-linear numerical results for System II. (b) Part of the experimental prototype of System II. (c) Frequency distribution graphs for different parameters of System II.

Further analyses of the numerical results were carried out by comparing them with those obtained through the mechanical testing of the physical prototypes. As can be observed from Figure 3.20 and Figure 3.21, the general trends obtained from the experimental prototypes were the same as those derived from the non-linear analysis. In fact, the experimental prototypes showed that these systems can indeed exhibit a negative Poisson's ratio that is strain independent up to a compression of 7%. However, for both the regular 3D perforated (System I) system and the more general system (System II), the values obtained experimentally for the Poisson's ratio differed significantly from those predicted by the non-linear simulations. In fact, for the regular 3D perforated system, the experimentally determined Poisson's ratios ν_{xy}, ν_{yz}, and ν_{zx} were measured to be −0.229, −0.224, and −0.301 respectively. These results suggest that some anisotropy is present in the regular 3D perforated system, something which was not expected based on the symmetry and the numerical results. Furthermore, in the case of the more general system, the ν_{xy}, ν_{yx}, ν_{xz}, ν_{zx}, ν_{yz}, and ν_{zy} were measured to be of −0.068, −0.471, −0.067, −0.276, −0.531, and −0.291 respectively so that these too deferred from those obtained using non-linear simulations.

To investigate the differences between the numerical and experimental results, the actual dimensions of the 3D printed structures were measured using microscopy as described in Section 3.3.3. For both System I and System II there were some discrepancies between the expected perforation dimensions and the actual dimensions. In fact, *s*, which should have been set to 0.8 mm, was found to vary between 0.9 mm and 1.5 mm in the case of the System I, and between 1.0 mm and 1.4 mm in the case of System II. This problem probably arose due to the poor drainage of the uncured resin from the edges of the perforations while cleaning the model with iso-propanol. The extra resin, which did not drain during the cleaning phase, then cured at the intersections during the post curing stage. A change in *s* is not expected to cause a large change in the Poisson's ratio. However, this change in *s* is necessarily accompanied with a

change in the dimensions of the perforations. Indeed, in the case of System I, *a* was found to vary between 3.7 and 4.3 mm whilst in the case of System II, *a* varied between 3.7 and 4.3 mm while *b* ranged between 4.5 and 5.1 mm. This means that in the case of System I, the perforations were not of the same dimension leading to an anisotropic behaviour of the structure. Similarly, the deviations of *a* and *b* from the intended ones can explain the discrepancies obtained between the simulated and experimental values. Such production problems can be resolved in different ways. When using additive manufacturing, the shape of the perforation can be optimised. For example, using ellipse shaped perforations instead of diamond ones allows for better resin drainage. This would require further research to study any changes in the mechanical properties because of this change in perforation shape. The proposed systems could also be produced using casting methods. This is possible as the pores in this 3D system are continuous and thus allow for the design of a mould with removable rods to produce the perforated system discussed in this study. Once casting is complete one would simply remove the rods and obtain the system which was investigated in this study. The systems investigated in this study could also be produced by a subtractive method. Subtractive methods are generally easier to implement than additive manufacturing, however, they may be less cost-effective due to material wastage. When using subtractive methods, the cost effectiveness would highly depend on the size of the perforations. For example, in the case of the regular 3D perforated system, using small values for angle θ will result in 'slit' like perforations. Production of such a system using subtractive methods will probably be cost effective as minimal material loss will occur. On the other hand, if large values for angle θ are used, subtractive methods may not be cost effective due to the large amount of lost material. This may be clearly inferred form Figure 3.9 where the volume fraction of the regular system for various values of θ is given.

3.5 Innovation and application of the study

At this stage it is important to point out that the 3D structures that result when using this novel design method with diamond shaped perforations are also innovative. First and foremost, such 3D structures can be fabricated using a number of fabrication methodologies. This is due to the fact that the perforations extend across the whole length of the cuboid in the *x*, *y*, and *z* directions (continuous voids of constant cross-sectional area). Thus, such systems can also be produced through casting by creating a mould chamber having interpenetrating and detachable diamond-shaped rods, an example of which is depicted in Figure 3.22. For ease of visualisation, the mould being shown here is for a system where diamond shaped perforations are performed across two perpendicular planes. The assembled mould itself would constitute the negative image of the perforated cuboid just presented with the diamond shaped rods creating the necessary voids. Furthermore, because of the presence of the continuous voids of constant cross-sectional area, these systems can also be produced through subtractive manufacturing. Such 3D systems would also show advantages when using additive manufacturing as they would have a clear drainage channel thus eliminating issues of cupping.

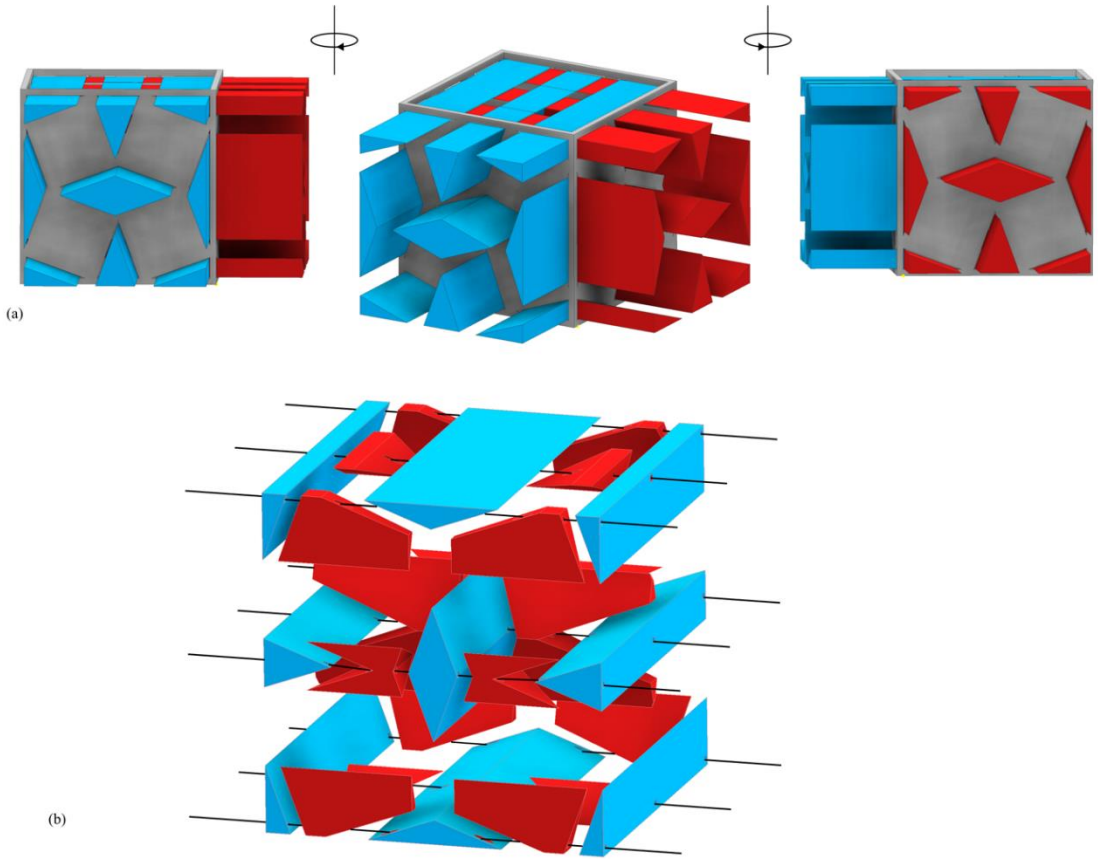

Figure 3.22. Proposed mould which can be used to produce the perforated systems.

Furthermore, the results obtained suggest that these 3D systems have a strain independent Poisson's ratio (up to the maximum strain used in this study). This is a desirable feature which is not obtained in numerous auxetic structures. For example, the 2D perforated systems that mimic the re-entrant honeycomb systems (Mizzi, Azzopardi, *et al.*, 2015) do not exhibit a strain independent Poisson's ratio. Moreover, the systems designed using equally sized diamond shaped perforations (the regular 3D perforated systems) where shown to have a nearly constant Poisson's ratio for a large degree of θ values (up to 60°). This is not the case for other 3D rotating polygons. For example, the rotating cubes proposed by Kim et. al (J. Kim *et al.*, 2017) were shown to have a Poisson's ratio that varies between −0.51 and −0.98 as the angles between the cubes change between 2° and 60°. It was also found that in the case of the

3D systems produced with diamond shaped perforations a Poisson's ratio of 0 can also be obtained when the distance between the perforations (s) is small, and θ has a value of 90°.

The perforated 3D systems proposed in this study may be used in a plethora of applications. For example, they can find use in protection equipment ranging from helmets to protective sports equipment. As discussed in Chapter 2, materials with a negative Poisson's ratio have superior indentation resistance since the material tends to move towards the zone of impact rather than away from it as is the case for positive Poisson's ratio materials. However, in the case of '2D' auxetic systems such as the rotating squares, one would expect that the material would move towards the direction of impact from only one orthogonal direction whilst in 3D auxetic systems, such as the regular 3D perforated system proposed here, one would expect that the material moves towards the zone of impact from all orthogonal directions, hence making the material more resistant to impact. 3D materials like the ones proposed in this study would also be useful for the production of 3D actuators, where an extension in the x direction would result in the perpendicular motion in the y and z directions. Furthermore, through the design of the perforation used, one may design a system which amplifies the strain in one of the orthogonal directions. Such applications are possible as the Poisson's ratio was found to be nearly linear with applied strain (up to the maximum strain used in this study, 7%). Furthermore, such perforated systems may find use in the production of prosthetics. For instance, recent studies have shown that tendons have a highly anisotropic Poisson's ratio, with a large negative Poisson's ratio in one plane (Gatt, Vella Wood, *et al.*, 2015). Thus, the mechanical properties of the proposed perforated systems may be fine-tuned to those of the tendon, with the aim of producing prosthetics that mimic the behaviour of real tendons.

3.6 Conclusion

In this study, it was shown that a novel design method may be employed to obtain auxetic 3D structures. This method utilises the application of continuous voids of constant cross-sectional area in multiple planes. The significant innovation of this work is that it shows that perforations i.e., continuous pores within a material may be used to design 3D auxetic structures. Since the pores are continuous and have the same cross-sectional area throughout the pore, several manufacturing techniques such as additive manufacturing, subtractive manufacturing and casting techniques can be employed to produce 3D auxetic structures. Due to their pore geometry, such systems are by far easier to produce when compared to current 3D auxetic systems with complex geometries. In order to exemplify the proposed design method, several 3D structures were constructed using a series of diamond shaped perforations applied at strategic locations on multiple planes. The 3D structures obtained are also novel due to a number of characteristics which they show. The simplest structure considered here has equal sized perforation in the *xy*, *yz*, and *zx* planes. Computational simulations have shown that this configuration has a negative Poisson's ratio of circa −0.5 in the *xy*, *yz*, and *zx* planes as long as the spacing between the perforations is relatively small. Furthermore, non-linear simulations indicate that the Poisson's ratio obtained for these systems is strain independent up to the maximum strain used in this study (7%). Also of interest is the fact that, when the distance between the perforations is small and the perforation angle is 90°, a system with a Poisson's ratio of zero may be obtained. A more general 3D system having diamond shaped perforations was also studied, whereby differently sized perforations were used. The results obtained showed that an array of structures exhibiting a range of anisotropic Poisson's ratios and Young's moduli can be obtained.

Chapter 4 : 3D Perforated Systems using elliptical and stadium-shaped perforations

Highlights

- This chapter builds on the work in Chapter 3 and makes use of the design method developed to design two new systems having elliptical and stadium-shaped perforations.
- The analysed systems were shown to exhibit a more negative Poisson's ratio when compared to diamond-shaped perforations, whilst having a better stress and strain distribution.
- The experimental prototypes of the analysed systems were found to have a strain independent Poisson's ratio up to at least 10% strain.

4.1 Introduction

A number of the 3D structures obtained when using diamond shaped perforations as an example of the novel design method proposed in Chapter 3 were found to exhibit a negative Poisson's ratio in a number of perpendicular planes (see Section 3.4.3.2). The notion of using perforations (i.e., continuous pores in the third direction) in multiple planes for the design of 3D auxetic structures is not limited to the adoption of diamond shaped perforations and other types of perforation shapes such as elliptical, rectangular, stadium and I-shaped perforations can be expected to lead to 3D auxetic structures when perforations are performed in multiple

planes as shown in Figure 4.1. In this chapter, 3D auxetic structures produced through elliptical and stadium shaped perforations will be investigated and analysed with respect to the 3D auxetic structures produced through diamond perforations.

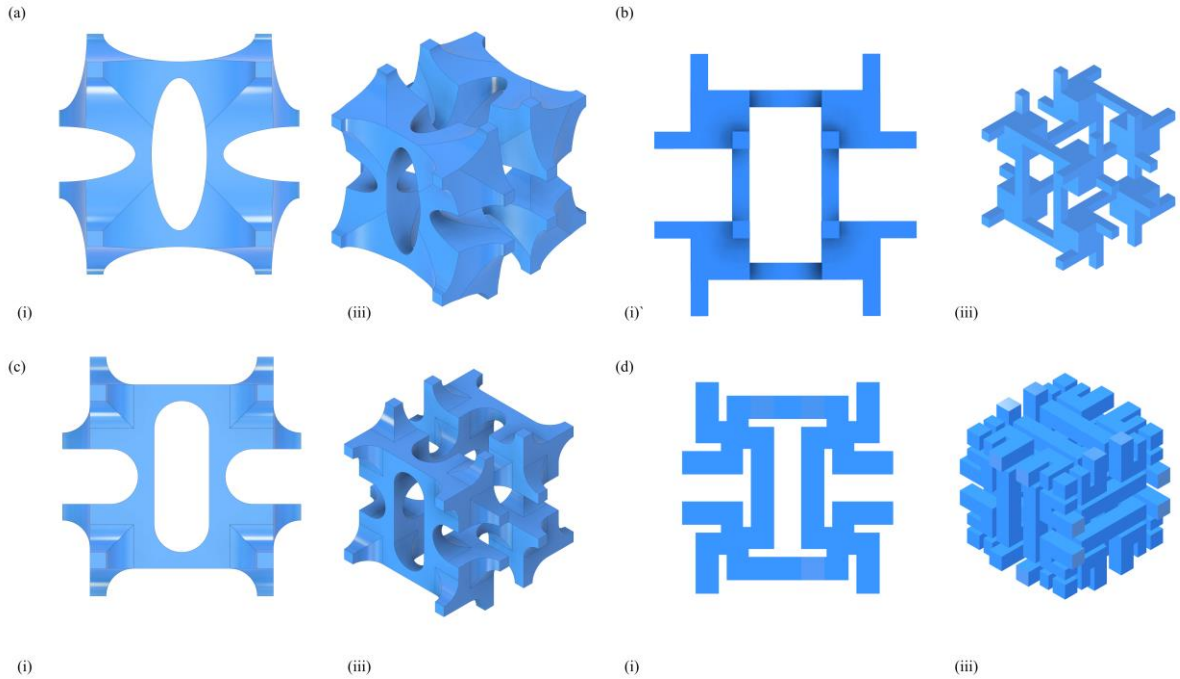

Figure 4.1. An illustration of possible 3D auxetic structure that may be obtained when using (a) elliptical, (b) rectangular, (c) stadium-shaped, (d) I-shaped perforation shapes. Panel (i) represents the projections of the 3D structures in the major planes while panel (ii) shows the 3D structure.

4.2 Materials and methods

4.2.1 The design of the 3D perforated systems

In this study, the perforations with a diamond shaped cross-sectional area explored in Chapter 3 will be compared to perforations having elliptical and stadium-shaped cross-sectional areas. To be in a position to assess the properties of the resulting structures, the perforations having elliptical, and stadium shaped cross-sectional areas were designed in such a way that a diamond shape can be inscribed inside of them. Referring to Figure 4.2,

perforations with a diamond shaped cross-sectional area having side length, a, and an aperture angle, θ, were used. The diagonals for this geometry may be given by:

$$h_d = 2a \cos\left(\frac{\theta}{2}\right) \tag{4.1}$$

$$w_d = 2a \sin\left(\frac{\theta}{2}\right) \tag{4.2}$$

Based on these, in order to inscribe a diamond shape in the elliptical cross-sectional area the major and minor semi axis of the ellipse need to have the following dimensions $r_b = h_d/2$ and $r_a = w_d/2$ respectively (see Figure 4.2). Similarly, the perforations with a stadium shaped cross-sectional area will have the radius of the semicircles $r_s = w_d/2$ and the length of the straight line $d = h_d - w_d$.

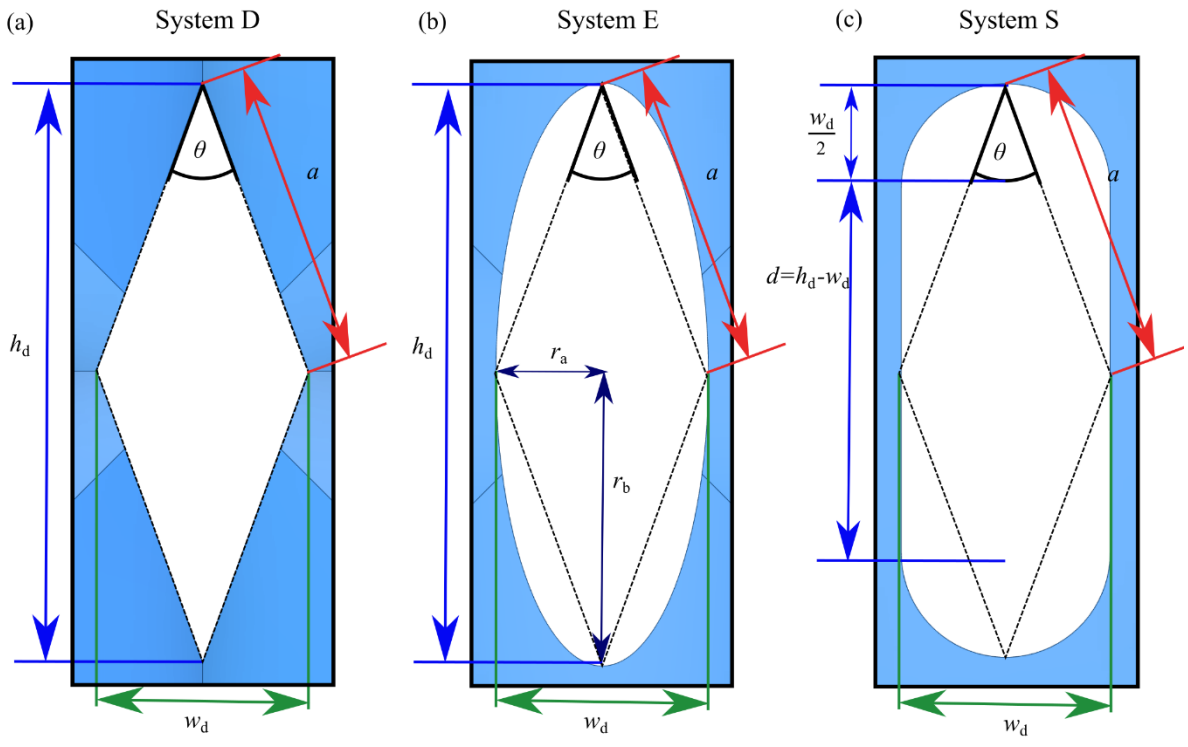

Figure 4.2.The figure depicts the parameters used to create (a) diamond perforations and how the parameters for (b) elliptical and (c) stadium-shaped perforations are derived.

Having established the dimensions of the perforation cross-sectional area, the resulting perforated structures were built in-silico using the auto-CAD software, Inventor 2022. This was done following the work done in Chapter 3 where continuous voids of constant cross-sectional area (perforations) were applied at strategic loci and in the *xy*, *yz* and *zx* planes of a block of material to produce complex 3D structures, as shown in Figure 4.3. The nearest corners of the diamond shaped perforations (or inscribed diamonds in the cased of the elliptical and stadium shaped perforations) were separated by an equal distance *s*.

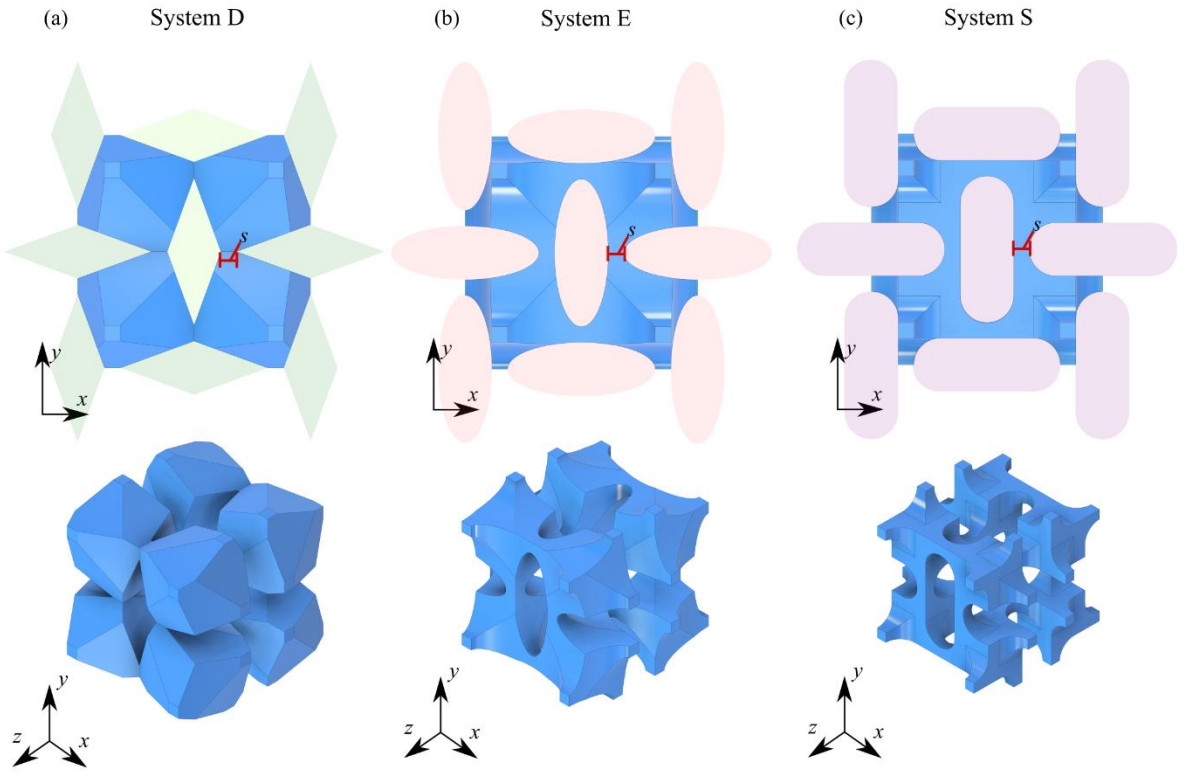

Figure 4.3.The figure depicts how the 3D structures were built using (a) diamond perforations (b) elliptical and (c) stadium-shaped perforations.

4.2.2 Finite element simulations

The perforated systems were then analysed using the Finite Element method via the commercially available software ANSYS® Mechanical APDL Release 13. Due to the symmetry that exists along lines parallel to the principal axes, only one eighth of the unit cell needed to be simulated (see Figure 4.4). This allowed the simulation of a smaller volume, representative of the larger structure, which decreased simulation time.

The boundary conditions were imposed in a similar fashion to Chapter 3 in Section 3.3.2.1. Referring to Figure 4.4, when loading in the *x* direction, a compressive strain was applied to the nodes having the minimum and maximum value in the *x* direction shown as black arrows. The nodes having the minimum value in the y-direction were constrained to not move in the *y* direction (depicted by rollers) whilst those having the maximum value in the *y* direction were coupled to move together in the same direction with the red boxes indicating coupled nodes. Similarly, the nodes having minimum value in the *z* direction were constrained to not move in the *z* direction whilst those having the maximum value in the *z* direction were coupled to move together in this direction. This allowed the structure to be modelled as an infinite system, with the results providing the bulk properties of the material when loaded in the *x* direction. This procedure was repeated for the loading in the *y*, or *z* directions by altering the boundary conditions accordingly.

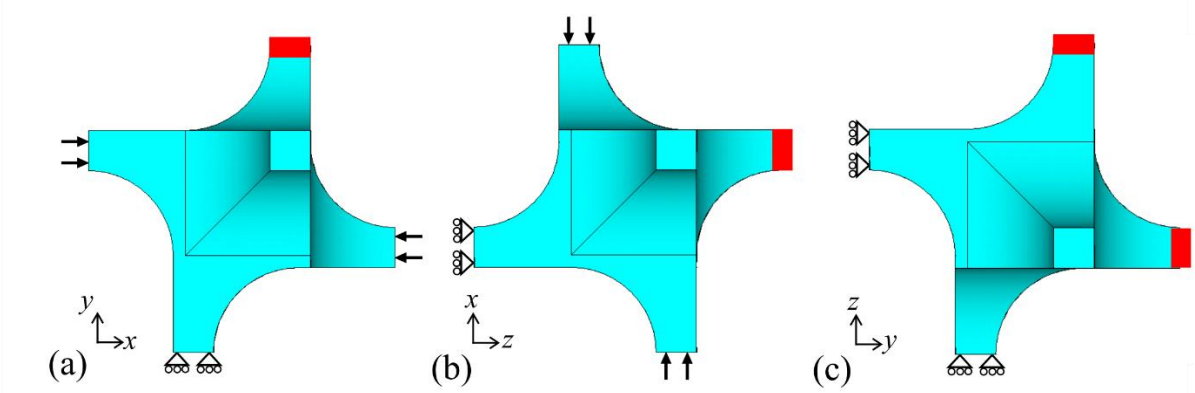

Figure 4.4. A representative drawing of the projections of the 3D perforated system on the (a) *xy*, (b) *yz*, and (c) *zx* planes together with the boundary conditions used for loading in the *x* direction.

The element type for the simulation was set to SOLID187, this being a higher order 3D element with quadratic displacement behaviour that is able to model both elastic and plastic behaviour, as well as allowing for irregular meshes (ANSYS Inc., 2010.). For the initial investigation, the mechanical properties of the material to be used were experimentally determined and in the linear region the Poisson's ratio was found to be 0.463 while the Young's modulus was estimated to be 972 MPa. These values were inputted in the numerical simulations. Mesh independence tests were then carried out for the three types of 3D perforated systems considered.

For ease of reference, the 3D perforated system having continuous voids of diamond shaped cross-sectional areas will be referred to as System D, the perforated system having continuous voids of elliptical cross-sectional area will be referred to as System E, whilst the system having continuous voids of stadium shaped cross-sectional area will be referred to as System S. For each system considered in this study (System D, System E and System S), referring to Figure 4.2 and Figure 4.3, parameter a was assigned a value of 10 mm, parameter s was given a value of 0.5 mm or 2.0 mm whilst θ was varied between 20° and 90° in increments of 5°. This resulted in a total of 90 structures or 270 simulations (for loading along the three principal directions).

From the numerical results obtained the engineering Poisson's ratios and Young's moduli in all loading directions were derived. Furthermore, the distribution of forces within the material was investigated through the use of the von Mises stresses. For the purpose, the strain concentration factor (K_ε) was used defined in Section 3.3.2.2.

To complement the linear analysis, nine non-linear simulations were also carried out on three structures from System D, System E and Systems S when loading in the x, y and z directions. The geometric parameters adopted for Systems D, E, and S were a = 4 mm, s = 0.8 mm, and θ = 50° (see Figure 4.5). In the case of this study, the non-linear simulations

were performed for relatively small strains, i.e., up to 2% strains. As for the previous cases, one eighth of the unit cell was simulated. Three non-linear simulations were carried out on each structure. For the purpose of simulations, the mechanical properties of the material to be used for the experimental prototypes were inputted in ANSYS APDL. The Poisson's ratio of the constituting material in the linear region was found to be 0.463 while the Young's modulus was estimated to be 972 MPa.

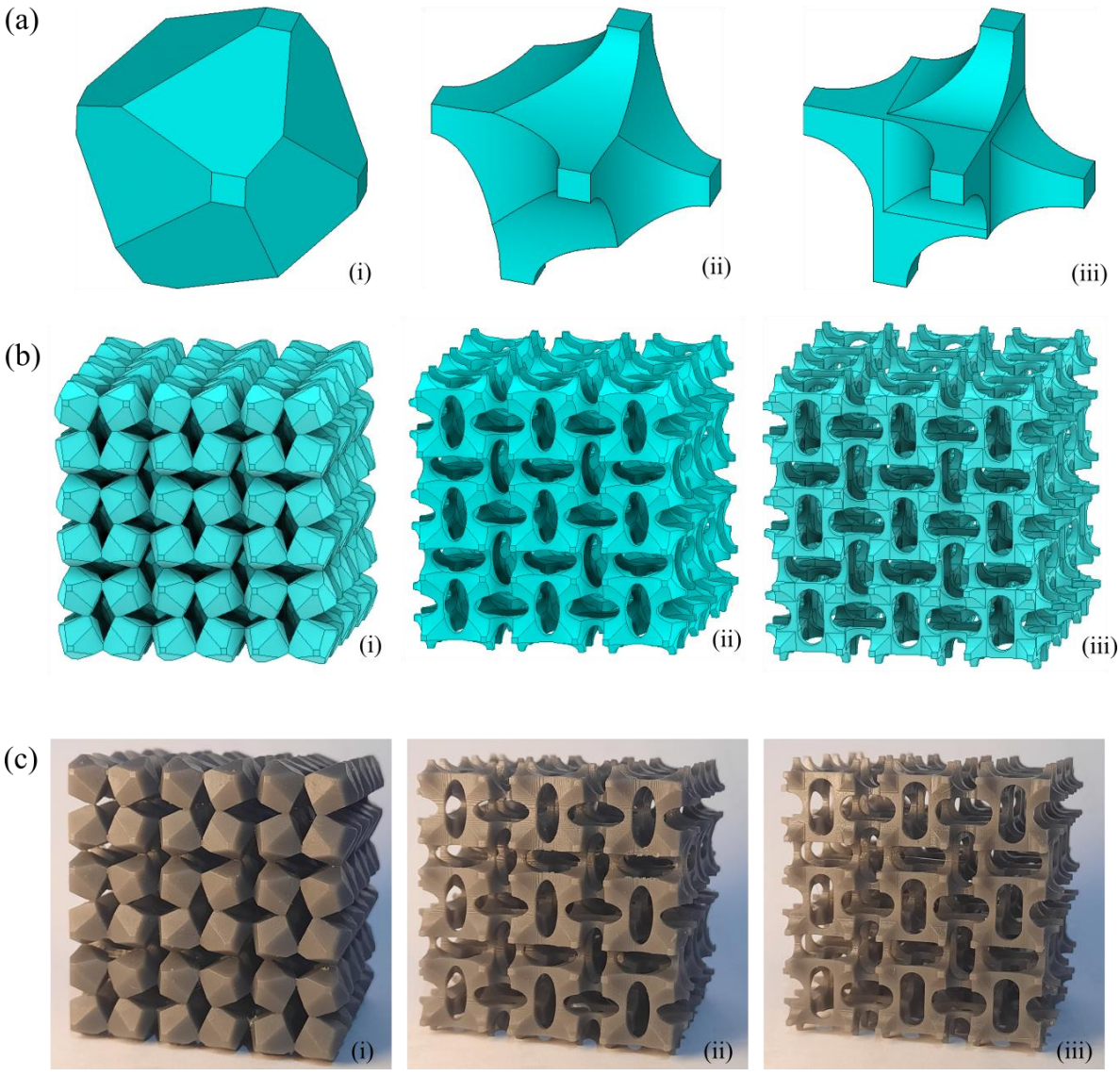

Figure 4.5.(a) The repeating unit of the three structures considered for the FEA non-linear simulations. (b) The CAD of the three structures considered composed of 3×3×3-unit cells. (c) the experimental counterparts of the three structures composed of 3×3×3-unit cells.

4.2.3 Experimental method

To verify the numerical results, experimental measurements were also carried out. These were carried out on three structures using the same parameters as those used for the non-linear simulations described above. The only difference was that the simulated systems and the experimental structures was that the latter were composed of 3×3×3-unit cells (see Figure 4.5). The experimental prototypes were 3D printed using Formlabs Form 3 SLA 3D printer employing the Formlabs Tough 2000 resin. The *xy* resolution was 50 µm and a layer thickness of 50 µm was adopted. Once printed the prototypes were washed with isopropyl alcohol (IPA) in the Formlabs Form Wash tank for 10 minutes. The parts were then detached from the build plate removing any supporting material in the process. The cleaned models were then washed once more for further 10 minutes in IPA. The washed prototypes were than post-cured for 60 minutes at 60 °C using the Formlabs Form Cure.

The cured prototypes were tested under compression using a Testometric universal loading machine (M350-20CT) with a 100 kg load cell (Serial Number: 31931). The edges within the printed structure were marked with white spots and were used to record the deformations in the axial and transverse directions (see Figure 4.6). A compressive strain was then slowly applied on the prototype at a rate of (10 mm min^{-1}). The deformation was recorded at a rate of 5 fps with a Daheng imaging camera (MER2-630-60U3M) having a resolution of 3088 × 2064 px and mounted with a Get Cameras lens (LCM-5MP-08MM-F1.4-1.5-ND1) having a focal length of 8 mm and less than 1% distortion. The camera and lens were stably fixed and levelled horizontally in front of the prototype. The change in lengths were monitored using an inhouse pattern recognition python script, using an in-built calibration procedure. Two sets of axial and transverse measurements were taken (one from each unit cell), from which the average Poisson's ratio was then determined. To the determine the average Poisson's ratio, the raw data was first fitted using a 6^{th} order polynomial from which values for the transverse strain

were calculated for particular values of the axial strain. The results were than compared to the set of non-linear simulations discussed above.

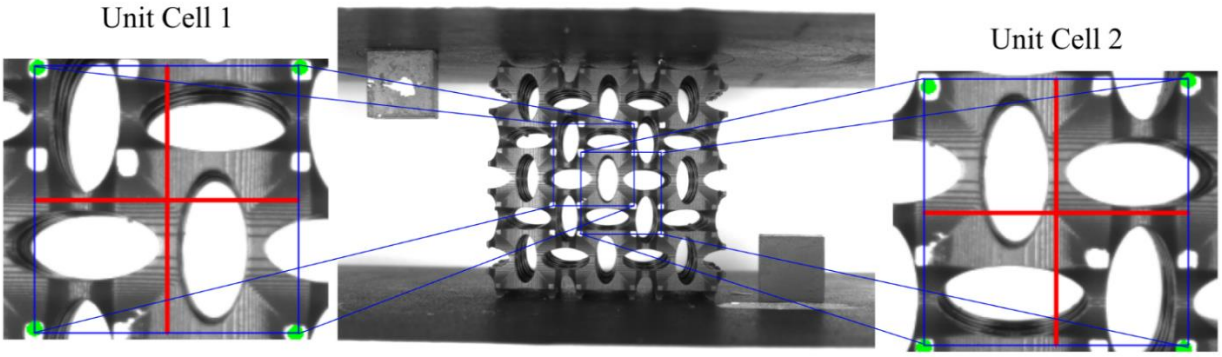

Figure 4.6. The image observed by the camera which is fed into the python script which analysed two-unit cells of the structure.

4.2.4 Deformation Analysis using FEA

Through the use of FEA, the deformation analysis is carried out to investigate the mechanisms leading to an NPR. To do so, linear simulations were carried out on a series of structures from System D, E and S, having s = 0.5 and θ ranging from 20° to 90° at 10° intervals. The irregular polygons' six (6) connecting points were mapped out and their displacements when a strain of −2% was applied, were noted. Following this, three diagonals; α, β and γ, were drawn connecting the centres of opposite connecting points as shown in Figure 4.7. The rotation angles φ_i, i = 1,2,3, and percentage change in length of these diagonals (and hence the polygons as a whole) could then be calculated from the deformed and undeformed structures.

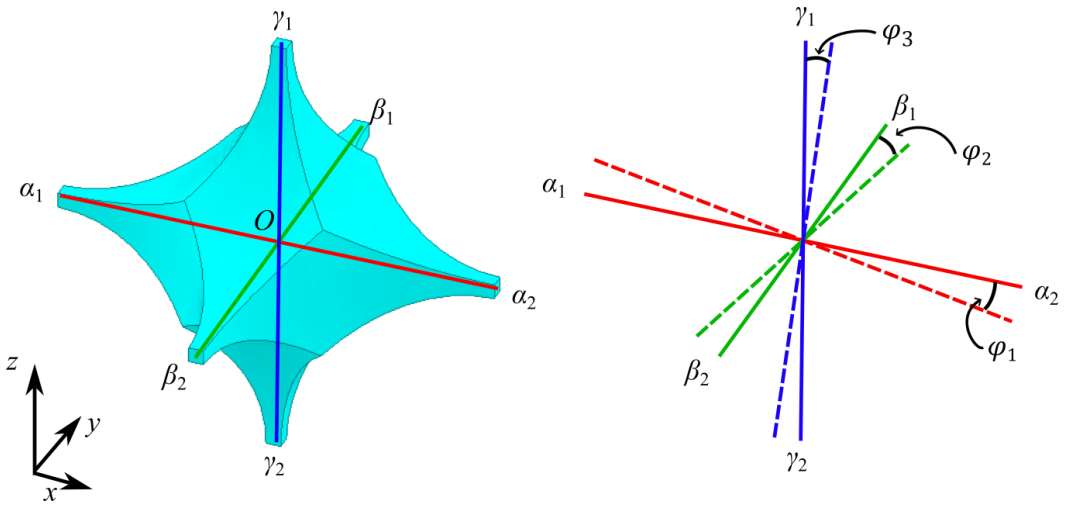

Figure 4.7. A depiction of a System E structure and the parameters used for the analysis of the deformation mechanism.

4.3 Results and Discussion

Prior to discussing the FEA results in detail, it is important to highlight the results obtained from the mesh independent studies carried out for Systems E and S. (Note that mesh independent studies for System D were carried in Chapter 3). Structures having a = 10 mm, s = 2.0 mm and θ = 50°, were meshed using element sizes ranging from 0.3 to 1.2 mm. In the case of element size 0.3 mm, mesh refinement was also applied, whereby thirteen degrees of increasing refinement were used. Each set was then compared to the finest mesh and the values for the calculated Poisson's ratio and Young's modulus were compared. The results obtained (see Figure 4.8) show that for Systems E and S, an element size of 0.3 mm is enough to obtain values of the Young's Modulus and Poisson's ratio within <0.01% of the finest set.

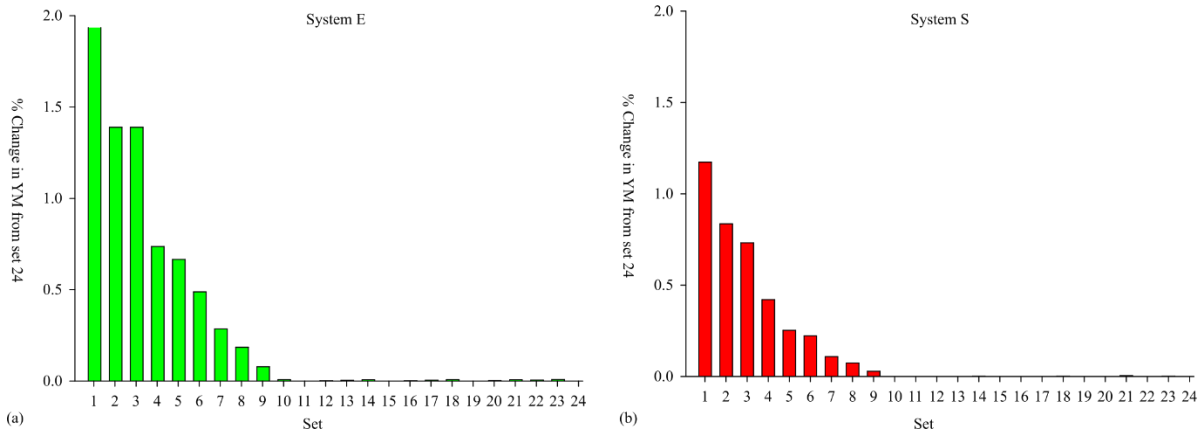

Figure 4.8. Mesh-independent studies carried out on System E and S.

As in the case of System D (see Chapter 3), Systems E and S were found to have the potential to exhibit auxetic behaviour, with the sign and magnitude of the Poisson's ratio depending on the values and magnitude of θ and s. The variation of the Poisson's ratio and Young's moduli of the 3D perforated systems analysed in this study are shown in Figure 4.9. As expected, given the symmetry of the analysed structures, the Poisson's ratios and Young's moduli were identical in the *xy*, *yz*, and *zx* planes and thus, only the results in the *xy* plane are shown. For all values of θ and s considered in this study the Poisson's ratio and the percentage ratio of the Young's modulus of the structures E to that of the material E_{M} ($\%E^* = \frac{E}{E_{\mathrm{M}}} \times 100\%$) obtained for Systems E and S are very similar. Calculations indicate that the maximum difference in the values of the Poisson's ratio is of 0.001, while in the case of $\%E^*$ it is 0.025%. On the other hand, the discrepancy in the values between System E and System D (as well as between System S and System D) is small only for relatively small values of s and θ, becoming, in the main, more pronounced as the values of s and θ increase. For example, when s = 0.5 mm and θ = 20°, the difference between the Poisson's ratio of Systems D and E (S) is 0.005 (0.008) while that in the $\%E^*$ is 0.003% (0.001%). On the other hand, when s = 2.0 mm and θ = 80°,

the difference between the Poisson ratio of Systems D and E (S) is 0.062 (0.053) while that in the $\%E^*$ is 4.35% (4.09%). From Figure 4.9 it also follows that the discrepancy is most noticeable in the case of the $\%E^*$.

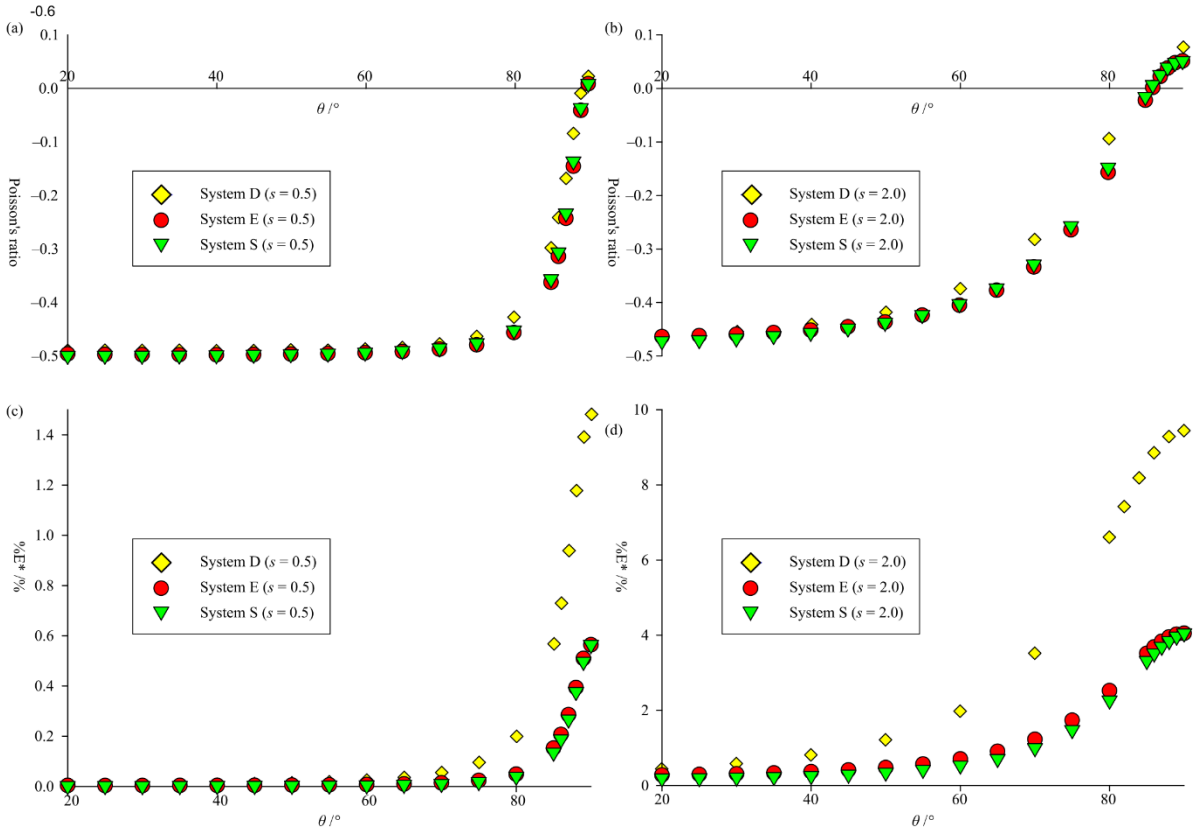

Figure 4.9(a-b) Graphs of Poisson's ratio against perforation angle comparing Systems E and S to System D. (c-d) Graphs of Young's Modulus against perforation angle comparing Systems E and S to System D

All this indicates that the Poisson's ratio and relative stiffness of Systems D, E and S may be tailored, to some extent depending on of the chosen values of θ and s. These tailored mechanical properties may also be coupled with different volume fractions that these systems may achieve. For a particular value of θ and a (see Figure 4.10), it is immediately clear that System E and S are expected to have a lower volume fraction when compared to System D as the former systems are designed in such a way that the diamond shape is inscribed inside the

perforation. Furthermore, it may be observed that the volume fraction of system E is always larger than that of System S, except when θ has a value of 90°, as in this case, both Systems E and S would result in the same geometry. Moreover, System S reaches a minimum at 70°, due to the nature of the stadium-shaped perforations which allows it to have a significantly lower volume fraction even when compared to System E. Referring to Figure 4.10, it is also interesting to note that for larger values of θ, the difference in volume fraction between Systems E and S and System D is larger than 50%. For example, for a system with a = 10 mm, s = 2 mm and θ = 70°, System D, E, and S have a volume fraction of 0.370, 0.160 and 0.122 respectively. These considerations would be important in industries where there is a need of high performing light materials, such as the aerospace industries and sports industries.

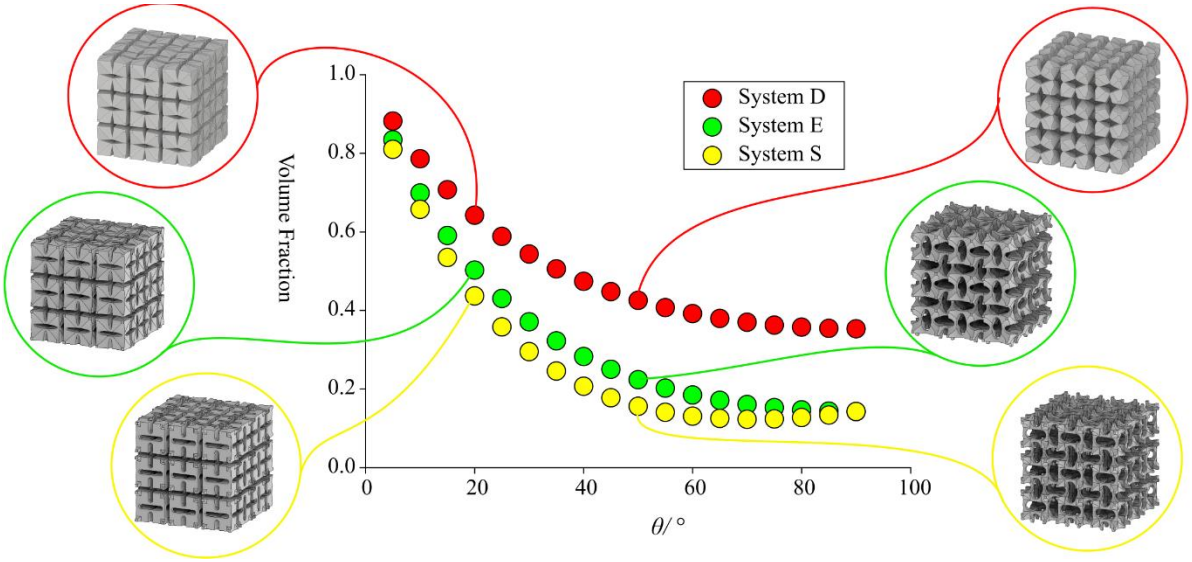

Figure 4.10. A graph of volume fraction with a change in θ, for the three considered systems. The insets are the structures at the corresponding θ values.

As mentioned in Chapter 2, the mechanical properties of auxetic materials are related to the geometry and the way the geometry deforms in response to an applied stress. In view of this, it would be very interesting to understand how the mechanical properties of Systems D, E and S arise from a deformation point of view. No attempt has been made so far to measure the

deformation of these systems. Thus, as a first step, one must understand how the measured negative Poisson's ratio in different planes is obtained. In view of this, an attempt is made to elucidate the way Systems D, E and S deform when a stress is applied.

As described in the methodology section, the deformation of the system was first evaluated by considering its movement in three dimensions. This was done by monitoring the changes in the angle and length of the diagonals between the vertices of the polyhedron that were connected together i.e., diagonals α_1-α_2, β_1-β_2 and γ_1-γ_2 (see Figure 4.7). These three diagonals pass through the centre of the polyhedron; however, they do not necessarily intersect each other perpendicularly. The angle between these diagonals is dependent on the initial value of angle θ. In fact, referring to Figure 4.11 and taking angles α-o-β and α-o-γ (see Figure 4.7) as an example, one notes that these angles tend to approach a value of 90° as the initial value of θ approaches 90°. Thus, in the case when θ is smaller than 90°, the lines between the connection points of the polyhedron are not representative of its axis. Monitoring the changes in the angles of these diagonals (angles φ_1, φ_2 and φ_3 in Figure 4.7) will thus only give an indication of the hinging of the polyhedron. Furthermore, an indication of the rigidity of the polyhedral unit may be obtained by monitoring the changes in angles between these diagonals (such as angles α-o-β and α-o-γ in Figure 4.7) and the changes in length of these diagonals.

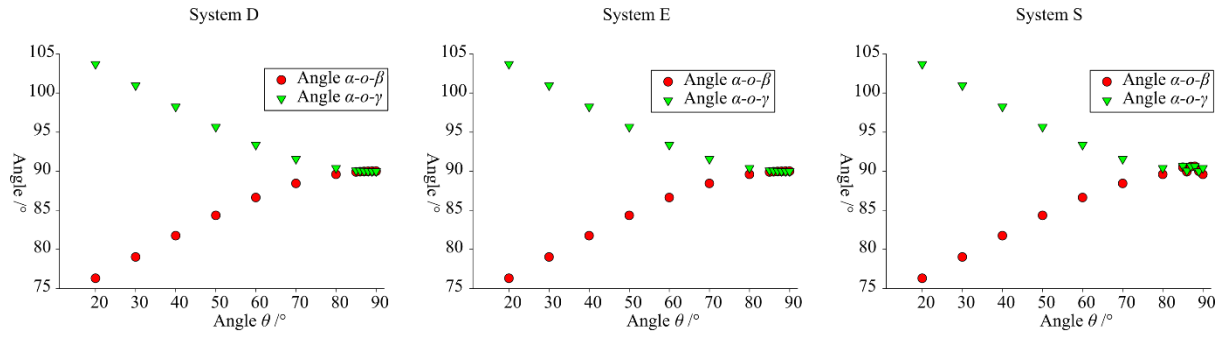

Figure 4.11. The value of angles α-o-β and α-o-γ (see Figure 4.7) for different values of θ. Note that System D, System E and System S result in the same profile.

To elucidate the deformation mechanism of these systems, System D was initially analysed. More specifically, System D having parameters of θ = 20°, a = 10 mm and s = 0.5 mm was studied when loaded under compression in the x-direction. A load in this direction results in a negative Poisson's ratio in the xy and zx planes, with the Poisson's ratio being of equal magnitude in the two planes. Referring to Figure 4.12 and Figure 4.7, one may note that in response to an applied compressive strain, angles φ_1, φ_2 and φ_3 undergo a substantial change, albeit not to the same extent with the ratio, $\varphi_2 : \varphi_1$ being approximately equal to 0.5, while the ratio $\varphi_3 : \varphi_1$ being approximately equal to 1. As described above, the fact that these three diagonals do not intersect perpendicularly at the centre must also be taken into consideration when interpreting these ratios. The angles where the diagonals α_1-α_2, β_1-β_2 and γ_1-γ_2 intersect (such as angles α-o-β, α-o-γ and β-o-γ, see Figure 4.7), undergo minimal changes with a maximum variation of 0.01° (a maximum change of 0.007° for each 1° rotation of φ_1). Diagonals α_1-α_2, β_1-β_2 and γ_1-γ_2, also experience a minimal change in length, to a maximum of 0.02% (a maximum change of 0.018% for each 1° rotation of φ_1). It is interesting to note that although the system is being compressed, the length of the diagonals between the connection points is increasing (i.e., it is under tension), albeit to a very small degree. Taking all this into consideration, one may conclude that in this case, the polyhedron is mainly acting as a rigid rotating unit, with the polyhedral units rotating in multiple directions.

Referring to Figure 4.9a-b, the Poisson's ratio of System D does not change considerably as the angle θ assumes different initial values, up to when θ = 70°. Referring to Figure 4.12, one may note that similarly to the case when θ = 20°, there is significant rotation of the polyhedron, with the amount of rotation of angles φ_1, φ_2 and φ_3 increasing as angle θ increases. Furthermore, the ratios, $\varphi_2 : \varphi_1$ and $\varphi_3 : \varphi_1$ start to approach each other with $\varphi_2 : \varphi_1$being equal to 0.58 and $\varphi_3 : \varphi_1$ being equal to 0.82 when the initial value of θ is 70°. This indicates that as the angles at the point where the diagonals intersect each other start to

approach 90°, the ratios $\varphi_2:\varphi_1$ and $\varphi_3:\varphi_1$ start to approach each other as well. Changes between the diagonals also increase with an increase in the initial value of θ. However, the changes in these angles are still very small and in fact when the initial value of θ is 70°, they change to a maximum of 0.15° (0.033° for each 1° rotation of φ_1), indicating that the polyhedra are not distorting to a large degree. When taking into consideration the changes in length of the polyhedron, one also notes that it is increasing slightly as angle θ increases. The maximum change of the polyhedron diagonals (α_1-α_2, β_1-β_2 and γ_1-γ_2) is of 0.23%, (a maximum change of 0.051% for each 1° rotation of φ_1) when θ = 70°. All this indicates that up to when the initial value of θ is 70°, the main deformation mechanism is the rotation of polyhedral units with the polyhedral units themselves distorting to a low degree.

For values of θ between 70° and 86°, the Poisson's ratio of System D starts to become less negative. Within this region of θ, the polyhedron tends to deform to a higher extent than what was measured previously. Changes between the angles of the diagonals (such as angles α-o-β, α-o-γ and β-o-γ, see Figure 4.7) increase to a substantial amount with an increase in the initial value of θ. When θ = 86°, they change to a maximum of 0.95° (0.089° for each 1° rotation of φ_1), indicating that the polyhedra start to distort. The change in length experienced by each polyhedron also increases within this range of θ, with the maximum change of the polyhedron diagonals (α_1-α_2, β_1-β_2 and γ_1-γ_2) being 0.93%, (a maximum change of 0.086% for each 1° rotation of φ_1) when the initial value of θ is 86°. However, the polyhedral units still rotate to a substantial amount (10.6° when θ = 86° for a strain of −2%). Referring to Figure 4.12, the ratios, $\varphi_2:\varphi_1$ and $\varphi_3:\varphi_1$ approach each other with the former having a value of 0.68 and the latter ratio having a value of 0.72 when θ = 86°. Although the rotation of the polyhedral unit is still very important, the rigidity of the same polyhedral units start to decrease, resulting in a mechanism that may be described as a semi-rigid rotating polyhedral system. This significant decrease in rigidity of the polyhedral units is accompanied by a decrease in the

auxeticity of the system. As the value of θ approaches 90°, the rotations of the polyhedral units start to decrease, until no rotation is present when the initial value of θ is 90° (fully open system). Also, changes in β_1-β_2 and γ_1-γ_2 begin to decrease as θ approaches 90° having a value of about 0.20% when θ = 89°. On the other hand, the change in α_1-α_2 increases (although within this range of theta the direction of deformation changes i.e., from tension to compression) with a change of −1.58% when θ = 89°. When θ = 90°, only α_1-α_2 experiences a change in length. The change in length of α_1-α_2 is equal to −2%, which is the same as the applied strain. This is because the main deformation mechanism of this conformation is contraction of the polyhedral units in the direction of the load, resulting in a Poisson's ratio of nearly zero (see Chapter 3).

An analysis of the 3D geometric parameters of Systems E and S when s = 0.5 mm and a = 10 mm reveals that a similar deformation mechanism as described for System D is taking place. In the range of $20° \leq \theta \leq 70°$, Systems E and S deform through rotation of rigid units. The largest change in the length of the polyhedron diagonals (α_1-α_2, β_1-β_2 and γ_1-γ_2) is of 0.14% (0.032% for each 1° rotation of φ_1) for System E and 0.13% (0.029% for each 1° rotation of φ_1) for System S. Note that in the case of System S, the change in length of the diagonals is slightly aiding to the auxetic behaviour as up to when θ = 50° all three diagonals are becoming smaller under compression (see Figure 4.12). However, this is expected to have a very small effect on the Poisson's ratio as these changes are very small. The changes of the angle between these diagonals is less than 0.07° (0.016° for each 1° rotation of φ_1) in the case of System E and 0.08° (0.019° for each 1° rotation of φ_1) in the case of System S. Similar to System D, for Systems E and S the ratio, $\varphi_2 : \varphi_1$ is about 0.58 while the ratio $\varphi_3 : \varphi_1$ is about 0.83. Thus, up to a value of θ = 70°, the auxetic behaviour of systems E and S may be described as rotation of rigid units, as was the case for System D.

When θ is in the range of $70° < \theta \leq 86°$, the polyhedral units become slightly less rigid with the polyhedron diagonals (α_1-α_2, β_1-β_2 and γ_1-γ_2) changing by a maximum of 2.28%

for System E and 2.49% for System S. The angles between these diagonals change by a maximum of 1.70° in the case of Systems E and S. The ratio, $\varphi_2 : \varphi_1$ is within the range of 0.57 and 0.68 for Systems E and S while the ratio $\varphi_3 : \varphi_1$ for these systems is within the range of 0.72 and 0.83. All this indicates that within this region of theta, Systems E and S are distorting to a higher degree than System D. However, at the same time, the rotation of the polyhedral units of Systems E and S is larger than that of System D (see Figure 4.12). This combination of deformation mechanisms results in a slightly more negative Poisson's ratio for Systems E and S when compared to System D.

As θ approaches 90°, rotations of the polyhedral units decrease as in the case of System D as the Systems start to adopt their fully open conformation. Comparing System D with System E and S one notes that the polyhedral units of Systems E and S elongate and distort to a slightly higher degree. This may be explained by the fact that Systems E and S have a smaller volume fraction for the same value of θ (see above) and therefore are expected to be less rigid as indicated by their Young's moduli (see Figure 4.9(c-d)).

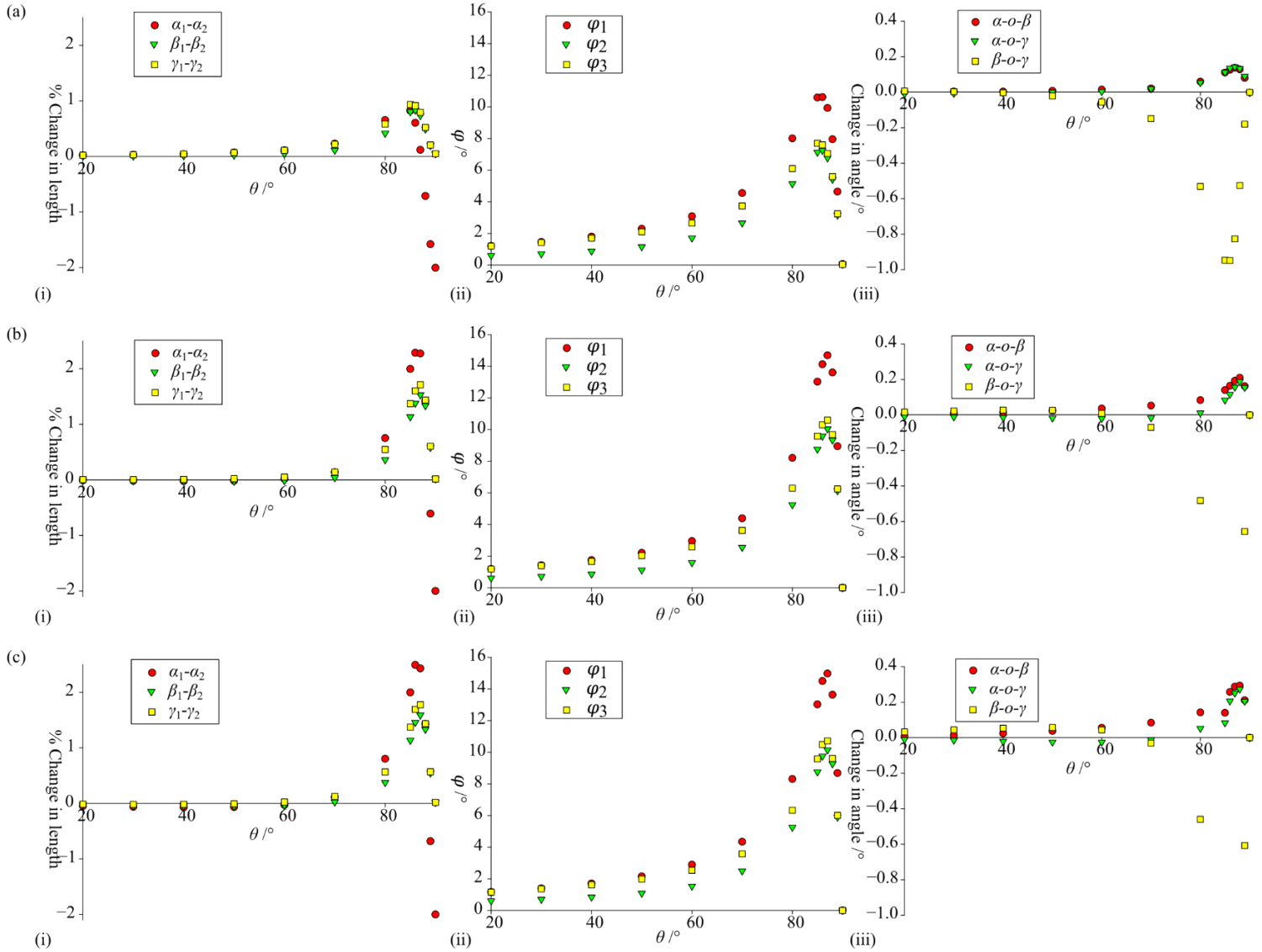

Figure 4.12. Graphs analysing the deformation of (a) System D, (b) System E and (c) System S when s = 0.5 mm

The observed changes in Poisson's ratio for Systems D, E, and S as parameter *s* increases provide an impetus to investigate the mechanistic changes brought about by a change in this parameter. As *s* increases, the Poisson's ratio of all three Systems tends to become more positive, particularly at higher values of θ. For example, referring to Figure 4.9(a-b), for θ = 50°, the Poisson's ratio for Systems D, E, and S is nearly −0.5 when *s* = 0.5 mm and circa −0.45 when *s* = 2.0 mm (the Poisson's ratio is slightly more positive for System D). On the other hand, when θ = 80°, the Poisson's ratio of Systems E and S change from about −0.456 to about −0.157, as *s* increases from 0.5 mm to 2.0 mm whilst the Poisson's ratio of System D changes from −0.429 to −0.095 for the same change in *s*.

An analysis of the deformation mechanism when *s* = 2.0 mm (see Figure 4.13) as compared to that when *s* = 0.5 mm (see Figure 4.12) indicates that at lower values of θ, a change in s does not result in a change of the polyhedral rotation. For example, when the initial value of θ is 50°, angle φ_1 changes by about 2.2° for Systems D, E, and S both when *s* is equal to 0.5 mm and *s* is equal to 2.0 mm. However, at higher values of θ, the rotation of the octahedron decreases as *s* increases. For example, when θ = 85° and *s* = 0.5 mm angle φ_1 changes by about 10.6° in the case of System D and by about 13.0° in the case of Systems E and S. On the other hand, when *s* increases to 2.0 mm, angle φ_1 changes by about 2.0° in the case of System D and by about 2.8° in the case of Systems E and S. This also shows that at higher values of θ, as *s* increases, the polyhedral units of Systems E and S are able to rotate to a higher extent when compared to System D.

It is also evident that as *s* increases, the polyhedron becomes less rigid. This is mainly shown from the changes in the polyhedron diagonals (α_1-α_2, β_1-β_2 and γ_1-γ_2). As *s* increases, the amount of change of these polyhedron diagonals increases as well. This is particularly true for diagonal α_1-α_2, for all values of θ. More specifically, when θ = 50°, as *s* is increased from

0.5 mm to 2.0 mm changes in α_1-α_2 vary from 0.07% to −0.12% in case of System D, from −0.02% to −0.017% in the case of System E and from −0.07% to −0.23% in the case of System S. These changes become larger as θ increases. Interestingly, the polyhedral units of Systems E and S deform to a higher extent than that those of System D even though Systems E and S have a more negative Poisson's ratio when compared to System D. The more negative Poisson's ratios of Systems E and S may be a result of the larger rotation of the polyhedral units. For Systems D, E, and S, as *s* increases, the angles where the diagonals α_1-α_2, β_1-β_2 and γ_1-γ_2 intersect (such as angles α-o-β, α-o-γ and β-o-γ, see Figure 4.7), start to deform to a lower extent, particularly angle β-o-γ.

Further insight in the deformation mechanism can be obtained from the stress distribution within the polyhedral units. Referring to Figure 4.14, Figure 4.15 and Figure 4.16, System E and S have lower peak values for the von Mises stresses and strain concentration factors, when compared to System D, even though Systems E and S were shown to deform to a larger extent. This is because the stresses are more distributed within System E and S and thus deform in a more uniform manner. On the other hand, in the case of System D, the stresses are more concentrated at the hinges, making more prone to failure at these points. Furthermore, as angle θ increases, the strain distribution factor increases for all considered Systems (Systems D, E, and S) indicating that the polyhedral are becoming less rigid, in accordance with the measurements conducted above. Another interesting comparison is when θ = 90° (shown in Figure 4.16). In this case, as already discussed above, the system is deforming through stretching of the polygons. The stress distribution indicates that the stress is not limited to the hinges and in all three cases it starts to move into the polygon. Thus, the Poisson's ratio is positive, however it is less positive that that of the material as two mechanisms are operating as discussed in Chapter 3.

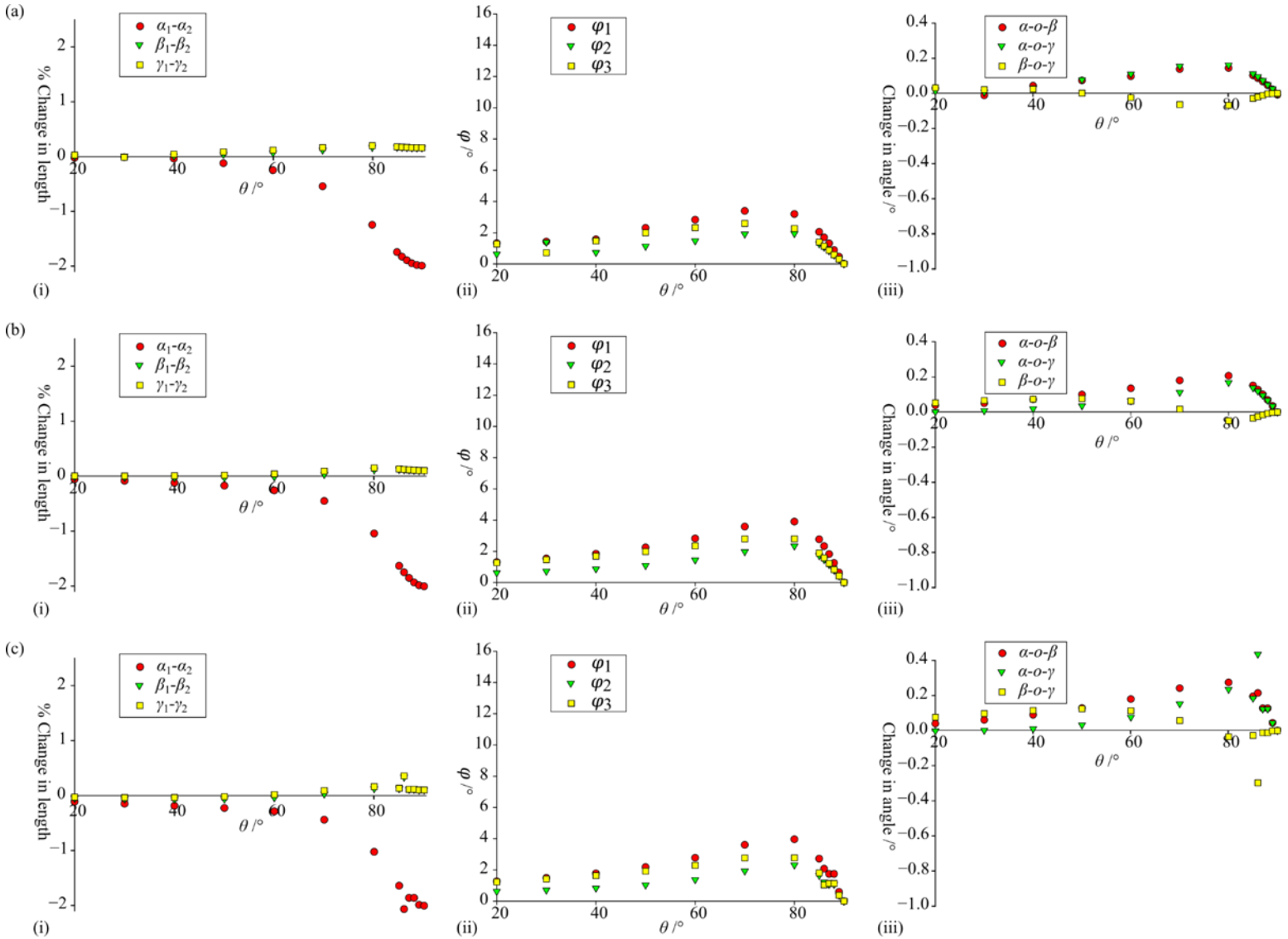

Figure 4.13. Graphs analysing the deformation of (a) System D, (b) System E and (c) System S when s = 2 mm.

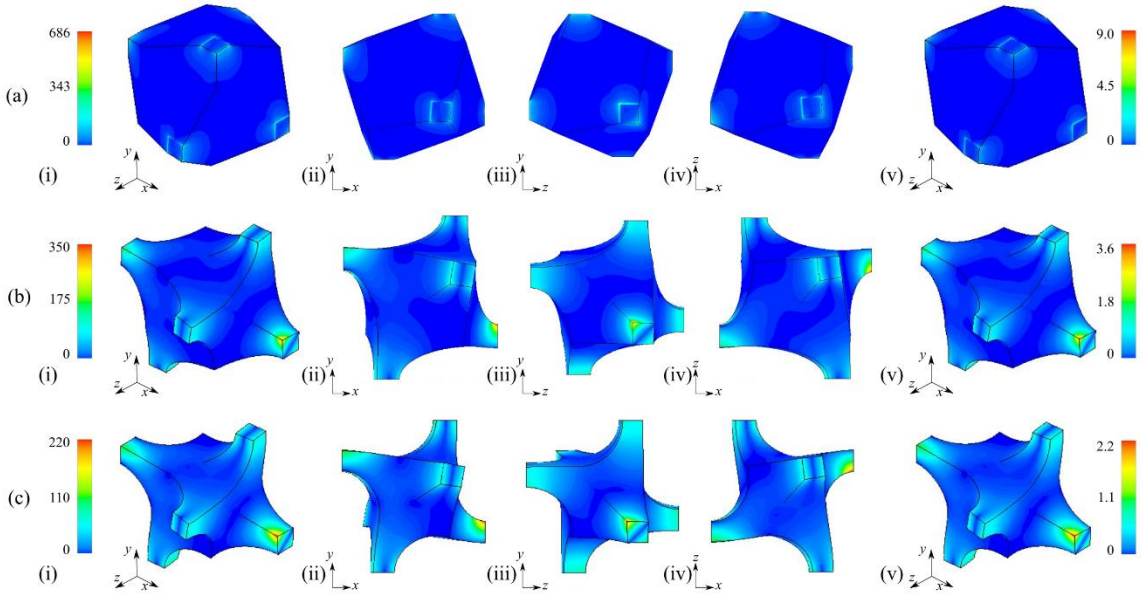

Figure 4.14.The results for the compressed (a) System D, (b) System E, (c) System S, having θ = 50°, which show the von Mises stresses along planes (i-iv) and the strain concentration factor (v). In all cases a = b = c = 10.0 mm and s = 2 mm.

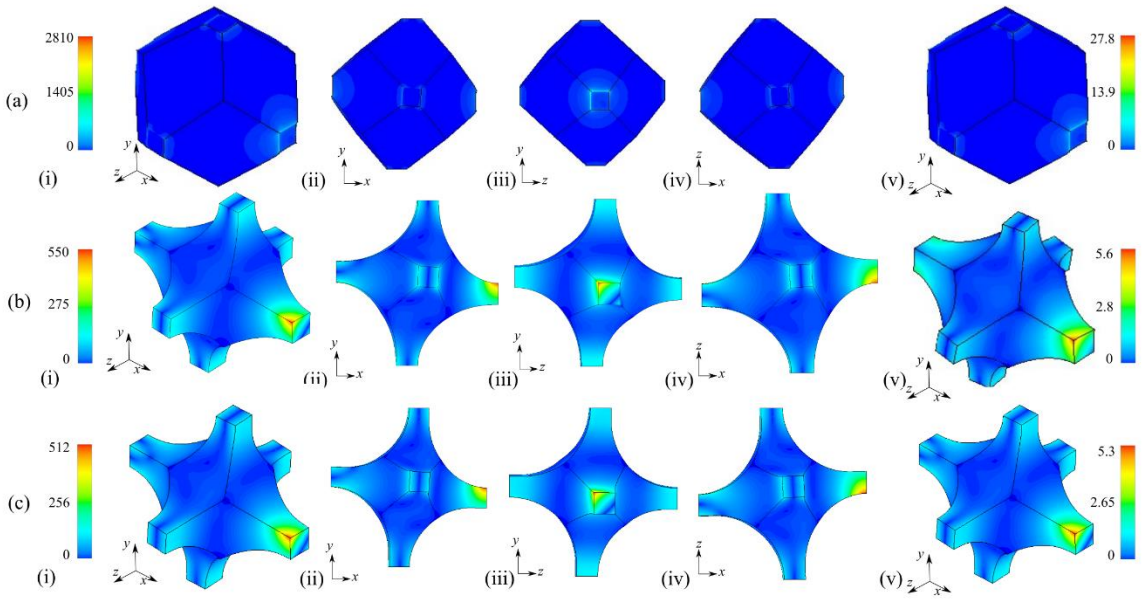

Figure 4.15.The results for the compressed (a) System D, (b) System E, (c) System S, having θ = 80°, which show the von Mises stresses along planes (i-iv) and the strain concentration factor (v). In all cases a = b = c = 10.0 mm and s = 2 mm.

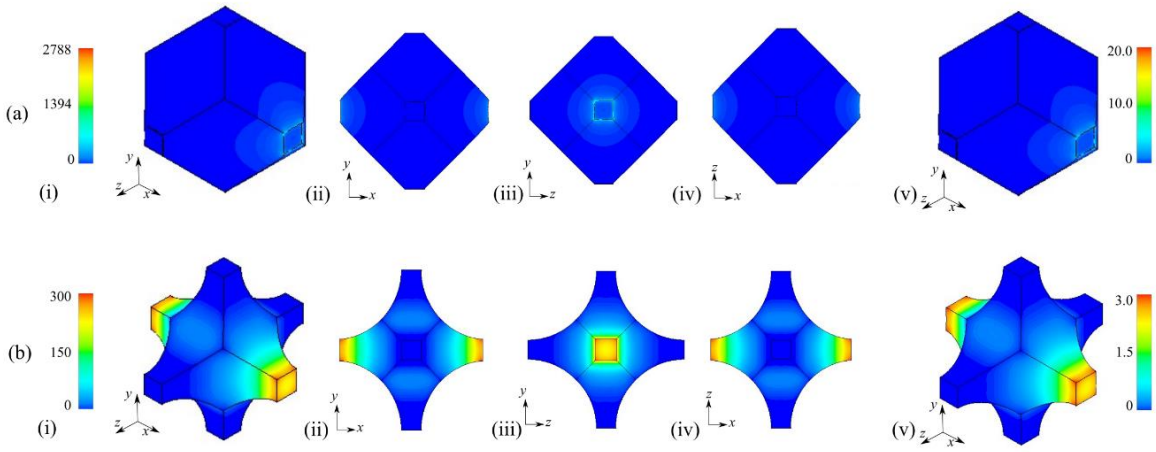

Figure 4.16. The results for the compressed (a) System D, (b) System E, having θ = 90°, which show the von Mises stresses along planes (i-iv) and the strain concentration factor (v). In all cases a = 10.0 mm and s = 2 mm.

Having established numerically that Systems D, E and S can exhibit a negative Poisson's ratio and having studied the way that this change is brought about (the deformation mechanism), the numerical results were validated experimentally. For the three experimental prototypes produced, (Systems D, E and S having target values of s = 0.8 mm, a = 4.0 mm and θ = 50°) the dimension of parameter s was measured as described in the methodology section (see Figure 4.17). This was done as to assess the accuracy of the printer *vis-à-vis* pore geometry as in Chapter 3 it was highlighted that when using diamond shaped perforations and elastic resin the printer used was unable to reproduce the target geometry. Furthermore, Tough 2000 resin was used instead of elastic resin (used in Chapter 3) in order to investigate whether the printing inaccuracies for System D in the previous chapter were due to the resin rather than the geometry of the structure. From the data obtained, it was found that a significant difference between System D and Systems E and S is present. In fact, the average value of parameter s for System D was 1.093±0.193 mm (similar to that obtained in Chapter 3) whereas Systems E and S has an average value of 0.870±0.045 mm and 0.841±0.060 mm, respectively.

Given that the target value for *s* was 0.8 mm, it is evident that the printed structures of Systems E and S are more representative of the target pore geometry. As discussed in Chapter 3, the small space at the vertices of the diamond shaped perforations could result in poor drainage of the uncured resin while cleaning. The extra resin would then cure at the intersections during the post curing stage changing the pore parameters. In the case of Systems E and S, due to their round geometry, such small spaces are not present and thus there is better drainage of the resin in the cleaning phase, resulting in more faithful prints, in terms of parameters.

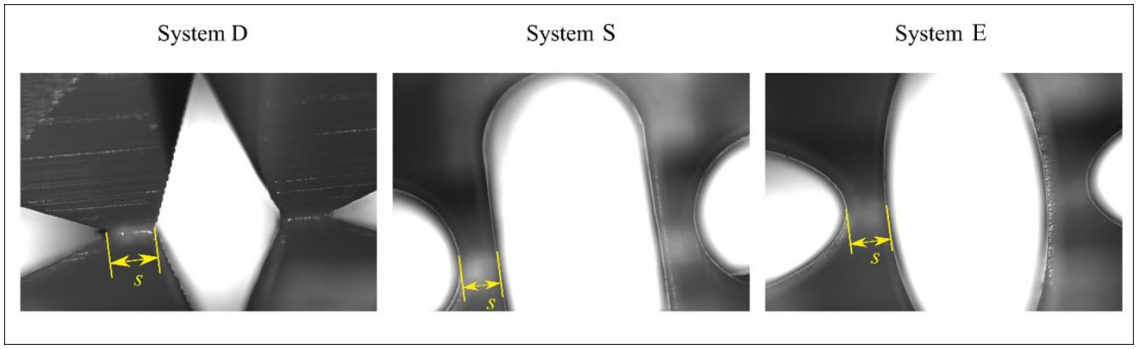

Figure 4.17. Images of Systems D, E and S structures, having an *s* of 0.8 mm, *a* of 4.0 mm and θ of 50°, under the microscope

Having established that target parameters are obtained for Systems E and S, their mechanical properties were measured experimentally and compared to those obtained from non-linear simulations having the same parameters. When a = 4.0 mm, s = 0.8 mm and θ = 50°, non-linear FEA simulation predicted a Poisson's ratio of −0.43 for both Systems E and S. The experimentally determined Poisson's ratio for Systems E and S having the same parameters were of −0.50 and −0.41 respectively, indicating a good agreement between the Poisson's ratio as obtained from the non-linear FEA simulations

and the experimental results, particularly for System S. It is important to note that when fitting the data of the experimental structures, the minimum value obtained for the R^2 was of 0.990. The experimentally undeformed and deformed structures for Systems E and S are shown in Figure 4.18. From this figure it may be discerned that upon deformation the projected squares are undergoing both rotation and distortions of the squares, as discussed above. Furthermore, the experimental results obtained (see Figure 4.19) show that that the Poisson's ratio of these systems is strain independent up to 10% axial strain, something which increases the possible applications of these systems as discussed in Chapter 3.

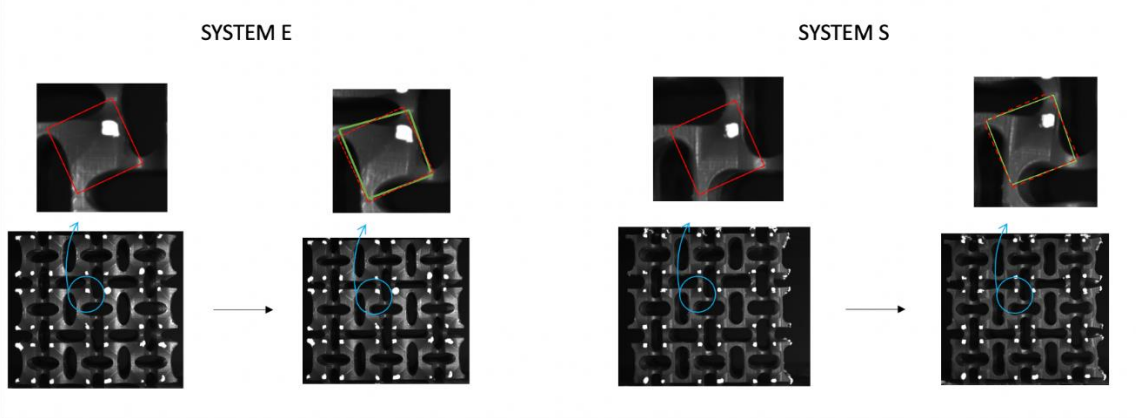

Figure 4.18. Depicts the experimental prototypes for System E and S, when loaded up to 8%

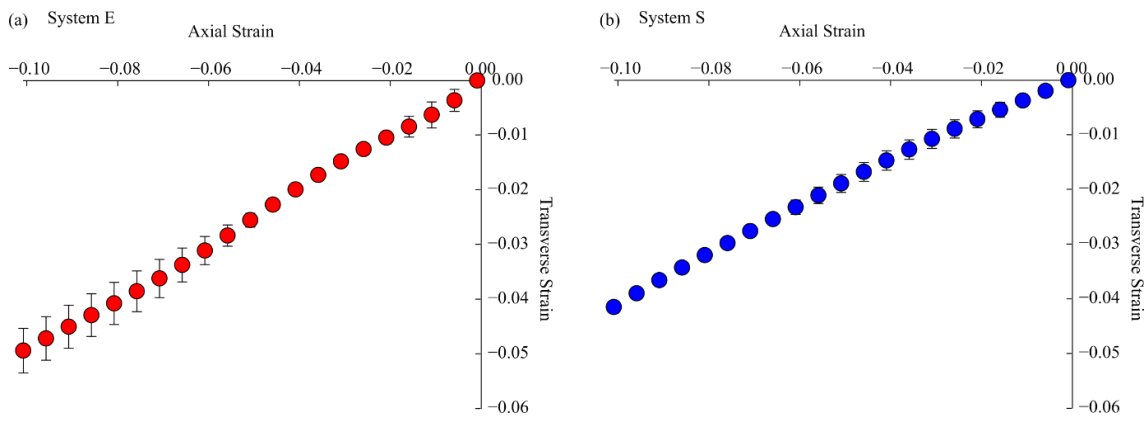

Figure 4.19. Plots depicting the axial strain-transverse strain curve for (a) System E and (b) System S

Before concluding it is important to note that the nature of the perforations investigated in this study (particularly System S) may be easily produced through milling as two circular perorations may be drilled at each end of the perforation and then joined to form the stadium shape. Such 3D auxetic perforated systems would be ideal for a number of applications such as shock absorbers, dampeners and body protection due to the known superior energy absorption performance (S. Hou *et al.*, 2015; Imbalzano *et al.*, 2016; L. Jiang & Hu, 2017) and impact resistance (K. K. Dudek *et al.*, 2019a) of auxetic materials. As discussed above, the experimental prototypes were shown to be strain independent up to at least 10% strain something which is usually a desirable trait. Furthermore, for small values of s and at when θ is smaller than 70°, the Poisson's ratio of all considered systems was circa −0.5. However, there were substantial differences in the Young's moduli and volume fractions which indicate that systems having similar Poisson's ratio but different Young's moduli and/or volume fractions can be produced.

4.4 Conclusion

In this study we investigate the use of elliptical and stadia-shaped perforations to create an auxetic material having a three-dimensional auxetic mechanism, *in lieu* of diamond-shaped perforations shown in Chapter 3. Through numerical simulations, it was shown that the new structures were able to distribute stresses better throughout the structure while exhibiting a more negative Poisson's ratio when the perforation angle (θ) is large. Furthermore, experimental studies indicate that the Poisson's ratio observed are strain independent up to at least 10% strain. The use of these perforation aimed to simplify the manufacturing process where elliptical and stadia-shaped perforations would allow the use of milling in addition to casting and cutting. This is a significant advancement as

currently most 3D auxetic systems can only be produced through the use of additive manufacturing techniques. Therefore, having an auxetic system with such versatility and ease of production would promote industrial development of manufacturing methods for the low-cost production of 3D auxetic systems which has so far been a major stumbling block.

Chapter 5 : Inclusion-based Magneto-Mechanical Metamaterial: Part 1[4]

Highlights

- A novel magneto-mechanical metamaterial which could collapse through hinging in response to an external magnetic field.
- Investigate the effect of dependant variables on the response to an external magnetic field.
- Shape restoration achieved via the proper distribution of magnetic inclusions.
- A multi-layer 3D system with tuneable properties able to exhibit positive, zero and negative Poisson's ratio.

5.1 Introduction

Despite the numerous applications that have been proposed for auxetic metamaterials and the continuously growing interest of the research community, auxetic mechanical metamaterials still have a number of limitations as discussed in Chapter 2. For instance, once manufactured, the mechanical properties of the auxetic metamaterials

[4] The work in this chapter has been published in two research articles;
Galea, R., Dudek, K. K., Farrugia, P. S., Mangion, L. Z., Grima, J. N., & Gatt, R. (2022). Reconfigurable magneto-mechanical metamaterials guided by magnetic fields. *Composite Structures*, *280*, 114921. **(Impact Factor 6.603)**
Galea, R., Farrugia, P. S., Dudek, K. K., Zammit Mangion, L., Grima, J. N., & Gatt, R. (2022). An Investigation of Reconfigurable Magnetomechanical Metamaterials. *physica status solidi (b)*, *259*(12), 2200420. **(Impact Factor 1.615)**

show a lack of tunability (Montgomery *et al.*, 2020). This limits the use of these materials, where more responsive and adaptable materials with mechanical functionalities beyond those offered by the traditional machines are needed (Lum *et al.*, 2016). To this end, a number of researchers started to investigate shape-programmable metamaterials, i.e., a type of active materials whose geometry can be controlled through specific stimuli such as heat, chemicals, electric and magnetic fields. These materials are capable of providing the more precise control needed in a plethora of applications (Q. Li *et al.*, 2017; Lum *et al.*, 2016; Montgomery *et al.*, 2020; Scarpa, 2008; S. L. Zhang *et al.*, 2017), see Chapter 2 for a detailed discussion. One promising class of shape-programmable materials is that of magnetically actuated materials, as their shape can be manipulated not only through the magnitude of the external stimulus, but also through its direction and spatial gradient as well as by the internal interactions between magnetic inclusions (K. K. Dudek *et al.*, 2019a; M. R. Dudek & Wojciechowski, 2008; J. N. Grima *et al.*, 2013; Jackson *et al.*, 2018; Lum *et al.*, 2016; Schaeffer & Ruzzene, 2015a; Slesarenko, 2020a).

Despite its potential, research in active materials is still at its infancy and researchers must better understand the science governing the evolution of such systems in order to discover their full potential. In view of the above, in the first section of this chapter, a novel accordion-like magneto-mechanical metamaterial with the ability to change its linear dimensions in a controllable manner upon being subjected to a uniform external magnetic field, will be investigated. In the second part of this chapter, the proposed accordion-like system will be considered as a building block for a larger three-dimensional system which may undergo a transition from the positive Poisson's ratio to a negative Poisson's ratio, depending solely on the magnitude and the orientation of the external magnetic field.

5.2 Accordion-like magneto-mechanical metamaterial

5.2.1 Introduction

To develop multi-layered active metamaterials, it was necessary to first design and investigate the fundamental unit, which in this study is the magnetically actuated accordion-like foldable structure. Thus, this section will provide an overview of the structure's conceptualisation and the design of the system itself. An experimental investigation will be carried out to study the structure and dependent variables.

The analysis of the system will be divided into two parts. In the first part, the control of the evolution of the proposed system through the use of an external magnetic field and its ability to exhibit shape recovery will be explored. In the second part, an investigation of changes in properties of the system when a number of parameters are altered will be carried out.

5.2.2 Concept

In this section, an accordion-like foldable non-magnetic structure with magnetic inclusions is proposed and its response to an external uniform magnetic field is investigated in order to assess its potential to act as an actuator. The basic system that will be considered can be described as having a non-magnetic backbone in the form of an accordion-like foldable structure as shown in Figure 5.1. Magnetic inclusions, consisting of permanent magnets, are inserted in the rigid arms (bars) of the backbone with the orientation being such that the internal magnetic forces allow the structure to attain an equilibrium position in the shape of an accordion. As shown in Figure 5.1(b), in the presence of an external magnetic field, the system may act as an actuator as it causes the mechanical folding of the entire structure along the *x*-direction. This stems from the fact

that the magnetic inclusions tend to align with the external magnetic field, and since they are fixed on the non-magnetic elements, their rotation, induced by the external magnetic field, must result in the rotation of non-magnetic rigid bars constituting the system. Once the external magnetic field is switched off, if the magnetic inclusions are oriented in such a way that they repel each other, it is expected that the internal repulsion between the respective magnetic inclusions will make it possible for the system to return to the initial configuration.

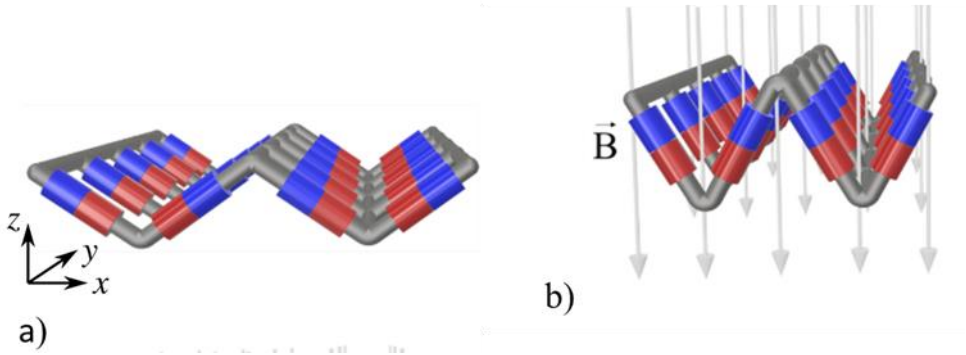

Figure 5.1 Panels show a) the graphical representation of the considered magneto-mechanical system, b) the deformation of the structure induced by the external magnetic field,

5.2.3 Design of the accordion-like foldable structure

The non-magnetic backbone can be described as ladders housing magnetic inclusions which are connected to each other through butt-hinges. The aim was to have hinges with minimal frictions while allowing a wide range of movement and to have magnet holders which had minimal effect on the magnetic moment of the magnetic inclusions. The latter was achieved by having a magnetic holder with two openings resulting in minimal material covering the magnets, as shown in Figure 5.2.

Figure 5.2. CAD design of magnet holder unit

The joints were initially designed in such a way that they protruded perpendicularly to the ‘ladder’ with each rung housing the magnetic inclusions as shown in Figure 5.3. The ladders were then connected to each other through copper rods. The prototype was produced following the procedure highlighted in Section 5.2.5.2.1 below. This was then suspended between the plates of an electromagnet using copper wires attached to the top and bottom of the central rod such that the structure was allowed to deform without having the structure spinning due to asymmetric movement. However, this setup resulted in a system with very high friction which restricted the degree of opening of the structure for a given external magnetic field. Furthermore, this structure was not able to open up into a flat plane due to the nature of the joints (as they were perpendicular to the magnetic inclusions).

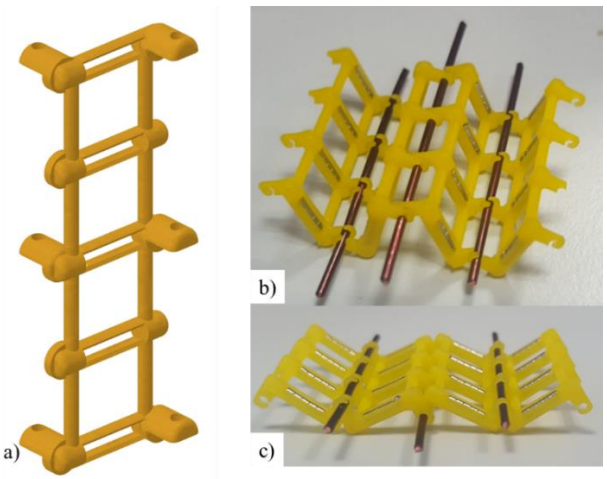

Figure 5.3. a) CAD design of one unit, b) Experimental prototype, c) Experimental prototype when fully extended

The design was then improved by replacing the rigid copper rods with copper wires to minimise the friction. In addition to this, connection bars were introduced in order to join the two adjacent ladders of the accordion-like structure to allow the structure to have a wider range of movement at the cost of increasing the degree of freedom of the system. The central connection bar was designed with a separate protrusion which allowed the structure to be suspended securely (see Figure 5.4). The prototypes produced were very brittle and thus assembly was particularly difficult.

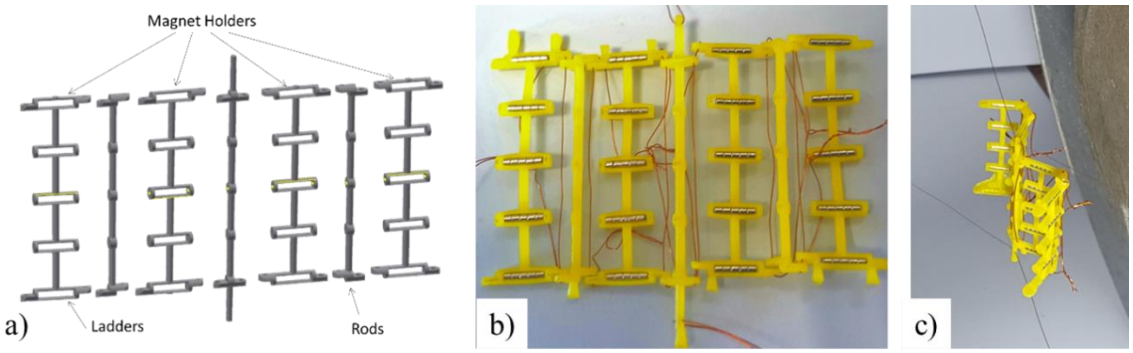

Figure 5.4. a) CAD design of the final prototype, b) 3D-printed structure with magnetic inclusions and copper wires, c) Structure suspended between the electromagnet's plates.

5.2.4 Geometric Parameters

The accordion-like structure is characterised by two composite angles, labelled θ_1 and θ_2, five lengths denoted by l_1, l_2, L, D_A, and D_M (Figure 5.5(a)) as well as the number of magnets used in the inclusions, *Mi*. Each ladder was attached to the connection bar using a copper wire (having a diameter of 0.2 mm). This introduced two extra degrees of freedom. Thus, in this simple configuration, the θ_1 and θ_2 represent the smallest angle that successive arms make with each other as indicated in Figure 6a. In an ideal model, θ_1 and θ_2 would be equal. However, θ_1 is untethered on one side which can induce it to exhibit edge effects whereas θ_2 is constrained from both ends. For this reason, the two angles can attain different values and hence need to be considered separately.

The length L gives the length between two corresponding arms while D_A gives the length of an arm. On the other hand, D_M represents the distance between the magnets in the out of plane direction. In order to simplify the analysis D_A and D_M were taken to have the same magnitude and are subsequently referred to as D. The lengths l_1 and l_2 represent the lengths of the side and centre connection bars respectively. The housing arms were designed to host magnetic inclusions which consisted of a number of cylindrical neodymium magnets (*Mi*, where *i* represents the number of magnets) each having a height and a diameter equal to 1 mm.

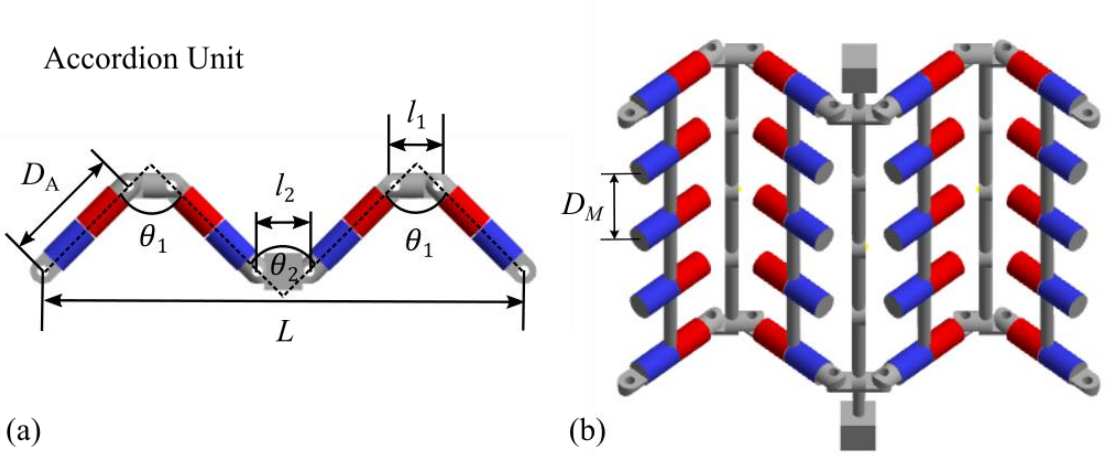

Figure 5.5. (a) Top and (b) tilted view of the accordion unit depicting the parameters considered in this study. (c-d) Top view of System I and System II arrangements indicating the orientation of the magnetic inclusions.

5.2.5 The magneto-mechanical accordion system: evolution under external magnetic field and shape recovery

5.2.5.1 Introduction

In this experimental study, the evolution of the magneto-mechanical accordion system under an external magnetic field will be explored. The foldability, shape restoration and reconfiguration time of the structure when exposed to an external magnetic field will be tested and discussed.

5.2.5.2 Methodology

5.2.5.2.1 3D printing of non-magnetic prototype backbone

The in-silico version of the non-magnetic backbone of the accordion-like system was build using Autodesk Inventor Professional 2019. The initial prototype (Mi = 5, D = 8.5 mm) was printed using an SLA 3D printer (Titan 2, Kudo3D) employing a resolution of 50 μm in the XY plane and layer height of 5 μm. 'Engineering Hard Resin' (Kudos 3D) having a reported Young's modulus of 1896 MPa was used. After printing, the structure was cleaned from excess resin by sonication in propanol for 30 minutes. The cleaned structure was then further cured in a UV chamber (Kudo 3D) for 60 minutes.

5.2.5.2.2 Assembly of structure and experimental study

The different printed parts were then assembled using copper wire having a diameter of 0.2 mm (see Figure 5.6). Five cylindrical neodymium magnets were inserted in each of the magnet holder ensuring they were oriented in the proper direction as shown in Figure 5.1(a). The assembled accordion-like system was then placed between two duly calibrated electromagnets which were able to generate a uniform magnetic field between them. To minimise the effect of friction on the deformation process, the entire structure was suspended in the air between the plates of electromagnets (see Figure 5.6) by means of auxiliary non-magnetic threads. Thus, the evolution of the system was primarily dependent on the interaction of magnetic inclusions with the external magnetic field and with each other. In addition, the spatial orientation of the system was very specific in order to ensure that the gravity would not affect the deformation process since the structure can only fold along the x-direction. Furthermore, to ensure the validity of experimental results, the evolution of the considered system was also analysed by means of computer simulations utilising a Molecular Dynamics approach, see Appendix I.

The extension/contraction of the accordion-like system was then studied at different external magnetic fields. The deformation of a structure was recorded through a camera situated above the structure. A frame was recorded every 0.033 of a second. In a typical experiment, the electromagnets were switched on and the accordion-like system was left to deform. When the system reached its equilibrium configuration, the electromagnets were switched off and any changes in the structure were also recorded. This was repeated for ten times for each external magnetic field tested. The changes in the parameters examined in the study i.e., θ_1, θ_2 and L were then measured using the software ImageJ.

The percentage shape restoration (R_s) for the accordion like system investigated in this study was calculated as follows:

$$R_s = \frac{L_f}{L_i} \times 100\% \qquad (5.1)$$

where, L_f is the length of the accordion like system after the external magnetic field was switched off and L_i is the length of the accordion like system before the magnetic field was switched on.

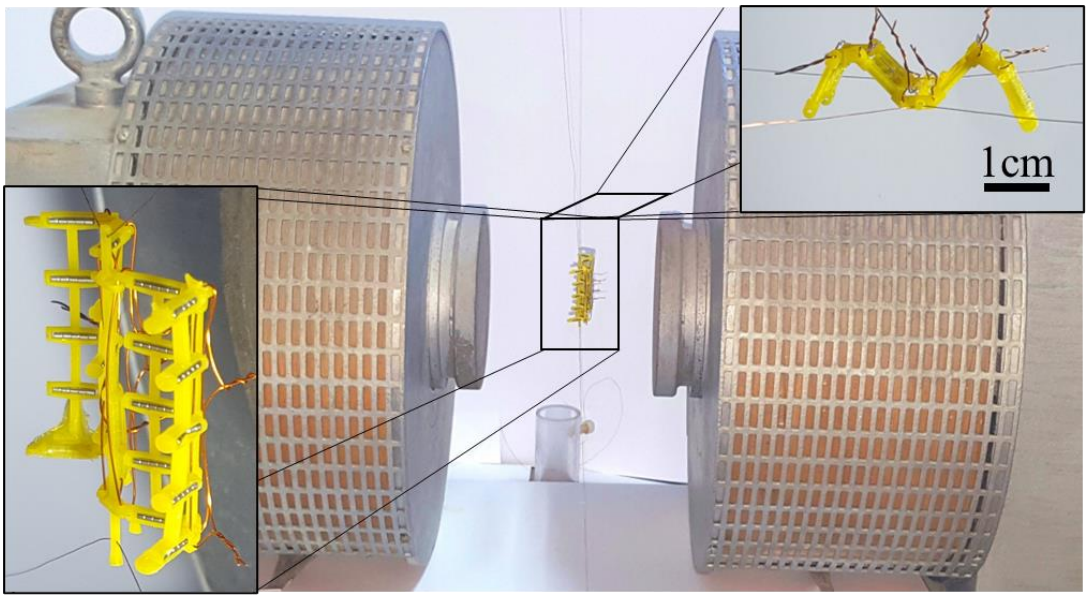

Figure 5.6: the setup of an experiment as well as pictures of the experimental prototype taken from different perspectives.

In this experimental study, the structure with the following initial geometrical parameters was analysed: ($\theta_1 = 0$) = 65.12°, ($\theta_2 = 0$) = 84.77°, l_1 = 2 mm, l_2 = 3.5 mm and D = 8.5 mm. The magnetic dipole moment of the magnetic inclusions was the same for all results presented and was equal to 0.00455 Am^2 (see Section 5.2.5.3.1). On the other hand, the external magnetic fields used in the experimental study were 4.5, 5.5, 6.5, 7.4, 8.5, 9.5, 11.5, 13.75, 15.7, 17.65, 19.9, 21.5, 25.75 mT.

5.2.5.2.3 Assessment of the Magnetic Dipole Moment of the magnetic inclusions

The aforementioned magnetic inclusions were composed of five neodymium magnets each having a diameter of 1 mm and a thickness of 1mm. In order to measure the magnetic moment of these magnetic inclusions, the following procedure was used. The z direction of a 3-axis hall magnetometer (Metrolab THM1176) was oriented perpendicular to the Earth's magnetic field. This was done to exclude any contribution

from the earth's magnetic field in this direction. A set of five magnets (the same amount used as one magnetic inclusion) was placed at a distance of 11.5 mm from the three-axis sensor and were oriented parallel to the *z*-axis of the sensor such that only the results in the *z*-axis were taken (see Figure 5.7). The magnetic field generated by these magnets was then measured. This procedure was repeated for an additional six distances and each measurement was repeated ten times, in order to minimise errors.

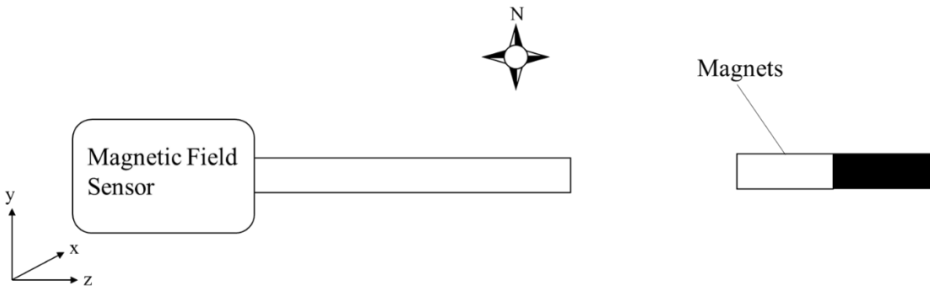

Figure 5.7. Schematic showing the experiment with the compass showing the magnetic field of the Earth.

It is known that magnetic field (*B*) is related to the distance as shown in equation 5.2,

$$B = \frac{2mr}{(r^2 + a^2)^2} \frac{\mu_0}{4\pi} \tag{5.2}$$

Where μ_0 is the permeability of free space ($4\pi \times 10^{-7}$), *m* is the magnetic moment, *a* is half the length of the dipole and *r* is the distance from the centre of the dipole and the probe. The experimental data obtained was used to produce a plot of the measured magnetic field (*B*) versus $\frac{r}{(r^2+a^2)^2}$. The gradient of the plot and equation 5.2, were then used to calculate the magnetic moment of the magnetic inclusions.

5.2.5.2.4 Relation between the current and magnetic field of the electromagnets used

The electromagnets used to generate a uniform external magnetic field were powered through a 150 W laboratory power supply (UNI-T UTP3315TFL-II). The relation between the supplied current and the magnetic field was analysed using the following procedure:

A 3-axis hall magnetometer (Metrolab THM1176) was positioned between the two electromagnets in the area where the structure was going to be placed and in such a way that the *x*-direction of the probe was oriented parallel to the generated magnetic field. The power supply was then switched on and the current adjusted to 0.1 A, using a multimeter (UNI-T UT39E) to read the current. The strength of the magnetic field generated for this current was then recorded. The power supply was then switched off. This experiment was repeated for two times in order to ensure that consistent results were obtained. This experiment was then repeated within the range 0.1 A and 2.0 A.

The data obtained was then plotted and the relationship between the supplied current and the generated magnetic field was determined.

5.2.5.3 Results and Discussion

5.2.5.3.1 Magnetic elements analysis

The magnetic moment of the neodymium magnetic inclusions was found by calculating the gradient of the plot of magnetic field (B) versus $\frac{r}{(r^2+a^2)^2}$ shown in Figure 5.8. The resulting gradient (9.03×10^{-10} T m^3) is equal to $\frac{2m\mu_0}{4\pi}$, from which the magnetic moment of the magnetic inclusions (which corresponds to five neodymium magnets) was found to be 4.55 mA m^2.

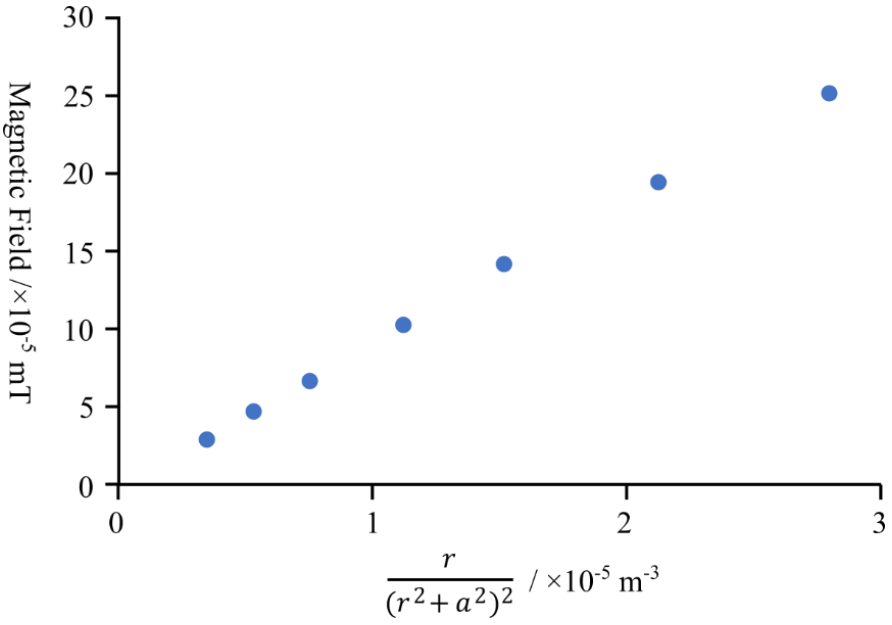

Figure 5.8. A graph calculating the magnetic moment.

The relationship between the current supplied and the magnetic field strength produced by the electromagnets was also investigated. The data obtained was plotted in Figure 5.9 which shows that the current and the magnetic field have a linear relationship up to the tested current. The results also show that the electromagnet outputs 20.822 mT per 1 A of current supplied. Furthermore, one notes that some residual magnetisation was present in the iron core of the electromagnets which is indicated by the non-zero *y*-intercept (circa 1.3 mT).

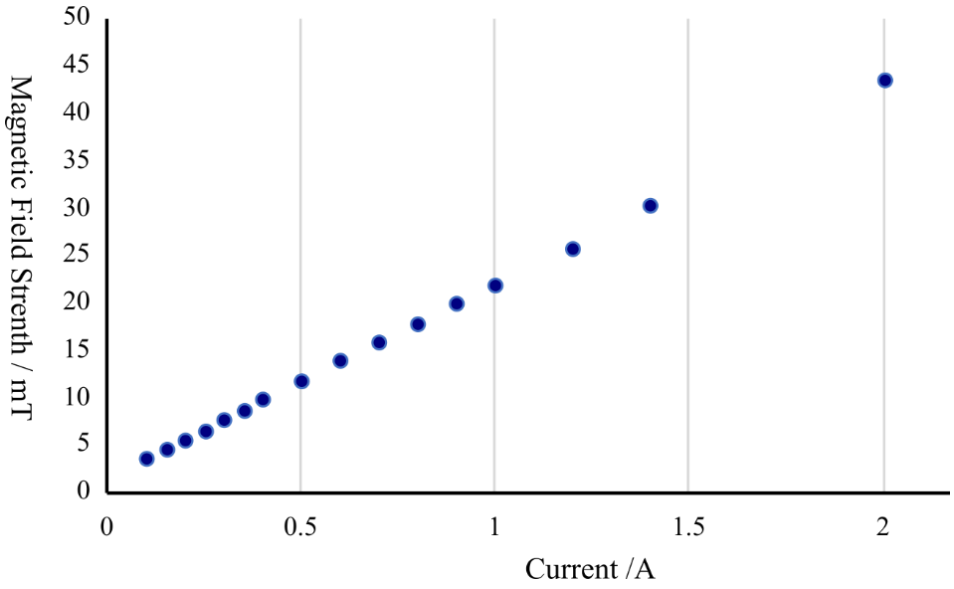

Figure 5.9. A graph of current against the magnetic field

5.2.5.3.2 The ability of the accordion-like foldable system to act as a linear actuator.

In this study, the extent of contraction of the proposed accordion-like system due to changes in the external magnetic field was investigated. This was done by monitoring the values of angles θ_1 and θ_2 (Figure 5.10). These angles represent the amount of contraction experienced by the structure at different magnetic fields, where the larger the extent of the contraction the smaller the values of θ_1 and θ_2 assumed by the equilibrium configuration of these structures.

To understand the behaviour of the proposed system when subjected to an external magnetic field, the experimental results obtained for a magnetic field of magnitude B = 28 mT were analysed first. Based on Figure 5.10(a), one can note that in response to the external magnetic field, the structure shrinks along the *x*-axis which leads to a decrease in the value of angles θ_1 and θ_2. The observed deformation stems from the fact that magnetic moments corresponding to respective magnetic inclusions tend to align with the external magnetic field, something that induces the folding (and thus contraction) of the

structure. As the accordion-like system starts to close, the interactions between magnetic inclusions become stronger as the magnetic inclusions are now approaching each other. However, unlike the external magnetic field, these interactions oppose the folding mechanism. Thus, as shown in Figure 5.10(a), the folding of the accordion-like structure continues until the point where the system assumes the equilibrium configuration for this specific external magnetic field.

Once the possibility of altering the dimensions of the system by subjecting it to an external magnetic field is established, it is important to analyse the general effect that the magnitude of the external magnetic field has on the evolution of the structure. According to Figure 5.10(c), the extent of contraction of the system changes with the magnitude of the external magnetic field. More specifically, the stronger the magnetic field, the smaller the values of angles θ_1 and θ_2 (which indicate that the accordion-like system is closing up). It is worth noting that for all of the results, the initial values of these angles were the same. In the case of the experiment, values of θ_1 and θ_2 changed from 48.3 ±3.0° and 61.0 ±0.57° to 27.4 ±1.4° and 25.0 ±1.3° respectively for the range of magnetic fields investigated in this study (between 4.5 mT and 30 mT). Also, referring to Figure 5.10(c), it is evident that the ten experimental repeats are concordant with each other, particularly for θ_2. The larger (but still relatively small) error found for θ_1 was expected as a result of the increased degrees of freedom due to the presence of the elements having a length l_1. Hence, the provided results further indicate that the dimensions of the system can be precisely controlled by changing the magnitude of the magnetic field and thus the proposed system can act as a linear actuator by precisely and reliably controlling its extension.

Similar results were obtained using computational methods (see Appendix I). All trends observed for the experimental system discussed above were qualitatively the same

to those obtained using computational studies. The discrepancies between the two sets of results arise from the fact that in the theoretical model there is no friction affecting the motion of hinges which is certainly present in the experiment. Also, in the experimental prototype, it is possible that despite our efforts there was some misalignment between the magnetic inclusions which may, up to some extent, have affected the result. Finally, the analytical expressions which were used in the numerical study to describe the interactions between magnetic inclusions serve only as an approximation of the real behaviour which is especially true for small separation distances between the magnets are expected to deviate from the experiment.

At this point, it is worth noting that even though the following topic does belong to the scope of this work, it is expected that the external magnetic field can also be used to change the stiffness of the system. This stems from the fact that the application of an external magnetic field would result in the change in net forces acting on respective structural elements constituting the system. Thus, should one consider deforming the analysed structure through the direct application of tensile forces, the variation in the magnitude of the external magnetic field could either accelerate or decelerate this process by fine-tuning its stiffness.

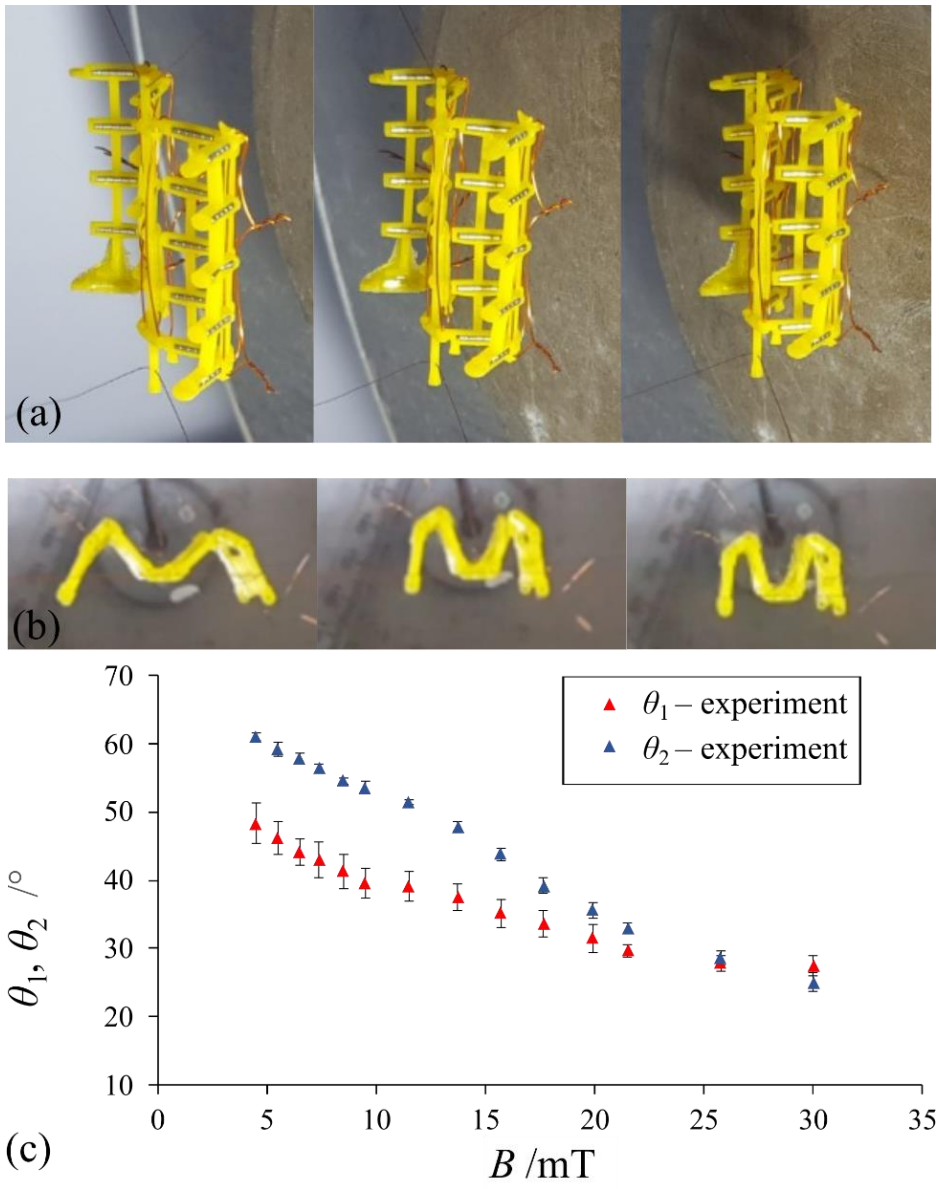

Figure 5.10. The evolution of the experimental prototype subjected to the uniform external magnetic field of magnitude 28 mT as viewed from (a) the side and (b) above. (c) A graph depicting the change in angles θ_1 and θ_2 for the system subjected to the external magnetic field of different magnitudes.

5.2.5.3.3 Shape Restoration

An important property of the accordion-like systems proposed in this study is its ability to return to its initial shape after switching off the external magnetic field. This property arises from the fact that the structure adopts a preferred configuration when no external forces are applied as a consequence of the internal repulsions between the magnetic inclusions. For example, referring to Figure 5.11(a), the proposed system (having an initial length of L_i) contracts along the *x*-axis when an external magnetic field (B_c = 26 mT in this case) is applied. However, upon switching off the external magnetic field, the system opens up again along the *x*-axis until the point where it assumes the equilibrium configuration corresponding to the dimension L_f. This means that the potential of the proposed system to return to its initial configurations can be assessed upon analysing the value of L_f.

According to Figure 5.11 (b), the accordion-like system exhibits a relatively good shape restoration irrespective of the magnitude of the external magnetic field. However, it can be noted that for relatively strong external magnetic fields, the difference in the linear dimension between the initial and the final configuration of the system is slightly larger than in the case of a relatively weak magnetic field. In fact, for small external magnetic fields (lower than 5 mT) the accordion-like system considered in this study nearly returned to its initial conformation ($R_s \approx 99\%$) when the external magnetic field was switched off. The shape restoration of the system was slightly lower for larger external magnetic fields, for example in the range from 14 to 25 mT, a 95% shape restoration was observed.

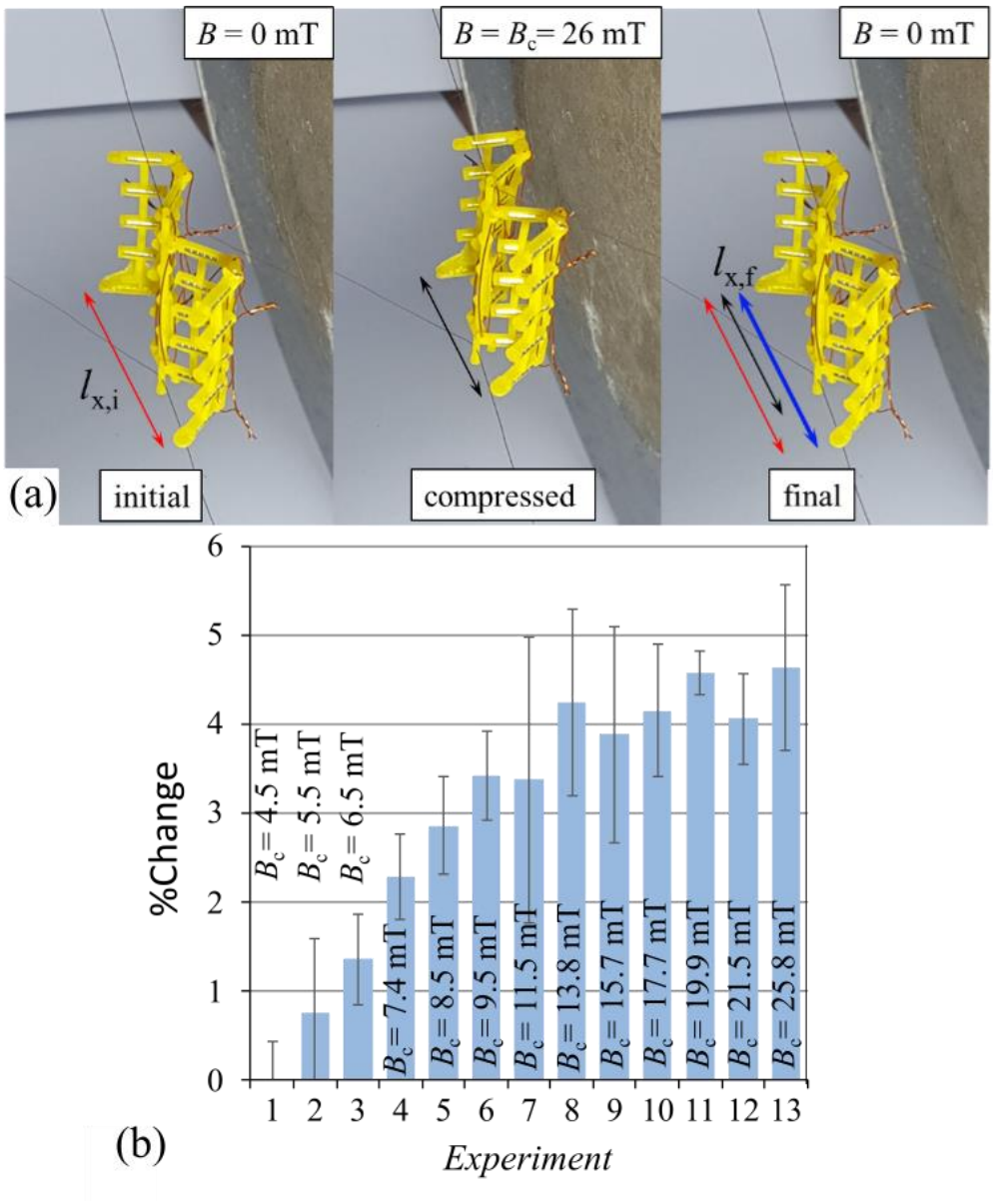

Figure 5.11 Panel (a) shows an example of the evolution of the system where after it was initially subjected to a specific magnetic field of magnitude B_c, the magnetic field was switched off so that the structure could assume the equilibrium configuration. Panel (b) describes the percentage change in the dimension of the structure subjected to the magnetic field of different magnitudes. The percentage change in the dimension for each of the analysed cases is measured along the *x*-axis upon comparing the initial configuration ($l_x = l_{x,i}$) corresponding to the situation before the magnetic field of magnitude B_c was switched on and the final equilibrium configuration ($l_x = l_{x,f}$) assumed by the system once the magnetic field was switched off.

5.2.5.3.4 Investigation of the delay for the structure to reconfigure to its original structure

The time taken for the experimental compressed structure to re-open after the external magnetic field was switched off was investigated for the external magnetic fields used in the experimental study. The results are shown in Figure 5.12 which revealed an average delay of circa 1.2 seconds. The delay depends on the interplay of two forces; the repulsion of the magnetic inclusions which increases as they are brought closer (in the case of our experiment this is achieved by a larger external magnetic field) and the opposing friction in the joints.

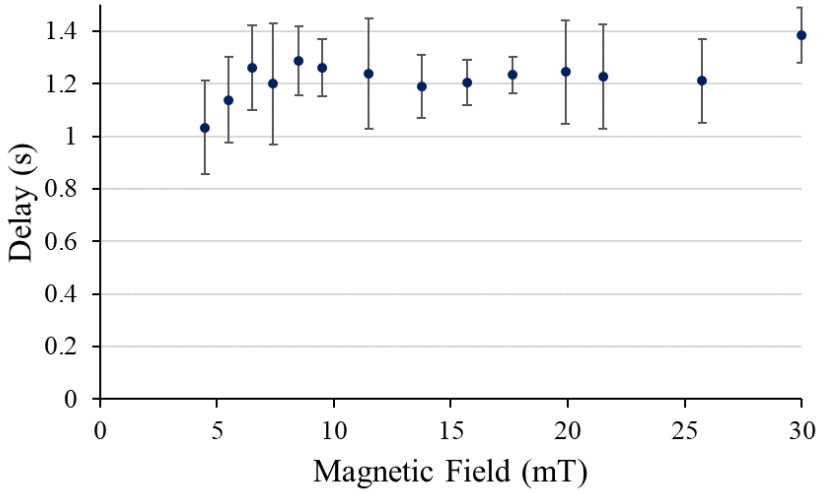

Figure 5.12. A graph of the delay at different external magnetic fields.

5.2.5.3.5 Reversing the polarity of the external magnetic field

Up to this point the compression of the system under an external magnetic field has been discussed. It was shown how upon being subjected to an external magnetic field the structure contracts from the at rest configuration shown in Figure 5.13(b) to the contracted structure depicted in Figure 5.13**(**c) which is the resultant equilibrium position when the applied field is 26 mT. Reversing the direction of the external magnetic field

caused the structure to open up to a flat sheet as depicted in Figure 5.13a which shows the induced flattening when acted upon a magnetic field of −13 mT. The system opens up as now the north poles of the magnetic inclusions are facing the north pole of the electromagnet, resulting in repulsion. Given that the magnetic inclusions are embedded in the non-magnetic elements, their rotation, induced by the external magnetic field, results in the rotation of non-magnetic rigid bars in such a way that the structure opens. In this case, when the magnetic field strength was increased, the structure started to spin. This may be due to the asymmetry present within the structure which led to a net torque on the structure.

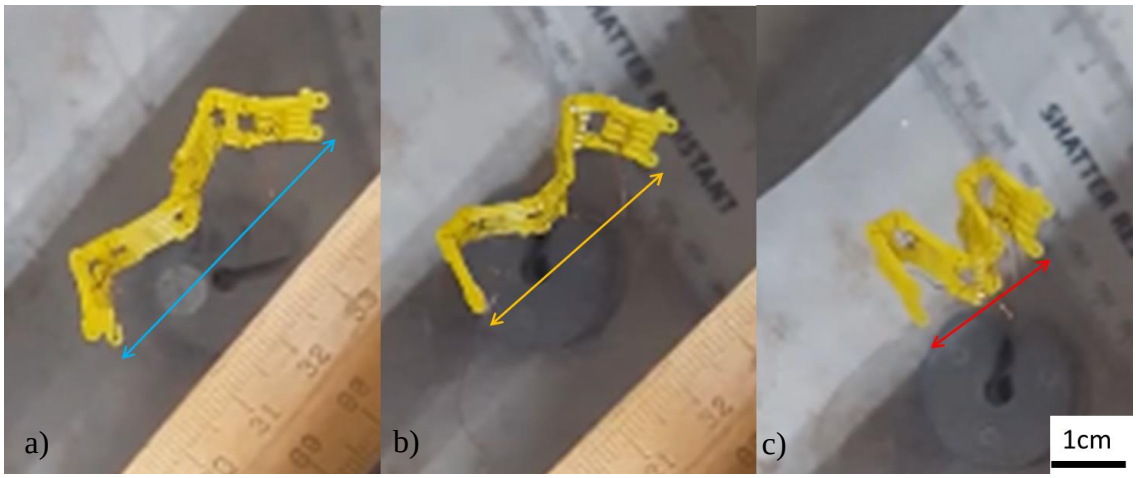

Figure 5.13. Pictures taken when (a) Polarities of the Magnetic field were reversed, (b) when at rest, (c) under a relatively large magnetic field.

5.2.5.4 Conclusion

In conclusion, it was shown that the proposed magneto-mechanical metamaterial can have its geometry controlled via an external magnetic field. It was also shown that it can return to its initial shape upon switching off the external magnetic field which indicates that the considered system can be redeployed multiple times. Depending on the direction and magnitude of the external magnetic field, the analysed structure can contract or extend depending on the magnitude and the direction of the magnetic field which adds

a second component to the active metamaterial and allows for more versatility in its applications.

5.2.6 An investigation of the dependent parameters

5.2.6.1 Introduction

As discussed above, the evolution of the system and hence the folding of the entire structure depends on the magnitude of the external magnetic field. However, the extent of contraction also depends on the geometrical parameters. This stems from the fact that the change in the geometric parameters alters the spatial orientation and the separation distance between the magnetic inclusions which affects their interactions. Furthermore, the amount of contraction for a system having the same initial geometrical parameters may also be altered by changing the magnetic moments corresponding to magnetic inclusions. Therefore, in this section, structures having different geometrical parameters and different magnetic moments will be investigated in order to understand the effect of these variables on the response of the accordion-like structure to an external magnetic field.

5.2.6.2 Methodology

5.2.6.2.1 3D printing of non-magnetic prototype backbone

As discussed in Section 5.2.3, the 3D printed non-magnetic backbones used were very brittle, therefore, a different material with higher elasticity was employed. This was accomplished by using a different SLA 3D printer. As described in Section 5.2.5.2.1, the accordion-like systems were initially designed in Autodesk Inventor Professional. These were then exported and printed with a stereolithography 3D printer (Formlabs, Form 3)

having a resolution of 25 μm in the *xy* plane and a layer height of 50 μm. Formlabs Tough 2000 Resin was used for the purpose. The prints were then cleaned in Formlabs Form Wash using isopropyl alcohol (IPA) for a total of 20 minutes. Following this the structure was cured in the Formlabs Form Cure at 60 °C for 1 hour.

5.2.6.2.2 Experimental setup and variables investigation

The dependent variables investigated were parameter *D* (see Figure 5.5) and the magnetic moment of the inclusions, *M*. To this end, six different structures were designed and built. Four of the structures had the parameter *D* set to 8.5 mm with the magnetic inclusion holders being modified to house two to five cylindrical neodymium magnets each having a height and a diameter equal to 1 mm. These structures were referred to as M*i*, where *i* represents the number of magnets. Experimental testing, described in section 5.2.5.3.1, had shown that the inclusions with five neodymium magnets (M5), had a dipole moment of 4.55 mA m^2. It was assumed that each neodymium magnet contributed equally to the total dipole moment and thus the dipole moment for the other inclusions was calculated through simple proportion. This resulted in a dipole moment of 1.82 mA m^2, 2.73 mA m^2 and 3.64 mA m^2, for M2, M3 and M4 respectively. The other two structures, referred to as D2 and D3, were designed to house five magnets while parameter *D* was set to 12 and 17 mm. These were used to study the effect of varying *D*. The relative orientation of successive magnetic inclusions was similar to the previous work, where adjacent magnetic inclusions repelled one another as indicated in Figure 5.5(b) (Blue represents the south pole and red represents the north pole).

The prototypes thus produced was set up as described in Section 5.2.5.2.2. The deformation of the structures when subjected to a magnetic field was then monitored

using an imaging camera (Daheng MER2-630-60U3M) mounted with a lens having a focal length of 1.4 (get-cameras LCM-5MP-08MM-F1.4-1.5-ND1) stably fixed and levelled vertically above the system (Figure 5.14 (a)).

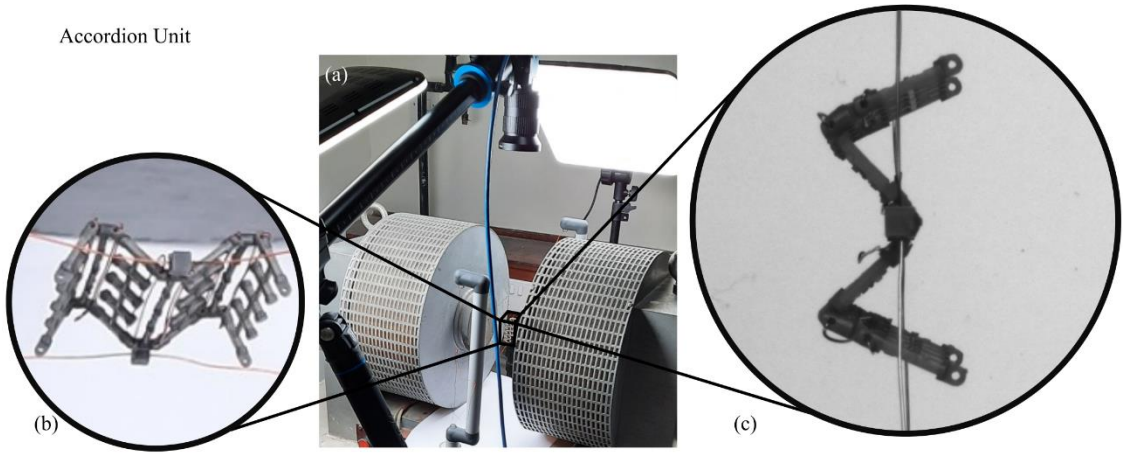

Figure 5.14**.** (a) A depiction of the setup used in the experiments including a (b) sideway image and (c) the image recorded by the camera for the experiment.

The extension/contraction of the accordion-like systems was then studied using an external magnetic field having values ranging between 4.0 and 43.4 mT. Similar to Section 5.2.5.2.2, in a typical experiment, the electromagnets were switched on and the accordion-like system was allowed to attain the new equilibrium position. At this point the electromagnets were switched off and the deformation was recorded by the camera. This was repeated ten times for each external magnetic field used. A python script was used to determine automatically θ_1, θ_2, and L from the images obtained. To do so, reference points were selected manually for each image. θ_1 and θ_2 were in practice determined by extrapolating the arms to a point connecting them. On the other hand, L was determined by measuring the distance between the external arms. Once the variables were calculated, the percentage change as compared to their values at the lowest external magnetic field (namely 4.0 mT) was determined. The use of the relative change in θ_1 and

θ_2, and L allowed for a better comparison of the deformation between structures having different parameters.

5.2.6.3 Results and Discussion

5.2.6.3.1 Effect of the variation in the magnitude of the magnetic moment corresponding to magnetic inclusions on the evolution of the system

The influence of the magnetic moment on the behaviour of the structure was studied first. Its importance stems from the fact that it establishes the internal repulsive forces present within the system that maintain the stability of the structure. It also dictates the system's interaction with the external magnetic field. The results can pave the way to the introduction of electromagnets in place of the permanent magnets that are able to exert a varying and controllable internal magnetic field. In doing so, it should be possible to control the equilibrium position of the structure. Furthermore, it would be possible to vary the conformation of the structure in real time allowing the system to attain a desired morphology by applying different magnetic fields in different regions or positions.

In order to study the effect of the magnetic moment of the magnetic inclusions on the deformation of the structure, four structures; M2, M3, M4 and M5, housing 2, 3, 4 and 5 magnets respectively, were subjected to different external magnetic fields. The results, which are shown in Figure 5.15, indicate that structure M2 had the smallest relative changes in θ_1, θ_2, and L, possibly due to the fact that the relatively low magnetic moment did not create sufficient torque to overcome the friction at the hinges. On the other hand, it can be noted that the changes in the angles θ_1 and θ_2 for all the other structures are basically the same. This suggests that once the friction at the hinges is overcome, the angles will increase to the same relative extent irrespective of the internal magnetic moment. Interestingly, this is not reflected in the change in L. There are various

reasons for this. One factor is that the reference equilibrium value of θ_1 and θ_2 (i.e., when no external field was present) differed according to the magnitude of the magnetic moment. Furthermore, the connecting bar provided additional degrees of freedom that altered the simple dependence between L and the angles as suggested from Figure 5.15(d-g). Even so, at relatively low magnetic fields, the value of L for M3, M4, and M5 are very similar. They start to diverge at around an external magnetic field of 15 mT. Remarkably, the smallest variation was that for M3 while the largest was for M4, with M5 being somewhere in between. This would suggest that there could be a reversal of the increasing of L with increasing internal magnetic moment which stems from the fact that in the case of relatively strong magnetic inclusions, their mutual repulsion is very significant, and the system cannot deform to a similar extent as would be the case for weaker magnetic inclusions.

Numerical simulations (see Appendix I) confirmed that the considered structure deforms differently depending on the magnitude of the magnetic moment, with stronger magnetic moment of the inclusions hindering the foldability of the structure. More specifically, initially an increase in the magnetic moment brought about a larger change in the mechanical deformation (measured along the x-axis) induced by the external magnetic field. However, upon further increasing the value of the magnetic moment, the extent of the change in the mechanical deformation diminished (see Appendix I), as in the case the experimental results.

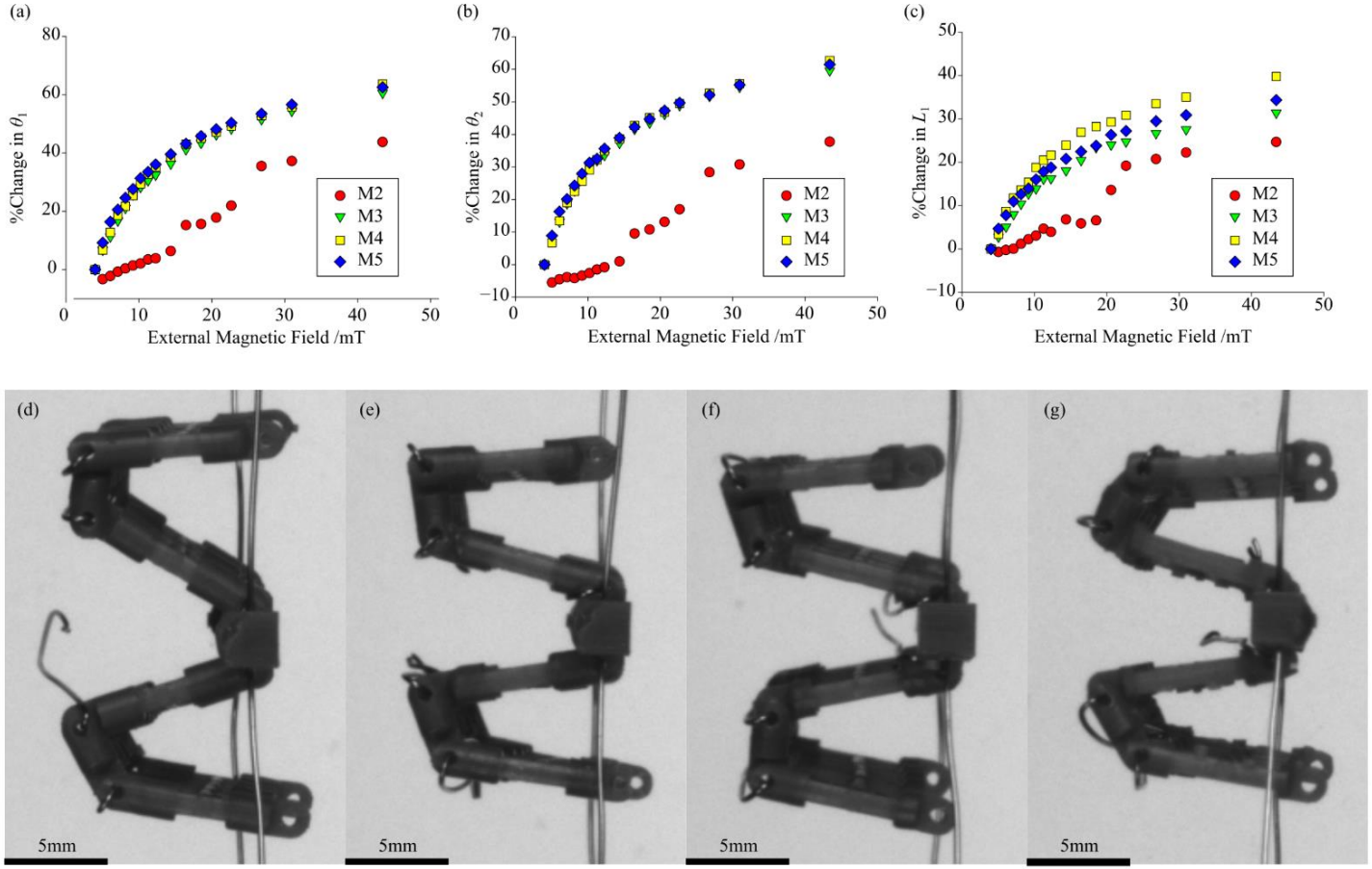

Figure 5.15**.** (a-c) Graphs representing the percentage change in θ_1, θ_2, and L respectively against the applied external magnetic field for structures Mi, where i = 2,…,5. (d-g) Images taken during the experiment when an external magnetic field of 43.4 mT was applied for structures Mi, where i = 2,…,5, respectively.

5.2.6.3.2 Effect of the variation in the value of the geometric parameter *D* on the behaviour of the structure

The changes induced by varying parameter *D* were studied next. This parameter dictates the moments induced about the hinges by the magnetic inclusions. The results are meant to shed light on how the behaviour of the system will change when the structure is scaled up or down (using the same magnetic inclusions) in order to accommodate a desired application and how the geometry affects the equilibrium configuration. Understanding the interplay of forces and moments acting on the structure is fundamental in order to design both miniature and larger devices based on the same principles presented here.

In order to study the effect of the parameter *D* on the deformation of the structure, the behaviour of M5 was compared with that of D2 and D3 when these were subjected to different magnetic fields. The structures M5, D2 and D3 had five embedded magnets but the value of parameter *D* was set to 8.5, 12, and 17 mm respectively. The results shown in Figure 5.16 indicate that the behaviour of M5 and D2 are similar but differ slightly from those of D3, particularly for the relative change in θ_1 and θ_2. In this case, the friction at the hinges should be similar for the three structures considered. As a matter of fact, the longer arms of D3 should have allowed it to exert a larger torque at the joints. However, by the same token, a small change in θ_1 and θ_2 would have moved the embedded magnetics of D3 farther away (or closer) than in the case of M5 and D2.

It is worth noting that the results for *L* are not too different from one another. Yet there does not seem to be a discernible pattern for the change in *L* with increasing *D*. Once again, this could be partially explained by the fact that the initial values of θ_1 and θ_2 were different for the three structures. In addition, the introduction of a connecting bar added further degrees of freedom to the motion. Geometric effects relating the angles

with *L* as well as inducing different internal forces between the magnets could also have played a role.

Numerical simulations (see Appendix I) deviated from the experimental results discussed above and behaved as expected. These simulations showed that the extent of the mechanical deformation of the considered system induced by the application of the external magnetic field changes depending on the value of the geometric parameter *D*. This behaviour originates from the fact that the increase in the value of *D* results in the increase in the separation distance between the magnetic inclusions. Thus, the mutual repulsion between the magnetic inclusions is weaker than is the case when magnetic inclusions are relatively close to each other. At the same time, one should remember that the magnitude of the external magnetic field does not depend on the geometric parameters of the system. Hence, the magnetic torque corresponding to each structural element with the magnetic inclusions remains approximately the same irrespective of the selection of the geometric parameters (given that the spatial orientation of magnetic inclusions remains almost unchanged). This difference between the numerical and experimental studies can be explained by the factors considered above.

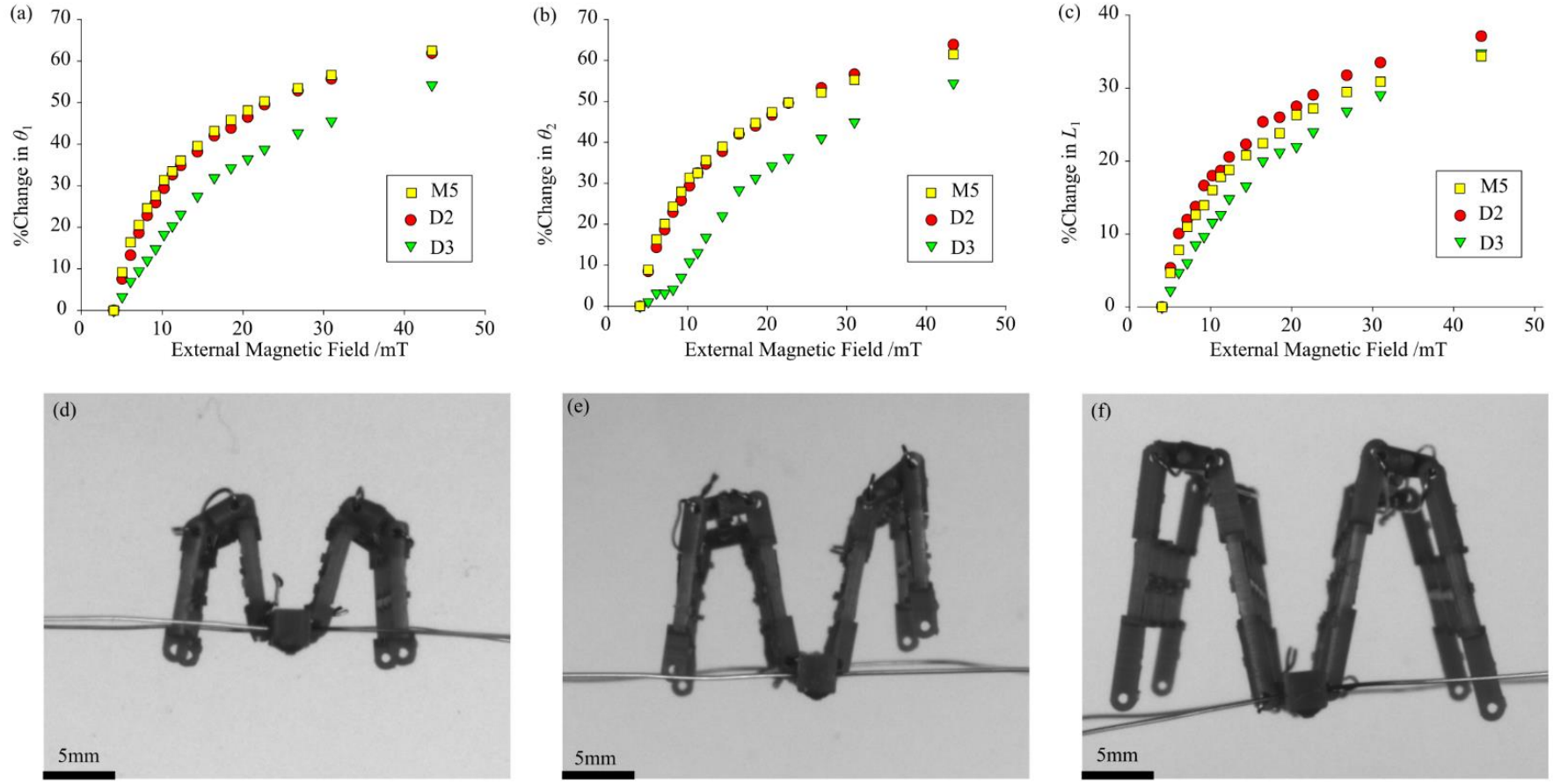

Figure 5.16. (a-c) Graphs representing the percentage change in θ_1, θ_2, and L respectively against the applied external magnetic field for structures M5, D2, and D3. (d-g) Images taken during the experiment when the external magnetic field was set to 43.4 mT for structures M5, D2, and D3 respectively.

5.2.6.4 Conclusion

The magnetomechanical accordion-like metamaterial was investigated further experimentally to determine how the magnetic moment of the emended magnets and the length of the arms affect the deformation of the structure when subjected to an external magnetic field. The investigation revealed that an increase in the magnetic moment led to a larger contraction under an external magnetic field, however, further increasing the magnetic moment had the opposite effect due to the increased internal repulsion. Similarly, an increase in the lengths of the arms led to a larger contraction under an external magnetic field, however, further increasing the lengths resulted in significant forces on the hinges which hindered the contraction. This study provided key insight in the dependant variables which opens up the possibility of replacing the permanent magnetic inclusions with electromagnets where the magnetic moment could be controlled. Furthermore, the investigation of the geometric parameters is key in understanding the properties when scaling the structure up or down.

5.2.7 Conclusion

In conclusion, it is shown that the proposed magneto-mechanical metamaterial can have its dimensions controlled via an external magnetic field. It is also shown that it can return to its equilibrium, which indicates that the considered system can be used multiple times which significantly increases its appeal from the practical point of view. Furthermore, the dependent variables were investigated experimentally to determine how the magnetic moment of the emended magnets and the length of the arms affect the deformation of the structure when subject to an external magnetic field. The high degree of turnability and control that can be exerted on the structure, as well as the fact that their behaviour can be altered interactively, can potentially lead to a multitude of applications.

5.3 Multi-layered systems – A proof of concept

5.3.1 Introduction

The basic accordion-like unit discussed above can be used as a building block to create multi-layered systems which have the potential of exhibiting an NPR. This can be carried out by stacking the accordion-like units in specific orientations and fixing the stacked units at strategic locations to achieve a multitude of structures, namely honeycomb, re-entrant honeycomb and semi re-entrant structures. Finally, the response of these structures to external magnetic fields will be observed and discussed. The aim of the investigation was to qualitatively show that the multi-layered systems would in fact behave in an expected manner under the influence of an external magnetic field and therefore, measuring the deformation was considered to be beyond the scope of the experiment.

5.3.2 Concept

Building on the concept of the shape-programmable material mentioned in Section 5.2, the basic accordion unit may be used to produce various 3D structures. This can be achieved by stacking and connecting a number of these units in the third direction. Different 3D structures can be achieved, depending on the orientation of successive layers and the manner in which these layers are attached (see Figure 5.17). For example, each subsequent layer can be stacked on each other so that each layer is in the same orientation (Case I), or each layer may be related through a mirror relation (Case II).

For Case I, attachment of subsequent layers in the third direction through non-continuous ligament results in a semi-re-entrant structure (shown in Figure 5.17(b)). On the other hand, if the layers in Case I are connected together in the third direction through

continuous ligaments, an accordion system (shown in Figure 5.17(a)) is formed. Both of these structures are known to exhibit a zero Poisson's ratio when deforming through a hinging mechanism.

For Case II, attachment of subsequent layers in the third direction through non-continuous ligaments can result in a re-entrant honeycomb structure (see Figure 5.17(d)) or a hexagonal honeycomb structure (see Figure 5.17(e)) depending on the attachment sites. Connecting the layers through corresponding ligaments in a continuous manner will also yield an accordion system in this case having a Poisson's ratio of zero (see Figure 5.17(c)). Thus, in Case II, assuming that the structure deforms by hinging, one may obtain structures which exhibits positive, negative or zero Poisson's ratios.

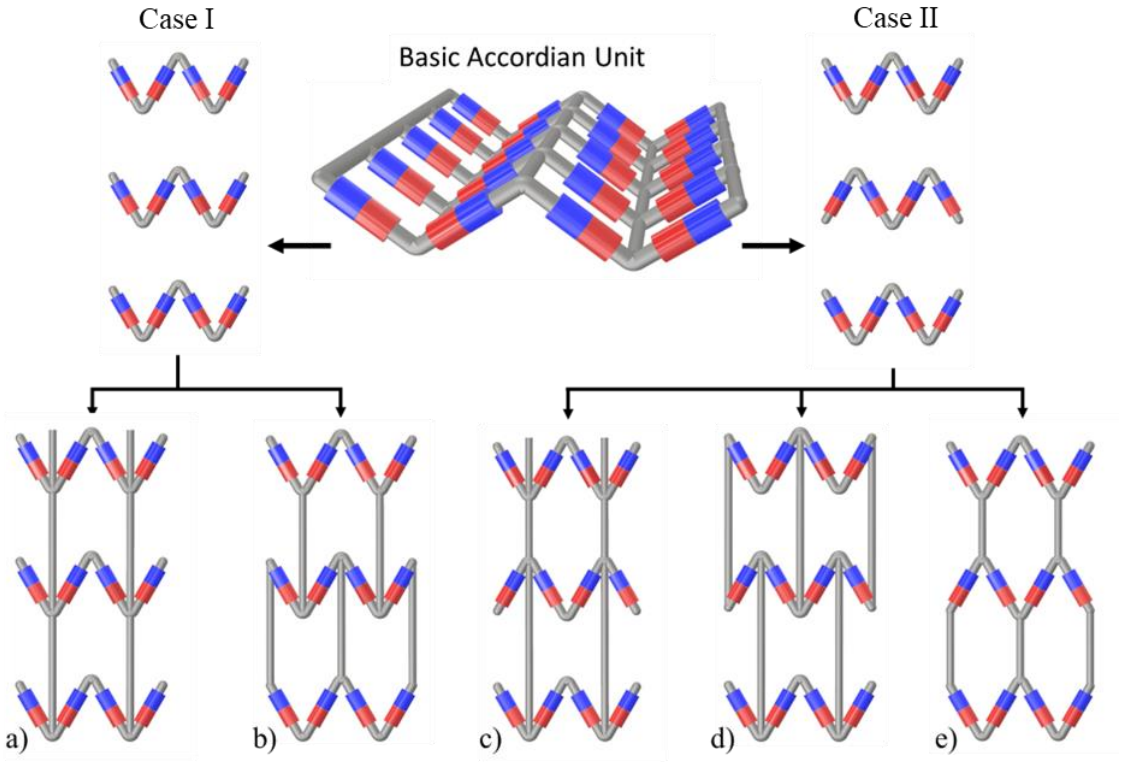

Figure 5.17. Possible structures by stacking the basic accordion structure namely (a) stacked accordions, (b) semi re-entrant honeycomb, (c) alternating accordions, (d) re-entrant honeycomb and (e) honeycomb structures.

5.3.3 Methodology

5.3.3.1 3D printing of the non-magnetic elements

The non-magnetic elements were 3D printed following the same procedure and parameters described in Section 5.2.6.2.1.

5.3.3.2 Assembly of multi-layer structures

The proof of concept was carried out using two structures, referred to as System SR (see Figure 5.17(b)) and System H (see Figure 5.17(d-e)). System SR was achieved through the stacking of accordion-like units having the same orientation of magnets. The stacked units were then connected via alternating corners as shown in Figure 5.18(a). Under the action of an external magnetic field, the system attains a shape that is akin to the semi-re-entrant honeycomb, which is well known to have a zero Poisson's ratio. On the other hand, System H was achieved by stacking accordion-like structures with opposite polarities of the magnetic inclusions as shown in Figure 5.18(b). The stacked units were then connected via alternating corners such that under the action of an external magnetic field the structures may take the form of a re-entrant or conventional honeycomb system depending on the direction of the external magnetic field. These structures are known to have a negative Poisson's ratio when in the re-entrant configuration and deforming through hinging, whilst the conventional honeycomb configuration is known to have a positive Poisson's ratio when deforming through hinging.

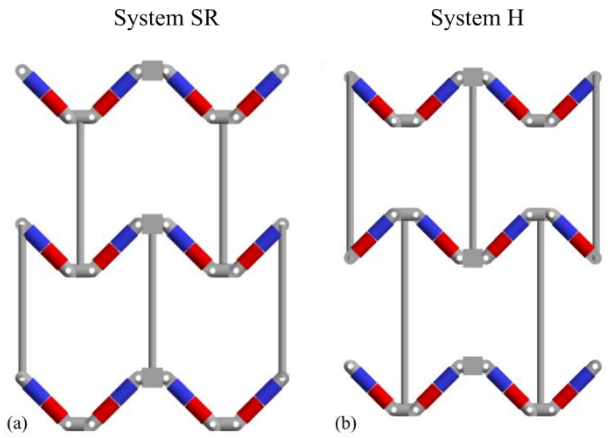

Figure 5.18 Top view of (a) System SR and (b) System H arrangements indicating the orientation of the magnetic inclusions.

5.3.3.3 Experimental study

As discussed above, the basic accordion-like configuration was stacked to achieve complex structures. The accordion-like structure used to construct the multi-layered structures was the M5. Systems SR and H were assembled as described in Section 5.3.2 above using copper wire having a diameter of 0.2 mm. Five cylindrical neodymium magnets were inserted in each of the magnet holder ensuring they were oriented in the proper direction as shown in Figure 5.18. The assembled accordion-like system was then placed between two duly calibrated electromagnets which were able to generate a uniform magnetic field between them. To minimise the effect of friction on the deformation process, the entire structure was suspended in the air between the plates of electromagnets by means of auxiliary non-magnetic threads. Thus, the evolution of the system was primarily dependent on the interaction of magnetic inclusions with the external magnetic field and with each other. In addition, the spatial orientation of the system was very specific in order to ensure that the gravity would not affect the deformation process since the structure can only fold along the *x* direction.

5.3.4 Results and Discussion

As described in the methodology, these accordion-like systems were used to construct three-dimensional honeycomb systems. The behaviour of System SR under the action of an increasing external magnetic field is depicted in Figure 5.19. The structure configured itself as a semi re-entrant hexagonal honeycomb under the action of a small external magnetic field when aligned as shown. This arrangement is known to have a theoretical Poisson's ratio of zero (J. N. Grima, Oliveri, *et al.*, 2010). In fact, the structure can be observed to contract laterally while keeping its length along the direction of the applied magnetic field. Deviation from the ideal behaviour was also observed. The reason for this is the relatively small number of repeating units which made edge effects significant. In fact, the outer parts showed a tendency to sheer. It should be further noted that when the direction of the external magnetic field was reversed, the structure reconfigured itself as shown in Figure 5.20(a-d). The arrangement can be described as a mirror image of the one adopted with the original magnetic field. However, apart from this exception, its behaviour was the same for both orientations of the external magnetic field.

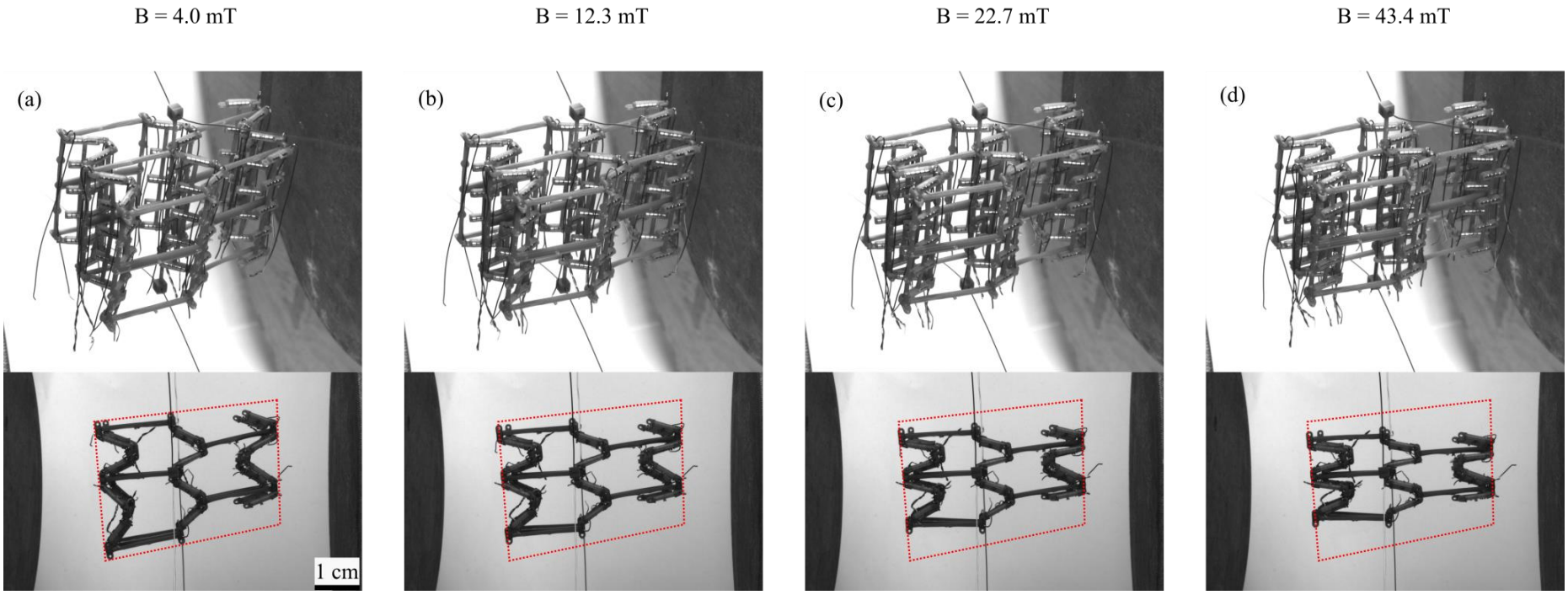

Figure 5.19. (a-d) Images from a side view and aerial view of a System SR structure under an external magnetic field of 4.0, 12.3, 22.7, 43.4 mT respectively.

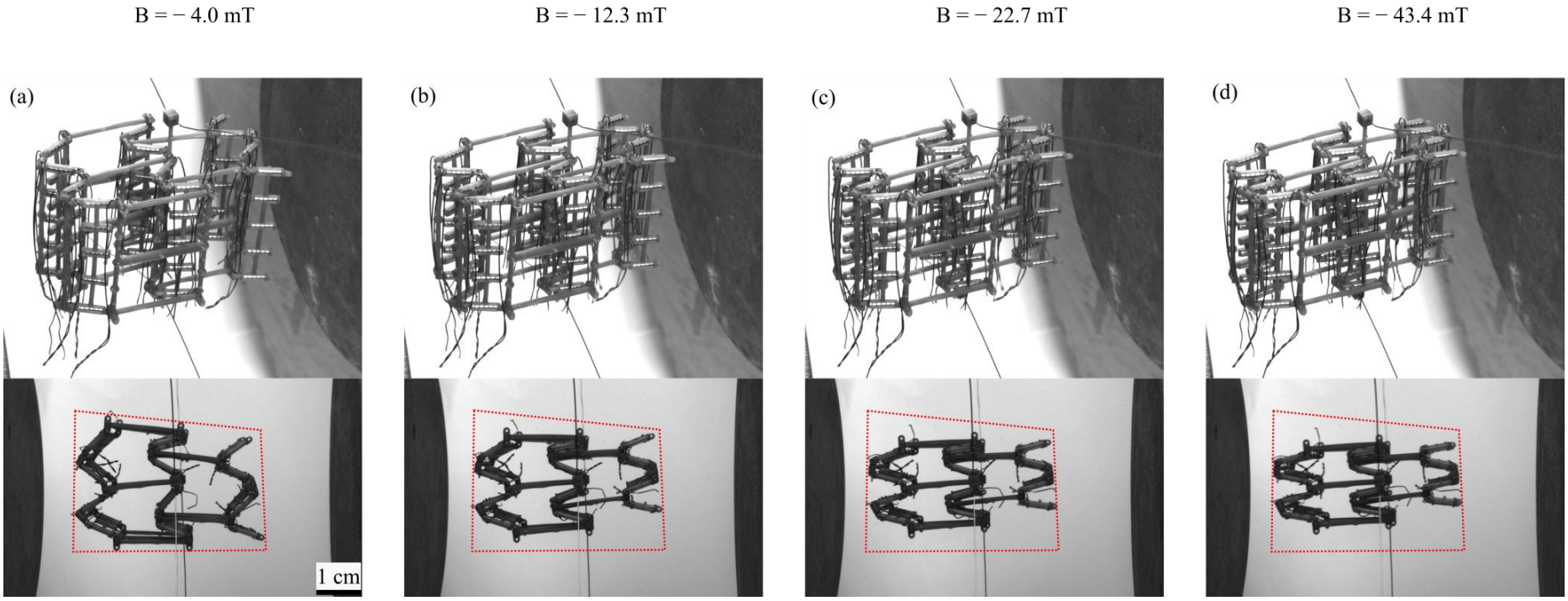

Figure 5.20. (a-d) Images from a side view and aerial view of a System SR structure under an external magnetic field of −4.0, −12.3, −22.7 and −43.4 mT respectively. The negative sign indicated that the external magnetic field is acting in the opposite direction.

The analogous results for System H are illustrated in Figure 5.21 and Figure 5.22. As it can be noted from these figures, when the external magnetic field was in one direction, the structure configured itself as a re-entrant hexagonal honeycomb (Figure 5.21), while when the external magnetic field acted in the opposite direction it arranged itself as a conventional hexagonal honeycomb (Figure 5.22). In the former case, upon increasing the external magnetic field, the structure shrunk as expected, since this shape is known to have a negative Poisson's ratio. The opposite is true in the latter case with the structure spreading out in the orthogonal direction. Again, this was expected since the conventional hexagonal honeycomb is known to have a positive Poisson's ratio. Yet, edge effects are visible, with some shearing clearly noticeable. The edge effects can be minimised by considering systems with a larger number of unit cells.

The results clearly indicate that the structure allows for detailed control of its dimension. In addition, it is possible to choose configurations that have negative, zero, or positive Poisson's ratio, with System H being able to flip between negative and positive Poisson's ratio arrangements simply by reversing the direction of the applied magnetic field. Furthermore, additional control can be achieved by replacing the emended permanent magnets with electromagnets. In this case it would be possible to selectively alter the magnetic moment locally inducing regional deformation effects.

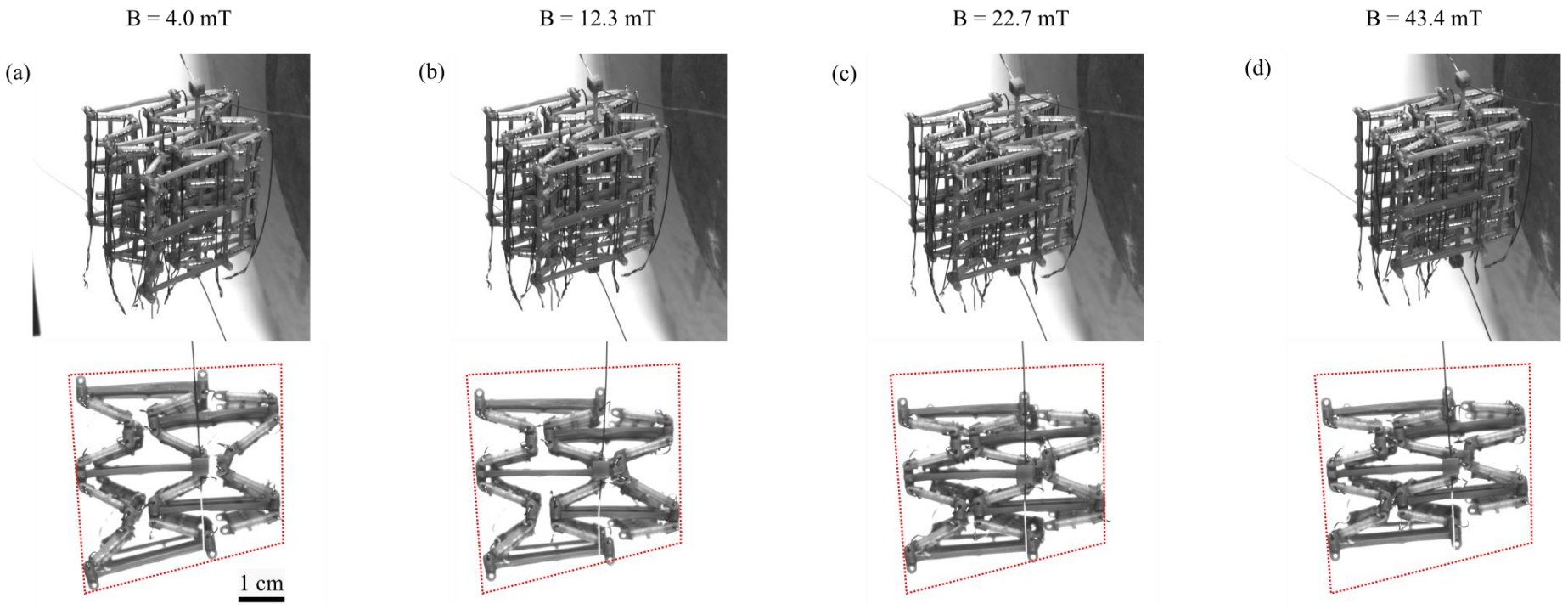

Figure 5.21. (a-d) Images from a side view and aerial view of a System H structure under an external magnetic field of 4.0, 12.3, 22.7, 43.4 mT respectively.

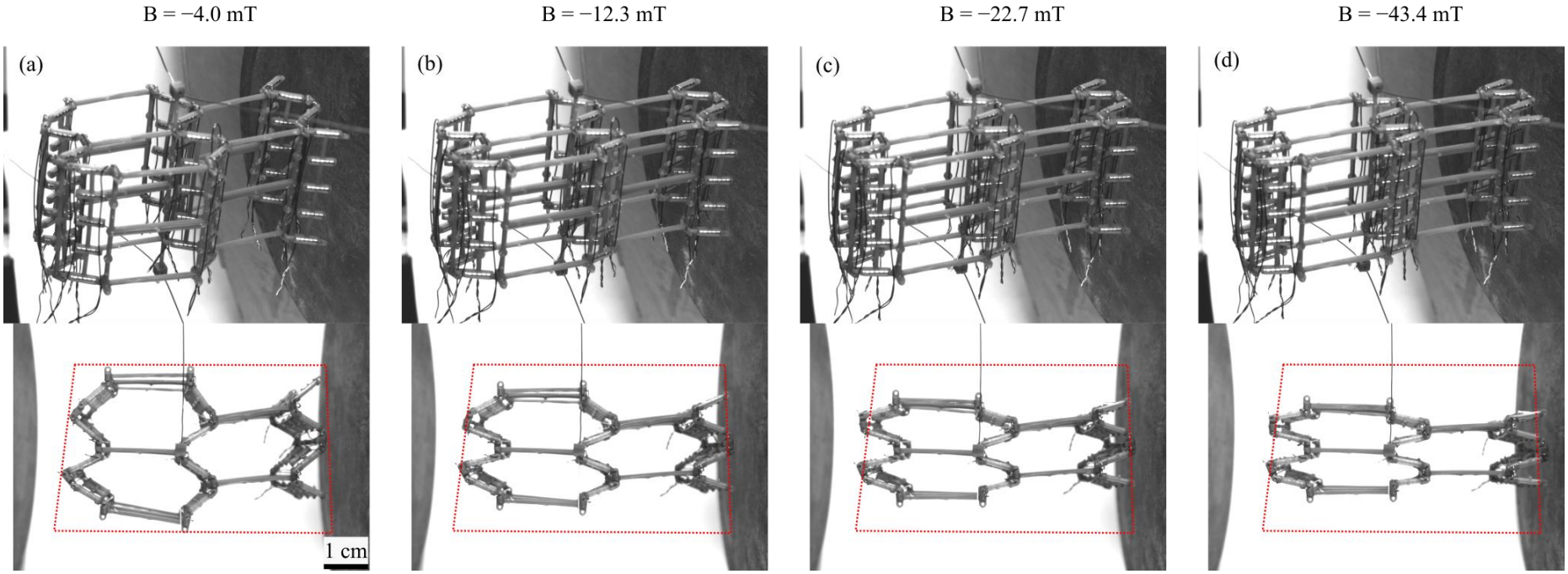

Figure 5.22(a-d) Images from a side view and aerial view of a System H structure under an external magnetic field of −4.0, −12.3, −22.7 and −43.4 mT respectively. The negative sign indicated that the external magnetic field is acting in the opposite direction.

5.3.5 Conclusion

In this section, multi-layered systems were constructed by stacking the basic accordion-like unit, created Systems SR and H. System H was shown to be able to flip between two configurations depending on the direction of the magnetic field from a conventional honeycomb known to exhibit a positive Poisson's ratio to a re-entrant honeycomb known to exhibit a negative Poisson's ratio (both when deforming through hinging). Furthermore, the geometry of the systems was manipulated through the external magnetic field, inducing contractions and extensions on the structures.

5.4 Possible applications

It is envisioned that a major potential application of the structures investigated in this work will be an untethered miniature multi-directional actuator that provides a high degree of real time control. The ability to modify the geometry of the structure interactively through the use of electromagnetics will allow it to be redeployed for different applications without the need of physically changing the geometry. Furthermore, the actuator could be used to impart controlled movement in two directions simultaneously. In fact, the possibility of switching between positive and negative Poisson's ratio implies that the direction of the force exerted in the plane of deformation could be either in the same or in opposite directions. Given its high adaptability and controllability, the actuator can be especially attractive in the aerospace, biomedical, and robotics industries. Apart from actuators, the properties exhibited by this structure can find potential use in deployable structures, including drones and satellites amongst others. In these cases, the system would be packed densely in the launching phase and subsequently deployed in situ through the use of magnetic fields. The process could allow

the system to lock in the desired configuration without the use of pistons and other traditional mechanical parts. Real-time adjustable variable pored sieves and sound proofing systems represent other possible applications of the structure.

5.5 Conclusion

In this chapter, an accordion-like magneto-mechanical metamaterial was designed and produced. The structure was able to react to an external magnetic field through changes in its geometry by contracting and extending. An investigation analysed the response of the structure and its dependence on the magnetic moment of the magnetic inclusions and the geometric parameters in order to gain a better understanding of the response. More importantly, the basic unit was stacked to construct multi-layer structures; System SR and H, and it is shown that depending on the direction and magnitude of the external magnetic field, the analysed structure H can undergo a transition from a structure known to show a positive Poisson's ratio to one known to exhibit a negative Poisson's ratio. All of these results indicate that the proposed concept can be used in a number of applications including programmable actuators at different scales and smart filters. It is also very promising from the point of view of novel devices used in medicine and robotics, i.e., fields where the possibility of having a remote control over the deformation pattern and the resulting mechanical properties of functional materials is of great significance.

Chapter 6 : Inclusion-based Auxetic Magneto-Mechanical Metamaterial: Part 2

6.1 Introduction

In Chapter 5, magneto-mechanical materials with embedded magnets were proposed which could undergo a rapid reconfiguration in response to an external magnetic field. Such active reconfiguration was shown to lead to a tuneable geometry that may exhibit Poisson's ratio, ranging from positive, zero Poisson's ratio to negative Poisson's ratio. However, despite these results being very promising, they share a number of limitations. Firstly, the structures proposed in these studies were built through the use of multiple separately fabricated components that were later connected through hinges in a pin-jointed manner. More specifically, all elements had to be manually aligned and connected through external rods passing through the joints. Such approach, despite being easy to reproduce, results in a situation where it is relatively difficult to scale the size of the system. Secondly, the nature of the pin-joints imparted excessive degrees of freedom resulting in an unstable structure, which deformed asymmetrically when exposed to an external magnetic field. Another limitation of the previous study is that the structure's smallest dimension is limited by the size of the magnetic inclusions, i.e., the permanent magnets. Furthermore, as discussed in Section 5.2.6.3.1, reducing the number of magnets in the magnetic inclusions drastically, had a negative effect on the response of the structure to an external magnetic field. The possibility of miniaturising the structure is particularly important as it opens the opportunity for applications in robotics and biomedical devices.

To address these shortcomings, this chapter will be divided into two parts. The first section will investigate the possibility of fabricating the magneto-mechanical metamaterial as a single undivided element. In this section, the prospect of an egg-rack-like structure will be explored, which would be able to shrink in multiple directions in response to an external magnetic field. On the other hand, the second part will investigate the use of nanoparticles *in lieu* of the magnetic inclusions; specifically iron nanoparticles capable of exhibiting superparamagnetism.

6.2 Fabricating an active magneto-mechanical metamaterial using bendable connecting arms

6.2.1 Introduction

This study aims to investigate the feasibility of constructing a magneto-mechanical metamaterial as a single undivided element, thereby facilitating the production of miniature systems which may deform when exposed to an external magnetic field. In the first section, different concepts of bendable connecting arms will be explored numerically *vis-à-vis* their ability to deform. The connecting arm which results to have the best properties will then be used in the second section to produce and investigate an experimental accordion-type prototype printed as one part. The differences between this prototype and the one produced in Chapter 5 will be discussed.

In the third section, an egg-rack-like structure (J. N. Grima, Williams, *et al.*, 2005) with magnetic inclusions, will be proposed and analysed when the system is subjected to an external magnetic field. The possibility of producing multi-layered structures which may exhibit an NPR in multiple directions will also be discussed.

6.2.2 Exploring different designs of Interconnecting Arms

6.2.2.1 Introduction

In this section, the issues governing the accordion-like structure discussed in section 5.2 will be addressed. Specifically, the aim was to redesign the hinges of the accordion-like structure. As discussed in Chapter 5, the connection bars used as part of the hinges of the structure, brought about a large degree of freedom which resulted in an unstable structure. This was shown in the large deviations in the geometric parameters analysed in section 5.2.5.3.2 and the shearing of the multi-layered structure discussed in section 5.3.4. Furthermore, the manual assembly of the structure introduced unnecessary human errors especially when tightening the butt-hinges. Therefore, in this section, a number of connecting arms designs will be proposed and tested numerically in order to choose the best hinge design for handling large deformations.

6.2.2.2 Methodology

6.2.2.2.1 Pre-processing FEA parameters

The mechanical properties of the four connecting arms designs proposed (see Figure 6.1) were studied using FEA simulations to select an appropriate connecting arm for the experimental prototype. For the purpose of the simulations, the symmetry lines were availed of, and thus only one section of the structures was simulated as shown in Figure 6.1. The parameters investigated were the thickness of the connecting arm, $T_{h,}$ and the length of the connecting arm, $L_{1,}$ as shown in Figure 6.1. In the case of Designs 2 and 4, L_1 was dependant on L_2 and L_3, where L_2 was always equal to L_3. All sharp edges were filleted to better distribute the internal strains. Furthermore, angle φ (see Figure 6.1) was used to describe the extension of the structure and is defined as the angle between the initial position of the rigid bar and the position of the rigid bar after the deformation is carried out.

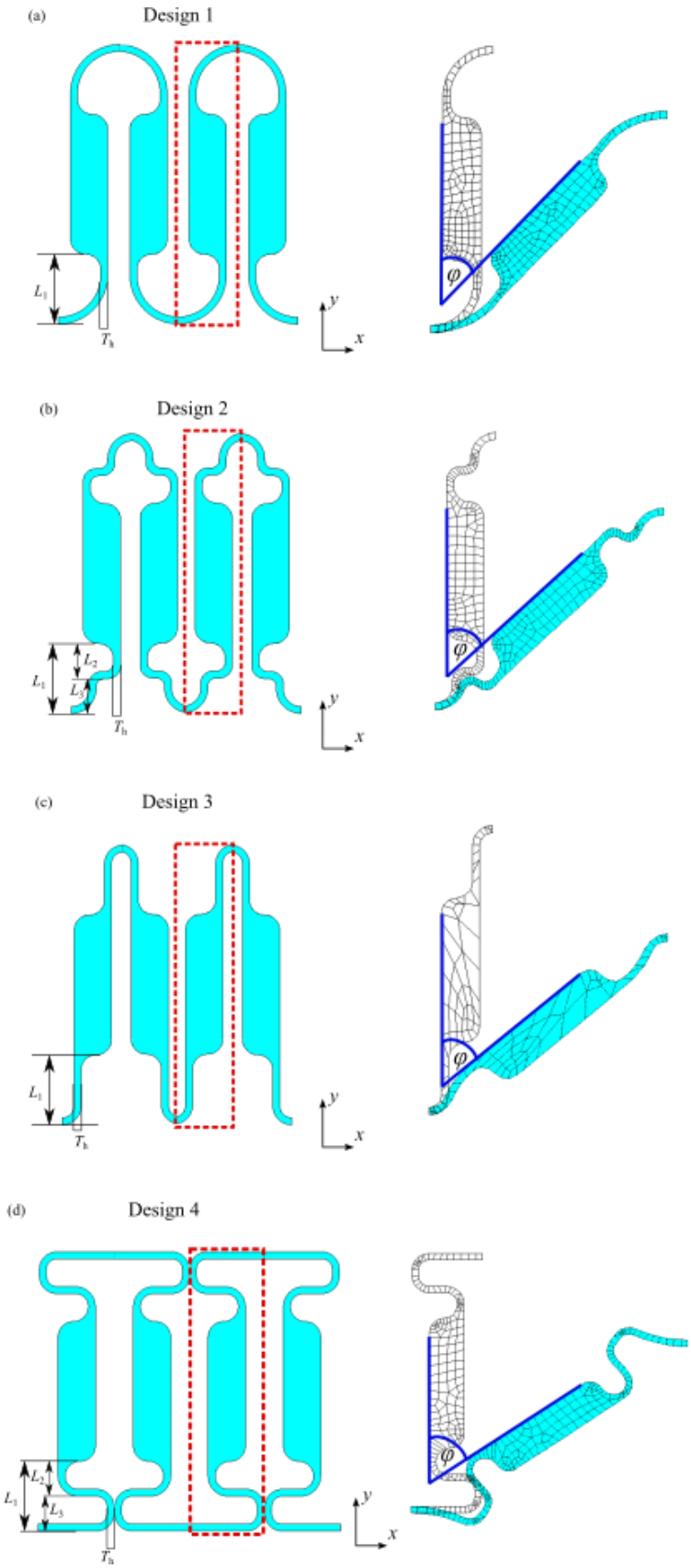

Figure 6.1. The four hinge designs tested numerically, outlining the parameters varied in the study.

The element type for the simulation was set to PLANE183, this being a 2D element able to model both elastic and plastic behaviour, as well as allowing for irregular meshes. Non-linear material properties as measured for the Tough2000 resin were used (see section 4.2.3), with an initial Young's modulus of 972 MPa, and a Poisson's ratio of 0.463.

Symmetry boundary conditions were used for the simulation. The structures were loaded in the *x* direction by applying a tensile strain on the nodes at the joint having the maximum value of the *x* coordinate aligned perpendicularly to the loading direction as shown in Figure 6.2 as a red arrow. The nodes at the joint having a minimum value of the *x* coordinate were set to have a zero displacement (depicted by rollers) in the *x* direction. The nodes having the minimum value of the *y* coordinate were set to have a zero displacement in the *y* direction.

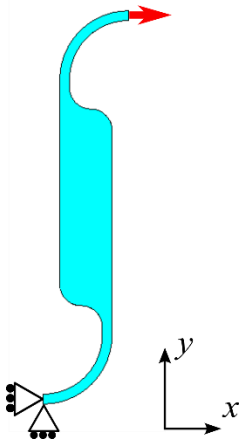

Figure 6.2. A representative drawing the boundary conditions used for loading in the *x* direction.

Non-linear numerical simulations using line searches were carried out. Large displacements were taken into consideration and automatic time stepping was used with the number of substeps set between 100 to 200. The structure was subjected to a maximum displacement of 700% L_x. A mesh-independent study was carried out in order to achieve a mesh that yielded accurate results while maintaining a low computational time. To this end, one structure was selected (Design 4, L_1 = 3.0 mm, T_h = 0.3 mm) and simulated using different smart sizes as described in Table 6.1 below.

Table 6.1: Different Levels and Depth use in different sets of mesh refinement.

Set	*Smart Size*	*Number of elements*
1	6	336
2	5	1217
3	4	20356
4	3	256008
5	1	317972

Each set was then compared to the finest mesh (set 5) and their deviations were analysed. The maximum percentage deviation from all computed stresses and strains was used to assess the difference between the generated results.

6.2.2.2.2 Parametric Analysis of the different connecting arm designs

For each connecting arm design, numerical simulations investigating the effect of the connecting arm thickness (T_h) and connecting arm length (L_1) as defined in Figure 6.1 were carried out. To this end nine structures for each connecting arm design were investigated with T_h having values of 0.2 mm, 0.3 mm and 0.4 mm, while L_1 had values of 1.5 mm, 3 mm and 4.5 mm. For each design the maximum von Mises stresses, σ_{max},

and the strain concentration factor, $K_{\varepsilon,}$ (see Equation 3.11, section 3.3.2.2) were obtained for each sub-step computed in the non-linear simulation.

6.2.2.3 Results and discussion

The aim of this section was to redesign a connecting arm for the foldable structure described in Chapter 5. The connecting arm should be capable of withstanding the folding and unfolding of the structure and the stresses induced by the deformation. Before discussing the actual results, it is important to assess that the mesh used did not create artefacts in the results. The mesh was investigated at φ = 1°, 45° and 85° to ensure that the selected mesh yielded precise results throughout the non-linear simulation. The results obtained indicate that using smart sizing of 1 or 3 led to constant results (within 0.0003% of each other), thus using a smart sizing of 3 would yield accurate results.

Structures having longer connecting arms bend less than structures having shorter connecting arms, when applying the same strain. In fact, taking structures from Design 1 having T_h = 0.2 mm as an example, when 300% strain was applied, angle φ changed by 68° for the shorter structure (L_1 = 1.5 mm), whereas angle φ changed by 48° and 38.5° for structures having L_1 of 3.0 mm and 4.5 mm respectively. When investigating the foldability of the proposed connecting arms, angle φ was used when comparing the von Mises stresses and strain concentration factor of different connecting arms, as the strain does not reflect clearly the extent of folding of the structure.

For each design, the effect of the variables T_h and L_1 on the strain concentration and maximum von Mises stress will be discussed. From the results obtained (see Figure 6.3 to Figure 6.6) it is evident that changes in T_h and L_1 have the same effect for all the connecting arm designs considered in this study. Thus, discussion of the effect of these two parameters will be limited to Design 1. As expected, an increase in the parameter T_h,

is accompanied by an increase in the strain concentration factor and maximum von Mises stress. More specifically, for structures having L_1 = 4.5 mm and φ = 45°, a strain concentration factor of 0.00724, 0.0114 and 0.0163 was recorded when T_h was 0.2 mm, 0.3 mm and 0.4 mm respectively, see Figure 6.3(e). Furthermore, the structures having a T_h of 0.2 mm were able to stretch more while maintaining a low strain concentration factor. In fact, the structure having a T_h of 0.2 mm had a significantly lower strain concentration factor and had relatively smaller changes as angle φ opened (up until φ = 70°), implying that such structure would not only experience lower localised strains but maintain it for a large extension. For the thicker connecting arms, at a T_h of 0.3 mm and a T_h of 0.4 mm, there are minimal changes in the strain concentration factor up until a φ of 60° and 50° respectively, after which it starts to increase considerably. This implies that after a certain extension, local strains arise in the structure which could result in local plastic deformation. This is complemented by the fact that the maximum von Mises stress increases with T_h, in fact a maximum von Mises stress of 0.0372, 0.100 and 0.310 MPa was recorded when T_h was 0.2 mm, 0.3 mm and 0.4 mm respectively (Figure 6.3f).

Figure 6.3a-f depicts the effect of increasing the length of the connecting arm and reveals that a longer connecting arms had a better strain distribution and experience lower local stresses. For structures having a T_h of 0.2 mm, one notes that the structure having a length of 4.5 mm and φ = 45° experienced a strain concentration factor of 0.00724 and a maximum internal stress of 0.0372 MPa. The structures having a length of 3 mm and 1.5 mm, are shown to have a higher strain concentration factor of 0.0140 and 0.0104 respectively, coupled with higher local stresses of 0.105 and 0.637 MPa respectively (Figure 6.3c-f). The effect of increasing L_1 was shown to reduce local stresses and improve the strain distribution and can be attributed to the stresses being distributed along a larger length of the connecting arm.

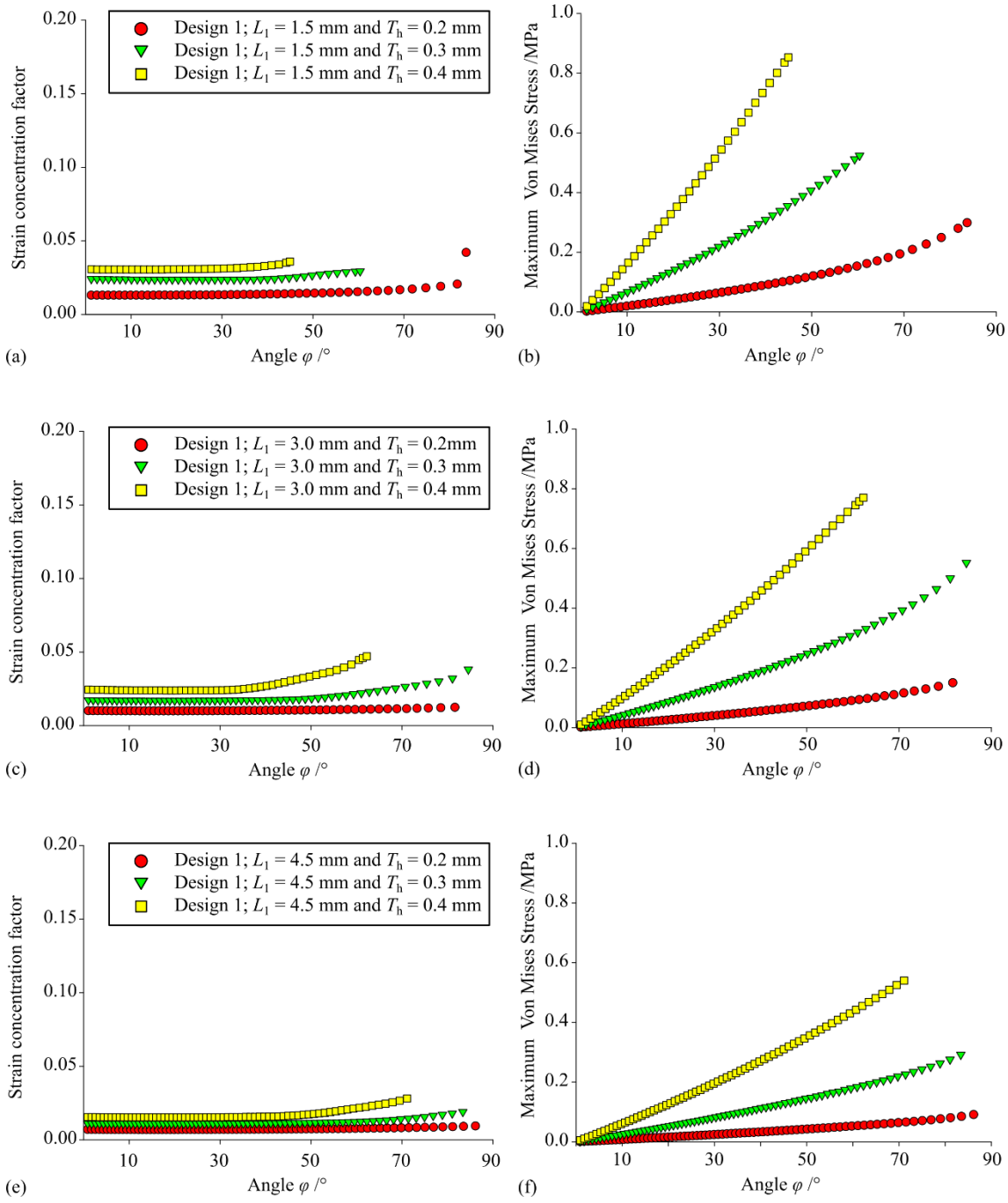

Figure 6.3. Investigation of the effect of variables L_1 and T_h on the strain concentration factor and maximum von Mises stress for Design 1 structures.

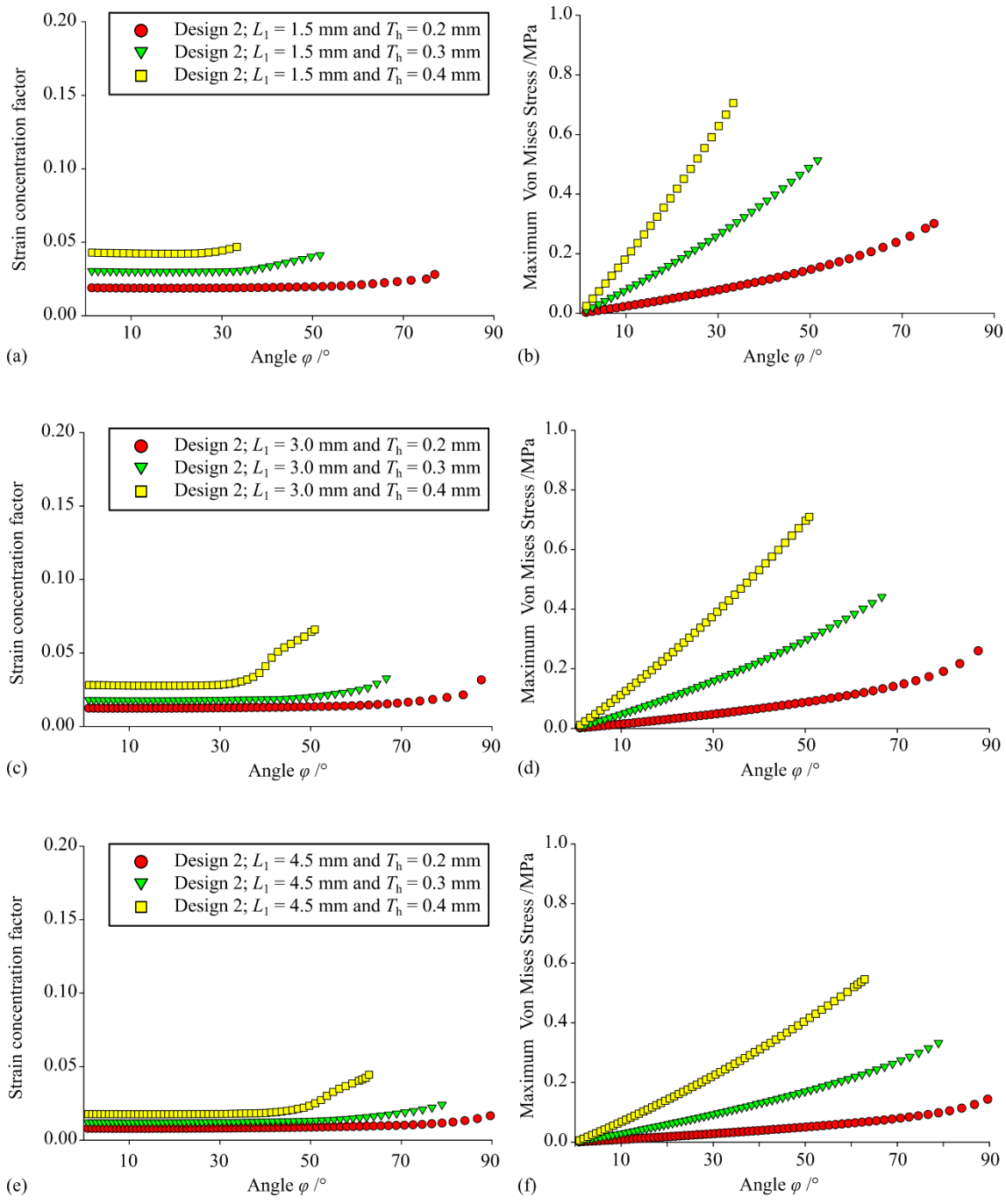

Figure 6.4. Investigation of the effect of variables L_1 and T_h on the strain concentration factor and maximum von Mises stress for Design 2 structures.

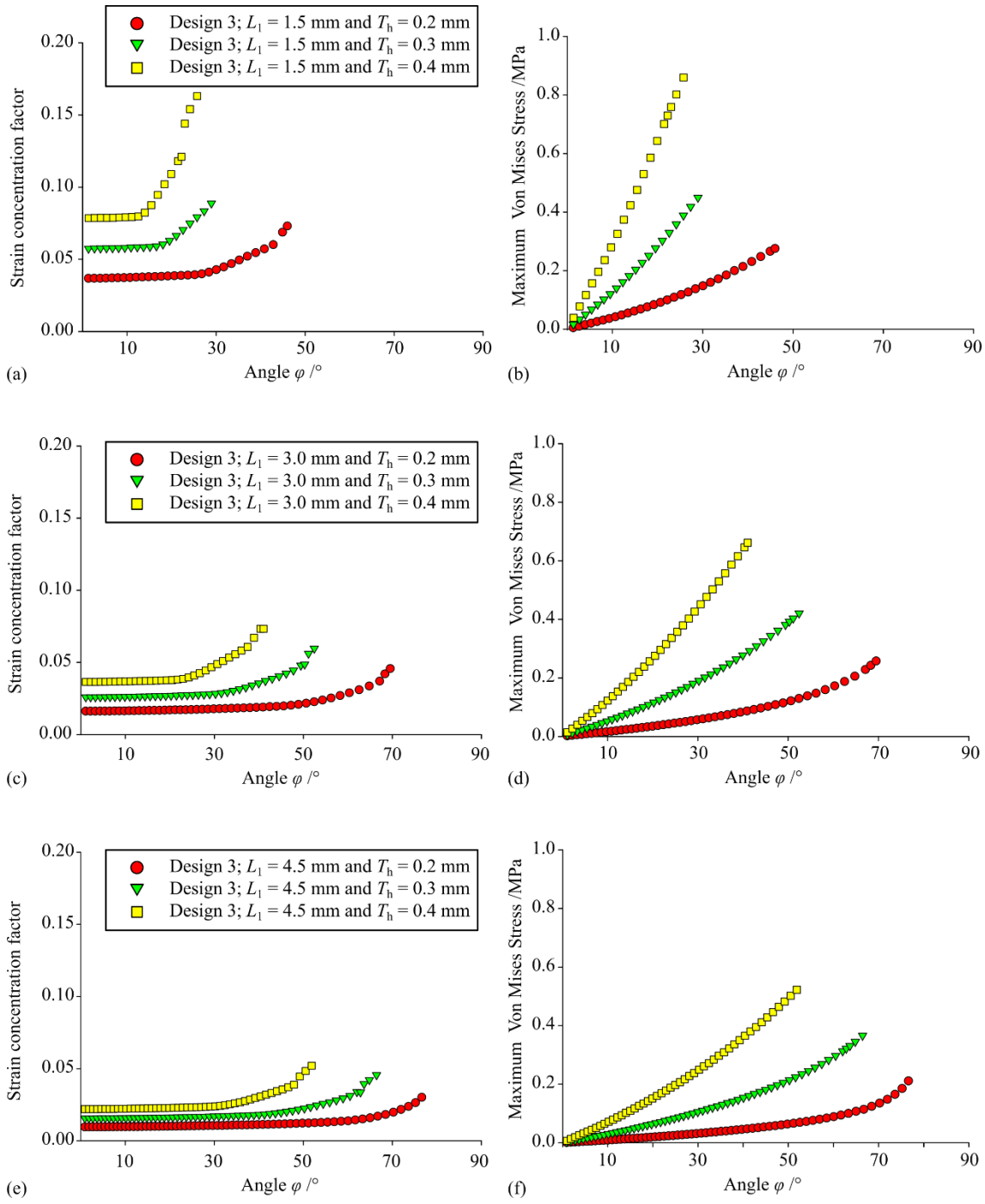

Figure 6.5. Investigation of the effect of variables L_1 and T_h on the strain concentration factor and maximum von Mises stress for Design 3 structures.

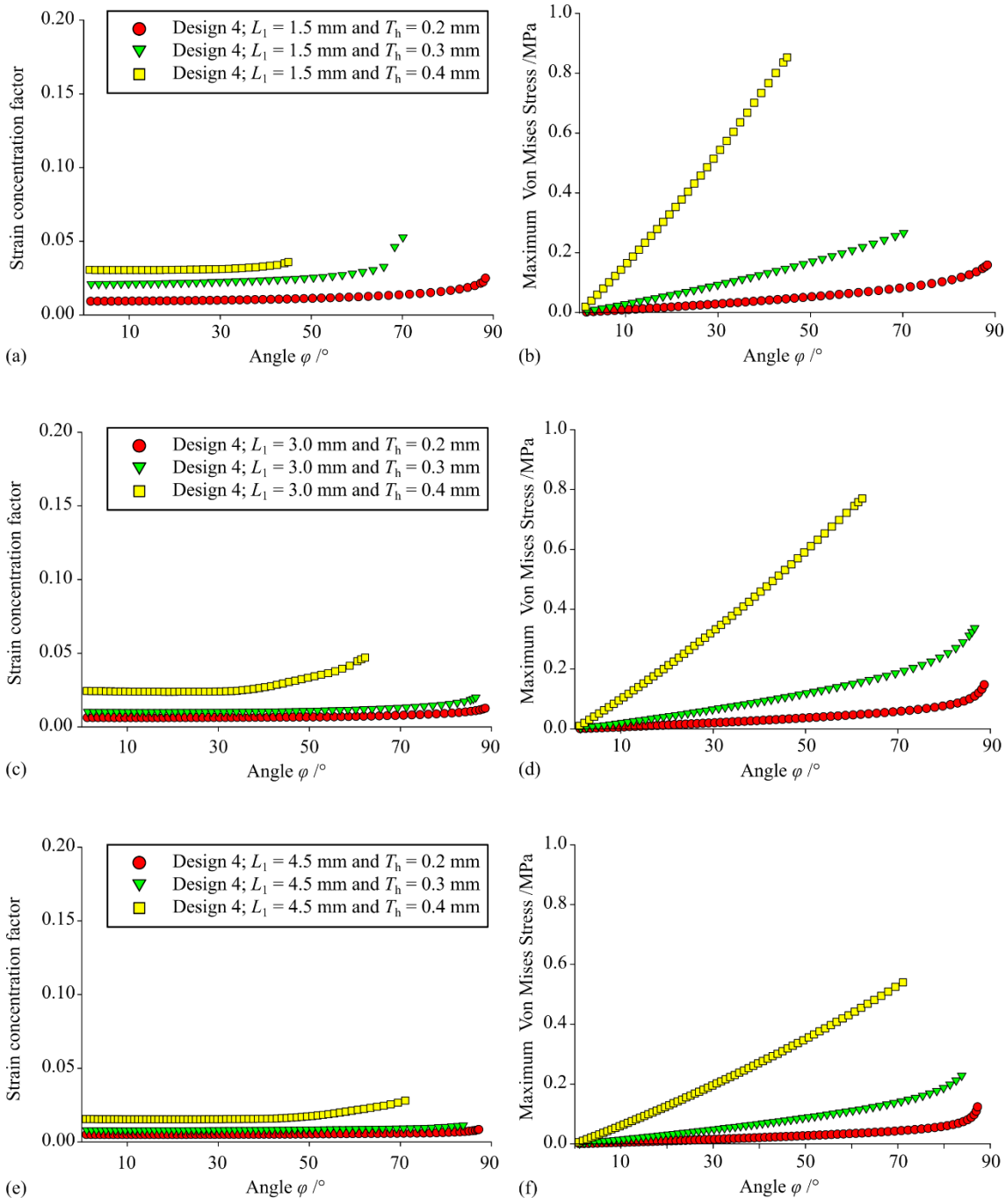

Figure 6.6. Investigation of the effect of variables L_1 and T_h on the strain concentration factor and maximum von Mises stress for Design 4 structures.

By comparing the four designs together, one notes that in general, structures of Design 4 had a lower strain concentration factor and lower maximum von Mises stress whilst on the other hand, Design 3 structures generally exhibited the largest strain concentration factor and maximum von Mises stress. Specifically, when comparing structures having a T_h of 0.3 mm, a L_1 of 4.5 mm and $\varphi = 45°$, a strain concentration factor of 0.0114, 0.0129, 0.0196 and 0.00840, and a maximum von Mises stress of 0.130, 0.150, 0.181 and 0.0757 MPa, for Design 1, Design 2, Design 3 and Design 4 respectively. In Figure 6.7 von Mises strain contour plots are shown for all four structures discussed above to better understand the strain distribution. It is immediately clear that Design 4 experiences significantly lower strains within the structure and distribute the strains more effectively from the small strains shown in the edges of the hinges, which can be attributed to the shape of the design. This was followed by Design 1 which seemed to exhibit a good strain distribution, whilst Design 2 and especially Design 3 had relatively high local strains at the hinges. The order of the most efficient design may vary depending on the variables; however, it was shown that Design 4 structures generally had a good strain distribution and low local stresses followed by Design 1, Design 2 and Design 3.

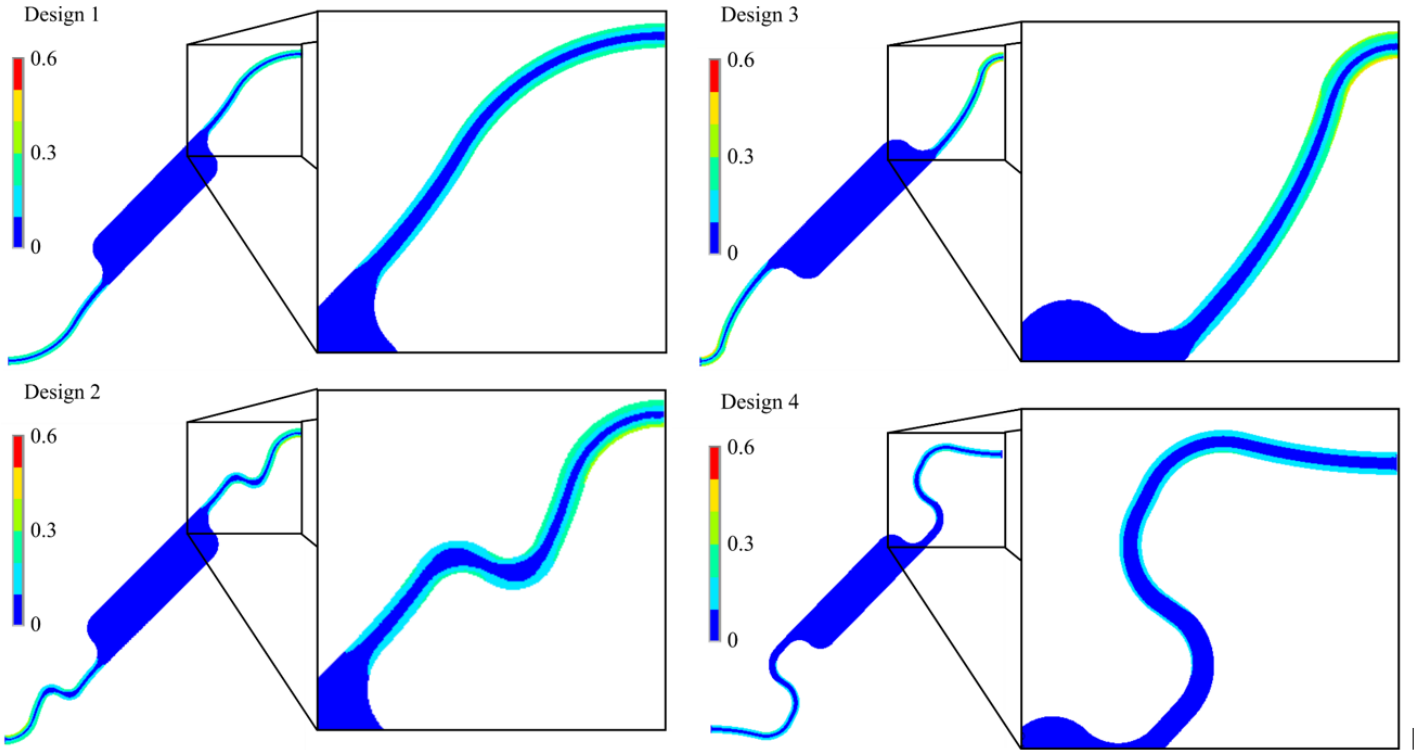

Figure 6.7. The strain distribution for structures having a T_h of 0.3 mm, a L_1 of 4.5 mm and φ = 45°

6.2.2.4 Conclusion

In this section, a redesign of the connecting mechanism for the accordion-like structure was investigated through FEA. The parametric investigation showed how the length of the arm and its thickness affected the strain distribution when deformed through hinging and concluded that Design 4 exhibited the best strain distribution followed by Design 1, Design 2 and Design 3.

6.2.2.5 One-part magneto-mechanical materials: Concept

In this section, the possibility of having a single undivided non-magnetic lattice with neodymium magnets distributed within the system will be explored. This would allow for minimal assembly and is expected to promote the structure's stability. Four connecting arms designs were investigated and discussed in section 6.2.2. It was shown that Design 4 had the lowest stresses and strain concentration factor followed by Design 1. Given the complexity associated when 3D printing Designs 4 (in terms of supports that would be needed), Design 1 was chosen as it had an effective strain distribution whilst being easier to 3D print. The connecting arms will serve to compose two types of structures; the accordion-like and egg-rack-like structures, referred to as Structure A and E respectively (see Figure 6.8). Structure A comprises non-magnetic connecting arms which link the rigid ladder of bars together in an accordion-like foldable structure as depicted in Figure 6.8a. It is expected that similar to the structure discussed in section 5.2.2, the magnetic inclusions housed in the rigid bars would induce a torque on the rigid ladder of bars, deforming the hinges and folding the structure in one direction.

Structure E is an egg-rack-like foldable structure composed of individual rigid bars connected to three other bars through connecting arms, as shown in Figure 6.8b. The rigid bars are identical to the ones used in Structure A and also incorporate magnetic

inclusions. The permanent magnets will be placed such that the adjacent magnetic inclusions repel each other. This will result in the egg-rack like structure to open up resulting in the initial equilibrium configuration. Upon the application of an external magnetic field, the magnetic inclusions experience a torque that makes them align with the magnetic field. The direction of the torque depends on the orientation of the external magnetic field. The torque causes the structure to hinge at the flexible connectors such that the structure bends in multiple directions and as a result the overall structure may close, open or even reverse the egg-rack-like folding pattern. Once the external magnetic field is removed, the structure is expected to revert back to its equilibrium position due to the internal forces within the structure itself.

6.2.3 Geometric Parameters

Structure A is characterised by three lengths denoted by L_1, D_A, and D_M and thickness, T_h, (as depicted in Figure 6.8a), whereas structure E is characterised by the variables; L_1, D_A and T_h (as depicted in Figure 6.8b). The length L_1 gives the length of the connecting arm while D_A gives the length of the rigid bar. On the other hand, D_M represents the distance between the magnets in the out of plane direction. In order to simplify the analysis for Structure A, D_A and D_M were taken to have the same magnitude and are subsequently referred to as D. Thickness, T_h, is defined as the thickness of the connecting arm.

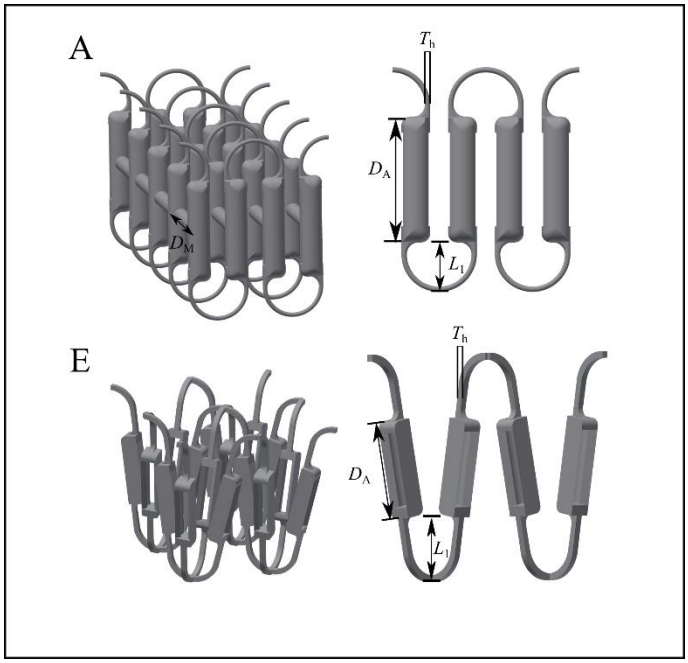

Figure 6.8. (a) A computer-generated model of the accordion-like structure as seen from the side and the front. (b) A computer-generated model of the egg rack-like structure as seen from the side and the front.

6.2.4 One-part accordion-like magneto-mechanical structure

6.2.4.1 Introduction

In this section, the new connecting arm will be implemented in the accordion-like magneto-mechanical structure. Additionally, the structure will be investigated experimentally to test the feasibility of the design when exposed to an external magnetic field. The stability of the structure and its controlled deformation to the external magnetic field will be discussed and compared briefly to the previous study.

6.2.4.2 Methodology

Structure A was designed in Autodesk Inventor Professional having T_h of 0.3, D = 8.5 mm and L_1 = 4.5 mm. The designs were then exported to be printed with an SLA 3D printer as described in section 5.2.6.2.1. The magnetic inclusions were then inserted into the bars - this setup consisted of five cylindrical neodymium magnets each having a

height and a diameter equal to 1 mm having a combined dipole moment of 4.55 mA m^2, described in detail in section 5.2.5.3.1. The magnetic inclusions were inserted such that the magnetic poles repelled the adjacent magnets.

The structures were then placed in between two large electromagnets generating an approximately uniform magnetic field at the location of the sample. Structure A was suspended through a rigid backbone using copper wires. The deformation of the structures when subjected to a magnetic field could then be monitored using an imaging camera (Daheng MER2-630-60U3M) mounted with a lens having a focal length of 1.4 (get cameras LCM-5MP-08MM-F1.4-1.5-ND1) stably fixed and levelled vertically above the system.

The extension/contraction of the Structure A was then studied using an external magnetic field having values ranging between 12.3 mT and 95.3 mT. In a typical experiment the electromagnets were switched on and the structure was allowed to attain the new equilibrium position. At this point the electromagnets were switched off with the deformation being recorded by the camera. This was repeated for ten times for each external magnetic field used. A python script was used to determine the observable parameters; θ_1, θ_2, θ_3, and L_x by selecting reference points for each image, shown as red dots in Figure 6.9. Once the variables were calculated, the percentage change of L_x as compared to its value at the lowest external magnetic field (12.3 mT) was determined.

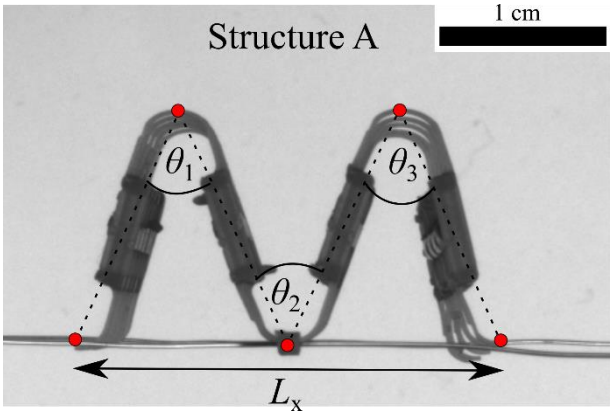

Figure 6.9. A depiction of the reference points and the parameters analysed for structure A

6.2.4.3 Results and Discussion

The use of bendable connecting arms was experimentally investigated to determine the viability of the proposed structure when compared to the butt-hinges used in section 5.2.5. In the experiment, structure A was shown to contract by 25%, from 21.6 mm under a magnetic field of 12.3 mT to 16.14 mm when the external magnetic field was 95.3 mT, as shown in Figure 6.10(a). Correspondingly, the angles observed decreased by around 13° each and as expected, θ_2 was slightly higher than θ_1 and θ_3, due to the edge effects discussed in the previous chapter. As in the case of the butt-hinges, this contraction is caused by the torque generated in the magnetic inclusions which in turn creates a moment around the hinges. Furthermore, as expected, when the external magnetic field was switched off the structure returned to its original configuration.

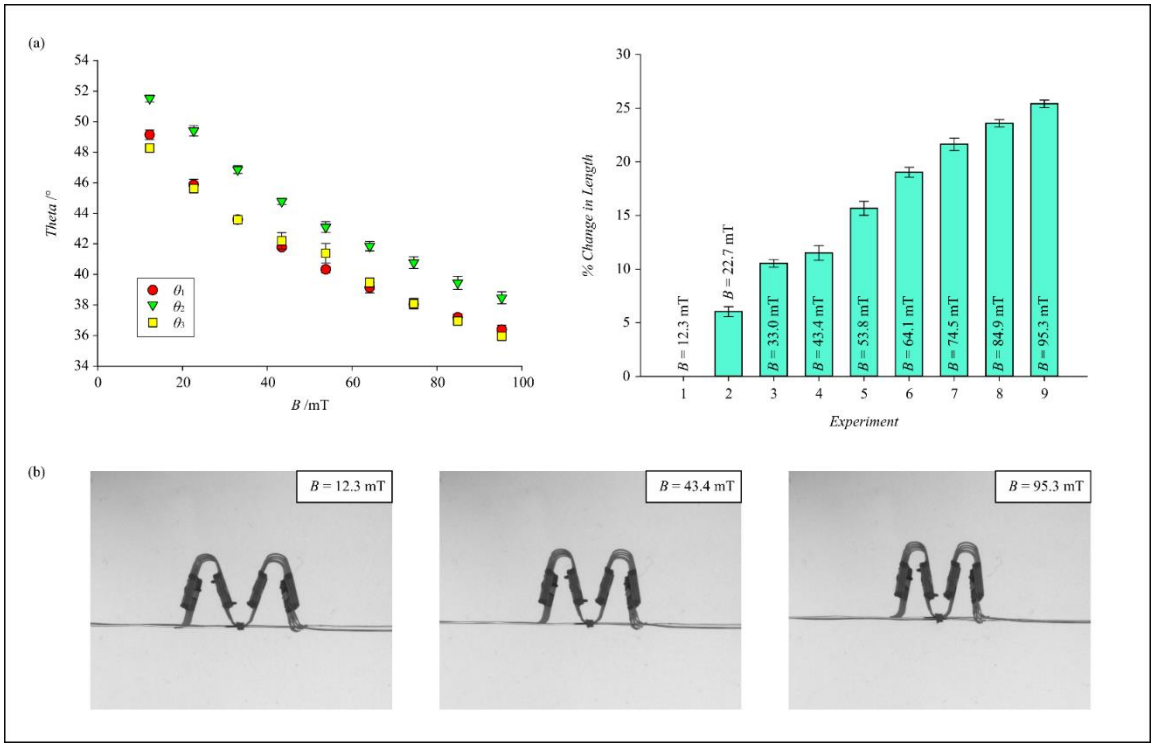

Figure 6.10(a) Graphs depicting the change in angles, θ_1, θ_2 and θ_3, and the % change in length with an increase in the magnetic field strength. (b) Images of structure A taken at different magnetic field strengths.

In order to investigate the effect of using connecting arms instead of butt-hinges, Structure A was compared with the equivalent structure composed of butt-hinges (Structure 5M, see section 5.2.5). In comparing the initial configurations when no external magnetic field is present, Structure 5M had a more open configuration than Structure A. This may be explained through the stiffness of the hinges. In Structure 5M there was minimal resistance to the repulsive forces generated by the magnetic inclusions since the hinges allowed relatively frictionless movement. On the other hand, in the case of the connecting arms, the internal magnetic repulsion had to overcome the stiffness of the hinge material which needed to bend for the structure to deform. The frictionless nature of the butt-hinges also allowed the structure to respond to lower external magnetic field, where a large contraction was recorded for a small increase in the external magnetic field

shown in Figure 6.11. On the other hand, Structure A required stronger external magnetic fields to contract by the same amount since as discussed above the torques caused by the magnetic inclusions had to overcome the stiffness of the material in the connecting arms.

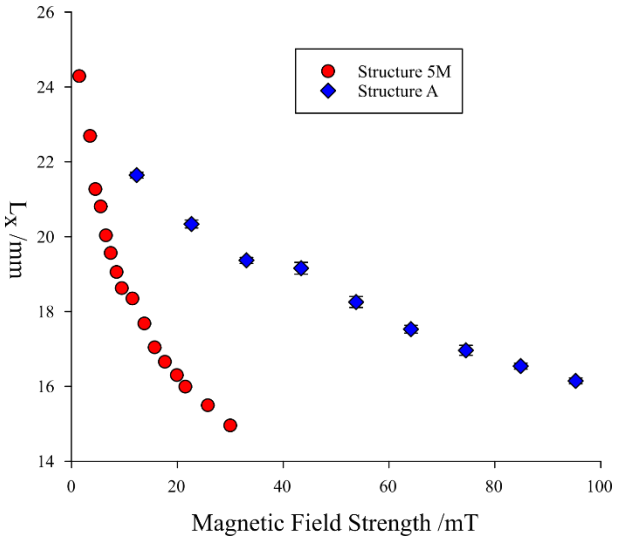

Figure 6.11. A graph depicting the change in length of Structures A and 5M as the external magnetic field was increased.

The deformation of the systems under an external magnetic field for Structure A and Structure 5M was also compared by observing the change in the angles; θ_1, θ_2 and θ_3. More specifically the ratios of θ_2 with θ_1 and θ_3 were investigated for both structures, as shown in Figure 6.12. At any value of the external magnetic field strength studied, the butt-hinge design shows a significant difference between the ratio θ_1/θ_2 and θ_3/θ_2. This implies that one side of the structure deforms to a larger extent than the other side. This asymmetric deformation can be attributed to the connection bars used in this design which introduced a large degree of freedom. Furthermore, the tautness of copper wire used in the hinges could have varied resulting in a side with preferential deformation. On the other hand, in the case of Structure A in general, for each value of the external magnetic field strength studied, the ratio θ_1/θ_2 and θ_3/θ_2 are almost identical (with the exception

of the values at 43.4 mT which may be due to an experimental error). This implies a very symmetric deformation, with both sides of the structure deforming similarly, something which may be explained by the fact that Structure A was 3D-printed with minimal assembly and thus the structure was more symmetrical resulting in similar forces on either side of the accordion-like structure.

Additionally, in Structure A, one notes that the ratios are close to one (between 0.92 and 0.99), whereas in the butt-hinges, the ratios deviate significantly from one especially for lower magnetic fields (between 0.70 and 1.15). This implies that for the bendable connecting arms there was minimal discrepancy between the angles at the edge and the one at the centre, which shows that the edge effect was less significant. This could be due to the bendable connecting arms having less degrees of freedom and higher stiffness that needs to be overcome by the torque generated by the magnetic inclusions in the external magnetic field, unlike what happens in the butt-hinges where the parts rotate freely. One notes that for Structure A, when under 43.4 mT, an outlier was observed for θ_3/θ_2. This can be attributed to imperfections in the 3D model as well as errors in measurement where the camera may have captured the images at an angle.

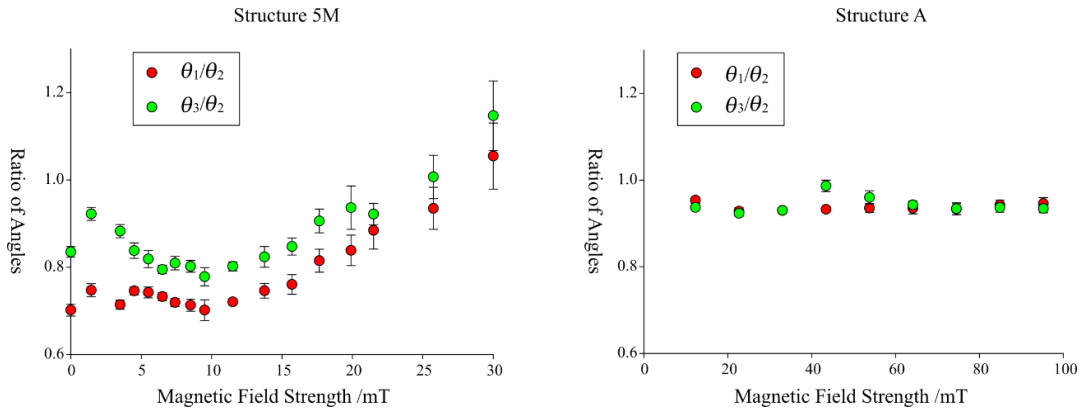

Figure 6.12. A comparison of the ratios θ_1/θ_2 and θ_3/θ_2 for structure 5M and A.

6.2.4.4 Conclusion

The proposed bendable connecting arms design was experimentally investigated and compared to the butt-hinge design mention in Section 5.2.5. It was shown to exhibit significant advantages over the butt-hinge design. Firstly, there was significantly less assembly required and therefore less human error involved in the assembly of the butt-hinges. This resulted in uniform connecting arms which resulted in a more symmetrical deformation. Furthermore, the structure was more stable when compared to the unsteady butt-hinges as the new design required the deformation of the connecting arms to move whereas previously the magnetic bars moved freely even at rest. This resulted in a structure capable of a controlled symmetrical deformation to an external magnetic field which could be produced as one part.

6.2.5 Egg-rack-like magneto-mechanical structure

6.2.5.1 Introduction

The use of connecting arms to produce magneto-mechanical structures makes the process of connecting two or more units together relatively easy to achieve. In view of this, in this section, an egg-rack-like magneto-mechanical structure will be proposed whereby four units with magnetic inclusions are connected together. This structure should be able to respond to an external magnetic field by contracting in two perpendicular directions. The prototype will be investigated experimentally and the concept of a magneto-mechanical structure capable of exhibiting an NPR in two directions will be discussed.

6.2.5.2 Methodology

Three structures were designed and built for Structure E; E1, E2, E3, having a thickness T_h of 0.2, 0.3 and 0.4 mm respectively, in order to assess the effect of the thickness of the hinge on the contraction observed. All structures had the following parameters: D = 8.5 mm and L_1 = 4.5 mm. The magnetic inclusions were then inserted into the bars such that the magnetic poles repelled the adjacent magnets.

The structures were then placed in between two large electromagnets generating an approximately uniform magnetic field at the location of the sample. Unlike previous prototypes, Structure E was fixed using a clamp connected through the central connecting arms as shown in Figure 6.13(a). Additionally, the structure was observed from two directions; from above the system, henceforth referred to as the transverse direction (see Figure 6.13(a)(iii)) and in a perpendicularly to the former direction henceforth referred to as the longitudinal direction (Figure 6.13(a)(iv)).

The extension/contraction of the Structure E was then studied using an external magnetic field having values ranging between 6.1 and 43.4 mT. In a typical experiment the electromagnets were switched on and the structure was allowed to attain the new equilibrium position. At this point the electromagnets were switched off with the deformation being recorded by the camera. This was repeated for ten times for each external magnetic field used. A python script was used to determine the observable parameters; θ_1, θ_2, θ_3, and L_x by selecting reference points for each image, shown as red dots in Figure 6.13(b). Once the variables were calculated, the percentage change of L_x as compared to its value at the lowest external magnetic field (6.1 mT) was determined.

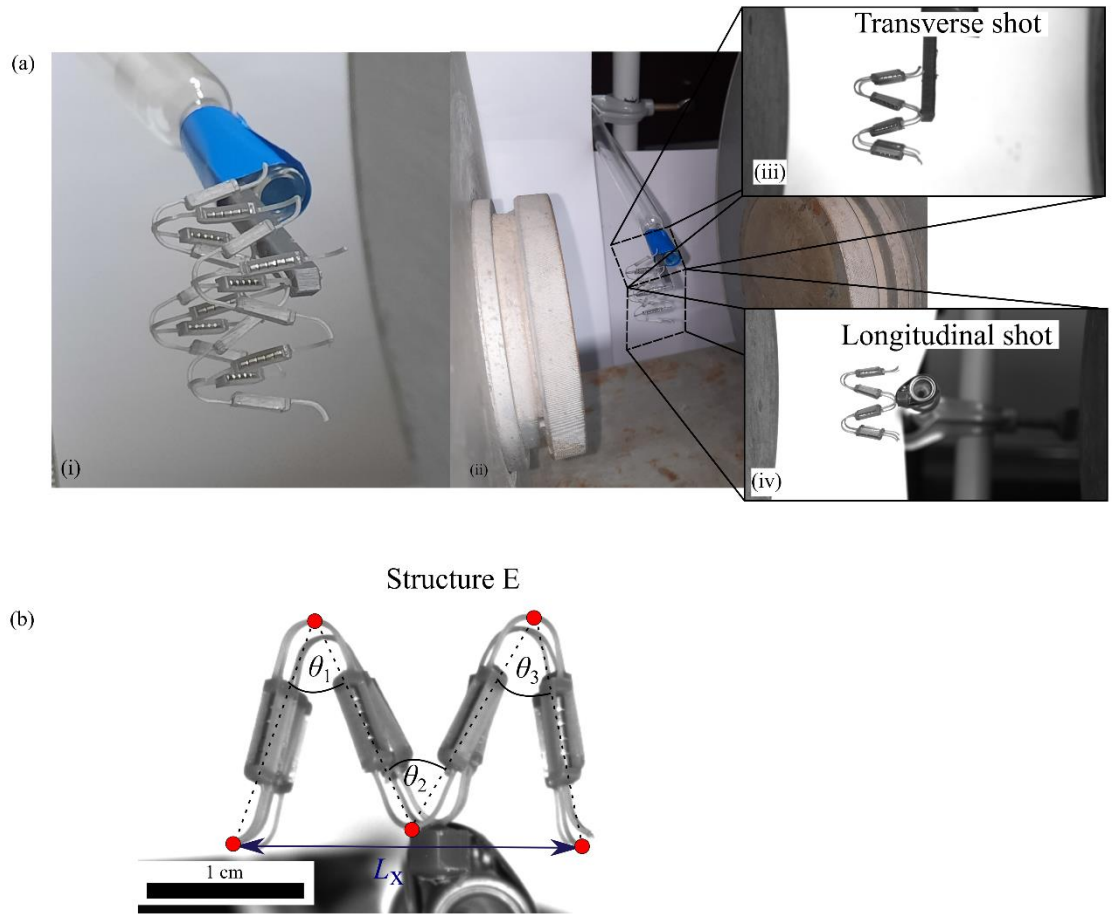

Figure 6.13. (a)(i) A close-up image of Structure E3 at an angle and (ii) a sideway image showing the orientation in the setup. Insets (iii) and (iv) show the transversal and longitudinal shot respectively. (b) Images showing the parameters considered for this study for Structure A

6.2.5.3 Results and Discussion

A number of challenges were present when performing the experiment using egg-rack-like structures. The first limitation was that the electromagnets used to produce the external magnetic field were fixed and therefore the external magnetic field could only be produced along an axis perpendicular to the Earth's gravitational field which restricted the orientation of magneto-mechanical structure. Furthermore, the egg-rack-like structure was designed to deform in multiple directions (unlike the accordion-like structure which deformed in one direction), and therefore structures E*i* (where *i* refers to 1, 2 or 3) had to

be fixed from one point. Taking into consideration the orientation of the magnetic inclusions, structures Ei were oriented such that the connection rod, see Figure 6.14, was oriented perpendicular to the Earth's gravitational field.

In this orientation, the downward force of gravity would impact the structure, causing it to move downward, particularly at its outer parts. From Figure 6.14, the longitudinal shots of Structures E1, E2 and E3, reveals that as expected the largest displacement occurs in the direction of gravity (the *y* direction), as the structure is pulled downward. Since the structure is fixed, there is also some displacement in the perpendicular direction (the *x* direction) as the structure rotates around the fixed point. It is worth noting that the transverse direction shows minimal changes when compared to the longitudinal direction, where in the latter case, the outermost bars significantly deviate from the position these bars would attain in the absence of a gravitational field. When comparing Structures E1, E2 and E3, one notes that thicker connecting arms result in significantly smaller displacement caused by gravity. This may be attributed to the fact that, while the weight of the structure remained approximately the same (since it was largely dependent on the weight of the magnetic inclusions), the connecting arms become stiffer, as demonstrated in the FEA simulations conducted in section 6.2.2. As a result, Structure E3 exhibited the least deformation due to gravity.

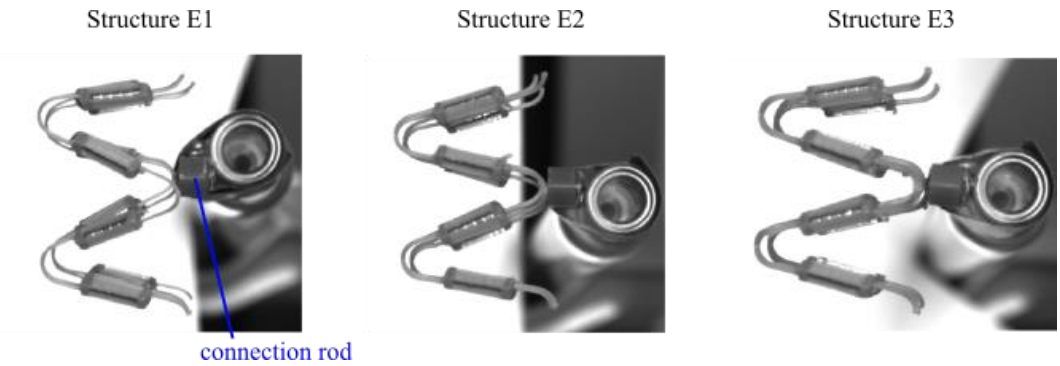

Figure 6.14. A depiction of the effect of gravity on structures E1, E2 and E3.

The behaviour of the experiment prototypes when subjected to an external magnetic field were analysed in the transversal and longitudinal direction of the egg-rack-like structures to investigate their ability to fold in multiple directions. For this study, measurements from the 2D projections of the outermost bars in the longitudinal and transversal direction were taken since the central bars were much less visible. It is important to note that since the measurements were taken from projected images, direct measurements of any out-of-plane rotation could not be obtained. However, the data collected from the projected images should give a good indication of the behaviour of the structure when subjected to an external magnetic field. Figure 6.15 and Figure 6.16 depict the contraction of structures E1, E2 and E3. Structure E1 experienced the largest contraction of 13.7% longitudinally and 23% transversally when increasing the external magnetic field from 6.1 mT to 43.4 mT. As expected, E2 and E3 had lower contraction values. When the external magnetic field was increased from 6.1 mT to 43.4 mT, E2 experienced a longitudinal and transversal contraction of 11.2% and 16.9% respectively while E3 experienced a longitudinal and transversal contraction of 7.5% and 9.6% respectively. Without losing sight of the fact that gravity is affecting the structure, the difference in contraction of E1, E2 and E3 may be explained by the different thickness of the connecting arms with the thicker connecting arm bending less for the same applied external magnetic field. The relation of the thickness of the connecting arm and the contraction observed was further analysed through the change in angles, θ_1, θ_2 and θ_3, shown in Figure 6.17. This confirmed that structure E1, having the thinnest connecting arm, exhibited the largest change in angles overall.

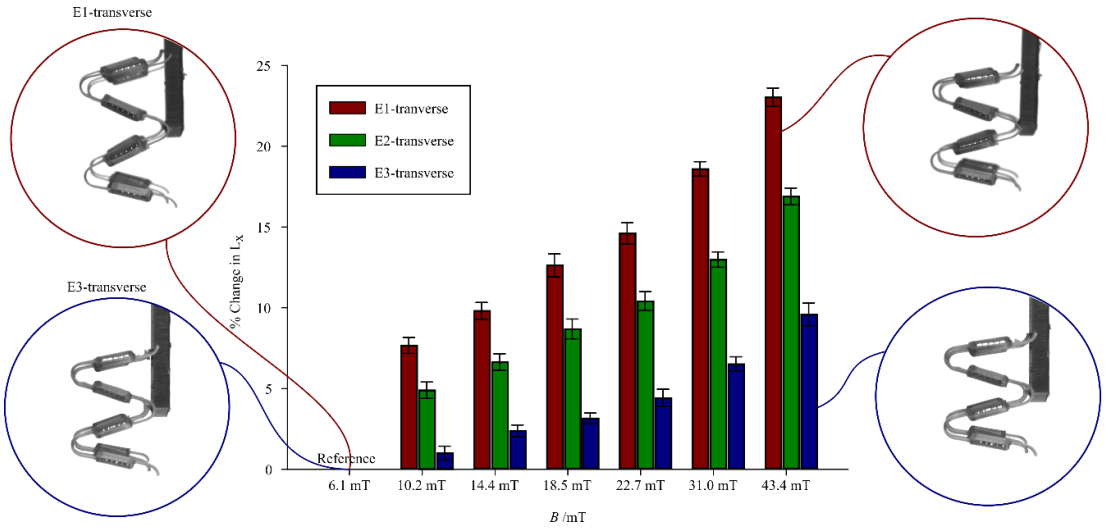

Figure 6.15. Bar graph depicting the % change in length recorded in the transverse direction of structures E1, E2 and E3 with increasing magnetic field strength. The insets show snapshots taken of the structure at different magnetic field strengths.

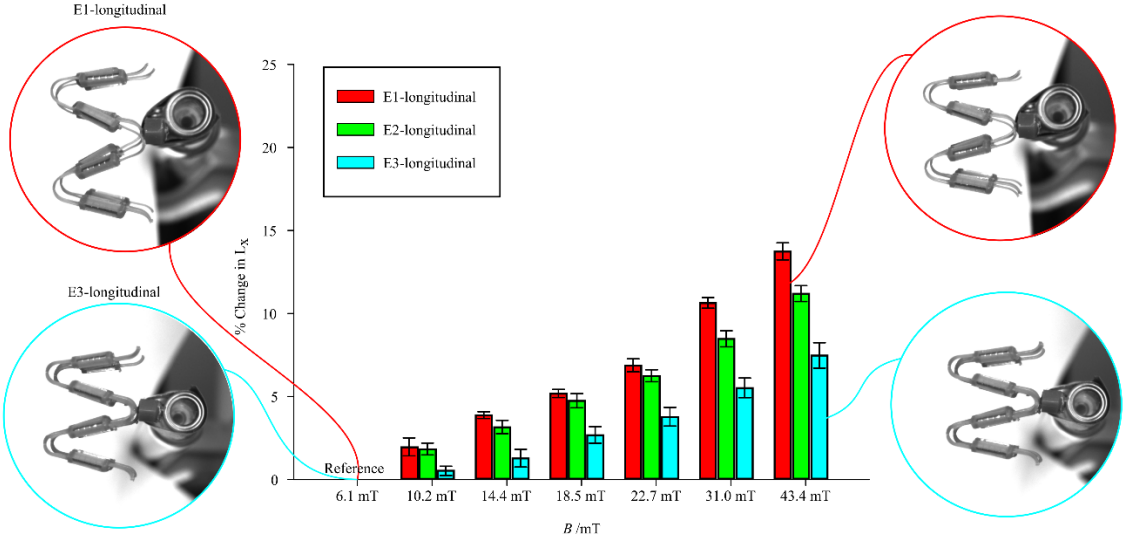

Figure 6.16.. Bar graph depicting the % change in length recorded in the longitudinal direction of structures E1, E2 and E3 with increasing magnetic field strength. The insets show snapshots taken of the structure at different magnetic field strengths.

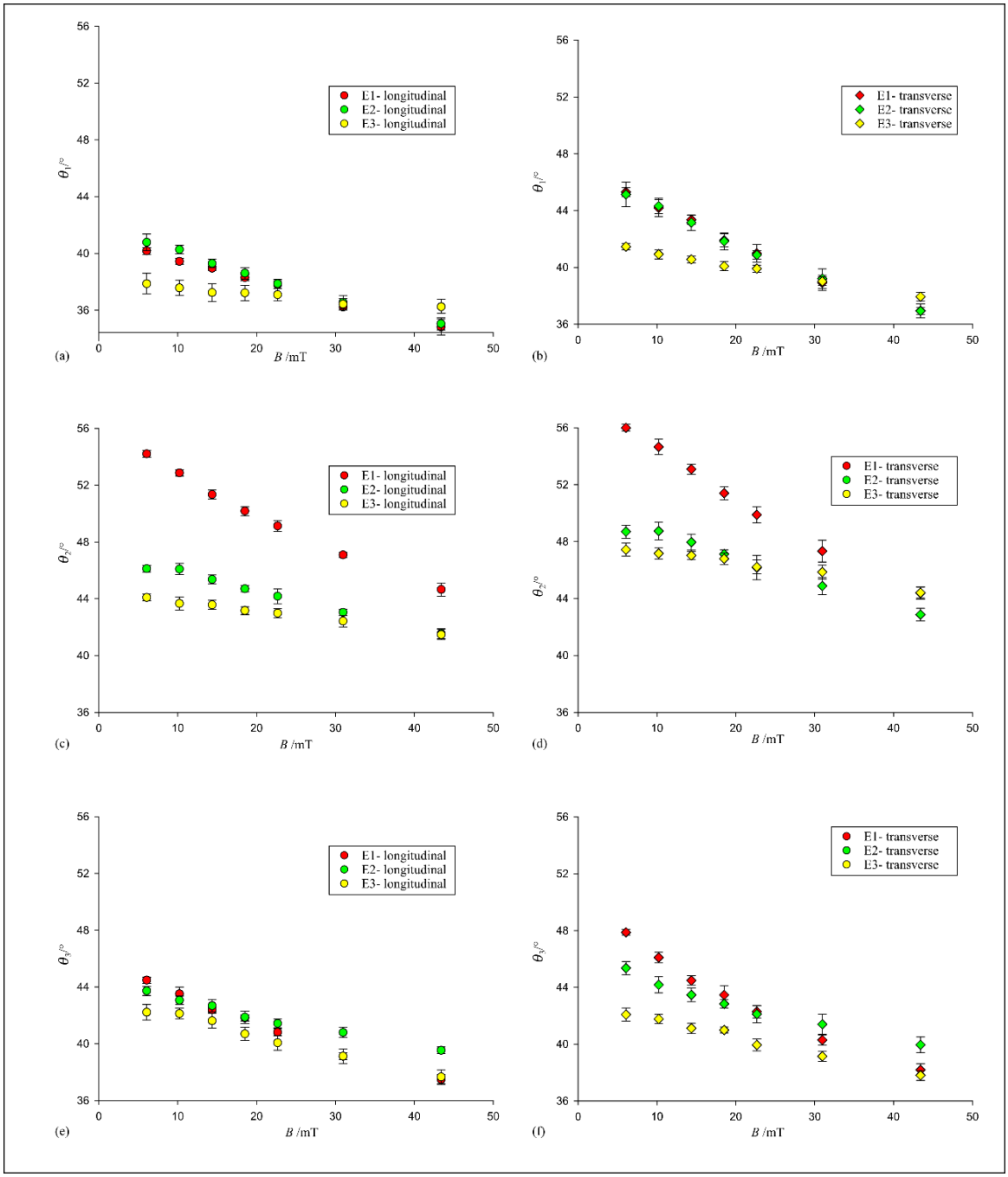

Figure 6.17.(a-f) Graphs depicting the change in angles, θ_1, θ_2 and θ_3, with an increase in magnetic field strength.

In accordance with the discussion about the effect of gravity, all the structures were more closed in the longitudinal direction when compared to the transverse direction. In fact, Figure 6.18 shows that the ratio between the longitudinal (L) and the transversal

(T) contraction (L/T) is smallest for structure E1 with a value of 0.255, followed by structure E2 with a value of 0.374 and structure E3 with a value of 0.514, all values quoted at an external magnetic field of 10.22 mT. Furthermore, as the strength of the external magnetic field is increased, the ratio L/T in general increased in the case of all structures. This may be due to the fact that as the external magnetic field increases, the ratio between the force exerted by the magnetic inclusion to align to the external field and the downward force due to gravity, shifts such that the former becomes more significant.

It is also interesting to compare how the individual angles measure within these structures behave when an external magnetic field is applied (see Figure 6.17). When the external magnetic field was set to 6.07 mT, the angles measured in the transverse direction for structure E1 had a value of 45.31, 56.00 and 47.86 for θ_1, θ_2 and θ_3 respectively. Increasing the external magnetic field strength to 43.4 mT, the values changed to 36.90, 44.38 and 38.17 for θ_1, θ_2 and θ_3 respectively. Even though at low magnetic fields the system in the transverse direction is already quite symmetrical, the system continues to deform in a more symmetrical manner as the external magnetic field is increasing. In the longitudinal direction, when the external magnetic field was set to 6.07 mT, the angles measured for structure E1 had a value of 40.18, 54.20 and 44.48 for θ_1, θ_2 and θ_3 respectively. Increasing the external magnetic field strength to 43.4 mT, the values changed to 34.77, 44.65 and 37.48 for θ_1, θ_2 and θ_3 respectively. This shows that the 2D projection in the longitudinal direction is less symmetrical than the transverse direction as discussed above, however, as the external magnetic field increase, the system deforms in a more symmetrical manner.

In structure E3, the angles measured in the transverse direction had a value of 41.46, 47.44 and 42.07 for θ_1, θ_2 and θ_3 respectively. Increasing the external magnetic field strength to 43.4 mT, the values changed to 37.94, 44.41 and 37.79 for θ_1, θ_2 and θ_3

respectively. On the other hand, in the longitudinal direction, when the external magnetic field was set to 6.07 mT, the angles measured for structure E1 had a value of 37.87, 44.08 and 42.22 for θ_1, θ_2 and θ_3 respectively. Increasing the external magnetic field strength to 43.4 mT, the values changed to 36.24, 41.47 and 37.66 for θ_1, θ_2 and θ_3 respectively. Similar to structure E1, as the external magnetic field increases, the structure become more symmetrical. Comparing structures E1 and E3 reveals that structure E3 is more symmetric which may be due to the stiffer connecting arms which increase the stability of the structure.

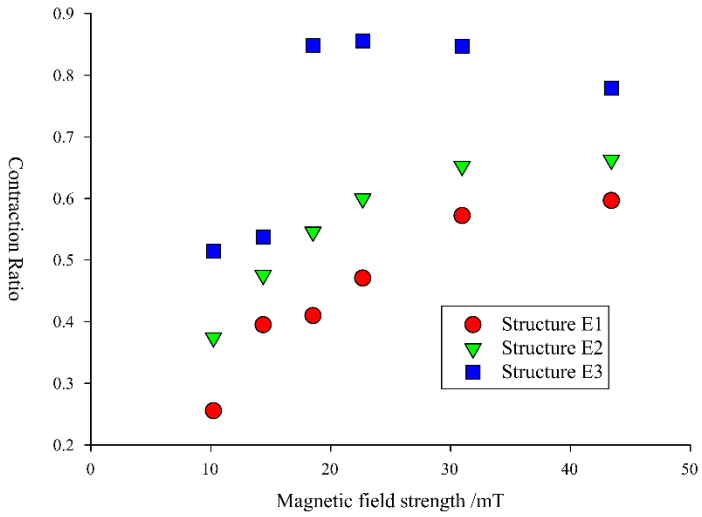

Figure 6.18. A graph of the change in Longitudinal/Transversal contraction ratio with magnetic field.

6.2.5.4 Conclusion

In this section the ability of an egg-rack-like shape programmable structure to fold in two directions in response to a relatively low external magnetic field was observed and the effect of the connecting arm thickness was investigated. The E1 structure exhibited the largest contraction of 23% in the transverse direction and 13% in longitudinal direction.

6.2.6 Possible applications

Both accordion and egg-rack-like systems showed tuneable folding in response to an external magnetic field. Combined with the ease of producing such units these systems can be implemented as a framework in deployable systems especially smart or remotely controlled systems. The package would be folded using magnetism, untethered, and therefore reducing any friction present in the conventional mechanisms. Once deployed the framework would no longer be under an external magnetic field and thus unfurl. For smarter systems, electromagnets could be attached at local point to contract or extend the system in real time as required by adjusting the external magnetic field. This would be combined with locking mechanisms which would keep the structure in the desired place once the batteries run out. The system would be initially contracted using the external magnetic field and the system would open up upon deployment. In the case of System E, the system would unfurl in two directions upon deployment akin to an umbrella in two dimensions. Deployable devices include satellites and drones where the use of magnetism would have a number of advantages over hard machines using pistons, mainly the concern of weight and fine, accurate control of small movements. Since these systems rely solely on the external magnetic field, they are able to generate forces and movement without contact, i.e., untethered. In fact, this can be used in applications such as the robotics industry, especially in milli- and micro-devices which could be controlled untethered and remotely. A possible use for this would be as stents in the biomedical industry. Moreover, both systems have great potential as actuators owing to the untethered manipulation of their dimensions through the use of an external magnetic field with System E being a strong candidate for multidirectional actuators as it extends and contracts in two planes. Furthermore, being magnetically actuated allows the structures to be controlled by the magnitude of the external magnetic field and thus the structures can be finely tuned in smart actuators.

Further research could investigate a sheet composed of multiple unit cells in which electromagnets would be implemented at strategic locations to produce localised external magnetic fields. Thus, the system could be controlled at a local level where segments contract and extend independently of each other. This allows for complex shapes and even doming given the auxetic nature of egg-rack models. This would find application in materials that need to adapt their morphology to a localised degree such as solar wings and satellites as well as smart textiles.

6.2.7 Conclusion

In this section, two foldable magneto-metamaterial systems with bendable hinges consisting of an additively manufactured structure hosting magnetic inclusions were proposed. Structure A consisted of an accordion-like structure with emended magnets which caused deformation when subjected to an external magnetic field resulting in the folding of the system in one direction. The concept was extended to an egg-rack-like model, Structure E, which was capable of folding in two perpendicular directions in response to an external magnetic field. The effect of the thickness of the hinges was investigated and it was found that structure E1 having a hinge thickness of 0.2 mm exhibited the largest contraction. Furthermore, the contraction of both systems can be finely controlled through the external magnetic field with a high degree of turnability and control. These systems offer untethered manipulation of the dimensions of the structure (one dimension for System A and two dimensions for System E) with high accuracy which finds possible uses in the design of scaffoldings for deployable structures, actuators, variable pored sieves, and sound proofing systems. Such systems can find utilisation in different industries such as the aerospace, biomedical, and robotics ones.

6.3 Magneto-mechanical metamaterial with iron nanoparticle inclusions

6.3.1 Introduction

As discussed above, magnetically actuated shape programmable systems find application in a number of industries as actuators and robotic systems amongst others. They offer several advantages over their traditional counterparts including accurate displacements, fine control and untethered manipulation of the structure (C. Ma *et al.*, 2022; Zou *et al.*, 2022). In the previous section, the concept of a magnetically actuated structure having magnetic inclusions was analysed and a number of were studied to investigate the possibility of scaling down the structure. However, the scaling down of such system is limited by the size of the smallest unit which are the neodymium magnetic inclusion.

In this part of the study, the use of a magneto-elastomer (henceforth referred to as ME), composed of 10 nm iron nanoparticles embedded in an elastomer, will be investigated *in lieu* of the neodymium permanent magnets. The response of these MEs to an external magnetic field will be investigated numerically and experimentally. Furthermore, the effect of the concentration of iron nanoparticles in relation to the response of the structure will be experimentally investigated. It should be noted that whilst in Appendix V attempts to synthesise iron nanoparticles were carried out, the iron nanoparticles used in this section were purchased.

6.3.2 Concept

The magneto-mechanical systems investigated up to this point had neodymium magnets having a diameter and height of 1 mm. As discussed above in order to investigate

the possibility of further miniaturisation of the proposed accordion and ‘egg-rack’ like systems, a composite made of spherical iron nanoparticles having a mean diameter of 10 nm, bound in a non-magnetic elastomer will be used. Iron nanoparticles were chosen as it has been reported in literature that they exhibit a superparamagnetic behaviour (H. Tang *et al.*, 2021). Superparamagnetism is the phenomenon that occurs in very small ferromagnetic nanoparticles where magnetisation can randomly flip due to temperature (Huber, 2005). In fact, it is known that as the size of the iron particles decreases, the Curie temperature decreases as well (Cao *et al.*, 2007). This implies that when no external magnetic field is present, and the particles are small enough, the particles have a randomly oriented magnetic dipole that result in no net magnetisation, however, when exposed to an external magnetic field, the magnetic dipoles align and become magnetic. Once the external magnetic field is removed, the magnetic dipoles flip randomly due to temperature and results in no net magnetisation. This implies that the particles have no magnetic memory, however, do retain a high magnetic susceptibility when compared to paramagnetic particles (Pamme, 2006).

In this part of the study, the whole accordion-like structure will be constructed from a composite made from spherical iron nanoparticles bound in a non-magnetic elastomer as depicted in Figure 6.19(a). When no external magnetic field is applied, the elastomer would have no net magnetisation, however when exposed to an external magnetic field, the dipoles of the iron nanoparticles are expected to align to the magnetic field generating forces along the structure. In theory, should the structure be perfectly in the centre between the two poles, the centre point would experience no net force since it is equidistant from the south and north pole and would experience the same force of attraction from both poles (see Figure 6.19b). On the other hand, the material off centre would experience a stronger force from the closest pole. Considering the magnetic force

is inversely proportion of the fourth power of the distance separating them, the material closest to the poles would experience the largest force of attraction (see Figure 6.19b). This is expected to result in the accordion-like structure folding in one direction.

It is important to note that in the previous structure, the permanent magnets inclusions aligned with the external magnetic field by exerted a torque around a pivot point. The direction of the torque was dependent on the direction of the external magnetic field and therefore the structure could contract, extend, or even flip. On the other hand, in this case, the nanoparticle inclusions in the magnetoelastomer do not have a magnetic field and do not have magnetic memory. This means that when exposed to an external magnetic field, the magnetic domains of the iron nanoparticles align with the magnetic field and a force of attraction is experienced that causes the structure to fold. Additionally, reversing the direction of the magnetic field will result in the same folding of the structure as the nanoparticles' domains flip. This is due to the fact that for iron nanoparticles of a sufficiently small size, the Curie temperature is equal to or below the room temperature.

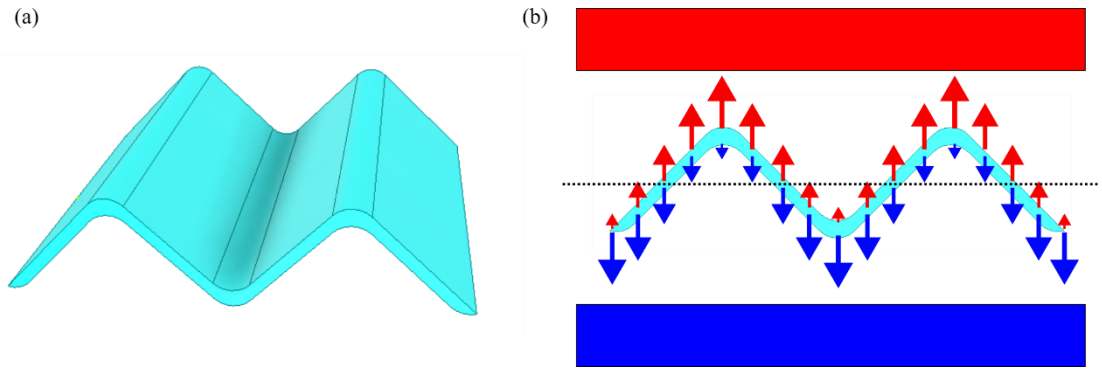

Figure 6.19 (a) A CAD generated design of the accordion-like structure. (b) the magnetic forces acting on the magneto elastomer when under an external magnetic field.

6.3.3 Geometrical Parameters

The accordion-like structure is defined by the following variables: the thickness of the arm, t, the length of the arm, L, the angle Φ, and radius, r_1, see Figure 6.20. Furthermore, a number of parameters were defined for the purpose of the investigation, t_{EFF}, the effective thickness (i.e., the thickness of the material perpendicular to the external magnetic field), and lengths L_x and L_y.

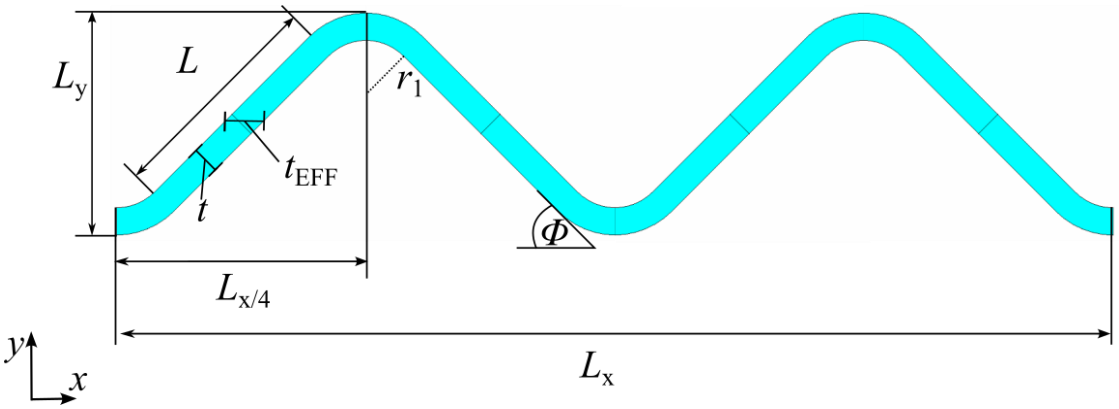

Figure 6.20. A depiction of the variables and parameters considered for the accordion-like structure.

6.3.4 Numerical Analysis

6.3.4.1 Introduction

The behaviour of the accordion-like system made up of this ME was first investigated numerically. Initially, the forces experienced by the ME when subjected to an external magnetic field will be quantified and assessed. The forces obtained will be used in FEA simulations to investigate the displacement of the accordion-like structure when the forces of attraction on the ME by the external magnetic field are applied. It is important to note, that as the structure deforms, the magnetic forces experienced by the

ME change significantly since parts of the structure would move closer to the magnetic poles. Therefore, after an FEA simulation, the forces would have to be recalculated and another simulation has to be performed using the new forces.

6.3.4.2 Methodology

The effect of the magnetic field on the magneto elastomer was analysed through FEMM and FEA simulations. Nine structures were considered, each having a length, L, of 8 mm and radius, r_1 of 2 mm, see Figure 6.20. For each structure, parameters t and Φ was varied as detailed in Table 6.2.

.

Table 6.2. The nine structures considered in this study.

Structure No.	***t* /mm**	***Φ* /°**	**t_{EFF} /mm**
1	0.5	30	1.00
2	0.5	45	0.71
3	0.5	60	0.58
4	1	30	2.00
5	1	45	1.41
6	1	60	1.15
7	1.5	30	3.00
8	1.5	45	2.12
9	1.5	60	1.73

6.3.4.2.1 Finite Element Method Magnetics (FEMM)

FEMM (an open-source finite element analysis software package for solving electromagnetic problems) was used to calculate the forces generated by an electromagnet on the ME. The simulated electromagnet consisted of a horseshoe metal core composed of 1010 Steel and a copper (22 AWG) coil having 1700 turns (see Figure 6.21). The

distance between the poles of the magnet was set to 21 mm. For simplicity, it was assumed that the ME had a constant thickness (t_{EFF}) throughout its length. The width of the accordion-like system was set to be equal to the width of the electromagnet i.e., 28 mm. The relative magnetic permeability of the ME was assigned a value of 1.34 based on the ME having 50%w/w (percentage by weight) of iron nanoparticles. The magnetic permeability of the ME was obtained using the well-known Maxwell-Garnett homogenising rule (Waki *et al.*, 2005). In the case of this study, it was assumed that the elastomer used had a relative magnetic permeability of 1, whilst the iron nanoparticles (99% purity) had a relative magnetic permeability of 1000 (Waki *et al.*, 2005). It is important to note that iron nanoparticles could have a higher relative magnetic permeability since 10 nm iron nanoparticles used are known to have a single domain (T. I. Yang *et al.*, 2011b).

The total force experienced by different regions of the ME located at different positions between the poles of the electromagnet was determined when acted upon by an external magnetic field generated by passing a current of 1 A through the electromagnet. The forces in different sections of the ME were obtained for the nine structures considered. Taking Structure 5 (see Table 6.2) as an example, the total force acting on sections of ME having dimensions of $0.5 \times 1.414 \times 28$ mm when positioned at different locations between the poles of electromagnet were simulated. The zero distance was set to be at the midpoint between the two poles of the electromagnet. From these measurements, a relation between the force and distance was determined. To confirm that the force distance relationship obtained was not an artifact of the size of the section being measured, for this particular system, the force-distance relationship was also measured for sections of ME having dimensions of $0.25 \times 1.414 \times 28$ mm.

Prior to the investigation two mesh independent study were carried out taking two distances from the centre; 3.75 mm and 9.75 mm to ensure that the mesh was suitable for the entire length. Ten mesh sizes were applied ranging from 0.01 to 0.1 mm in increments of 0.01 mm. The force exerted was then acquired and compared to the finest mesh level.

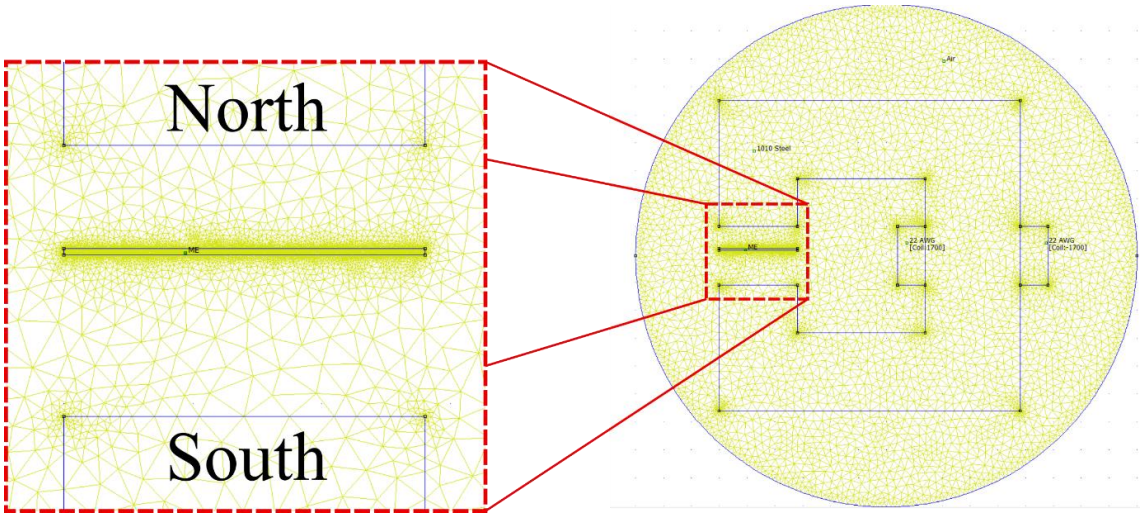

Figure 6.21. A depiction of the setup design in the FEMM. The inset depicts the 20 segments taken into consideration and depicts their position with respect to the magnetic poles.

6.3.4.2.2 Finite Element Analysis simulation

Following the FEMM simulations, the deformation of the structure in response to an external magnetic field was simulated through FEA. The accordion-like structure was designed and was meshed as described in section 6.2.2.2.1. The element type for the simulations was set to PLANE183 using plane stress and boundary conditions were used to simulate one quarter of the structure as a representation of the whole structure, as shown in Figure 6.22, in order to use the computational power more efficiently. To this end, the nodes having the minimum x values were coupled to move together in the x direction and similarly the nodes having the maximum x values were coupled to move

together in the *x* direction (depicted in green in Figure 6.22). The central node, depicted as a black dot in Figure 6.22, was fixed in the *x* and *y* direction.

Following this, the forces acquired through FEMM were applied along the structure. A 6^{th} order polynomial was fitted to the data obtained from FEMM in order to obtain a relation between the force experienced by the ME and the distance from the centre between the electromagnet poles. The accordion-like structure was divided into 40 equal regions. The total force experienced by each region due to the external magnetic field was calculated from the integral of the polynomial fit described above. The total force on the region was then divided equally onto the nodes making up the region and a non-linear geometrical simulation was carried out using a linear elastic material model having a Young's modulus of 202.50 KPa and a Poisson's ratio of 0.49. It is important to note that as the structure deformed, the distance of the nodes from the centre changes. Since the magnetic forces change significantly with distance, the magnetic forces had to be recalculated and subsequent simulations were carried out on the deformed structure. This was repeated until the displacement of the structure was within less than 0.5% of the previous simulation. Furthermore, the deformation caused the structure to bend and therefore after every simulation the variable t_{EFF} was recalculated and the forces acting on the regions were adjusted accordingly to accurately simulate the deformation of the structure. The procedure was then carried out for all nine structures described in Table 6.2.

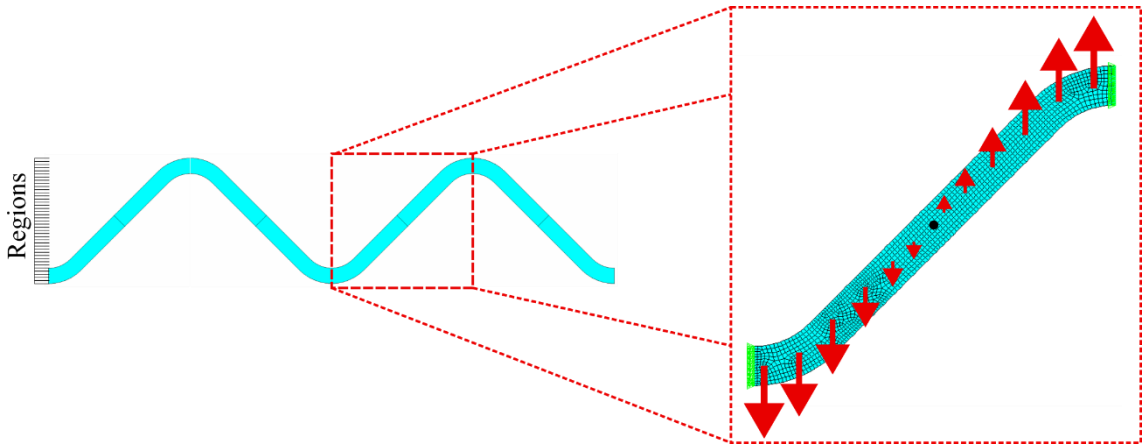

Figure 6.22. Depicts the simulated section of the structure. The inset shows the boundary conditions (green), the fixed point (black) and the forces applied to the nodes (red arrows). The lines on the left depict the 40 regions into which the accordion-like structure was divided to apply the forces as calculated by the FEMM simulations.

6.3.4.3 Results and Discussion

The simulations showed that the structure contracts in the *x* direction in response to an external magnetic field and thus a magneto-elastomer can be used instead of magnetic inclusions, something which as discussed above, would be advantageous for miniaturisation of the structure. As highlighted in the methodology above, a mesh independent study for the FEMM was first carried out. The results obtained revealed that a mesh size of 0.3 mm was within 0.5% of the finest mesh size (0.01 mm) used for both segments considered. In a typical simulation (see Figure 6.23(c)), a segment is suspended between the poles and the force experienced by the segment is acquired. From preliminary simulations, it was found that subdividing the distance between the poles of the electromagnet into segments of 0.5 mm, was enough to accurately calculate the forces at different distances from the centre of the structure. This was confirmed by measuring the forces using segments of 0.25 mm from which the same relationship between the magnetic force and the distance from the centre between the poles of the electromagnet was obtained as shown in Figure 6.23(d).

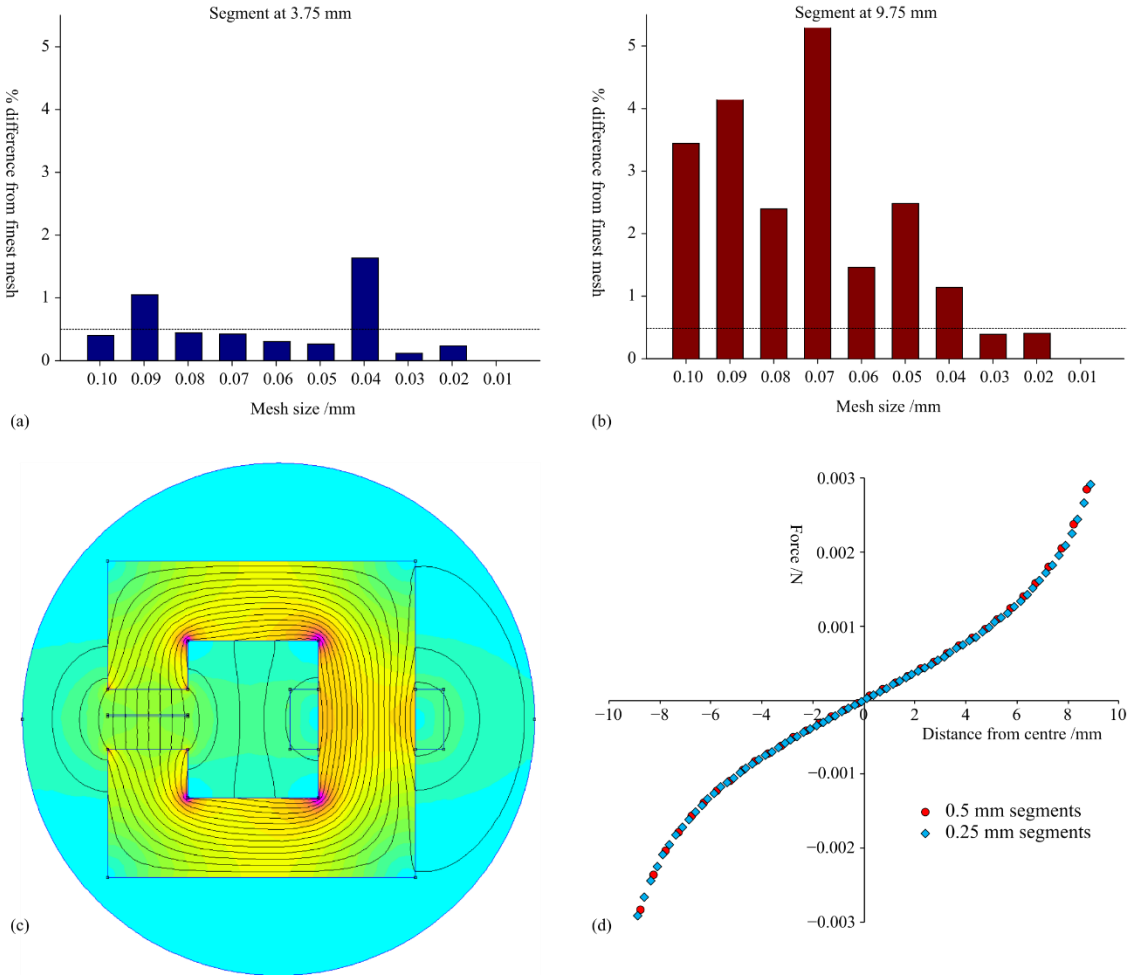

Figure 6.23(a-b) Mesh independent studies carried out at to distances from the centre point (c) Depicts the results of the simulation carried out on one segment. (d) A plot showing the relation between the force exerted on Structure 5 (see Table 6.2) at different distances from the centre of the structure using segments of 0.25 and 0.5 mm.

Finite element analysis was then carried out on the nine structures described in the methodology (see Table 6.2) to investigate the effect of two geometrical parameters, *t* and *Φ*, on the behaviour of the structure to an external magnetic field. The forces obtained through FEMM simulations were applied to the ME as described in the

methodology above. As discussed previously, subsequent simulations had to be carried out on the deformed structure until the displacement of the structure was within less than 0.5% of the previous simulation. This is exemplified in Figure 6.24 which shows the % change in displacement between two consecutive simulations steps observed on Structure 5. One notes that there is a large change initially and thus the magnetic force increases accordingly. With subsequent steps the changes become smaller as the structure approaches the equilibrium position. In this case, eleven steps had to be carried out until the structure's displacement remained within 0.5% of the previous simulation.

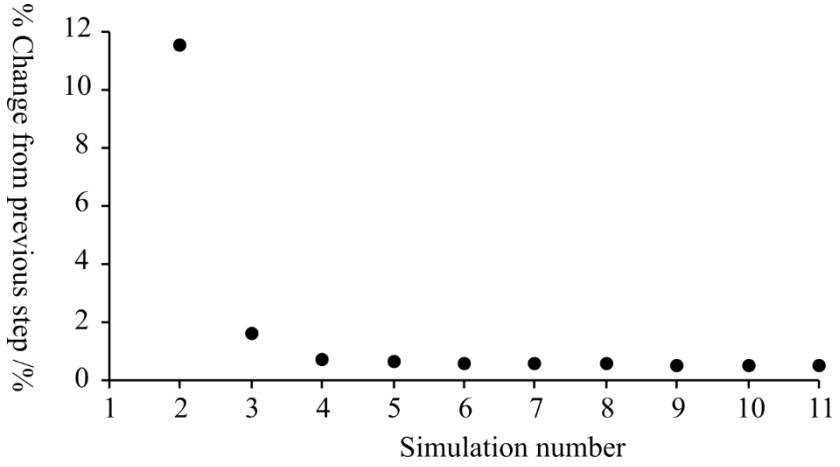

Figure 6.24. A graph depicting the % change from previous step after each subsequent simulation.

An analysis of the effect of the thickness of the structure on its contraction revealed that upon increasing the thickness of the structure a larger % change in $L_{x/4}$ is observed (see Figure 6.25). In fact, for Φ = 45°, a % change of 55.13%, 39.05% and 26.19% in the x direction was recorded for Structures 2, 5 and 8 respectively (having t = 0.5, 1.0 and 1.5 mm respectively). Taking the total upward force on the top half of the structure (since taking the net force on the whole structure would be zero) it was shown that while the force increased significantly with an increase in t, from 0.92 mN in

Structure 2 to 1.99 mN in Structure 5 and 3.27 mN in Structure 8, a thinner structure still exhibited the largest deformation. This is due to the fact that a thicker structure requires the deformation of more material at the hinges and thus offers more resistance to deformation. This trend is reflected for structures having Φ of 30° and 60°. Future work could investigate a structure having variable thickness, where thinner hinges would be used, whilst having thick arms, thus benefitting from the increased magnetic forces and the lower resistance to deformation.

Parameter Φ was also shown to have a significant role in the % change in $L_{x/4}$. In fact, when considering Structures 1, 2 and 3 (structures having t = 0.5 mm and Φ having a value of 30°, 45° and 60° respectively), the % change in $L_{x/4}$ recorded was 80.64%, 55.13% and 44.37%. This seems counterintuitive as one would expect that as Φ increases the structures peripheries would be closer to the magnetic poles and thus the structure would experience a higher total force. However, as the Φ value increases, the variable t_{EFF} decreases significantly and therefore the magnitude of the magnetic force acting on the regions is decreased. In fact, the total upward force experienced by the top half of Structures 1, 2 and 3 was of 1.08 mN, 0.92 mN and 0.86 mN respectively (for a t_{EFF} of 1, 0.71 and 0.58 mm respectively). It is interesting to note that for Structures 4, 5 and 6, having t = 1.0 mm, the same trend is observed albeit to a smaller extent with a % change in $L_{x/4}$ of 48.25%, 39.05% and 34.84% was recorded. Furthermore, for the thicker structures, Structures 7, 8 and 9 having t = 1.5 mm, different Φ values yielded similar % change in the x direction exhibiting a change of 28.01%, 26.2% and 26.96% respectively. In contrast to the previously mentioned trend, Structure 8 having Φ = 45° exhibits the lowest contraction whilst Structure 9 having Φ = 60° is slightly higher. This clearly outlines the two competing factors determining the total force experienced by the structure: (1) the variable t_{EFF} and (2) the distance from magnetic poles. As the value of

Φ increases from 30° to 45° to 60°, for t = 1.5 mm, the variable t_{EFF} decreases from 3 to 2.12 to 1.73 mm respectively. On the other hand, the structure's extremities become closer to the magnetic poles which results in larger forces per unit thickness. This can be noted from the total upward force experienced by the top half of the structure i.e., 3.36 mN, 3.27 mN and 3.32 mN for Structures 7, 8 and 9 respectively.

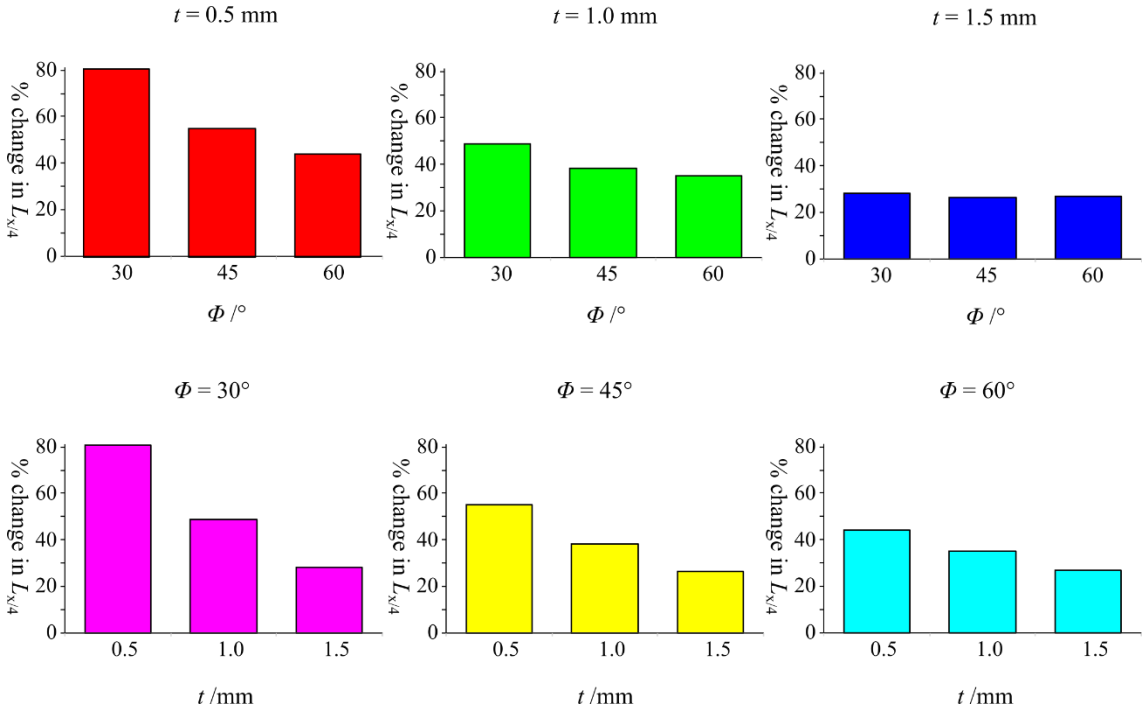

Figure 6.25. Graphs depicting % change in length for the nine structures investigated.

Therefore, when producing such MEs, one must consider that for thinner sheets, a lower value of Φ yields a higher contraction, however, thicker sheets could have a higher contraction when the value of Φ is higher. Future studies would be required to fully investigate the relationship between Φ and t in order to achieve the optimal combination for specific applications.

6.3.4.4 Conclusion

In this section the relation between the force experienced by the segments and their distance from the centre of the structure was obtained through FEMM. Furthermore, through the FEA simulations, the effect of parameters, t and Φ, on the behaviour of the structure to an external magnetic field was investigated. It was concluded that a thinner structure would exhibit a larger deformation and that parameter Φ had two opposing effects where on one hand, an increase in Φ closed the gap between the structure and the magnetic poles whilst on the other hand decreased the effective thickness of the structure thus experiencing less magnetic force.

6.3.5 Experimental Investigation

6.3.5.1 Introduction

In the simulations above, the concept of using a ME having 50%w/w of iron nanoparticles was investigated and it was shown that an external magnetic field was able to elicit a contraction in the material. In this section, experimental prototypes will be investigated and the effect of magnetic field strength and nanoparticle concentration in the ME on the contraction will be analysed using five structures with different concentrations of nanoparticles.

6.3.5.2 Methodology

Four MEs were synthesised having 20, 30, 40 and 50%w/w of iron nanoparticles and labelled as ME20, ME30, ME40 and ME50 respectively. The MEs were produced using spherical zero-valent iron nanoparticles (99% pure) having an average particle size

of 10 nm which were passivated with 3% oleic acid (Nanoshell). The iron nanoparticles were then bound in a silicone rubber matrix by using a two-part casting liquid silicone rubber. In a typical experiment, the iron nanoparticles were mixed thoroughly with the first component of the rubber. The second component was then added and mixed for 5 minutes after which the mixture was injected into a mould of the accordion-like structure (see Figure 6.26). The material solidified over 30 minutes after which the ME was extracted from the mould.

Figure 6.26.(top & bottom) CAD of the moulds used, and (middle) the ME structure produced.

The deformation of the MEs produced in response to an external magnetic field was then experimentally tested. As in the case of the simulations discussed above, a horseshoe magnet made of 1010 Steel was used which was wound by a copper (22 AWG) coil having 1700 turns, see Figure 6.27. The copper coils were then connected to a power

supply having a variable current. In a typical experiment a plastic case was placed on the bottom magnet and lubricated with WD40. The ME was then placed on the lubricated surface and oriented in the middle of the magnet's poles (see Figure 6.27). The extension/contraction of the ME was then recorded when exposed to an external magnetic field generated by a range of 0.2 and 2.0 A.

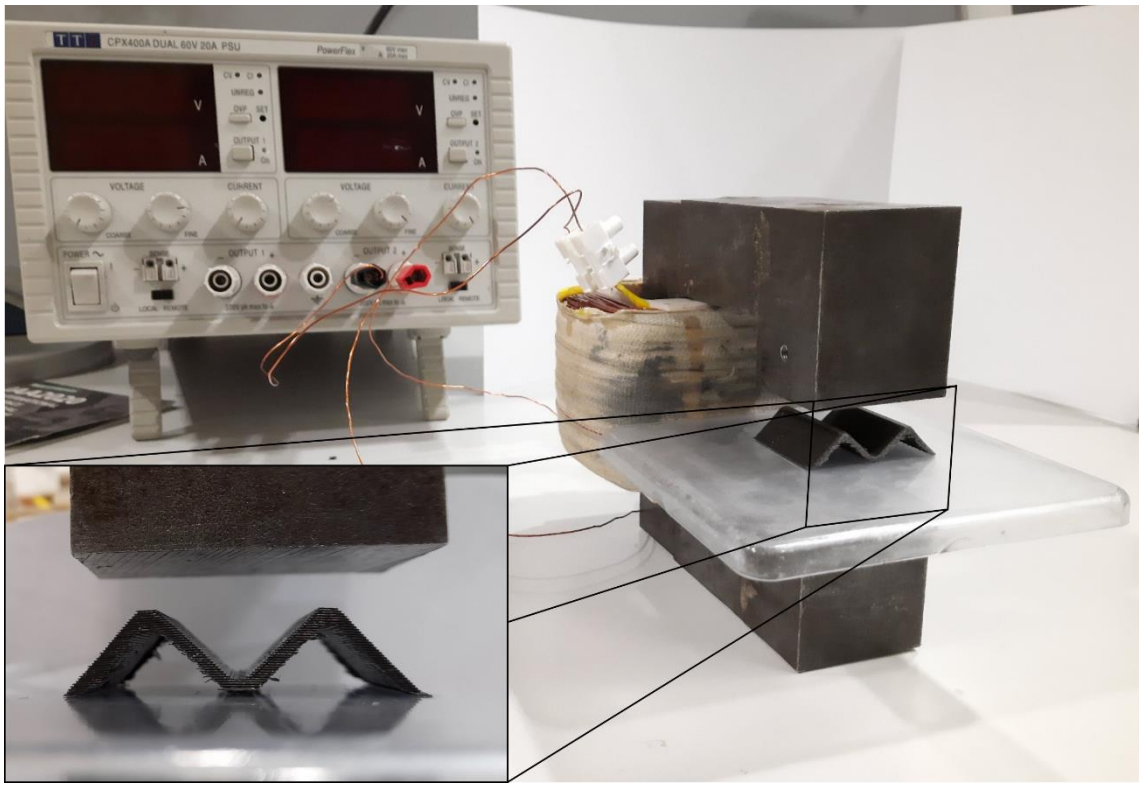

Figure 6.27. A depiction of the experimental setup. The inset shows the structure as recorded by the camera for the analysis.

6.3.5.3 Results and Discussion

In this section, experimental studies will be used to confirm the numerical simulations in Section 6.3.4.3 and later will be used to investigate the effect of iron nanoparticles concentration on the contraction of the structure due to an external magnetic

field. The experimental prototypes investigated in this section were based on the geometry of Structure 5 (see Table 6.2). The comparison between the numerical simulations and experimental tests was carried out on structures ME40 and ME50. In order to carry out this comparison, two additional sets of numerical simulations were performed following the methodology outlined in Section 6.2.2.2 to simulate structures ME40 and ME50 (having a magnetic permeability of 1.20 and 1.30, respectively). For each set of simulations, five different currents were used: 0.2, 0.6, 1.0, 1.6 and 2.0 A, in order to compare the contraction to the experimental prototypes. In Figure 6.28, the contraction of the experimental prototypes ME40 and ME50 are shown in relation to their numerical counterparts. In general, a good agreement was obtained between the experimental and numerical results, in particular for the ME50 system. One notes that the numerical simulations reflect the trend observed in the experimental data where the structure's contraction increase with current until a certain point (around 1.5 A) where the rate in increase of contraction decreases. Furthermore, it is shown that Structure ME50 has less of a discrepancy with the numerical data than Structure ME40. This can be attributed to the fact that ME50 experiences a larger force due to the larger magnetic permeability which allows it to overcome any friction and other experimental limitations as discussed below.

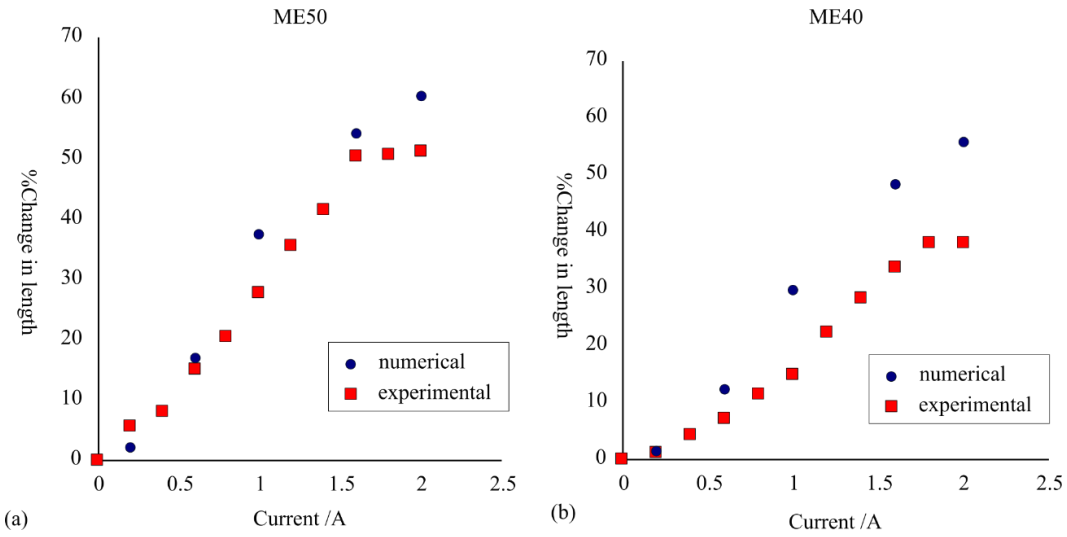

Figure 6.28. Graphs depicting the % change in length at varying currents obtained from the experimental and numerical studies.

The discrepancy between the experimental and numerical results may be attributed to gravity and friction, which were not considered in the numerical simulations. Furthermore, in the numerical simulations the structure was suspended in the centre between the electromagnet's poles. This was not the case in the experiment as the structure was resting on a plate placed on the lower magnetic pole. Therefore, the structure experiences larger downward forces, increasing the friction with the plate. The structure experienced smaller upward forces since the experimental prototype was farther away from the magnetic pole above it. Other factors that may have attributed to the discrepancy in the results include the values of the magnetic permeability used in the simulations as this was an estimation and was not experimentally measured. Additionally, the calculations of the forces were based on the assumption that the structure had a constant thickness. This was not true at the hinges due to the curved shape of the structure which may have led to some inaccuracies. Furthermore, some errors can

be attributed to the FDM 3D printed mould having striations and the alignment of the top and bottom mould which may have produced slightly uneven ME thickness.

Following the validation of the numerical methodology with experimental data, it is interesting to explore the effect of iron nanoparticles concentration on the contraction of the structure in response to an external magnetic field. To this end, five prototypes were analysed experimentally to acquire the % change in L_x and the change in angles θ_1, θ_2 and θ_3 in response to varying magnetic fields. In Figure 6.29, it is shown that, as expected, ME50 exhibited the largest contraction followed by ME40, ME30 and ME20. In fact, for an external magnetic field generated by a current of 2 A, a contraction of 51.1%, 37.9%, 28.6% and 11.3% was recorded for ME50, ME40, ME30 and ME20, respectively. This can be explained by the increase in magnetic inclusions which results in an increase of the relative magnetic permeability of the material and hence results in larger forces which pull the structures toward the closest pole. Using the Maxwell-Garnett homogenising rule (Waki *et al.*, 2005) one finds the relative magnetic permeability is 1.30, 1.20, 1.12 and 1.05 for ME50, ME40, ME30 and ME20 respectively.

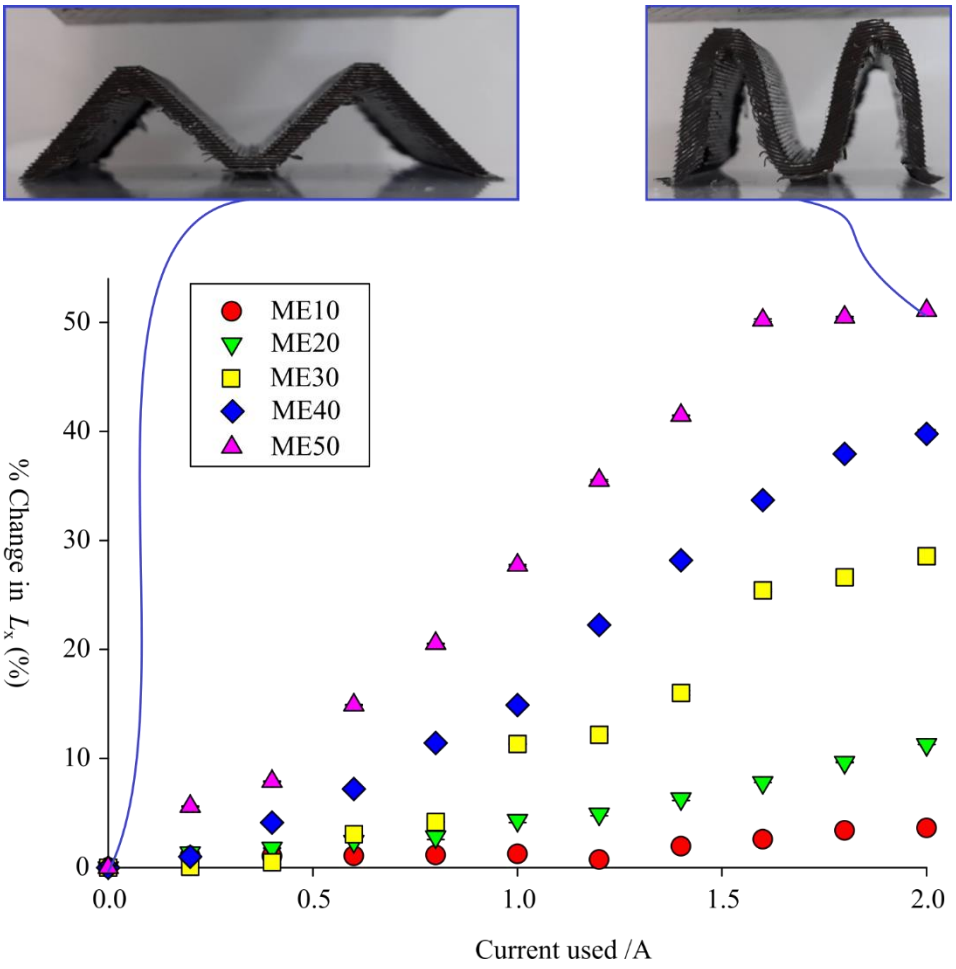

Figure 6.29. Graph of the % change in L_x corresponding to an increase in the external magnetic field.

This trend was confirmed by the change in angles θ_1, θ_2 and θ_3 (see Figure 6.30). When exposed to an external magnetic field generated by 2 A, structure ME50 showed a change of 49.1°, 47.6° and 52.5° in θ_1, θ_2 and θ_3, respectively. On the other hand, for the same external magnetic field, structure ME10 showed a change of 5.4°, 6.1° and 6.6° in θ_1, θ_2 and θ_3 respectively.

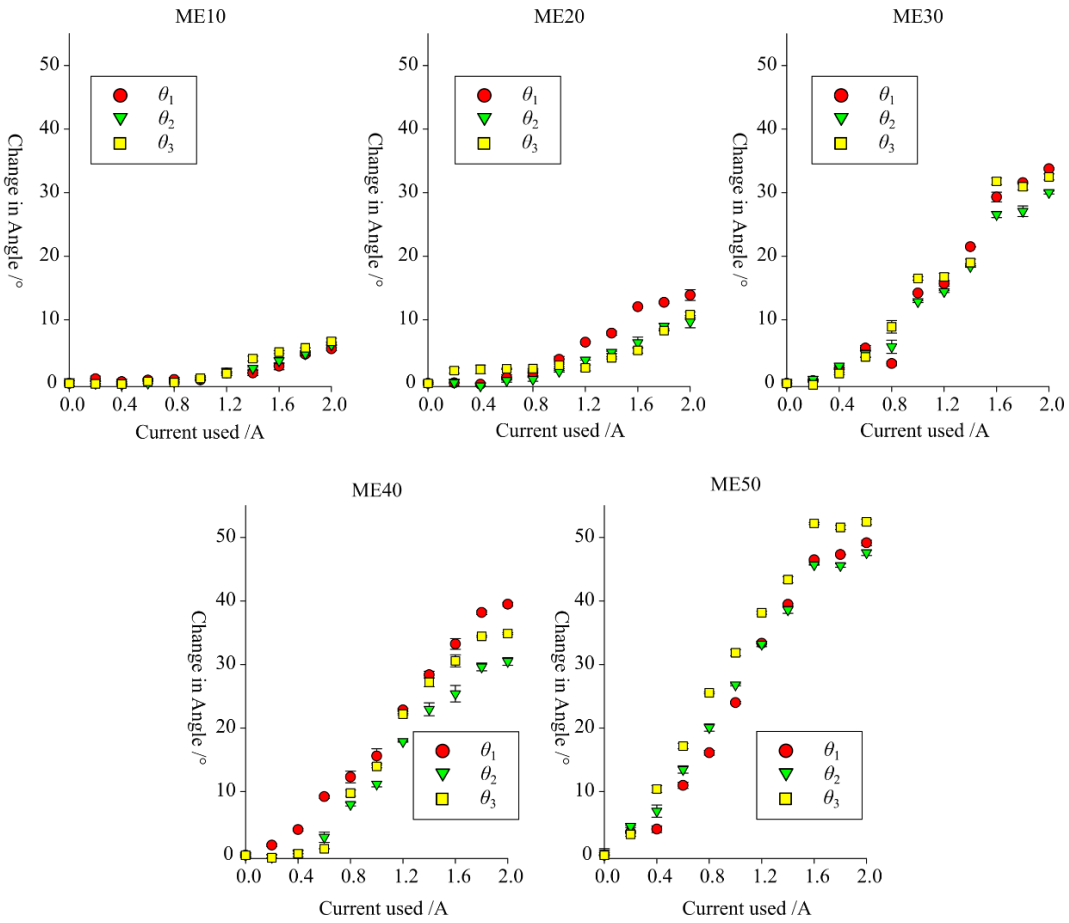

Figure 6.30. Depicts the change in angles θ_1, θ_2 and θ_3 with increasing magnetic field for structures M10, M20, M30, M40 and ME50.

6.3.5.4 Conclusion

In this section, the iron-nanoparticle inclusion based ME prototypes were produced, and experimental studies were conducted to validate the numerical simulations discussed in Section 6.3.4. It was concluded that the numerical and experimental data had good agreement. Furthermore, four structures were investigated to understand the effect of iron nanoparticle concentration on the contraction of the structure in response to an external magnetic field. It was shown that an increase in iron nanoparticle concentration resulted in a larger contraction in the *x* direction and in fact structure ME50, having 50%w/w iron nanoparticle concentration, exhibited the largest contraction of more than 50% in the *x* direction.

6.3.6 Conclusion

In the work above the viability of iron nanoparticles in a silicone rubber as magnetic inclusions instead of permanent magnets was studied. It was numerically and experimentally shown that the ME responded to an external magnetic field by contracting in one direction. Furthermore, the effect of nanoparticle concentration was investigated concluding that a higher nanoparticle concentration resulted in a larger contraction.

6.4 Conclusion

In this chapter the accordion-like magneto-mechanical structure design was improved using bendable connecting arms and extended to the egg-rack-like magneto-mechanical metamaterial. The foldable structures, Structure A and E, were investigated experimentally and their response to an external magnetic field was recorded. It was shown that the contraction of both systems can be finely controlled through the external magnetic field with a high degree of turnability and control.

A novel magneto-mechanical design was also proposed composed of iron nanoparticles *in lieu* of the permanent magnetic inclusions. The iron nanoparticles were fixed in a silicone elastomer during the moulding process resulting in a magnetoelastomer. Four MEs were synthesised having different iron nanoparticle concentration and their response to an external magnetic field was investigated. This showed that the structures contracted in response to an external magnetic field with ME50 recording a contraction of more than 50%. The concept of a nanoparticle inclusion-based magneto-mechanical metamaterial opens up the possibility of scaling down the structure to be included in micro- and possibly nano-sized devices as the structure is no longer restricted by the 1 mm neodymium magnetic inclusions.

Chapter 7 : General Discussion, Conclusions and Future Perspective

Significant strides in technology have stimulated the quest for novel materials having properties which can be applied in numerous high-tech applications. As discussed in the literature review, recent decades have witnessed extensive research into mechanical metamaterials, i.e. materials that are characterised by counterintuitive mechanical traits like negative stiffness (Carrella *et al.*, 2008; K. K. Dudek, Gatt, *et al.*, 2018; Jaglinski & Lakes, 2007), negative compressibility (Errandonea *et al.*, 2010; Grima-Cornish *et al.*, 2021; Lim, 2019), and negative Poisson's ratio, (commonly known as auxetic materials)(Z. Chen *et al.*, 2020; Gambin *et al.*, 2023; H.-H. Huang *et al.*, 2016). As discussed in Chapter 2, a plethora of mechanical metamaterials have been designed and investigated for their properties, for example, auxetic metamaterials have been shown to exhibit superior impact and indentation resistance (Duncan *et al.*, 2018; R. S. Lakes & Elms, 1993; Shah, Khan, Saeid, *et al.*, 2022) as well as synclastic behaviour (A. Alderson, Alderson, Chirima, *et al.*, 2010; Moroney *et al.*, 2018; Peliński & Smardzewski, 2022). Due to their superior properties, a number of metamaterials have already found their way to the market in niche products such as protective gear (Nallavan, 2020; Newton-Mann *et al.*, 2018) and biomedical devices (A. Alderson *et al.*, 2001; M. N. Ali *et al.*, 2014b; Y. Kim *et al.*, 2021). With the advent of additive manufacturing (mainly 3D printing) research involving 3D mechanical metamaterials, particularly 3D auxetic metamaterials (systems which exhibit auxetic behaviour in more than one direction), has intensified. This heightened interest in 3D auxetic metamaterials comes from the fact the 3D auxetic

metamaterials may be used in applications such as textiles (Grimmelsmann *et al.*, 2016; Krödel *et al.*, 2014; P. Ma *et al.*, 2017; Zeng *et al.*, 2017), protective equipment (Faraci *et al.*, 2021; Teng *et al.*, 2022; C. Yang *et al.*, 2018), biomedical (Y. Kim *et al.*, 2021; Shukla & Behera, 2022; W. Wu *et al.*, 2019)and electronic devices as sensors and actuators (X. Ren, Das, *et al.*, 2018; Yuan *et al.*, 2017).

Active materials have also been at the forefront of materials research as discussed in Section 2.3.1. The ability to tune the geometry and mechanical properties of these materials post fabrication has placed active materials in high demand for several applications (Lum *et al.*, 2016; Mu *et al.*, 2015; Ze *et al.*, 2020). Additionally, several studies have designed active auxetic metamaterials with the ability to tune their geometry and mechanical properties through external stimuli, thus benefitting from the unique properties attributed to auxetic materials and the tunability of active materials. Of the wide range of active materials, the magnetically actuated metamaterials have stood out for their versatility. Their response to a magnetic field is not limited to simply the presence and absence of the stimuli but also the magnitude and direction of the magnetic field. In fact, over the past decade, a number of studies have proposed magnetically actuated active metamaterials ranging from magneto-elastic lattices and magneto-mechanical foams (Fang *et al.*, 2019; Raghunath & Flatau, 2015; X. Tan *et al.*, 2019) to reconfigurable magneto-mechanical metamaterials (Jackson *et al.*, 2018; Lum *et al.*, 2016; Montgomery *et al.*, 2020; Z. Ren *et al.*, 2019; K. Singh *et al.*, 2013).

Given the potentials in the fields of 3D auxetic metamaterial and active auxetic metamaterials, this thesis aimed: (1) to propose 3D auxetic systems having continuous voids of constant cross-sectional area and investigate them *vis-à-vis* their Poisson's ratio and (2) to develop a scalable inclusion-based magneto-mechanical metamaterial. As explained in Chapter 2, the thesis was divided into two main parts, each part focusing on

each of these aims. In fact, Chapters 3 and 4 investigated the possibility of having 3D auxetic systems with continuous voids of constant cross-sectional area whilst chapters 5 and 6 focused on active auxetic metamaterials and their miniaturisation. As discussed later in this chapter, the auxetic systems proposed in Chapters 3 and 4 of this thesis were designed in such a way that in the future they may be used as the auxetic matrix for active auxetic metamaterials.

The search for a simple method to produce 3D auxetic structures inadvertently led to the development of a novel design method that can be used to manufacture a plethora of 3D auxetic metamaterial. The method that was developed in this thesis to produce 3D auxetic system was inspired from the methods used to produce perforated 2D sheets. When producing perforated sheets, slits and/or perforations are introduced on mundane materials transforming them into 2D auxetic systems. In this thesis, this method was extended to 3D systems by strategically introducing continuous voids of constant cross-sectional area in different planes of a block of material. The resultant structures were investigated numerically and experimentally and were shown to exhibit an NPR in multiple directions. Since the structures produced have continuous voids of constant cross-sectional area, these systems can be produced through various methods, including additive manufacturing (3D printing), subtractive manufacturing (such as milling) and moulding.

The simplest system considered in Chapter 3 was constructed by introducing equally sized voids having diamond shaped cross-sectional area in the three major planes of a cubic block of material. This resulted in a system that may be described as polygons connected together from six vertices. It was shown that the structures (the regular 3D perforated systems) exhibited a nearly constant Poisson's ratio of −0.5 in the *xy*, *yz*, and *zx* planes, for a large degree of θ values (up to 60°). This suggests that these systems can

be designed in such a way that they exhibit a constant Poisson's ratio when deforming. In fact, non-linear simulations revealed that these systems exhibited a strain independent NPR for the maximum compressive strain used in this study (7%). Interestingly, similar systems proposed by Attard and co-workers (J. N. Grima, Caruana-Gauci, *et al.*, 2012b) and Kim et. al (J. Kim *et al.*, 2017), the 3D rotating cubes, do not share this property and their Poisson's ratio changes as the angles between the connected cubes change. It was also shown that for the regular 3D perforated systems having $\theta = 90°$, the system exhibited a Poisson's ratio of 0 (when the distance between the voids, parameter *s*, had a small value), something which may have applications of its own.

The regular 3D perforated system having diamond-shaped voids was also extended to other/more general systems. In Chapter 3, structures having voids with a diamond shaped cross-sectional area of different sizes were explored. The asymmetry in the size of the voids having a diamond cross-sectional area led to a plethora of structures exhibiting a range of anisotropic Poisson's ratios and Young's moduli. This means that a catalogue could be obtained where 3D auxetics could be produced depending on the mechanical properties required.

Additionally, it was shown that the 3D perforated systems are not limited to diamond-shaped voids and in Chapter 4, voids having elliptical and stadia-shaped cross-sectional areas were used to create 3D auxetic metamaterial. Whilst the new structures were not space-filling auxetic structures, numerical simulations showed that the structures were able to distribute stresses better throughout the structure while exhibiting a larger negative Poisson's ratio, particularly at higher values of θ and when the voids were placed at larger distances from each other (larger *s* parameter). Experimental prototypes of these systems were shown to be strain independent up to at least 10 % strain. Furthermore, for small values of *s* and when θ was smaller than 70°, the Poisson's ratio of these systems

was also shown to be circa −0.5 as in the case when the voids had a diamond shaped cross-sectional area. However, there were substantial differences in the Young's moduli and volume fractions which indicate that systems having similar Poisson's ratio but different Young's moduli and / or volume fractions can be produced. An advantage of this new design method is that a number of manufacturing techniques can be used for the production of such 3D auxetic systems. For example, such systems can be manufactured using additive, subtractive and casting methods. This presents a significant advancement as currently most 3D auxetic systems can only be produced through the use of additive manufacturing techniques or through assembly. Therefore, having an auxetic system with such versatility and ease of production could promote industrial manufacturing for the low-cost production of 3D auxetic systems.

These 3D auxetic systems having voids of constant cross-sectional area would be ideal for numerous applications. For instance auxetic systems are known to exhibit superior energy absorption performance (S. Hou *et al.*, 2015; Imbalzano *et al.*, 2016; L. Jiang & Hu, 2017) and impact resistance (K. K. Dudek *et al.*, 2019a). Having 3D auxetic materials would offer the advantage that these properties would manifest from multiple directions. Therefore, these 3D auxetic systems would be particularly suitable for applications where impacts and indentation can occur from multiple directions. It is also worth discussing the wide array of anisotropic designs presented in Chapter 3 of this thesis. The plethora of structures yield a large number of anisotropic Poisson's ratio and therefore, through the design of the voids used, one may produce a system which amplifies the strain in one of the orthogonal directions. This could be taken advantage of in various technological areas, such as in the production of directional strain sensors. Another area where such anisotropy could be utilised is in the production of prosthetics. For example, it is known that tendons have a highly anisotropic Poisson's ratio, with a

negative Poisson's ratio in one plane (Gatt, Vella Wood, *et al.*, 2015) and a large positive Poisson's ratio in the orthogonal plane. Thus, the mechanical properties of the proposed perforated systems may be fine-tuned to produce prosthetics that mimic the behaviour of real tendons.

In the second part of this thesis, the potential of a number of systems to act as active metamaterials was explored. In Chapter 5, an accordion-like unit was developed, using a non-magnetic matrix embedded with permanent magnets. In this chapter, the non-magnetic matrix of the accordion like unit was assembled using copper wire to resemble a hinging system. In itself the unit was not auxetic, however, as shown in this chapter, the accordion-like unit can serve as a building block for more complex active metamaterials, including auxetic structures. In the presence of an external magnetic field, the accordion-like unit deformed, with the magnitude and the direction of deformation (contraction or extension) depending on the magnitude and direction of the external magnetic field. The deformation of these systems was attributed to a torque generated by the magnetic inclusions when an external magnetic field was present. In the second part of Chapter 5, the basic accordion-like unit was used to design multi-layer structures modelled on established structures in literature which are known to exhibit positive, zero and negative Poisson's ratio. Two of the proposed designs were produced experimentally with the first one being a semi-re-entrant system which is known for exhibiting a zero Poisson's ratio (structure SR). It was shown that the structure's extent of folding can be controlled by an external magnetic field. A change in the direction of the magnetic field resulted in an inversion of the structure. In this case, the inverted structure still retained its semi-re-entrant configuration (which is known to exhibit a zero Poisson's ratio). The second structure that was investigated was based on a hexagonal honeycomb system (structure H), which is known to exhibit a positive Poisson's ratio when deforming through hinging.

In this case, the amount of deformation was also controlled by the strength of the external magnetic field. However, when the direction of the external magnetic field acting on the structure was reversed, structure H, reconfigured to a re-entrant honeycomb, a configuration which is known to exhibit a negative Poisson's ratio when deforming through hinging. The ability to not only control the geometry of the structure but to also change the configuration of the system has significant application which will be discussed below.

In the first part of Chapter 6, the concept of the accordion-like unit was further explored by designing a non-magnetic matrix which does not require assembly, i.e., a non-magnetic matrix that is produced as one part. This was done by employing bendable joints. It was found that the overall stability of system and ease of manufacture of the system was increased when using such designs. A preliminary study to choose a good design for the 'bendable joints' was also conducted. Using the same concept, an egg-rack-like structure (structure E), which is known to exhibit an NPR, was designed, and tested. The investigations showed that these systems can deform in two planes in response to an external magnetic field. Systems based on the egg-rack-like structure discussed above could also be used to create 3D auxetic structures. For example, Figure 7.1 depicts a 3D re-entrant honeycomb configuration which is expected to exhibit an NPR in multiple planes. The degree of openness of such system (and hence the Poisson's ratio) could be controlled by the magnitude and direction of the magnetic field. In fact, it would be expected that a reversal of the magnetic field would result in a conventional 3D honeycomb configuration, which would be expected to exhibit a positive Poisson's ratio.

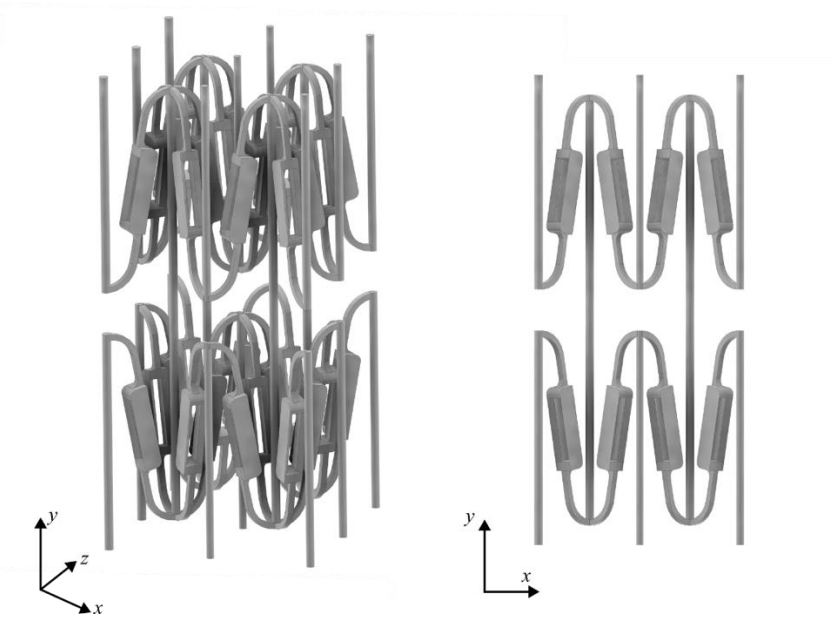

Figure 7.1. A CAD of the proposed 3D auxetic re-entrant honeycomb structure.

Having successfully designed and tested the concept of a magnetomechanical metamaterial, the next step was to use iron nanoparticles *in lieu* of the permanent magnetic inclusions. This would further contribute to the possible miniaturisation of these systems. In section 6.3, a novel magneto-mechanical material composed of iron nanoparticles embedded in an elastic matrix was proposed. In this case, the magnetic field of the inclusions would align with the external magnetic field and thus, deformation of the system would occur due to an attraction between the poles of the external magnetic field and the embedded nanoparticles. It was experimentally and numerically shown that the structure contracted when a constant external magnetic field was applied. This research serves to prove the concept of using iron nanoparticle inclusions to produce an active material. This concept lays the groundwork for further research on active metamaterials having iron nanoparticle inclusions. Firstly, the concept can easily be extended to egg-rack-like structure by having a sheet with protrusions as shown in Figure 7.2. The structure could be produced through injection moulding (see Figure 7.2) however

further research is required to investigate any restriction in movement and perhaps whether slits that may allow for smoother movement should be introduced.

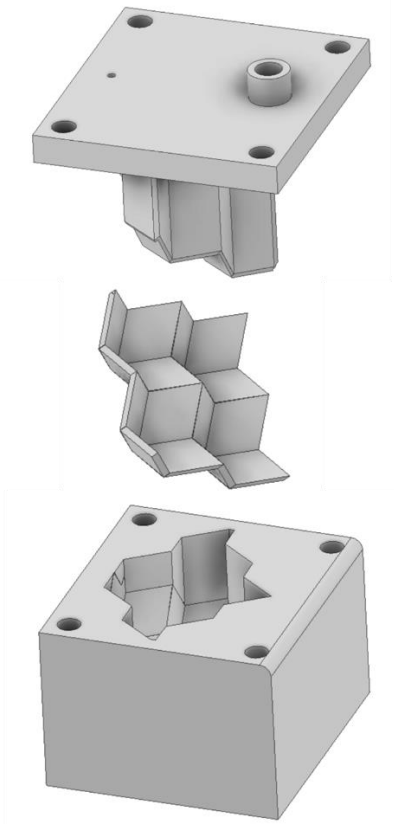

Figure 7.2. Designs for the top and bottom mould and a depiction of the resulting egg-rack-like structure.

Iron nanoparticles could also be embedded in the 3D auxetics designed in chapters 3 and 4. For example, considering the mould proposed in Section 3.5, a two-part silicone rubber could be used whereby, iron particles would be suspended evenly in the liquid rubber. The mixture would be poured into the mould and upon setting, the mould would be disassembled leaving the auxetic rubber with iron nanoparticles inclusions. A milling process could also be implemented whereby a block of material having iron particle inclusions could be produced and then perforations could be performed strategically either through a cutter or a drill. The use of drilling would be advantageous when considering stadia and elliptical-shaped perforations over the diamond-shaped ones due

to the geometry. This process would require less assembly and disassembly; however, this would result in the loss of material when cutting. Another possibility would be SLA 3D printing using resin with suspended iron particles where the resin would solidify and entrap the iron particles. However, this would require further research to analyse the effect of UV light on iron particles and on maintaining an evenly distributed suspension of iron particles since 3D printing is a relatively slow process. Future research could then consider the active metamaterial when exposed to an external magnetic field. The iron particles within the auxetic matrix would become magnetised and align with the external magnetic field. In turn they may exert internal forces, and should the forces be significant enough they may cause the structure to expand. An investigation on the concentration of iron particles would be required to understand what concentration could produce an observable expansion for the strength of external magnetic field used. The degree of expansion in the three axes would be dependent on the chosen geometry of the structure and the direction and magnitude of the external field. Furthermore, the use of iron nanoparticles and 3D printing could lead to intricate and fine designs which would be suitable for miniature devices. One may consider multilayered designs having electromagnets fixed in strategic places to generate external magnetic fields. Such multilayered designs would consist of sheets of magnetoelastomers with electromagnets fixed in between. The resultant structure would be able to contract in local areas and thus morphing into complex geometries as shown in Figure 7.3.

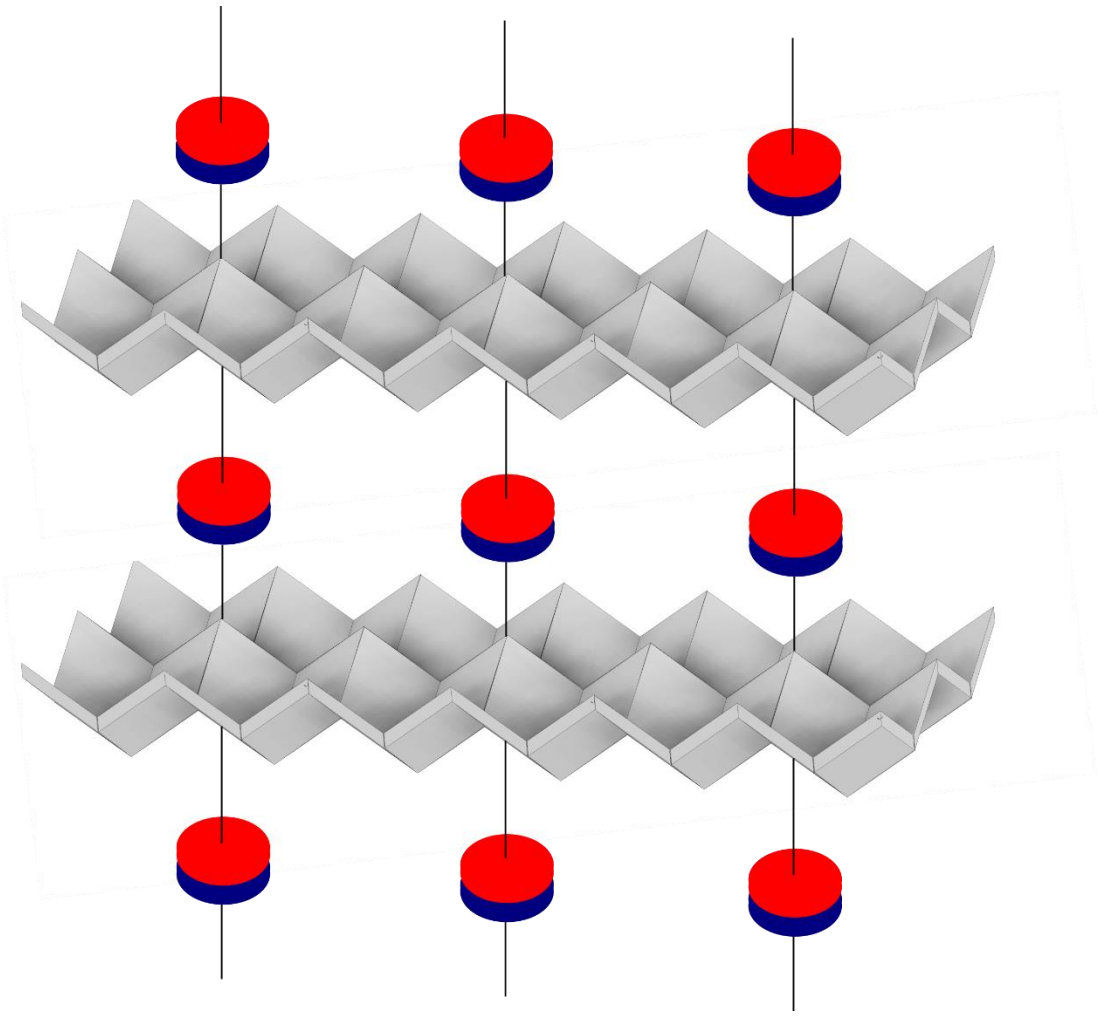

Figure 7.3. A proposed design for a multilayered structure composed of electromagnets and egg-rack-like sheets.

The next step would be active magneto-mechanical metamaterials on a molecular level. Given that the trend is designing smaller and more compact devices, researchers may shift focus to developing materials to use in nanoactuators and other parts. Using the proposed accordion-like structure, one may consider polymeric chains in a zig-zag pattern laced with iron nanoparticles. Research in iron nanoparticles has already produced iron nanoparticles coated with organic shells, which allows functionalisation. The strand would deform in response to an external magnetic field. This could be further combined

with the concepts discussed above extending this to egg-rack-like structures and multilayered structures.

Inclusions that may be used are not limited to iron nanoparticles, but other inclusions such as silver nanoparticles can also be used. This would offer advantages when such devises need to have antiseptic properties, such as in the case of prosthetics. Although not included in the main body of this thesis, a new method for the synthesis of silver nanoparticles was developed during this period. The results obtained in this study are included in Appendix III, where it is shown that silver nanoparticles were successfully synthesised through a new approach. In the case of this new method, the solution was chilled to sub-zero temperature. This gave more control on the size of the nanoparticles produced and in fact, silver nanoparticles having an average size of 19 ± 6 nm were produced. Preliminary experiments on the anti-microbial activity of the produced silver nanoparticles were also conducted (see Appendix IV) and it was shown that they may possess very good anti-microbial properties. All this is very relevant as silver NPs are already being used in the medical industry when sterile environments are required, such as in bedding and bandages (Haider & Kang, 2015; Juknius *et al.*, 2016; Pourzahedi & Eckelman, 2015; Prasath & Palaniappan, 2019). The interaction between the silver NPs and the auxetic matrix has to be explored and the antimicrobial activity of the material would have to be investigated. It is worth noting that silver nanoparticles may also impart increased electrical conductivity which would be particularly interesting for smart textiles and smart devices. This property could be used to create metamaterials where an electrical current could locally heat areas within the structure and thus control the mechanical properties and deformation mechanisms of the structure.

The magnetomechanical systems discussed here offer promising applications in scenarios where real-time geometric modifications with precise control are essential.

These systems can prove particularly valuable as untethered miniature multi-directional actuators, enabling controlled movement in two directions simultaneously. Moreover, leveraging magnetic fields to open pores presents opportunities for enhanced functionality. For instance, it can facilitate the cleaning of filtration devices located in hard-to-reach areas or within clean environments where physical access to the actuator might risk contaminating the surroundings. Aside from actuation, the ability to control the mechanical properties of these systems to shift its mechanical properties, especially shifting from a positive to a negative Poisson's ratio configuration, could have several applications.

In future research, the exploration of innovative systems could involve the design of systems having localized external magnetic fields. These fields could induce real-time contractions or extensions in the system as needed by adjusting the local external magnetic field. This approach would impart precise local control, enabling segments to contract and extend independently. This would result in the production of intricate geometries and/or behaviours (such as doming in the case of auxetic designs). Another intriguing avenue to explore is a system where the magnetic inclusions are electromagnets rather than permanent magnets or nanoparticles. In this configuration, one could eliminate the need for an external electromagnetic field, instead directly controlling the attraction and repulsion between the electromagnets. Moreover, such systems would offer an enhanced level of control as each magnetic inclusion could be individually manipulated in terms of magnetic field strength and direction. Such adaptable structures hold promising for applications in materials requiring localized morphological adjustments, such as solar wings, satellites, and smart textiles.

In summary, the work carried out in this thesis is intended to serve as ground work for future studies to develop industrial applications for active auxetic materials. The

uptake of the 3D perforated models by industry could see the application of 3D auxetic rotating rigid units to improve existing materials such as in construction materials and in the automotive industry due to their enhanced impact resistance. The work on magneto-mechanical metamaterials also aims to replace conventional pistons in miniature robotics, offering a lightweight, untethered alternative. Further work can incorporate the findings presented into miniature devices for uses in robotics and the biomedical industry. Of particular interest is the magnetoelastomer proposed which could be scaled to be implemented in the micro-devices of the future.

Chapter 8 : References

Abbaslou, M., Hashemi, R., & Etemadi, E. (2023). Novel hybrid 3D-printed auxetic vascular stent based on re-entrant and meta-trichiral unit cells: Finite element simulation with experimental verifications. *Materials Today Communications*, *35*, 105742. https://doi.org/10.1016/J.MTCOMM.2023.105742

Abd El-Sayed, F. K., Jones, R., & Burgess, I. W. (1979). A theoretical approach to the deformation of honeycomb based composite materials. *Composites*, *10*(4), 209–214. https://doi.org/10.1016/0010-4361(79)90021-1

Abdeen, M., Sabry, S., Ghozlan, H., El-Gendy, A. A., & Carpenter, E. E. (2016). Microbial-Physical Synthesis of Fe and Fe3O4 Magnetic Nanoparticles Using Aspergillus Niger YESM1 and Supercritical Condition of Ethanol. *Journal of Nanomaterials*. https://doi.org/10.1155/2016/9174891

Abdel-Mohsen, A. M., Hrdina, R., Burgert, L., Krylová, G., Abdel-Rahman, R. M., Krejčová, A., Steinhart, M., & Beneš, L. (2012). Green synthesis of hyaluronan fibers with silver nanoparticles. *Carbohydrate Polymers*, *89*(2), 411–422. https://doi.org/10.1016/j.carbpol.2012.03.022

Abou El-Nour, K. M. M., Eftaiha, A., Al-Warthan, A., & Ammar, R. A. A. (2010). Synthesis and applications of silver nanoparticles. *Arabian Journal of Chemistry*, *3*(3), 135–140. https://doi.org/10.1016/j.arabjc.2010.04.008

Abudabbus, M. M., Jevremović, I., Janković, A., Perić-Grujić, A., Matić, I., Vukašinović-Sekulić, M., Hui, D., Rhee, K. Y., & Mišković-Stanković, V. (2016). Biological activity of electrochemically synthesized silver doped polyvinyl alcohol/graphene composite hydrogel discs for biomedical applications. *Composites Part B: Engineering*. https://doi.org/10.1016/j.compositesb.2016.08.024

Acuna, D., Gutiérrez, F., Silva, R., Palza, H., Nunez, A. S., & Düring, G. (2022). A three step recipe for designing auxetic materials on demand. *Communications Physics*, *5*(1), 1–9. https://doi.org/10.1038/s42005-022-00876-5

Afdhal, Jirousek, O., Palar, P. S., Falta, J., & Dwianto, Y. B. (2023). Design exploration of additively manufactured chiral auxetic structure using explainable machine learning. *Materials & Design*, *232*, 112128. https://doi.org/10.1016/J.MATDES.2023.112128

Afshar, A., & Rezvanpour, H. (2022). Computational Study of Non-Porous Auxetic Plates with Diamond Shape Inclusions. *Journal of Composites Science 2022, Vol. 6, Page 192*, *6*(7), 192. https://doi.org/10.3390/JCS6070192

Agnihotri, S., Mukherji, S., & Mukherji, S. (2014). Size-controlled silver nanoparticles synthesized over the range 5-100 nm using the same protocol and their antibacterial efficacy. *RSC Advances*, *4*(8), 3974–3983. https://doi.org/10.1039/c3ra44507k

Ahmad, S., Munir, S., Zeb, N., Ullah, A., Khan, B., Ali, J., Bilal, M., Omer, M., Alamzeb, M., Salman, S. M., & Ali, S. (2019). Green nanotechnology: A review on green synthesis of silver nanoparticles — An ecofriendly approach. *International Journal of Nanomedicine*, *14*, 5087–5107. https://doi.org/10.2147/IJN.S200254

Alderson, A. (1999). A triumph of lateral thought. *Chemistry and Industry*, *10*, 384–391.

Alderson, A., Alderson, K. L., Attard, D., Evans, K. E., Gatt, R., Grima, J. N., Miller, W., Ravirala, N., Smith, C. W., & Zied, K. (2010). Elastic constants of 3-, 4- and 6-connected chiral and anti-chiral honeycombs subject to uniaxial in-plane loading. *Composites Science and Technology*, *70*(7), 1042–1048. https://doi.org/10.1016/j.compscitech.2009.07.009

Alderson, A., Alderson, K. L., Chirima, G., Ravirala, N., & Zied, K. M. (2010). The in-plane linear elastic constants and out-of-plane bending of 3-coordinated ligament and cylinder-ligament honeycombs. *Composites Science and Technology*, *70*(7), 1034–1041. https://doi.org/10.1016/J.COMPSCITECH.2009.07.010

Alderson, A., & Evans, K. E. (1995). Microstructural modelling of auxetic microporous polymers. *Journal of Materials Science*, *30*(13), 3319–3332. https://doi.org/10.1007/BF00349875

Alderson, A., Rasburn, J., Ameer-Beg, S., Mullarkey, P. G., Perrie, W., & Evans, K. E. (2000). An auxetic filter: A tuneable filter displaying enhanced size selectivity or defouling properties. *Industrial and Engineering Chemistry Research*, *39*(3), 654–665. https://doi.org/10.1021/ie990572w

Alderson, A., Rasburn, J., Evans, K. E., & Grima, J. N. (2001). Auxetic polymeric filters display enhanced de-fouling and pressure- compensation properties. *Membrane Technology*, *137*, 6–8.

Alderson, K. L., Alderson, A., & Evans, K. E. (1997). The interpretation of the strain-dependent Poisson's ratio in auxetic polyethylene. *Journal of Strain Analysis*, *32*.

Alderson, K. L., Alderson, A., Smart, G., Simkins, V. R., & Davies, P. J. (2002). Auxetic polypropylene fibres:Part 1 - Manufacture and characterisation. *Plastics, Rubber and Composites*, *31*(8), 344–349. https://doi.org/10.1179/146580102225006495

Alderson, K. L., & Evans, K. E. (1993). Strain-dependent behaviour of microporous polyethylene with a negative Poisson's ratio. *Journal of Materials Science*, *28*(15), 4092–4098. https://doi.org/10.1007/BF00351238/METRICS

Alderson, K. L., Simkins, V. R., Coenen, V. L., Davies, P. J., Alderson, A., & Evans, K. E. (2005). How to make auxetic fibre reinforced composites. *Physica Status Solidi (B)*, *242*(3), 509–518. https://doi.org/10.1002/pssb.200460371

Alhamid, M. Z., Hadi, B. S., & Khumaeni, A. (2019). Synthesis of silver nanoparticles using laser ablation method utilizing Nd:YAG laser. *AIP Conference Proceedings*, *2202*(December). https://doi.org/10.1063/1.5141626

Ali, K., Ahmed, B., Dwivedi, S., Saquib, Q., Al-Khedhairy, A. A., & Musarrat, J. (2015). Microwave accelerated green synthesis of stable silver nanoparticles with Eucalyptus globulus leaf extract and their antibacterial and antibiofilm activity on clinical isolates. *PLoS ONE*, *10*(7), 1–20. https://doi.org/10.1371/journal.pone.0131178

Ali, M. N., Busfield, J. J. C. C., & Rehman, I. U. (2014). Auxetic oesophageal stents: structure and mechanical properties. *Journal of Materials Science: Materials in Medicine*, *25*(2), 527–553. https://doi.org/10.1007/s10856-013-5067-2

Alimohammadi, F., Gashti, M. P., Shamei, A., & Kiumarsi, A. (2012). Deposition of

silver nanoparticles on carbon nanotube by chemical reduction method: Evaluation of surface, thermal and optical properties. *Superlattices and Microstructures*, *52*(1), 50–62. https://doi.org/10.1016/j.spmi.2012.04.015

Allen, T., Haake, S., & Goodwill, S. (2009). Comparison of a finite element model of a tennis racket to experimental data. *Sports Engineering*, *12*(2), 87–98. https://doi.org/10.1007/S12283-009-0032-5/FIGURES/14

Allen, T., Hewage, T., Newton-Mann, C., Wang, W., Duncan, O., & Alderson, A. (2017). Fabrication of Auxetic Foam Sheets for Sports Applications. *Physica Status Solidi (B)*, *254*(12). https://doi.org/10.1002/pssb.201700596

Allen, T., Shepherd, J., Hewage, T. A. M., Senior, T., Foster, L., & Alderson, A. (2015). Low-kinetic energy impact response of auxetic and conventional open-cell polyurethane foams. *Physica Status Solidi (B) Basic Research*, *252*(7), 1631–1639. https://doi.org/10.1002/pssb.201451715

Almgren, R. F. (1985). An isotropic three-dimensional structure with Poisson's ratio =-1. *Journal of Elasticity*, *15*(4), 427–430. https://doi.org/10.1007/BF00042531

Alomarah, A., Ruan, D., & Masood, S. (2018). Tensile properties of an auxetic structure with re-entrant and chiral features—a finite element study. *International Journal of Advanced Manufacturing Technology*, *99*(9–12), 2425–2440. https://doi.org/10.1007/S00170-018-2637-Y/METRICS

Alomarah, A., Ruan, D., Masood, S., & Gao, Z. (2019). Compressive properties of a novel additively manufactured 3D auxetic structure. *Smart Materials and Structures*, *28*(8), 085019. https://doi.org/10.1088/1361-665X/AB0DD6

Alomarah, A., Xu, S., Masood, S. H., & Ruan, D. (2020). Dynamic performance of auxetic structures: experiments and simulation. *Smart Materials and Structures*, *29*(5), 055031. https://doi.org/10.1088/1361-665X/AB79BB

Alqadi, M. K., Abo Noqtah, O. A., Alzoubi, F. Y., Alzouby, J., & Aljarrah, K. (2014). PH effect on the aggregation of silver nanoparticles synthesized by chemical reduction. *Materials Science- Poland*, *32*(1), 107–111. https://doi.org/10.2478/s13536-013-0166-9

Alqudami, A., Alhemiary, N. A., & Munassar, S. (2012). Removal of Pb(II) and Cd(II) ions from water by Fe and Ag nanoparticles prepared using electro-exploding wire technique. *Environmental Science and Pollution Research*, *19*(7), 2832–2841. https://doi.org/10.1007/s11356-012-0788-1

Alqudami, A., & Annapoorni, S. (2007). Fluorescence from metallic silver and iron nanoparticles prepared by exploding wire technique. *Plasmonics*, *2*(1), 5–13. https://doi.org/10.1007/s11468-006-9019-2

Alqudami, A., Annapoorni, S., Govind, & Shivaprasad, S. M. (2008). Ag-Au alloy nanoparticles prepared by electro-exploding wire technique. *Journal of Nanoparticle Research*, *10*(6), 1027–1036. https://doi.org/10.1007/s11051-007-9333-4

Alqudami, A., Annapoorni, S., Lamba, S., Kothari, P. C., & Kotnala, R. K. (2007). Magnetic properties of iron nanoparticles prepared by exploding wire technique. *Journal of Nanoscience and Nanotechnology*, *7*(6), 1898–1903.

https://doi.org/10.1166/jnn.2007.738

Alqudami, A., Annapoorni, S., Sen, P., & Rawat, R. S. (2007). The incorporation of silver nanoparticles into polypyrrole: Conductivity changes. *Synthetic Metals*, *157*(1), 53–59. https://doi.org/10.1016/j.synthmet.2006.12.006

Alvarez-Puebla, R. A., & Aroca, R. F. (2009). Synthesis of silver nanoparticles with controllable surface charge and their application to surface-enhanced Raman scattering. *Analytical Chemistry*, *81*(6), 2280–2285. https://doi.org/10.1021/ac8024416

Amara, D., Felner, I., Nowik, I., & Margel, S. (2009). Synthesis and characterization of Fe and Fe3O4 nanoparticles by thermal decomposition of triiron dodecacarbonyl. *Colloids and Surfaces A: Physicochemical and Engineering Aspects*, *339*(1–3), 106–110. https://doi.org/10.1016/j.colsurfa.2009.02.003

Amendola, V., Riello, P., & Meneghetti, M. (2011). Magnetic nanoparticles of iron carbide, iron oxide, iron@iron oxide, and metal iron synthesized by laser ablation in organic solvents. *Journal of Physical Chemistry C*, *115*(12), 5140–5146. https://doi.org/10.1021/jp109371m

Andò, B., Ascia, A., Baglio, S., & Pitrone, N. (2006). Development of novel ferrofluidic pumps. *Annual International Conference of the IEEE Engineering in Medicine and Biology - Proceedings*, 2828–2831. https://doi.org/10.1109/IEMBS.2006.260239

Andrade, C., Ha, C. S., & Lakes, R. S. (2018). Extreme Cosserat elastic cube structure with c'S ratio. *Journal of Mechanics of Materials and Structures*, *13*(1), 93–101. https://doi.org/10.2140/jomms.2018.13.93

Andreas, E., & Howard, C. V. (2013). Toxicology of nanoparticles. *Nanomedicine in Drug Delivery*, *64*(2), 337–354. https://doi.org/10.1201/b14802

Andriya, N., Dutta, V., & Vani, V. V. (2022). Study on 3D printed auxetic structure-based non-pneumatic tyres (NPT'S). *Https://Doi.Org/10.1080/10426914.2022.2039692*, *37*(11), 1280–1297. https://doi.org/10.1080/10426914.2022.2039692

ANSYS Inc. ANSYS Mechanical APDL Element Reference, Release 13. Pennsylvania, USA. (2010).

Aouni, N., & Wheeler, L. (2008). Auxeticity of Calcite and Aragonite polymorphs of CaCO and crystals of similar structure. *Physica Status Solidi (B)*, *245*(11), 2454–2462. https://doi.org/10.1002/pssb.200880264

Aparna, J., Maiti, S., & Jessy, P. (2021). Polyether ether ketone – As an alternative biomaterial for Metal Richmond crown-3-dimensional finite element analysis. *Journal of Conservative Dentistry : JCD*, *24*(6), 553. https://doi.org/10.4103/JCD.JCD_638_20

Archana, R., Sreeja, B., Nagarajan, K., Radha, S., BalajiBhargav, P., Balaji, C., & Padmalaya, G. (2020). Development of Highly Sensitive Ag NPs Decorated Graphene FET Sensor for Detection of Glucose Concentration. *Journal of Inorganic and Organometallic Polymers and Materials*. https://doi.org/10.1007/s10904-020-01541-6

Argatov, I. I., Guinovart-Díaz, R., & Sabina, F. J. (2012). On local indentation and impact compliance of isotropic auxetic materials from the continuum mechanics viewpoint.

International Journal of Engineering Science, *54*, 42–57. https://doi.org/10.1016/j.ijengsci.2012.01.010

Asanithi, P., Chaiyakun, S., & Limsuwan, P. (2012). Growth of silver nanoparticles by DC magnetron sputtering. *Journal of Nanomaterials*, *2012*. https://doi.org/10.1155/2012/963609

Ashkarran, A. A. (2010). A novel method for synthesis of colloidal silver nanoparticles by arc discharge in liquid. *Current Applied Physics*, *10*(6), 1442–1447. https://doi.org/10.1016/j.cap.2010.05.010

Ashkarran, A. A., Iraji Zad, A., Ahadian, M. M., & Hormozi Nezhad, M. R. (2009). Stability, size and optical properties of colloidal silver nanoparticles prepared by electrical arc discharge in water. *EPJ Applied Physics*, *48*(1). https://doi.org/10.1051/epjap/2009113

Ashraf, H., Anjum, T., Riaz, S., & Naseem, S. (2020). Microwave-Assisted Green Synthesis and Characterization of Silver Nanoparticles Using Melia azedarach for the Management of Fusarium Wilt in Tomato. *Frontiers in Microbiology*, *11*(March), 1–22. https://doi.org/10.3389/fmicb.2020.00238

Atilla Yolcu, D., & Okutan Baba, B. (2022). Measurement of Poisson's ratio of the auxetic structure. *Measurement: Journal of the International Measurement Confederation*, *204*(May), 112040. https://doi.org/10.1016/j.measurement.2022.112040

Attard, D., Caruana-Gauci, R., Gatt, R., Caruana-Gauci, R., Gatt, R., & Grima, J. N. (2016). Negative linear compressibility from rotating rigid units. *Physica Status Solidi (B)*, *253*(7), 1410–1418. https://doi.org/10.1002/pssb.201600092

Attard, D., Farrugia, P. S., Gatt, R., & Grima, J. N. (2020). Starchirals – A novel class of auxetic hierarchal structures. *International Journal of Mechanical Sciences*, *179*(March). https://doi.org/10.1016/j.ijmecsci.2020.105631

Attard, D., & Grima, J. N. (2008). Auxetic behaviour from rotating rhombi. *Physica Status Solidi (B)*, *245*(11). https://doi.org/10.1002/pssb.200880269

Attard, D., & Grima, J. N. (2012). A three-dimensional rotating rigid units network exhibiting negative Poisson's ratios. *Physica Status Solidi (B)*, *249*(7), 1330–1338. https://doi.org/10.1002/pssb.201084223

Attard, D., Manicaro, E., Gatt, R., & Grima, J. N. (2009). On the properties of auxetic rotating stretching squares. *Physica Status Solidi (B)*, *246*(9). https://doi.org/10.1002/pssb.200982035

Attard, D., Manicaro, E., & Grima, J. (2009a). On rotating rigid parallelograms and their potential for exhibiting auxetic behaviour. *Physica Status Solidi*, *249*(7), 1330–1338. https://doi.org/10.1002/pssb.201084223

Attard, D., Manicaro, E., & Grima, J. N. (2009b). On rotating rigid parallelograms and their potential for exhibiting auxetic behaviour. *Physica Status Solidi (B)*, *246*(9), 2033–2044. https://doi.org/10.1002/pssb.200982034

Aymonier, C., Schlotterbeck, U., Antonietti, L., Zacharias, P., Thomann, R., Tiller, J. C., & Mecking, S. (2002). Hybrids of silver nanoparticles with amphiphilic hyperbranched macromolecules exhibiting antimicrobial properties. *Chemical*

Communications, *24*, 3018–3019. https://doi.org/10.1039/b208575e

Baker, C., Shah, S. I., & Hasanain, S. K. (2004). Magnetic behavior of iron and iron-oxide nanoparticle/polymer composites. *Journal of Magnetism and Magnetic Materials*, *280*(2–3), 412–418. https://doi.org/10.1016/j.jmmm.2004.03.037

Baker, C., Shah, S. I., Hasanain, S. K., Ali, B., Shah, L., Li, G., Ekiert, T., & Unruh, K. M. (2002). Inert gas condensation of iron and iron-oxide nanoparticles. *Materials Research Society Symposium - Proceedings*, *746*, 201–206.

Bakina, O. V, Pervikov, A. V, Glazkova, E. A., Svarovskaya, N. V, Lozhkomoev, A. S., Lerner, M. I., & Avgustinovich, A. V. (2019). New magnetic bimetallic yanus-like ag-fe nanoparticles for antitumine therapy. *Siberian Journal of Oncology*, *18*(1), 65–70. https://doi.org/10.21294/1814-4861-2019-18-1-65-70

Baláž, M., Daneu, N., Balážová, Ľ., Dutková, E., Tkáčiková, Ľ., Briančin, J., Vargová, M., Balážová, M., Zorkovská, A., & Baláž, P. (2019). Corrigendum to "Bio-mechanochemical synthesis of silver nanoparticles with antibacterial activity" (Advanced Powder Technology (2017) 28(12) (3307–3312), (S0921883117303758) (10.1016/j.apt.2017.09.028)). *Advanced Powder Technology*, *30*(1), 219–220. https://doi.org/10.1016/j.apt.2018.11.018

Ban, Z., Barnakov, Y. A., Li, F., Golub, V. O., & O'Connor, C. J. (2005). The synthesis of core-shell iron@gold nanoparticles and their characterization. *Journal of Materials Chemistry*, *15*(43), 4660–4662. https://doi.org/10.1039/b504304b

Bandi, R., Alle, M., Park, C., Han, S., Kwon, G., Kim, J., & Lee, S. (2020). Rapid synchronous synthesis of Ag nanoparticles and Ag nanoparticles/holocellulose nanofibrils: Hg(II) detection and dye discoloration. *Carbohydrate Polymers*. https://doi.org/10.1016/j.carbpol.2020.116356

Bartlett, N. W., Tolley, M. T., Overvelde, J. T. B., Weaver, J. C., Mosadegh, B., Bertoldi, K., Whitesides, G. M., & Wood, R. J. (2015). A 3D-printed, functionally graded soft robot powered by combustion. *Science*, *349*(6244), 161–165. https://doi.org/10.1126/SCIENCE.AAB0129/SUPPL_FILE/AAB0129S2.MP4

Baruah, P. K., Singh, A., Rangan, L., Sharma, A. K., & Khare, A. (2020). Elucidation of size, structure, surface plasmon resonance, and photoluminescence of Ag nanoparticles synthesized by pulsed laser ablation in distilled water and its viability as SERS substrate. *Applied Physics A: Materials Science and Processing*, *126*(3), 1–14. https://doi.org/10.1007/s00339-020-3375-1

Baruwati, B., Polshettiwar, V., & Varma, R. S. (2009). Glutathione promoted expeditious green synthesis of silver nanoparticles in water using microwaves. *Green Chemistry*, *11*(7), 926–930. https://doi.org/10.1039/b902184a

Baughman, R. H., Stafström, S., Cui, C., & Dantas, S. O. (1998). Materials with negative compressibilities in one or more dimensions. *Science*, *279*(5356), 1522–1524. https://doi.org/10.1126/science.279.5356.1522

Berlincourt, D., & Jaffe, H. (1958). Elastic and Piezoelectric Coefficients of Single-Crystal Barium Titanate. *Physical Review*, *111*(1), 143–148. https://doi.org/10.1103/PhysRev.111.143

Bertoldi, K., Reis, P. M., Willshaw, S., & Mullin, T. (2010). Negative Poisson's Ratio

Behavior Induced by an Elastic Instability. *Advanced Materials*, *22*(3), 361–366. https://doi.org/10.1002/adma.200901956

Bezazi, A., Remillat, C., Innocenti, P., & Scarpa, F. (2008). In-plane mechanical and thermal conductivity properties of a rectangular-hexagonal honeycomb structure. *Composite Structures*, *84*(3), 248–255. https://doi.org/10.1016/j.compstruct.2007.08.005

Bezazi, A., & Scarpa, F. (2009). Tensile fatigue of conventional and negative Poisson's ratio open cell PU foams. *International Journal of Fatigue*, *31*(3), 488–494. https://doi.org/10.1016/j.ijfatigue.2008.05.005

Bezazi, A., Scarpa, F., & Remillat, C. (2005). A novel centresymmetric honeycomb composite structure. *Composite Structures*, *71*(3), 356–364. https://doi.org/10.1016/j.compstruct.2005.09.035

Bharde, A., Rautaray, D., Bansal, V., Ahmad, A., Sarkar, I., Yusuf, S. M., Sanyal, M., & Sastry, M. (2006). Extracellular biosynthesis of magnetite using fungi. *Small*, *2*(1), 135–141. https://doi.org/10.1002/smll.200500180

Bhattacharyya, S., & Gedanken, A. (2008). Microwave-assisted insertion of silver nanoparticles into 3-D mesoporous zinc oxide nanocomposites and nanorods. *Journal of Physical Chemistry C*, *112*(3), 659–665. https://doi.org/10.1021/jp0760253

Bhullar, S. K., Ko, J., Ahmed, F., & Jun, M. B. G. (2014). Design and Fabrication of Stent with Negative Poisson's Ratio. *International Journal of Mechanical and Mechatronics Engineering*, *8*(2), 448–454. https://doi.org/10.5281/zenodo.1091366

Billon, K., Ouisse, M., Sadoulet-Reboul, E., Scarpa, F., & Collet, M. (2016). Parametric study of wave propagation in hierarchical auxetic perforated metamaterials. *Https://Doi.Org/10.1117/12.2221895*, *9799*, 18–24. https://doi.org/10.1117/12.2221895

Billon, K., Zampetakis, I., Scarpa, F., Ouisse, M., Sadoulet-Reboul, E., Collet, M., Perriman, A., & Hetherington, A. (2017). Mechanics and band gaps in hierarchical auxetic rectangular perforated composite metamaterials. *Composite Structures*, *160*, 1042–1050. https://doi.org/10.1016/J.COMPSTRUCT.2016.10.121

Bodaghi, M., Namvar, N., Yousefi, A., Teymouri, H., Demoly, F., & Zolfagharian, A. (2023). Metamaterial boat fenders with supreme shape recovery and energy absorption/dissipation via FFF 4D printing. *Smart Materials and Structures*, *32*(9), 095028. https://doi.org/10.1088/1361-665X/ACEDDE

Bonet, F., Grugeon, S., Urbina, R. H., Tekaia-Elhsissen, K., & Tarascon, J. M. (2002). In situ deposition of silver and palladium nanoparticles prepared by the polyol process, and their performance as catalytic converters of automobile exhaust gases. *Solid State Sciences*, *4*(5), 665–670. https://doi.org/10.1016/S1293-2558(02)01311-0

Bonet, F., Guéry, C., Guyomard, D., Herrera Urbina, R., Tekaia-Elhsissen, K., & Tarascon, J. M. (1999). Electrochemical reduction of noble metal compounds in ethylene glycol. *International Journal of Inorganic Materials*, *1*(1), 47–51. https://doi.org/10.1016/S1463-0176(99)00007-1

Bonfanti, A., & Bhaskar, A. (2019). Elastic stabilization of wrinkles in thin films by

auxetic microstructure. *Extreme Mechanics Letters*, *33*, 100556. https://doi.org/10.1016/J.EML.2019.100556

Boppart, H., Treindl, A., Wachter, P., & Roth, S. (1980). First observation of a negative elastic constant in intermediate valent TmSe. *Solid State Communications*, *35*(6), 483–486. https://doi.org/10.1016/0038-1098(80)90253-7

Borysiuk, J., Grabias, A., Szczytko, J., Bystrzejewski, M., Twardowski, A., & Lange, H. (2008). Structure and magnetic properties of carbon encapsulated Fe nanoparticles obtained by arc plasma and combustion synthesis. *Carbon*, *46*(13), 1693–1701. https://doi.org/10.1016/j.carbon.2008.07.011

Bryaskova, R., Pencheva, D., Nikolov, S., & Kantardjiev, T. (2011). Synthesis and comparative study on the antimicrobial activity of hybrid materials based on silver nanoparticles (AgNps) stabilized by polyvinylpyrrolidone (PVP). *Journal of Chemical Biology*, *4*(4), 185–191. https://doi.org/10.1007/s12154-011-0063-9

Burke, N. A. D., Stover, H. D. H., & Dawson, F. P. (2002). Magnetic nanocomposites: Preparation and characterization of Polymer-Coated Iron nanoparticles. *Chem Mater*, *14*, 4752–4761. https://doi.org/10.1016/j.colsurfa.2006.02.005

Bystrzejewski, M., Károly, Z., Szépvölgyi, J., Huczko, A., & Lange, H. (2011). Continuous synthesis of controlled size carbon-encapsulated iron nanoparticles. *Materials Research Bulletin*, *46*(12), 2408–2417. https://doi.org/10.1016/j.materresbull.2011.08.047

Bystrzejewski Michałand Huczko, A., Lange, H., Cudziło, S., & Kiciński, W. (2007). Combustion synthesis route to carbon-encapsulated iron nanoparticles. *Diamond and Related Materials*, *16*(2), 225–228. https://doi.org/10.1016/j.diamond.2006.05.002

Caddock, B. D., & Evans, K. E. (1989). Microporous materials with negative Poisson ' s ratios . I . Microstructure and mechanical properties. *J. Phys. D: Appl. Phys.*, *1877*, 1877–1882. https://doi.org/10.1088/0022-3727/22/12/012

Cai, W., Chettiar, U. K., Kildishev, A. V, & Shalaev, V. M. (2007). Optical cloaking with metamaterials. *Nature Photonics 2007 1:4*, *1*(4), 224–227. https://doi.org/10.1038/nphoton.2007.28

Cañamares, M. V, Garcia-Ramos, J. V, Gómez-Varga, J. D., Domingo, C., & Sanchez-Cortes, S. (2005). Comparative study of the morphology, aggregation, adherence to glass, and surface-enhanced Raman scattering activity of silver nanoparticles prepared by chemical reduction of Ag+ using citrate and hydroxylamine. *Langmuir*, *21*(18), 8546–8553. https://doi.org/10.1021/la050030l

Cañamares, M. V, Garcia-Ramos, J. V, Sanchez-Cortes, S., Castillejo, M., & Oujja, M. (2008). Comparative SERS effectiveness of silver nanoparticles prepared by different methods: A study of the enhancement factor and the interfacial properties. *Journal of Colloid and Interface Science*, *326*(1), 103–109. https://doi.org/10.1016/j.jcis.2008.06.052

Cao, L. fei, Xie, D., Guo, M. xing, Park, H. S., & Fujita, T. (2007). Size and shape effects on Curie temperature of ferromagnetic nanoparticles. *Transactions of Nonferrous Metals Society of China*, *17*(6), 1451–1455. https://doi.org/10.1016/S1003-6326(07)60293-3

Carpenter, E. E. (2001). Iron nanoparticles as potential magnetic carriers. *Journal of Magnetism and Magnetic Materials*, *225*(1–2), 17–20. https://doi.org/10.1016/S0304-8853(00)01222-1

Carrella, A., Brennan, M. J., Waters, T. P., & Shin, K. (2008). On the design of a high-static-low-dynamic stiffness isolator using linear mechanical springs and magnets. *Journal of Sound and Vibration*, *315*(3), 712–720. https://doi.org/10.1016/j.jsv.2008.01.046

Carta, G., Brun, M., & Baldi, A. (2016). Design of a porous material with isotropic negative Poisson's ratio. *Mechanics of Materials*.

Catauro, M., Tranquillo, E., Dal Poggetto, G., Pasquali, M., Dell'Era, A., & Ciprioti, S. V. (2018). Influence of the heat treatment on the particles size and on the crystalline phase of TiO2 synthesized by the sol-gel method. *Materials*, *11*(12). https://doi.org/10.3390/ma11122364

Cetin, H. (2017). Silver Nanoparticle Synthesis Through Arc-Discharge in Deionized Water Medium. *Journal of Optoelectronic and Biomedical Materials*, *9*(4), 153–157.

Chang, Y., Liu, Y., & Hu, H. (2023). A finite element analysis of auxetic composite fabric with rotating square structure. *Https://Doi.Org/10.1177/15280837231173153*, *53*, 152808372311731. https://doi.org/10.1177/15280837231173153

Changfang, Z., Changlin, Z., Jianlin, Z., Hongwei, Z., Kebin, Z., & Yangzuo, L. (2022). Compressive mechanical behavior for surface auxetic structures. *Journal of Alloys and Compounds*, *894*, 162427. https://doi.org/10.1016/j.jallcom.2021.162427

Chen, C., Wang, L., Jiang, G., Zhou, J., Chen, X., Yu, H., & Yang, Q. (2006). Study on the synthesis of silver nanowires with adjustable diameters through the polyol process. *Nanotechnology*, *17*(15), 3933–3938. https://doi.org/10.1088/0957-4484/17/15/054

Chen, D. H., & Ozaki, S. (2009). Analysis of in-plane elastic modulus for a hexagonal honeycomb core: Effect of core height and proposed analytical method. *Composite Structures*, *88*(1), 17–25. https://doi.org/10.1016/J.COMPSTRUCT.2008.02.021

Chen, J., Wang, J., Zhang, X., & Jin, Y. (2008). Microwave-assisted green synthesis of silver nanoparticles by carboxymethyl cellulose sodium and silver nitrate. *Materials Chemistry and Physics*, *108*(2–3), 421–424. https://doi.org/10.1016/j.matchemphys.2007.10.019

Chen, K., Gao, Q., Fang, S., Zou, D., Yang, Z., & Liao, W. H. (2021). An auxetic nonlinear piezoelectric energy harvester for enhancing efficiency and bandwidth. *Applied Energy*, *298*, 117274. https://doi.org/10.1016/J.APENERGY.2021.117274

Chen, M., Feng, Y. G., Wang, X., Li, T. C., Zhang, J. Y., & Qian, D. J. (2007). Silver nanoparticles capped by oleylamine: Formation, growth, and self-organization. *Langmuir*, *23*(10), 5296–5304. https://doi.org/10.1021/la700553d

Chen, Y., Fu, M., Hu, H., & Xiong, J. (2022). Curved inserts in auxetic honeycomb for property enhancement and design flexibility. *Composite Structures*, *280*(September 2021), 114892. https://doi.org/10.1016/j.compstruct.2021.114892

Chen, Y. H., & Yeh, C. S. (2002). Laser ablation method: Use of surfactants to form the

dispersed Ag nanoparticles. *Colloids and Surfaces A: Physicochemical and Engineering Aspects*, *197*(1–3), 133–139. https://doi.org/10.1016/S0927-7757(01)00854-8

Chen, Y., & He, Q. (2020). 3D-printed short carbon fibre reinforced perforated structures with negative Poisson's ratios: Mechanisms and design. *Composite Structures*, *236*(October 2019), 111859. https://doi.org/10.1016/j.compstruct.2020.111859

Chen, Z., Wu, X., Min, Y., Wang, Z., & Zhou, S. (2020). Re-entrant auxetic lattices with enhanced stiffness : A numerical study. *International Journal of Mechanical Sciences*, *178*, 105619. https://doi.org/10.1016/j.ijmecsci.2020.105619

Cheng, X., Wu, B., Yang, Y., & Li, Y. (2011). Synthesis of iron nanoparticles in water-in-oil microemulsions for liquid-phase Fischer-Tropsch synthesis in polyethylene glycol. *Catalysis Communications*, *12*(6), 431–435. https://doi.org/10.1016/j.catcom.2010.11.011

Cheng, X., Zhang, Y., Ren, X., Han, D., Jiang, W., Zhang, X. G., Luo, H. C., & Xie, Y. M. (2022). Design and mechanical characteristics of auxetic metamaterial with tunable stiffness. *International Journal of Mechanical Sciences*, *223*, 107286. https://doi.org/j.ijmecsci.2022.107286

Cheong, S., Ferguson, P., Feindel, K. W., Hermans, I. F., Callaghan, P. T., Meyer, C., Slocombe, A., Su, C.-H., Cheng, F.-Y., Yeh, C.-S., Ingham, B., Toney, M. F., & Tilley, R. D. (2011). Simple Synthesis and Functionalization of Iron Nanoparticles for Magnetic Resonance Imaging. *Angewandte Chemie*, *123*(18), 4292–4295. https://doi.org/10.1002/ange.201100562

Chetcuti, E., Ellul, B., Manicaro, E., Brincat, J. P. J.-P., Attard, D., Gatt, R., & Grima, J. N. (2014). Modeling auxetic foams through semi-rigid rotating triangles. *Physica Status Solidi (B)*, *251*(2), 297–306. https://doi.org/10.1002/pssb.201384252

Chimentão, R. J., Kirm, I., Medina, F., Rodríguez, X., Cesteros, Y., Salagre, P., & Sueiras, J. E. (2004). Different morphologies of silver nanoparticles as catalysts for the selective oxidation of styrene in the gas phase. *Chemical Communications*, *4*(7), 846–847. https://doi.org/10.1039/b400762j

Chirima, G. T., Zied, K. M., Ravirala, N., Burgess, A. N., Dooling, P. J., Alderson, K. L., & Alderson, A. (2009). Modelling of auxetic particulate-filled polymeric composites. *17th International Conference on Composite Materials*.

Cho, C., Choi, Y. W., Kang, C., & Lee, G. W. (2007). Effects of the medium on synthesis of nanopowders by wire explosion process. *Applied Physics Letters*, *91*(14), 1–4. https://doi.org/10.1063/1.2794724

Cho, Y., Shin, J. H., Costa, A., Kim, T. A., Kunin, V., Li, J., Lee, S. Y., Yang, S., Han, H. N., Choi, I. S., & Srolovitz, D. J. (2014). Engineering the shape and structure of materials by fractal cut. *Proceedings of the National Academy of Sciences of the United States of America*, *111*(49), 17390–17395.

Choi, C. J., Tolochko, O., & Kim, B. K. (2002). Preparation of iron nanoparticles by chemical vapor condensation. *Materials Letters*, *56*(3), 289–294. https://doi.org/10.1016/S0167-577X(02)00457-3

Choi, J. B., & Lakes, R. S. (1995). Analysis of elastic modulus of conventional foams

and of re-entrant foam materials with a negative Poisson's ratio. *International Journal of Mechanical Sciences*, *37*(1), 51–59. https://doi.org/10.1016/0020-7403(94)00047-N

Chook, S. W., Chia, C. H., Zakaria, S., Ayob, M. K., Chee, K. L., Huang, N. M., Neoh, H. M., Lim, H. N., Jamal, R., & Rahman, R. M. F. R. A. (2012). Antibacterial performance of Ag nanoparticles and AgGO nanocomposites prepared via rapid microwave-assisted synthesis method. *Nanoscale Research Letters*, *7*, 1–7. https://doi.org/10.1186/1556-276X-7-541

Choudhary, A., Mukherjee, G. S., Banerjee, M., & Nagar, S. (2020). Studies on structural and magnetic properties of PMMA/Co/Ag nanocomposite film. *3Rd International Conference on Condensed Matter and Applied Physics (Icc-2019)*, *May*. https://doi.org/10.1063/5.0001417

Chow, G. M., Md, B., Schoen, P. E., & Kurihara, L. K. (1998). Nanostructured Metallic Powders and Films via an Alcoholic Sovent Process. *United States Patent*, *19*.

Chow, L., Yick, K. lun, Wong, K. H., Leung, M. S. hang, Sun, Y., Kwan, M. ying, Ning, K., Yu, A., Yip, J., Chan, Y. fan, & Ng, S. pui. (2022). 3D Printing Auxetic Architectures for Hypertrophic Scar Therapy. *Macromolecular Materials and Engineering*, *307*, 2100866. https://doi.org/10.1002/mame.202100866

Chung, W. H., Hwang, Y. T., Lee, S. H., & Kim, H. S. (2016). Electrical wire explosion process of copper/silver hybrid nano-particle ink and its sintering via flash white light to achieve high electrical conductivity. *Nanotechnology*, *27*(20), 1–13. https://doi.org/10.1088/0957-4484/27/20/205704

Cirtiu, C. M., Raychoudhury, T., Ghoshal, S., & Moores, A. (2011). Systematic comparison of the size, surface characteristics and colloidal stability of zero valent iron nanoparticles pre- and post-grafted with common polymers. *Colloids and Surfaces A: Physicochemical and Engineering Aspects*, *390*(1–3), 95–104. https://doi.org/10.1016/j.colsurfa.2011.09.011

Coenen, V. L., & Alderson, K. L. (2011). Mechanisms of failure in the static indentation resistance of auxetic carbon fibre laminates. *Physica Status Solidi (B) Basic Research*, *248*(1), 66–72. https://doi.org/10.1002/pssb.201083977

Coskun, S., Aksoy, B., & Unalan, H. E. (2011). Polyol synthesis of silver nanowires: An extensive parametric study. *Crystal Growth and Design*, *11*(11), 4963–4969. https://doi.org/10.1021/cg200874g

Courant, R. (1943). *Variational methods for the solution of problems of equilibrium and vibrations*. https://community.ams.org/journals/bull/1943-49-01/S0002-9904-1943-07818-4/S0002-9904-1943-07818-4.pdf

Crane, R. A., & Scott, T. B. (2012). Nanoscale zero-valent iron: Future prospects for an emerging water treatment technology. *Journal of Hazardous Materials*, *211–212*, 112–125. https://doi.org/10.1016/j.jhazmat.2011.11.073

Creighton, J.A.; Blatchford, C.G.; Albrecht, M. G. (1978). Plasma Resonance Enhancement of Raman Scattering by Pyridine Adsorbed on Silver or Gold Sol Particles of Size. *Journal of Chemical Society -Faraday Transactions*, *75*, 790–798.

Cremonesi, M., Franci, A., Idelsohn, S., & Oñate, E. (2020). A State of the Art Review

of the Particle Finite Element Method (PFEM). *Archives of Computational Methods in Engineering*, *27*(5), 1709–1735. https://doi.org/10.1007/S11831-020-09468-4/FIGURES/22

Crespo, J., Duncan, O., Alderson, A., & Montáns, F. J. (2020). Auxetic orthotropic materials: Numerical determination of a phenomenological spline-based stored density energy and its implementation for finite element analysis. *Computer Methods in Applied Mechanics and Engineering*, *371*, 113300. https://doi.org/10.1016/j.cma.2020.113300

Crumm, A. T., & Halloran, J. W. (2007). Negative Poisson's ratio structures produced from zirconia and nickel using co-extrusion. *Journal of Materials Science*, *42*(4), 1336–1342. https://doi.org/10.1007/S10853-006-1209-Y/FIGURES/10

Dadashi, S., Poursalehi, R., & Delavari, H. (2015). Structural and Optical Properties of Pure Iron and Iron Oxide Nanoparticles Prepared via Pulsed Nd:YAG Laser Ablation in Liquid. *Procedia Materials Science*, *11*, 722–726. https://doi.org/10.1016/j.mspro.2015.11.052

Dang, T. M. D., Le, T. T. T., Fribourg-Blanc, E., & Dang, M. C. (2012). Influence of surfactant on the preparation of silver nanoparticles by polyol method. *Advances in Natural Sciences: Nanoscience and Nanotechnology*, *3*(3). https://doi.org/10.1088/2043-6262/3/3/035004

Darroudi, M., Ahmad, M. Bin, Abdullah, A. H., Ibrahim, N. A., & Shameli, K. (2010). Effect of accelerator in green synthesis of silver nanoparticles. *International Journal of Molecular Sciences*, *11*(10), 3898–3905. https://doi.org/10.3390/ijms11103898

De Bonis, A., Lovaglio, T., Galasso, A., Santagata, A., & Teghil, R. (2015). Iron and iron oxide nanoparticles obtained by ultra-short laser ablation in liquid. *Applied Surface Science*, *353*, 433–438. https://doi.org/10.1016/j.apsusc.2015.06.145

Del Bianco, L., Hernando, A., Multigner, M., Prados, C., Sánchez-López, J. C., Fernández, A., Conde, C. F., & Conde, A. (1998). Evidence of spin disorder at the surface-core interface of oxygen passivated Fe nanoparticles. *Journal of Applied Physics*, *84*(4), 2189–2192. https://doi.org/10.1063/1.368282

Dell'Aglio, M., & De Giacomo, A. (2020). Plasma charging effect on the nanoparticles releasing from the cavitation bubble to the solution during nanosecond Pulsed Laser Ablation in Liquid. *Applied Surface Science*. https://doi.org/10.1016/j.apsusc.2020.146031

Demchenko, V., Riabov, S., Kobylinskyi, S., Goncharenko, L., Rybalchenko, N., Kruk, A., Moskalenko, O., & Shut, M. (2020). Effect of the type of reducing agents of silver ions in interpolyelectrolyte-metal complexes on the structure, morphology and properties of silver-containing nanocomposites. *Scientific Reports*, *10*(1), 1–9. https://doi.org/10.1038/s41598-020-64079-0

Deng, Z. Y., Chen, K. L., & Wu, C. H. (2019). Improving the SERS signals of biomolecules using a stacked biochip containing Fe2O3/Au nanoparticles and a DC magnetic field. *Scientific Reports*, *9*(1), 1–8. https://doi.org/10.1038/s41598-019-45879-5

Devasenan, S., Beevi, N. H., Jayanthi, S. S., & Sivakami, G. (2016). *Journal of Chemical and Pharmaceutical Research , 2016 , 8 (3): 314-319 Research Article Synthesis*

and characterization of silver nanoparticles by using glycerol and their antimicrobial activity. *8*(3), 314–319.

Devatha, C. P., Thalla, A. K., & Katte, S. Y. (2016). Green synthesis of iron nanoparticles using different leaf extracts for treatment of domestic waste water. *Journal of Cleaner Production*, *139*, 1425–1435. https://doi.org/10.1016/j.jclepro.2016.09.019

Dijith, K. S., Aiswarya, R., Praveen, M., Pillai, S., & Surendran, K. P. (2018). Polyol derived Ni and NiFe alloys for effective shielding of electromagnetic interference. *Materials Chemistry Frontiers*, *2*(10), 1829–1841. https://doi.org/10.1039/c8qm00264a

Dimitrijevic, N. M., Bartels, D. M., Jonah, C. D., Takahashi, K., & Rajh, T. (2001). Radiolytically induced formation and optical absorption spectra of colloidal silver nanoparticles in supercritical ethane. *Journal of Physical Chemistry B*, *105*(5), 954–959. https://doi.org/10.1021/jp0028296

Djeddou, K., Bouloudenine, M., Soualah Alila, H., & Bououdina, M. (2020). Formation of Silver Nanoparticles by a Novel Irradiation Method Without a Reducing Agent and Their Impact on Four Pathogenic Bacterial Strains. *Journal of Inorganic and Organometallic Polymers and Materials*. https://doi.org/10.1007/s10904-020-01466-0

Djekoun, A., Boudinar, N., Chebli, A., Otmani, A., Benabdeslem, M., Bouzabata, B., & Greneche, J. M. (2009). Characterization of Fe and Fe50Ni50 ultrafine nanoparticles synthesized by inert gas-condensation method. *Physica B: Condensed Matter*, *404*(20), 3824–3829. https://doi.org/10.1016/j.physb.2009.07.074

Dmitriev, S. V. (2007). Auxetic behavior of crystals from rotational degrees of freedom. *Ferroelectrics*, *349*(1), 33–44. https://doi.org/10.1080/00150190701260660

Dmitriev, S. V., Vasiliev, A. A., Yoshikawa, N., Shigenari, T., & Ishibashi, Y. (2005). Multi-cell continuum approximation for discrete medium with microscopic rotations. *Physica Status Solidi (B)*, *242*(3), 528–537. https://doi.org/10.1002/pssb.200460373

Dong, X., Ji, X., Jing, J., Li, M., Li, J., & Yang, W. (2010). Synthesis of triangular silver nanoprisms by stepwise reduction of sodium borohydride and trisodium citrate. *Journal of Physical Chemistry C*, *114*(5), 2070–2074. https://doi.org/10.1021/jp909964k

Dudek, K. K. (2018). *Properties of mechanical metamaterials with the focus on magnetic inclusions* (Issue April). https://www.um.edu.mt/library/oar/handle/123456789/36877

Dudek, K. K., Gatt, R., Dudek, M. R., & Grima, J. N. (2018). Negative and positive stiffness in auxetic magneto-mechanical metamaterials. *Proceedings of the Royal Society A: Mathematical, Physical and Engineering Sciences*, *474*(2215). https://doi.org/10.1098/rspa.2018.0003

Dudek, K. K., Gatt, R., & Grima, J. N. (2020). 3D composite metamaterial with magnetic inclusions exhibiting negative stiffness and auxetic behaviour. *Materials and Design*, *187*, 108403. https://doi.org/10.1016/j.matdes.2019.108403

Dudek, K. K., Gatt, R., Mizzi, L., Dudek, M. R., Attard, D., Evans, K. E., & Grima, J. N.

(2017). On the dynamics and control of mechanical properties of hierarchical rotating rigid unit auxetics. *Scientific Reports*, *7*(1), 46529. https://doi.org/10.1038/srep46529

Dudek, K. K., Iglesias Martínez, J. A., & Kadic, M. (2022). Variable Dual Auxeticity of the Hierarchical Mechanical Metamaterial Composed of Re-Entrant Structural Motifs. *Physica Status Solidi (B)*, *259*(12), 2200404. https://doi.org/10.1002/pssb.202200404

Dudek, K. K., Wojciechowski, K. W., Dudek, M. R., Gatt, R., Mizzi, L., & Grima, J. N. (2018). Potential of mechanical metamaterials to induce their own global rotational motion. *Smart Materials and Structures*, *27*(5). https://doi.org/10.1088/1361-665X/aabbf6

Dudek, K. K., Wolak, W., Dudek, M. R., Caruana-Gauci, R., Gatt, R., Wojciechowski, K. W., & Grima, J. N. (2017). Programmable magnetic domain evolution in magnetic auxetic systems. *Physica Status Solidi - Rapid Research Letters*, *11*(8), 1–6. https://doi.org/10.1002/pssr.201700122

Dudek, K. K., Wolak, W., Gatt, R., & Grima, J. N. (2019a). Impact resistance of composite magnetic metamaterials. *Scientific Reports*, *9*(1), 65–69. https://doi.org/10.1038/s41598-019-40610-w

Dudek, K. K., Wolak, W., Gatt, R., & Grima, J. N. (2019b). Impact resistance of composite magnetic metamaterials. *Scientific Reports*, *9*(1). https://doi.org/10.1038/s41598-019-40610-w

Dudek, M. R., Dudek, K. K., Wolak, W., Wojciechowski, K. W., & Grima, J. N. (2019). Magnetocaloric materials with ultra-small magnetic nanoparticles working at room temperature. *Scientific Reports*, *9*(1). https://doi.org/10.1038/s41598-019-53617-0

Dudek, M. R., Grabiec, B., & Wojciechowski, K. W. (2007). Molecular dynamics simulations of auxetic ferrogel. *Reviews on Advanced Materials Science*, *14*, 167–173. http://www.ipme.ru/e-journals/RAMS/no_21407/dudek.pdf

Dudek, M. R., & Wojciechowski, K. W. (2008). Magnetic films of negative Poisson's ratio in rotating magnetic fields. *Journal of Non-Crystalline Solids*, *354*(35–39), 4304–4308. https://doi.org/10.1016/j.jnoncrysol.2008.06.086

Duncan, O., Shepherd, T., Moroney, C., Foster, L., Venkatraman, P., Winwood, K., Allen, T., & Alderson, A. (2018). Review of Auxetic Materials for Sports Applications: Expanding Options in Comfort and Protection. *Applied Sciences*, *8*(6), 941. https://doi.org/10.3390/app8060941

Dung, N. T., Long, N. V., Tam, L. T. T., Nam, P. H., Tung, L. D., Phuc, N. X., Lu, L. T., & Kim Thanh, N. T. (2017). High magnetisation, monodisperse and water-dispersible CoFe@Pt core/shell nanoparticles. *Nanoscale*, *9*(26), 8952–8961. https://doi.org/10.1039/c6nr09325f

Edel, J. B., Ma, Y., & Kornyshev, A. A. (2023). Electrochemical photonics: a pathway towards electrovariable optical metamaterials. *Nanophotonics*, *12*(14), 2717–2744. https://doi.org/10.1515/NANOPH-2023-0053/ASSET/GRAPHIC/J_NANOPH-2023-0053_FIG_016.JPG

El-Gendy, A. A., Ibrahim, E. M. M., Khavrus, V. O., Krupskaya, Y., Hampel, S.,

Leonhardt, A., Büchner, B., & Klingeler, R. (2009). The synthesis of carbon coated Fe, Co and Ni nanoparticles and an examination of their magnetic properties. *Carbon*, *47*(12), 2821–2828. https://doi.org/10.1016/j.carbon.2009.06.025

El-Khatib, A. M., Badawi, M. S., Ghatass, Z. F., Mohamed, M. M., & Elkhatib, M. (2018). Synthesize of Silver Nanoparticles by Arc Discharge Method Using Two Different Rotational Electrode Shapes. *Journal of Cluster Science*, *29*(6), 1169–1175. https://doi.org/10.1007/s10876-018-1430-2

Elmaci, G. (2020). Microwave Assisted Green Synthesis of Ag/AgO Nanocatalyst as An Efficient OER Catalyst in Neutral Media. *Hittite Journal of Science & Engineering*, *7*(1), 61–65. https://doi.org/10.17350/hjse19030000174

Errandonea, D., Santamaria-Perez, D., Bondarenko, T., & Khyzhun, O. (2010). New high-pressure phase of HfTiO4and ZrTiO4ceramics. *Materials Research Bulletin*, *45*(11), 1732–1735. https://doi.org/10.1016/j.materresbull.2010.06.061

Etemadi, E., Gholikord, M., Zeeshan, M., & Hu, H. (2023). Improved mechanical characteristics of new auxetic structures based on stretch-dominated-mechanism deformation under compressive and tensile loadings. *Thin-Walled Structures*, *184*, 110491. https://doi.org/10.1016/j.tws.2022.110491

Evans, K. E. (1991a). Auxetic polymers: a new range of materials. *Endeavour*, *15*(4), 170–174. https://doi.org/10.1016/0160-9327(91)90123-S

Evans, K. E. (1991b). The design of doubly curved sandwich panels with honeycomb cores. *Composite Structures*, *17*(2), 95–111. https://doi.org/10.1016/0263-8223(91)90064-6

Evans, K. E., Alderson, A., & Christian, F. R. (1995). Auxetic two-dimensional polymer networks. An example of tailoring geometry for specific mechanical properties. *Journal of the Chemical Society, Faraday Transactions*, *91*(16), 2671. https://doi.org/10.1039/ft9959102671

Evans, K. E., Nkansah, M. A., & Hutchinson, I. J. (1994). Auxetic foams: Modelling negative Poisson's ratios. *Acta Metallurgica Et Materialiaetall, Mater.*, *42*(4), 1289–1294. https://doi.org/10.1016/0956-7151(94)90145-7

Fadiji, T., Coetzee, C. J., Berry, T. M., Ambaw, A., & Opara, U. L. (2018). The efficacy of finite element analysis (FEA) as a design tool for food packaging: A review. *Biosystems Engineering*, *174*, 20–40. https://doi.org/10.1016/J.BIOSYSTEMSENG.2018.06.015

Fan, M. De, Yuan, P., Chen, T. H., He, H. P., Yuan, A. H., Chen, K. M., Zhu, J. X., & Liu, D. (2010). Synthesis, characterization and size control of zerovalent iron nanoparticles anchored on montmorillonite. *Chinese Science Bulletin*, *55*(11), 1092–1099. https://doi.org/10.1007/s11434-010-0062-1

Fan, G. Z., Ren, X., Wang, S. L., Luo, C., & Xie, Y. M. (2022). A novel cement-based auxetic foam composite: Experimental study. *Case Studies in Construction Materials*, *17*, e01159. https://doi.org/10.1016/J.CSCM.2022.E01159

Fang, H., Chang, T.-S., & Wang, K. W. (2019). Magneto-origami structures: engineering multi-stability and dynamics via magnetic-elastic coupling. *Smart Materials and Structures*.

Faraci, D., Driemeier, L., & Comi, C. (2021). Bending-Dominated Auxetic Materials for Wearable Protective Devices Against Impact. *Journal of Dynamic Behavior of Materials*, *7*(3), 425–435. https://doi.org/10.1007/s40870-020-00284-2

Fatimah, I. (2016). Green synthesis of silver nanoparticles using extract of Parkia speciosa Hassk pods assisted by microwave irradiation. *Journal of Advanced Research*, *7*(6), 961–969. https://doi.org/10.1016/j.jare.2016.10.002

Fazlzadeh, M., Rahmani, K., Zarei, A., Abdoallahzadeh, H., Nasiri, F., & Khosravi, R. (2017). A novel green synthesis of zero valent iron nanoparticles (NZVI) using three plant extracts and their efficient application for removal of Cr(VI) from aqueous solutions. *Advanced Powder Technology*, *28*(1), 122–130. https://doi.org/10.1016/j.apt.2016.09.003

Fernández-Pacheco, R., Arruebo, M., Marquina, C., Ibarra, R., Arbiol, J., & Santamaría, J. (2006). Highly magnetic silica-coated iron nanoparticles prepared by the arc-discharge method. *Nanotechnology*, *17*(5), 1188–1192. https://doi.org/10.1088/0957-4484/17/5/004

Fievet, F., Lagier, J. P., Blin, B., Beaudoin, B., & Figlarz, M. (1989). Homogeneous and heterogeneous nucleations in the polyol process for the preparation of micron and submicron size metal particles. *Solid State Ionics*, *32–33*(PART 1), 198–205. https://doi.org/10.1016/0167-2738(89)90222-1

Fievet, F., Lagier, J. P., & Figlarz, M. (1989). Preparing Monodisperse Metal Powders in Micrometer and Submicrometer Sizes by the Polyol Process. *MRS Bulletin*, *14*(12), 29–34. https://doi.org/10.1557/S0883769400060930

Foster, L., Peketi, P., Allen, T., Senior, T., Duncan, O., & Alderson, A. (2018). Application of Auxetic Foam in Sports Helmets. *Applied Sciences*, *8*(3), 354. https://doi.org/10.3390/app8030354

Francesconi, L., Baldi, A., Dominguez, G., & Taylor, M. (2020). An Investigation of the Enhanced Fatigue Performance of Low-porosity Auxetic Metamaterials. *Experimental Mechanics*, *60*(1), 93–107. https://doi.org/10.1007/S11340-019-00539-7/FIGURES/12

Frattini, A., Pellegri, N., Nicastro, D., & De Sanctis, O. (2005). Effect of amine groups in the synthesis of Ag nanoparticles using aminosilanes. *Materials Chemistry and Physics*, *94*(1), 148–152. https://doi.org/10.1016/j.matchemphys.2005.04.023

Frenzel, T., Kadic, M., & Wegener, M. (2017). Three-dimensional mechanical metamaterials with a twist. *Science*, *358*(6366), 1072–1074. https://doi.org/10.1126/SCIENCE.AAO4640/SUPPL_FILE/AAO4640_MOVIE_S1.MP4

Frey, N. A., Peng, S., Cheng, K., & Sun, S. (2009). Magnetic nanoparticles: Synthesis, functionalization, and applications in bioimaging and magnetic energy storage. *Chemical Society Reviews*, *38*(9), 2532–2542. https://doi.org/10.1039/b815548h

Friis, E. A., Lakes, R. S., & Park, J. B. (1988). Negative Poisson's ratio polymeric and metallic foams. *Journal of Materials Science*, *23*(12), 4406–4414. https://doi.org/10.1007/BF00551939

Fuku, K., Hayashi, R., Takakura, S., Kamegawa, T., Mori, K., & Yamashita, H. (2013).

The synthesis of size- and color-controlled silver nanoparticles by using microwave heating and their enhanced catalytic activity by localized surface plasmon resonance. *Angewandte Chemie - International Edition*, *52*(29), 7446–7450. https://doi.org/10.1002/anie.201301652

Fung, K. K., Qin, B., & Zhang, X. X. (2000). Passivation of α-Fe nanoparticle by epitaxial γ-Fe2O3 shell. *Materials Science and Engineering A*, *286*(1), 135–138. https://doi.org/10.1016/S0921-5093(00)00717-6

Galati, M., Calignano, F., & Minosi, F. (2022). Numerical and experimental investigations of a novel 3D bucklicrystal auxetic structure produced by metal additive manufacturing. *Thin-Walled Structures*, *180*, 109850. https://doi.org/10.1016/J.TWS.2022.109850

Galbusera, F., Casaroli, G., Chande, R., Lindsey, D., Villa, T., Yerby, S., Mesiwala, A., Panico, M., Gallazzi, E., & Brayda-Bruno, M. (2020). Biomechanics of sacropelvic fixation: a comprehensive finite element comparison of three techniques. *European Spine Journal*, *29*(2), 295–305. https://doi.org/10.1007/S00586-019-06225-5/TABLES/2

Gambin, D., Grima, J. N., & Gatt, R. (2023). Unusual Mechanical Properties of CO2-V: Auxetic Potential in a High-Pressure Polymorph of Carbon Dioxide. *Journal of Physics and Chemistry of Solids*, *178*(111349). https://doi.org/10.2139/ssrn.4221807

Gandhi, H., & Khan, S. (2016). Biological Synthesis of Silver Nanoparticles and Its Antibacterial Activity. *Journal of Nanomedicine & Nanotechnology*, *07*(02), 2–4. https://doi.org/10.4172/2157-7439.1000366

Gang, X., Ren, X., Jiang, W., Yu, X., Luo, C., Zhang, Y., & Min, Y. (2022). A novel auxetic chiral lattice composite : Experimental and numerical study. *Composite Structures*, *282*, 115043. https://doi.org/10.1016/j.compstruct.2021.115043

Gangwar, M. S., Singh, A. K., & Agarwal, P. (2020). Synthesis and characterization of metallic nanoparticles on different substrates for light trapping applications in thin film solar cells. *3Rd International Conference on Condensed Matter and Applied Physics (Icc-2019)*, *2220*. https://doi.org/10.1063/5.0001410

Gao, D., Wang, S., Zhang, M., & Zhang, C. (2021). Experimental and numerical investigation on in-plane impact behaviour of chiral auxetic structure. *Composite Structures*, *267*(February), 113922. https://doi.org/10.1016/j.compstruct.2021.113922

Gao, J., Xu, W., & Ding, Z. (2006). 3D finite element mesh generation of complicated tooth model based on CT slices. *Computer Methods and Programs in Biomedicine*, *82*(2), 97–105. https://doi.org/10.1016/J.CMPB.2006.02.008

Gao, Q., Zhao, X., Wang, C., Wang, L., & Ma, Z. (2018). Multi-objective crashworthiness optimization for an auxetic cylindrical structure under axial impact loading. *Materials & Design*, *143*, 120–130. https://doi.org/10.1016/j.matdes.2018.01.063

Gao, Y., Jiang, P., Song, L., Liu, L., Yan, X., Zhou, Z., Liu, D., Wang, J., Yuan, H., Zhang, Z., Zhao, X., Dou, X., Zhou, W., Wang, G., & Xie, S. (2005). Growth mechanism of silver nanowires synthesized by polyvinylpyrrolidone-assisted polyol

reduction. *Journal of Physics D: Applied Physics*, *38*(7), 1061–1067. https://doi.org/10.1088/0022-3727/38/7/015

Gao, Y., Wei, X., Han, X., Zhou, Z., & Xiong, J. (2021). Novel 3D auxetic lattice structures developed based on the rotating rigid mechanism. *International Journal of Solids and Structures*, *233*, 111232. https://doi.org/10.1016/J.IJSOLSTR.2021.111232

Gaspar, N., Smith, C. W., Alderson, A., Grima, J. N., & Evans, K. E. (2011). A generalised three-dimensional tethered-nodule model for auxetic materials. *Journal of Materials Science*, *46*(2), 372–384. https://doi.org/10.1007/s10853-010-4846-0

Gatt, R., Attard, D., & Grima, J. N. (2009). On the behaviour of bi-material strips when subjected to changes in external hydrostatic pressure. *Scripta Materialia*, *60*(2). https://doi.org/10.1016/j.scriptamat.2008.08.045

Gatt, R., Cauchi, R., & Grima, J. N. (2012). Honeycomb metamaterials exhibiting anomalous mechanical and thermal properties. *Mechanics of Nano, Micro and Macro Composite Structures*. http://paginas.fe.up.pt/~icnmmcs/http://www.auxetic.info/http://staff.um.edu.mt/jgri1/

Gatt, R., Mizzi, L., Azzopardi, J. I., Azzopardi, K. M., Attard, D., Casha, A., Briffa, J., & Grima, J. N. (2015). Hierarchical Auxetic Mechanical Metamaterials. *Scientific Reports*, *5*(1), 8395. https://doi.org/10.1038/srep08395

Gatt, R., Vella Wood, M., Gatt, A., Zarb, F., Formosa, C., Azzopardi, K. M., Casha, A., Agius, T. P., Schembri-Wismayer, P., Attard, L., Chockalingam, N., & Grima, J. N. (2015). Negative Poisson's ratios in tendons: An unexpected mechanical response. *Acta Biomaterialia*, *24*, 201–208. https://doi.org/10.1016/j.actbio.2015.06.018

Gawande, M. B., Goswami, A., Asefa, T., Guo, H., Biradar, A. V, Peng, D. L., Zboril, R., & Varma, R. S. (2015). Core-shell nanoparticles: synthesis and applications in catalysis and electrocatalysis. *Chemical Society Reviews*, *44*(21), 7540–7590. https://doi.org/10.1039/c5cs00343a

Geng, L. C., Ruan, X. L., Wu, W. W., Xia, R., & Fang, D. N. (2019). Mechanical Properties of Selective Laser Sintering (SLS) Additive Manufactured Chiral Auxetic Cylindrical Stent. *Experimental Mechanics*, *59*(6), 913–925. https://doi.org/10.1007/S11340-019-00489-0/FIGURES/13

Ghozlan, H. A., Abouelkheir, S. S., & Sabry, S. A. (2018). Microbial Fabrication of Magnetic Nanoparticles and Their Applications. In *Magnetic Nanostructured Materials*. Elsevier Inc. https://doi.org/10.1016/b978-0-12-813904-2.00004-8

Gibson, L. J., & Ashby, M. F. (1997). *Cellular Solids: Structure and Properties* (2nd ed.). Cambridge University Press. https://openlibrary.org/books/OL993071M/Cellular_solids

Gibson, L. J. J., Ashby, M. F. F., Schajer, G. S. S., & Robertson, C. I. I. (1982). The Mechanics of Two-Dimensional Cellular Materials. *Proceedings of the Royal Society A: Mathematical, Physical and Engineering Sciences*, *382*(1782), 25–42. https://doi.org/10.1098/rspa.1982.0087

Giri, A. K. (1997). Magnetic properties of iron-polyethylene nanocomposites prepared

by high energy ball milling. *Journal of Applied Physics*, *81*(3), 1348–1350. https://doi.org/10.1063/1.363870

Gleiter, H. (1990). N a N O C R Y S T a L L I N E Materials. *Progress*, *33*, 223–315.

Gohar, S., Hussain, G., Ilyas, M., & Ali, A. (2021). Performance of 3D printed topologically optimized novel auxetic structures under compressive loading: experimental and FE analyses. *Journal of Materials Research and Technology*, *15*, 394–408. https://doi.org/10.1016/j.jmrt.2021.07.149

Golubeva, O. Y., Shamova, O. V, Orlov, D. S., Pazina, T. Y., Boldina, A. S., & Kokryakov, V. N. (2010). Study of antimicrobial and hemolytic activities of silver nanoparticles prepared by chemical reduction. *Glass Physics and Chemistry*, *36*(5), 628–634. https://doi.org/10.1134/S1087659610050135

Gomes, J. F., Garcia, A. C., Ferreira, E. B., Pires, C., Oliveira, V. L., Tremiliosi-Filho, G., & Gasparotto, L. H. S. (2015). New insights into the formation mechanism of Ag, Au and AgAu nanoparticles in aqueous alkaline media: Alkoxides from alcohols, aldehydes and ketones as universal reducing agents. *Physical Chemistry Chemical Physics*, *17*(33), 21683–21693. https://doi.org/10.1039/c5cp02155c

Gordanshekan, A., Heib, T., Ripplinger, W., Herrmann, H. G., & Diebels, S. (2022). Experimental and Theoretical Investigations of Auxetic Sheet Metal. *Advanced Structured Materials*, *175*, 689–707. https://doi.org/10.1007/978-3-031-04548-6_32/COVER

Grediac, M. (1993). A finite element study of the transverse shear in honeycomb cores. *International Journal of Solids and Structures*, *30*(13), 1777–1788. https://doi.org/10.1016/0020-7683(93)90233-W

Grima-Cornish, J. N., Grima, J. N., & Attard, D. (2020). Negative Mechanical Materials and Metamaterials: Giant Out-of-Plane Auxeticity from Multi-Dimensional Wine-Rack-like Motifs. *MRS Advances*, *5*, 717–725. https://doi.org/10.1557/adv.2020.48

Grima-Cornish, J. N., Vella-Zarb, L., Wojciechowski, K. W., & Grima, J. N. (2021). Shearing Deformations of β -Cristobalite-Like Boron Arsenate. *Symmetry*, *13*(6), 977. https://doi.org/https://doi.org/10.3390/sym13060977

Grima, J., Alderson, A., & Evans, K. (2004). Negative Poisson's ratios from rotating rectangles. *Comput. Methods Sci.* https://doi.org/10.12921/cmst.2004.10.02.137-145

Grima, J., Gatt, R., & Alderson, A. (2005). On the auxetic properties of "rotating rectangles" with different connectivity. *Journal of the Physical Society of Japan*, *74*(10), 2866–2867. https://doi.org/10.1143/JPSJ.74.2866

Grima, J., Mizzi, L., Azzopardi, K. M., & Gatt, R. (2016). Auxetic Perforated Mechanical Metamaterials with Randomly Oriented Cuts. *Advanced Materials*, *28*(2), 385–389. https://doi.org/10.1002/adma.201503653

Grima, J. N. (2000). New Auxetic Materials. In *Ph.D thesis*. University of Exeter, United Kingdom.

Grima, J. N., & Caruana-Gauci, R. (2012). Mechanical Metamaterials - Materials that push back. *Nature Materials*, *11*(7), 565–566. https://doi.org/10.1038/nmat3364

Grima, J. N., Caruana-Gauci, R., Attard, D., & Gatt, R. (2012a). Three-dimensional cellular structures with negative Poisson's ratio and negative compressibility properties. *Proceedings of the Royal Society A: Mathematical, Physical and Engineering Sciences*, *468*(2146), 3121–3138. https://doi.org/10.1098/rspa.2011.0667

Grima, J. N., Caruana-Gauci, R., Attard, D., & Gatt, R. (2012b). Three-dimensional cellular structures with negative Poisson's ratio and negative compressibility properties. *Proceedings of the Royal Society A: Mathematical, Physical and Engineering Sciences*, *468*(2146), 3121–3138. https://doi.org/10.1098/RSPA.2011.0667

Grima, J. N., Caruana-Gauci, R., Dudek, M. R., Wojciechowski, K. W. K. W., & Gatt, R. (2013). Smart metamaterials with tunable auxetic and other properties. *Smart Materials and Structures*, *22*(8), 084016. https://doi.org/10.1088/0964-1726/22/8/084016

Grima, J. N., Cauchi, R., Gatt, R., & Attard, D. (2013). Honeycomb composites with auxetic out-of-plane characteristics. *Composite Structures*, *106*. https://doi.org/10.1016/j.compstruct.2013.06.009

Grima, J. N., Chetcuti, E., Manicaro, E., Attard, D., Camilleri, M., Gatt, R., & Evans, K. E. (2012). On the auxetic properties of generic rotating rigid triangles. *Proceedings of the Royal Society A: Mathematical, Physical and Engineering Sciences*, *468*(2139), 810–830. https://doi.org/10.1098/RSPA.2011.0273

Grima, J. N., & Evans, K. E. (2000a). Auxetic behavior from rotating squares. *Journal of Materials Science Letters*, *19*(17), 1563–1565. https://doi.org/10.1023/A:1006781224002

Grima, J. N., & Evans, K. E. (2000b). *Self expanding molecular networks*. https://doi.org/10.1039/b004305m

Grima, J. N., & Evans, K. E. (2006). Auxetic behavior from rotating triangles. *Journal of Materials Science*, *41*(10), 3193–3196. https://doi.org/10.1007/s10853-006-6339-8

Grima, J. N., Farrugia, P. S., Caruana, C., Gatt, R., & Attard, D. (2008). Auxetic behaviour from stretching connected squares. *Journal of Materials Science*, *43*(17), 5962–5971. https://doi.org/10.1007/s10853-008-2765-0

Grima, J. N., Farrugia, P. S., Gatt, R., & Attard, D. (2008a). On the auxetic properties of rotating rhombi and parallelograms: A preliminary investigation. *Physica Status Solidi (B)*, *245*(3). https://doi.org/10.1002/pssb.200777705

Grima, J. N., Farrugia, P. S., Gatt, R., & Attard, D. (2008b). On the auxetic properties of rotating rhombi and parallelograms: A preliminary investigation. *Physica Status Solidi (B)*, *245*(3), 521–529. https://doi.org/10.1002/pssb.200777705

Grima, J. N., & Gatt, R. (2010). Perforated sheets exhibiting negative Poisson's ratios. *Advanced Engineering Materials*, *12*(6), 460–464. https://doi.org/10.1002/adem.201000005

Grima, J. N., Gatt, R., Alderson, A., & Evans, K. (2005a). On the Auxetic Properties of `Rotating Rectangles' with Different Connectivity. *Journal of the Physical Society of Japan*, *74*(10), 2866–2867. https://doi.org/10.1143/JPSJ.74.2866

Grima, J. N., Gatt, R., Alderson, A., & Evans, K. E. (2005b). On the potential of connected stars as auxetic systems. *Molecular Simulation*, *31*(13). https://doi.org/10.1080/08927020500401139

Grima, J. N., Gatt, R., Alderson, A., & Evans, K. E. (2005c). On the auxetic properties of "rotating rectangles" with different connectivity. *Journal of the Physical Society of Japan*, *74*(10), 2866–2867. https://doi.org/10.1143/JPSJ.74.2866

Grima, J. N., Gatt, R., Ellul, B., & Chetcuti, E. (2010). Auxetic behaviour in non-crystalline materials having star or triangular shaped perforations. *Journal of Non-Crystalline Solids*, *356*(37–40), 1980–1987. https://doi.org/10.1016/j.jnoncrysol.2010.05.074

Grima, J. N., Gatt, R., & Farrugia, P.-S. (2008). On the properties of auxetic meta-tetrachiral structures. *Physica Status Solidi (B)*, *245*(3). https://doi.org/10.1002/pssb.200777704

Grima, J. N., Manicaro, E., & Attard, D. (2011). Auxetic behaviour from connected different-sized squares and rectangles. *Proceedings of the Royal Society A: Mathematical, Physical and Engineering Sciences*, *467*(2126), 439–458. https://doi.org/10.1098/rspa.2010.0171

Grima, J. N., Oliveri, L., Attard, D., Ellul, B., Gatt, R., Cicala, G., & Recca, G. (2010). Hexagonal honeycombs with zero Poisson's ratios and enhanced stiffness. *Advanced Engineering Materials*, *12*(9), 855–862. https://doi.org/10.1002/adem.201000140

Grima, J. N., Williams, J. J., & Evans, K. E. (2005). Networked calix[4]arene polymers with unusual mechanical properties. *Chemical Communications*, *32*, 4065. https://doi.org/10.1039/b505839b

Grima, J. N., Zammit, V., Gatt, R., Alderson, A., & Evans, K. E. (2007). Auxetic behaviour from rotating semi-rigid units. *Physica Status Solidi (B)*, *244*(3), 866–882. https://doi.org/10.1002/pssb.200572706

Grimmelsmann, N., Meissner, H., & Ehrmann, A. (2016). 3D printed auxetic forms on knitted fabrics for adjustable permeability and mechanical properties. *IOP Conference Series: Materials Science and Engineering*, *137*(1). https://doi.org/10.1088/1757-899X/137/1/012011

Grishina, Y. S., Borgardt, N. I., Volkov, R. L., Gromov, D. G., & Savitskiy, A. I. (2019). Electron Microscopy Study of Silver Nanoparticles Obtained by Thermal Evaporation. *Semiconductors*, *53*(15), 1986–1991. https://doi.org/10.1134/S1063782619150089

Gromov, D. G., Lebedev, E. A., Savitskiy, A. I., Trifonov, A. Y., Rubcov, V. V, Borgardt, N. I., & Grishina, Y. S. (2015). Investigation of condensation of small portions of Ag at thermal evaporation in vacuum. *Journal of Physics: Conference Series*, *643*(1). https://doi.org/10.1088/1742-6596/643/1/012014

Gubin, S. P., Spichkin, Y. I., Yurkov, G. Y., & Tishin, A. M. (2002). Nanomaterial for high-density magnetic data storage. *Russian Journal of Inorganic Chemistry*, *47*(SUPPL.).

Gul, U., Kanwal, S., Tabassum, S., Gilani, M. A., & Rahim, A. (2020). Microwave-assisted synthesis of carbon dots as reductant and stabilizer for silver nanoparticles

with enhanced-peroxidase like activity for colorimetric determination of hydrogen peroxide and glucose. *Microchimica Acta*, *187*(2). https://doi.org/10.1007/s00604-019-4098-x

Gunaydin, K., Gallina, F. G., Airoldi, A. A., Sala, G., Grande, A. M., Gunaydin, K., Gallina, F. G., Airoldi, A., Sala, G., & Grande, A. M. (2019). Numerical and experimental crushing behaviour investigation of EBM printed auxetic chiral lattices. *Sim-AM 2019 : II International Conference on Simulation for Additive Manufacturing*, 408–416. https://upcommons.upc.edu/handle/2117/334900

Gunaydin, K., & Turkmen, H. S. (2019). In-plane quasi-static crushing finite element analysis of auxetic lattices. *Proceedings of 9th International Conference on Recent Advances in Space Technologies, RAST 2019*, 645–648. https://doi.org/10.1109/RAST.2019.8767839

Guo, J., Wang, R., Tjiu, W. W., Pan, J., & Liu, T. (2012). Synthesis of Fe nanoparticles@graphene composites for environmental applications. *Journal of Hazardous Materials*, *225–226*, 63–73. https://doi.org/10.1016/j.jhazmat.2012.04.065

Guo, M. F., Yang, H., & Ma, L. (2020). Design and analysis of 2D double-U auxetic honeycombs. *Thin-Walled Structures*, *155*(February). https://doi.org/10.1016/j.tws.2020.106915

Guo, S., & Sun, S. (2012). FePt nanoparticles assembled on graphene as enhanced catalyst for oxygen reduction reaction. *Journal of the American Chemical Society*, *134*(5), 2492–2495. https://doi.org/10.1021/ja2104334

Gurunathan, S. (2019). Rapid biological synthesis of silver nanoparticles and their enhanced antibacterial effects against Escherichia fergusonii and Streptococcus mutans. *Arabian Journal of Chemistry*, *12*(2), 168–180. https://doi.org/10.1016/j.arabjc.2014.11.014

Guzman, M., Dille, J., & Godet, S. (2009). Synthesis of silver nanoparticles by chemical reduction method and their antibacterial activity. *International Journal of Chemical and Biomolecular Engineering*, *2*(3). https://doi.org/10.1007/s11814-010-0067-0

Guzman, M., Dille, J., & Godet, S. (2012). Synthesis and antibacterial activity of silver nanoparticles against gram-positive and gram-negative bacteria. *Nanomedicine: Nanotechnology, Biology, and Medicine*, *8*(1), 37–45. https://doi.org/10.1016/j.nano.2011.05.007

Gyrylov, E. I. (2019). Research of silicon and silver nanoparticles obtained by laser ablation in liquid. *IOP Conference Series: Materials Science and Engineering*, *704*(1). https://doi.org/10.1088/1757-899X/704/1/012019

Hadjipanayis, C. G., Bonder, M. J., Balakrishnan, S., Wang, X., Mao, H., & Hadjipanayis, G. C. (2008). Metallic iron nanoparticles for MRI contrast enhancement and local hyperthermia. *Small*, *4*(11), 1925–1929. https://doi.org/10.1002/smll.200800261

Hah, H. O. E. J. I. N., Koo, S. M. A. N., & Lee, S. H. (2003). *R_hah_JSolGelScTec26_467_2003.pdf*. 467–471.

Haider, A., & Kang, I. K. (2015). Preparation of silver nanoparticles and their industrial and biomedical applications: A comprehensive review. *Advances in Materials*

Science and Engineering. https://doi.org/10.1155/2015/165257

Hamidi, A., Taghavizadeh Yazdi, M. E., Amiri, M. S., Hosseini, H. A., & Darroudi, M. (2019). Biological synthesis of silver nanoparticles in Tribulus terrestris L. extract and evaluation of their photocatalyst, antibacterial, and cytotoxicity effects. *Research on Chemical Intermediates*, *45*(5), 2915–2925. https://doi.org/10.1007/s11164-019-03770-y

Han, D., Ren, X., Zhang, Y., Yu Zhang, X., Gang Zhang, X., Luo, C., & Min Xie, Y. (2022). Lightweight auxetic metamaterials: Design and characteristic study. *Composite Structures*, *293*, 115706. https://doi.org/10.1016/J.COMPSTRUCT.2022.115706

Han, D., Zhang, Y., Yu, X., Min, Y., & Ren, X. (2022). Mechanical characterization of a novel thickness gradient auxetic tubular structure under inclined load. *Engineering Structures*, *273*(October), 115079. https://doi.org/10.1016/j.engstruct.2022.115079

Han, W., Gao, W., & Wang, X. (2021). A novel magneto-mechanical metamaterial cell structure with large, reversible and rapid two-way shape alteration. *Smart Materials and Structures*, *30*(3), 35018. https://doi.org/10.1088/1361-665X/ABDCFE

Han, Y. C., Cha, H. G., Kim, C. W., Kim, Y. H., & Kang, Y. S. (2007). Synthesis of highly magnetized iron nanoparticles by a solventless thermal decomposition method. *Journal of Physical Chemistry C*, *111*(17), 6275–6280. https://doi.org/10.1021/jp0686285

Hao, J., Han, D., Zhang, X. G. X. Y., Zhang, Y., Jiang, W., Teng, X. C., Lang, J. P., Pan, Y., Ni, X. H., Zhang, X. G. X. Y., Xie, Y. M., & Ren, X. (2022). Novel dual-platform lightweight metamaterials with auxeticity. *Engineering Structures*, *270*, 114891. https://doi.org/10.1016/J.ENGSTRUCT.2022.114891

Harada, M., Asakura, K., & Toshima, N. (1993). Catalytic activity and structural analysis of polymer-protected Au/Pd bimetallic clusters prepared by the successive reduction of HAuCl4 and PdCl2. *Journal of Physical Chemistry*, *97*(19), 5103–5114. https://doi.org/10.1002/chin.199334024

Harinarayana, V. (2022). *THREE-DIMENSIONAL MICROFABRICATION OF MECHANICAL METAMATERIALS VIA STEREOLITHOGRAPHY AND TWO-PHOTON POLYMERIZATION*. https://doi.org/10.25394/PGS.21674612.V1

Harinarayana, V., & Shin, Y. C. (2022). Design and evaluation of three–dimensional axisymmetric mechanical metamaterial exhibiting negative Poisson's ratio. *Journal of Materials Research and Technology*, *19*, 1390–1406. https://doi.org/10.1016/J.JMRT.2022.05.131

Harkati, E., Daoudi, N., Bezazi, A., Haddad, A., & Scarpa, F. (2017). In-plane elasticity of a multi re-entrant auxetic honeycomb. *Composite Structures*, *180*, 130–139. https://doi.org/10.1016/j.compstruct.2017.08.014

Harshiny, M., Iswarya, C. N., & Matheswaran, M. (2015). Biogenic synthesis of iron nanoparticles using Amaranthus dubius leaf extract as a reducing agent. *Powder Technology*, *286*, 744–749. https://doi.org/10.1016/j.powtec.2015.09.021

He, F., & Zhao, D. (2005). Preparation and characterization of a new class of starch-stabilized bimetallic nanoparticles for degradation of chlorinated hydrocarbons in

water. *Environmental Science and Technology*, *39*(9), 3314–3320. https://doi.org/10.1021/es048743y

He, F., & Zhao, D. (2007). Manipulating the size and dispersibility of zerovalent iron nanoparticles by use of carboxymethyl cellulose stabilizers. *Environmental Science and Technology*, *41*(17), 6216–6221. https://doi.org/10.1021/es0705543

He, Y., Sahoo, Y., Wang, S., Luo, H., Prasad, P. N., & Swihart, M. T. (2006). Laser-driven synthesis and magnetic properties of iron nanoparticles. *Journal of Nanoparticle Research*, *8*(3–4), 335–342. https://doi.org/10.1007/s11051-005-9008-y

Hebbalalu, D., Lalley, J., Nadagouda, M. N., & Varma, R. S. (2013). Greener techniques for the synthesis of silver nanoparticles using plant extracts, enzymes, bacteria, biodegradable polymers, and microwaves. *ACS Sustainable Chemistry and Engineering*, *1*(7), 703–712. https://doi.org/10.1021/sc4000362

Hebeish, A., Shaheen, T. I., & El-Naggar, M. E. (2016). Solid state synthesis of starch-capped silver nanoparticles. *International Journal of Biological Macromolecules*, *87*, 70–76. https://doi.org/10.1016/j.ijbiomac.2016.02.046

Henglein, A. (1989). Small-Particle Research: Physicochemical Properties of Extremely Small Colloidal Metal and Semiconductor Particles. *Chemical Reviews*, *89*(8), 1861–1873. https://doi.org/10.1021/cr00098a010

Henglein, A., & Meisel, D. (1998). Spectrophotometric Observations of the Adsorption of Organosulfur Compounds on Colloidal Silver Nanoparticles. *The Journal of Physical Chemistry B*, *102*(43), 8364–8366. https://doi.org/10.1021/jp982900w

Hernández, S. (Santiago), Brebbia, C. A., & El-Sayed, M. E. M. (2003). Helmet Optimisation Based On Head-helmet Modelling. *WIT Transactions on The Built Environment*, *67*, 339. https://doi.org/10.2495/OP030311

Herr, U., Jing, J., Birringer, R., Gonser, U., & Gleiter, H. (1987). Investigation of nanocrystalline iron materials by Mössbauer spectroscopy. *Applied Physics Letters*, *50*(8), 472–474. https://doi.org/10.1063/1.98177

Hewage, T. A. M., Alderson, K. L., Alderson, A., & Scarpa, F. (2016). Double-Negative Mechanical Metamaterials Displaying Simultaneous Negative Stiffness and Negative Poisson's Ratio Properties. *Advanced Materials*, *28*(46), 10323–10332. https://doi.org/10.1002/adma.201603959

Hewage, T. A. M., Alderson, K. L., Alderson, A., Scarpa, F., M Hewage, T. A., Alderson, K. L., Alderson, A., Scarpa A M Hewage, F. T., Alderson, A., Alderson, K. L., Lane, P., & Scarpa, F. (2016). Double-Negative Mechanical Metamaterials Displaying Simultaneous Negative Stiffness and Negative Poisson's Ratio Properties. *Advanced Materials*, *28*(46), 10323–10332. https://doi.org/10.1002/adma.201603959

Hoag, G. E., Collins, J. B., Holcomb, J. L., Hoag, J. R., Nadagouda, M. N., & Varma, R. S. (2009). Degradation of bromothymol blue by "greener" nano-scale zero-valent iron synthesized using tea polyphenols. *Journal of Materials Chemistry*, *19*(45), 8671–8677. https://doi.org/10.1039/b909148c

Hong, X., Wen, J., Xiong, X., & Hu, Y. (2016). Shape effect on the antibacterial activity of silver nanoparticles synthesized via a microwave-assisted method. *Environmental*

Science and Pollution Research, *23*(5), 4489–4497. https://doi.org/10.1007/s11356-015-5668-z

Hostetler, M. J., Zhong, C. J., Yen, B. K. H., Anderegg, J., Gross, S. M., Evans, N. D., Porter, M., & Murray, R. W. (1998). Stable, monolayer-protected metal alloy clusters [18]. *Journal of the American Chemical Society*, *120*(36), 9396–9397. https://doi.org/10.1021/ja981454n

Hou, F., Xiao, S., & Wang, H. (2021). Mechanical properties characterization and zero Poisson's ratio design for perforated auxetic metamaterial by computational homogenized method. *Https://Doi.Org/10.1080/15376494.2021.2004268*. https://doi.org/10.1080/15376494.2021.2004268

Hou, S., Liu, T., Zhang, Z., Han, X., & Li, Q. (2015). How does negative Poisson's ratio of foam filler affect crashworthiness? *Materials and Design*, *82*, 247–259. https://doi.org/10.1016/j.matdes.2015.05.050

Hrennikoff, A. (1941). Solution of Problems of Elasticity by the Framework Method. *Journal of Applied Mechanics*, *8*(4), A169–A175. https://doi.org/10.1115/1.4009129

Hu, B., Wang, S. B., Wang, K., Zhang, M., & Yu, S. H. (2008). Microwave-assisted rapid facile "green" synthesis of uniform silver nanoparticles: Self-assembly into multilayered films and their optical properties. *Journal of Physical Chemistry C*, *112*(30), 11169–11174. https://doi.org/10.1021/jp801267j

Hu, L. L., Zhou, M. Z., & Deng, H. (2019). Dynamic indentation of auxetic and non-auxetic honeycombs under large deformation. *Composite Structures*, *207*(August 2018), 323–330. https://doi.org/10.1016/j.compstruct.2018.09.066

Huang, H.-H., Wong, B.-L., & Chou, Y.-C. (2016). Design and properties of 3D-printed chiral auxetic metamaterials by reconfigurable connections. *Physica Status Solidi (B)*, *253*(8), 1557–1564. https://doi.org/10.1002/pssb.201600027

Huang, J., Zhang, Q., Scarpa, F., Liu, Y., & Leng, J. (2017). In-plane elasticity of a novel auxetic honeycomb design. *Composites Part B-Engineering*, *110*, 72–82. https://doi.org/10.1016/j.compositesb.2016.11.011

Huang, K. C., & Ehrman, S. H. (2007). Synthesis of iron nanoparticles via chemical reduction with palladium ion seeds. *Langmuir*, *23*(3), 1419–1426. https://doi.org/10.1021/la0618364

Huang, L., Weng, X., Chen, Z., Megharaj, M., & Naidu, R. (2014a). Green synthesis of iron nanoparticles by various tea extracts: Comparative study of the reactivity. *Spectrochimica Acta - Part A: Molecular and Biomolecular Spectroscopy*, *130*, 295–301. https://doi.org/10.1016/j.saa.2014.04.037

Huang, L., Weng, X., Chen, Z., Megharaj, M., & Naidu, R. (2014b). Synthesis of iron-based nanoparticles using oolong tea extract for the degradation of malachite green. *Spectrochimica Acta - Part A: Molecular and Biomolecular Spectroscopy*, *117*, 801–804. https://doi.org/10.1016/j.saa.2013.09.054

Huber, D. L. (2005). Synthesis, properties, and applications of iron nanoparticles. *Small*, *1*(5), 482–501. https://doi.org/10.1002/smll.200500006

Huiskes, R., & Chao, E. Y. S. (1983). A survey of finite element analysis in orthopedic

biomechanics: The first decade. *Journal of Biomechanics*, *16*(6), 385–409. https://doi.org/10.1016/0021-9290(83)90072-6

Humud, H. R., Wasfi, A. S., & Makia, A. M. (2014). Preparation of Silver Nanoparticles by Exploding Wire in Different Liquids. *Asian Journal of Applied Science and Engineering*, *3*(7), 23. https://doi.org/10.15590/ajase/2014/v3i7/53572

Huo, J., Song, H., & Chen, X. (2004). Preparation of carbon-encapsulated iron nanoparticles by co-carbonization of aromatic heavy oil and ferrocene. *Carbon*, *42*(15), 3177–3182. https://doi.org/10.1016/j.carbon.2004.08.007

Hur, J. M., Seo, D. S., Kim, K., Lee, J. K., Lee, K. J., Kim, Y. Y., & Kim, D. N. (2021). Harnessing distinct deformation modes of auxetic patterns for stiffness design of tubular structures. *Materials & Design*, *198*, 109376. https://doi.org/10.1016/J.MATDES.2020.109376

Huynh, K. A., & Chen, K. L. (2011). Aggregation kinetics of citrate and polyvinylpyrrolidone coated silver nanoparticles in monovalent and divalent electrolyte solutions. *Environmental Science and Technology*, *45*(13), 5564–5571. https://doi.org/10.1021/es200157h

Hyeon, T., Su Seong Lee, Park, J., Chung, Y., & Hyon Bin Na. (2001). Synthesis of highly crystalline and monodisperse maghemite nanocrystallites without a size-selection process. *Journal of the American Chemical Society*, *123*(51), 12798–12801. https://doi.org/10.1021/ja016812s

Imbalzano, G., Tran, P., Ngo, T. D., & Lee, P. V. S. (2016). A numerical study of auxetic composite panels under blast loadings. *Composite Structures*, *135*, 339–352. https://doi.org/10.1016/j.compstruct.2015.09.038

Inoue, M., Hayashi, Y., Takizawa, H., & Suganuma, K. (2018). Nanoparticle fabrication. *Nanopackaging: Nanotechnologies and Electronics Packaging, Second Edition*, 219–242. https://doi.org/10.1007/978-3-319-90362-0_7

Iravani, S., Korbekandi, H., Mirmohammadi, S. V, & Zolfaghari, B. (2014). Synthesis of silver nanoparticles: Chemical, physical and biological methods. *Research in Pharmaceutical Sciences*, *9*(6), 385–406.

Irzh, A., Perkas, N., & Gedanken, A. (2007). Microwave-assisted coating of PMMA beads by silver nanoparticles. *Langmuir*, *23*(19), 9891–9897. https://doi.org/10.1021/la701385m

Ishibashi, Y., & Iwata, M. (2000). A microscopic model of a negative Poisson's ratio in some crystals. *Journal of the Physical Society of Japan*, *69*(8), 2702–2703. https://doi.org/10.1143/JPSJ.69.2702

Islam, M. N., Abbas, M., & Kim, C. (2013). Synthesis of monodisperse and high moment nickel-iron (NiFe) nanoparticles using modified polyol process. *Current Applied Physics*, *13*(9), 2010–2013. https://doi.org/10.1016/j.cap.2013.08.020

Jackson, J. A., Messner, M. C., Dudukovic, N. A., Smith, W. L., Bekker, L., Moran, B., Golobic, A. M., Pascall, A. J., Duoss, E. B., Loh, K. J., & Spadaccini, C. M. (2018). Field responsive mechanical metamaterials. *Science Advances*, *4*(12), 1–10. https://doi.org/10.1126/sciadv.aau6419

Jafari, T., Simchi, A., & Khakpash, N. (2010). Synthesis and cytotoxicity assessment of

superparamagnetic iron-gold core-shell nanoparticles coated with polyglycerol. *Journal of Colloid and Interface Science*, *345*(1), 64–71. https://doi.org/10.1016/j.jcis.2010.01.038

Jaglinski, T. M., & Lakes, R. S. (2007). Negative Stiffness and Negative Poisson's Ratio in Materials which Undergo a Phase Transformation. *Adaptive Structures: Engineering Applications*, 231–246. https://doi.org/10.1002/9780470512067.ch8

Jain, N., Bhosale, P., Tale, V., Henry, R., & Pawar, J. (2019). Hydrothermal assisted biological synthesis of silver nanoparticles by using honey and gomutra (Cow urine) for qualitative determination of its antibacterial efficacy against pseudomonas sp.isolated from contact lenses. *EurAsian Journal of BioSciences*, *13*(1), 27–33.

Jaiswal, J., Tiwari, P., & Chandra, R. (2020). Tunable plasmonic properties of silver nanoparticles embedded in amorphous-carbon ultrathin films deposited by co-sputtering. *3Rd International Conference on Condensed Matter and Applied Physics (Icc-2019)*, *2220*. https://doi.org/10.1063/5.0001149

Jana, N. R., Gearheart, L., & Murphy, C. J. (2001). Wet chemical synthesis of silver nanorods and nanowires of controllable aspect ratio. *Chemical Communications*, *7*, 617–618. https://doi.org/10.1039/b100521i

Jia, X., Yao, Y., Yu, G., Qu, L., Li, T., Li, Z., & Xu, C. (2020). Synthesis of gold-silver nanoalloys under microwave-assisted irradiation by deposition of silver on gold nanoclusters/triple helix glucan and antifungal activity. *Carbohydrate Polymers*, *238*(November 2019), 116169. https://doi.org/10.1016/j.carbpol.2020.116169

Jianbao, L., Wang, Y. S., & Zhang, C. (2008). Finite element method for analysis of band structures of three dimensonal phononic crystals. *Proceedings - IEEE Ultrasonics Symposium*, 1468–1471. https://doi.org/10.1109/ULTSYM.2008.0357

Jiang, H., Moon, K. S., Zhang, Z., Pothukuchi, S., & Wong, C. P. (2006). Variable frequency microwave synthesis of silver nanoparticles. *Journal of Nanoparticle Research*, *8*(1), 117–124. https://doi.org/10.1007/s11051-005-7522-6

Jiang, H., Ren, Y., Jin, Q., Zhu, G., Hu, Y., & Cheng, F. (2020). Crashworthiness of novel concentric auxetic reentrant honeycomb with negative Poisson ' s ratio biologically inspired by coconut palm. *Thin-Walled Structures*, *154*(June), 106911. https://doi.org/10.1016/j.tws.2020.106911

Jiang, L., & Hu, H. (2017). Low-velocity impact response of multilayer orthogonal structural composite with auxetic effect. *Composite Structures*, *169*, 62–68. https://doi.org/10.1016/j.compstruct.2016.10.018

Jiang, S. X., Qin, W. F., Guo, R. H., & Zhang, L. (2010). Surface functionalization of nanostructured silver-coated polyester fabric by magnetron sputtering. *Surface and Coatings Technology*, *204*(21–22), 3662–3667. https://doi.org/10.1016/j.surfcoat.2010.04.042

Jiang, X. C., Chen, W. M., Chen, C. Y., Xiong, S. X., & Yu, A. B. (2011). Role of Temperature in the Growth of Silver Nanoparticles Through a Synergetic Reduction Approach. *Nanoscale Research Letters*, *6*(1), 1–9. https://doi.org/10.1007/s11671-010-9780-1

Joseph, S., & Mathew, B. (2015). Microwave-assisted green synthesis of silver

nanoparticles and the study on catalytic activity in the degradation of dyes. *Journal of Molecular Liquids*, *204*, 184–191. https://doi.org/10.1016/j.molliq.2015.01.027

Ju, J., & Summers, J. D. (2011). Compliant hexagonal periodic lattice structures having both high shear strength and high shear strain. *Materials & Design*, *32*(2), 512–524. https://doi.org/10.1016/J.MATDES.2010.08.029

Juknius, T., Ružauskas, M., Tamulevičius, T., Šiugždiniene, R., Jukniene, I., Vasiliauskas, A., Jurkevičiute, A., & Tamulevičius, S. (2016). Antimicrobial Properties of Diamond-Like Carbon/Silver Nanocomposite Thin Films Deposited on Textiles: Towards Smart Bandages. *Materials 2016, Vol. 9, Page 371*, *9*(5), 371. https://doi.org/10.3390/MA9050371

Jung, J. H., Cheol Oh, H., Soo Noh, H., Ji, J. H., & Soo Kim, S. (2006). Metal nanoparticle generation using a small ceramic heater with a local heating area. *Journal of Aerosol Science*, *37*(12), 1662–1670. https://doi.org/10.1016/j.jaerosci.2006.09.002

Kądzioła, K., Piwoński, I., Kisielewska, A., Szczukocki, D., Krawczyk, B., & Sielski, J. (2014). The photoactivity of titanium dioxide coatings with silver nanoparticles prepared by sol-gel and reactive magnetron sputtering methods - Comparative studies. *Applied Surface Science*, *288*, 503–512. https://doi.org/10.1016/j.apsusc.2013.10.061

Kahrilas, G. A., Wally, L. M., Fredrick, S. J., Hiskey, M., Prieto, A. L., & Owens, J. E. (2014). Microwave-assisted green synthesis of silver nanoparticles using orange peel extract. *ACS Sustainable Chemistry and Engineering*, *2*(3), 367–376. https://doi.org/10.1021/sc4003664

Kandarp Mavani, M. S. (2013). Synthesis of Silver Nanoparticles by using Sodium Borohydride as a Reducing Agent. *International Journal of Engineering Research and Technology*, *2*(4), 388–397. https://doi.org/10.13140/2.1.3116.8648

Kanel, S. R., Manning, B., Charlet, L., & Choi, H. (2005). Removal of arsenic(III) from groundwater by nanoscale zero-valent iron. *Environmental Science and Technology*, *39*(5), 1291–1298. https://doi.org/10.1021/es048991u

Kapoor, S. (2000). Effect of ligand on the redox reactions of thallium metal clusters. *Langmuir*, *16*(12), 5496–5498. https://doi.org/10.1021/la991064u

Kassaee, M. Z., Motamedi, E., Mikhak, A., & Rahnemaie, R. (2011). Nitrate removal from water using iron nanoparticles produced by arc discharge vs. reduction. *Chemical Engineering Journal*, *166*(2), 490–495. https://doi.org/10.1016/j.cej.2010.10.077

Kasthuri, J., Veerapandian, S., & Rajendiran, N. (2009). Biological synthesis of silver and gold nanoparticles using apiin as reducing agent. *Colloids and Surfaces B: Biointerfaces*, *68*(1), 55–60. https://doi.org/10.1016/j.colsurfb.2008.09.021

Kavakli, H. S., & Ali, D. (2023). Enhancing the Mechanical Properties of Auxetic Metamaterials by Incorporating Nonrectangular Cross Sections into Their Component Rods: A Finite Element Analysis. *Physica Status Solidi (B)*, *260*(3), 2200194. https://doi.org/10.1002/PSSB.202200194

Kays, B. T., & Smith, L. V. (2017). Effect of ice hockey stick stiffness on performance. *Sports Engineering*, *20*(4), 245–254. https://doi.org/10.1007/S12283-017-0232-

3/FIGURES/14

Kelsen, V., Wendt, B., Werkmeister, S., Junge, K., Beller, M., & Chaudret, B. (2013). The use of ultrasmall iron(0) nanoparticles as catalysts for the selective hydrogenation of unsaturated C-C bonds. *Chemical Communications*, *49*(33), 3416–3418. https://doi.org/10.1039/c3cc00152k

Khadem-Reza, L., Etemadi, E., Abbaslou, M., & Hu, H. (2022). Design of novel 3D auxetic structures based on S-shaped unit-cells. *Smart Materials and Structures*, *31*(7), 075024. https://doi.org/10.1088/1361-665X/AC7681

Khan, A., El-Toni, A. M., Alrokayan, S., Alsalhi, M., Alhoshan, M., & Aldwayyan, A. S. (2011). Microwave-assisted synthesis of silver nanoparticles using poly-N-isopropylacrylamide/acrylic acid microgel particles. *Colloids and Surfaces A: Physicochemical and Engineering Aspects*, *377*(1–3), 356–360. https://doi.org/10.1016/j.colsurfa.2011.01.042

Khan, S. Z., Mustahsan, F., Mahmoud, E. R. I., & Masood, S. H. (2019). A novel modified re-entrant honeycomb structure to enhance the auxetic behavior: Analytical and numerical study by FEA. *Materials Today: Proceedings*, *39*(xxxx), 1041–1045. https://doi.org/10.1016/j.matpr.2020.05.083

Khan, Z., Al-Thabaiti, S. A., Obaid, A. Y., & Al-Youbi, A. O. (2011). Preparation and characterization of silver nanoparticles by chemical reduction method. *Colloids and Surfaces B: Biointerfaces*, *82*(2), 513–517. https://doi.org/10.1016/j.colsurfb.2010.10.008

Khandel, P., & Kumar Shahi, S. (2016). Microbes mediated synthesis of metal nanoparticles: current status and future prospects. *International Journal of Nanomaterials and Biostructures*, *6*(1), 1–24.

Khanna, P. K., Singh, N., Charan, S., Subbarao, V. V. V. S., Gokhale, R., & Mulik, U. P. (2005). Synthesis and characterization of Ag/PVA nanocomposite by chemical reduction method. *Materials Chemistry and Physics*, *93*(1), 117–121. https://doi.org/10.1016/j.matchemphys.2005.02.029

Khayati, G. R., & Janghorban, K. (2012). The nanostructure evolution of Ag powder synthesized by high energy ball milling. *Advanced Powder Technology*, *23*(3), 393–397. https://doi.org/10.1016/j.apt.2011.05.005

Kim, D., Jeong, S., & Moon, J. (2006). Synthesis of silver nanoparticles using the polyol process and the influence of precursor injection. *Nanotechnology*, *17*(16), 4019–4024. https://doi.org/10.1088/0957-4484/17/16/004

Kim, D., Park, J., An, K., Yang, N. K., Park, J. G., & Hyeon, T. (2007). Synthesis of hollow iron nanoframes. *Journal of the American Chemical Society*, *129*(18), 5812–5813. https://doi.org/10.1021/ja070667m

Kim, K. Do, Han, D. N., Lee, J. B., & Kim, H. T. (2006). Formation and characterization of Ag-deposited TiO2 nanoparticles by chemical reduction method. *Scripta Materialia*, *54*(2), 143–146. https://doi.org/10.1016/j.scriptamat.2005.09.054

Kim, J. S., Kuk, E., Yu, K. N., Kim, J. H., Park, S. J., Lee, H. J., Kim, S. H., Park, Y. K., Park, Y. H., Hwang, C. Y., Kim, Y. K., Lee, Y. S., Jeong, D. H., & Cho, M. H. (2007). Antimicrobial effects of silver nanoparticles. *Nanomedicine:*

Nanotechnology, Biology, and Medicine, *3*(1), 95–101. https://doi.org/10.1016/j.nano.2006.12.001

Kim, J., Shin, D., Yoo, D.-S., & Kim, K. (2017). Regularly configured structures with polygonal prisms for three-dimensional auxetic behaviour. *Proceedings of the Royal Society A: Mathematical, Physical and Engineering Sciences*, *473*(2202). https://doi.org/10.1098/rspa.2016.0926

Kim, Y., Son, K., & Lee, J. (2021). Auxetic structures for tissue engineering scaffolds and biomedical devices. *Materials*, *14*(22), 1–17. https://doi.org/10.3390/ma14226821

Kim, Y., Yuk, H., Zhao, R., Chester, S. A., & Zhao, X. (2018). Printing ferromagnetic domains for untethered fast-transforming soft materials. *Nature*, *558*(7709), 274–279. https://doi.org/10.1038/s41586-018-0185-0

Kittinger, E., Tichý, J., & Bertagnolli, E. (1981). Example of a Negative Effective Poisson's Ratio. *Physical Review Letters*, *47*(10), 712–714. https://doi.org/10.1103/PhysRevLett.47.712

Klačanová, K., Fodran, P., Šimon, P., Rapta, P., Boča, R., Jorík, V., Miglierini, M., Kolek, E., & Čaplovič, L. (2013). Formation of Fe(0)-nanoparticles via reduction of Fe(II) compounds by amino acids and their subsequent oxidation to iron oxides. *Journal of Chemistry*, *Ii*. https://doi.org/10.1155/2013/961629

Koltypin, Y., Perkas, N., & Gedanken, A. (2004). Commercial edible oils as new solvents for ultrasonic synthesis of nanoparticles: The preparation of air stable nanocrystalline iron particles. *Journal of Materials Chemistry*, *14*(20), 2975–2977. https://doi.org/10.1039/b411983e

Kotov, Y. A. (2003). Electric explosion of wires as a method for preparation of nanopowders. *Journal of Nanoparticle Research*, *5*(5–6), 539–550. https://doi.org/10.1023/B:NANO.0000006069.45073.0b

Kotov, Y. A., Samatov, O. M., Rhee, C. K., Murzakaev, A. M., Timoshenkova, O. R., Medvedev, A. I., & Shtolts, A. K. (2003). Nanopowders prepared by simultaneous electrical explosion of Al and Fe wires. *Proc. of 10th APAM Topical Seminar and 3rd Conf. 'Materials of Siberia, Nanoscience and Technology'','* 128–130.

Koutsianitis, P. I., Tairidis, G. K., Drosopoulos, G. A., & Stavroulakis, G. E. (2019). Conventional and star-shaped auxetic materials for the creation of band gaps. *Archive of Applied Mechanics*, *89*(12), 2545–2562. https://doi.org/10.1007/s00419-019-01594-1

Koutsianitis, P. I., Tairidis, G. K., & Stavroulakis, G. E. (2021). Shunted piezoelectric patches on auxetic microstructures for the enhancement of band gaps. *Archive of Applied Mechanics*, *91*(2), 739–751. https://doi.org/10.1007/s00419-020-01804-1

Krämer, J., Redel, E., Thomann, R., & Janiak, C. (2008). Supporting Information for Use of ionic liquids for the synthesis of Fe , Ru and Os nanoparticles from their metal carbonyl precursors. *Organometallics*, *3*, 1976–1978. https://doi.org/10.1021/om800056z

Krödel, S., Delpero, T., Bergamini, A., Ermanni, P., & Kochmann, D. M. (2014). 3D Auxetic Microlattices with Independently Controllable Acoustic Band Gaps and

Quasi-Static Elastic Moduli. *Advanced Engineering Materials*, *16*(4), 357–363. https://doi.org/10.1002/ADEM.201300264

Kumar, S., & Sardana, S. K. (2020). Optical Properties of Silver Nanoparticles Deposited on Glass and Silicon Substrates. *AIP Conference Proceedings*.

Kundu, S., Wang, K., & Liang, H. (2009). Size-controlled synthesis and self-assembly of silver nanoparticles within a minute using microwave irradiation. *Journal of Physical Chemistry C*, *113*(1), 134–141. https://doi.org/10.1021/jp808292s

Kurihara, L. K., Chow, G. M., & Schoen, P. E. (1995). Nanocrystalline metallic powders and films produced by the polyol method. *Nanostructured Materials*, *5*(6), 607–613. https://doi.org/10.1016/0965-9773(95)00275-J

Kvítek, L., Panáček, A., Soukupová, J., Kolář, M., Večeřová, R., Prucek, R., Holecová, M., & Zbořil, R. (2008). Effect of surfactants and polymers on stability and antibacterial activity of silver nanoparticles (NPs). *Journal of Physical Chemistry C*, *112*(15), 5825–5834. https://doi.org/10.1021/jp711616v

Lacroix, L. M., Lachaize, S., Falqui, A., Blon, T., Carrey, J., Respaud, M., Dumestre, F., Amiens, C., Margeat, O., Chaudret, B., Lecante, P., & Snoeck, E. (2008). Ultrasmall iron nanoparticles: Effect of size reduction on anisotropy and magnetization. *Journal of Applied Physics*, *103*(7), 7–10. https://doi.org/10.1063/1.2837625

Lahoz, R., Natividad, E., Mayoral, Á., Rentenberger, C., Díaz-Fernández, D., Félix, E. J., Soriano, L., Kautek, W., & Bomati-Miguel, O. (2020). Pursuit of optimal synthetic conditions for obtaining colloidal zero-valent iron nanoparticles by scanning pulsed laser ablation in liquids. *Journal of Industrial and Engineering Chemistry*, *81*, 340–351. https://doi.org/10.1016/j.jiec.2019.09.024

Lakes, R. (1987). Foam structures with a negative Poisson's ratio. *Science*, *235*, 1038–1040. https://doi.org/10.1126/science.235.4792.1038

Lakes, R. S. (1991). Deformation mechanisms in negative Poisson's ratio materials: structural aspects. *Journal of Materials Science*, *26*(9), 2287–2292. https://doi.org/10.1007/BF01130170

Lakes, R. S., & Elms, K. (1993). Indentability of Conventional and Negative Poisson's Ratio Foams. *Journal of Composite Materials*, *27*(12), 1193–1202. https://doi.org/10.1177/002199839302701203

Larsen, U. D., Sigmund, O., & Bouwstra, S. (1997). Design and fabrication of compliant micromechanisms and structures with negative Poisson's ratio. *Journal of Microelectromechanical Systems*, *6*(2), 99–106. https://doi.org/10.1109/84.585787

Laurent, S., Forge, D., Port, M., Roch, A., Robic, C., Vander Elst, L., & Muller, R. N. (2010). Erratum: Magnetic iron oxide nanoparticles: Synthesis, stabilization, vectorization, physicochemical characterizations, and biological applications (Chemical Reviews (2008) 108 (2064)). *Chemical Reviews*, *110*(4), 2574. https://doi.org/10.1021/cr900197g

Lee, D. Y., Lee, K. H., Kim, B. Y., & Cho, N. I. (2010). Silver nanoparticles dispersed in electrospun polyacrylonitrile nanofibers via chemical reduction. *Journal of Sol-Gel Science and Technology*, *54*(1), 63–68. https://doi.org/10.1007/s10971-010-2158-0

Lee, G. J., Shin, S. Il, Kim, Y. C., & Oh, S. G. (2004). Preparation of silver nanorods

through the control of temperature and pH of reaction medium. *Materials Chemistry and Physics*, *84*(2–3), 197–204. https://doi.org/10.1016/j.matchemphys.2003.11.024

Lee, J., Choi, J. B., & Choi, K. (1996). Application of homogenization FEM analysis to regular and re-entrant honeycomb structures. *Journal of Materials Science*, *31*(February 1996), 4105–4110. https://doi.org/10.1007/BF00352675

Lee, J. M., Kim, D. W., Jun, Y. D., & Oh, S. G. (2006). Preparation of silica-silver heterogeneous nanocomposite particles by one-pot preparation strategy using polyol process: Size-controlled immobilization of silver nanoparticles. *Materials Research Bulletin*, *41*(8), 1407–1416. https://doi.org/10.1016/j.materresbull.2006.02.010

Lee, K. J., Nallathamby, P. D., Browning, L. M., Osgood, C. J., & Xu, X.-H. N. (2017). In Vivo Imaging of Transport and Biocompatibility of Single Silver Nanoparticles in Early Development of Zebrafish Embryos. *PLoS ONE*, *32*(7), 736–740. https://doi.org/10.1371/journal.pone.0178059

Lee, P. C., & Meisel, D. (1982). Adsorption and surface-enhanced Raman of dyes on silver and gold sols. *Journal of Physical Chemistry*, *86*(17), 3391–3395. https://doi.org/10.1021/j100214a025

Lee, S. M., Song, K. C., & Lee, B. S. (2010). Antibacterial activity of silver nanoparticles prepared by a chemical reduction method. *Korean Journal of Chemical Engineering*, *27*(2), 688–692. https://doi.org/10.1007/s11814-010-0067-0

Lee, Y. C., Chen, S. J., & Huang, C. L. (2010). Finding a facile method to synthesize decahedral silver nanoparticles through a systematic study of temperature effect on photomediated silver nanostructure growth. *Journal of the Chinese Chemical Society*, *57*(3 A), 325–331. https://doi.org/10.1002/jccs.201000048

Lee, Y. T., Im, S. H., Wiley, B., & Xia, Y. (2005). Quick formation of single-crystal nanocubes of silver through dual functions of hydrogen gas in polyol synthesis. *Chemical Physics Letters*, *411*(4–6), 479–483. https://doi.org/10.1016/j.cplett.2005.06.080

Lendlein, A., Jiang, H., Jünger, O., & Langer, R. (2005). Light-induced shape-memory polymers. *Nature 2005 434:7035*, *434*(7035), 879–882. https://doi.org/10.1038/nature03496

Li, C., Shen, H. S., & Wang, H. (2021). Full-scale finite element modeling and nonlinear bending analysis of sandwich plates with functionally graded auxetic 3D lattice core. *Journal of Sandwich Structures and Materials*, *23*(7), 3113–3138. https://doi.org/10.1177/1099636220924657/ASSET/IMAGES/LARGE/10.1177_1099636220924657-FIG11.JPEG

Li, C., Shen, H. S., Wang, H., & Yu, Z. (2020). Large amplitude vibration of sandwich plates with functionally graded auxetic 3D lattice core. *International Journal of Mechanical Sciences*, *174*(November 2019), 105472. https://doi.org/10.1016/j.ijmecsci.2020.105472

Li, J., & Fang, Y. (2007). An investigation of the surface enhanced Raman scattering (SERS) from a new substrate of silver-modified silver electrode by magnetron sputtering. *Spectrochimica Acta - Part A: Molecular and Biomolecular Spectroscopy*, *66*(4–5), 994–1000. https://doi.org/10.1016/j.saa.2006.05.012

Li, J. M., Ma, W. F., Wei, C., You, L. J., Guo, J., Hu, J., & Wang, C. C. (2011). Detecting trace melamine in solution by SERS using Ag nanoparticle coated poly(styrene-co-acrylic acid) nanospheres as novel active substrates. *Langmuir*, *27*(23), 14539–14544. https://doi.org/10.1021/la203049k

Li, J., Wang, Y. S., & Zhang, C. (2009). Finite element method for analysis of band structures of phononic crystal slabs with archimedean-like tilings. *Proceedings - IEEE Ultrasonics Symposium*, 1548–1551. https://doi.org/10.1109/ULTSYM.2009.5442087

Li, L., Fan, M., Brown, R., Leeuwen, J., Wang, J., Wang, W., Song, Y., & Zhang, P. (2006). Synthesis, properties and environmental applications of nanoscale iron-based materials: A review. *Comments on Inorganic Chemistry*, *27*(1–2), 1–32. https://doi.org/10.1080/02603590500496721

Li, Q., Kuang, Y., & Zhu, M. (2017). Auxetic piezoelectric energy harvesters for increased electric power output. *AIP Advances*, *7*(1). https://doi.org/10.1063/1.4974310

Li, S., Yan, W., & Zhang, W. X. (2009). Solvent-free production of nanoscale zero-valent iron (nZVI) with precision milling. *Green Chemistry*, *11*(10), 1618–1626. https://doi.org/10.1039/b913056j

Li, T., Liu, F., & Wang, L. (2020a). Chan. *Composites Part B: Engineering*, *198*, 108229. https://doi.org/10.1016/j.compositesb.2020.108229

Li, T., Liu, F., & Wang, L. (2020b). Enhancing indentation and impact resistance in auxetic composite materials. *Composites Part B*, *198*(June), 108229. https://doi.org/10.1016/j.compositesb.2020.108229

Li, W., Camargo, P. H. C., Lu, X., & Xia, Y. (2009). Dimers of silver nanospheres: Facile synthesis and their use as hot spots for surface-enhanced raman scattering. *Nano Letters*, *9*(1), 485–490. https://doi.org/10.1021/nl803621x

Li, X., Fan, R., Fan, Z., & Lu, Y. (2021). Programmable mechanical metamaterials based on hierarchical rotating structures. *International Journal of Solids and Structures*, *216*, 145–155. https://doi.org/10.1016/J.IJSOLSTR.2021.01.028

Li, X. Q., & Zhang, W. X. (2006). Iron nanoparticles: The core-shell structure and unique properties for Ni(II) sequestration. *Langmuir*, *22*(10), 4638–4642. https://doi.org/10.1021/la060057k

Li, X. Q., & Zhang, W. X. (2007). Sequestration of metal cations with zerovalent iron nanoparticles - A study with high resolution x-ray photoelectron spectroscopy (HR-XPS). *Journal of Physical Chemistry C*, *111*(19), 6939–6946. https://doi.org/10.1021/jp0702189

Li, Y., Wu, Y., & Ong, B. S. (2005). Facile synthesis of silver nanoparticles useful for fabrication of high-conductivity elements for printed electronics. *Journal of the American Chemical Society*, *127*(10), 3266–3267. https://doi.org/10.1021/ja043425k

Li, Z.-Y. Y., Wang, X.-T. T., Ma, L., Wu, L.-Z. Z., & Wang, L. (2023). Auxetic and failure characteristics of composite stacked origami cellular materials under compression. *Thin-Walled Structures*, *184*, 110453.

https://doi.org/10.1016/j.tws.2022.110453

Li, Z., Gao, Q., Yang, S., Wang, L., & Tang, J. (2019). Comparative study of the in-plane uniaxial and biaxial crushing of hexagonal, re-entrant, and mixed honeycombs. *Journal of Sandwich Structures & Materials*, *21*(6), 1991–2013. https://doi.org/10.1177/1099636218755294

Li, Z., Wang, K. F., & Wang, B. L. (2021). Indentation resistance of brittle auxetic structures : Combining discrete representation and continuum model. *Engineering Fracture Mechanics*, *252*(November 2020), 107824. https://doi.org/10.1016/j.engfracmech.2021.107824

Li, Z. Y., Wang, X. T., Ma, L., & Wu, L. Z. (2022). Study on the mechanical properties of CFRP composite auxetic structures consist of corrugated sheets and tubes. *Composite Structures*, *292*(December 2021). https://doi.org/10.1016/j.compstruct.2022.115655

Liang, X., Ali, M. Z., & Zhang, H. (2020). Induction motors fault diagnosis using finite element method: A review. *IEEE Transactions on Industry Applications*, *56*(2), 1205–1217. https://doi.org/10.1109/TIA.2019.2958908

Liang, X., Fu, H., & Crosby, A. J. (2022). Phase-transforming metamaterial with magnetic interactions. *Proceedings of the National Academy of Sciences of the United States of America*, *119*(1), e2118161119. https://doi.org/10.1073/PNAS.2118161119/SUPPL_FILE/PNAS.2118161119.SM05.MP4

Liang, Y. C., & Deng, X. S. (2013). Structure dependent luminescence evolution of c-axis-oriented ZnO nanofilms embedded with silver nanoparticles and clusters prepared by sputtering. *Journal of Alloys and Compounds*, *569*, 144–149. https://doi.org/10.1016/j.jallcom.2013.03.169

Liaqat, M., Samad, H. A., Hamdani, S. T. A., & Nawab, Y. (2017). The development of novel auxetic woven structure for impact applications. *Journal of the Textile Institute*, *108*(7), 1264–1270. https://doi.org/10.1080/00405000.2016.1239330

Lim, T. C. (2019). Composite metamaterial with sign-switchable coefficients of hygroscopic, thermal and pressure expansions. *Advanced Composites and Hybrid Materials*, *2*, 657–669. https://doi.org/10.1007/s42114-019-00118-3

Lin, J. Y., Hsueh, Y. L., & Huang, J. J. (2014). The concentration effect of capping agent for synthesis of silver nanowire by using the polyol method. *Journal of Solid State Chemistry*, *214*, 2–6. https://doi.org/10.1016/j.jssc.2013.12.017

Lin, J., Zhou, W., Kumbhar, A., Wiemann, J., Fang, J., Carpenter, E. E., & O'Connor, C. J. (2001). Gold-coated iron (Fe@Au) nanoparticles: Synthesis, characterization, and magnetic field-induced self-assembly. *Journal of Solid State Chemistry*, *159*(1), 26–31. https://doi.org/10.1006/jssc.2001.9117

Linforth, S., Ngo, T., Tran, P., Ruan, D., & Odish, R. (2021). Investigation of the auxetic oval structure for energy absorption through quasi-static and dynamic experiments. *International Journal of Impact Engineering*, *147*, 103741.

Ling, X., Li, J., Zhu, W., Zhu, Y., Sun, X., Shen, J., Han, W., & Wang, L. (2012). Synthesis of nanoscale zero-valent iron/ordered mesoporous carbon for adsorption

and synergistic reduction of nitrobenzene. *Chemosphere*, *87*(6), 655–660. https://doi.org/10.1016/j.chemosphere.2012.02.002

Liou, Y. H., Lo, S. L., Kuan, W. H., Lin, C. J., & Weng, S. C. (2006). Effect of precursor concentration on the characteristics of nanoscale zerovalent iron and its reactivity of nitrate. *Water Research*, *40*(13), 2485–2492. https://doi.org/10.1016/j.watres.2006.04.048

Liu, J., Li, X., & Zeng, X. (2010). Silver nanoparticles prepared by chemical reduction-protection method, and their application in electrically conductive silver nanopaste. *Journal of Alloys and Compounds*, *494*(1–2), 84–87. https://doi.org/10.1016/j.jallcom.2010.01.079

Liu, J., & Liu, H. (2022). Energy absorption characteristics and stability of novel bionic negative Poisson ' s ratio honeycomb under oblique compression. *Engineering Structures*, *267*, 114682. https://doi.org/10.1016/j.engstruct.2022.114682

Liu, P., & Zhao, M. (2009). Silver nanoparticle supported on halloysite nanotubes catalyzed reduction of 4-nitrophenol (4-NP). *Applied Surface Science*, *255*(7), 3989–3993. https://doi.org/10.1016/j.apsusc.2008.10.094

Liu, W., Wang, N., Luo, T., & Lin, Z. (2016). In-plane dynamic crushing of re-entrant auxetic cellular structure. *MATERIALS & DESIGN*, *100*, 84–91. https://doi.org/10.1016/j.matdes.2016.03.086

Liu, Y., Goebl, J., & Yin, Y. (2013). Templated synthesis of nanostructured materials. *Chemical Society Reviews*, *42*(7), 2610–2653. https://doi.org/10.1039/c2cs35369e

Logakannan, K. P., Ramachandran, V., Rengaswamy, J., Gao, Z., & Ruan, D. (2020). Quasi-static and dynamic compression behaviors of a novel auxetic structure. *Composite Structures*, *254*(July), 112853. https://doi.org/10.1016/j.compstruct.2020.112853

Logakannan, K. P., Ramachandran, V., Rengaswamy, J., & Ruan, D. (2022). Stiffened star-shaped auxetic structure with tri-directional symmetry. *Composite Structures*, *279*, 114773. https://doi.org/10.1016/J.COMPSTRUCT.2021.114773

Lorato, A., Innocenti, P., Scarpa, F., Alderson, A., Alderson, K. L., Zied, K. M., Ravirala, N., Miller, W., Smith, C. W., & Evans, K. E. (2010). The transverse elastic properties of chiral honeycombs. *Composites Science and Technology*, *70*(7), 1057–1063. https://doi.org/10.1016/J.COMPSCITECH.2009.07.008

Lozhkomoev, A. S., Kazantsev, S. O., Pervikov, A. V, Fomenko, A. N., & Gotman, I. (2019). New approach to production of antimicrobial Al2O3-Ag nanocomposites by electrical explosion of two wires. *Materials Research Bulletin*, *119*(July). https://doi.org/10.1016/j.materresbull.2019.110545

Lu, H., Wang, X., & Chen, T. (2021). In-plane dynamics crushing of a combined auxetic honeycomb with negative Poisson ' s ratio and enhanced energy absorption. *Thin-Walled Structures*, *160*(November 2020), 107366. https://doi.org/10.1016/j.tws.2020.107366

Lu, L., Wang, H., Zhou, Y., Xi, S., Zhang, H., Hu, J., & Zhao, B. (2002). Seed-mediated growth of large, monodisperse core-shell gold-silver nanoparticles with Ag-like optical properties. *Chemical Communications*, *2*(2), 144–145.

https://doi.org/10.1039/b108473a

Lu, Z., Li, X., Yang, Z., & Xie, F. (2016). *Novel structure with negative Poisson ' s ratio and enhanced Young ' s modulus*. *138*, 243–252. https://doi.org/10.1016/j.compstruct.2015.11.036

Lum, G. Z., Ye, Z., Dong, X., Marvi, H., Erin, O., Hu, W., & Sitti, M. (2016). Shape-programmable magnetic soft matter. *Proceedings of the National Academy of Sciences of the United States of America*, *113*(41), E6007--E6015. https://doi.org/10.1073/pnas.1608193113

Luo, S., Yang, S., Sun, C., & Gu, J. D. (2012). Improved debromination of polybrominated diphenyl ethers by bimetallic iron-silver nanoparticles coupled with microwave energy. *Science of the Total Environment*, *429*, 300–308. https://doi.org/10.1016/j.scitotenv.2012.04.051

Lvov, V. A., Senatov, F. S., Korsunsky, A. M., & Salimon, A. I. (2020). Design and mechanical properties of 3D-printed auxetic honeycomb structure. *Materials Today Communications*, *24*, 101173. https://doi.org/10.1016/J.MTCOMM.2020.101173

Lyngdoh, G. A., Kelter, N. K., Doner, S., Krishnan, N. M. A., & Das, S. (2022). Elucidating the auxetic behavior of cementitious cellular composites using finite element analysis and interpretable machine learning. *Materials and Design*, *213*(April). https://doi.org/10.1016/j.matdes.2021.110341

M.C. Daniel, D. A. (2004). Gold nanoparticles: assembly, supramolecularchemistry, quantum-size-related properties, and applications toward. *Chem. Rev.*, *104*, 293–346.

Ma, C., Chang, Y., Wu, S., & Zhao, R. R. (2022). Deep Learning-Accelerated Designs of Tunable Magneto-Mechanical Metamaterials. *ACS Applied Materials and Interfaces*. https://doi.org/10.1021/ACSAMI.2C09052/SUPPL_FILE/AM2C09052_SI_001.PDF

Ma, P., Chang, Y., Boakye, A., & Jiang, G. (2017). Review on the knitted structures with auxetic effect. *The Journal of The Textile Institute*. https://doi.org/10.1080/00405000.2016.1204901

Ma, Y., Scarpa, F., Zhang, D., Zhu, B., Chen, L., & Hong, J. (2013). A nonlinear auxetic structural vibration damper with metal rubber particles. *Smart Materials and Structures*, *22*(8). https://doi.org/10.1088/0964-1726/22/8/084012

Mahmudin, L., Suharyadi, E., Utomo, A. B. S., & Abraha, K. (2015). Optical Properties of Silver Nanoparticles for Surface Plasmon Resonance (SPR)-Based Biosensor Applications. *Journal of Modern Physics*, *06*(08), 1071–1076. https://doi.org/10.4236/jmp.2015.68111

Maliszewska, I., Szewczyk, K., & Waszak, K. (2009). Biological synthesis of silver nanoparticles. *Journal of Physics: Conference Series*, *146*. https://doi.org/10.1088/1742-6596/146/1/012025

Margeat, O., Dumestre, F., Amiens, C., Chaudret, B., Lecante, P., & Respaud, M. (2005). Synthesis of iron nanoparticles: Size effects, shape control and organisation. *Progress in Solid State Chemistry*, *33*(2-4 SPEC. ISS.), 71–79.

https://doi.org/10.1016/j.progsolidstchem.2005.11.002

Marsich, L., Bonifacio, A., Mandal, S., Krol, S., Beleites, C., & Sergo, V. (2012). Poly-L-lysine-coated silver nanoparticles as positively charged substrates for surface-enhanced Raman scattering. *Langmuir*, *28*(37), 13166–13171. https://doi.org/10.1021/la302383r

Masters, I. G., & Evans, K. E. (1996). Models for the elastic deformation of honeycombs. *Composite Structures*, *35*(4), 403–422. https://doi.org/10.1016/S0263-8223(96)00054-2

Maurya, K. C., Caligiuri, V., Pillai, A. I. K., Garbrecht, M., Krahne, R., & Saha, B. (2023). Radiative volume plasmon and phonon-polariton resonances in TiN-based plasmonic/polar-dielectric hyperbolic optical metamaterials. *Applied Physics Letters*, *122*(22). https://doi.org/10.1063/5.0150185/2893932

Mazzonello, A., Valdramidis, V. P., Grima, J., Gatt, R., & Farrugia, C. (2015). Synthesis and Characterization of Silver Nanoparticles. *Materials Science Forum*, *802*(April), 135–139. https://doi.org/10.4028/www.scientific.net/msf.802.135

McFarland, A. D., & Van Duyne, R. P. (2003). Single silver nanoparticles as real-time optical sensors with zeptomole sensitivity. *Nano Letters*, *3*(8), 1057–1062. https://doi.org/10.1021/nl034372s

Menazea, A. A. (2020). Femtosecond laser ablation-assisted synthesis of silver nanoparticles in organic and inorganic liquids medium and their antibacterial efficiency. *Radiation Physics and Chemistry*, *168*. https://doi.org/10.1016/j.radphyschem.2019.108616

Meng, F., & Sun, Z. (2009). Enhanced photocatalytic activity of silver nanoparticles modified TiO2 thin films prepared by RF magnetron sputtering. *Materials Chemistry and Physics*, *118*(2–3), 349–353. https://doi.org/10.1016/j.matchemphys.2009.07.068

Mengoni, M. (2020). Biomechanical modelling of the facet joints: a review of methods and validation processes in finite element analysis. *Biomechanics and Modeling in Mechanobiology 2020 20:2*, *20*(2), 389–401. https://doi.org/10.1007/S10237-020-01403-7

Menon, H. G., Dutta, S., Krishnan, A., & Hariprasad, M. P. (2022). Proposed auxetic cluster designs for lightweight structural beams with improved load bearing capacity. *Engineering Structures*, *260*(November 2021), 114241. https://doi.org/10.1016/j.engstruct.2022.114241

Miller, W., Smith, C. W., Scarpa, F., & Evans, K. E. (2010). Flatwise buckling optimization of hexachiral and tetrachiral honeycombs. *Composites Science and Technology*, *70*(7), 1049–1056. https://doi.org/10.1016/J.COMPSCITECH.2009.10.022

Mishra, Y. K., Mohapatra, S., Kabiraj, D., Mohanta, B., Lalla, N. P., Pivin, J. C., & Avasthi, D. K. (2007). Synthesis and characterization of Ag nanoparticles in silica matrix by atom beam sputtering. *Scripta Materialia*, *56*(7), 629–632. https://doi.org/10.1016/j.scriptamat.2006.12.008

Mizzi, L., Attard, D., Evans, K. E., Gatt, R., & Grima, J. N. (2021). Auxetic mechanical

metamaterials with diamond and elliptically shaped perforations. *Acta Mechanica*, *232*(2), 779–791. https://doi.org/10.1007/S00707-020-02881-7/FIGURES/9

Mizzi, L., Attard, D., Gatt, R., Farrugia, P. S., & Grima, J. N. (2018). An analytical and finite element study on the mechanical properties of irregular hexachiral honeycombs. *Smart Materials and Structures*, *27*(10), 105016. https://doi.org/10.1088/1361-665X/aad3f6

Mizzi, L., Azzopardi, K. M., Attard, D., Grima, J. N., & Gatt, R. (2015). Auxetic metamaterials exhibiting giant negative Poisson's ratios. *Physica Status Solidi (RRL) - Rapid Research Letters*, *9*(7), 425–430. https://doi.org/10.1002/pssr.201510178

Mizzi, L., Gatt, R., & Grima, J. N. (2015). Non-porous grooved single-material auxetics. *Physica Status Solidi (B)*, *252*(7). https://doi.org/10.1002/pssb.201552218

Mizzi, L., Grima, J. N., Gatt, R., & Attard, D. (2019). Analysis of the Deformation Behavior and Mechanical Properties of Slit-Perforated Auxetic Metamaterials. *Physica Status Solidi (B) Basic Research*, *256*(1). https://doi.org/10.1002/pssb.201800153

Mizzi, L., Mahdi, E. M., Titov, K., Gatt, R., Attard, D., Evans, K. E., Grima, J. N., & Tan, J.-C. J.-C. (2018). Mechanical metamaterials with star-shaped pores exhibiting negative and zero Poisson's ratio. *Materials and Design*, *146*(2017), 28–37. https://doi.org/10.1016/j.matdes.2018.02.051

Mizzi, L., Salvati, E., Spaggiari, A., Tan, J.-C. C., & Korsunsky, A. M. (2020a). 2D auxetic metamaterials with tuneable micro-/nanoscale apertures. *Applied Materials Today*, *20*, 100780. https://doi.org/10.1016/j.apmt.2020.100780

Mizzi, L., Salvati, E., Spaggiari, A., Tan, J. C., & Korsunsky, A. M. (2020b). Highly stretchable two-dimensional auxetic metamaterial sheets fabricated via direct-laser cutting. *International Journal of Mechanical Sciences*, *167*, 105242. https://doi.org/10.1016/j.ijmecsci.2019.105242

Mizzi, L., & Spaggiari, A. (2020). Lightweight mechanical metamaterials designed using hierarchical truss elements. *Smart Materials and Structures*, *29*(10), 105036. https://doi.org/10.1088/1361-665X/ABA53C

Moens, D., & Vandepitte, D. (2006). Recent advances in non-probabilistic approaches for non-deterministic dynamic finite element analysis. *Archives of Computational Methods in Engineering*, *13*(3), 389–464. https://doi.org/10.1007/BF02736398/METRICS

Mohan Kumar, K., Mandal, B. K., Siva Kumar, K., Sreedhara Reddy, P., & Sreedhar, B. (2013). Biobased green method to synthesise palladium and iron nanoparticles using Terminalia chebula aqueous extract. *Spectrochimica Acta - Part A: Molecular and Biomolecular Spectroscopy*, *102*, 128–133. https://doi.org/10.1016/j.saa.2012.10.015

Mohanraj, H., Filho Ribeiro, S. L. M., Panzera, T. H., Scarpa, F., Farrow, I. R., Jones, R., Davies-Smith, A., Remillat, C. D. L., Walters, P., & Peng, H. X. (2016). Hybrid auxetic foam and perforated plate composites for human body support. *Physica Status Solidi (B)*, *253*(7), 1378–1386. https://doi.org/10.1002/PSSB.201600106

Mohr, R., Kratz, K., Weigel, T., Lucka-Gabor, M., Moneke, M., & Lendlein, A. (2006). Initiation of shape-memory effect by inductive heating of magnetic nanoparticles in thermoplastic polymers. *Proceedings of the National Academy of Sciences of the United States of America*, *103*(10), 3540–3545. https://doi.org/10.1073/PNAS.0600079103

Mohsenizadeh, S., Ahmad, Z., Alipour, R., Majid, R. A., & Prawoto, Y. (2019). Quasi Tri-Axial Method for the Fabrication of Optimized Polyurethane Auxetic Foams. *Physica Status Solidi (B)*, *256*(10), 1–14. https://doi.org/10.1002/pssb.201800587

Mokhtari, N., Daneshpajouh, S., Seyedbagheri, S., Atashdehghan, R., Abdi, K., Sarkar, S., Minaian, S., Shahverdi, H. R., & Shahverdi, A. R. (2009). Biological synthesis of very small silver nanoparticles by culture supernatant of Klebsiella pneumonia: The effects of visible-light irradiation and the liquid mixing process. *Materials Research Bulletin*, *44*(6), 1415–1421. https://doi.org/10.1016/j.materresbull.2008.11.021

Montgomery, S. M., Wu, S., Kuang, X., Armstrong, C. D., Zemelka, C., Ze, Q., Zhang, R., Zhao, R., & Qi, H. J. (2020). Magneto-Mechanical Metamaterials with Widely Tunable Mechanical Properties and Acoustic Bandgaps. *Advanced Functional Materials*, *2005319*(3), 1–10. https://doi.org/10.1002/adfm.202005319

Morin-Martinez, A. A., Arcudia, J., Zarate, X., Cifuentes-Quintal, M. E., & Merino, G. (2023). The quest for a bidirectional auxetic, elastic, and enhanced fracture toughness material: Revisiting the mechanical properties of the BeH2 monolayers. *Journal of Computational Chemistry*, *44*(3), 248–255. https://doi.org/10.1002/JCC.26875

Morita, T., Yasuda, Y., Ide, E., Akada, Y., & Hirose, A. (2008). Bonding technique using micro-scaled silver-oxide particles for in-situ formation of silver nanoparticles. *Materials Transactions*, *49*(12), 2875–2880. https://doi.org/10.2320/matertrans.MRA2008269

Moroney, C., Alderson, A., Allen, T., Sanami, M., & Venkatraman, P. (2018). *The Application of Auxetic Material for Protective Sports Apparel*. 251. https://doi.org/10.3390/proceedings2060251

Moshfegh, A., Jalali, A., Salehzadeh, A., & Jozani, A. S. (2019). Biological synthesis of silver nanoparticles by cell-free extract of Polysiphonia algae and their anticancer activity against breast cancer MCF-7 cell lines. *Micro and Nano Letters*, *14*(5), 581–584. https://doi.org/10.1049/mnl.2018.5260

Mosleh, Y., Cajka, M., Depreitere, B., Sloten, J. Vander, & Ivens, J. (2018). Designing safer composite helmets to reduce rotational accelerations during oblique impacts. *J Engineering in Medicine*, *232*(5), 479–491. https://doi.org/10.1177/0954411918762622

Motol, R. K. C., Espineli, C. A., Tapit, C. M. V, & Tiangco, C. E. (2020). Synthesis and characterization of silver nanoparticles as a potential sensor for volatile organosulfides for visual detection of postharvest storage in garlic. *IOP Conference Series: Materials Science and Engineering*, *778*(1). https://doi.org/10.1088/1757-899X/778/1/012002

Mu, J., Hou, C., Wang, H., Li, Y., Zhang, Q., & Zhu, M. (2015). Origami-inspired active

Graphene-Based paper for programmable instant self-folding walking devices. *Science Advances*, *1*(10). https://doi.org/10.1126/SCIADV.1500533/SUPPL_FILE/1500533_SM.PDF

Mulfinger, L., Solomon, S. D., Bahadory, M., Jeyarajasingam, A. V, Rutkowsky, S. A., & Boritz, C. (2007). Synthesis and Study of Silver Nanoparticles. *Journal of Chemical Education*, *84*(2), 322. https://doi.org/10.1021/ed084p322

Mullin, T., Deschanel, S., Bertoldi, K., & Boyce, M. C. (2007). Pattern transformation triggered by deformation. *Physical Review Letters*, *99*(8). https://doi.org/10.1103/PHYSREVLETT.99.084301

Mullin, T., Willshaw, S., & Box, F. (2013). Pattern switching in soft cellular solids under compression. *Soft Matter*, *9*(20), 4951–4955. https://doi.org/10.1039/C3SM27677E

Mulvaney, P. (1996). Surface plasmon spectroscopy of nanosized metal particles. *Langmuir*, *12*(3), 788–800. https://doi.org/10.1021/la9502711

Munkhbayar, B., Tanshen, M. R., Jeoun, J., Chung, H., & Jeong, H. (2013). Surfactant-free dispersion of silver nanoparticles into MWCNT-aqueous nanofluids prepared by one-step technique and their thermal characteristics. *Ceramics International*, *39*(6), 6415–6425. https://doi.org/10.1016/j.ceramint.2013.01.069

Muñoz, J. E., Cervantes, J., Esparza, R., & Rosas, G. (2007). Iron nanoparticles produced by high-energy ball milling. *Journal of Nanoparticle Research*, *9*(5), 945–950. https://doi.org/10.1007/s11051-007-9226-6

Murzakaev, A. M. (2017). Size dependence of the phase composition of silver nanoparticles formed by the electric explosion of a wire. *Physics of Metals and Metallography*, *118*(5), 459–465. https://doi.org/10.1134/S0031918X1705009X

Mustahsan, F., Khan, S. Z., Zaidi, A. A., Alahmadi, Y. H., Mahmoud, E. R. I., & Almohamadi, H. (2022). Re-Entrant Honeycomb Auxetic Structure with Enhanced Directional Properties. *Materials*, *15*(22). https://doi.org/10.3390/ma15228022

Müzel, S. D., Bonhin, E. P., Guimarães, N. M., & Guidi, E. S. (2020). Application of the Finite Element Method in the Analysis of Composite Materials: A Review. *Polymers 2020, Vol. 12, Page 818*, *12*(4), 818. https://doi.org/10.3390/POLYM12040818

Na, H. Bin, Song, I. C., & Hyeon, T. (2009). Inorganic nanoparticles for MRI contrast agents. *Advanced Materials*, *21*(21), 2133–2148. https://doi.org/10.1002/adma.200802366

Nallavan, G. (2020). Impact of recent developments in fabrication of auxetic materials on safety and protection in sport. *AIP Conference Proceedings*, *2271*(1), 030006. https://doi.org/10.1063/5.0024805

Naoui, Y., Settar, A., Chetehouna, K., Bouleklab, M. C., Revo, S., & Hamamda, S. (2020). Effect of multiwall carbon nanotube (MWCNT) content on thermal and structural properties enhancement of FeCu–MWCNT nanocomposites synthesized by high-energy ball milling. *Applied Physics A: Materials Science and Processing*, *126*(4). https://doi.org/10.1007/s00339-020-03474-w

Narojczyk, J. W., Bilski, M., Grima, J. N., Kędziora, P., Morozow, D., Rucki, M., & Wojciechowski, K. W. (2022). Removing Auxetic Properties in f.c.c. Hard Sphere Crystals by Orthogonal Nanochannels with Hard Spheres of Another Diameter.

Materials 2022, Vol. 15, Page 1134, *15*(3), 1134. https://doi.org/10.3390/MA15031134

Narojczyk, J. W., Kowalik, M., & Wojciechowski, K. W. (2016). Influence of nanochannels on Poisson's ratio of degenerate crystal of hard dimers. *Physica Status Solidi (B)*, *253*(7), 1324–1330. https://doi.org/10.1002/pssb.201600212

Narojczyk, J. W., Tretiakov, K. V, & Wojciechowski, K. W. (2022). Partially Auxetic Properties of Face-Centered Cubic Hard-Sphere Crystals with Nanochannels of Different Sizes, Parallel to [001]-Direction and Filled by Other Hard Spheres. *Physica Status Solidi (B)*, *259*(6), 2200006. https://doi.org/10.1002/PSSB.202200006

Narojczyk, J. W., Wojciechowski, K. W., Tretiakov, K. V, Smardzewski, J., Scarpa, F., Piglowski, P. M., Kowalik, M., Imre, A. R., & Bilski, M. (2019). Auxetic Properties of a f.c.c. Crystal of Hard Spheres with an Array of [001]-Nanochannels Filled by Hard Spheres of Another Diameter. *Physica Status Solidi (B)*, *256*(1), 1800611. https://doi.org/10.1002/PSSB.201800611

Naseem, T., & Farrukh, M. A. (2015). Antibacterial activity of green synthesis of iron nanoparticles using lawsonia inermis and gardenia jasminoides leaves extract. *Journal of Chemistry*. https://doi.org/10.1155/2015/912342

Nasim, M. S., & Etemadi, E. (2018). Three dimensional modeling of warp and woof periodic auxetic cellular structure. *International Journal of Mechanical Sciences*, *136*(December 2017), 475–481. https://doi.org/10.1016/j.ijmecsci.2018.01.002

Nečemer, B., Glodež, S., Novak, N., & Kramberger, J. (2020). Numerical modelling of a chiral auxetic cellular structure under multiaxial loading conditions. *Theoretical and Applied Fracture Mechanics*, *107*, 102514. https://doi.org/10.1016/J.TAFMEC.2020.102514

Nedoushan, R. J., & Yu, W. R. (2020). A new auxetic structure with enhanced stiffness via stiffened elliptical perforations. *Functional Composites and Structures*, *2*(4), 45006. https://iopscience.iop.org/article/10.1088/2631-6331/abd373

Nel, A., Xia, T., Mädler, L., & Li, N. (2006). Toxic potential of materials at the nanolevel. *Science*, *311*(5761), 622–627. https://doi.org/10.1126/science.1114397

Nene, A. G., Takahashi, M., & Somani, P. R. (2016). Fe 3 O 4 and Fe Nanoparticles by Chemical Reduction of Fe(acac) 3 by Ascorbic Acid: Role of Water Keywords Fe 3 O 4 Nanoparticles, Fe-Nanoparticles, Iron Oxide, Chemical Reduction Method. *World Journal of Nano Science and Engineering*, *6*(March), 20–28. https://doi.org/10.4236/wjnse.2016.61002

Newton-Mann, C., Winwood, K., Driscoll, H., Hamilton, N., & Allen, T. (2018). Finite Element Model of an Impact on a Palmar Pad from a Snowboard Wrist Protector. *Proceedings 2018, Vol. 2, Page 314*, *2*(6), 314. https://doi.org/10.3390/PROCEEDINGS2060314

Ngo, T. D., Kashani, A., Imbalzano, G., Nguyen, K. T. Q., & Hui, D. (2018). Additive manufacturing (3D printing): A review of materials, methods, applications and challenges. *Composites Part B: Engineering*, *143*(December 2017), 172–196. https://doi.org/10.1016/j.compositesb.2018.02.012

Nguyen, M. T., Yu, K., Tokunaga, T., Boonyaperm, K., Kheawhom, S., Arita, M., & Yonezawa, T. (2019). Green Synthesis of Size-Tunable Iron Oxides and Iron Nanoparticles in a Salt Matrix. *ACS Sustainable Chemistry and Engineering*, *7*(21), 17697–17705. https://doi.org/10.1021/acssuschemeng.9b03950

Ni, X., Zheng, Z., Xiao, X., Huang, L., & He, L. (2010). Silica-coated iron nanoparticles: Shape-controlled synthesis, magnetism and microwave absorption properties. *Materials Chemistry and Physics*, *120*(1), 206–212. https://doi.org/10.1016/j.matchemphys.2009.10.047

Nicolaou, Z. G., & Motter, A. E. (2012). Mechanical metamaterials with negative compressibility transitions. *Nature Materials*, *11*(7), 608–613. https://doi.org/10.1038/nmat3331

Nilavukkarasi, M., Vijayakumar, S., & Prathip Kumar, S. (2020). Biological synthesis and characterization of silver nanoparticles with Capparis zeylanica L. leaf extract for potent antimicrobial and anti proliferation efficiency. *Materials Science for Energy Technologies*, *3*, 371–376. https://doi.org/10.1016/j.mset.2020.02.008

Nirmala Grace, A., & Pandian, K. (2007). One pot synthesis of polymer protected Pt, Pd, Ag and Ru nanoparticles and nanoprisms under reflux and microwave mode of heating in glycerol-A comparative study. *Materials Chemistry and Physics*, *104*(1), 191–198. https://doi.org/10.1016/j.matchemphys.2007.03.009

Nishioka, M., Miyakawa, M., Kataoka, H., Koda, H., Sato, K., & Suzuki, T. M. (2011). Continuous synthesis of monodispersed silver nanoparticles using a homogeneous heating microwave reactor system. *Nanoscale*, *3*(6), 2621–2626. https://doi.org/10.1039/c1nr10199d

Nkansah, M. A., Evans, K. E., & Hutchinson, I. J. (1993). Modelling the effects of negative Poisson's ratios in continuous-fibre composites. *Journal of Materials Science*, *28*(10), 2687–2692. https://doi.org/10.1007/BF00356204/METRICS

Novak, N., Mauko, A., Ulbin, M., Krstulović-Opara, L., Ren, Z., & Vesenjak, M. (2022). Development and characterisation of novel three-dimensional axisymmetric chiral auxetic structures. *Journal of Materials Research and Technology*, *17*, 2701–2713. https://doi.org/10.1016/J.JMRT.2022.02.025

Novak, N., Nowak, M., Vesenjak, M., & Ren, Z. (2022). Structural Optimization of the Novel 3D Graded Axisymmetric Chiral Auxetic Structure. *Physica Status Solidi (B)*, *259*(12), 2200409. https://doi.org/10.1002/PSSB.202200409

Novak, N., Vesenjak, M., Kennedy, G., Thadhani, N., & Ren, Z. (2019). Response of Chiral Auxetic Composite Sandwich Panel to Fragment Simulating Projectile Impact. *Physica Status Solidi (B)*, *1*, 1900099. https://doi.org/10.1002/pssb.201900099

Novak, N., Vesenjak, M., & Ren, Z. (2016). Auxetic Cellular Materials - a Review. *Strojniški Vestnik – Journal of Mechanical Engineering*, *62*(9), 485–493. https://doi.org/10.5545/sv-jme.2016.3656

Novak, N., Vesenjak, M., Tanaka, S., Hokamoto, K., & Ren, Z. (2020). Compressive behaviour of chiral auxetic cellular structures at diferent strain rates. *International Journal of Impact Engineering*, *141*, 103566. https://doi.org/10.1016/j.ijimpeng.2020.103566

Novelino, L. S., Ze, Q., Wu, S., Paulino, G. H., & Zhao, R. (2020). Untethered control of functional origami microrobots with distributed actuation. *Proceedings of the National Academy of Sciences of the United States of America*, *117*(39), 24096–24101. https://doi.org/10.1073/PNAS.2013292117/SUPPL_FILE/PNAS.2013292117.SM04.MP4

Nuntawong, N., Horprathum, M., Eiamchai, P., Wong-Ek, K., Patthanasettakul, V., & Chindaudom, P. (2010). Surface-enhanced Raman scattering substrate of silver nanoparticles depositing on AAO template fabricated by magnetron sputtering. *Vacuum*, *84*(12), 1415–1418. https://doi.org/10.1016/j.vacuum.2009.12.020

Nurmi, J. T., Tratnyek, P. G., Amonette, J. E., Pecher, K., Wang, C., Linehan, J. C., Matson, D. W., Penn, R. L. E. E., & Driessen, M. D. (2005). Characterization and Properties of Metallic Iron Nanoparticles: Spectroscopy, Electrochemistry and Kinetics. *Environ. Sci. Technol.*, 1221–1230.

Okada, T., Saiki, T., Taniguchi, S., Ueda, T., Nakamura, K., Nishikawa, Y., & Iida, Y. (2013). Hydrogen Production Using Reduced-Iron Nanoparticles by Laser Ablation in Liquids. *ISRN Renewable Energy*, *2013*, 1–7. https://doi.org/10.1155/2013/827681

Oliveira, M. M., Ugarte, D., Zanchet, D., & Zarbin, A. J. G. (2005). Influence of synthetic parameters on the size, structure, and stability of dodecanethiol-stabilized silver nanoparticles. *Journal of Colloid and Interface Science*, *292*(2), 429–435. https://doi.org/10.1016/j.jcis.2005.05.068

Orhan, S. N., & Erden, Ş. (2022). Numerical investigation of the mechanical properties of 2D and 3D auxetic structures. *Smart Materials and Structures*, *31*(6), 65011. https://doi.org/10.1088/1361-665X/AC6918

Ou, Y., Yan, S., & Wen, P. (2021). In-Plane Impact Dynamics Analysis of Re-Entrant Honeycomb with Variable Cross-Section. *Computer Modeling in Engineering & Sciences*, *127*, 209–222. https://doi.org/10.32604/cmes.2021.014828

Overaker, D. W., Cuitiño, A. M., & Langrana, N. A. (1998). Effects of morphology and orientation on the behavior of two-dimensional hexagonal foams and application in a re-entrant foam anchor model. *Mechanics of Materials*, *29*(1), 43–52. https://doi.org/10.1016/S0167-6636(98)00004-0

Pacioni, N. L., Borsarelli, C. D., Rey, V., & Veglia, A. V. (2015). *Silver Nanoparticle Applications*. https://doi.org/10.1007/978-3-319-11262-6

Pal, A., Shah, S., & Devi, S. (2009). Microwave-assisted synthesis of silver nanoparticles using ethanol as a reducing agent. *Materials Chemistry and Physics*, *114*(2–3), 530–532. https://doi.org/10.1016/j.matchemphys.2008.11.056

Pamme, N. (2006). Magnetism and microfluidics. *Lab on a Chip*, *6*(1), 24–38. https://doi.org/10.1039/B513005K

Panáček, A., Kolář, M., Večeřová, R., Prucek, R., Soukupová, J., Kryštof, V., Hamal, P., Zbořil, R., & Kvítek, L. (2009). Antifungal activity of silver nanoparticles against Candida spp. *Biomaterials*, *30*(31), 6333–6340. https://doi.org/10.1016/j.biomaterials.2009.07.065

Park, E. J., Lee, S. W., Bang, I. C., & Park, H. W. (2011). Optimal synthesis and characterization of Ag nanofluids by electrical explosion of wires in liquids. *Nanoscale Research Letters*, *6*(1), 1–10. https://doi.org/10.1186/1556-276X-6-223

Park, J. B., Jeong, S. H., Jeong, M. S., Kim, J. Y., & Cho, B. K. (2008). Synthesis of carbon-encapsulated magnetic nanoparticles by pulsed laser irradiation of solution. *Carbon*, *46*(11), 1369–1377. https://doi.org/10.1016/j.carbon.2008.05.011

Park, S. J., Kim, S., Lee, S., Khim, Z. G., Char, K., & Hyeon, T. (2000). Synthesis and magnetic studies of uniform iron nanorods and nanospheres [12]. *Journal of the American Chemical Society*, *122*(35), 8581–8582. https://doi.org/10.1021/ja001628c

Parveen, M., Ahmad, F., Malla, A. M., & Azaz, S. (2016). Microwave-assisted green synthesis of silver nanoparticles from Fraxinus excelsior leaf extract and its antioxidant assay. *Applied Nanoscience (Switzerland)*, *6*(2), 267–276. https://doi.org/10.1007/s13204-015-0433-7

Peliński, K., & Smardzewski, J. (2022). Static response of synclastic sandwich panel with auxetic wood-based honeycomb cores subject to compression. *Thin-Walled Structures*, *179*, 109559. https://doi.org/10.1016/j.tws.2022.109559

Peng, H., Yang, A., & Xiong, J. (2013). Green, microwave-assisted synthesis of silver nanoparticles using bamboo hemicelluloses and glucose in an aqueous medium. *Carbohydrate Polymers*, *91*(1), 348–355. https://doi.org/10.1016/j.carbpol.2012.08.073

Peng, L., Guo, R., Lan, J., Jiang, S., & Lin, S. (2016). Microwave-assisted deposition of silver nanoparticles on bamboo pulp fabric through dopamine functionalization. *Applied Surface Science*, *386*, 151–159. https://doi.org/10.1016/j.apsusc.2016.05.170

Peng, S., Wang, C., Xie, J., & Sun, S. (2006). Synthesis and stabilization of monodisperse Fe nanoparticles. *Journal of the American Chemical Society*, *128*(33), 10676–10677. https://doi.org/10.1021/ja063969h

Peter, John, H. J. T., & Cooper. (1951). A study of the nucleation and growth process in the synthesis of colloidal gold. *Discussions of the Faraday Society*, *55*(c), 55–75. https://doi.org/10.1039/df9511100055

Phellan, R., Hachem, B., Clin, J., Mac-Thiong, J. M., & Duong, L. (2021). Real-time biomechanics using the finite element method and machine learning: Review and perspective. *Medical Physics*, *48*(1), 7–18. https://doi.org/10.1002/MP.14602

Photiou, D., Avraam, S., Sillani, F., Verga, F., Jay, O., & Papadakis, L. (2021). Experimental and numerical analysis of 3d printed polymer tetra-petal auxetic structures under compression. *Applied Sciences (Switzerland)*, *11*(21). https://doi.org/10.3390/app112110362

Pickles, A. P., Webber, R. S., Alderson, K. L., Neale, P. J., & Evans, K. E. (1995). The effect of the processing parameters on the fabrication of auxetic polyethylene. *Journal of Materials Science*, *30*(16), 4059–4068. https://doi.org/10.1007/BF00360709

Pigłowski, P. M., Wojciechowski, K. W., & Tretiakov, K. V. (2016). Partial auxeticity

induced by nanoslits in the Yukawa crystal. *Physica Status Solidi - Rapid Research Letters*, *10*(7), 566–569. https://doi.org/10.1002/pssr.201600119

Ponder, S. M., Darab, J. G., & Mallouk, T. E. (2000). Remediation of Cr(VI) and Pb(II) aqueous solutions using supported, nanoscale zero-valent iron. *Environmental Science and Technology*, *34*(12), 2564–2569. https://doi.org/10.1021/es9911420

Pourzahedi, L., & Eckelman, M. J. (2015). Environmental life cycle assessment of nanosilver-enabled bandages. *Environmental Science and Technology*, *49*(1), 361–368. https://doi.org/10.1021/ES504655Y/SUPPL_FILE/ES504655Y_SI_001.PDF

Poźniak, A. A. A., Wojciechowski, K. W., Grima, J. N., & Mizzi, L. (2016). Planar auxeticity from elliptic inclusions. *Composites Part B: Engineering*, *94*, 379–388. https://doi.org/10.1016/j.compositesb.2016.03.003

Prall, D., & Lakes, R. S. (1997). Properties of a chiral honeycomb with a poisson's ratio of -1. *International Journal of Mechanical Sciences*, *39*(3), 305–314. https://doi.org/10.1016/S0020-7403(96)00025-2

Prasath, S., & Palaniappan, K. (2019). Is using nanosilver mattresses/pillows safe? A review of potential health implications of silver nanoparticles on human health. *Environmental Geochemistry and Health 2019 41:5*, *41*(5), 2295–2313. https://doi.org/10.1007/S10653-019-00240-7

Qi, C., Jiang, F., Yang, S., & Remennikov, A. (2021). Multi-scale characterization of novel re-entrant circular auxetic honeycombs under quasi-static crushing. *Thin-Walled Structures*, *169*, 108314. https://doi.org/10.1016/j.tws.2021.108314

Qi, C., Jiang, F., Yu, C., & Yang, S. (2019). In-plane crushing response of tetra-chiral honeycombs. *International Journal of Impact Engineering*, *130*, 247–265. https://doi.org/10.1016/j.ijimpeng.2019.04.019

Qi, D., Yu, H., Hu, W., He, C., Wu, W., & Ma, Y. (2019). Bandgap and wave attenuation mechanisms of innovative reentrant and anti-chiral hybrid auxetic metastructure. *Extreme Mechanics Letters*, *28*, 58–68. https://doi.org/10.1016/J.EML.2019.02.005

Qiao, J., & Chen, C. Q. (2015). Analyses on the in-plane impact resistance of auxetic double arrowhead honeycombs. *Journal of Applied Mechanics, Transactions ASME*, *82*(5). https://doi.org/10.1115/1.4030007/421913

Qiao, J. X., & Chen, C. Q. (2015). Impact resistance of uniform and functionally graded auxetic double arrowhead honeycombs. *International Journal of Impact Engineering*, *83*, 47–58. https://doi.org/10.1016/J.IJIMPENG.2015.04.005

Rad, M. S., Ahmad, Z., & Alias, A. (2015). *Computational Approach in Formulating Mechanical Characteristics of 3D Star Honeycomb Auxetic Structure*. *2015*.

Rad, M. S., Hatami, H., Ahmad, Z., & Yasuri, A. K. (2019). Analytical solution and finite element approach to the dense re-entrant unit cells of auxetic structures. *Acta Mechanica*, *230*(6), 2171–2185. https://doi.org/10.1007/S00707-019-02387-X/METRICS

Rafsanjani, A., & Pasini, D. (2016). Bistable auxetic mechanical metamaterials inspired by ancient geometric motifs. *Extreme Mechanics Letters*, *9*, *Part 2*, 291–296. https://doi.org/https://doi.org/10.1016/j.eml.2016.09.001

Raghunandan, D., Mahesh, B. D., Basavaraja, S., Balaji, S. D., Manjunath, S. Y., & Venkataraman, A. (2011). Microwave-assisted rapid extracellular synthesis of stable bio-functionalized silver nanoparticles from guava (Psidium guajava) leaf extract. *Journal of Nanoparticle Research*, *13*(5), 2021–2028. https://doi.org/10.1007/s11051-010-9956-8

Raghunath, G., & Flatau, A. B. (2015). Study of magnetic domain evolution in an auxetic plane of Galfenol using Kerr microscopy. *Journal of Applied Physics*, *117*(17), 1–5. https://doi.org/10.1063/1.4913727

Rashed, H. H. (2016). Silver Nanoparticles Prepared by Electrical Arc Discharge Method in DIW. *Journal of Enginnering and Technology*, *34*(2), 295–301.

Ratyakshi, & Chauhan, R. P. (2009). Colloidal synthesis of silver nano particles. *Asian Journal of Chemistry*, *21*(10), 113–116.

Ravirala, N., Alderson, A., Alderson, K. L., & Davies, P. J. (2005). Auxetic polypropylene films. *Polymer Engineering and Science*. https://doi.org/10.1002/pen.20307

Ravirala, N., Alderson, K. L., Davies, P. J., Simkins, V. R., & Alderson, A. (2006). Negative Poisson's Ratio Polyester Fibers. *Textile Research Journal*, *76*(7), 540–546. https://doi.org/10.1177/0040517506065255

Rele, M., Kapoor, S., Sharma, G., & Mukherjee, T. (2004). Reduction and aggregation of silver and thallium ions in viscous media. *Physical Chemistry Chemical Physics*, 590–595. https://doi.org/10.1039/b311540b

Ren, X., Das, R., Tran, P., Ngo, T. D., & Xie, Y. M. (2018). Auxetic metamaterials and structures: A review. *Smart Materials and Structures*, *27*(2). https://doi.org/10.1088/1361-665X/aaa61c

Ren, X., Shen, J., Tran, P., Ngo, T. D., & Xie, Y. M. (2018). Auxetic nail: Design and experimental study. *Composite Structures*, *184*, 288–298. https://doi.org/10.1016/j.compstruct.2017.10.013

Ren, Z., Hu, W., Dong, X., & Sitti, M. (2019). Multi-functional soft-bodied jellyfish-like swimming. *Nature Communications*, *10*(1). https://doi.org/10.1038/s41467-019-10549-7

Ripplinger, W., Schwarz, M., Diebels, S., & Herrmann, H. G. (2018). Auxetic aluminum sheets in lightweight structures. *Materialpruefung/Materials Testing*, *60*(11), 1071. https://doi.org/10.3139/120.111250/MACHINEREADABLECITATION/RIS

Roche, J., Lockette, P. Von, & Lofland, S. (2011). Study of Hard-and Soft-Magnetorheological Elastomers (MRE's) Actuation Capabilities. *COMSOL*.

Rojas, T. C., Sánchez-López, J. C., Greneche, J. M., Conde, A., & Fernández, A. (2004). Characterization of oxygen passivated iron nanoparticles and thermal evolution to $γ$-Fe2O3. *Journal of Materials Science*, *39*(15), 4877–4885. https://doi.org/10.1023/B:JMSC.0000035328.99440.8d

Rose, G. K., Soni, R., Rishi, P., & Soni, S. K. (2019). Optimization of the biological synthesis of silver nanoparticles using Penicillium oxalicum GRS-1 and their antimicrobial effects against common food-borne pathogens. *Green Processing and Synthesis*, *8*(1), 144–156. https://doi.org/10.1515/gps-2018-0042

Ruan, X. L., Li, J. J., Song, X. K., Zhou, H. J., Yuan, W. X., Wu, W. W., & Xia, R. (2019). Mechanical Design of Antichiral-Reentrant Hybrid Intravascular Stent. *Https://Doi.Org/10.1142/S1758825118501053*, *10*(10). https://doi.org/10.1142/S1758825118501053

S.A. Vorobyova , A.I. Lesnikovich, N. S. S., & Research. (2008). Preparation of Silver Nanoparticles by Chemical Reduction Method. **安徽工**业大学学报：自然科学版, *2*(25), 120–122.

Sadegh, M., Ranjbar, M., Boldrin, L., Scarpa, F., Patsias, S., & Ozada, N. (2018). Vibroacoustics of 2D gradient auxetic hexagonal honeycomb sandwich panels. *Composite Structures*, *187*(October 2017), 593–603. https://doi.org/10.1016/j.compstruct.2017.10.077

Sajitha, E. P., Prasad, V., Subramanyam, S. V, Eto, S., Takai, K., & Enoki, T. (2004). Synthesis and characteristics of iron nanoparticles in a carbon matrix along with the catalytic graphitization of amorphous carbon. *Carbon*, *42*(14), 2815–2820. https://doi.org/10.1016/j.carbon.2004.06.027

Sanami, M., Ravirala, N., Alderson, K., & Alderson, A. (2014). Auxetic materials for sports applications. *Procedia Engineering*. https://doi.org/10.1016/j.proeng.2014.06.079

Sánche-Lópeaz, J. C., Justo, A., Fernández, A., Conde, C. F., & Conde, A. (1997). Preparation and thermal evolution of vapour-condensed nanocrystalline iron. *Philosophical Magazine B: Physics of Condensed Matter; Statistical Mechanics, Electronic, Optical and Magnetic Properties*, *76*(4), 663–667. https://doi.org/10.1080/01418639708241132

Sang, H. I., Yun, T. L., Wiley, B., & Xia, Y. (2005). Large-scale synthesis of silver nanocubes: The role of HCl in promoting cube perfection and monodispersity. *Angewandte Chemie - International Edition*, *44*(14), 2154–2157. https://doi.org/10.1002/anie.200462208

Sarkar, A., Kapoor, S., & Mukherjee, T. (2010). Synthesis and characterisation of silver nanoparticles in viscous solvents and its transfer into non-polar solvents. *Research on Chemical Intermediates*, *36*(4), 411–421. https://doi.org/10.1007/s11164-010-0151-4

Scarpa, F. (2008). Auxetic materials for bioprostheses. *IEEE Signal Processing Magazine*, *25*(5). https://doi.org/10.1109/MSP.2008.926663

Scarpa, F., Blain, S., Lew, T., Perrott, D., Ruzzene, M., & Yates, J. R. (2007). Elastic buckling of hexagonal chiral cell honeycombs. *Composites Part A: Applied Science and Manufacturing*, *38*(2), 280–289. https://doi.org/10.1016/J.COMPOSITESA.2006.04.007

Scarpa, F., Bullough, W. A., & Lumley, P. (2004). Trends in acoustic properties of iron particle seeded auxetic polyurethane foam. *Proceedings of the Institution of Mechanical Engineers, Part C: Journal of Mechanical Engineering Science*, *218*(2), 241–244. https://doi.org/10.1243/095440604322887099

Scarpa, F., Panayiotou, P., & Tomlinson, G. (2000). Numerical and experimental uniaxial loading on in-plane auxetic honeycombs. *The Journal of Strain Analysis for*

Engineering Design, *35*(5), 383–388. https://doi.org/10.1243/0309324001514152

Scarpa, F., Pastorino, P., Garelli, A., Patsias, S., & Ruzzene, M. (2005). Auxetic compliant flexible PU foams: static and dynamic properties. *Physica Status Solidi (B)*, *242*(3), 681–694. https://doi.org/10.1002/pssb.200460386

Scarpa, F., & Smith, F. C. (2004). Passive and MR fluid-coated auxetic PU foam - Mechanical, acoustic, and electromagnetic properties. *Journal of Intelligent Material Systems and Structures*, *15*(12), 973–979. https://doi.org/10.1177/1045389X04046610

Scarpa, F., Yates, J. R., Ciffo, L. G., & Patsias, S. (2002). Dynamic crushing of auxetic open-cell polyurethane foam. *Proceedings of the Institution of Mechanical Engineers, Part C: Journal of Mechanical Engineering Science*, *216*(12), 1153–1156. https://doi.org/10.1243/095440602321029382

Schaeffer, M., & Ruzzene, M. (2015a). Homogenization of 1D and 2D magnetoelastic lattices. *EPJ Applied Metamaterials*, *2*. https://doi.org/10.1051/epjam/2015013

Schaeffer, M., & Ruzzene, M. (2015b). Wave propagation in multistable magneto-elastic lattices. *International Journal of Solids and Structures*, *56*, 78–95. https://doi.org/10.1016/j.ijsolstr.2014.12.003

Schaeffer, M., & Ruzzene, M. (2015c). Wave propagation in reconfigurable magneto-elastic kagome lattice structures. *Journal of Applied Physics*, *117*(19), 1–7. https://doi.org/10.1063/1.4921358

Schroeders, B. (2021). *Design of magneto-active mechanical metamaterials with mechanical target properties* (G. Balint, B. Antala, C. Carty, J.-M. A. Mabieme, I. B. Amar, & A. Kaplanova (Eds.); Vol. 7, Issue 1) [Uniwersytet Śląski. WydziałMatematyki, Fizyki i Chemii]. https://doi.org/10.2/JQUERY.MIN.JS

Schwerdtfeger, J., Schury, F., Stingl, M., Wein, F., Singer, R. F., & Körner, C. (2012). Mechanical characterisation of a periodic auxetic structure produced by SEBM. *Physica Status Solidi (B)*, *249*(7), 1347–1352. https://doi.org/10.1002/PSSB.201084211

Scown, T. M., Santos, E. M., Johnston, B. D., Gaiser, B., Baalousha, M., Mitov, S., Lead, J. R., Stone, V., Fernandes, T. F., Jepson, M., van Aerle, R., & Tyler, C. R. (2010). Effects of aqueous exposure to silver nanoparticles of different sizes in rainbow trout. *Toxicological Sciences*, *115*(2), 521–534. https://doi.org/10.1093/toxsci/kfq076

Seip, C. T., & O'Connor, C. J. (1999). Fabrication and organization of self-assembled metallic nanoparticles formed in reverse micelles. *Nanostructured Materials*, *12*(1), 183–186. https://doi.org/10.1016/S0965-9773(99)00094-X

Sen, P., Ghosh, J., Abdullah, A., Kumar, P., & Vandana. (2003). Preparation of Cu, Ag, Fe and Al nanoparticles by the exploding wire technique. *Proceedings of the Indian Academy of Sciences: Chemical Sciences*, *115*(5-6 SPEC. ISS.), 499–508. https://doi.org/10.1007/bf02708241

Sergeev, G. B. (2003). Cryochemistry of metal nanoparticles. *Journal of Nanoparticle Research*, *5*(5–6), 529–537. https://doi.org/10.1023/B:NANO.0000006153.65107.42

Sergeev, G. B., & Shabatina, T. I. (2008). Cryochemistry of nanometals. *Colloids and Surfaces A: Physicochemical and Engineering Aspects*, *313–314*, 18–22. https://doi.org/10.1016/j.colsurfa.2007.04.064

Shah, I. A., Khan, R., Koloor, S. S. R., Petrů, M., Badshah, S., Ahmad, S., & Amjad, M. (2022). Finite Element Analysis of the Ballistic Impact on Auxetic Sandwich Composite Human Body Armor. *Materials 2022, Vol. 15, Page 2064*, *15*(6), 2064. https://doi.org/10.3390/MA15062064

Shalaev, V. M. (2007). Optical negative-index metamaterials. *Nature Photonics*, *1*(1), 41–48. https://doi.org/10.1038/nphoton.2006.49

Shameli, K., Ahmad, M. Bin, Yunus, W. Z. W., Ibrahim, N. A., & Darroudi, M. (2010). Synthesis and characterization of silver/talc nanocomposites using the wet chemical reduction method. *International Journal of Nanomedicine*, *5*(1), 743–751. https://doi.org/10.2147/IJN.S13227

Shan, S., Kang, S. H., Zhao, Z., Fang, L., & Bertoldi, K. (2015). Design of planar isotropic negative Poisson's ratio structures. *Extreme Mechanics Letters*, *4*, 96–102. https://doi.org/10.1016/j.eml.2015.05.002

Sharma, S., Kushawah, D., & Rawal, A. (2019). Designing nonwoven auxetic metamaterials with spatially textured functionalities. *Materials Letters*, *241*, 214–218. https://doi.org/10.1016/J.MATLET.2019.01.038

Shavel, A., Rodríguez-González, B., Spasova, M., Farle, M., & Liz-Marzán, L. M. (2007). Synthesis and characterization of iron/iron oxide core/shell nanocubes. *Advanced Functional Materials*, *17*(18), 3870–3876. https://doi.org/10.1002/adfm.200700494

Shen, J., Zhou, S., Huang, X., & Xie, Y. M. (2014). Simple cubic three-dimensional auxetic metamaterials. *Physica Status Solidi (B)*, *251*(8). https://doi.org/10.1002/pssb.201451304

Shepherd, T., Winwood, K., Venkatraman, P., Alderson, A., & Allen, T. (2020). Validation of a Finite Element Modeling Process for Auxetic Structures under Impact. *Physica Status Solidi (B)*, *257*(10), 1900197. https://doi.org/10.1002/PSSB.201900197

Shervani, Z., Ikushima, Y., Sato, M., Kawanami, H., Hakuta, Y., Yokoyama, T., Nagase, T., Kuneida, H., & Aramaki, K. (2008). Morphology and size-controlled synthesis of silver nanoparticles in aqueous surfactant polymer solutions. *Colloid and Polymer Science*, *286*(4), 403–410. https://doi.org/10.1007/s00396-007-1784-8

Shim, J., Shan, S., Košmrlj, A., Kang, S. H., Chen, E. R., Weaver, J. C., & Bertoldi, K. (2013). Harnessing instabilities for design of soft reconfigurable auxetic/chiral materials. *Soft Matter*, *9*(34), 8198–8202. https://doi.org/10.1039/C3SM51148K

Shokri Rad, M., Prawoto, Y., & Ahmad, Z. (2014). Analytical solution and finite element approach to the 3D re-entrant structures of auxetic materials. *Mechanics of Materials*, *74*, 76–87. https://doi.org/10.1016/j.mechmat.2014.03.012

Shukla, S., & Behera, B. K. (2022). Auxetic fibrous materials and structures in medical engineering–a review. *Journal of the Textile Institute*. https://doi.org/10.1080/00405000.2022.2116549

Si, P. Z., Zhang, Z. D., Geng, D. Y., You, C. Y., Zhao, X. G., & Zhang, W. S. (2003). Synthesis and characteristics of carbon-coated iron and nickel nanocapsules produced by arc discharge in ethanol vapor. *Carbon*, *41*(2), 247–251. https://doi.org/10.1016/S0008-6223(02)00280-4

Siddiqui, N., Bhardwaj, A., Hada, R., Yadav, V. S., & Goyal, D. (2018). Synthesis, characterization and antimicrobial study of poly (methyl methacrylate)/Ag nanocomposites. *Vacuum*, *153*, 6–11. https://doi.org/10.1016/j.vacuum.2018.03.036

Siegel, J., Kvítek, O., Ulbrich, P., Kolská, Z., Slepička, P., & Švorčík, V. (2012). Progressive approach for metal nanoparticle synthesis. *Materials Letters*, *89*, 47–50. https://doi.org/10.1016/j.matlet.2012.08.048

Siekkinen, A. R., McLellan, J. M., Chen, J., & Xia, Y. (2006). Rapid synthesis of small silver nanocubes by mediating polyol reduction with a trace amount of sodium sulfide or sodium hydrosulfide. *Chemical Physics Letters*, *432*(4–6), 491–496. https://doi.org/10.1016/j.cplett.2006.10.095

Sigmund, O. (1995). Tailoring materials with prescribed elastic properties. *Mechanics of Materials*, *20*(4), 351–368. https://doi.org/10.1016/0167-6636(94)00069-7

Sigmund, O., & Torquato, S. (1999). Design of smart composite materials using topology optimization. *Smart Materials and Structures*, *8*(3), 365–379. https://doi.org/10.1088/0964-1726/8/3/308

Sigmund, O., Torquato, S., & Aksay, I. A. (1998). On the design of 1–3 piezocomposites using topology optimization. *Journal of Materials Research*, *13*(04), 1038–1048. https://doi.org/10.1557/JMR.1998.0145

Šileikaitė, A., Prosyčevas, I., Puišo, J., Juraitis, A., & Guobienė, A. (2006). Analysis of Silver Nanoparticles Produced by Chemical Reduction of Silver Salt Solution. *Materials Science (Medžiagotyra)*, *12*(4), 1320–1392. https://doi.org/10.1002/jid

Singh, K., Tipton, C. R., Han, E., & Mullin, T. (2013). Magneto-elastic buckling of an Euler beam. *Proceedings of the Royal Society A: Mathematical, Physical and Engineering Sciences*, *469*(2155). https://doi.org/10.1098/rspa.2013.0111

Singh, M., Sinha, I., & Mandal, R. K. (2009). Role of pH in the green synthesis of silver nanoparticles. *Materials Letters*, *63*(3–4), 425–427. https://doi.org/10.1016/j.matlet.2008.10.067

Singh, R., Javanbakht, Z., & Hall, W. (2021). On the inclined static loading of honeycomb re-entrant auxetics. *Composite Structures*, *273*(May), 114289. https://doi.org/10.1016/j.compstruct.2021.114289

Siwach, O. P., & Sen, P. (2008a). Fluorescence properties of Ag nanoparticles in water. *Spectrochimica Acta - Part A: Molecular and Biomolecular Spectroscopy*, *69*(2), 659–663. https://doi.org/10.1016/j.saa.2007.05.018

Siwach, O. P., & Sen, P. (2008b). Fluorescence properties of Fe nanoparticles prepared by electro-explosion of wires. *Materials Science and Engineering B: Solid-State Materials for Advanced Technology*, *149*(1), 99–104. https://doi.org/10.1016/j.mseb.2007.12.007

Siwach, O. P., & Sen, P. (2009). Fluorescence properties of Ag nanoparticles in water, methanol and hexane. *Journal of Luminescence*, *129*(1), 6–11.

https://doi.org/10.1016/j.jlumin.2008.07.010

Skrzyńska, E., Zaid, S., Addad, A., Girardon, J. S., Capron, M., & Dumeignil, F. (2016). Performance of Ag/Al2O3 catalysts in the liquid phase oxidation of glycerol-effect of preparation method and reaction conditions. *Catalysis Science and Technology*, *6*(9), 3182–3196. https://doi.org/10.1039/c5cy01581b

Slann, A., White, W., Scarpa, F., Boba, K., & Farrow, I. (2015). Cellular plates with auxetic rectangular perforations. *Physica Status Solidi (B) Basic Research*, *252*(7), 1533–1539. https://doi.org/10.1002/pssb.201451740

Slavin, Y. N., Asnis, J., Häfeli, U. O., & Bach, H. (2017). Metal nanoparticles: Understanding the mechanisms behind antibacterial activity. *Journal of Nanobiotechnology*, *15*(1), 1–20. https://doi.org/10.1186/s12951-017-0308-z

Slepička, P., Elashnikov, R., Ulbrich, P., Staszek, M., Kolská, Z., & Švorčík, V. (2015). Stabilization of sputtered gold and silver nanoparticles in PEG colloid solutions. *Journal of Nanoparticle Research*, *17*(1). https://doi.org/10.1007/s11051-014-2850-z

Slesarenko, V. (2020). Planar Mechanical Metamaterials with Embedded Permanent Magnets. *Materials*, *13*(6), 1313. https://doi.org/10.3390/ma13061313

Smith, D. R., Pendry, J. B., & Wiltshire, M. C. K. (2004). Metamaterials and Negative Refractive Index. *Science*, *305*(788). https://doi.org/10.1126/science.1096796

Song, D. H., Uhm, S. H., Kim, S. E., Kwon, J. S., Han, J. G., & Kim, K. N. (2012). Synthesis of titanium oxide thin films containing antibacterial silver nanoparticles by a reactive magnetron co-sputtering system for application in biomedical implants. *Materials Research Bulletin*, *47*(10), 2994–2998. https://doi.org/10.1016/j.materresbull.2012.04.085

Song, J. Y., & Kim, B. S. (2009). Rapid biological synthesis of silver nanoparticles using plant leaf extracts. *Bioprocess and Biosystems Engineering*, *32*(1), 79–84. https://doi.org/10.1007/s00449-008-0224-6

Song, K. C., Lee, S. M., Park, T. S., & Lee, B. S. (2009). Preparation of colloidal silver nanoparticles by chemical reduction method. *Korean Journal of Chemical Engineering*, *26*(1), 153–155.

Sorensen, C. M., & Klabunde, K. J. (2001). Nanoscale materials in Chemistry. *Inc.: New York, NJ*, 169–221.

Sorrentino, A., & Castagnetti, D. (2023a). Novel polyhedral mechanical metamaterial exhibiting negative Poisson's ratio. *Smart Materials and Structures*, *32*(3), 035008. https://doi.org/10.1088/1361-665X/ACB3A3

Sorrentino, A., & Castagnetti, D. (2023b). Novel polyhedral mechanical metamaterial exhibiting negative Poisson's ratio. *Smart Materials and Structures*, *32*(3), 35008. https://doi.org/10.1088/1361-665X/ACB3A3

Sorrentino, A., Castagnetti, D., Mizzi, L., & Spaggiari, A. (2021). Rotating squares auxetic metamaterials with improved strain tolerance. *Smart Materials and Structures*, *30*(3), 035015. https://doi.org/10.1088/1361-665X/abde50

Soukupová, J., Kvítek, L., Panáček, A., Nevěčná, T., & Zbořil, R. (2008). Comprehensive

study on surfactant role on silver nanoparticles (NPs) prepared via modified Tollens process. *Materials Chemistry and Physics*, *111*(1), 77–81. https://doi.org/10.1016/j.matchemphys.2008.03.018

Spadoni, A., Ruzzene, M., & Scarpa, F. (2005). Global and local linear buckling behavior of a chiral cellular structure. *Physica Status Solidi (B)*, *242*(3), 695–709. https://doi.org/10.1002/PSSB.200460387

Spagnoli, A., Brighenti, R., Lanfranchi, M., & Soncini, F. (2015). On the Auxetic Behaviour of Metamaterials with Re-entrant Cell Structures. *Procedia Engineering*, *109*, 410–417. https://doi.org/10.1016/J.PROENG.2015.06.252

Sparavigna, A. (2007a). Phonons dispersions in auxetic lattices. In *Journal of Physics: Conference Series*. https://doi.org/10.1088/1742-6596/92/1/012100

Sparavigna, A. (2007b). Phonons in conventional and auxetic honeycomb lattices. *Physical Review B - Condensed Matter and Materials Physics*, *76*, 134302. https://doi.org/10.1103/PhysRevB.76.134302

Sportelli, M. C., Izzi, M., Volpe, A., Clemente, M., Picca, R. A., Ancona, A., & Cioffi, N. (2020). Novel polyethylene oxide coatings implementing ultra-stable laser-ablated silver nanoparticles. *Applied Surface Science*, *507*(September 2019). https://doi.org/10.1016/j.apsusc.2019.145156

Sreeram, K. J., Nidhin, M., & Nair, B. U. (2008). Microwave assisted template synthesis of silver nanoparticles. *Bulletin of Materials Science*, *31*(7), 937–942. https://doi.org/10.1007/s12034-008-0149-3

Srirekha, A., & Bashetty, K. (2010). Infinite to finite: An overview of finite element analysis. *Indian Journal of Dental Research*, *21*(3), 425. https://doi.org/10.4103/0970-9290.70813

Stamplecoskie, K. G., Scaiano, J. C., Tiwari, V. S., & Anis, H. (2011). Optimal size of silver nanoparticles for surface-enhanced raman spectroscopy. *Journal of Physical Chemistry C*, *115*(5), 1403–1409. https://doi.org/10.1021/jp106666t

Starowicz, M., Stypuła, B., & Banaś, J. (2006). Electrochemical synthesis of silver nanoparticles. *Electrochemistry Communications*, *8*(2), 227–230. https://doi.org/10.1016/j.elecom.2005.11.018

State, S. (1988). New approaches to in situ characterization ultrafine agglomerates a. schmidt-ott. *Solid State Physics*, *19*(5).

Stavric, M., & Wiltsche, A. (2019). Geometrical Elaboration of Auxetic Structures. *Nexus Network Journal*, *21*(1), 79–90. https://doi.org/10.1007/s00004-019-00428-5

Steffens, F., Oliveira, F. R., & Fangueiro, R. (2021). Energy absorption from composite reinforced with high performance auxetic textile structure. *Journal of Composite Materials*, *55*(7), 1003–1013. https://doi.org/10.1177/0021998320964552/ASSET/IMAGES/LARGE/10.1177_0021998320964552-FIG7.JPEG

Steinigeweg, D., & Schlücker, S. (2012). Monodispersity and size control in the synthesis of 20-100 nm quasi-spherical silver nanoparticles by citrate and ascorbic acid reduction in glycerol-water mixtures. *Chemical Communications*, *48*(69), 8682–8684. https://doi.org/10.1039/c2cc33850e

Su, Y., Xu, X., Shi, J., & Huang, G. (2021). A 3D Mechanism-driven Hexagonal Metamaterial: Evaluation of Auxetic Behavior. *International Journal of Mechanical Sciences*, *209*(July), 106699. https://doi.org/10.1016/j.ijmecsci.2021.106699

Suber, L., Sondi, I., Matijević, E., & Goia, D. V. (2005). Preparation and the mechanisms of formation of silver particles of different morphologies in homogeneous solutions. *Journal of Colloid and Interface Science*, *288*(2), 489–495. https://doi.org/10.1016/j.jcis.2005.03.017

Sukhov, I. A., Simakin, A. V, Shafeev, G. A., Viau, G., & Garcia, C. (2012). Formation of nanoparticles during laser ablation of an iron target in a liquid. *Quantum Electronics*, *42*(5), 453–456. https://doi.org/10.1070/qe2012v042n05abeh014753

Sun, S., Anders, S., Thomson, T., Baglin, J. E. E., Toney, M. F., Hamann, H. F., Murray, C. B., & Terris, B. D. (2003). Controlled synthesis and assembly of FePt nanoparticles. *Journal of Physical Chemistry B*, *107*(23), 5419–5425. https://doi.org/10.1021/jp027314o

Sun, S., & Zeng, H. (2002). Size-controlled synthesis of magnetite nanoparticles. *Journal of the American Chemical Society*, *124*(28), 8204–8205. https://doi.org/10.1021/ja026501x

Sun, Y., Mayers, B., Herricks, T., & Xia, Y. (2003). Polyol synthesis of uniform silver nanowires: A plausible growth mechanism and the supporting evidence. *Nano Letters*, *3*(7), 955–960. https://doi.org/10.1021/nl034312m

Sun, Y. P., Li, X. Q., Zhang, W. X., & Wang, H. P. (2007). A method for the preparation of stable dispersion of zero-valent iron nanoparticles. *Colloids and Surfaces A: Physicochemical and Engineering Aspects*, *308*(1–3), 60–66. https://doi.org/10.1016/j.colsurfa.2007.05.029

Sun, Y., & Xia, Y. (2002). Shape-Controlled Synthesis of Gold and Silver Nanoparticles. *Science*, *298*(5601), 2176–2179.

Sun, Y., Yin, Y., Mayers, B. T., Herricks, T., & Xia, Y. (2002). Uniform silver nanowires synthesis by reducing AgNO3 with ethylene glycol in the presence of seeds and poly(vinyl pyrrolidone). *Chemistry of Materials*, *14*(11), 4736–4745. https://doi.org/10.1021/cm020587b

Suriati, G., Mariatti, M., & Azizan, A. (2014). SYNTHESIS OF SILVER NANOPARTICLES BY CHEMICAL REDUCTION METHOD: EFFECT OF REDUCING AGENT AND SURFACTANT CONCENTRATION. *International Journal of Automotive and Mechanical Engineering (IJAME)*, *10*(December).

Suslick, K. S., Fang, M., & Hyeon, T. (1996). Sonochemical synthesis of iron colloids. *Journal of the American Chemical Society*, *118*(47), 11960–11961. https://doi.org/10.1021/ja961807n

Svarovskaya, N. V, Bakina, O. V, Pervikov, A. V, Rubtsov, K. V, & Lerner, M. I. (2020). Electrical Explosion of Wires for Manufacturing Bimetallic Antibacterial Ti–Ag and Fe–Ag Nanoparticles. *Russian Physics Journal*, *62*(9), 1580–1586. https://doi.org/10.1007/s11182-020-01879-x

Syed, A., Saraswati, S., Kundu, G. C., & Ahmad, A. (2013). Biological synthesis of silver nanoparticles using the fungus Humicola sp. And evaluation of their cytoxicity using

normal and cancer cell lines. *Spectrochimica Acta - Part A: Molecular and Biomolecular Spectroscopy*, *114*, 144–147. https://doi.org/10.1016/j.saa.2013.05.030

Sylvere, A. S., Justin, M., David, V., Joseph, M., & Betchewe, G. (2021). Impact of fractional effects on modulational instability and bright soliton in fractional optical metamaterials. *Https://Doi.Org/10.1080/17455030.2021.1880668*, *33*(2), 414–427. https://doi.org/10.1080/17455030.2021.1880668

Szczepanowicz, K., Stefańska, J., Socha, R. P., & Warszyński, P. (2010). Preparation of silver nanoparticles via chemical reduction and their antimicrobial activity. *Physicochemical Problems of Mineral Processing*, *45*(March 2014), 85–98.

Taglietti, A., A. Diaz Fernandez, Y., Amato, E., Cucca, L., Dacarro, G., Grisoli, P., Necchi, V., Pallavicini, P., Pasotti, L., & Patrini, M. (2012). Antibacterial Activity of Glutathione-Coated Silver Nanoparticles against Gram Positive and Gram Negative Bacteria. *Langmuir*, *28*(21), 8140–8148. https://doi.org/10.1021/la3003838

Tan, H. L., He, Z. C., Li, K. X., Li, E., Cheng, A. G., & Xu, B. (2019). *In-plane crashworthiness of re-entrant hierarchical honeycombs with negative Poisson ' s ratio*. *229*(July). https://doi.org/10.1016/j.compstruct.2019.111415

Tan, X., Wang, B., Yao, K., Zhu, S., Chen, S., Xu, P., Wang, L., & Sun, Y. (2019). Novel multi-stable mechanical metamaterials for trapping energy through shear deformation. *International Journal of Mechanical Sciences*, *164*(September). https://doi.org/10.1016/j.ijmecsci.2019.105168

Tanaka, H., Asao, S., Shibutani, Y., Huu Phuoc Street, L., Dinh, M., Tu Liem District, N., Noi, H., & Nam, V. (2021). Auxetic vibration behaviours of periodic tetrahedral units with a shared edge. *Royal Society Open Science*, *8*(10). https://doi.org/10.1098/RSOS.210768

Tang, H., Jiang, X., Ling, L., Li, L., & Hu, Y. (2020). Highly tailorable electromechanical properties of auxetic piezoelectric ceramics with ultra-low porosity. *Journal of the American Ceramic Society*, *103*(11), 6330–6347. https://doi.org/10.1111/JACE.17356

Tang, H., Wang, J., Zhang, S., Pang, H., Wang, X., Chen, Z., Li, M., Song, G., Qiu, M., & Yu, S. (2021). Recent advances in nanoscale zero-valent iron-based materials: Characteristics, environmental remediation and challenges. *Journal of Cleaner Production*, *319*. https://doi.org/10.1016/j.jclepro.2021.128641

Tang, Y., & Yin, J. (2017). Design of cut unit geometry in hierarchical kirigami-based auxetic metamaterials for high stretchability and compressibility. *Extreme Mechanics Letters*, *12*, 77–85. https://doi.org/10.1016/J.EML.2016.07.005

Tao, A., Sinsermsuksakul, P., & Yang, P. (2006). Polyhedral silver nanocrystals with distinct scattering signatures. *Angewandte Chemie - International Edition*, *45*(28), 4597–4601. https://doi.org/10.1002/anie.200601277

Tarafdar, J. C., & Raliya, R. (2013). Rapid, Low-Cost, and Ecofriendly Approach for Iron Nanoparticle Synthesis Using Aspergillus oryzae TFR9 . *Journal of Nanoparticles*, *2013*, 1–4. https://doi.org/10.1155/2013/141274

Tatarciuc, M., Maftei, G. A., Vitalariu, A., Luchian, I., Martu, I., & Diaconu-Popa, D. (2021). Inlay-Retained Dental Bridges—A Finite Element Analysis. *Applied Sciences 2021, Vol. 11, Page 3770*, *11*(9), 3770. https://doi.org/10.3390/APP11093770

Taylor, A., Krupskaya, Y., Costa, S., Oswald, S., Kramer, K., Füssel, S., Klingeler, R., Büchner, B., Borowiak-Palen, E., & Wirth, M. P. (2010). Functionalization of carbon encapsulated iron nanoparticles. *Journal of Nanoparticle Research*, *12*(2), 513–519. https://doi.org/10.1007/s11051-009-9773-0

Taylor, M., Francesconi, L., Gerendás, M. M., Shanian, A., Carson, C., Bertoldi, K., Taylor, M., Francesconi, L., Gerendás, M. M., Shanian, A., Carson, C., & Bertoldi, K. (2014). Low porosity metallic periodic structures with negative poisson's ratio. *Advanced Materials*, *26*(15), 2365–2370. https://doi.org/10.1002/adma.201304464

Teng, X. C., Ren, X., Zhang, Y., Jiang, W., Pan, Y., Zhang, X. G., Zhang, X. Y., & Xie, Y. M. (2022). A simple 3D re-entrant auxetic metamaterial with enhanced energy absorption. *International Journal of Mechanical Sciences*, *229*, 107524. https://doi.org/10.1016/J.IJMECSCI.2022.107524

Thresher, R. W., & Saito, G. E. (1973). The stress analysis of human teeth. *Journal of Biomechanics*, *6*(5), 443–449. https://doi.org/10.1016/0021-9290(73)90003-1

Tian, X., Chen, W., Gao, R., Liu, S., & Wang, J. (2020). Design of pore layout for perforated auxetic metamaterials with low-frequency band gaps. *Applied Physics Express*, *13*(4), 45503. https://doi.org/10.35848/1882-0786/AB7F5B

Tien, D. C., Liao, C. Y., Huang, J. C., Tseng, K. H., Lung, J. K., Tsung, T. T., Kao, W. S., Tsai, T. H., Cheng, T. W., Yu, B. S., Lin, H. M., & Stobinski, L. (2008). Novel technique for preparing a nano-silver water suspension by the arc-discharge method. *Reviews on Advanced Materials Science*, *18*(8), 752–758.

Tien, D. C., Tseng, K. H., Liao, C. Y., Huang, J. C., & Tsung, T. T. (2008). Discovery of ionic silver in silver nanoparticle suspension fabricated by arc discharge method. *Journal of Alloys and Compounds*, *463*(1–2), 408–411. https://doi.org/10.1016/j.jallcom.2007.09.048

Tikariha, A. K., Saurabh, N., Gudipadu, V., & Patel, S. (2022). Effect of auxetic structures parameters variation on PVDF-based piezoelectric energy harvesters. *Journal of Applied Physics*, *132*(24), 244105. https://doi.org/10.1063/5.0119742

Tipton, C. R., Han, E., & Mullin, T. (2012). Magneto-elastic buckling of a soft cellular solid. *Soft Matter*, *8*(26), 6880–6883. https://doi.org/10.1039/c2sm25965f

Tokoi, Y., Josho, K., Izuari, Y. M., Suzuki, T., Nakayama, T., Suematsu, H., Lee, W., Fu, Z., & Niihara, K. (2011). Particle size control of silver nanoparticles prepared by pulsed wire discharge in liquid media. *IOP Conference Series: Materials Science and Engineering*, *20*(1). https://doi.org/10.1088/1757-899X/20/1/012008

Toneguzzo, P., Viau, G., Acher, O., Fiévet-Vincent, F., & Fiévet, F. (1998). Monodisperse ferromagnetic particles for microwave applications. *Advanced Materials*, *10*(13), 1032–1035. https://doi.org/10.1002/(SICI)1521-4095(199809)10:13<1032::AID-ADMA1032>3.0.CO;2-M

Torras, M., & Roig, A. (2020). From Silver Plates to Spherical Nanoparticles: Snapshots

of Microwave-Assisted Polyol Synthesis. *ACS Omega*, *5*(11), 5731–5738. https://doi.org/10.1021/acsomega.9b03748

Tretiakov, K. V. (2009). Negative Poisson's ratio of two-dimensional hard cyclic tetramers. *Journal of Non-Crystalline Solids*, *355*(24–27), 1435–1438. https://doi.org/10.1016/j.jnoncrysol.2009.05.043

Tretiakov, K. V., Pigłowski, P. M., Hyżorek, K., & Wojciechowski, K. W. (2016). Enhanced auxeticity in Yukawa systems due to introduction of nanochannels in [001]-direction. *Smart Materials and Structures*, *25*(5), 054007. https://doi.org/10.1088/0964-1726/25/5/054007

Tretiakov, K. V., & Wojciechowski, K. W. (2005a). Poisson's ratio of the fcc hard sphere crystal at high densities. *Journal of Chemical Physics*, *123*(7), 074509. https://doi.org/10.1063/1.1949206

Tretiakov, K. V., & Wojciechowski, K. W. (2006). Elastic properties of the degenerate crystalline phase of two-dimensional hard dimers. *Journal of Non-Crystalline Solids*, *352*(40–41), 4221–4228. https://doi.org/10.1016/J.JNONCRYSOL.2006.08.004

Tretiakov, K. V., & Wojciechowski, K. W. (2014). Partially auxetic behavior in fcc crystals of hard-core repulsive Yukawa particles. *Physica Status Solidi (B)*, *251*(2), 383–387. https://doi.org/10.1002/pssb.201384244

Tretiakov, K. V., & Wojciechowski, K. W. (2020). Auxetic, Partially Auxetic, and Nonauxetic Behaviour in 2D Crystals of Hard Cyclic Tetramers. *Physica Status Solidi - Rapid Research Letters*, *14*(7), 2000198. https://doi.org/10.1002/pssr.202000198

Tretiakov, K. V., & Wojciechowski, K. W. (2022). Auxeticity and Its Pressure Dependence for Strongly Anisotropic Hard Cyclic Tetramers. *Physica Status Solidi - Rapid Research Letters*, 2200288. https://doi.org/10.1002/pssr.202200288

Tretiakov, K. V, & Wojciechowski, K. W. (2005b). Monte Carlo simulation of two-dimensional hard body systems with extreme values of the Poisson's ratio. *Physica Status Solidi (B)*, *242*(3), 730–741. https://doi.org/10.1002/pssb.200460390

Tretiakov, K. V, & Wojciechowski, K. W. (2007). Poisson's ratio of simple planar 'isotropic'' solids in two dimensions.' *Physica Status Solidi (B)*, *244*(3), 1038–1046. https://doi.org/10.1002/pssb.200572721

Trivedi, S. (2014). Finite element analysis: A boon to dentistry. *Journal of Oral Biology and Craniofacial Research*, *4*(3), 200–203. https://doi.org/10.1016/J.JOBCR.2014.11.008

Tseng, K. H., Chen, Y. C., & Shyue, J. J. (2011). Continuous synthesis of colloidal silver nanoparticles by electrochemical discharge in aqueous solutions. *Journal of Nanoparticle Research*, *13*(5), 1865–1872. https://doi.org/10.1007/s11051-010-9937-y

Tseng, K. H., Chou, C. J., Liu, T. C., Haung, Y. H., & Chung, M. Y. (2016). Preparation of Ag-Cu composite nanoparticles by the submerged arc discharge method in aqueous media. *Materials Transactions*, *57*(3), 294–301. https://doi.org/10.2320/matertrans.M2015288

Tseng, K. H., Chou, C. J., Liu, T. C., Tien, D. C., Chang, C. Y., & Stobinski, L. (2018). Relationship between Ag nanoparticles and Ag ions prepared by arc discharge method. *Nanotechnology Reviews*, *7*(1), 1–9. https://doi.org/10.1515/ntrev-2017-0167

Tseng, K. H., Lin, Y. H., Tien, D. C., & Chung, M. Y. (2018). The study of nanosilver colloid with/without ammonia prepare by Submerged Arc Discharge Method. *Proceedings of the 13th IEEE Conference on Industrial Electronics and Applications, ICIEA 2018*, 379–383. https://doi.org/10.1109/ICIEA.2018.8397746

Tung, D. K., Manh, D. H., Phong, L. T. H., Nam, P. H., Nam, D. N. H., Anh, N. T. N., Nong, H. T. T., Phan, M. H., & Phuc, N. X. (2016). Iron Nanoparticles Fabricated by High-Energy Ball Milling for Magnetic Hyperthermia. *Journal of Electronic Materials*, *45*(5), 2644–2650. https://doi.org/10.1007/s11664-016-4457-x

Tuval, T., & Gedanken, A. (2007). A microwave-assisted polyol method for the deposition of silver nanoparticles on silica spheres. *Nanotechnology*, *18*(25). https://doi.org/10.1088/0957-4484/18/25/255601

Uddin, K. Z., Pagliocca, N., Anni, I. A., Youssef, G., & Koohbor, B. (2022). Multiscale Strain Field Characterization in Flexible Planar Auxetic Metamaterials with Rotating Squares. *Advanced Engineering Materials*, 2201248. https://doi.org/10.1002/ADEM.202201248

Ulbin, M., Borovinšek, M., Vesenjak, M., & Glodež, S. (2020). Computational Fatigue Analysis of Auxetic Cellular Structures Made of SLM AlSi10Mg Alloy. *Metals 2020, Vol. 10, Page 945*, *10*(7), 945. https://doi.org/10.3390/MET10070945

Underwood, S., & Mulvaney, P. (1994). Effect of the Solution Refractive Index on the Color of Gold Colloids. *Langmuir*, *10*(10), 3427–3430. https://doi.org/10.1021/la00022a011

Usta, F., Türkmen, H. S., & Scarpa, F. (2021). Low-velocity impact resistance of composite sandwich panels with various types of auxetic and non-auxetic core structures. *Thin-Walled Structures*, *163*, 107738. https://doi.org/10.1016/j.tws.2021.107738

Usta, F., Türkmen, H. S., & Scarpa, F. (2022). High-velocity impact resistance of doubly curved sandwich panels with re-entrant honeycomb and foam core. *International Journal of Impact Engineering*, *165*, 104230. https://doi.org/10.1016/J.IJIMPENG.2022.104230

Valentini, P. P., Pennestrì, E., & Quattrociocchi, L. (2016). Biomechanical model for simulating impacts against protective padding of sport facility. *Sports Engineering*, *19*(1), 47–57. https://doi.org/10.1007/s12283-015-0187-1

Valera-Jiménez, J. F., Burgueño-Barris, G., Gómez-González, S., López-López, J., Valmaseda-Castellón, E., & Fernández-Aguado, E. (2020). Finite element analysis of narrow dental implants. *Dental Materials*, *36*(7), 927–935. https://doi.org/10.1016/J.DENTAL.2020.04.013

Vandana, & Sen, P. (2005). Nanometre scale surface modification in a needle-plate exploding system. *Journal of Physics Condensed Matter*, *17*(35), 5327–5334. https://doi.org/10.1088/0953-8984/17/35/001

Varas, D., Pernas-Sánchez, J., Fjeldberg, N., & Martín-Montal, J. (2023). Experimental analysis at different loading rates of 3D printed polymeric auxetic structure based on cylindrical elements. *Polymer Testing*, *119*, 107930. https://doi.org/10.1016/J.POLYMERTESTING.2023.107930

Veronda, D. R., & Westmann, R. A. (1970). Mechanical characterization of skin-Finite deformations. *Journal of Biomechanics*, *3*(1). https://doi.org/10.1016/0021-9290(70)90055-2

Viau, G., Fiévet-Vincent, F., & Fiévet, F. (1996a). Monodisperse iron-based particles: Precipitation in liquid polyols. *Journal of Materials Chemistry*, *6*(6), 1047–1053. https://doi.org/10.1039/JM9960601047

Viau, G., Fiévet-Vincent, F., & Fiévet, F. (1996b). Nucleation and growth of bimetallic CoNi and FeNi monodisperse particles prepared in polyols. *Solid State Ionics*, *84*(3–4), 259–270. https://doi.org/10.1016/0167-2738(96)00005-7

Viau, G., Piquemal, J. Y., Esparrica, M., Ung, D., Chakroune, N., Warmont, F., & Fiévet, F. (2003). Formation of assembled silver nanowires by reduction of silver thiolate in polyol/toluene medium. *Chemical Communications*, *3*(17), 2216–2217. https://doi.org/10.1039/b304021f

Viceconti, M., Zannoni, C., Testi, D., Petrone, M., Perticoni, S., Quadrani, P., Taddei, F., Imboden, S., & Clapworthy, G. (2007). The multimod application framework: A rapid application development tool for computer aided medicine. *Computer Methods and Programs in Biomedicine*, *85*(2), 138–151. https://doi.org/10.1016/J.CMPB.2006.09.010

Vigneshwaran, N., Ashtaputre, N. M., Varadarajan, P. V, Nachane, R. P., Paralikar, K. M., & Balasubramanya, R. H. (2007). Biological synthesis of silver nanoparticles using the fungus Aspergillus flavus. *Materials Letters*, *61*(6), 1413–1418. https://doi.org/10.1016/j.matlet.2006.07.042

Vitta, Y., Piscitelli, V., Fernandez, A., Gonzalez-Jimenez, F., & Castillo, J. (2011). α-Fe nanoparticles produced by laser ablation: Optical and magnetic properties. *Chemical Physics Letters*, *512*(1–3), 96–98. https://doi.org/10.1016/j.cplett.2011.07.020

Vivekanandhan. (2009). Biological Synthesis of Silver Nanoparticles Using Glycine max (Soybean) Leaf Extract: An Investigation on Different Soybean Varieties. *Journal of Nanoscience and Nanotechnology*, *9*(12), 6828–6833. https://doi.org/10.1166/jnn.2009.2201

Vyavahare, S., & Kumar, S. (2021). Numerical and experimental investigation of FDM fabricated re-entrant auxetic structures of ABS and PLA materials under compressive loading. *Rapid Prototyping Journal*, *27*(2), 223–244. https://doi.org/10.1108/RPJ-10-2019-0271/FULL/PDF

Wagner, J., Tshikhudo, T. R., & Köhler, J. M. (2007). Microfluidic generation of metal nanoparticles by borohydride reduction. *Chemical Engineering Journal*, *135*(SUPPL. 1), 104–109. https://doi.org/10.1016/j.cej.2007.07.046

Waki, H., Igarashi, H., & Honma, T. (2005). Estimation of effective permeability of magnetic composite materials. *IEEE Transactions on Magnetics*, *41*(5), 1520–1523. https://doi.org/10.1109/TMAG.2005.845071

Wan, M., Yu, K., & Sun, H. (2022). 4D printed programmable auxetic metamaterials with shape memory effects. *Composite Structures*, *279*(September 2021), 114791. https://doi.org/10.1016/j.compstruct.2021.114791

Wan, Y., Guo, Z., Jiang, X., Fang, K., Lu, X., Zhang, Y., & Gu, N. (2013). Quasi-spherical silver nanoparticles: Aqueous synthesis and size control by the seed-mediated Lee-Meisel method. *Journal of Colloid and Interface Science*, *394*(1), 263–268. https://doi.org/10.1016/j.jcis.2012.12.037

Wang, B., Zhang, L., & Zhou, X. (2014). Synthesis of silver nanocubes as a SERS substrate for the determination of pesticide paraoxon and thiram. *Spectrochimica Acta - Part A: Molecular and Biomolecular Spectroscopy*, *121*, 63–69. https://doi.org/10.1016/j.saa.2013.10.013

Wang, H., Lu, Z., Yang, Z., & Li, X. (2019). A novel re-entrant auxetic honeycomb with enhanced in-plane impact resistance. *Composite Structures*, *208*, 758–770. https://doi.org/10.1016/j.compstruct.2018.10.024

Wang, H., Qiao, X., Chen, J., & Ding, S. (2005). Preparation of silver nanoparticles by chemical reduction method. *Colloids and Surfaces A: Physicochemical and Engineering Aspects*, *256*(2–3), 111–115. https://doi.org/10.1016/j.colsurfa.2004.12.058

Wang, H., Xiao, S. H., & Zhang, C. (2021). Novel Planar Auxetic Metamaterial Perforated with Orthogonally Aligned Oval-Shaped Holes and Machine Learning Solutions. *Advanced Engineering Materials*, *23*(7), 2100102. https://onlinelibrary.wiley.com/doi/full/10.1002/adem.202100102

Wang, H., Xiao, S., & Wang, J. (2021). Disordered auxetic metamaterials architected by random peanut-shaped perturbations. *Materials & Design*, *212*, 110291. https://doi.org/10.1016/J.MATDES.2021.110291

Wang, K., Chang, Y. H., Chen, Y. W., Zhang, C., & Wang, B. (2015). Designable dual-material auxetic metamaterials using three-dimensional printing. *Materials & Design*, *67*, 159–164. https://doi.org/10.1016/J.MATDES.2014.11.033

Wang, L., Ulliac, G., Wang, B., Iglesias Martínez, J. A., Dudek, K. K., Laude, V., & Kadic, M. (2022). 3D Auxetic Metamaterials with Elastically-Stable Continuous Phase Transition. *Advanced Science*, *9*(34), 2204721. https://doi.org/10.1002/ADVS.202204721

Wang, Q., Yang, Z., Lu, Z., & Li, X. (2020). Mechanical responses of 3D cross-chiral auxetic materials under uniaxial compression. *Materials & Design*, *186*, 108226. https://doi.org/10.1016/J.MATDES.2019.108226

Wang, S., Deng, C., Ojo, O., Akinrinlola, B., Kozub, J., & Wu, N. (2022). Design and modeling of a novel three dimensional auxetic reentrant honeycomb structure for energy absorption. *Composite Structures*, *280*, 114882. https://doi.org/10.1016/J.COMPSTRUCT.2021.114882

Wang, T., Jin, X., Chen, Z., Megharaj, M., & Naidu, R. (2014). Green synthesis of Fe nanoparticles using eucalyptus leaf extracts for treatment of eutrophic wastewater. *Science of the Total Environment*, *466–467*, 210–213. https://doi.org/10.1016/j.scitotenv.2013.07.022

Wang, T., Li, Z., Wang, L., Ma, Z., & Hulbert, G. M. (2019). *Dynamic Crushing Analysis of a Three-Dimensional Re-Entrant Auxetic Cellular Structure*. https://doi.org/10.3390/ma12030460

Wang, T., Xie, Y., Wang, L., Zhang, X., & Ma, Z. (2022). Size effects of elastic properties for auxetic cellular structures : bending energy-based method. *Materials Today Communications*, *31*(December 2021), 103585. https://doi.org/10.1016/j.mtcomm.2022.103585

Wang, W., & Asher, S. A. (2001). Photochemical Incorporation of Silver Quantum Dots in Monodisperse Silica Colloids for Photonic Crystal Applications. *J. Am. Chem. Soc.*, *123*, 12528–12535. https://doi.org/10.1021/ja011262j

Wang, W., Zhang, W., Guo, M., Yang, J., & Ma, L. (2023). Energy absorption characteristics of a lightweight auxetic honeycomb under low-velocity impact loading. *Thin-Walled StructuresWalled Structures*, *185*(October 2022), 110577. https://doi.org/10.1016/j.tws.2023.110577

Wang, X.-T., Wang, B., Li, X., & Ma, L. (2017). Mechanical properties of 3D re-entrant auxetic cellular structures. *International Journal of Mechanical Sciences*, *131–132*, 396–407. https://doi.org/10.1016/j.ijmecsci.2017.05.048

Wang, Y. C., & Lakes, R. (2002). Analytical parametric analysis of the contact problem of human buttocks and negative Poisson's ratio foam cushions. *International Journal of Solids and Structures*, *39*(18), 4825–4838. https://doi.org/10.1016/S0020-7683(02)00379-7

Wang, Y., Zhao, W., Zhou, G., & Wang, C. (2018). International Journal of Mechanical Sciences Analysis and parametric optimization of a novel sandwich panel with double-V auxetic structure core under air blast loading. *International Journal of Mechanical Sciences*, *142–143*(May), 245–254. https://doi.org/10.1016/j.ijmecsci.2018.05.001

Wang, Z., Chen, X., Liu, J., Zhang, M., & Qian, Y. (2004). Glucose reduction route synthesis of uniform silver nanowires in large-scale. *Chemistry Letters*, *33*(9), 1160–1161. https://doi.org/10.1246/cl.2004.1160

Wang, Z., Li, X., Gao, M., & Zeng, X. (2012). One-step preparation of amorphous iron nanoparticles by laser ablation. *Powder Technology*, *215–216*, 147–150. https://doi.org/10.1016/j.powtec.2011.09.039

Wang, Z., Zulifqar, A., & Hu, H. (2016). Auxetic composites in aerospace engineering. In *Advanced Composite Materials for Aerospace Engineering* (pp. 213–240). Elsevier. https://doi.org/10.1016/b978-0-08-100037-3.00007-9

Wani, I. A., Ganguly, A., Ahmed, J., & Ahmad, T. (2011). Silver nanoparticles: Ultrasonic wave assisted synthesis, optical characterization and surface area studies. *Materials Letters*, *65*(3), 520–522. https://doi.org/10.1016/j.matlet.2010.11.003

Warmuth, F., Osmanlic, F., Adler, L., Lodes, M. A., & Körner, C. (2017). Fabrication and characterisation of a fully auxetic 3D lattice structure via selective electron beam melting. *Smart Materials and Structures*, *26*(2). https://doi.org/10.1088/1361-665X/26/2/025013

Wei, L., Zhao, X., Yu, Q., & Zhu, G. (2020). A novel star auxetic honeycomb with

enhanced in-plane crushing strength. *Thin-Walled Structures*, *149*, 106623. https://doi.org/10.1016/j.tws.2020.106623

Wei, Y. L., Yang, Q. S., & Tao, R. (2021). SMP-based chiral auxetic mechanical metamaterial with tunable bandgap function. *International Journal of Mechanical Sciences*, *195*, 106267. https://doi.org/10.1016/J.IJMECSCI.2021.106267

Whitty, J. P. M., Nazare, F., & Alderson, A. (2002). Modelling the effects of density variations on the in-plane Poisson's ratios and Young's moduli of periodic conventional and re-entrant honeycombs - Part 1: Rib thickness variations. *Cellular Polymers*, *21*(2), 69–98.

Wiley, B., Herricks, T., Sun, Y., & Xia, Y. (2004). Polyol synthesis of silver nanoparticles: Use of chloride and oxygen to promote the formation of single-crystal, truncated cubes and tetrahedrons. *Nano Letters*, *4*(9), 1733–1739. https://doi.org/10.1021/nl048912c

Wiley, B. J., Chen, Y., Mclellan, J. M., Xiong, Y., Li, Z., Ginger, D., & Xia, Y. (2007). *Synthesis and Optical Properties of Silver Nanobars and Nanorice*.

Wiley, B. J., Skrabalak, S. E., Xia, Y., Kim, M., & Formo, E. V. (2008). On the Polyol Synthesis of Silver Nanostructures: Glycolaldehyde as a Reducing Agent. *Nano Letters*, *8*(7), 2077–2081. https://doi.org/10.1021/nl800910d

Wiley, B., Sun, Y., Mayers, B., & Xia, Y. (2005). Shape-controlled synthesis of metal nanostructures: The case of silver. *Chemistry - A European Journal*, *11*(2), 454–463. https://doi.org/10.1002/chem.200400927

Wiley, B., Sun, Y., & Xia, Y. (2005). Polyol synthesis of silver nanostructures: Control of product morphology with Fe(II) or Fe(III) Species. *Langmuir*, *21*(18), 8077–8080. https://doi.org/10.1021/la050887i

Williams, D. (2008). The relationship between biomaterials and nanotechnology. *Biomaterials*, *29*(12), 1737–1738. https://doi.org/10.1016/j.biomaterials.2008.01.003

Wojciechowski, K. W. (1987). Constant thermodynamic tension Monte Carlo studies of elastic properties of a two-dimensional system of hard cyclic hexamers. *Molecular Physics*, *61*(5), 1247–1258. https://doi.org/10.1080/00268978700101761

Wojciechowski, K. W. (1989). Two-dimensional isotropic system with a negative poisson ratio. *Physics Letters A*, *137*(1–2), 60–64. https://doi.org/10.1016/0375-9601(89)90971-7

Wojciechowski, K. W. (1995). Negative Poisson's Ratios at Negative Pressures. *Molec. Phys. Reports*, *10*, 129–136. http://www.ifmpan.poznan.pl/mol/dokumenty/010-10.pdf

Wojciechowski, K. W., & Brańka, A. C. (1989). Elastic moduli of a perfect hard disc crystal in two dimensions. *Physics Letters A*, *134*(5), 314–318. https://doi.org/10.1016/0375-9601(89)90642-7

Wojciechowski K.W., Branka, A. C. (1994). Auxetics: Materials and Models with Negative Poisson's Ratios. *Molec. Phys. Reports* , *6*, 71–85.

Wong-Ek, K., Eiamchai, P., Horprathum, M., Patthanasettakul, V., Limnonthakul, P.,

Chindaudom, P., & Nuntawong, N. (2010). Silver nanoparticles deposited on anodic aluminum oxide template using magnetron sputtering for surface-enhanced Raman scattering substrate. *Thin Solid Films*, *518*(23), 7128–7132. https://doi.org/10.1016/j.tsf.2010.07.017

Wood, I., Jawad, Z., Paisley, C., & Brunton, P. (2008). Non-carious cervical tooth surface loss: a literature review. *Journal of Dentistry*, *36*(10), 759–766. https://doi.org/10.1016/J.JDENT.2008.06.004

Wu, G., Cho, Y., Choi, I. S., Ge, D., Li, J., Han, H. N., Lubensky, T., & Yang, S. (2015). Directing the deformation paths of soft metamaterials with prescribed asymmetric units. *Advanced Materials*, *27*(17), 2747–2752. https://doi.org/10.1002/adma.201500716

Wu, K., Zhao, X., Bifano, T. G., Anderson, S. W., & Zhang, X. (2022). Auxetics-Inspired Tunable Metamaterials for Magnetic Resonance Imaging. *Advanced Materials*, *34*(6), 2109032. https://doi.org/10.1002/adma.202109032

Wu, S., Eichenberger, J., Dai, J., Chang, Y., Ghalichechian, N., & Zhao, R. R. (2022). Magnetically Actuated Reconfigurable Metamaterials as Conformal Electromagnetic Filters. *Advanced Intelligent Systems*, *4*(9), 2200106. https://doi.org/10.1002/AISY.202200106

Wu, S., Ze, Q., Zhang, R., Hu, N., Cheng, Y., Yang, F., & Zhao, R. (2019). Symmetry-Breaking Actuation Mechanism for Soft Robotics and Active Metamaterials. *ACS Applied Materials and Interfaces*, *11*(44), 41649–41658. https://doi.org/10.1021/ACSAMI.9B13840/ASSET/IMAGES/LARGE/AM9B13840_0007.JPEG

Wu, T., Li, M., Zhu, X., & Lu, X. (2021). Research on non-pneumatic tire with gradient anti-tetrachiral structures. *Mechanics of Advanced Materials and Structures*, *28*(22), 2351–2359. https://doi.org/10.1080/15376494.2020.1734888

Wu, W., Hu, W., Qian, G., Liao, H., Xu, X., & Berto, F. (2019). Mechanical design and multifunctional applications of chiral mechanical metamaterials: A review. *Materials and Design*, *180*(June), 107950. https://doi.org/10.1016/j.matdes.2019.107950

Wu, W., Song, X., Liang, J., Xia, R., Qian, G., & Fang, D. (2018). Mechanical properties of anti-tetrachiral auxetic stents. *Composite Structures*, *185*, 381–392. https://doi.org/10.1016/j.compstruct.2017.11.048

Wu, Y., Li, Y., & Ong, B. S. (2006). Printed silver ohmic contacts for high-mobility organic thin-film transistors. *Journal of the American Chemical Society*, *128*(13), 4202–4203. https://doi.org/10.1021/ja058725w

Wu, Y., Zhou, Q., Li, H., Liu, W., Wang, T., & Jiang, G. (2010). Effects of silver nanoparticles on the development and histopathology biomarkers of Japanese medaka (Oryzias latipes) using the partial-life test. *Aquatic Toxicology*, *100*(2), 160–167. https://doi.org/10.1016/j.aquatox.2009.11.014

Xiao, S., Shen, M., Guo, R., Wang, S., & Shi, X. (2009). Immobilization of Zerovalent Iron Nanoparticles into Electrospun Polymer Nanofibers: Synthesis, Characterization, and Potential Environmental Applications. *Journal of Physical Chemistry C*, *113*(42), 18062–18068. https://doi.org/10.1021/jp905542g

Xu, N., Liu, H., An, M., & Wang, L. (2021). *Novel 2D star-shaped honeycombs with enhanced effective Young ' s modulus and negative Poisson ' s ratio*. *43*. https://doi.org/10.1016/j.eml.2020.101164

Xu, W., Dong, Z., & Ma, P. (2020). Finite element analyses of auxetic warp-knitted fabric deformation behaviors under low-velocity impact loading. *The Journal of The Textile Institute*. https://doi.org/10.1080/00405000.2020.1714273

Yamamoto, T., Wada, Y., Sakata, T., Mori, H., Goto, M., Hibino, S., & Yanagida, S. (2004). Microwave-assisted preparation of silver nanoparticles. *Chemistry Letters*, *33*(2), 158–159. https://doi.org/10.1246/cl.2004.158

Yang, C., Chang, Y. B., & Lee, D. (2020). Nonlinearity of Enhanced Cell Structures Having Auxetic Material Properties. *ASME International Mechanical Engineering Congress and Exposition, Proceedings (IMECE)*, *12*. https://doi.org/10.1115/IMECE2019-11361

Yang, C., Vora, H. D., & Chang, Y. (2018). Behavior of auxetic structures under compression and impact forces. *Smart Materials and Structures*, *27*(2). https://doi.org/10.1088/1361-665X/aaa3cf

Yang, D. U., Lee, S., & Huang, F. Y. (2003). Geometric effects on micropolar elastic honeycomb structure with negative Poisson's ratio using the finite element method. *Finite Elements in Analysis and Design*, *39*(3), 187–205. https://doi.org/10.1016/S0168-874X(02)00066-5

Yang, T. I., Brown, R. N. C., Kempel, L. C., & Kofinas, P. (2011a). Controlled synthesis of core-shell iron-silica nanoparticles and their magneto-dielectric properties in polymer composites. *Nanotechnology*, *22*(10). https://doi.org/10.1088/0957-4484/22/10/105601

Yang, T. I., Brown, R. N. C., Kempel, L. C., & Kofinas, P. (2011b). Controlled synthesis of core–shell iron–silica nanoparticles and their magneto-dielectricproperties in polymer composites. *Nanotechnology*, *22*(10), 105601. https://doi.org/10.1088/0957-4484/22/10/105601

Yang, W., Huang, R., Liu, J. J., Liu, J. J., & Huang, W. (2022). Ballistic impact responses and failure mechanism of composite double-arrow auxetic structure. *Thin-Walled Structures*, *174*, 109087. https://doi.org/10.1016/J.TWS.2022.109087

Yang, W., Li, Z.-M., Shi, W., Xie, B.-H., & Yang, M.-B. (2004). Review On auxetic materials. *Journal of Materials Science*, *39*, 3269–3279.

Yao, J., Sun, R., Scarpa, F., Remillat, C., Gao, Y., & Su, Y. (2021). Two-dimensional graded metamaterials with auxetic rectangular perforations. *Composite Structures*, *261*, 113313. https://doi.org/10.1016/j.compstruct.2020.113313

Yeon, H., Lee, H., Kim, Y., Lee, D., Lee, Y., Lee, J. S. J., Shin, J., Choi, C., Kang, J. H., Suh, J. M., Kim, H., Kum, H. S., Lee, J. S. J., Kim, D., Ko, K., Ma, B. S., Lin, P., Han, S., Kim, S., … Kim, J. (2021). Long-term reliable physical health monitoring by sweat pore–inspired perforated electronic skins. *Science Advances*, *7*(27). https://doi.org/10.1126/SCIADV.ABG8459/SUPPL_FILE/ABG8459_SM.PDF

Yildirimer, L., Thanh, N. T. K., Loizidou, M., & Seifalian, A. M. (2011). Toxicological considerations of clinically applicable nanoparticles. *Nano Today*, *6*(6), 585–607.

https://doi.org/10.1016/j.nantod.2011.10.001

Yin, H., Yamamoto, T., Wada, Y., & Yanagida, S. (2004). Large-scale and size-controlled synthesis of silver nanoparticles under microwave irradiation. *Materials Chemistry and Physics*, *83*(1), 66–70. https://doi.org/10.1016/j.matchemphys.2003.09.006

Yin, Y., Li, Z. Y., Zhong, Z., Gates, B., Xia, Y., & Venkateswaran, S. (2002). Synthesis and characterization of stable aqueous dispersions of silver nanoparticles through the Tollens process. *Journal of Materials Chemistry*, *12*(3), 522–527. https://doi.org/10.1039/b107469e

Yu, D. G. (2007). Formation of colloidal silver nanoparticles stabilized by Na+-poly($γ$-glutamic acid)-silver nitrate complex via chemical reduction process. *Colloids and Surfaces B: Biointerfaces*, *59*(2), 171–178. https://doi.org/10.1016/j.colsurfb.2007.05.007

Yuan, S., Shen, F., Bai, J., Chua, C. K., Wei, J., & Zhou, K. (2017). 3D soft auxetic lattice structures fabricated by selective laser sintering: TPU powder evaluation and process optimization. *Materials and Design*, *120*, 317–327. https://doi.org/10.1016/j.matdes.2017.01.098

Yun, G. S., Bac, L. H., Kim, J. S., Kwon, Y. S., Choi, H. S., & Kim, J. C. (2011). Preparation and dispersive properties of Ag colloid by electrical explosion of wire. *Journal of Alloys and Compounds*, *509*(SUPPL. 1), S348--S352. https://doi.org/10.1016/j.jallcom.2011.01.142

Yusuf İnan, C., Yusuf Inan, C., & Evis, Z. (2023). *The effect of the geometric influence of trichiral structures on mechanical properties*. https://doi.org/10.21203/RS.3.RS-3268583/V1

Zang, L., Wang, X., Yan, P., & Zhao, Z. (2021). Structural design and characteristics of a non-pneumatic tire with honeycomb structure. *Https://Doi.Org/10.1080/15376494.2021.1919800*, *29*(25), 4066–4073. https://doi.org/10.1080/15376494.2021.1919800

Ze, Q., Kuang, X., Wu, S., Wong, J., Macrae Montgomery, S., Zhang, R., Kovitz, J. M., Yang, F., Jerry Qi, H., Zhao, R., Ze, Q., Wu, S., Zhang, R., Zhao, R., Kuang, X., Wong, J., Montgomery, S. M., Qi, H. J., Kovitz, J. M., & Yang, F. (2020). Magnetic Shape Memory Polymers with Integrated Multifunctional Shape Manipulation. *Advanced Materials*, *32*(4), 1906657. https://doi.org/10.1002/ADMA.201906657

Zeng, J., Hu, H., & Zhou, L. (2017). A study on negative Poisson's ratio effect of 3D auxetic orthogonal textile composites under compression. *Smart Materials and Structures*, *26*(6). https://doi.org/10.1088/1361-665X/aa6fe6

Zhan, C., Li, M., Mccoy, R., Zhao, L., & Lu, W. (2022). 3D printed hierarchical re-entrant honeycombs : Enhanced mechanical properties and the underlying deformation mechanisms. *Composite Structures*, *290*, 115550. https://doi.org/10.1016/j.compstruct.2022.115550

Zhang, D., Klabunde, K., Sorensen, C., & Hadjipanayis, G. (1998). Magnetization temperature dependence in iron nanoparticles. *Physical Review B - Condensed Matter and Materials Physics*, *58*(21), 14167–14170. https://doi.org/10.1103/PhysRevB.58.14167

Zhang, D., Qi, L., Yang, J., Ma, J., Cheng, H., & Huang, L. (2004). Wet Chemical Synthesis of Silver Nanowire Thin Films at Ambient Temperature. *Chemistry of Materials*, *16*(5), 872–876. https://doi.org/10.1021/cm0350737

Zhang, H., Zou, G., Liu, L., Li, Y., Tong, H., Sun, Z., & Zhou, Y. N. (2016). A comparative study of silver nanoparticles synthesized by arc discharge and femtosecond laser ablation in aqueous solution. *Applied Physics A: Materials Science and Processing*, *122*(10), 1–14. https://doi.org/10.1007/s00339-016-0424-x

Zhang, H., Zou, G., Liu, L., Tong, H., Li, Y., Bai, H., & Wu, A. (2017). Synthesis of silver nanoparticles using large-area arc discharge and its application in electronic packaging. *Journal of Materials Science*, *52*(6), 3375–3387. https://doi.org/10.1007/s10853-016-0626-9

Zhang, J., Lu, G., Ruan, D., & Wang, Z. (2018). Tensile behavior of an auxetic structure: Analytical modeling and finite element analysis. *International Journal of Mechanical Sciences*, *136*, 143–154. https://doi.org/10.1016/J.IJMECSCI.2017.12.029

Zhang, J., Lu, G., Wang, Z., Ruan, D., Alomarah, A., & Durandet, Y. (2018). Large deformation of an auxetic structure in tension: Experiments and finite element analysis. *Composite Structures*, *184*, 92–101. https://doi.org/10.1016/J.COMPSTRUCT.2017.09.076

Zhang, J., Post, M., Veres, T., Jakubek, Z. J., Guan, J., Wang, D., Normandin, F., Deslandes, Y., & Simard, B. (2006). Laser-assisted synthesis of superparamagnetic Fe@Au core-shell nanoparticles. *Journal of Physical Chemistry B*, *110*(14), 7122–7128. https://doi.org/10.1021/jp0560967

Zhang, K., Zhao, P., Zhao, C., Hong, F., & Deng, Z. (2020). Study on the mechanism of band gap and directional wave propagation of the auxetic chiral lattices. *Composite Structures*, *238*, 111952. https://doi.org/10.1016/J.COMPSTRUCT.2020.111952

Zhang, S. L., Lai, Y. C., He, X., Liu, R., Zi, Y., & Wang, Z. L. (2017). Auxetic Foam-Based Contact-Mode Triboelectric Nanogenerator with Highly Sensitive Self-Powered Strain Sensing Capabilities to Monitor Human Body Movement. *Advanced Functional Materials*, *27*(25), 1–7. https://doi.org/10.1002/adfm.201606695

Zhang, T., Wang, L., Chen, Q., & Chen, C. (2014). Cytotoxic potential of silver nanoparticles. *Yonsei Medical Journal*, *55*(2), 283–291. https://doi.org/10.3349/ymj.2014.55.2.283

Zhang, W.-X., & Wang, C.-B. (1997). Rapid and complete dechlorination of TCE and PCBs by nanoscale Fe and Pd/Fe particles. *Environ. Sci. Technol.*, *37*(7), 2154–2156.

Zhang, W., Yao, Y., Li, K., Huang, Y., & Chen, Y. (2011). Influence of dissolved oxygen on aggregation kinetics of citrate-coated silver nanoparticles. *Environmental Pollution*, *159*(12), 3757–3762. https://doi.org/10.1016/j.envpol.2011.07.013

Zhang, W., Zhao, S., Scarpa, F., Wang, J., & Sun, R. (2021). In-plane mechanical behavior of novel auxetic hybrid metamaterials. *Thin-Walled Structures*, *159*, 107191. https://doi.org/10.1016/j.tws.2020.107191

Zhang, X. F., Liu, Z. G., Shen, W., & Gurunathan, S. (2016). Silver nanoparticles:

Synthesis, characterization, properties, applications, and therapeutic approaches. *International Journal of Molecular Sciences*, *17*(9). https://doi.org/10.3390/ijms17091534

Zhang, X. Y., Ren, X., Wang, X. Y., Zhang, Y., & Xie, Y. M. (2021). A novel combined auxetic tubular structure with enhanced tunable stiffness. *Composites Part B: Engineering*, *226*, 109303. https://doi.org/10.1016/J.COMPOSITESB.2021.109303

Zhang, Y., Ren, X., Han, D., Cheng, X., Jiang, W., Zhang, X. G., Zhang, X. Y., & Xie, Y. M. (2022). Static and dynamic properties of a perforated metallic auxetic metamaterial with tunable stiffness and energy absorption. *International Journal of Impact Engineering*, *164*, 104193. https://doi.org/10.1016/J.IJIMPENG.2022.104193

Zhang, Y., Ren, X., Zhang, X. Y., Huang, T. T., Sun, L., & Xie, Y. M. (2021). A novel buckling-restrained brace with auxetic perforated core: Experimental and numerical studies. *Engineering Structures*, *249*, 113223. https://doi.org/10.1016/J.ENGSTRUCT.2021.113223

Zhang, Z., Hu, H., Liu, S., & Xu, B. (2013). Study of an auxetic structure made of tubes and corrugated sheets. *Physica Status Solidi (B)*, *250*(10), 1996–2001. https://doi.org/10.1002/PSSB.201248349

Zhang, Z. K., Hu, H., & Xu, B. G. (2013). An elastic analysis of a honeycomb structure with negative Poisson's ratio. *Smart Materials and Structures*, *22*(8), 084006. https://doi.org/10.1088/0964-1726/22/8/084006

Zhao, T., Sun, R., Yu, S., Zhang, Z., Zhou, L., Huang, H., & Du, R. (2010). Size-controlled preparation of silver nanoparticles by a modified polyol method. *Colloids and Surfaces A: Physicochemical and Engineering Aspects*, *366*(1–3), 197–202. https://doi.org/10.1016/j.colsurfa.2010.06.005

Zhao, X., Liu, W., Cai, Z., Han, B., Qian, T., & Zhao, D. (2016). An overview of preparation and applications of stabilized zero-valent iron nanoparticles for soil and groundwater remediation. *Water Research*, *100*, 245–266. https://doi.org/10.1016/j.watres.2016.05.019

Zhao, X., Xia, Y., Li, Q., Ma, X., Quan, F., Geng, C., & Han, Z. (2014). Microwave-assisted synthesis of silver nanoparticles using sodium alginate and their antibacterial activity. *Colloids and Surfaces A: Physicochemical and Engineering Aspects*, *444*, 180–188. https://doi.org/10.1016/j.colsurfa.2013.12.008

Zheng, X., Guo, X., & Watanabe, I. (2021). A mathematically defined 3D auxetic metamaterial with tunable mechanical and conduction properties. *Materials & Design*, *198*, 109313. https://doi.org/10.1016/J.MATDES.2020.109313

Zhou, W. L., Carpenter, E. E., Lin, L., Kumbhar, A., Sims, J., & O'Connor, C. J. (2001). Nanostructures of gold coated iron core-shell nanoparticles and the nanobands assembled under magnetic field. *European Physical Journal D*, *8*(3), 289–292. https://doi.org/10.1007/s100530170112

Zhou, Y., Gao, L., & Li, H. (2023). A ready-to-manufacture optimization design of 3D chiral auxetics for additive manufacturing. *Engineering with Computers*, 1–22. https://doi.org/10.1007/S00366-023-01880-1/TABLES/6

Zhou, Y., Yu, S. H., Cui, X. P., Wang, G. Y., & Chen, Z. Y. (1999). Formation of silver nanowires by a novel solid-liquid phase arc discharge method. *Chemistry of Materials*, *11*(3), 545–546. https://doi.org/10.1021/cm981122h

Zhu, Y., Luo, Y., Gao, D., Yu, C., Ren, X., & Zhang, C. (2022). In-plane elastic properties of a novel re-entrant auxetic honeycomb with zigzag inclined ligaments. *Engineering Structures*, *268*(August), 114788. https://doi.org/10.1016/j.engstruct.2022.114788

Zhuge, Y., Li, Y., Xu, X., Zhang, D., Zhang, H., Liu, W., & Yue, M. (2020). Morphology and magnetic properties of Sm2Co7/α-Fe nanocomposite magnets produced by high energy ball milling and spark plasma sintering. *Journal of Rare Earths*. https://doi.org/10.1016/j.jre.2020.02.015

Zied, K., Osman, M., & Elmahdy, T. (2015). Enhancement of the in-plane stiffness of the hexagonal re-entrant auxetic honeycomb cores. *Physica Status Solidi (B)*, *252*(12), 2685–2692. https://doi.org/10.1002/PSSB.201552164

Zielińska, A., Skwarek, E., Zaleska, A., Gazda, M., & Hupka, J. (2009). Preparation of silver nanoparticles with controlled particle size. *Procedia Chemistry*, *1*(2), 1560–1566. https://doi.org/10.1016/j.proche.2009.11.004

Zienkiewicz-Strzałka, M., Pasieczna-Patkowska, S., Kozak, M., & Pikus, S. (2013). Silver nanoparticles incorporated onto ordered mesoporous silica from Tollen's reagent. *Applied Surface Science*, *266*, 337–343. https://doi.org/10.1016/j.apsusc.2012.12.021

Zou, B., Liang, Z., Cui, Z., Xiao, K., Shao, S., & Ju, J. (2022). *Magneto-thermomechanically triggered active mechanical metamaterials -- untethered, reversible, reprogrammable transformations with shape locking*. https://doi.org/10.48550/arxiv.2207.03177

Appendix I: Numerical simulations on the accordion-like magneto mechanical structure

I.1 Introduction

The work in Chapter 5 was carried out in conjunction with a numerical investigation with the aim of replicating the experimental results through simulations. In this case, magnetic inclusions were represented by means of individual magnetic moments having the same magnitude μ which was identical as in the case the experiment. The non-magnetic foldable lattice used in the simulations had the same dimensions as the experimental prototype and it was assumed that rigid bar-like elements constituting the system were connected to each other by means of frictionless hinges.

I.2 Methodology

In this work, a theoretical model was designed which was used to validate the results obtained by means of the experimental approach. In this case, the evolution of the system was analysed through the use of the Molecular Dynamics simulations utilising the fourth-order Runge–Kutta method for a constant time step $\Delta t = 10^{-6}$ s. Furthermore, in the simulations, the analysed structure was represented by a set of point masses connected to each other by means of very stiff two-body bonded interactions which made it possible to represent the behaviour of rigid nonmagnetic rod-like elements constituting the system. In addition, the magnetic inclusions present in the experimental prototype were

represented by individual magnetic moments having a magnitude of $\mu = 0.0045$ A m^2 and the same orientation as shown schematically for the magnets depicted in Fig. I.1.

In terms of geometry, the analysed model is a lattice which consists of seven rigid rectangular building blocks having dimensions either of $d \times 4d$, $l_1 \times 4d$ or $l_2 \times 4d$ depending on their position within the system. These building blocks are connected to each other at their edges (having a length $4d$) through hinges resulting in a system resembling a foldable accordion-like sheet. In this case, the hinging motion is assumed to be controlled through a harmonic potential corresponding to a stiffness constant $K_h = 0.2 \times 10^{-4}$ J rad^{-2} for each of the hinges. Furthermore, the building blocks are composed of a set of pairs of points having a mass $m = 0.15$ g that are connected to each other by means of rigid bonds. The length of such bonds is also controlled through a harmonic potential corresponding to a stiffness constant $k = 2 \times 10^4$ N m^{-1} so that the bonds and structural units would remain rigid throughout the entire deformation process. Thus, one can imagine that the pairs of points connected to each other by rigid bonds act as macroscopic rigid bars.

In addition to the non-magnetic accordion-like lattice, the considered system is also composed of magnetic inclusions. As shown in the Chapter 5, magnetic inclusions are located at the centre of some of the rigid bars having a length of d similarly to the distribution of neodymium magnets in the experimental prototype. In this case, magnetic inclusions are represented by means of individual magnetic dipoles corresponding to the magnetic moment of magnitude μ, where the orientation of magnetic moments is identical to that used for the experimental prototype. All the magnetic dipoles are collinear with rigid bars to which they are attached and oriented as described in Chapter 5, i.e., the same orientation as is the case of the experimental prototype. At this point, it is important to note the system in question is embedded within the external uniform magnetic field of

magnitude B which is the main factor governing the deformation process of the entire structure.

In the considered model, there are several types of magnetic interactions contributing to the deformation process of the entire structure. The main cause of the deformation process is the external magnetic field which results in the torque having a magnitude of τ_{ext} being applied to all the magnetic dipoles within the structure. This in turn leads to the rotation of structural building blocks around the axis which is parallel to the x-axis and passes through their centres of mass. In general, $\boldsymbol{\tau}_{ext}$ corresponding to a specific i-th magnetic dipole can be defined as $\boldsymbol{\tau}_{ext,\,i} = \boldsymbol{\mu}_i \times \boldsymbol{B}$ which means that it leads to the clockwise or the anticlockwise rotation of structural units in the yz plane depending on their location within the structure. In addition to the interaction with the external magnetic field, magnetic inclusions present within the system also interact with each other. In fact, there are two types of such interactions which must be considered to reliably represent the behaviour of the experimental prototype. The first of these interactions corresponds to the explicit repulsion or attraction between any two magnetic dipoles where the force due to an arbitrary magnetic moment i acting on the magnetic moment j can in general be written down as follows:

$$\vec{F}_{ij} = \frac{3\mu_0}{4\pi r^5}\left[(\vec{\mu}_i \bullet \vec{r})\vec{\mu}_j + (\vec{\mu}_j \bullet \vec{r})\vec{\mu}_i + (\vec{\mu}_i \bullet \vec{\mu}_j)\vec{r} - \frac{5(\vec{\mu}_i \bullet \vec{r})(\vec{\mu}_j \bullet \vec{r})}{r^2}\vec{r}\right]$$

Equation I.1

where, μ_0 is the vacuum permeability and $\boldsymbol{r}$ stands for the distance vector pointing from the i-th to the j-th magnetic moment. The second type of interaction between magnetic inclusions is related to the torque applied to each of the magnetic dipoles which originates from the magnetic field corresponding to all the surrounding magnetic moments. Thus,

the torque applied to a given *i*-th magnetic dipole can be expressed as: $\boldsymbol{\tau}_i = \boldsymbol{\mu}_i \times \boldsymbol{B}_i$ where $\boldsymbol{B}_i$ stands for the magnetic field originating from the magnetic dipoles surrounding the *i*-th magnetic moment.

I.3 Results and Discussion

Before conducting a full analysis of the behaviour of the considered system for different magnetic fields, it is first worth to focus on an example of the structure deformed by a specific magnetic field, i.e. B = 28 mT. Based on Figure I.1(a), one can note that in response to the external stimulus, the structure shrinks in time along the *x*-axis which leads to the decrease in the value of angles θ_1, θ_2 as well as l_x. This behaviour stems from the fact that magnetic moments corresponding to respective magnetic inclusions tend to align with the external magnetic field which induces the deformation of the structure. However, this process is also accompanied by the interactions between the magnetic inclusions that become stronger as magnetic inclusions approach each other and unlike the external magnetic field oppose the folding mechanism. In view of this, as shown in Figure I.1(a), the folding of the considered accordion-like structure continues until the point where the system assumes the equilibrium configuration for the specific external magnetic field. Furthermore, it is important to note that as shown in Figure I.1(b), a similar behaviour to that observed in the experiment can be observed in the case of computer simulations conducted for the system with the same initial parameters. Particularly interesting in this regard can be the evolution of the structure portrayed in the *xz* plane (see Figure I.1(c)) as it clearly showcases the decrease in the value of angles θ_1 and θ_2 which behaviour is indicative of the structure being capable of acting as an actuator.

Once we visualised the possibility of altering the dimensions of the system by subjecting it to the external stimulus, it is important to analyse the general effect which the magnitude of the external magnetic field has on the evolution of the structure. According to Figure I.1(d), both in the case of experimental and computational studies, the extent of contraction of the system changes with the magnitude of the external magnetic field. More specifically, the stronger the magnetic field, the lower the dimension of the structure measured along the *x*-axis which corresponds to the decrease in the value of $\theta 1$ and $\theta 2$. It is important to emphasise that such behaviour is indicative of the fact that dimensions of the system can be controlled via the external stimulus. Furthermore, it is worth to note that in the case of the experiment, the variation in the magnetic field was investigated at the range between 4.5 mT and 30 mT, where each experiment was repeated ten times to estimate the size of the corresponding error. At this interval, values of θ_1 and $\theta 2$ have changed from 48.3 ±3.0° and 61.0 ±0.57° to 27.4 ±1.4° and 25.0 ±1.3° respectively. Furthermore, a similar analysis was also conducted through the use of computer simulations where the magnetic field used to deform the structure for different simulations assumed values from the range between 10 mT and 30 mT. At this interval, values of angles θ_1 and θ_2 have changed from 60.0° and 71.0° to 32.2° and 35.2° respectively.

Based on results shown in Figure I.1(d), it is clear that all trends observed for the analysed system are qualitatively the same both for the experimental as well as computational studies. Some discrepancies between the two sets of results arise amongst others from the fact that in the theoretical model there is no friction affecting the motion of hinges which is certainly present in the experiment. In addition, in the experimental prototype, it is possible that despite our efforts there is some misalignment between the magnetic inclusions which may, up to some extent, affect the result. Another factor was

the use of non-magnetic joints which while necessary to introduce some degrees of freedom in the experimental prototype were not present in the theoretical design. Finally, it is important to remember that analytical expressions describing interactions between magnetic inclusions serve only as an approximation of the real behaviour and especially for small separation distances between the magnets are expected to deviate from the experiment.

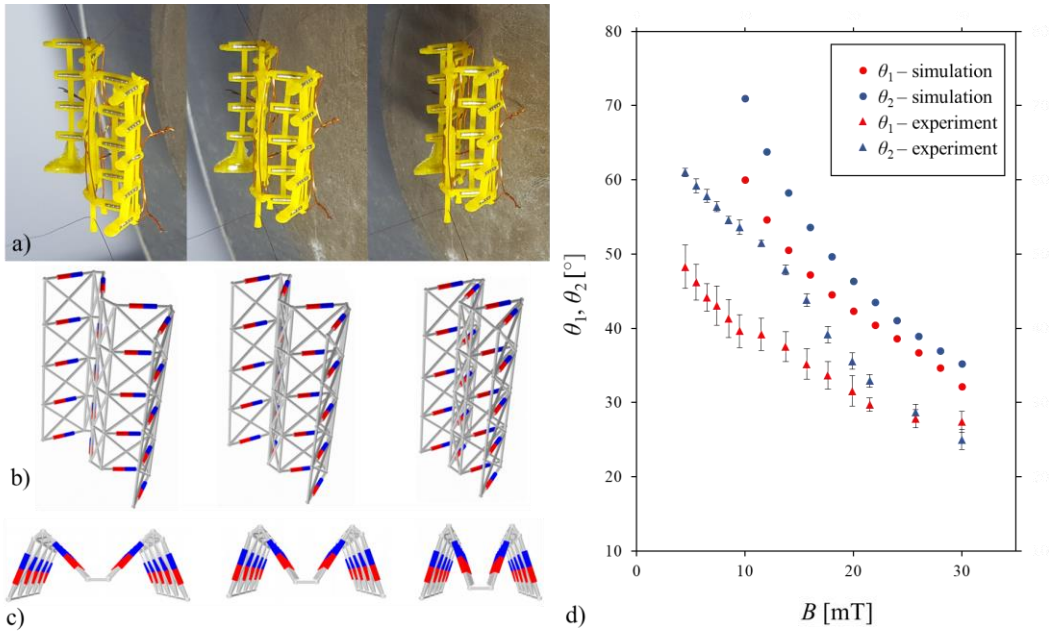

Figure I.1: Panels show: a) the evolution of the experimental prototype subjected to the uniform external magnetic field of magnitude 28 mT, b) visualisation of the evolution of the system corresponding to the computational simulations of the structure closely resembling the experimental prototype, c) the evolution corresponding to computer simulations portrayed in the xz plane and d) equilibrium values of angles θ_1 and $\theta_2$for the system subjected to the external magnetic field of different magnitudes.

At this point, it is worth to note that even though the following topic does belong to the scope of this work, it is expected that the external magnetic field can also be used in order to change stiffness of the system. This stems from the fact that the application of the external stimulus would result in the change in net forces acting on respective structural elements constituting the system. Thus, should one consider deforming the analysed structure through the direct application of tensile forces, the variation in the

magnitude of the external magnetic field could either accelerate or decelerate this process by fine-tuning its stiffness. Of course, a similar effect could also be also achieved through the use of magnetic inclusions in a form of electromagnets as opposed to standard permanent magnets where the magnetic moment corresponding to magnetic inclusions could be conveniently adjusted by altering the intensity of the provided current.

I.3.1 Effect of the variation in the magnitude of the magnetic moment corresponding to magnetic inclusions on the evolution of the system

As shown in Figure I.2, according to the theoretical model analysed though the use of computer simulations, the considered structure deforms differently depending on the magnitude of the magnetic moments corresponding to magnetic inclusions present within the system. More specifically, the larger the value of the magnetic moment, the smaller the extent of the mechanical deformation (measured along the *x*-axis) induced by the external magnetic field. This stems from the fact that in the case of relatively strong magnetic inclusions, their mutual repulsion is very significant, and the system cannot deform to a similar extent as would be the case for weaker magnetic inclusions. In fact, as shown in Figure I.3, this behaviour can be also described in terms of the change in the magnitude of the equilibrium length l_x for structures corresponding to different values of the magnetic moment associated with magnetic inclusions.

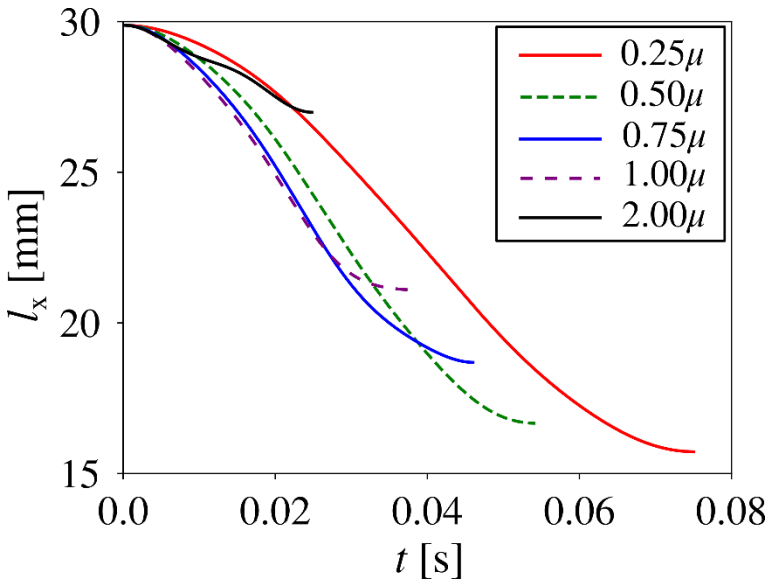

Figure I.2: The change in the linear dimension l_x plotted against time for the considered structure corresponding to different values of the magnetic moment associated with magnetic inclusions where μ is the magnetic moment calculated experimentally ($0.0045 Am^2$). All of the results were generated for the same external magnetic field of magnitude B = 26 mT.

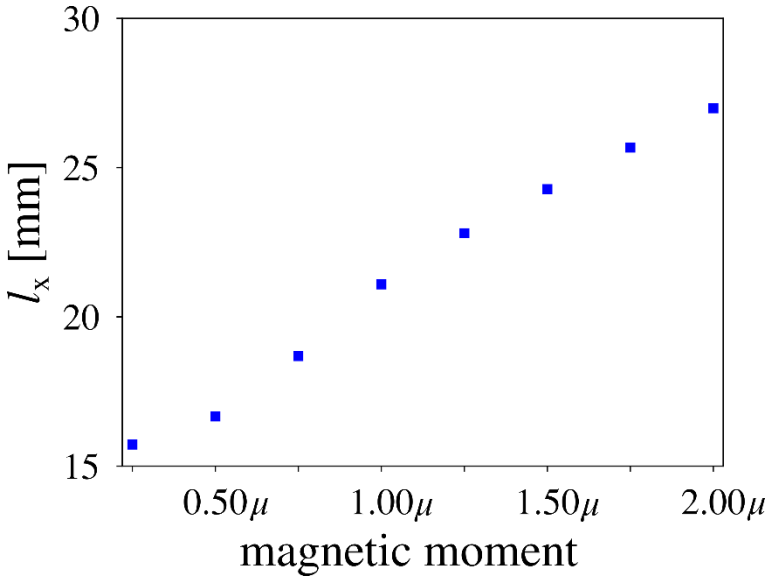

Figure I.3: The change in the equilibrium value of the linear dimension l_x plotted against the magnetic moment associated with its magnetic inclusions where μ is the magnetic moment calculated experimentally ($0.0045 Am^2$).

I.3.2 Effect of the variation in the value of the geometric parameter *d* on the behaviour of the structure

According to Figure I.4 which displays the results of computational studies, the extent of the mechanical deformation of the considered system induced by the application of the external magnetic field changes depending on the value of the geometric parameter *d* defined in the main text. Upon having a closer look at the generated results, it is possible to note that for large values of *d*, the analysed structure can deform to a greater extent than for small values of this parameter. This behaviour originates from the fact that the increase in the value of *d* results in the increase in the separation distance between the magnetic inclusions. Thus, the mutual repulsion between the magnetic inclusions is weaker than is the case when magnetic inclusions are relatively close to each other. At the same time, one should remember that the magnitude of the external magnetic field does not depend on the geometric parameters of the system. Hence, the magnetic torque corresponding to each structural element with the magnetic inclusions remains approximately the same irrespective of the selection of the geometric parameters (given that the spatial orientation of magnetic inclusions remains almost unchanged). On the other hand, one must remember that as the length of the nonmagnetic elements with magnetic inclusions is being altered, the internal forces originating from the torque induced by the external magnetic field must also change.

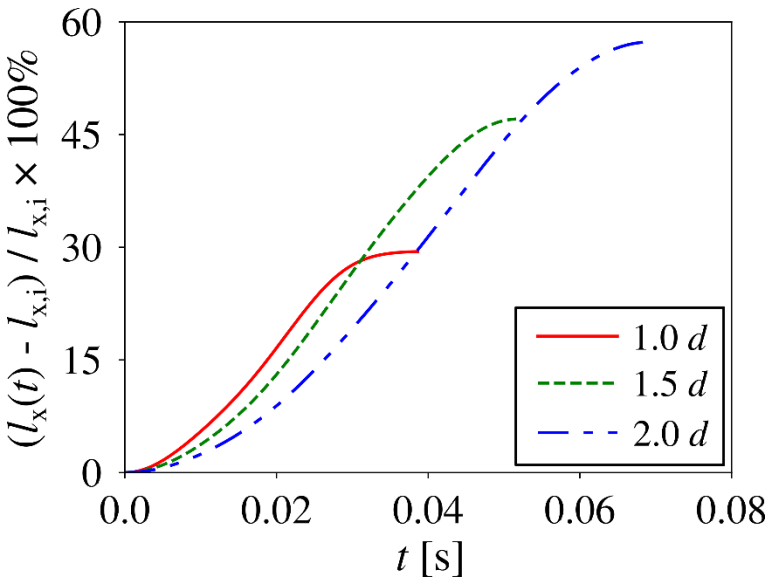

Figure I.4:. The percentage change in the linear dimension l_x plotted against time for the considered structure corresponding to different values of the geometric parameter d, which is defined in the main paper. In this case, l_x(t) and $l_{x,f}$ correspond the length of the structure measured along the x-axis at its current (measured at the time t) and the final configuration respectively. In this case, all of the results were generated for the same external magnetic field of magnitude B = 26 mT.

As shown in Figure I.5, a similar analysis to that provided above can be conducted upon considering the percentage change in the linear dimension of the system in the case of the evolution of structures associated with different values of the geometric parameter d. According to these results, the equilibrium length of the system measured along the x-axis changes to a significantly greater extent for relatively large value of d than is the case for small values of this parameter. This in turn is indicative of the same behaviour of the system to that shown in Figure I.4.

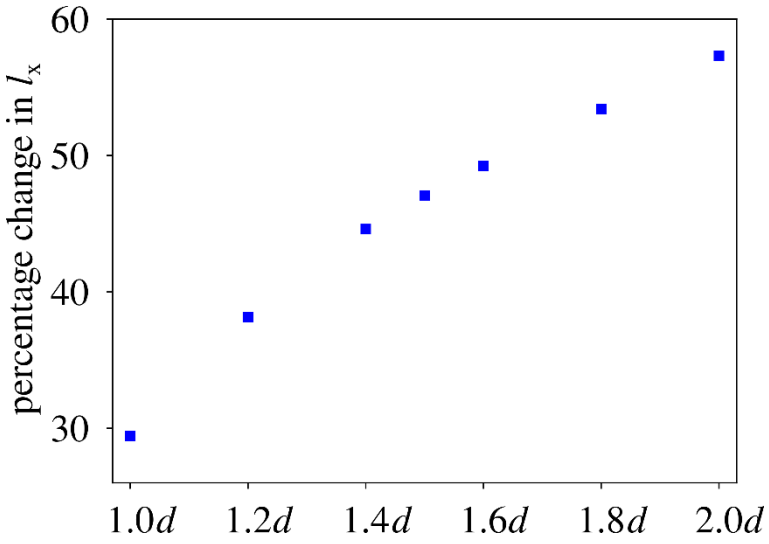

Figure I.5: Percentage change in the linear dimension of the system corresponding to different values of the geometric parameter defined as d in the main text. In this case, all the results were generated for the same external magnetic field of magnitude $B = 26$ mT.

I.3.3 The dynamics of a change in the value of angles for different parameters

In the main text, we have already analysed how the value of the internal angles θ_1 and θ_2 change with the magnitude of the external magnetic field. However, it is also interesting to investigate how these quantities change in time as they change to attain the equilibrium position. As shown in Figure I.6, both angles θ_1 and θ_2 evolve differently in time depending on the magnitude of the applied external magnetic field. More specifically, similarly to the results presented in the main text, both of the considered angles change to a larger extent for relatively high values of B than is the case for low values of this parameter. However, the provided results also make it possible to note that in the presence of a strong external magnetic field, the rate of the mechanical deformation (determined by the slope of the graph) is significantly larger than for low values of B.

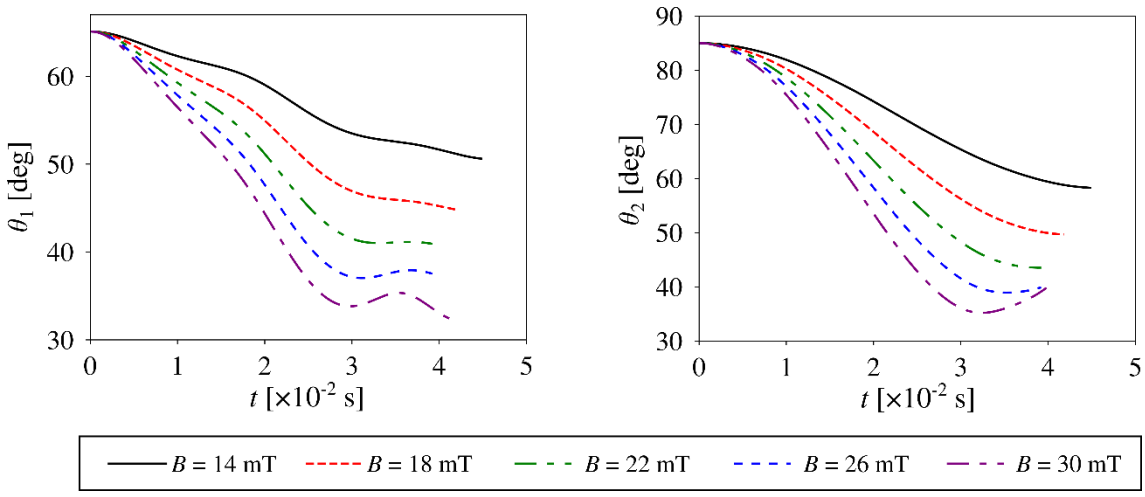

Figure I.6: The time evolution of the system subjected to different magnitudes of the external magnetic field. In this case, the deformation of the structure is discussed in terms of the variation in the angles θ_1 and θ_2.

In addition to the above results, it is also interesting to analyse the time evolution of the system for structures composed of magnetic inclusions corresponding to different values of the magnetic moment. As shown in Figure I.7, angles θ_1 and θ_2 change to the largest extent when the magnetic moment of the magnetic inclusions is relatively small. In fact, this aspect was already reported in the main text and does not offer a new insight into the complexity of the behaviour of the considered system. However, upon having a closer look at the provided results, one can note that, irrespective of the magnitude of the magnetic moment corresponding to magnetic inclusions, the rate at which the system is being deformed by the external magnetic field remains approximately unchanged. In fact, it is possible to observe that as opposed to the rate of the mechanical deformation, the quantity that changes upon comparing the behaviour of different systems is the total evolution time.

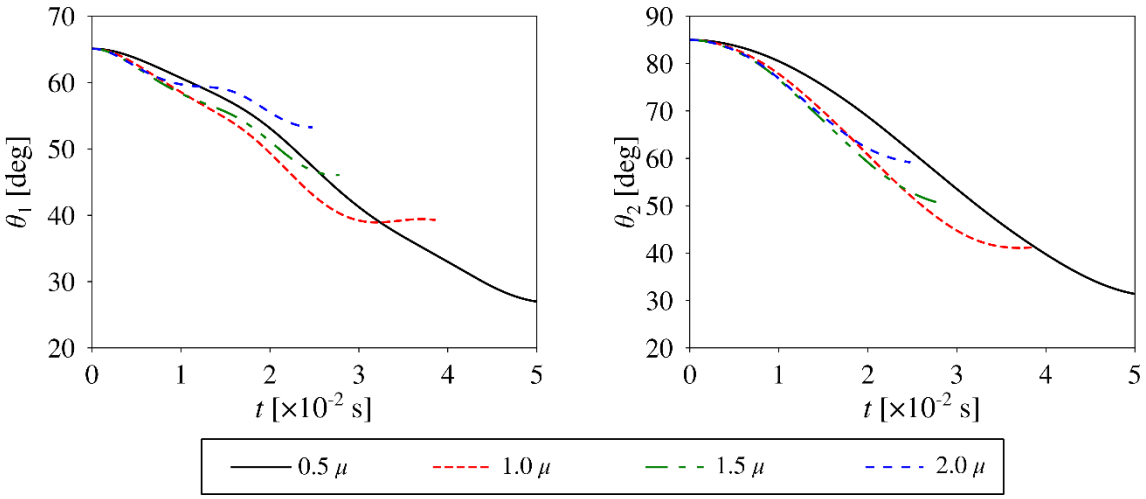

Figure I.7: The time evolution of structures corresponding to different values of the magnetic moment associated with magnetic inclusions where μ is the magnetic moment calculated experimentally and used in the main paper.

I.3.4 Extrapolating to a three-dimensional system

Once the basic structure was tested, and both experimental and computational studies confirmed that it is possible to control its deformation via the the external magnetic field, it is important to note that the considered system can be extended upon stacking several single-layer accordion-like structures on top of each other and connecting them by means of rigid nonmagnetic structural elements as shown in Figure I.8(a). As a result, the orientation of the accordion-like structure and the position of the connective nonmagnetic elements can give rise to a number of structures exhibiting positive, zero or negative Poisson's ratio. Thus, in this work, in order to investigate its behaviour and the corresponding mechanical properties, the evolution of such structure was analysed by means of computer simulations with specific details related to the model definition being provided in the Methodology section.

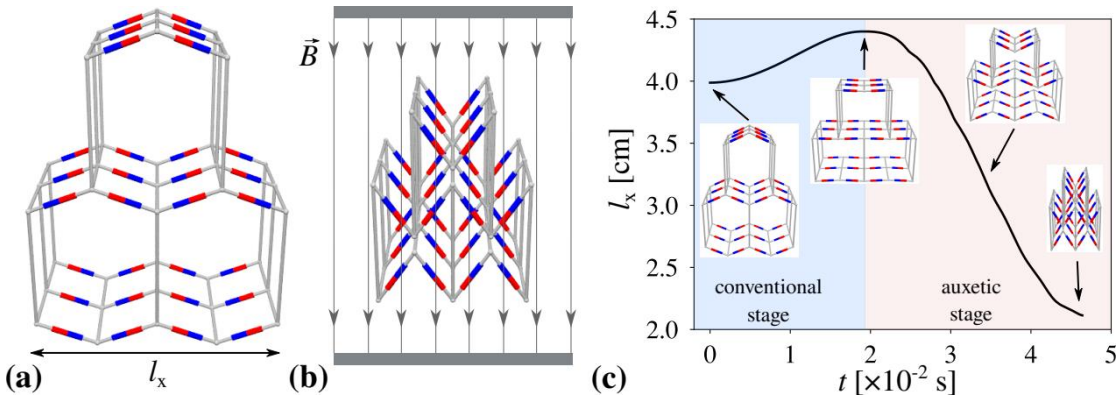

Figure I.8: Panels show: (a) the initial configuration of the three-dimensional system, (b) the deformed system subjected to the uniform external magnetic field and (c) the variation in the linear dimension of the analysed system measured during the deformation process induced by the application of the external magnetic field.

As shown schematically in Figure I.8(b) and analysed quantitatively in Figure I.8(c), similarly to its simpler counterpart, the shape and the linear dimension of the extended structure can be modified through the application of the uniform external magnetic field. However, as visualised in Figure I.8, it is important to note that during its evolution, the analysed system undergoes a transition from the conventional configuration characterised by the positive Poisson's ratio to the auxetic system. This in turn is of great significance as it indicates that mechanical properties of the analysed structure can be controlled via the external magnetic field and significantly changed without the need of reconstructing the system.

I.3.5 The evolution of the multi-layer structure

The results presented in Figure I.9, correspond to the multi-layer structure subjected to the external magnetic field of magnitude B = 10 mT. Based on Figure I.9, one can note that during the initial stage of the deformation process, the vertical dimension of the structure corresponding to the l_z variable is decreasing while the horizontal dimension of the system is increasing (l_x). However, as shown in the main text,

as the system deforms, at one point it assumes the configuration where its cross-section in the *xz* plane assumes the shape of a rectangle. After surpassing this point of the time evolution of the considered multi-layer system, the structure starts to shrink both in the horizontal (decrease in the value of l_x) as well as in the vertical dimension (decrease in the value of l_z). Thus, at beginning of the deformation process, the configuration assumed by the system corresponds to that of the conventional honeycomb system where after surpassing the aforementioned threshold configuration the system assumes the auxetic configuration.

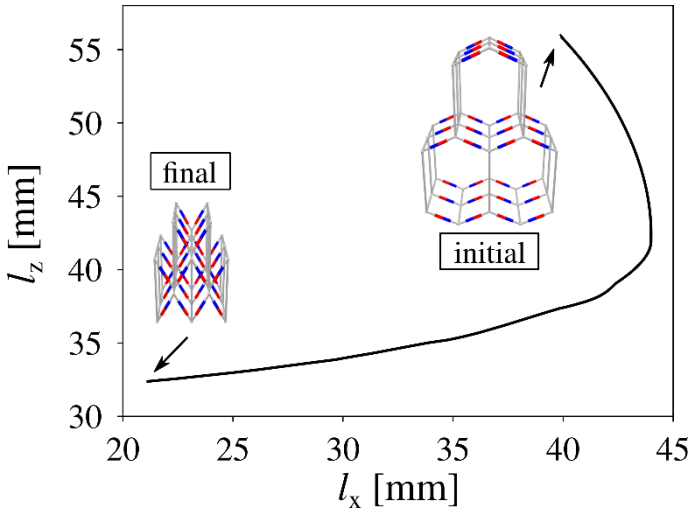

Figure I.9: The variation in the linear dimensions measured along the *x* and *z* axes throughout the deformation process.

I.4 Conclusion

The numerical simulations and experimental investigation showed a good agreement where both structures exhibited a contraction in response to an external magnetic field and the extent of contraction was shown to be dependant on the external magnetic field. Furthermore, the numerical analysis on the effect of the inclusions' magnetic moment and geometric parameters was validated using experimental studies in Section 5.2.6.3.

Appendix II: Literature review on Silver and Iron nanoparticles

II.1 Nanoparticles

Nanoscience is an interdisciplinary science encompassing all knowledge on the properties of nano-sized objects (Sergeev, 2003; Sergeev & Shabatina, 2008). The term 'nano' indicates one billionth of a unit, and while the size limits of nanoparticles are still relatively loose, in most study groups; a NP is defined as a cluster of atoms with at least one dimension ranging from one to a hundred manometers (Abou El-Nour *et al.*, 2010; Williams, 2008).

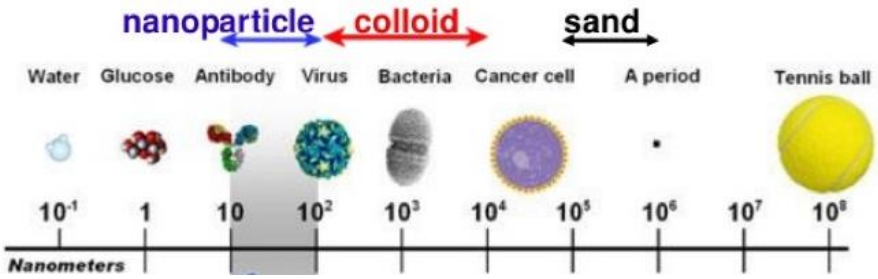

Figure II.1**:** A diagram comparing nanoparticles' size with relatable objects.

Nanotechnology research has experienced an exponential growth with several studies focusing on the synthesis and characterisation aspects(Abou El-Nour *et al.*, 2010). The synthesis of metallic NPs was given special attention due to their application in a wide range of industries namely health care and biomedical industry, environmental health, aerospace applications as well as material science amongst others(Iravani *et al.*, 2014). Metallic NPs, when at the nano-scale, exhibit a wide range of unique properties (shown in Figure II.2)(Dimitrijevic *et al.*, 2001; Harada *et al.*, 1993; Henglein, 1989;

Henglein & Meisel, 1998; Hostetler *et al.*, 1998; Kapoor, 2000; M.C. Daniel, 2004; Mulvaney, 1996; Rele *et al.*, 2004; Sarkar *et al.*, 2010; Underwood & Mulvaney, 1994) ranging from electronic and magnetic ones, to properties affecting their chemical reactions and in turn affecting their bioactivity. This can be attributed to their high percentage of atoms at the surface which results in quantum effects.

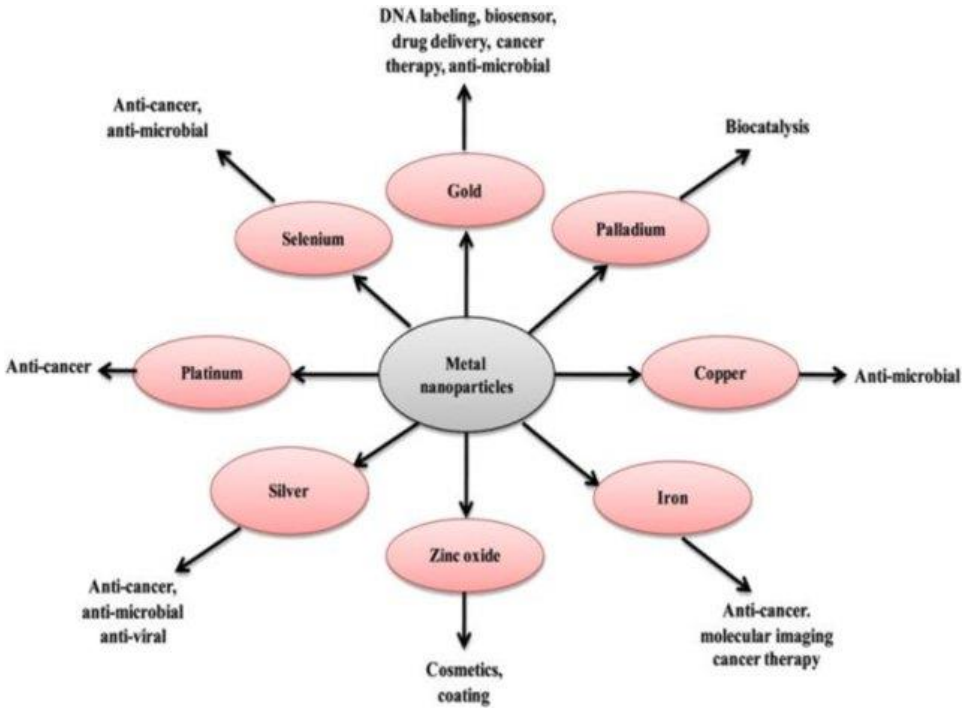

Figure II.2:Applications of metallic NPs. Image adapted from Khandel *et al.*(Khandel & Kumar Shahi, 2016)

II.1.1 Silver Nanoparticles

II.1.1.1 Introduction

In this review, the main focus are silver NPs, mainly their synthesis and their characterisation. As with most metallic NPs, at the nanoscale, silver NPs exhibit unusual properties, quite different from the bulk metal. There have been several studies detailing the optical, electronic, chemical and the characteristic antimicrobial properties which were found to depend on the size and shape (D. Kim *et al.*, 2006; Suber *et al.*, 2005; Y.

Sun *et al.*, 2002; D. Zhang *et al.*, 2004). Some applications derived from these properties include the use of silver NPs in catalysis reactions (Chimentão *et al.*, 2004), antimicrobial coatings(Aymonier *et al.*, 2002), optical sensors(McFarland & Van Duyne, 2003), printed electronics(Y. Li *et al.*, 2005; Y. Wu *et al.*, 2006) and in photonics (W. Wang & Asher, 2001) amongst others. Silver NPs have also been used extensively in applications concerning surface-enhanced spectroscopy(Alvarez-Puebla & Aroca, 2009; J. M. Li *et al.*, 2011; W. Li *et al.*, 2009; Marsich *et al.*, 2012; Pacioni *et al.*, 2015; Stamplecoskie *et al.*, 2011; B. Wang *et al.*, 2014).

II.1.1.2 Synthetic Methods

With an increase in the demand for silver NPs, a number of synthesis techniques have been proposed for the preparation of silver NPs(D. Kim *et al.*, 2006). In this review, an overview of these methods will be presented, categorising them into three main techniques.

- The physical methods, which tend to follow a top-down approach and
- Chemical and
- Biological methods; which follow a bottom-up approach(Pacioni *et al.*, 2015).

II.1.1.2.1 Physical methods:

As mentioned previously, physical methods generally involve using a top-down approach, whereby the material is broken down to NPs. Therefore, these methods would usually involve mechanical energy; high-energy lasers such as in laser ablation, and others. A common disadvantage of these techniques is the requirement of large amounts of energy in the form of heat, power, pressure or otherwise.

II.1.1.2.1.1 Evaporation-Condensation

Through this process, the material is vaporised at high temperatures in a tube oven and the vapour is then allowed to condense(State, 1988). The benefits of such processes comprise mainly of the lack of solvent contamination, and the uniformity in the NPs' distribution. However, with regards to the use of a tube furnace, there are several disadvantages. Primarily, the furnace itself occupies a lot of physical space, besides it also requires large amounts of energy to raise the temperature inside its chamber in order to heat up the metal. It is also relatively time-consuming, as it has to attain and maintain thermal stability. To minimise these disadvantages, Jung *et al.* modified the method by using a small ceramic heater which allowed for a local heating area, using a reaction temperature of around 1300°C(Jung *et al.*, 2006). Using Transmission Electron Microscopy (TEM), they observed spherical NPs ranging from 6.2 to 21.5 nm (shown in Figure II.3) and observed an increase in the NP size as temperature was increased. Using X-Ray Diffractometry (XRD), pure silver was confirmed to have been produced and not silver oxide(Jung *et al.*, 2006).

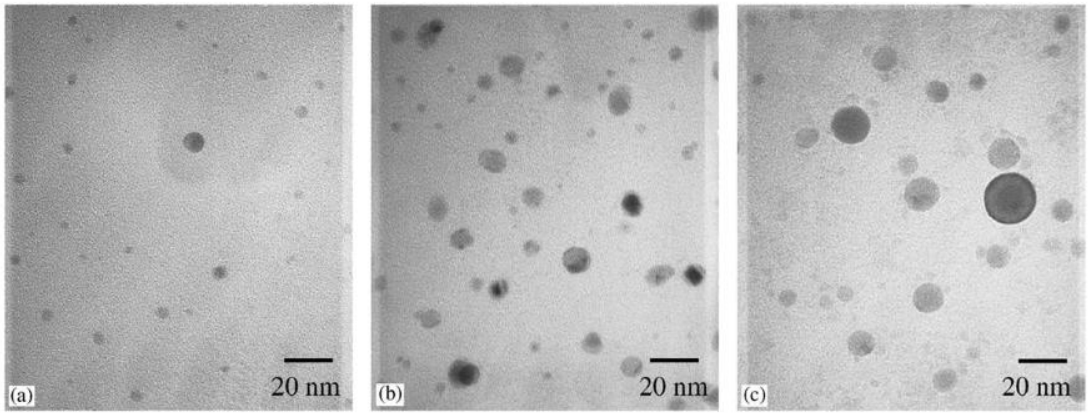

Figure II.3:TEM images taken from Jung *et al.*(Jung *et al.*, 2006)

More recently, the use of vacuum thermal evaporation has been investigated, achieving NPs ranging from 2 to 10nm. High-Resolution TEM (HRTEM) was used which revealed polycrystalline NPs, as well as the presence of single-crystal NPs with icosahedral and dodecahedral structures(Grishina *et al.*, 2019; Gromov *et al.*, 2015).

II.1.1.2.1.2 The Exploding Wire Method

Also known as Electric Explosion of Wire (EEW), the exploding wire method is a top-down approach that uses high current density to vaporise a thin metal wire when it comes in contact with an anodic plate(Sen *et al.*, 2003). This result is small fragments of condensed NPs. In this method, the main variables investigated were the current density(Sen *et al.*, 2003; Siwach & Sen, 2009) and breakdown voltage (related to the relative energy)(Chung *et al.*, 2016), dimensions of the wire(E. J. Park *et al.*, 2011; Sen *et al.*, 2003; Siwach & Sen, 2008a, 2009; Yun *et al.*, 2011), dispersion medium(Alqudami, Annapoorni, Sen, *et al.*, 2007; C. Cho *et al.*, 2007; Chung *et al.*, 2016; Humud *et al.*, 2014; Murzakaev, 2017; E. J. Park *et al.*, 2011; Siwach & Sen, 2008a, 2009), and the ambient temperature(Yun *et al.*, 2011). Studies have also investigated the use of this method to produce composite (or alloy) NPs such as Ag-Au(Alqudami *et al.*, 2008), Al_2O_3-Ag(Lozhkomoev *et al.*, 2019), Ag-Ti(Svarovskaya *et al.*, 2020) and Ag-Fe(Bakina *et al.*, 2019; Svarovskaya *et al.*, 2020). Research have also been conducted on pulsed wire explosion (PWE). Munkbayer *et al.* used pulses of 300 V in an Argon/Oxygen atmosphere achieving Ag NPs about 100 nm in size(Munkhbayar *et al.*, 2013).

Studies have also reported EEW to have a production rate of up to 200 g/h in a gaseous medium, yielding NPs of between 20 nm to a 100 nm; depending on the explosion conditions(Kotov, 2003). A more recent study by Park *et al.* also proposed the

optimal conditions for a manufacturing application. In this study they described the use of deionised water as a medium and the nanoparticles were observed using TEM imaging shown in Figure II.4. The silver NPs achieved in the method had an average size of 118.9nm(E. J. Park *et al.*, 2011).

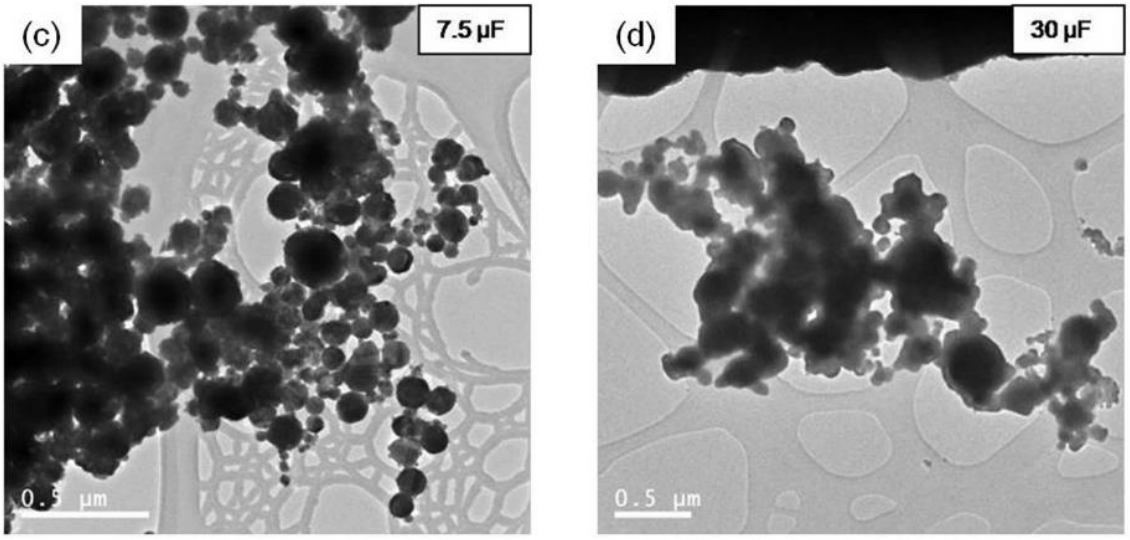

Figure II.4: TEM images of nanoparticles produced by Park *et al.*(E. J. Park *et al.*, 2011)

II.1.1.2.1.3 Laser Ablation

In Laser ablation, a high energy laser is pulsed onto the target bulk metal, vaporising the metal, which then sublimes in the solution forming NPs as illustrated in Figure II.5. The ablation method yields clean NPs in suspension due to the absence of chemical reagents(Gyrylov, 2019).

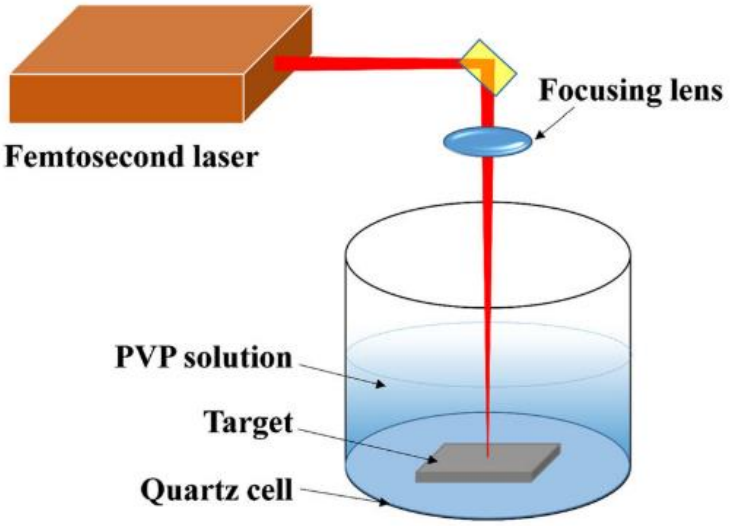

Figure II.5**:** Schematic diagram of a Laser ablation setup(H. Zhang *et al.*, 2016)

Several studies have investigated the parameters influencing the size and shape of silver NPs formed, including the wavelength of the laser(Alhamid *et al.*, 2019), irradiation time(Baruah *et al.*, 2020);nano-(Baruah *et al.*, 2020; Sportelli *et al.*, 2020), pico-, femto-(Menazea, 2020)second irradiation, the laser fluence(Baruah *et al.*, 2020) (optical energy delivered per unit area), the plasma charging effect(Dell'Aglio & De Giacomo, 2020), as well as the solvent(Menazea, 2020; Sportelli *et al.*, 2020) and coating agents(Y. H. Chen & Yeh, 2002; Sportelli *et al.*, 2020) used. In one study, to ensure the stability of the NPs, the silver NPs were incorporated in a biodegradable polymer matrix and used an organic solution(Sportelli *et al.*, 2020). This yielded spherical NPs with an average size of 9 ± 3 nm shown in the TEM images in Figure II.6.

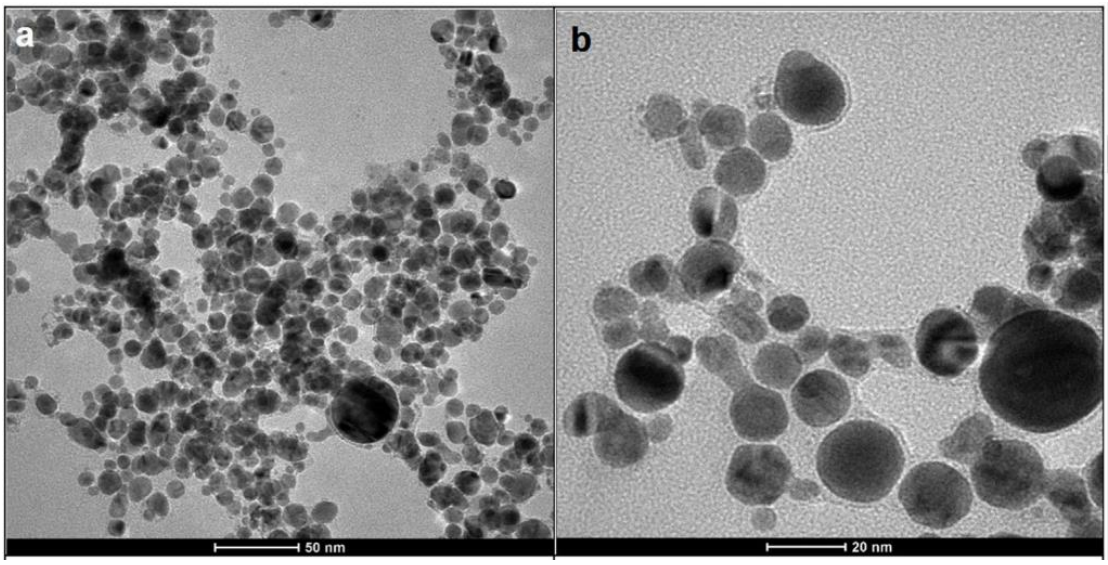

Figure II.6: TEM images of the silver NPs produced by Sportelli *et al.*(Sportelli *et al.*, 2020)

II.1.1.2.1.4 Sputtering

In sputtering, the target metal is bombarded with highly energetic particles such as plasma and as a result, nanoparticles are ejected from the surface. Several synthetic methods have been developed such as Vacuum Sputtering, Magnetron Sputtering as well as RF Magnetron Sputtering amongst others. Vacuum sputtering consists of a potential difference between two electrodes which creates an energised plasma on the target metal. Using this method, silver nanoparticles, 3.5 nm in diameter were synthesised by Siegel *et al.*(Siegel *et al.*, 2012).In this study, a glycerol-water media was used which was shown to stabilise the silver NPs formed. In another study, a PEG-water mixture was used yielding silver NPs of around 10 nm in size and observed that the particle size increased as a result of an increase in sputtering time and current(Slepička *et al.*, 2015).

Magneton Sputtering is a modification on Vacuum Sputtering, where a magnetic field is used. By introducing a magnetic field, the charged plasma particles become denser and thus increasing the sputtering rate. Using this method, several studies have been

conducted to synthesis of thin films of titanium oxide(Meng & Sun, 2009; D. H. Song *et al.*, 2012) and zinc oxide(Y. C. Liang & Deng, 2013) containing silver NPs as well as a PMMA/Co/Ag nanocomposite film(Choudhary *et al.*, 2020), depositing and embedding silver NPs on materials such as alumina templates(Nuntawong *et al.*, 2010; Wong-Ek *et al.*, 2010), amorphous carbon films(Jaiswal *et al.*, 2020), polyester fabric(S. X. Jiang *et al.*, 2010), silica and glass matrix(Gangwar *et al.*, 2020; Kumar & Sardana, 2020; Mishra *et al.*, 2007), as well as on pure silver electrodes(J. Li & Fang, 2007) and coating of graphene(Archana *et al.*, 2020) and titanium oxide(Kądzioła *et al.*, 2014) with silver NPs.

Asanithi *et al.* described the use of magnetron sputtering to produce silver NPs as small as 3.8 nm in diameter(Asanithi *et al.*, 2012). They also investigated the effect of several parameters where they showed that an increase in target-substrate distance yielded smaller nanoparticles and an increase in current resulted in a shift from spherical to worm-like morphologies shown in the TEM images in Figure II.7.

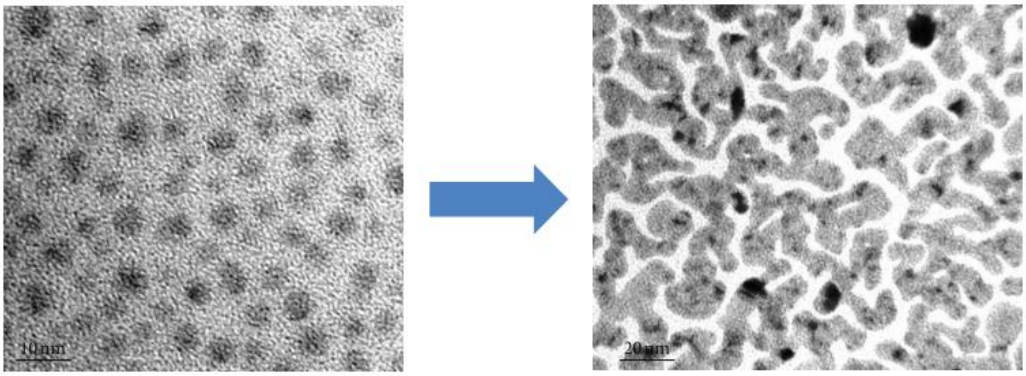

Figure II.7**:** TEM images depicting the shift in the morphologies when the current was increased. Taken from Asanithi *et al.*(Asanithi *et al.*, 2012).

II.1.1.2.1.5 Arc-discharge method

The Arc-discharge has been compared to the laser ablation method, as both methods provide a relatively green, economical techniques for the synthesis of silver NPs

with low impurity-contamination. In an arc-discharge, the electric discharge results in localised high temperatures at the silver electrodes, reaching temperatures of several thousands of degrees Celsius(Rashed, 2016; Tseng, Lin, *et al.*, 2018). This results in the vaporisation of silver, which then quickly condenses as a colloidal suspension of silver NPs in the solvent present(Rashed, 2016; Tseng, Lin, *et al.*, 2018). Several studies have successfully synthesised silver NPs using water as a solvent and silver electrodes(Ashkarran *et al.*, 2009; Cetin, 2017; El-Khatib *et al.*, 2018; Rashed, 2016; Tien, Liao, *et al.*, 2008; Tien, Tseng, *et al.*, 2008; Tseng *et al.*, 2016; Tseng, Chou, *et al.*, 2018; Tseng, Lin, *et al.*, 2018; H. Zhang *et al.*, 2016; X. F. Zhang *et al.*, 2016; Y. Zhou *et al.*, 1999); using different breakdown voltages(H. Zhang *et al.*, 2016), arc currents(Ashkarran *et al.*, 2009), different liquid mediums(Tseng *et al.*, 2016), different electrode systems(El-Khatib *et al.*, 2018), different coating agents(Cetin, 2017; Tseng, Lin, *et al.*, 2018) as well as scaling the process to a large-scale producing a production rate of up to 350 mg/min(H. Zhang *et al.*, 2017). Modifications to this method have resulted in the Submerged Arc Discharged Method (SADM) (Tseng *et al.*, 2016; Tseng, Chou, *et al.*, 2018; Tseng, Lin, *et al.*, 2018) and electrochemical arc-discharge, which combined the arc-discharge method with the chemical reduction of silver ions(Tseng *et al.*, 2011). A study has also synthesised composite Ag-Cu nanoparticles using the SADM(Tseng *et al.*, 2016). Another modification was presented which combined the arc-discharge and electric exploding wire with pulsed discharged, proposing the Pulsed Wire Discharge (PWD)(Tokoi *et al.*, 2011).

In a comparative study, arc-discharge synthesis (described in Figure II.8) yielded 6 mg/min whereas the femto-second laser ablation method yielded 3mg/min, with both techniques achieving silver NPs smaller than 20 nm which were coated by polyvinylpyrrolidone (PVP)(H. Zhang *et al.*, 2016). In the same study, they also

investigated the effect of increase the breakdown voltage potential in the arc using 60, 90 and 120 V and found that the mean NP size increased from 9.1 nm at 60 V to 12.7 nm at 120 V(H. Zhang *et al.*, 2016).

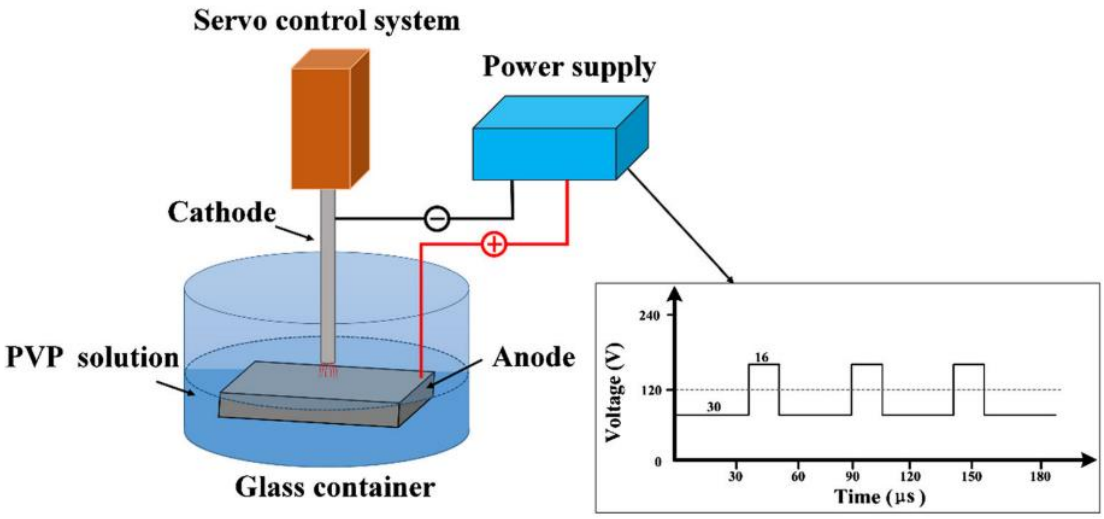

Figure II.8: Setup for Arc-discharge synthesis taken from Zhang *et al.* (H. Zhang *et al.*, 2016)

A novel method using arc-discharge, electrochemical discharge (ECD)(Tseng *et al.*, 2011), has also been used in research groups. Starowicz *et al.* made use of an ethanol solution with sodium nitrate to improve conductivity. A pure silver anode released silver ions which were reduced to form silver NPs approximately 20 nm in size(Starowicz *et al.*, 2006). Ashkarran *et al.* also used this procedure using titanium electrodes. In this chemical method, the silver ions in solution were reduced by electrons from the cathode. The main advantage of this technique is that it is a bottom up approach, which yields a narrower size distribution of silver NPs when compared to the top down approaches, which have a broad size distribution (such as arc discharge). Using citrate as a capping agent and silver nitrate as the silver precursor, they achieved spherical NPs with an average diameter of 28 nm(Ashkarran, 2010).

II.1.1.2.1.6 High Energy Ball Milling Mechanochemistry

High Energy Ball Milling is a technique that has been used in the synthesis of metal nanoparticles in which the metal powder is inserted in a mill and is broken down into a nanopowder using high energy collisions. For silver, however, many research groups have combined this technique with the chemical reduction of silver salts. A research by Khayati and Janghorban described the use of silver oxide and graphite which acts as a reducing agent(Khayati & Janghorban, 2012). The mixture was placed in the high energy ball mill and after 22 hours of ball milling, nanostructured silver with an average diameter of 28 nm was produced. In another research, a green synthesis of this technique was proposed using biomaterial as a reducing agent(Baláž *et al.*, 2019). The reducing agent and silver nitrate were milled for up to 45 minutes, after which two fractions of NPs having an average particle size of 2.9±1.3 nm and 34.4±16.1 nm.

II.1.1.2.2 Chemical method

II.1.1.2.2.1 Chemical reduction

Chemical reduction is one of the most popular method for the synthesis of silver NPs. In this method, the reducing agent is used to reduce silver ions, provided by a precursor compound, to metallic silver, which leads to the agglomeration of the silver atoms into clusters

$$Ag^{+} + e^{-} \rightarrow Ag^{0} \qquad \text{(II.1)}$$

The clusters eventually form metallic colloidal particles. Being one of the most common and simplest methods, chemical reduction has been investigated extensively. A multitude of studies have employed the use of different reducing agents such as sodium borohydride(Borysiuk *et al.*, 2008; Bryaskova *et al.*, 2011; Demchenko *et al.*, 2020; Dong

et al., 2010; Y. Gao *et al.*, 2005; Golubeva *et al.*, 2010; Jana *et al.*, 2001; Kandarp Mavani, 2013; Song *et al.*, 2009; J. S. Kim *et al.*, 2007; S. M. Lee *et al.*, 2010; J. Liu *et al.*, 2010; Motol *et al.*, 2020; Mulfinger *et al.*, 2007; Oliveira *et al.*, 2005; S.A. Vorobyova , A.I. Lesnikovich & Research, 2008; Shameli *et al.*, 2010; Skrzyńska *et al.*, 2016; Wani *et al.*, 2011; W. Zhang *et al.*, 2011; Zielińska *et al.*, 2009), trisodium citrate(Cañamares *et al.*, 2005, 2008; Guzman *et al.*, 2009, 2012; Mahmudin *et al.*, 2015; Mazzonello *et al.*, 2015; Ratyakshi & Chauhan, 2009; Šileikaitė *et al.*, 2006; Steinigeweg & Schlücker, 2012; Suriati *et al.*, 2014; Y. Wan *et al.*, 2013; H. Yin *et al.*, 2004), oleylamine(M. Chen *et al.*, 2007), DMF(Alimohammadi *et al.*, 2012; D. Y. Lee *et al.*, 2010; Siddiqui *et al.*, 2018), formaldehyde(Skrzyńska *et al.*, 2016), formalin(Szczepanowicz *et al.*, 2010), hydrazine hydrate(Demchenko *et al.*, 2020; Guzman *et al.*, 2009, 2012; Khanna *et al.*, 2005; K. Do Kim *et al.*, 2006; Skrzyńska *et al.*, 2016; Szczepanowicz *et al.*, 2010), tannin (Golubeva *et al.*, 2010), ascorbic acid (Alqadi *et al.*, 2014; Demchenko *et al.*, 2020; L. Lu *et al.*, 2002; Ni *et al.*, 2010; Szczepanowicz *et al.*, 2010), hydroxylamine (Cañamares *et al.*, 2005, 2008), Aminosilanes (Frattini *et al.*, 2005), hydrochloride (Cañamares *et al.*, 2005, 2008) ,aniline (Z. Khan *et al.*, 2011), Sodium formaldehyde sulfonate (SFS) (Khanna *et al.*, 2005) and polyols(P. Liu & Zhao, 2009).

The most popular production method is the Creighton method, in which sodium borohydride acts as the reducing agent by reducing silver ions as shown in (Creighton, J.A.; Blatchford, C.G.; Albrecht, 1978). A study by Demchenko in 2020 found that silver NPs' size decreased with an increasing activity of reducing agent(Demchenko *et al.*, 2020). Sodium borohydride, being a strong reducing agent, yields very small NPs and is therefore thoroughly researched in literature.

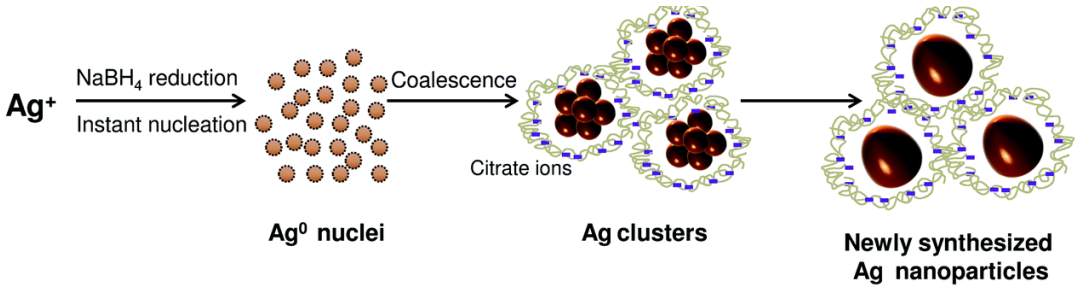

Figure II.9**:** Formation of silver NPs through the Creighton method. Image adapted from Agnihotri *et al.*(Agnihotri *et al.*, 2014)

Apart from the reducing agent, many methods employ the use of a capping agent or stabiliser. This is used in order to control the growth of NPs and stabilise the dispersed NPs preventing agglomeration. Several studies have been conducted on the use of stabilisers and capping agents such as dodecane thiol (Oliveira *et al.*, 2005), trisodium citrate(Alqadi *et al.*, 2014; Golubeva *et al.*, 2010; Guzman *et al.*, 2009; Jana *et al.*, 2001; W. Zhang *et al.*, 2011), PEG(Motol *et al.*, 2020), PVP(Bryaskova *et al.*, 2011; Kandarp Mavani, 2013; Tao *et al.*, 2006; W. Zhang *et al.*, 2011), H_2O_2(W. Zhang *et al.*, 2011), SDS(Guzman *et al.*, 2009, 2012; Song *et al.* 2009; K. Do Kim *et al.*, 2006; S. M. Lee *et al.*, 2010; Szczepanowicz *et al.*, 2010), ascorbic acid(Suriati *et al.*, 2014), gelatin(Golubeva *et al.*, 2010), organoalkoxysilanes (Hah *et al.*, 2003),PVA(Khanna *et al.*, 2005; P. Liu & Zhao, 2009; Mahmudin *et al.*, 2015), CTAB(Z. Khan *et al.*, 2011; L. Lu *et al.*, 2002) and have found that some stabilisers promote the growth of different shapes such as nanorods(Jana *et al.*, 2001), nanowires(Jana *et al.*, 2001; Y. Sun *et al.*, 2003), nanocubes(Y. T. Lee *et al.*, 2005; Sang *et al.*, 2005; Y. Sun & Xia, 2002; Tao *et al.*, 2006; B. Wiley *et al.*, 2004; B. Wiley, Sun, & Xia, 2005; B. Wiley, Sun, Mayers, *et al.*, 2005), truncated cubes(Tao *et al.*, 2006), cuboctahedra(Tao *et al.*, 2006), truncated octahedra(Tao *et al.*, 2006), octahedral(Tao *et al.*, 2006), nanobars(B. J. Wiley *et al.*, 2007) and nanorice(B. J. Wiley *et al.*, 2007). The use of other chemical agents was also

investigated, as exemplified by NaOH, NH4OH and their role as an accelerator(Cañamares *et al.*, 2005, 2008; Gomes *et al.*, 2015; L. Lu *et al.*, 2002; Sarkar *et al.*, 2010; Yu, 2007), seeds which aided the nucleation process such as TiO_2 seeds(K. Do Kim *et al.*, 2006), gold seeds(L. Lu *et al.*, 2002). Research conducted on the variables affecting NPs' growth and shape included the concentration of capping agent(Oliveira *et al.*, 2005) as well as the capping agent used(W. Zhang *et al.*, 2011).

Of particular interest are the syntheses of composite and alloyed silver nanoparticles. Examples of this include PMMA/Ag nanocomposite(Siddiqui *et al.*, 2018), Ag-Alumina NPs(Skrzyńska *et al.*, 2016), Ag-carbon nanotubes(CNT)(Alimohammadi *et al.*, 2012), Ag-PVA nanocomposite(Khanna *et al.*, 2005), Ag-Titania(K. Do Kim *et al.*, 2006), Ag-PAN nanofibers(D. Y. Lee *et al.*, 2010), Ag-talc nanocomposites(Shameli *et al.*, 2010) and Ag-Au nanoalloys (Gomes *et al.*, 2015; L. Lu *et al.*, 2002)

II.1.1.2.2.1.1 Polyol Method

Polyols fall under the bracket of organic solvents synthesis, however, given their versatility and their unique shape-control, which give silver NPs with different morphology by simple changes to ratios and such, allows them to be analysed separately from the other organic solvents. Polyols are characterized by the multiple -hydroxide groups in the molecule (such as glycerol and EG shown in Figure II.10) which are responsible for their unique properties(Pacioni *et al.*, 2015).

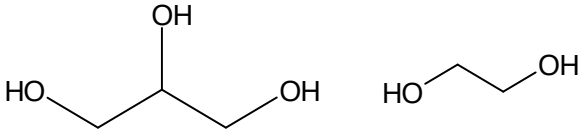

Figure II.10: Structure of (Left) Glycerol (Right) Ethylene glycol

Introduced by Fievet *et al.*, several metal NPs have been produced through this method as well as alloyed NPs(Bonet *et al.*, 1999, 2002; Fievet, Lagier, & Figlarz, 1989; Fievet, Lagier, Blin, *et al.*, 1989; Henglein, 1989; Toneguzzo *et al.*, 1998; Viau *et al.*, 1996a, 1996b, 2003). The main benefit of this method was that the viscosity and solvent-NPs interaction allowed for a more controlled reaction where the morphology and the size of NPs could be easily tailored to one's need.

Following this, Sun *et al.* proposed a suitable polyol technique for the synthesis of silver NPs using the precursor silver nitrate, ethylene glycol (EG) as a solvent and reducing agent and polyvinylpyrrolidone (PVP) as a stabiliser to yield silver nanowires in the range of 30-60 nm. In this study they investigated the effect of changing the molar ratio of silver nitrate and polyvinylpyrrolidone (PVP) on the shape of NPs, in particular the formation of nanowires. The degree of polymerisation of PVP was also found to influence the yield and quality of the nanowires produced(Y. Sun *et al.*, 2002, 2003; Y. Sun & Xia, 2002).

Since then, several studies have investigated the mechanics of the polyol method and have improved it by focusing on the different parameters to obtain desired morphologies. (Bonet *et al.*, 1999, 2002; Fievet, Lagier, & Figlarz, 1989; Fievet, Lagier, Blin, *et al.*, 1989; Henglein, 1989; J. Y. Lin *et al.*, 2014; Y. Sun *et al.*, 2002, 2003; Y. Sun & Xia, 2002; Toneguzzo *et al.*, 1998; Viau *et al.*, 2003, 1996b, 1996a; T. Zhao *et al.*, 2010). Kim *et al.* investigated the effect of the reaction temperature and heating rate as well as the injection rate. At a reaction temperature of 100 °C and an injection rate of 2.5 mL/s, they obtained quasi-spherical NPs about 17 nm in diameter(D. Kim *et al.*, 2006). Similarly, in another study (J. Y. Lin *et al.*, 2014) investigated the effect of synthesis temperature, PVP's molecular weight, reactant concentrations and injection rates were shown to affect the growth of silver nanowires. Dungdang *et al.* focused their efforts on

the PVP concentration, obtaining NPs in the range of 3-12 nm using 0.003 M PVP concentration(Dang *et al.*, 2012). Coskun *et al.* investigated the PVP's role which showed that PVP was able to passivate the [100] facet(Coskun *et al.*, 2011).

Other studies introduced trace amounts of different compounds in particular seeding agents such as Gao *et al.*, where platinum seeds were used to produce silver nanowires 3 nm in diameter(Y. Gao *et al.*, 2005). Palladium seeds were also used by Bonet *et al.* producing nanospheres 15 nm in diameter(Bonet *et al.*, 2002). Wiley *et al.* also introduced iron (II) and iron(III) species, producing nanocubes and nanowires about 25 nm large(B. Wiley, Sun, & Xia, 2005). In this study, etching using chloride and oxygen were implemented. In 2006, Siekkinen *et al.* used sodium sulphide and sodium hydrosulphide to produce silver nanocubes of 25-45 nm in edge length(Siekkinen *et al.*, 2006). Similarly, Skrabalak *et al.* used sodium sulphide and copper chloride in the polyol method to produce nanocubes and nanowires respectively(B. J. Wiley *et al.*, 2008). Through this study, the mechanism of the reduction was better understood, postulating that EG was transformed to glycolaldehyde upon heating, which acted as the reducing agent. Other compounds were used, such as ammonia as a complexing agent(T. Zhao *et al.*, 2010) ,sodium chloride(B. Wiley *et al.*, 2004) as well as a large amount of control agents, ranging from inorganic compounds to organic reducers- such as ascorbic acid in the study by Chen *et al.*(C. Chen *et al.*, 2006).

In 2006, two separate studies, Lee *et al.* and Tao *et al.*, were conducted on silica coatings(J. M. Lee *et al.*, 2006; Tao *et al.*, 2006). Lee *et al.*, using the conventional polyol method, produced spherical NPs in the 320 nm range with a silver cubic phase of 8.4 nm. Meanwhile Tao *et al.*, used 1,5-pentanediol as both a solvent and reducing agent to produce a NPs with different morphologies including cubes, truncated cubes, octahedra and others. Other reducing agents used include citrate and ascorbic acid in a glycerol-

water medium yielding quasi-spherical NPs of about 30 nm(Steinigeweg & Schlücker, 2012). Also, recently, glycerol has been used as both a solvent and a reducing agent. Hajara *et al.* produced NPs 5-10 nm in diameter using glycerol and heating(Devasenan *et al.*, 2016).

Apart from conventional heating in polyol synthesis, MW heating was also used to achieve homogenous heating. In a comparative study of MW heating and heating by reflux, Grace *et al.* synthesised several noble metals NPs including Ag NPs and found that reflux heating yielded more spherical NPs whereas MW heating encouraged nucleation along a plane leading to prisms(Nirmala Grace & Pandian, 2007).

II.1.1.2.2.1.2 Reduction using Silver Oxide

Another reduction method is using silver oxide, which is a mild oxidising agent and is therefore easily reduced to its metallic state. The main advantage of such a reduction is that a less aggressive reducing agent is required. In fact, these preparations typically make use of weak reducing agents such as alcohols or sugars. In 2008, Morita *et al.* used silver-oxide microparticles and added a primary alcohol to reduce it with heating(Morita *et al.*, 2008). They reported that at 220 ^{o}C, silver NPs ranging from 10 to 50 nm were formed on the silver-oxide microparticles.

In many studies, silver oxide was prepared in situ by using silver nitrate and an alkali such as NaOH:

$$2\,AgNO_3 + 2NaOH \rightarrow\ Ag_2O + 2NaNO_3 + H_2O \qquad \text{(II.2)}$$

Typically this reaction is accompanied by heating to 60-70 ^{o}C using different stabilisers(Abdel-Mohsen *et al.*, 2012; Darroudi *et al.*, 2010; Hebeish *et al.*, 2016; Shervani *et al.*, 2008; M. Singh *et al.*, 2009; H. Wang *et al.*, 2005) and reducing sugars.

Lanje *et al.*, using PVP as the capping agent, achieved NPs with a mean diameter of 15 nm. Other studies investigated the effect of different amounts of NaOH added, and also that of pH on the size of NPs(Abdel-Mohsen *et al.*, 2012; Darroudi *et al.*, 2010; M. Singh *et al.*, 2009; H. Wang *et al.*, 2005). In another study, ammonium hydroxide was used instead of NaOH, and sonication provided the necessary energy instead of conventional heating. This yielded NPs ranging from 20 to 50 nm(Y. Yin *et al.*, 2002).

In 2010, Sarkar *et al.* described the synthesis of silver nanoparticles by adding NaOH using EG and glycerol without any external reducing agent or heat, providing a more economical process while gaining the benefits of a polyol synthesis. In this study, NPs of about 25 nm were produced using PVP, silica or SDS as a capping agent(Sarkar *et al.*, 2010). Similar studies used this method to produce silver NPs and bimetallic Ag-Au NPs, and investigated the effect of pH on the resulting NPs(Gomes *et al.*, 2015).

II.1.1.2.2.2 Reduction using Tollen's Reagent

Silver Nanoparticles were also produced using the classical Tollen's reagent test. By modifying the reaction, the silver precursor complexes with ammonia and this complex is then reduced by reducing sugars. The fundamental reaction here can be shown in the following equation:

$$2\mathrm{Ag(NH_3)_2}^{+}{}_{\mathrm{aq}} + 2\mathrm{OH}^{-}{}_{aq} + \mathrm{RCHO}_{\mathrm{aq}} \rightarrow 2\mathrm{Ag_s} + \mathrm{RCOOH_{aq}} + 4\mathrm{NH_3}{}_{g} + \mathrm{H_2O}_{l} \qquad (\mathrm{II}.3)$$

A typical synthesis involved the use of silver nitrate which was mixed with ammonia and sodium hydroxide. The complex in turn was reduced by simple reducing sugars such as glucose and galactose. These conditions yielded a wide size distribution 45-300 nm(Kvítek *et al.*, 2008) and 25-450 nm(Panáček *et al.*, 2009), however, in two other studies, ammonia was replaced by ammonium hydroxide and with the aid of

sonication, silver NPs in range of 20-50 nm(Y. Yin *et al.*, 2002) and 57-87 nm(Huynh & Chen, 2011) was achieved. Zienkiewicz-Strzalka *et al.* used a similar method without sonicating, to produce silver NPs incorporated in porous silica. Spherical NPs, 4nm in diameter and nanowires were achieved(Zienkiewicz-Strzałka *et al.*, 2013). A study was carried out focusing on the role of surfactant in the Tollen's process in which it was determined that the surfactants used Tween-80, CTAC and SDS affect size, polydispersity and zeta potential and investigated the difference between ionic and non-ionic surfactants(Soukupová *et al.*, 2008).

II.1.1.2.2.3 Microwave Assisted Synthesis

Microwave (MW) irradiation has been used extensively in synthetic methods, in particular; silver nanoparticles(Nishioka *et al.*, 2011). The use of microwave heating allows for a controlled rapid, homogenous heating which increases the yield and reaction rate. This homogeneity allows for a narrow size distribution and smaller nanoparticles while also being a more eco-friendly method of heating(Hebbalalu *et al.*, 2013). When compared to conventional heating, microwave heating is much easier to control with specific irradiation times and power input, which allow for the manipulation of the size and morphology of silver NPs produced (Hebbalalu *et al.*, 2013). Most research studies describe the use of MW to assist chemical reduction(Djeddou *et al.*, 2020; B. Hu *et al.*, 2008; Kundu *et al.*, 2009; Pal *et al.*, 2009; Sreeram *et al.*, 2008; Yamamoto *et al.*, 2004; X. Zhao *et al.*, 2014) by increasing the temperature and studied the effect of MW power(Baruwati *et al.*, 2009) and irradiation time(Fuku *et al.*, 2013; B. Hu *et al.*, 2008; H. Peng *et al.*, 2013; Torras & Roig, 2020; X. Zhao *et al.*, 2014), capping agent(J. Chen *et al.*, 2008), concentration of silver precursor(Gul *et al.*, 2020; H. Peng *et al.*, 2013) and other variables(H. Jiang *et al.*, 2006; X. Zhao *et al.*, 2014). Yin *et al.* proposed a large-

scale synthesis for MW-assisted chemical reduction where they achieved NPs of about 24 nm(H. Yin *et al.*, 2004). In particular several research groups used MW- assisted polyol reduction using EG(Bhattacharyya & Gedanken, 2008; Hong *et al.*, 2016; H. Jiang *et al.*, 2006; Nishioka *et al.*, 2011; Torras & Roig, 2020; Tuval & Gedanken, 2007), PEG as solvent(Tuval & Gedanken, 2007), reducing and sometimes capping agent. Hong *et al.* managed to synthesise nanocubes, nanospheres and nanowires using this method and also investigated their microbial effect(Hong *et al.*, 2016).

Several research studies have used MW assisted biological methods to compensate for the characteristic slow nature of biological techniques, while still being cost-effective and environmentally friendly(Joseph & Mathew, 2015). Several leaf and fruit extracts(K. Ali *et al.*, 2015; Ashraf *et al.*, 2020; Fatimah, 2016; Joseph & Mathew, 2015; Kahrilas *et al.*, 2014; Parveen *et al.*, 2016; H. Peng *et al.*, 2013; Raghunandan *et al.*, 2011) were used, as well as fungal extracts(Jia *et al.*, 2020) to reduce and stabilise silver NPs. Joseph *et al.* also proposed a large scale synthesis for biological MW-assisted silver NP synthesis(Joseph & Mathew, 2015).

Chau *et al.* also used MW to assist in the thermal decomposition of silver carbonate yielding NPs of about 9 nm. Research was carried out on the deposition of silver NPs on fibres (Bandi *et al.*, 2020; L. Peng *et al.*, 2016), microgels(A. Khan *et al.*, 2011) and PMMA beads(Irzh *et al.*, 2007) using microwave . Other investigations were also carried out on the use of MW to assist in producing nanoalloys and nanocomposites (NC) such as ZnO-Ag NC(Bhattacharyya & Gedanken, 2008), Fe-Ag Nanoalloys(Luo *et al.*, 2012), Ag-Graphene oxide NC (Chook *et al.*, 2012), Au-Ag alloys(Jia *et al.*, 2020), Ag-AgO NC(Elmaci, 2020), Ag-Carbon dot(CD)(Gul *et al.*, 2020).

II.1.1.2.3 Biological Methods

The main disadvantages of chemical techniques are the use of toxic solvents and reagents and the use of energy in the form of microwave or heating. Biological approaches provide a green alternative to this by making use of organisms to reduce silver ions(Ahmad *et al.*, 2019; Iravani *et al.*, 2014). The organisms that have been studied range from the simple bacteria to fungi and plants.

Extracts from plant leaves have been investigated and used as alternatives to chemical agents. Examples include Soybean(Vivekanandhan, 2009), Pine(J. Y. Song & Kim, 2009), Henna leaves(Kasthuri *et al.*, 2009) amongst others(Hamidi *et al.*, 2019; Nilavukkarasi *et al.*, 2020; J. Y. Song & Kim, 2009). On the other hand, when using micro-organisms such as bacteria and fungi, the reaction generally occurs within the cell itself. Studies have made use of several fungi including; *Penicillium* spp. (Maliszewska *et al.*, 2009; Rose *et al.*, 2019), *Humicola* spp. (Syed *et al.*, 2013), *Asperigus flavus*(Vigneshwaran *et al.*, 2007) and also bacteria such as; *Klebsiella pneumonia*(Mokhtari *et al.*, 2009), *Bacillus cereus*(Gurunathan, 2019), *Streptococcus mutans*(Gurunathan, 2019) *and Escherichia fergusonii*(Gurunathan, 2019).

Apart from the aforementioned organisms, recently some studies also explored the use of algae, Polysiphonia(Moshfegh *et al.*, 2019), as well as animal by-products namely cow urine(Jain *et al.*, 2019).

II.1.1.2.3 Conclusion

Silver NPs have been applied in a multitude of industries including textiles, electronics, water treating applications, biotechnology as well as medicine amongst

others. This variety of applications is due to their unique antimicrobial properties, conductivity and mechanical properties.

A wide range of synthetic processes can be executed, with variables that can easily be controlled to yield the size, size distribution and shape of NPs required for the application. To this end, research has delved deeper into the effect of these reaction conditions on the NPs produced. The different synthetic procedures described in this review all provide a different set of variables which are used to tailor make silver nanoparticles to the need of the user. As a general rule, physical methods tend to consume more energy and have a wider size distribution of nanoparticles, chemical methods on the other hand use less energy and yield nanoparticles with a narrow size distribution, however generally making use of toxic solvents. It is worth noting that polyol synthesis, especially using accelerator agents instead of heating, provide an economical yet accurate method of nanoparticle synthesis. The interactions of the polyols, as well as the viscosity of the solution, aid in controlling the shape and size of nanoparticles.

II.1.2 Iron Nanoparticles

II.1.2.1 Introduction

The term nanoparticles is a relatively new term which came into use in the late 1970s (Huber, 2005) and is quite a loose term with some arguing that based on the SI units system they are particles between 1-10 nm while some hold that it is anything between 1 to a 1000 nm (Sorensen, C. M. & Klabunde, 2001). What distinguishes such particles is that a series of their properties depend on their particular size in the nanoscale region. In this intermediary region, neither quantum nor classic laws of physics hold.

Therefore, by being able to produce uniform nanoparticles of a certain size, one can tailor the size-dependant properties as required. This is possible due to their immensely huge surface energy which allows the bulk properties to be synonymous to the surface properties. In some cases, spherical nanoparticles in the 3 nm range can have up to 50% of their atoms on the surface and this allows the manipulation of NPs properties by altering their size and morphology (L. Li *et al.*, 2006; Nel *et al.*, 2006).

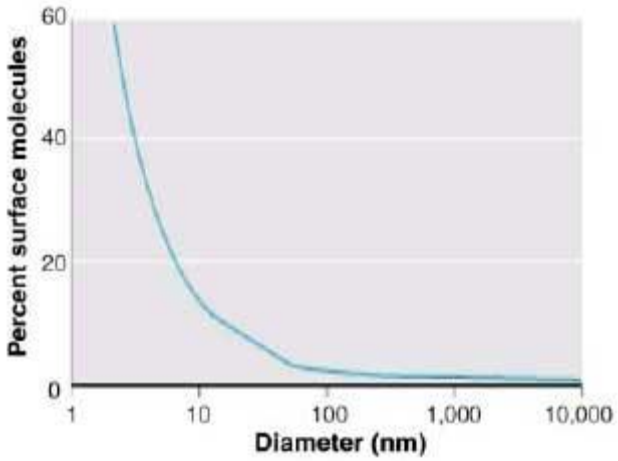

Figure II.11**:** Image taken from Nel *et al.* (Nel *et al.*, 2006) illustrating the inverse relation of diameter and percent surface molecules.

Having such a huge surface energy results in a higher intrinsic reactivity (Crane & Scott, 2012; Huber, 2005a; L. Li *et al.*, 2006) which can be explained through several classical equations such as the Gibbs-Thompson relation between particle size and energy. This shows how as the size is decreased, it approaches the size of specific lengths namely the electron mean-free path. As a result, these quantum size effects change the electronic structure and their properties. This affects the reactivity of the compound and hence properties such as magnetism and others due to changes in the Fermi level and band gap (Huber, 2005a; D. Zhang *et al.*, 1998). This coupled with other properties mentioned previously give nanoparticles the ability to perform optimally in certain applications.

Amongst the multitude of unique properties of nanoparticles, we will be focusing on magnetic nanoparticles whose properties has resulted in their potential use in a wide range of applications including data storage (Gubin *et al.*, 2002), magnetic pumps (Andò *et al.*, 2006), water purification (Crane & Scott, 2012), biochips (Deng *et al.*, 2019) as well as magnetism and biomedicine, namely magnetic hyperthermia (Hadjipanayis *et al.*, 2008), bio separation and MRI contrast agents (Hadjipanayis *et al.*, 2008; Na *et al.*, 2009).

Of all nanoparticles, iron nanoparticles have filled a particular niche of applications. Iron as a metal exhibits ferromagnetism and is one of the highest saturation magnetisation of the elements. Besides, iron NPs, below a certain size exhibit a different type of magnetism, superparamagnetism (Huber, 2005). These magnetic properties in addition to iron's biocompatibility, make it the suitable material ideal for several application such as MRI contrast agents, biosensors and in drug delivery amongst others.

Whilst research on magnetic and iron nanoparticles specifically has been carried out since the late seventies, it is only in the past few decades that the synthesis of iron NPs has been improved. While spherical nanoparticles have been successfully synthesised, controlling their size and shape has proved quite difficult. As a matter of fact, only recently have non-spherical iron nanoparticles been achieved (Shavel *et al.*, 2007). Another limitation is the fact that pure metallic NPs are susceptible to being oxidised as a result of their high surface area and reactivity, therefore metallic oxides are used which have a weaker magnetisation. Another issue that arises is that since iron nanoparticles are magnetic, they agglomerate and as a result of their superparamagnetic properties pack together which reduces the effect of properties characteristic to the nanoscale (Krämer *et al.*, 2008).

A solution to the problems discussed was to coat the nanoparticles. Magnetic nanoparticles in particular iron nanoparticles coated by non-magnetic capping agents have gained significant interest due to their stability (Sajitha *et al.*, 2004). This, however, effects the properties of the nanoparticles which includes a reduction in its magnetic properties.

II.1.2.2 Iron Nanoparticle Synthesis Techniques

In this review, several techniques to synthesise iron nanoparticles will be explored with close reference to the literature that has been performed in this field. Most of the conducted studies produced iron oxide which is the result of the oxidation during or after the formation of iron nanoparticles. While iron oxide nanoparticles have significant importance, the main aim of this review will be regarding zero-valent iron nanoparticles with some mentions to the iron-iron oxide core-shell structures.

When talking about nanoparticle synthetic pathways, we can classify them into three broad categories: Physical methods, Chemical methods and Biological methods.

II.1.2.2.1 Physical Synthesis Techniques

The physical methods usually consist of top-down techniques, i.e., techniques which involve the breakdown of bulk iron. The main advantages of such methods over the chemical and biological methods are that no toxic chemicals are used and most of them are relatively fast. On the other hand these methods are uneconomical due to the high temperatures, equipment and other expensive requirements for the techniques (X. Zhao *et al.*, 2016).

II.1.2.2.1.1 Inert Gas Condensation

Inert gas condensation is one of the first techniques developed for the synthesis of metallic nanoparticles. In this method, the metal material is vaporised by evaporating, sputtering or ablating into an inert atmosphere, and is then condensed under controlled conditions to produce particles of a desired size (Gleiter, 1990) as shown in

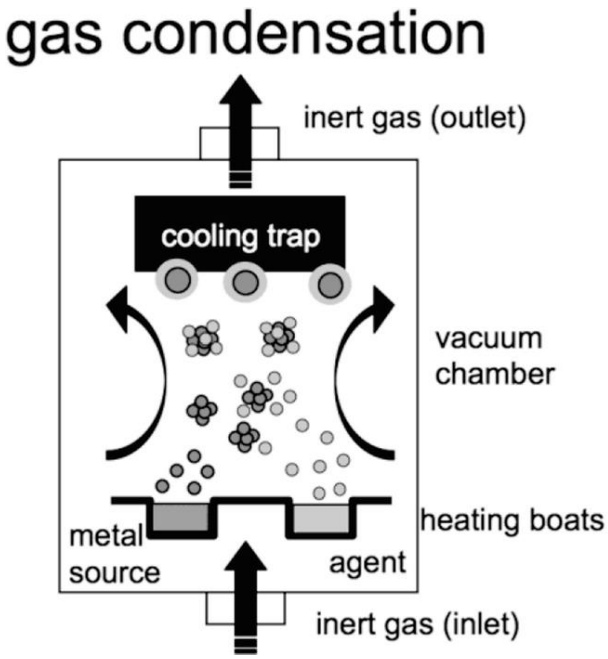

Figure II.12: A diagram illustrating the Inert Gas Condensation process taken from Inoue *et al.*(Inoue *et al.*, 2018).

In 1987, Gleiter *et al.* described one of the first iron nanoparticle synthesis through inert gas condensation (Herr *et al.*, 1987). Following this, Sanchez-Lopez managed to synthesise iron nanoparticles having an average diameter of 17nm (Sánche-Lópeaz *et al.*, 1997). Fung *et al.* later showed that iron NPs produced through this technique exhibited superior oxidation resistance (Fung *et al.*, 2000) due to the iron oxide shell. Similar studies investigated the passivation through oxidation as well as the magnetism of the nanoparticles produced (Baker *et al.*, 2002; Del Bianco *et al.*, 1998; Rojas *et al.*, 2004).

Some groups also investigated iron-polymer composites (Baker *et al.*, 2004) and alloying NPs (Djekoun *et al.*, 2009).

II.1.2.2.1.2 Laser Ablation

Laser ablation is a simple and flexible technique in which a solid target is irradiated by a laser beam. A plasma plume is formed and as it condenses, nanoparticles are produced in the medium. Several research groups have investigated this method namely Vitta *et al.*, where they characterised the iron NPs produced. In this study, SDS was used as a surfactant in an alcohol-water medium to obtain zero-valent iron NPs with a mean size of 17 nm (Vitta *et al.*, 2011). Over the years, research has been conducted on the variables of this method including the irradiation time (De Bonis *et al.*, 2015; Okada *et al.*, 2013; Sukhov *et al.*, 2012), different lasers (Sukhov *et al.*, 2012) as well as different liquid media (Amendola *et al.*, 2011; Okada *et al.*, 2013; Sukhov *et al.*, 2012), in some cases gaseous media (Z. Wang *et al.*, 2012). The use of pulsed laser irradiation was also explored (Amendola *et al.*, 2011; De Bonis *et al.*, 2015; Lahoz *et al.*, 2020; Okada *et al.*, 2013), an example of this is a study by Dadashi *et al.* where iron nanoparticles were synthesised by pulsed Nd:YAG laser ablation in a solution of water and acetone. These nanoparticles had a narrow -size distribution with an average size of 30 nm (Dadashi *et al.*, 2015).

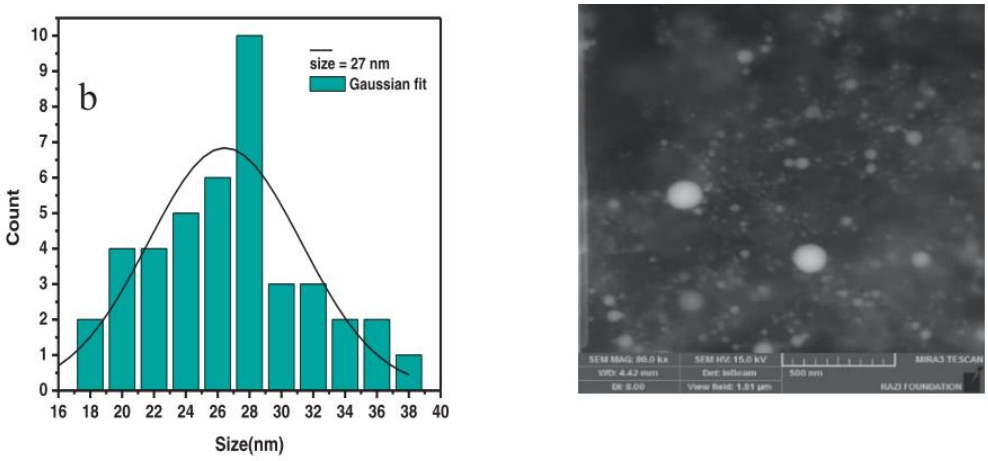

Figure II.13: TEM image and histogram showing the NPs and their size (produced by Dadashi *et al.* (Dadashi *et al.*, 2015))

II.1.2.2.1.3 The Exploding Wire Technique

In this process, a high-density current pulse is applied to a thin metal wire. The metal wire in turn is heated enough for it to vaporise resulting in it exploding into small fragments (Alqudami & Annapoorni, 2007; Kotov, 2003; Sen *et al.*, 2003; Siwach & Sen, 2008b; Vandana & Sen, 2005). A number of research groups have investigated this method and have explored the effect of variables such as wire diameter, current as well as the medium used (Alqudami, Annapoorni, Lamba, *et al.*, 2007).

In 2007, Alqudami *et al.* investigated the use of the capping agent PVP. The explosion medium for the iron wires used was water with PVP polymer dissolved using different concentrations of PVP which yielded NPs approximately 4 nm in diameter. They also investigated the effect of the coating on the magnetic properties of the iron NPs produced and found that the coating reduces the saturation magnetism (Alqudami *et al.*, 2012; Alqudami, Annapoorni, Lamba, *et al.*, 2007; Alqudami & Annapoorni, 2007). Other research groups have also explored the synthesis of bimetallic NPs by exploding two different wires simultaneously such as Al and Fe wires (Kotov *et al.*, 2003).

II.1.2.2.1.4 High Energy Ball Milling

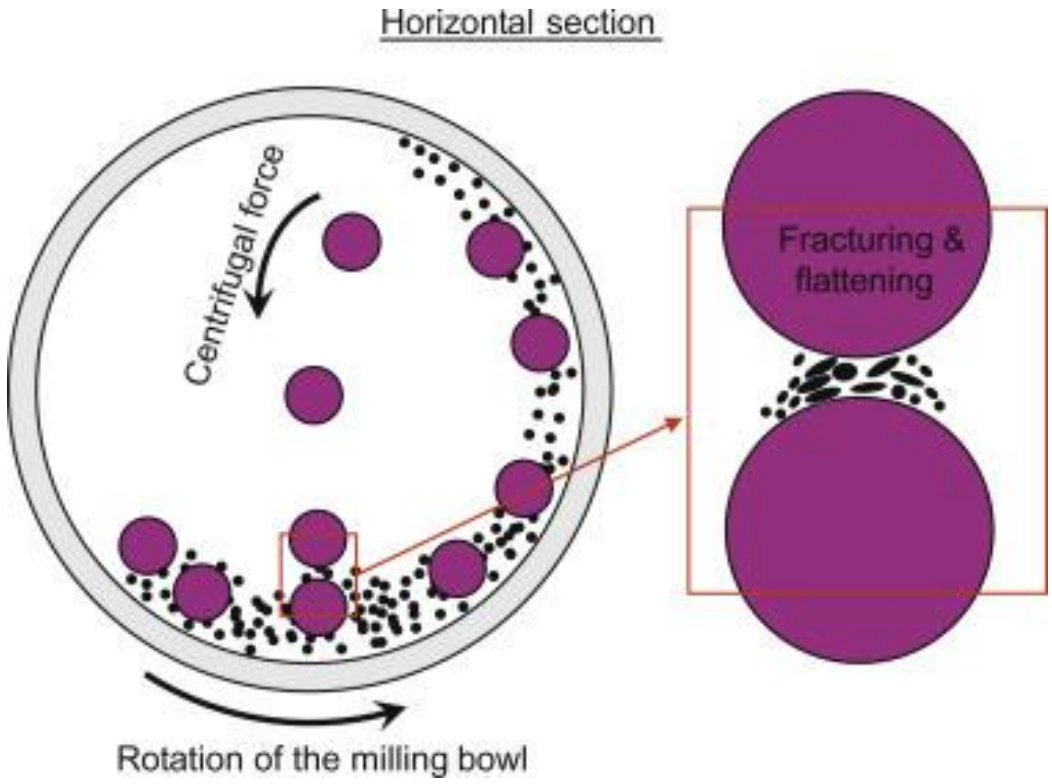

Figure II.14:Diagram illustrating the high-energy ball milling process

In ball-milling, micron-sized iron powder is fed into the mill and is broken down into smaller sizes by using the high energy collisions that occur in ball milling as shown in Figure II.14. Li *et al.* used iron powder having a mean size of 2 micrometres which after the milling process broke down into iron nanoparticles ranging from 40-60 nm (S. Li *et al.*, 2009). The resulting nanoparticles had comparable reactivity to those formed using the conventional borohydride reduction technique which will be discussed further on. Other research groups have also produced iron NPs using this method such as Tung *et al.* where they achieved NPs 10 nm in size (Tung *et al.*, 2016) and Munoz *et al.* where they described the production of nanoparticles having a mean size of 3 nm with HREM images (Muñoz *et al.*, 2007). In the latter study the use of ethanol as a processing control agent was employed which aided the cold-welding processes and fracturing (Muñoz *et*

al., 2007). In a study by Zhao *et al.*, the researchers produced nanoparticles with relatively small sizes using three methods; Wet chemical reduction, Gas-phase reduction and the high energy ball milling technique. The latter was found to be an energy-efficient and time-efficient process which singled it as a possibility for mass production (S. Li *et al.*, 2009; X. Zhao *et al.*, 2016). The main disadvantage of such technique is the inevitable surface defects that arise in the nanoparticles due to the collisions.

This technique has also been used to synthesise nanocomposites. In 1997, Giri prepared a iron-polyethylene NC by milling for 200 hours at room temperature (Giri, 1997). More recently studies have synthesised Fe/$Fe_{2-3}N$ NC, Sm_2Co_7/α-Fe NC(Zhuge *et al.*, 2020) and with the popularity of multi-walled carbon nanotubes, FeCu-MWCNT NC were also produced (Naoui *et al.*, 2020).

II.1.2.2.2 Chemical Synthesis Techniques

Chemical methods generally adopt a bottom up approach in which the atoms are produced from a precursor ion and come together to form clusters and stabilise as nanoparticles. These methods are extensively used particularly in metal nanoparticles synthesis due to their control on the morphology of nanoparticles via reaction parameters (X. Zhao *et al.*, 2016).

II.1.2.2.2.1 Arc discharge Technique

In this technique, electrodes are used to create an arc which ionises the atmosphere usually containing an inert gas producing plasma. The arc channels current into the electrolytic solution resulting in the reduction of the ions present. This process is a simple one-step procedure which yields homogeneous and well-coated particles. In 2006,

Fernandez-Pacheco successfully produced iron nanoparticles coated with a silica shell of an average size 56 nm(Fernández-Pacheco *et al.*, 2006). In another study by Kassaee *et al.*, iron nanoparticles 37 nm in diameter were obtained using the arc-discharge method and were compared to the iron nanoparticles obtained via borohydride reduction(Kassaee *et al.*, 2011).

II.1.2.2.2.2 Chemical Vapour condensation

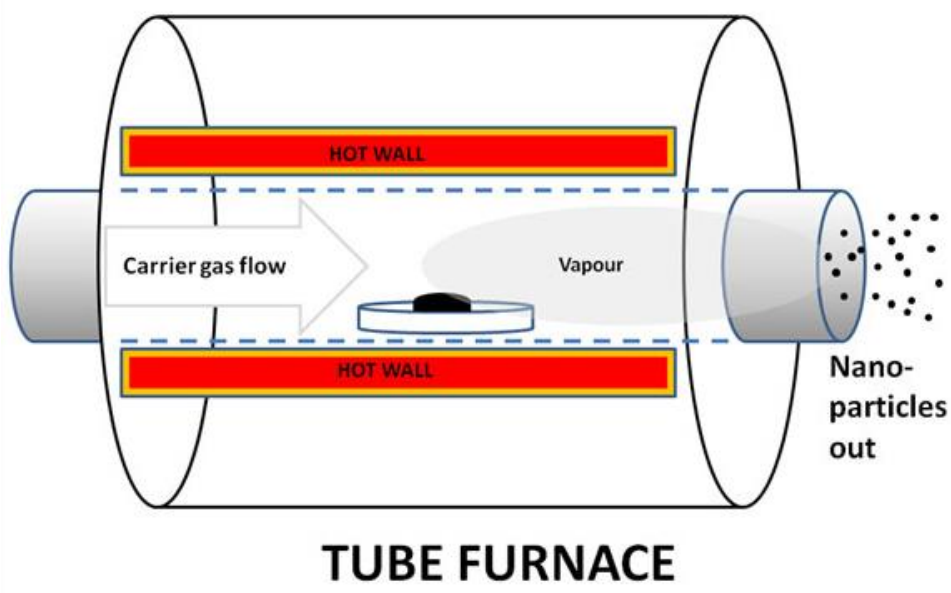

Figure II.15: A diagram illustrating the chemical vapour deposition process.

Chemical vapour condensation (CVC) is a process versatile process which can be used with a variety of precursors. It is similar in concept to Inert Gas Condensation mentioned previously however instead of vaporising the target metal, the metal nuclei are formed from a metal precursor. Choi *et al.* described a method where iron nanoparticles have been produced through this process via the pyrolysis of the precursor iron pentacarbonyl(C. J. Choi *et al.*, 2002). It was reported that iron NPs ranging from 5 to 13nm in size were produced with a uniform distribution.

II.1.2.2.2.3 Decomposition

Decomposition is one of the most popular syntheses for metallic NPs, owing to its simplicity. Metal precursors (generally metalloorganic compounds) are used which are then decomposed, when exposed to conditions such as heat, ultrasound and laser amongst others, to produced metal NPs. Metal carbonyls and their related derivatives are very popular as they are usually readily available (Krämer *et al.*, 2008) and due to the nature of the carbonyl ligand which is easily removed forming the metal clusters which grow into NPs (Amara *et al.*, 2009; Frey *et al.*, 2009).

II.1.2.2.2.3.1 Thermal Decomposition

Thermal decomposition is the use of heat energy to decompose a metal precursor yielding metal nanoparticles. of iron pentacarbonyl with different surfactants such as dioctyl ether solvent and oleic acid and oleyl amine yielded iron nanoparticles with sizes ranging from 5 to 19 nm (Amara *et al.*, 2009; Y. Gao *et al.*, 2005; Y. C. Han *et al.*, 2007)**.** However, it has proven to be an uneconomical process due to the elevated temperatures and expensive highly toxic precursors needed (K. C. Huang & Ehrman, 2007). Other researchers used different types of iron precursor such as Fe_3CO_{12} giving iron nanoparticles between 5 to 8 nm (Amara *et al.*, 2009) and $\{Fe(N[Si(CH_3)_3]_2)_2\}_2$ producing iron nanoparticles of 1.5 nm (Lacroix *et al.*, 2008) and 2 nm (Kelsen *et al.*, 2013) in two separate studies. A green synthesis was proposed by Nguyen *et al.* combining thermal decomposition and chemical reduction where iron(iii) oleate in a NaCl matrix was decomposed at high temperatures in the presence of a hydrogen atmosphere to produce iron nanoparticles (Nguyen *et al.*, 2019).

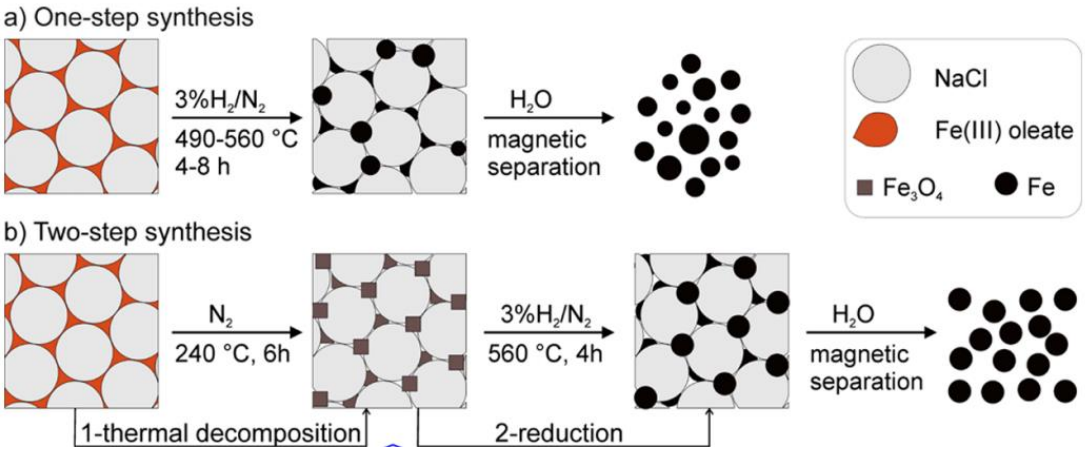

Figure II.16: A diagram explaining the synthesis through thermal decomposition by Nguyen *et al.*(Nguyen *et al.*, 2019).

Different experimental condition and stabilisers have been investigated such as trioctylphosphine oxide used by Park *et al.* to produce iron nanoparticles of about 2 nm from iron pentacarbonyl (S. J. Park *et al.*, 2000). Shavel *et al.* improving on the work of Hyeon and his co-workers (Hyeon *et al.*, 2001), was also able to produce cubic core shell iron-iron oxide nanoparticles through the use of sodium oleate and by varying the experiments conditions (Shavel *et al.*, 2007). Kim *et al.* also investigated the effect of sodium oleate and found that in some cases the nanocubes were transformed to hollow nanoframes (D. Kim *et al.*, 2007).

This technique has also been use to create alloy nanoparticles such as bimetallic CoFe alloy particles produced by the decomposition of $Fe(CO)_5$ and $Co_2(CO)_8$ in 1,2-dichlorobenzene (Dung *et al.*, 2017).

II.1.2.2.2.3.2 Other Decomposition techniques

Apart from the thermal decomposition, Suslick *et al.* (Suslick *et al.*, 1996) and Koltypin *et al.* (Koltypin *et al.*, 2004) have provided a sonochemical method using ultrasound irradiation of iron pentacarbonyl in the presence of polyvinyl pyrrolidine and

oleic acid. Laser-driven decomposition of iron pentacarbonyl vapour has also led to the formation of iron nanoparticles. In this method, an laser is used to rapidly heat a mixture of precursor vapours which results in the localised thermal decomposition of the precursor which yields NPs (Y. He *et al.*, 2006). Park *et al.* used pulsed laser decomposition of ferrocene to form carbon encapsulated iron nanoparticles with the particles produced ranging from 10-30 nm (J. B. Park *et al.*, 2008). He *et al.* also used this technique on iron pentacarbonyl vapour yielding iron nanoparticles 5 nm in diameter (Y. He *et al.*, 2006).

II.1.2.2.2.4 Chemical Reduction

According to the majority of studies, this method is the easiest, most efficient and one of the most popular technique for the synthesis of iron nanoparticles (J. Guo *et al.*, 2012). In this method, a reducing agent converts the ferrous and ferric ions to metal ions forming nanoparticles. Several studies have investigated the use of different reducing agents to synthesise these NPs with some of the most common being the hydrides; sodium borohydride (Carpenter, 2001; K. C. Huang & Ehrman, 2007; Jafari *et al.*, 2010; Kanel *et al.*, 2005; J. Lin *et al.*, 2001; Liou *et al.*, 2006; Ponder *et al.*, 2000; Y. P. Sun *et al.*, 2007; W.-X. Zhang & Wang, 1997; W. L. Zhou *et al.*, 2001) and lithium superhydride(S. Sun *et al.*, 2003). Other reducing agents used including hydrazine(Seip & O'Connor, 1999), dihydrogen gas (Margeat *et al.*, 2005), amino acids (Klačanová *et al.*, 2013) and polyols (G. M. Chow *et al.*, 1998; Dijith *et al.*, 2018; Kurihara *et al.*, 1995; Nene *et al.*, 2016)

This reduction generally is performed in a solvent medium and therefore the nanoparticles are obtained as a dispersion of solid nanoparticles in the solvent. This brings up the main disadvantage of this method, the oxidation and the aggregation of the

nanoparticles. However it is possible to mitigate this effect by employing the use of surfactants and capping agents during their synthesis which will be discussed later on (J. Guo *et al.*, 2012; Ling *et al.*, 2012).

One advantage of chemical reduction methods is the manipulation of morphology by controlling the reaction parameters; chemicals used and reaction conditions. There are two differing techniques in chemical reduction techniques; Ones which use aqueous mediums and those which use non-aqueous mediums.

Aqueous methods: In these techniques, an inert atmosphere and antioxidants are employed to prevent the oxidation of the nanoparticles produced. Many studies in this area have investigated the effect of capping agent/surfactant, pH reaction conditions and seeding agents on the morphological structure.

Huang *et al.* reported a method using palladium ion seeds as nucleating agents for iron nanoparticles (K. C. Huang & Ehrman, 2007). In this study, sodium borohydride was used as a reducing agent and polyacrylic acid as a capping agent. Iron nanoparticles produced were about 6 nm whereas under the same conditions, excluding the palladium ions, the size of nanoparticles was 110 nm implying that the seeds aided the formation of smaller nanoparticles. Yang *et al.* also introduced palladium chloride as a nucleating agent which upon reduction became palladium seeds (T. I. Yang *et al.*, 2011a). The iron nanoparticles produced ranged from 200 to 9 nm depending on the capping agent and the amount of capping agent. In this study it was shown that by increasing the amount of Citric Acid results in a uniform size distribution of smaller nanoparticles. However, being a strong chelating agent for iron, it is not feasible to use Citric acid alone. Oleic acid was also used and was shown to be ineffective in controlling nanoparticle formation however when used in conjunction to citric acid, 8.2 nm nanoparticles were produced with a much

narrower size distribution while eliminating the re-dissolution of iron. Sun *et al.* introduced polyvinyl alcohol-co-vinyl acetate-co-itaconic acid, a surfactant which produced spherical nanoparticles about 7.9 nm which when compared to the bare nanoparticles (without surfactant), which were about 59.4 nm shows the reduction in size while reducing aggregation. It was also shown how the polymer stabilised the surface energy (Y. P. Sun *et al.*, 2007).

Klacanova *et al.* also investigated the use of amino acids as reducing agents. Iron (II) Sulphate was reduced to produce iron nanoparticles ranging from 8 to 11 nm with aliphatic amino acids producing nanoparticles with higher magneto activity (mass susceptibility, mass magnetisation in saturation, remnant magnetism and magnetic hysteresis coercive field)(Klačanová *et al.*, 2013)

The non-aqueous techniques can be performed under inert gas or also without an inert atmosphere. In this synthesis, capping agents and surfactants are used to attain the morphology desired while also controlling temperatures and molar ratios (Margeat *et al.*, 2005). A class of reducing agents of interest are polyols, especially polyols having adjacent hydroxyl groups. These class of compounds have gained interest due to their versatility as they act as a solvent, reducing agent and capping agent in the reaction (Frey *et al.*, 2009). A technique called the Polyol method was developed and described by Islam *et al.* (Islam *et al.*, 2013). In this method, the precursor compound such as sulphates, halides and others were dissolved in the polyol. The mixture is then heated usually at a certain pH resulting in the reduction of the precursor into metal particles which in turn are coated by the polyol itself. It has been reported that to reduce particle size one can increase the reaction temperature(Catauro *et al.*, 2018).

While nanoparticles of nickel and cobalt are relatively easily produced due to nickel and cobalt ions being easily reduced using polyols, iron ions are less electronegative and therefore their reduction requires harsh conditions.

In 2002, Sun *et al.* proposed an approach in which iron (III) acetylacetonate, $Fe(acac)_3$ was dissolved in a diphenyl ether medium and exposed to a high-temperature (265 °C) (S. Sun & Zeng, 2002). Then chemical agents such as alcohols, oleic acid, and oleyl amine were used to reduce the iron ions to monodisperse magnetite nanoparticles. This magnetite in turn could be transformed into iron nanoparticles by annealing at different temperatures.

Following this, Nene *et al.* proposed the use of ascorbic acid to reduce iron acetylacetonate (acac)(Nene *et al.*, 2016). The iron acetylacetonate was dissolved in diphenyl-ether medium and kept under a nitrogen atmosphere. In the absence of water and by heating to 70°C, this yielded iron nanoparticles of around 7 nm. The presence of water resulted in iron oxide nanoparticles instead, 15 nm in size.

Viau *et al.*, described a method for using propylene glycol and ethylene glycol as solvents, reducing agents and capping agents. In this technique, sodium hydroxide was used accompanied with heating to yield nanoparticles ranging from 200 to 500 nm (Viau *et al.*, 1996a). In a later study, Viau *et al.* described the bimetallic synthesis of iron with cobalt and nickel via the polyol method (Viau *et al.*, 1996b). In two studies, Chow and Kurihara developed the reduction of iron acetate using both ethylene glycol and tetra ethylene glycol yielding nanoparticles of about 20 nm (G. M. Chow *et al.*, 1998; Kurihara *et al.*, 1995). More recently, Kesa *et al.* used PEG in the reduction of iron(II) chloride however the polyol did not provide adequate protection resulting in an iron oxide rich phase (Dijith *et al.*, 2018). However in 2011, Cheng *et al.* reported the successful use of

PEG as a stabiliser in borohydride reduction via the reverse micelle method discussed later on(Cheng *et al.*, 2011).

In general, non-aqueous methods yield nanoparticles with better morphological control than their aqueous counterparts however most of the techniques involve toxic chemicals and heating which make them environmentally unfavourable.

II.1.2.2.2.5 Reverse Micelle Technique

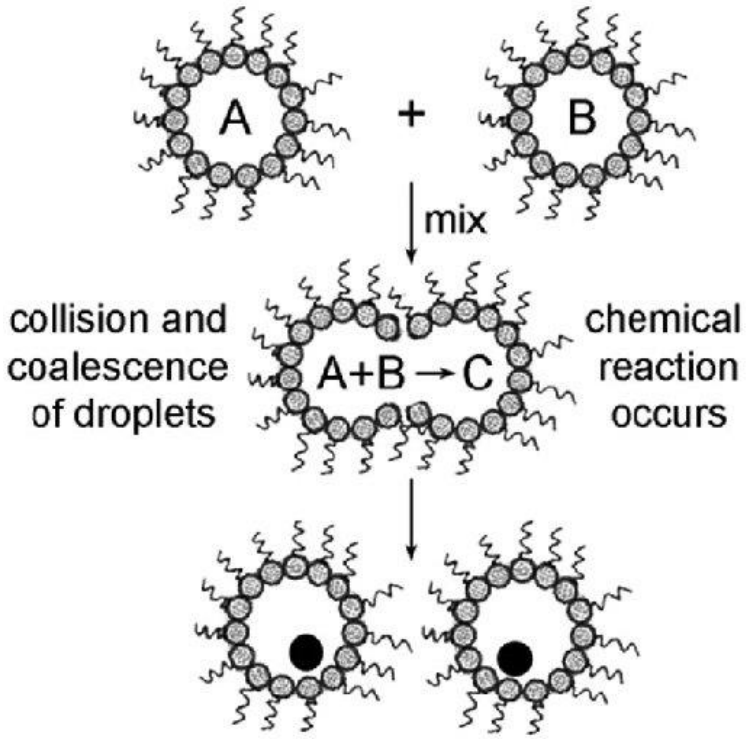

Figure II.0.17**:** A schematic diagram showing the synthesis of nanoparticles through the reverse micelle process(Y. Liu *et al.*, 2013)

The reverse micelle method is a technique that has been used frequently as it is an excellent method to prepare nanoparticles with a small size distribution and uniform morphology can be produced (Carpenter, 2001). In this process, micelles containing extremely small quantities of the reactants come together resulting in a very controlled

reaction to occur as shown in Figure II.0.17. Carpenter used a system containing cetyltrimethylammonium bromide (CTAB) was used as the surfactant, with octane as the oil phase, n-butanol and an aqueous reactant to reduce ferrous ions using the reducing agent sodium borohydride. The nanoparticles produced were then protected by a thin layer of gold. Building on this research, several researchers modified the process producing gold shells of different thickness as well as iron cores of different sizes(Jafari *et al.*, 2010; J. Lin *et al.*, 2001; W. L. Zhou *et al.*, 2001). In a study in 2001, Zhou *et al.* found that by varying the water to surfactant ratio ([H2O]/[CTAB]), they were able to carefully control the particle size, ranging from 5 to 30 nm(W. L. Zhou *et al.*, 2001). In 2011, Cheng *et al.* showed how the size and morphology of the iron nanoparticles were affected by the interfacial properties of the micelle as well as its size(Cheng *et al.*, 2011). The main disadvantage of such method is the use of organic solvents which makes them environmentally unfavourable.

II.1.2.2.3 Biological Synthesis Techniques

Iron NPs have also been synthesised through the use of a multitude of microorganisms ranging from bacteria and fungi to plants. In 2006, Bharde *et al.* reported the synthesis of iron oxide NPs using the fungi *F. oxysporum* and *Verticillium* spp. (Bharde *et al.*, 2006). A later study by Tarafdar et al, successfully synthesised zero-valent iron nanoparticle by *Aspergillus oryzae* (TFR9) using $FeCl_3$ as a precursor metal salt. Using this method, nanoparticles ranging between 10 to 25 nm were achieved(Tarafdar & Raliya, 2013).

In a more recent study, metallic iron nanoparticles were synthesised using *Aspergillus niger* (YESM1). In this process, iron sulphate decomposed to iron sulphide

which in turn are bioreduced to form iron sulphide nanoparticles. When exposed to the supercritical ethanol, iron nanoparticles are formed with the evolution of H_2S gas which protects the iron nanoparticles from oxidation. The iron nanoparticles produced by this method had an average size of 18 nm and were shown to exhibit superparamagnetism(Abdeen *et al.*, 2016; Ghozlan *et al.*, 2018).

Bio-extracts of plants such as flavonoids, proteins, terpenoids have also been used as both reducing agents as well as capping agents in the synthesis of iron NPs. Generally, such methods are referred to as green synthesis due to the eco-friendly aspect of the method. A wide variety of plant extracts have already been studied; *Azadiracta indica*(Devatha *et al.*, 2016) yielding 50-100 nm large nanoparticles, *Magnifera indica*(Devatha *et al.*, 2016), giving nanoparticles in the size range 50 to 150 nm, *Magnolia champaca*(Devatha *et al.*, 2016), yielding nanoparticles in the size range 99 to 200 nm, *Rosa damascene*(Fazlzadeh *et al.*, 2017) producing nanoparticles of about 100nm, *Thymus vulgaris*(Fazlzadeh *et al.*, 2017) producing nanoparticles of about 100 nm, *Urtica dioica*(Fazlzadeh *et al.*, 2017) producing nanoparticles of about 100 nm, *Amaranthus dubius*(Harshiny *et al.*, 2015) giving a wide size distribution of nanoparticles, 43-700 nm, *Terminalia chebula*(Mohan Kumar *et al.*, 2013) yielding nanoparticles in the size range of 80 nm, *Lawsonia inermis*(Naseem & Farrukh, 2015) producing iron particles 21 nm in diameter, *Gardenia jasminoides*(Naseem & Farrukh, 2015) giving nanoparticles 32 nm in diameter, *Camellia sinensis* (green tea) (Hoag *et al.*, 2009) giving nanoparticles ranging from 5-15 nm, and other tea extracts such as black tea and oolong tea giving particles with a diameter of 40-50 nm(L. Huang *et al.*, 2014b, 2014a) as well as eucalyptus leaves extract(T. Wang *et al.*, 2014) yielding particles of around 20 to 80 nm.

II.1.3 Major Issues and Solutions

The main concerns in the synthesis of Iron NPs are the aggregation and the oxidation of these particles(Ling *et al.*, 2012).

II.1.3.1 Oxidisation

It has been found that under ambient conditions iron NPs smaller than 8 nm oxidise completely upon exposure to air whereas larger nanoparticles form an oxide shell(Cheong *et al.*, 2011). This is due to iron's reactivity coupled with the high surface energy on nanoparticles. In fact, when iron nanoparticles are produced, the outer layer oxidises producing an oxide shell which gradually increases as oxidation(X. Q. Li & Zhang, 2006, 2007). However, studies have shown that if a crystalline Fe_3O_4 shell is formed, the iron core would be protected from further oxidation as opposed to an amorphous one which allows oxygen to seep through and come in contact with zero-valent iron resulting in oxidation(S. Peng *et al.*, 2006).

This oxidation can also be mitigated completely by applying shell coatings which will be discussed further on. However the resultant properties are inevitably affected by the shell's properties(S. Guo & Sun, 2012).

II.1.3.2 Aggregation

Another problem is the fact that magnetic nanoparticles tend to aggregate due to strong dipole-dipole interactions(Amara *et al.*, 2009)as aggregation is a thermodynamically favourable process(F. He & Zhao, 2005, 2007; Laurent *et al.*, 2010; S. Sun & Zeng, 2002). The issue with this is that the agglomeration of nanoparticles into

larger clusters results in a change in properties due to the change in the reactive surface area(Nurmi *et al.*, 2005).

There are two ways in which aggregation has been dealt with over the past few years. Ling *et al.* and other researchers controlled this issue by immobilizing nanoparticles in or on supports(Ling *et al.*, 2012). Xiao immobilised iron nanoparticles within electrospun polymer nanofibers through the in-situ reduction of Fe(III) ions complexed with the water-insoluble nanofibrous mats(Xiao *et al.*, 2009). An alternative is coating with organic compounds or surfactants(Amara *et al.*, 2009).

II.1.3.3 Stabilising Iron Nanoparticles

An effective solution to aggregation and oxidation is coating the iron nanoparticles with a layer of inert compounds which are termed stabilizers or dispersing agents(M. De Fan *et al.*, 2010). Different compounds impart different properties to the nanoparticles. Generally stabilisers fall into three categories; metals, organic compounds and surfactants, however other compounds such as dendrimers, resins, alumina, active carbon, zeolites and clay minerals are also used(M. De Fan *et al.*, 2010).

To stabilize these nanoparticles, there are two strategies that are usually used: Pre-aggregation stabilization or post-aggregation stabilization. As the name implies, pre-aggregation stabilization is when stabilizers are applied before the nanoparticles aggregate whilst, post-aggregation stabilization is when the aggregates are broken down and a stabilizer is added to the nanoparticles(Gawande *et al.*, 2015; F. He & Zhao, 2007).

Organic compounds have been used extensively as stabilizers. This is since an organic coating can allow the binding of other biological molecules (such as proteins) effectively functionalizing the nanoparticles' surface (Amara *et al.*, 2009). This is of high

importance in drug delivery and biomedical applications. He *et al.* in 2007 also used carboxymethyl cellulose as a stabilizer(F. He & Zhao, 2007). Burke *et al.* also investigated different polymer shells consisting of polyisobutylene, polyethylene or polystyrene chains which were functionalised with tetraethylenepentamine(Burke *et al.*, 2002). The effect of other polymers were investigated such as carboxy methyl cellulose , poly(styrene sulfonate), poly(acrylic acid) and polyacrylamide by Cirtiu *et al.*(Cirtiu *et al.*, 2011). All the polymers were negatively charged with the exception of the non-ionic polyacrilamide(Cirtiu *et al.*, 2011). Another organic compound is polyethylene glycol which is a cheap, and stable polymer making it a suitable stabiliser(Cheng *et al.*, 2011).

As discussed previously, coating helps to functionalise the particles, but it also enhances their biocompatibility and hence reduces the extent of clearance by the reticuloendothelial system. The inorganic silica is both biocompatible and non-toxic, it also has hydroxyl surface groups which allow functionalisation making it a suitable stabiliser(Fernández-Pacheco *et al.*, 2006; Ni *et al.*, 2010).

One of the main problems with organic compounds is that being non-magnetic, the coating layer reduces the particles magnetic properties. This problem can be mitigated, by using gold as a passivating layer(J. Lin *et al.*, 2001). Gold coating has become a favoured coating material as it protects the magnetic core from oxidation without have a large impact on the decrease in magnetisation(Ban *et al.*, 2005). Zhang *et al.* have shown a method of synthesising core-shell iron-gold nanoparticles using laser irradiation(J. Zhang *et al.*, 2006).

Another coating involves carbon encapsulation which enhances stability and prevents agglomeration and oxidation by isolating the particles magnetically from each other. Graphite has several desirable properties namely being light and resistant to acids,

bases, greases and high temperatures and more importantly, having the potential of functionalising, allowing for surface engineering(Bystrzejewski *et al.*, 2011; Huo *et al.*, 2004). In fact several studies have obtained Carbon-encapsulated magnetic nanoparticles (CEMN) consisting of graphite layers that cover an iron core(Bystrzejewski Michałand Huczko *et al.*, 2007; El-Gendy *et al.*, 2009; Si *et al.*, 2003; A. Taylor *et al.*, 2010).

Iron oxide can also be used for surface coating however it was shown that an amorphous layer of iron oxide is ineffective as it allows deep oxidation. On the other hand a crystalline layer prevents this such as a γ-Fe_2O_3 shell(Fung *et al.*, 2000).

Appendix III: Silver Nanoparticle Synthesis and Characterisation

III.1 Introduction

At the nano-scale, a material has a significant portion of its atoms on the surface resulting in a high surface area to volume ratio. This phenomenon drastically changes the properties of the material from the bulk material. In metals this is clearly observed in the colour changes as well as physical and chemical properties. Silver nanoparticles have been especially distinguished for their antimicrobial efficacy as well as their very unique optical, electric and chemical activity(D. Kim *et al.*, 2006; Suber *et al.*, 2005; Y. Sun *et al.*, 2002; D. Zhang *et al.*, 2004).

In order to produce uniform nanoparticles, synthetic techniques were developed to realize the production of nanoparticles of different sizes and shapes which in turn yielded different properties. For silver nanoparticles, one of the most popular production techniques is the Creighton method (Creighton, J.A.; Blatchford, C.G.; Albrecht, 1978) where sodium borohydride is used to reduce silver in conjunction with a capping agent such as PVP (Borysiuk *et al.*, 2008; Dong *et al.*, 2010; Kandarp Mavani, 2013; Song *et al.* 2009; J. S. Kim *et al.*, 2007; Mulfinger *et al.*, 2007; S.A. Vorobyova , A.I. Lesnikovich & Research, 2008; Wagner *et al.*, 2007; Wani *et al.*, 2011; Zielińska *et al.*, 2009). Another promising technique is the Lee-Meisel method (P. C. Lee & Meisel, 1982), based on the Turkevich method developed in 1951 (Peter *et al.*, 1951), which is a chemical synthesis using trisodium citrate as the reducing and capping agent. However since trisodium citrate only acts as a reducing agent above 60°C, this reaction is accompanied by heating the solution to boiling (Mazzonello *et al.*, 2015; Ratyakshi & Chauhan, 2009; Steinigeweg &

Schlücker, 2012; Y. Wan *et al.*, 2013; H. Yin *et al.*, 2004). Agnihotri *et al.*(Agnihotri *et al.*, 2014), showed that they were able to control the reducing ability of trisodium citrate in a co-reduction method (Agnihotri *et al.*, 2014) by varying the reaction temperature,. In addition to this, there are studies that have shown that the size of nanoparticles increases with increasing temperature (Agnihotri *et al.*, 2014; X. C. Jiang *et al.*, 2011; G. J. Lee *et al.*, 2004). It was also shown that with higher temperatures, the nanoparticles obtained were more monodisperse, homogenous and had uniform shapes (G. J. Lee *et al.*, 2004; Y. C. Lee *et al.*, 2010). In 2012, Steinigeweg *et al.*, introduced the use of the highly viscous glycerol at 95°C (Steinigeweg & Schlücker, 2012). This resulted in a decrease in nucleation speed and reducing power which yielded smaller nanoparticles of about 30 nm in size. Apart from this, glycerol also exhibited stabilizing effects which suppressed the ripening process(Steinigeweg & Schlücker, 2012). A modified method using NaOH as an accelerator of the reaction was suggested in which glycerol or EG was used as both the reducing agent and the solvent in conjunction with stabilisers such as PVP (Sarkar *et al.*, 2010). This reaction was carried out at room temperature and produced monodisperse silver nanoparticles, 25 nm in size. To the best of our knowledge, there are no studies carried out using glycerol at zero and sub-zero temperatures (°C) and there is lack of research regarding the effect of glycerol and of low temperatures on the nanoparticle shape and size.

In view of the above, the main objective of this chapter is to synthesise, characterise and understand the underlying mechanism for the production of silver nanoparticles using a glycerol-mediated reduction of silver ions using potassium hydroxide as an accelerator at low temperatures.

In particular this study aims to.

- Study the effect of low temperatures on the size and morphology of silver nanoparticles when using this method
- Study the effect different capping agents, namely trisodium citrate and PVP, have on the size and morphology of silver nanoparticles. This includes investigating the effect of using PVP with different molecular weights.

III.2 Methodology

III.2.1 Synthesis

A solution of silver nitrate (Biochem Chemopharma, France, 99%, CAS: 7761-88-8) was prepared by dissolving 0.20 g (weighed using an analytical balance, Precisa XT220) of silver nitrate in 10 g of ultra-pure water (18 MΩ/cm). A solution of trisodium citrate (Scharlab, Spain, 99-100.5%, CAS: 6132-04-3) was then prepared by dissolving 3.47 g of trisodium citrate in 10 g of ultra-pure water. The latter two solutions were then added to 170 g of glycerol (food grade glycerol CAS:56-81-5) present in a 500 mL beaker. This results in a system having a 1:10 molar ratio between silver nitrate and trisodium citrate. The beaker was then covered with aluminium foil to block sunlight and was placed in an insulated reaction chamber, wrapped with aluminium foil to further reduce exposure to light. As shown in Figure III.1, the beaker was surrounded by a hollow copper coil through which cooled liquid was passed from a circulating chiller (WCR-P8 refrigerated bath circulator) set at a temperature of 20°C. Copper being a good heat conductor allows efficient transfer of heat to the beaker and its surroundings. The body of liquid surrounding the beaker and the expanded polystyrene reduce thermal fluctuations. To achieve homogeneity, the contents of the beaker were stirred at 500 RPM using an overhead stirrer (AM120Z-H Laboratory mixer).

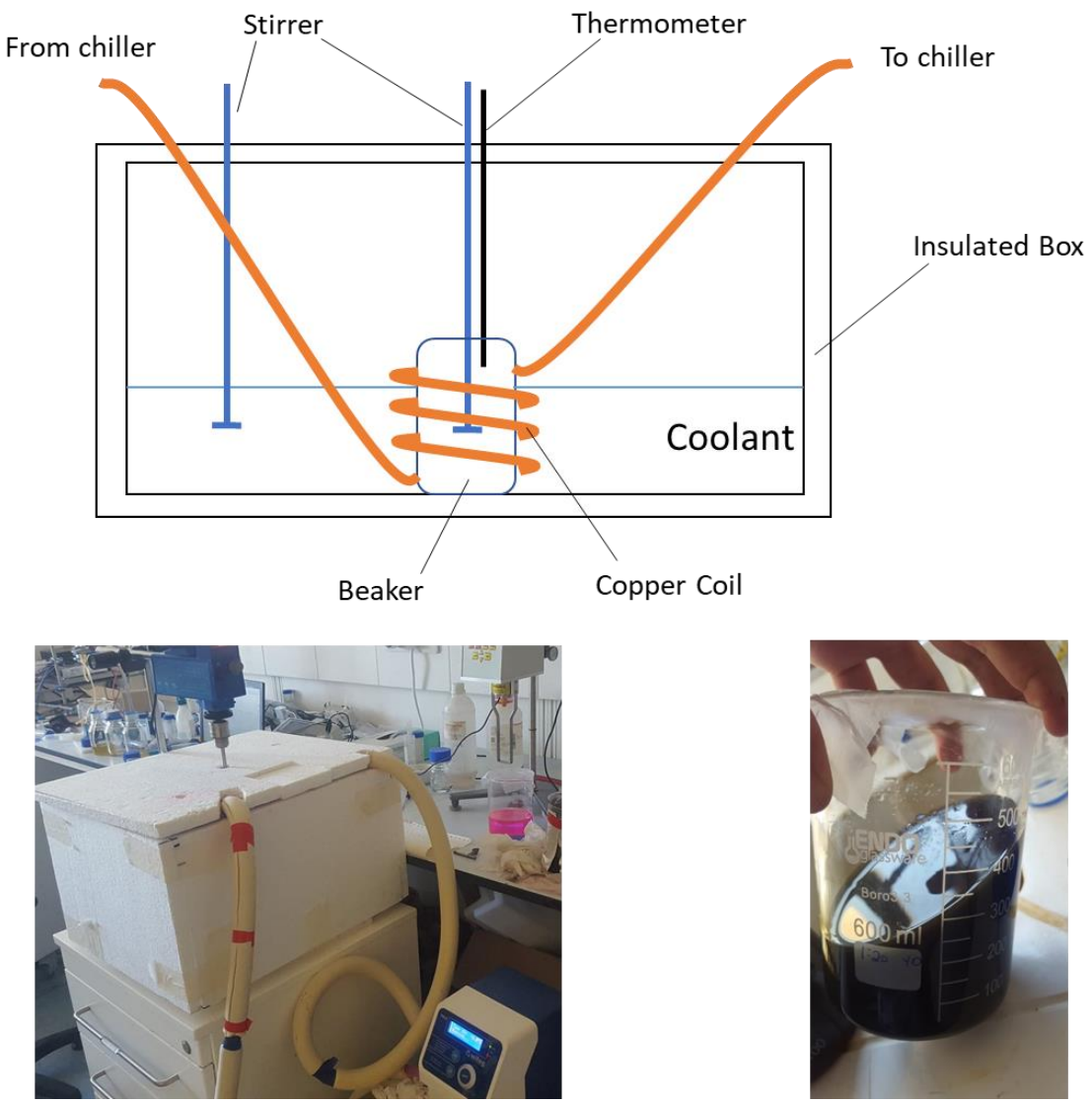

Figure III.1 (Top) Schematic of the reaction chamber (Left) Insulated reaction chamber (Right) Black solution formed at -10°C using a 1:20 Silver nitrate: Trisodium citrate ratio

After that the solution reached the temperature of the water bath a solution containing 1.4 g of potassium hydroxide (Carlo Erba, Italy, 85%, CAS: 1310-58-3) dissolved in 10 g of water were added. The mixture was mixed for one hour after which a dark liquid was collected. This methodology was then repeated using different reaction

times of 15, 30, 60 and 120 minutes, trisodium citrate concentration yielding a silver : citrate ratio of 1:1, 1:2, 1:5, 1:10, 1:15 and 1:20 and temperatures ranging from 20°C to -20°C in increments of 5°C.

III.2.2 Purification

First 15 mL of the suspension was poured into a 50 mL centrifuge tube to which 10 mL of water and 15 mL of acetone were added. The solution was thoroughly mixed to avoid any separation of layers. Hereafter, centrifugation was applied at 13480 ×g for 10 minutes using a TG16 Yingtai centrifuge. The supernatant was then removed and the solid was re-suspended in 2 mL of water to which 38 mL of acetone were added. This procedure was repeated twice. Thereafter, the supernatant was removed and left to dry in the dark overnight.

The dry solid that remained was then re-suspended in 100 mL of water by sonication for 15 minutes. The suspended nanoparticles were then filtered through a 200 nm membrane (Kinesis, KX Syringe filters, SFS-PES-25-022, 1706260007) and were stored in the dark at 4°C.

III.2.3 Characterisation

III.2.3.1 UV-Vis analysis

UV-Vis analysis within the range of 200–900 nm was then carried out using an Ultraviolet-visible (UV-vis) spectrophotometer (Shimadzu Single monochromator UV-2600, Japan). The samples were first diluted in order not to have any absorption above a

value of 2. The results obtained were then modulated in order to be able to compare the UV-Vis spectra of different samples.

III.2.3.2 X-Ray diffraction

Due to the limited amount of silver nanoparticles produced an epoxy sample holder was designed and build. The sample was tightly packed inside the container and X-Ray diffraction was carried out using a diffractometer (Bruker D8 Advance, BW/509/98/Ro, Erz Nr. 7Kp2025, F. Nr. D8-00/08-233) between angles of 30° and 90°. These angles were chosen to avoid the broad peak of the epoxy holder at around 25°.

III.2.3.3 ICP-MS

The silver and capping agent concentration within the nanoparticles suspension was studied using ICP-MS. The dispersion was first digested using concentrated nitric acid and the sample was injected in a Thermo Scientific iCAP Q ICP-MS using the kinetic energy discrimination measurement mode, a Dwell time of 0.01s and a spacing of 0.1.

III.2.3.4 TEM

In order to analyse the size and the morphology of the nanoparticles produced, Transmission Electron Microscopy (Tecnai T12 Biotwin TEM run at 100kv accelerating voltage, images captured using a Megaview II Soft Imaging camera system with Analysis software package) was used. A few milligrams of the sample were suspended (using a vortexer) in a 1:2 acetone: water mixture which was determined shown to be able to suspend and disperse the nanoparticles. Then one drop of the solution was pipetted onto

a TEM grid and a filter paper was used to dry the excess liquid. The grid was allowed to dry after which it was placed in the Microscope.

III.3 Results and Discussion

In this study silver nanoparticles were successfully synthesised as initially indicated by the characteristic colour change that occurred during the reaction. The presence of silver nanoparticles was confirmed by the characteristic UV-VIS spectra obtained (see below). Two main features of the spectra obtained were the peak at around 400 nm which represents the spherical nanoparticles and broad peaks at higher wavelengths indicative of nanoparticle morphologies other than spherical. The production of silver nanoparticles was further verified by XRD spectra. Referring to Figure III.2, the XRD spectra of silver nanoparticles shows the presence of pure silver characterised by the peaks at about 38°, 45°, 65° and 78° which correspond to the [111], [200], [220] and [311] planes respectively. However, the spectra were noisy due to the limited amount of silver nanoparticles used in the test.

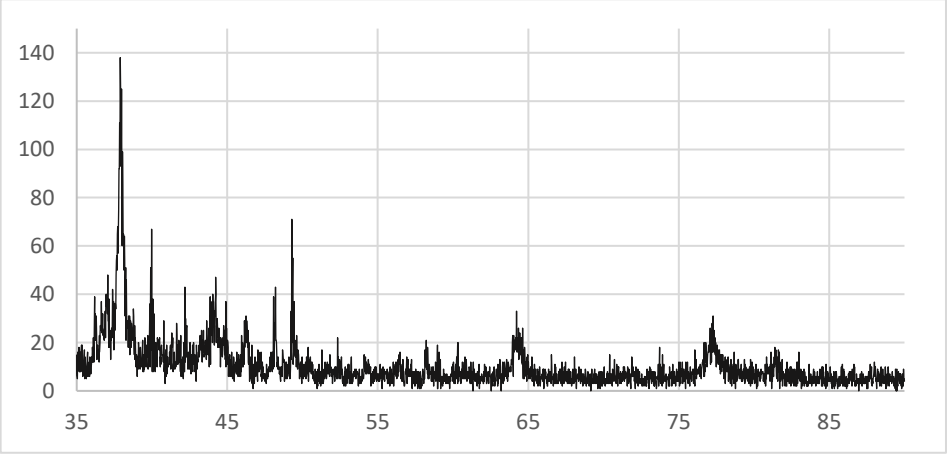

Figure III.2: XRD spectra of silver nanoparticles, produced at -5°C with a silver:citrate ratio of 1:10 and a reaction time of half an hour.

In the first part of this study, the effect of temperature was investigated. As shown in Figure III.3,a change in temperature may result in different morphologies as indicated by the broad peak at around 550 nm in the case of the nanoparticles produced at -1°C when compared to those produced at -20°C. The size distribution and size of nanoparticles remain relatively constant with changes in temperature. In fact, referring to Figure III.3 which shows TEM images of silver nanoparticles, one may observe that the nanoparticles produced at a temperature of -20°C have a diameter of circa 19 ± 6 nm whilst those produced at a temperature of -1°C have a diameter of circa 20 ± 5 nm.

a.

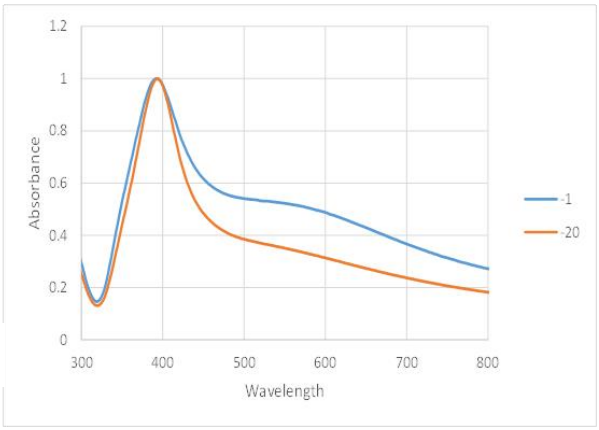

b.

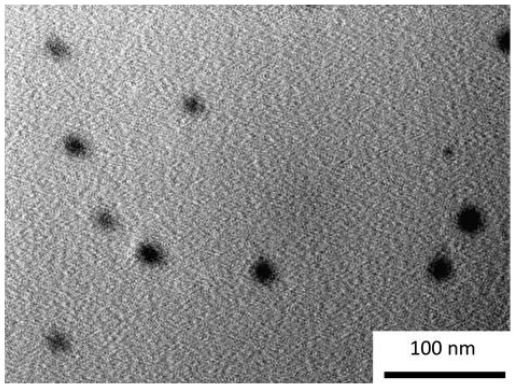

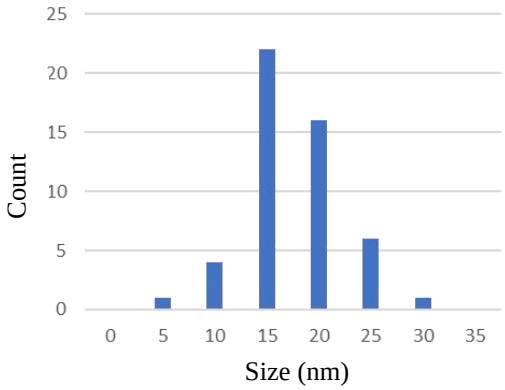

c.

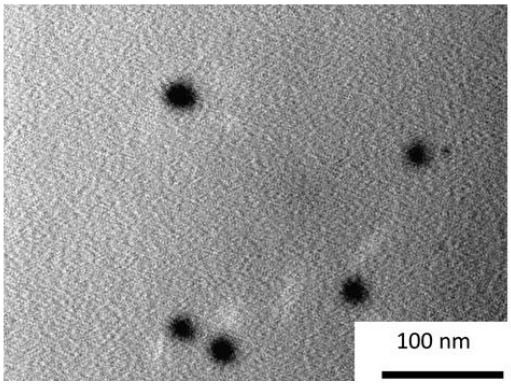

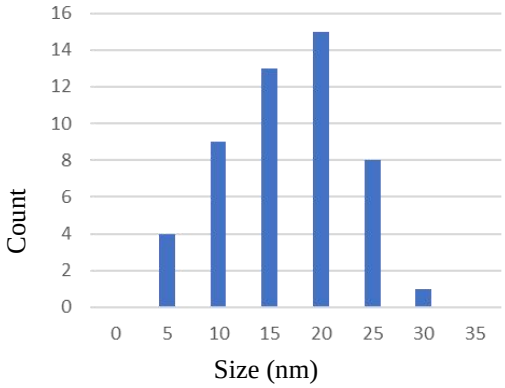

Figure III.3(a) UV-VIS spectra and (b & c) TEM images for silver nanoparticles produced at different temperatures using a 1:5, silver nitrate: sodium tricitrate ratio at -1°C and -20°C respectively.

The effect of changing the concentration of trisodium citrate at -20°C was then assessed. A relatively sharp peak at circa 390 nm together with a distinct broad peak at 550 nm was observed when using a low concentration of citrate (1:2 silver:citrate). The latter peak is indicative of a second morphology. Increasing the citrate concentration to a

silver: citrate ratio of 1:5 results in the reduction of the broad peak found at circa 550nm, which indicates that more spherical nanoparticles are being produced. A further increase in the concentration of silver: citrate ratio to 1:10, yields a very broad secondary peak, indicating that the production of spherical nanoparticles relative to the other morphologies present is being reduced once again. Finally, when using a silver: citrate ratio of 1:20 a distinctive secondary peak at about 450 nm is observed.

It is also interesting to note the absorbance of the primary peak which gives an indication of the size of the spherical nanoparticles. As shown in Figure III.5a, at low citrate concentrations, the spherical nanoparticles were larger having a maximum wavelength of 392 nm and 393 nm for a silver nitrate: trisodium citrate ratio of 1:2 and 1:5 respectively whilst at a ratio of 1:20, the peak shifted to 385 nm, indicating that smaller spherical nanoparticles were being produced.

This is in accordance to the TEM images shown in Figure III.5c & d where for a 1:2 ratio the nanoparticles were reported to be approximately 19±7 nm in size whereas for a 1:20 ratio the nanoparticles were 9.4±4 nm in size. With regards to the peak at higher wavelengths indicating a different type of morphology, some nanoparticles observed had an oval shape as depicted in Figure III.5c which could be cause by different morphologies namely rods. To confirm this observation TEM images with higher resolutions will have to be performed.

The change of citrate concentration was also observed at -1°C, shown in Figure III.5b, where a similar trend was observed with a reduction in the broad peak at around 550nm as the citrate concentration increases. This implies that the nanoparticles have opted for a spherical arrangement rather than other morphologies. On the other hand with regards to the main peak at 390nm, (shown in Figure III.5b) started relatively high for a

1:2 ratio after which a decrease was observed followed by an increase in concentration however for a 1:20 ratio, the peak increased slightly.

Once again, the TEM images (shown in Figure III.5e & f) seem to confirm what has been observed in the UV spectra where for a 1:2 silver: citrate ratio, large particles approximately 24±8 nm in size were recorded with the presence of non-spherical nanoparticles as indicated by the broad peak at 550 nm. Meanwhile for a 1:20 silver: citrate ratio, smaller nanoparticles 17±7nm in size were observed. It is worth noting that a decrease in reaction temperature was accompanied by a decrease in size in both cases.

a.

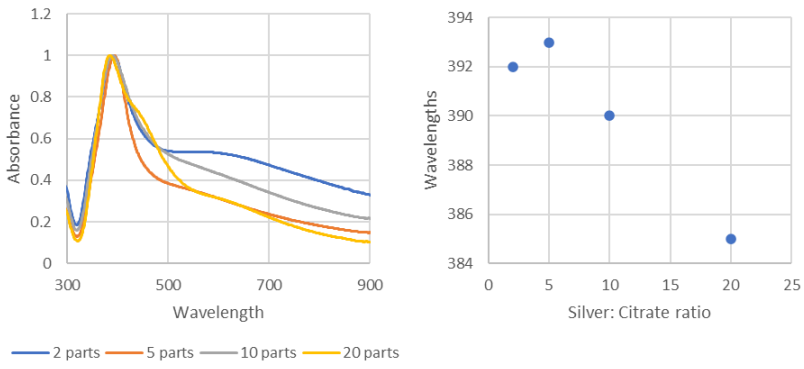

b.

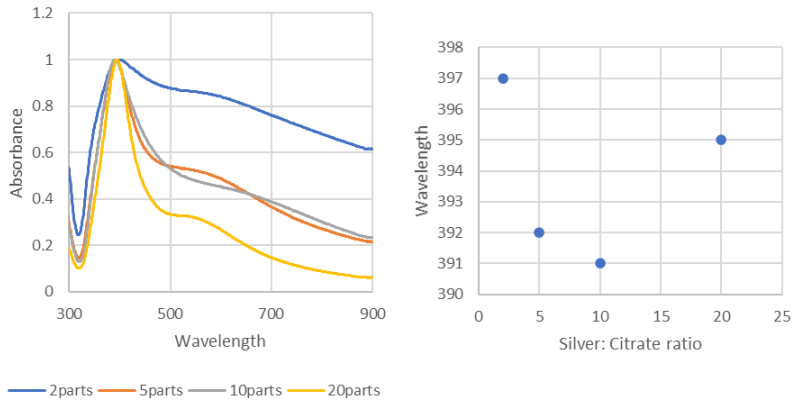

Figure III.4. (a & b) UV spectra of silver nanoparticles produced through different silver: citrate ratios at -20°C and -1°C respectively, and the relation between the silver: citrate ratio and the maximum wavelength in the UV spectra.

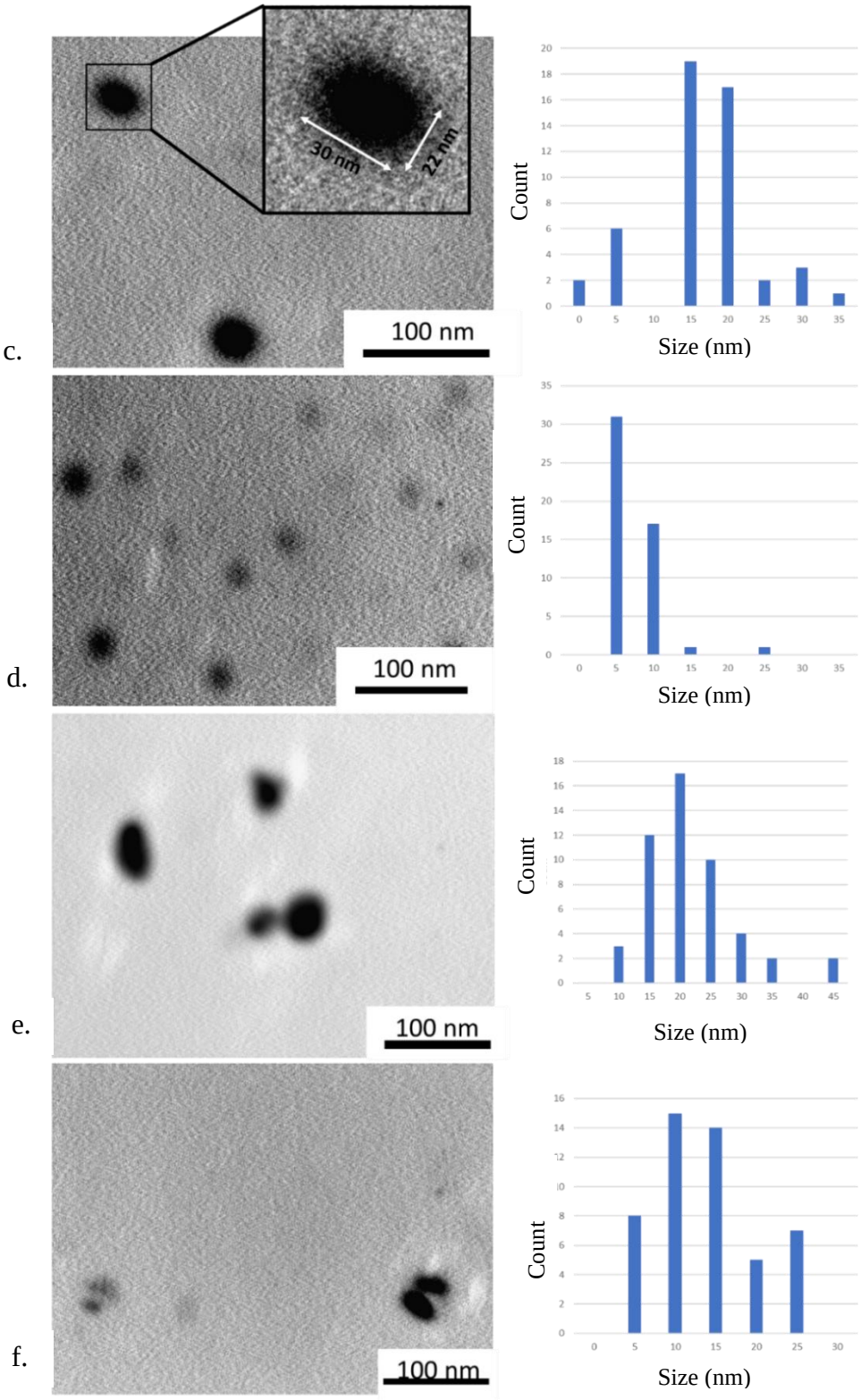

Figure III.5: (c - f) TEM images of silver nanoparticles produced at -20°C with silver: citrate ratios of 1:2 and 1:20 and -1°C with silver: citrate ratios of 1:2 and 1:20 respectively.

It is also important to look at the amount of citrate bound to the silver nanoparticles. In this study, this was done through the use of ICP-MS, wherein the silver and sodium content in the nanoparticles suspension was quantified. The sodium is indicative of the amount of trisodium citrate bound to the nanoparticles. Referring to Table III-1,one may note that the water used to suspend the nanoparticles did not contain significant amounts of silver and sodium ions. As one would expect, increasing the amount of trisodium citrate during the production of the silver nanoparticles increases the amount of citrate bound to the silver nanoparticles. Using a silver: citrate ration of 1:20 results in the production of nanoparticles wherein the majority of these particles is composed of citrate ions. This may be due to the small size of the nanoparticles, (large surface area where the citrate ions may interact with the silver atoms).

Table III-1: A table showing the data from the ICP-MS and the citrate: silver ratio in the nanoparticles.

Sample	**Na (g/100g)**	**Moles of Na (moles)**	**Moles of citrate (moles)**	**Ag (g/100g)**	**Moles of Ag (moles)**	**Citrate: Silver**
Water	2×10^{-5}			4.55×10^{-4}		
1:2 -20°C	8.12×10^{-3}	3.53×10^{-4}	1.18×10^{-4}	9.32×10^{-2}	8.64×10^{-4}	1.36×10^{-1}
1:20 -20°C	1.37×10^{-1}	5.95×10^{-3}	1.98×10^{-3}	1.04×10^{-1}	9.62×10^{-4}	2.06
1:2 -10°C	1.68×10^{-3}	7.30×10^{-5}	2.43E-05	6.55×10^{-2}	6.07×10^{-4}	4.01×10^{-2}
1:20 -10°C	2.49×10^{-1}	1.08×10^{-2}	3.61×10^{-3}	5.77×10^{-2}	5.36×10^{-4}	6.75

The effect of the reaction time on the produced silver nanoparticles was studied by preparing silver nanoparticles using different reaction times (15, 30, 60 and 120 minutes), as explained in the methodology section above using a silver: citrate ratio of

1:10 and at -10°C. From the results obtained (see Figure III.6), it is evident that the reaction time has an important effect on the shape and size-distribution of the nanoparticles. Referring to Figure III.6, one can note that after 15 minutes of reaction, the nanoparticles produced are quite spherical, and have a wider size distribution when compared to the nanoparticles taken from longer reaction times. As the reaction is allowed to proceed the nanoparticles start becoming less spherical and their size distribution becomes narrower. As the reaction time increases to the maximum reaction time allowed in this study, one notes that once again, nearly spherical nanoparticles are obtained, with their sizes continuing to increase once again when compared to the ones obtained from a reaction time of 30 and 60 minutes.

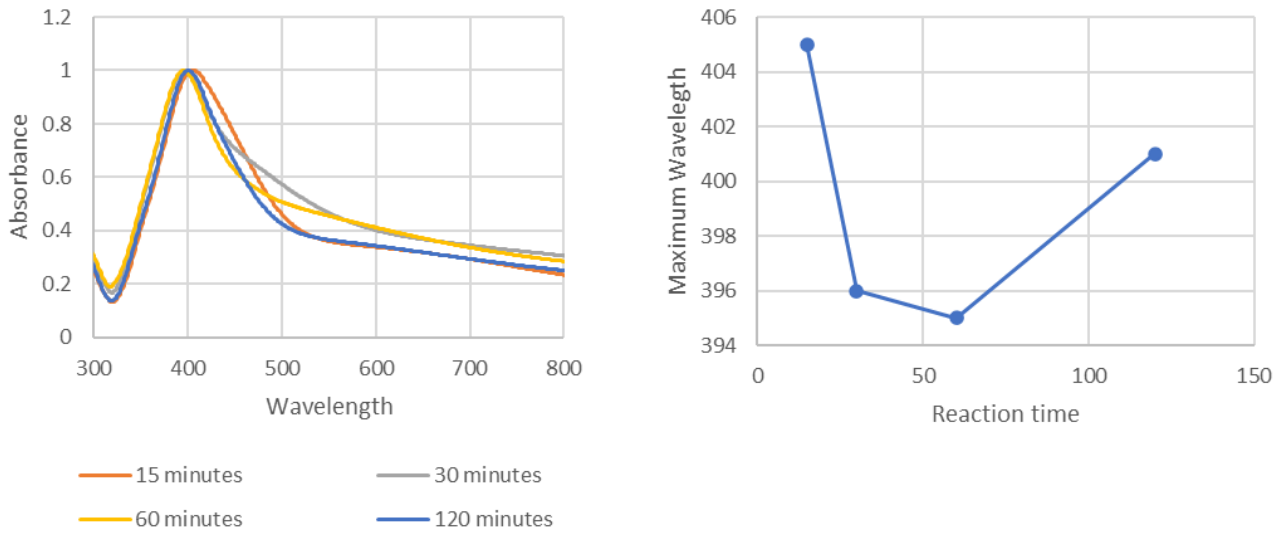

Figure III.6: UV spectra taken silver nanoparticles produced through different reaction times: Orange: 15 minutes, Purple: 30 minutes, Yellow: 60 minutes, Blue: 120 minutes.

The stability of the nanoparticles was also investigated. From the results obtained (see Figure III.7), the nanoparticles produced were in general shown to be stable for at least one week. However, the nanoparticles produced at +20°C using different citrate

concentrations gave different stability. For a 1:1 and 1:15 silver: citrate ratio, the nanoparticles did not exhibit any significant change. For a 1:5 and 1:10 silver: citrate ratio, however, there was a significant change in the 550 nm peak which indicates unstable morphologies shifting to a more stable conformation.

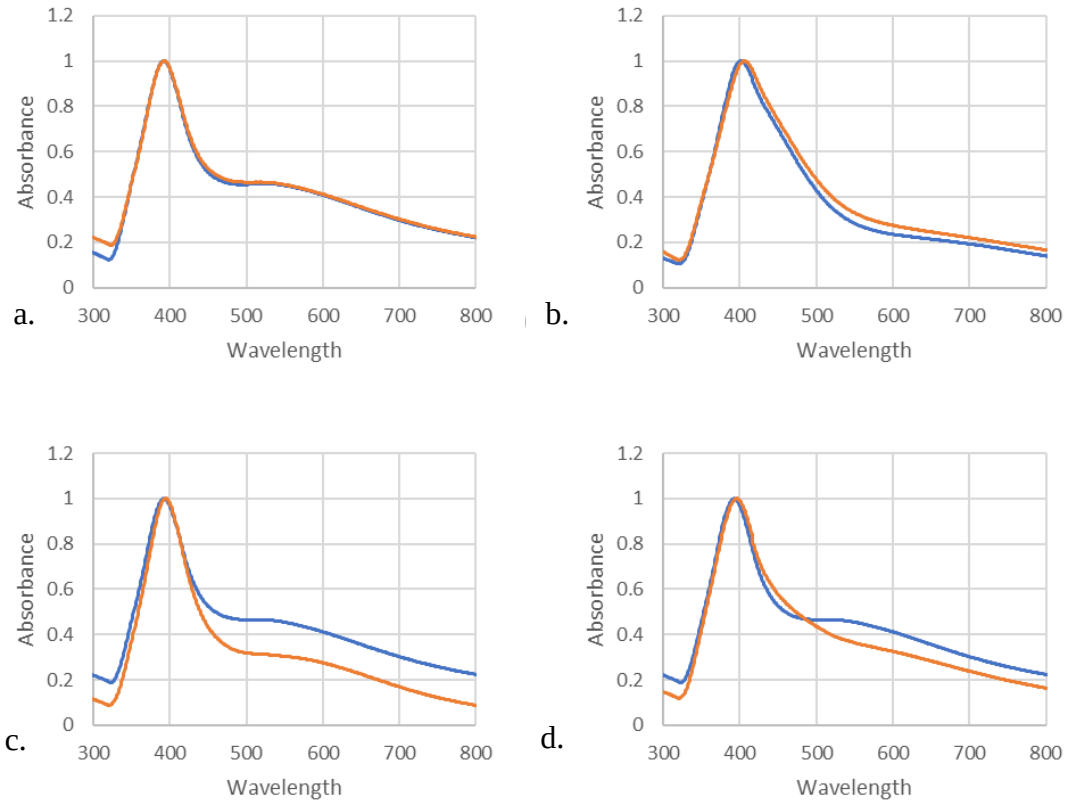

Figure III.7: UV spectra for silver nanoparticles produced with a silver: citrate ratio of a) 1:1, b) 1:15, c) 1:5 and d) 1:10 with the orange line depicting the initial UV spectra and the blue line depicting the UV spectra taking one week after the experiment.

Appendix IV: Antimicrobial and cytotoxicity of Silver Nanoparticles

IV.1 Introduction

One major application of silver nanoparticles is in the medical industry as an antimicrobial agent (T. Zhang *et al.*, 2014). In the past few decades, silver nanoparticles have been used extensively in medical applications such as wound-dressings (Haider & Kang, 2015; Z. Wang *et al.*, 2004)**,** surgical instruments, and bone prostheses (Abudabbus *et al.*, 2016). Silver nanoparticles' antimicrobial activities against pathogens such as Gram-positive and Gram negative bacteria have been reported (Gandhi & Khan, 2016; Taglietti *et al.*, 2012). Silver nanoparticles were also studied for their ability to damage bacterial cell walls such as that of *Escherichia coli* (Slavin *et al.*, 2017).

While research on nanotechnology and production of nanoparticles is growing exponentially, the research on the toxicity and their impact on human health and the environment is still lacking (Andreas & Howard, 2013). The main concerning factor is that while the toxicity of parent bulk materials is well-known, nanoparticles have a very high surface area to volume ratio, which leads to a higher reactivity and an alteration in the biological activity (Yildirimer *et al.*, 2011). Animal models, namely *Caenorhabditis elegans* and *Japanese medaka*, have been used to investigate the cytotoxicity of silver nanoparticles which have shown effects on the development, reproduction as well as mortality rate, depending on the dose (K. J. Lee *et al.*, 2017; Scown *et al.*, 2010; Y. Wu *et al.*, 2010; T. Zhang *et al.*, 2014). Additionally, research performed at the cell level has shown that exposure to silver nanoparticles could affect the cell's shape and reduce cell viability as a result of the oxidation stress brought about by silver nanoparticles (T. Zhang

et al., 2014). All this shows that research is *vis-à-vis* antimicrobial efficiency and cytotoxicity is still lacking and needs to be investigated.

Considering the above, this chapter aims to investigate the antimicrobial activity and cytotoxicity of the nanoparticles produced in the previous chapter. More specifically this chapter aims to:

- Investigate the antimicrobial activity of silver nanoparticles particularly identifying the non- inhibitory concentration (NIC) and the minimum inhibitory concentration (MIC) by monitoring the optical density responses at different concentrations of the silver nanoparticles and by measuring the bacterial population levels for different exposure times.
- Investigate the effect of silver nanoparticles on different bacteria and analyse the differences. The bacteria that have been proposed are *Listeria monocytogenes*, *Salmonella enterica* and *Escherichia coli*.
- Investigate the difference in the antimicrobial activity between silver nanoparticles produced under different producing conditions. Different capping agents, different morphologies and different sizes may have an impact on the antimicrobial activity of the silver nanoparticles.
- Investigate the cytotoxicity of silver nanoparticles using normal human dermal fibroblasts (NHDF).

IV.2 Antimicrobial activity

The two methods used were the multi-well method and the assay by plate counting. The former resulted in the precipitation of silver nanoparticles which effectively removed them from solution whilst the latter yielded some promising results.

IV.2.1 Multi well Method

IV.2.1.1 Methodology

For the microbiological testing of the silver nanoparticles dispersions, different strains of Listeria, were used. The bacterial cultures were stored in vials at -80°C. In order to activate the bacteria, 10 μL were taken using an inoculation loop and were streaked onto Brain Heart Infusion (BHI) agar. The plate was then incubated for 20 h at 37°C and kept at 4°C.

Two different colonies were picked under sterile conditions from the stock with a 10 μL loop and were transferred to 2 different tubes with 5 mL of BHI Broth. The tubes were then incubated again for 21 ± 3 h at 37°C, in order to reach stationary phase. This was repeated one more time.

The *Listeria* strains were then streaked on BHI agar plates and five wells were made on the agar. In three of the wells 50 μL silver nanoparticles suspension of 1, 10, 100 μg/mL were poured and a negative (water) and positive control (penicillin) in the other two. The plates were then incubated for 21 ± 3 h at 37°C and colony plate counting procedure was followed.

IV.2.1.2 Results and Discussion

The plates in Figure IV.1 show the bacterial inhibition around the wells. It is evident that no antimicrobial activity was observed except for the positive control. This is a very unexpected result and may be giving a false reading due to the fact that it was not designed to test the antimicrobial effect of nanoparticles. In fact, it may happen that the silver nanoparticles agglomerate, effectively removing them from suspension or they

were not able to diffuse into the agar gel. In view of this, a second method was set up to study the antimicrobial effects of silver nanoparticles.

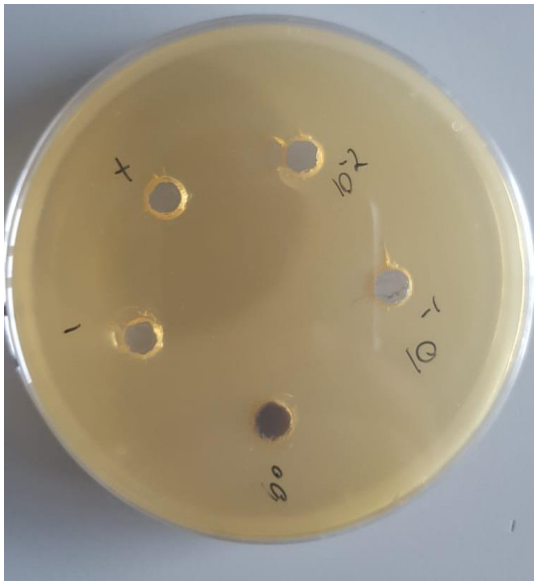

Figure IV.1: BHI agar plate with Listeria and five wells.

IV.2.2 Bacterial Inactivation Assay by Plate Counting

IV.2.2.1 Methodology

Salmonella enterica cultures were stored in vials at -80°C. As with the *Listeria*, a 10 µL inoculation loop was used to transfer the cultures and to streak onto Tryptic Soya Agar (TSA) plate. The plate was then incubated for 20 h at 37°C and kept at 4°C.

Two different colonies were picked under sterile conditions from the stock with a 10 µL loop and were transferred to 2 different tubes with 9 mL of Tryptic Soya Broth without dextrose (TSB-D) (Scharlau, Spain). The tubes were then incubated again for 24 ± 2 h at 37°C, allowing the bacteria to reach stationary phase (10^8-10^9 log CFU/mL). To obtain the final inoculum, 5 mL of the suspension of each tube (after stirring it with Vortex) was centrifuged (6400 g) for 20 minutes and the supernatants were discarded.

The same volume of sterile water was added in each centrifuge tube, resulting in a concentration of 10^6 CFU/mL.

1 mL of each inoculum was transferred to 9 mL of nanoparticles' dispersion and another 1 mL of each inoculum was transferred to 9 mL of distilled water. The tubes with the nanoparticles' dispersion were covered with Aluminium foil and survival studies were performed for the following time intervals: 0, 2, 4, 6 h. Duplicated samples from each inoculum (the blank and the one with the nanoparticles' dispersion) were diluted with Ringer's solution (Scharlau, Sentmenat, Spain and were spread plated on TSA (Oxoid, UK). Samples were incubated for 24 ± 2 h at 37°C, and colony plate counting procedure was followed.

IV.2.2.2 Results and Discussion

Using this method, the antimicrobial properties of the silver nanoparticles produced were measured. In fact, preliminary studies showed that the silver nanoparticles produced in this study have a strong antimicrobial effect even at low concentrations of 5 ppm. However, for the data to be conclusive, repeated tests have to be performed having different concentrations.

Appendix V: Iron Nanoparticle Synthesis and Characterisation

V.1 Introduction

Magnetic nanoparticles are attracting the interest of researchers from several disciplines given their wide range of applications such as in data storage (Gubin *et al.*, 2002), magnetic pumps (Andò *et al.*, 2006), water purification (Crane & Scott, 2012), biochips (Deng *et al.*, 2019) as well as biomedicine and in biomedical applications, namely magnetic hyperthermia (Hadjipanayis *et al.*, 2008), bio separation and magnetic resonance imaging (MRI) contrast agents (Hadjipanayis *et al.*, 2008; Na *et al.*, 2009).

Of all nanoparticles, iron nanoparticles have filled a particular niche of applications. Iron as a metal exhibits ferromagnetism and is one of the highest saturation magnetisation of the elements. Besides, iron NPs, below a certain size exhibit a different type of magnetism, superparamagnetism (Huber, 2005). These magnetic properties in addition to iron's biocompatibility, make it the suitable material ideal for several application such as MRI contrast agents, biosensors and in drug delivery amongst others.

Whilst research on magnetic and iron nanoparticles specifically has been carried out since the late seventies, it is only in the past few decades that the synthesis of iron NPs has been improved. While spherical nanoparticles have been successfully synthesised, controlling their size and shape has proved quite difficult. As a matter of fact, only recently have non-spherical iron nanoparticles been achieved(Shavel *et al.*, 2007). Another limitation is the fact that pure metallic NPs are susceptible to being oxidised as a result of their high surface area and reactivity, therefore metallic oxides are used which have a weaker magnetisation. Another issue that arises is that since iron nanoparticles are

magnetic, they agglomerate and as a result of their superparamagnetic properties pack together which reduces the effect of properties characteristic to the nanoscale(Krämer *et al.*, 2008).

In view of the above, the main objective of this chapter is to synthesise, characterise and understand the underlying mechanism for the production of iron nanoparticles using a glycerol-mediated reduction of iron ions using sodium hydroxide as an accelerator and using arc-discharge techniques under cold plasma conditions.

In particular this chapter aims to.

- Develop a synthesis technique for the reduction of iron ions through chemical reduction and through an electric arc discharge process
- Investigate the effect different capping agents, namely PVP and glucose, have on the size and morphology of iron nanoparticles. This includes investigating the effect of using PVP with different molecular weights.
- Investigating the effect different iron precursors have on the size and morphology of iron nanoparticles and the effect the anion may have on the reduction process.
- Study the effect of capping agent concentration on the size and morphology of iron nanoparticles
- Investigate the role of glycerol and to study the effect glycerol content has on the morphology and size of iron nanoparticles
- Study the role of potassium hydroxide as an accelerator in chemical reduction and the effect potassium hydroxide concentration has on the size and morphology of the iron nanoparticles

- Study the role of current and exposure time in the electric arc discharge process and the effect it has size and morphology of iron nanoparticles.

V.2 Methodology

V.2.1 Arc-discharge synthesis

In a typical synthesis by arc-discharge, 6.15 g of iron (II) sulphate (Biochem CAS: 7782-63-0) were weighed using an analytical balance (Precisa XT220)). This was then added to 200 g of a 25% w/w glycerol-water mixture (food grade glycerol CAS:56-81-5). This was followed by the addition of 3.5 g of D-(+)-glucose (Labkem CAS: 50-99-7). The solution was then mixed thoroughly for two hours using an overhead stirrer at 500 RPM to ensure complete dissolution.

The Arc-discharge synthesis was performed in an in-house build reactor, shown in Figure V.1. The main aim of this reactor was to provide an anoxic environment in which an electric arc reduces the iron ions in the solution. The setup consists of two chambers, with a titanium cathode (Alfa Aeser 99.99%) placed in the first chamber and an iron anode (Alfa 40500.DJ 99.99% pure) placed in the second chamber. The cathode and anode chambers of the circuit were electrically connected through the solution as shown in Figure V.1. The anode was placed in a second chamber due to the fact that electrochemical reactions may take place on the submerged anode. Argon gas was allowed to flow at a rate of 500 mL / min in the cathode chamber. Although the argon gas was allowed to leave from the same chamber, a slight increase in pressure was noted. This pushes the liquid from the first chamber to the second chamber, something that was counteracted by pushing the plunger of the second chamber, equilibrating the pressures between the two chambers once again. Any formation of gases in the second chamber results in the plunger being pushed up. The High Voltage (HV) power supply and the

replenishing of the solution through a peristaltic pump was controlled using an Arduino nano micro-controller to which a custom made circuitry was attached in order to measure the current at the cathode.

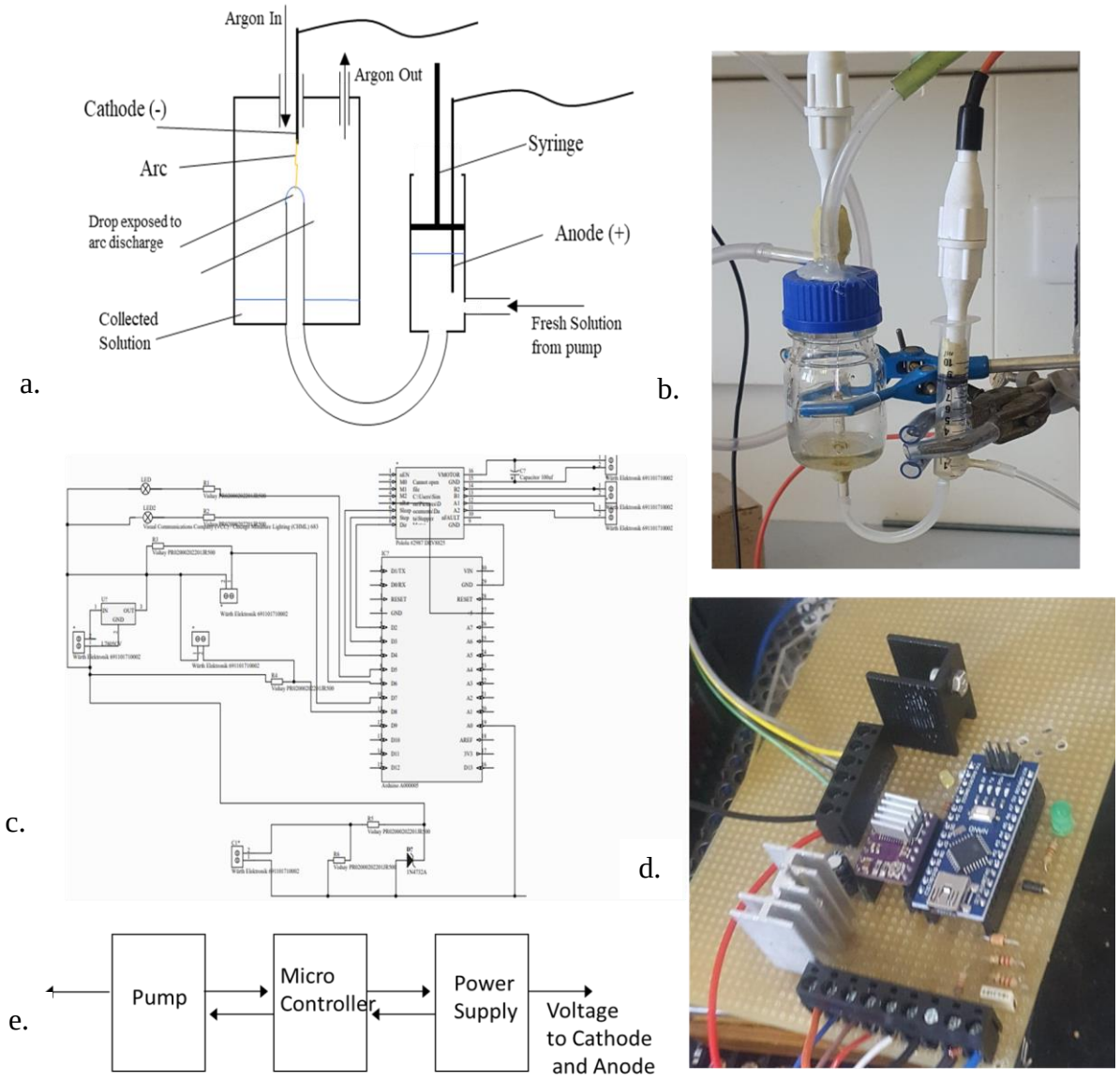

Figure V.1: Reaction chamber for arc-discharge synthesis

The microcontroller was then programmed (see code below) to coordinate the peristaltic pump and the HV power supply. Through this system, the solution was pumped into the reaction chamber, drop by drop, providing a fresh supply of iron ions while

removing the iron nanoparticles. Each drop was exposed to an arc discharge (with a voltage of circa 10KV and a current set at 10 mA) for a predetermined duration which would reduce iron and the iron nanoparticles would be collected.

This experiment was repeated for different current, exposure time, cooling time, pumping speed and frequency, different electrodes as well as different solutions, specifically by varying the iron sulphate concentration, glucose concentration, w/w% of glycerol.

V.2.1.1 Arduino Code

```
const int pinButton = 7;
const int LED =2;
const int pinButton2 = 8;
const int LED2 =3;
const int dirPin = 4;
const int stepPin = 5;
const int powerPin = 10;
const int slpPin = 6;
const int stepsPerRevolution = 200;
const long burnTime =120000; // time that plasma is active in ms
int pulses = 1 ; // number of pulses
int pulse_pause = 1000; // time between pulses in ms
int dir = 2; // 1 = clockwise direction, 2 = anti-clockwise direction
int RPM =70; //70 for soln
int turns = 80; //80 for sol
int turns2 = 1;
int flag = 0;
long stepper_delay;
int delay2;
float voltage = 0.1;
int voltage_analog;
float curr;
float req_curr = 7.0;//required current in mA
unsigned long time_at_start;
void setup() {    // Defining the inputs and outputs of the system
  Serial.begin(9600);
```

```
  pinMode(pinButton, INPUT);
  pinMode(LED, OUTPUT);
  pinMode(pinButton2, INPUT);
  pinMode(LED2, OUTPUT);
  pinMode(stepPin, OUTPUT);
  pinMode(dirPin, OUTPUT);
  pinMode(powerPin, OUTPUT);
  pinMode(slpPin, OUTPUT);
}
void loop() {
  analogWrite(powerPin, 0);
  digitalWrite(slpPin, LOW);
  int stateButton = digitalRead(pinButton); //read the state of the switch
  int stateButton2 = digitalRead(pinButton2);
  while(stateButton == 1) { // while switch 1 is on
    stateButton = digitalRead(pinButton);
    digitalWrite(LED,HIGH); // LED is on
   if (flag == 0) {
          voltage_analog = 10;
        do {
           stateButton = digitalRead(pinButton);
           if (stateButton == 0) {
           break;
           }
           analogWrite(powerPin, voltage_analog);
           curr = current_read();
           voltage_analog = voltage_analog + 1;
           } while (curr < (0.95*req_curr));
        analogWrite(powerPin, 0);
        flag = 1;
        analogWrite(powerPin, 0);
    delay (pulse_pause);
     }
      if (stateButton == 0) {
           break;
      }
     for(int z = 0; z < pulses; z++) {
    analogWrite(powerPin, voltage_analog);
    time_at_start = millis();
    while ((millis() - time_at_start) <= burnTime) {
      stateButton = digitalRead(pinButton);
        if (stateButton == 0) {
          break;
        }
```

```
 curr = current_read();
 Serial.print (curr);
 Serial.print (",");
 Serial.print (voltage_analog);
 if ((curr < 0.95 * req_curr) || (curr > 1.05 * req_curr)) {
  stateButton = digitalRead(pinButton);

    if (stateButton == 0) {
     break;
    }
  while (curr < (0.95*req_curr)){
    stateButton = digitalRead(pinButton);

    if (stateButton == 0) {
      break;
    }
    voltage_analog = voltage_analog + 1;
    analogWrite(powerPin, voltage_analog);
    curr = current_read();
  }
   while (curr> (1.05*req_curr)){
    stateButton = digitalRead(pinButton);

    if (stateButton == 0) {
     break;
    }
    voltage_analog = voltage_analog - 1;
    analogWrite(powerPin, voltage_analog);
    curr = current_read();
  }
 }
}
Serial.println("smallmotor");
motorcontrol(7,3,dir,stepsPerRevolution,pinButton);
delay (pulse_pause);
 }
analogWrite(powerPin, 0);
Serial.println("Motor");
motorcontrol(turns,RPM,dir,stepsPerRevolution,pinButton);
digitalWrite(slpPin, LOW);
stateButton = digitalRead(pinButton);

    if (stateButton == 0) {
     break;
```

```
        }
  }
  digitalWrite(LED, LOW);
  digitalWrite(slpPin, LOW);
  while ((stateButton == 0) && (stateButton2 == 1)) { // if switch 1 is off and switch 2 is
on, LED2 is on
    stateButton = digitalRead(pinButton);
    stateButton2 = digitalRead(pinButton2);
    digitalWrite(LED2,HIGH);
     if (dir == 1) {
      digitalWrite(dirPin, HIGH); // direction of the motor is set
     } else {
      digitalWrite(dirPin, LOW);
     }
    stepper_delay =(60*1000000)/(stepsPerRevolution*80); // RPM set to 80
    while ((stateButton == 0) && (stateButton2 == 1)) { //when switch2 is on, stepper
motor is on
     stateButton = digitalRead(pinButton);
     stateButton2 = digitalRead(pinButton2);
     digitalWrite(slpPin, HIGH);
     digitalWrite(stepPin, HIGH);
     delayMicroseconds(500);
     digitalWrite(stepPin, LOW);
     delayMicroseconds(500);
     delay2 = (stepper_delay-1000)/1000;
     delay(delay2);
     }
     digitalWrite(slpPin, LOW);
  }
  digitalWrite(LED2,LOW);
  analogWrite(powerPin, 0);
  digitalWrite(slpPin, LOW);
}
float current_read() { // Float current command
  unsigned long time_before;
  float current;
  float tot_for_av;
  unsigned int reps;
  reps = 0;
  tot_for_av = 0;
  time_before = millis();
  while (millis() - time_before <= 100) {
    int sensorValue = analogRead(A0);
    tot_for_av = tot_for_av + (((sensorValue * (5.0 / 1023)) / 220) * 1000);
```

```
   reps = reps + 1;
  }
 current = tot_for_av / reps;
 return current;
}
int motorcontrol (int turns_, int RPM_, int direction_, int stepsPerRevolution_,int pinButton_) {
  if (direction_ == 1) {
    digitalWrite(dirPin, HIGH); // direction of the motor is set
  } else if (direction_ == 2) {
    digitalWrite(dirPin, LOW);
  }

    stepper_delay =(60*1000000)/(stepsPerRevolution_*RPM_); //delay is set

    for(int x = 0; x < turns_; x++) { //loop depending on the number of turns
      digitalWrite(slpPin, HIGH);
      int stateButton_ = digitalRead(pinButton_); // read whether switch 1 is on or off

      if (stateButton_ == 0) { // if off break the for loop
        digitalWrite(slpPin, LOW);
        break;
      }
      digitalWrite(stepPin, HIGH); //switch on stepper motor
      delayMicroseconds(500);
      digitalWrite(stepPin, LOW); // switch off
      delayMicroseconds(500);
      delay2 =(stepper_delay-1000)/1000;
      delay(delay2);  //wait
      }
      digitalWrite(slpPin, LOW);
}
```

V.2.2 Chemical reduction synthesis

V.2.2.1 Synthesis

50 g of glycerol (food grade glycerol CAS:56-81-5), weighed using an analytical balance (Precisa XT220), were placed in a 500 ml beaker and 150 g of ultra-pure water (18 MΩ/cm) were added to it. This mixture was then stirred using an overhead stirrer (AM120Z-H Laboratory mixer) for 30 minutes at 500 RPM. This resulted in a of 25%

w/w glycerol-water mixture. To this, 6.15 g of iron(II) sulphate (BIOCHEM CAS:7782-63-0) and were added and 3.5 g of PVP (molecular weight 1406.9g) were added. This solution was then sonicated for 30 minutes to ensure dissolution. Finally, 2 g of the accelerator KOH (Carlo Erba CAS:1310-58-3) was added and the solution was stirred at room temperature using an overhead stirrer for 30 minutes at 500 RPM.

This procedure was repeated for different w/w% glycerol, concentrations of iron sulphate, PVP concentration, concentrations of accelerator KOH.

V.2.2.2 Purification

Once sufficient amount of the nanoparticle suspension was collected, the arc was switched off and the solution was poured into a plastic tube. Using neodymium magnets (mm in diameter) to keep the iron nanoparticles in place, the solution was decanted. Due to the viscous nature of glycerol, 25 mL of water were added and mixed thoroughly. Once again, the mixture was decanted using the magnets to keep iron nanoparticles in place. This was repeated until there was no trace of the iron sulphate solution. Then the nanoparticles were washed with 10 mL of propanol and stored under propanol.

V.2.3 Characterisation

V.2.3.1 UV-VIS

UV-Vis analysis within the range of 200–900 nm was then carried out as explained in Appendix III above.

V.2.3.2 X-Ray diffraction

X-Ray diffraction was carried out using the diffractometer between angles of 30° and 90°, as explained in section Appendix III above.

V.2.3.3 SEM

In order to analyse the size and the morphology of the nanoparticles produced, a Field Emission Scanning Electron Microscope (FESEM) with a Gemini II column was used in conjunction with energy dispersive X-ray spectroscopy (EDS) (under EHT of 15 KV and I probe of 1 nA).

V.2.3.4 TEM

Transmission Electron Microscopy (Tecnai T12 Biotwin TEM run at 100kv accelerating voltage, images captured using a Megaview II Soft Imaging camera system with Analysis software package) was used as described above.

V.3 Results and Discussion

Iron nanoparticles were successfully produced through the arc discharge method as shown by the XRD taken with the characteristic peaks at 44°, 65°, 82° owing to the [110], [200], [211] planes respectively. Through TEM imaging, the size and size distribution of the iron nanoparticles was collected. From the data gathered, iron nanoparticles obtained were about 10 ±6 nm in size. The relatively large standard deviation may be attributed to the few large particles which could be agglomerates.

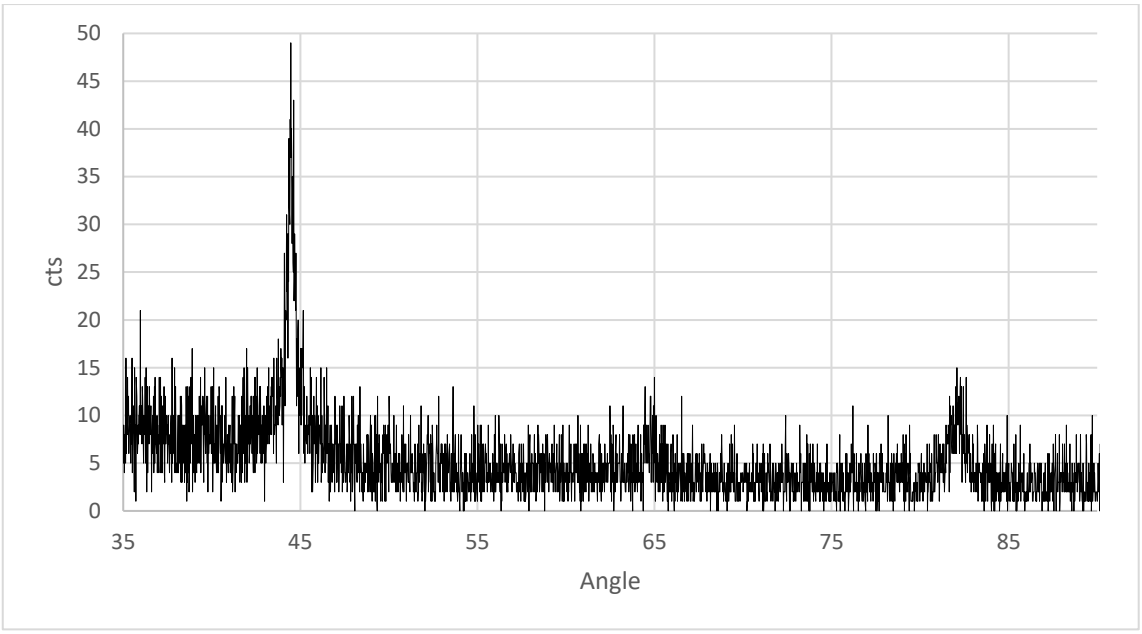

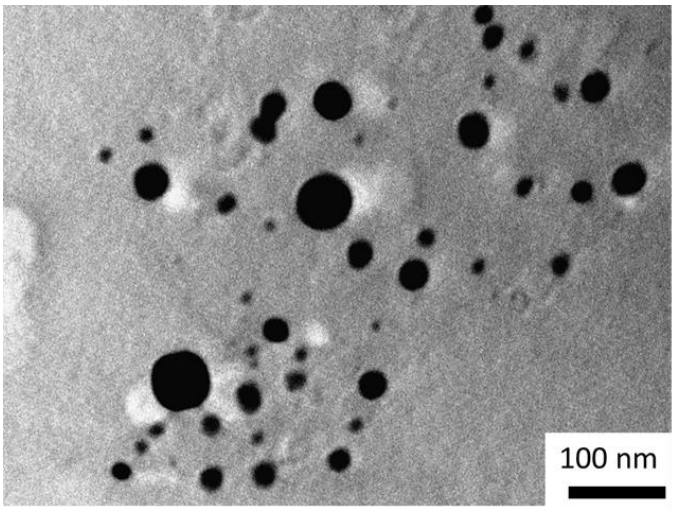

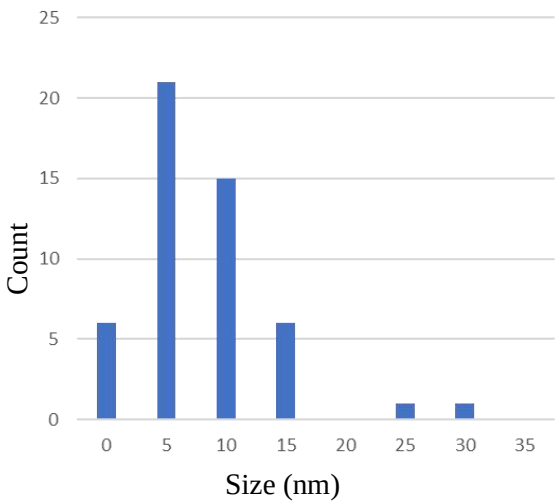

Figure V.2:(Top) XRD of zero-valent iron nanoparticles produced when using 21.25g of iron sulphate, 13 g of glucose in 20 mL of 2:5 glycerol: water mixture, (Left) TEM image of iron nanoparticles (Right) size distribution of iron nanoparticles

When using the chemical method, Iron oxide nanoparticles were obtained. Figure V.3 shows an XRD for these nanoparticles with the characteristic peaks at peaks at 35°, 42°, 57°, 62° and 68° owing to the [311], [400], [511], [440] and [533] planes respectively. Some peaks were covered by the noise however it was quite clear that the nanoparticles had oxidised.

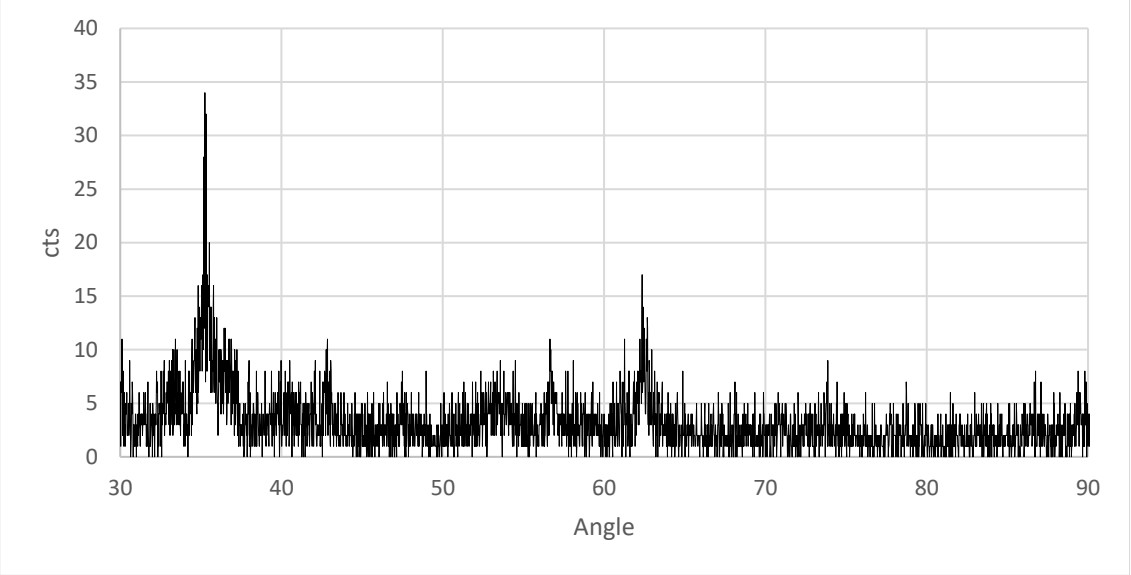

Figure V.3: XRD of iron oxide nanoparticles when using Chemical reduction.

The SEM images obtained were analysed and it was immediately clear that the iron oxide nanoparticles had agglomerated perhaps due to the method used to prepare the sample. However, at high magnifications, one can observe a dense set of agglomerates approximately 200 nm large. The EDS analysis shown in Figure V.4 also confirms the presence of iron oxide however could indicate that the core of the nanoparticles is in fact zero-valent iron.

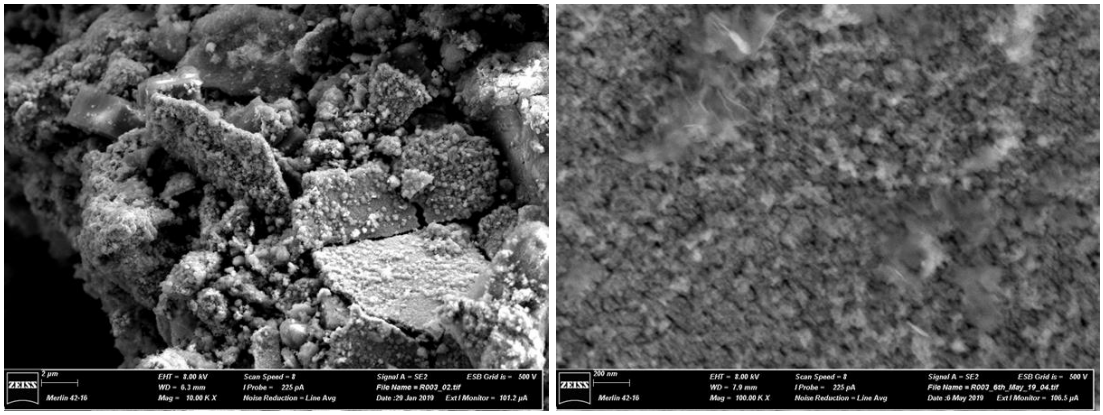

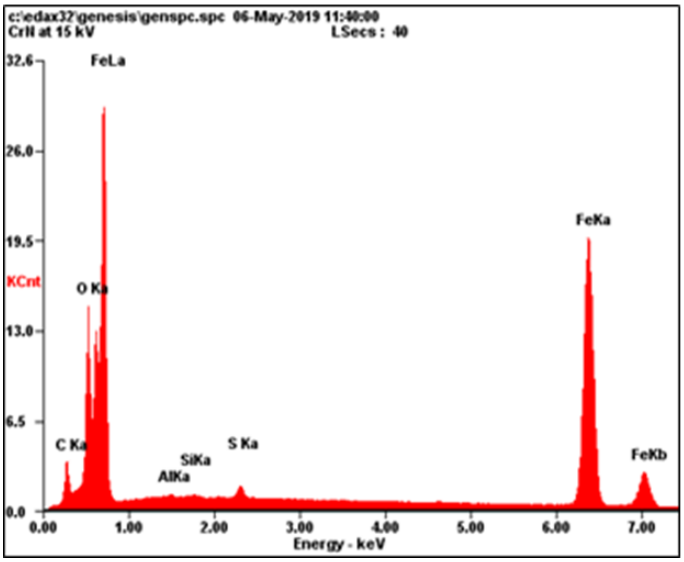

Element	Wt %	At %
C K	09.32	27.89
O K	08.24	18.50
AlK	00.17	00.22
SiK	00.14	00.18
S K	00.69	00.78
FeK	81.44	52.42

Figure V.4:SEM imaging of Iron Nanoparticles at a magnification of 10,000× and 100,000× along with the EDS results.